CATALYTIC SCIENCE SERIES — VOL. 11
Series Editor: Graham J. Hutchings

Supported Metals in Catalysis

2nd Edition

edited by
James A Anderson
Marcos Fernández García

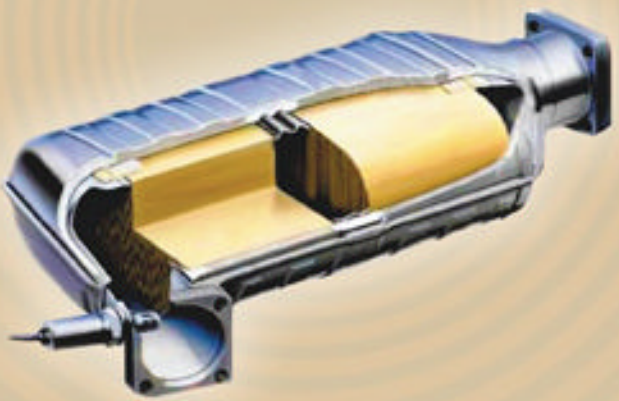

Imperial College Press

Supported Metals in Catalysis

2nd Edition

CATALYTIC SCIENCE SERIES

Series Editor: Graham J. Hutchings *(Cardiff University)*

Published

Vol. 1 Environmental Catalysis
edited by F. J. J. G. Janssen and R. A. van Santen

Vol. 2 Catalysis by Ceria and Related Materials
edited by A. Trovarelli

Vol. 3 Zeolites for Cleaner Technologies
edited by M. Guisnet and J.-P. Gilson

Vol. 4 Isotopes in Heterogeneous Catalysis
edited by Justin S. J. Hargreaves, S. D. Jackson and G. Webb

Vol. 5 Supported Metals in Catalysis
edited by J. A. Anderson and M. F. García

Vol. 6 Catalysis by Gold
edited by G. C. Bond, C. Louis and D. T. Thompson

Vol. 7 Combinatorial Development of Solid Catalytic Materials:
Design of High-Throughput Experiments, Data Analysis,
Data Mining
edited by M. Baerns and M. Holeňa

Vol. 8 Petrochemical Economics: Technology Selection in a Carbon Constrained World
edited by D. Seddon

Vol. 9 Deactivation and Regeneration of Zeolite Catalysts
edited by M. Guisnet and F. R. Ribeiro

Vol. 10 Concepts in Syngas Manufacture
edited by J. Rostrup-Nielsen and L. J. Christiansen

Vol. 11 Supported Metals in Catalysis (2nd Edition)
edited by J. A. Anderson and M. F. García

CATALYTIC SCIENCE SERIES — VOL. 11
Series Editor: Graham J. Hutchings

Supported Metals in Catalysis

2nd Edition

edited by
James A Anderson
Marcos Fernández García

ICP
Imperial College Press

Published by

Imperial College Press
57 Shelton Street
Covent Garden
London WC2H 9HE

Distributed by

World Scientific Publishing Co. Pte. Ltd.
5 Toh Tuck Link, Singapore 596224
USA office: 27 Warren Street, Suite 401-402, Hackensack, NJ 07601
UK office: 57 Shelton Street, Covent Garden, London WC2H 9HE

British Library Cataloguing-in-Publication Data
A catalogue record for this book is available from the British Library.

Catalytic Science Series — Vol. 11
SUPPORTED METALS IN CATALYSIS
2nd Edition

ISBN-13 978-1-84816-677-6
ISBN-10 1-84816-677-X

Typeset by Stallion Press
Email: enquiries@stallionpress.com

Printed in Singapore.

CONTENTS

This page intentionally left blank

PREFACE TO THE FIRST EDITION

The quantity of information available on a subject so apparently restricted as 'Supported Metal Catalysts' is such that no single mind can fully comprehend it all. We must therefore welcome every effort that is made to reduce it to manageable proportions and to present it to us in a readily digestible form. The problems that I have encountered when faced with a similar task have been to discriminate between the important and the not so important, and then to order the former in as logical a fashion as possible. I cannot claim always to have succeeded, but at least I recognise some of the qualities that are needed, even if I do not possess them myself to the extent I would wish. Long experience in the field is one, and a fair helping of that valuable commodity 'wisdom', which was once defined as 'knowing where to find knowledge'.

When I started research in 1948 there was obviously much less known about everything and about supported catalysts in particular. To quote a recent authority, there were things we didn't know we didn't know. Life was simpler then, and it has become progressively more complicated as tools have become available to extend our knowledge of the materials we use. But as J.W. von Goethe put it succinctly: *We know accurately only when we know little; with knowledge, doubt increases.* More optimistically, however, Francis Bacon, Lord Verulam, believed that *If a man begin with certainties, he shall end in doubts; but if he will be content to begin with doubts, he shall end in certainties.*

The scientific method is a kind of perpetual motion machine in which our doubts and uncertainties stimulate us to continued effort to resolve them in the hope that we may come to at least a few certainties. For this we need the guidance of the wise who are prepared

to invest their time and energy to create a book such as this. It deals with the preparation, characterisation and use of supported metal catalyst in vitally important areas, as well as informing us of theoretical developments. An overview such as this will be of tremendous value to all who work or are thinking to work in this field.

So what is the criterion by which 'wisdom' should be judged? Many years ago I read the following advice, which in my view encapsulates a good deal of common sense.

> *He who knows not, and knows not he knows not, he is a fool: leave him.*
> *He who knows not, and knows he knows not, he is willing: teach him.*
> *He who knows, and knows not he knows, he is asleep: wake him.*
> *He who knows, and knows he knows, he is wise: follow him.*

If you wish to be better informed about supported metal catalysts, read the following chapters, written by people who know that they know.

Geoff Bond

PREFACE TO THE SECOND EDITION

It seems appropriate that I should find myself writing the preface during a journey between Madrid and Aberdeen given that the second edition of *Supported Metals in Catalysis* once again draws heavily from contributors with Spanish and Celtic connections (apologies Guido, perhaps there is something in your ancestry?). I am hugely grateful for the time and effort that all contributors have committed to providing these chapters and hope they are well received by readers. When we were initially asked to write and edit the first edition, it was not envisaged that the full print run would go on to sell out (or that it would appear on Amazon's list of bestsellers in catalysis listings) and so there were no thoughts at that stage of how we would deal with a second edition. Circumstances therefore have allowed us to review, revise and update the contents to provide this second edition. We have omitted some of the chapters which appeared in the first edition where, in cases, the topics dealt with more established uses of supported metals and where developments in the field over the last five years were limited and where additional literature on the subject was minimal. This has allowed us to include new chapters where we have looked at emerging and fast-developing fields where supported metals will play a role. We are grateful to Sergio Rojas and colleagues for providing the chapter on application of supported metals for fuel cell applications and to Jose Rodriguez who provides an insight into some of the many reactions for which gold catalysts are currently receiving attention. Similarly, it was felt that the continuing advances made in our understanding of supported metal particle-based catalysts, as a result of technical advances in electron microscopy including the use of aberration

correcting devices, warranted a chapter of its own rather than appearing as a subsection of a chapter on determination of particle size. I thank Andy Herzing and Chris Kiely for contributing this chapter and hope they forgive me for all of the harassing which I gave them in trying to meet the publisher's deadlines. All of the other chapters have been thoroughly revised and will hopefully provide the reader with a route to access literature published on these topics up to 2010.

Lastly it was an enormous pleasure to have been able to have a preface to the first edition written by Geoff Bond who has made and continues to make such huge contributions to the field of supported metal catalysis. It has been a privilege over the years to attend and contribute to the UK RSC SURCAT group meetings at which Geoff participated, and I often aspire to be able to contribute to the field of supported metal catalysis to the extent which he has. Alas, however, I do not aspire to write such beautiful prose as Geoff and therefore ask forgiveness of those who purchase the second edition and consequently find an inferior preface. I do hope however that the standard of the proceeding chapters more than compensate.

Jim Anderson
February 2011

CHAPTER 1

PREPARATION OF SUPPORTED METAL CATALYSTS

Guido Mul[1] and Jacob A. Moulijn[2]

[1]*Photocatalytic Synthesis Group, IMPACT Institute, University of Twente, P.O. Box 217, 7500AE Enschede, The Netherlands*

[2]*Reactor and Catalysis Engineering Group, Delft ChemTech, Delft University of Technology, Julianalaan 136, 2628 BL Delft, The Netherlands*

1.1 Introduction

In the chemical industry, the majority of the reactions take place at the surfaces of heterogeneous catalysts. The efficiency of a heterogeneous catalytic process is thus largely determined by the quality of the catalysts used, i.e. the exposed surface area of active phase and the stability. It is instructive to show the correlation between the exposed (specific) surface area, and the particle size of the catalytic material. Let us suppose that the active phase (density ρ in kg/m^3) consists of uniform spherical particles. The specific area can be calculated as follows:

Volume of one particle, $V = 1/6\ \pi\ d^3$ (m^3)
Weight of one particle, $W = 1/6\ \rho\ \pi\ d^3$ (kg)
Surface area of one particle, $S_p = \pi\ d^2$ (m^2)
Specific surface area, $S_A = S_p/W = \pi\ d^2/(\rho\ 1/6\ \pi\ d^3) = 6/\rho\ d$ (m^2/kg)

Figure 1.1 shows a plot of this calculation. As an example, nickel has been chosen. It is obvious that only at low values of the particle sizes

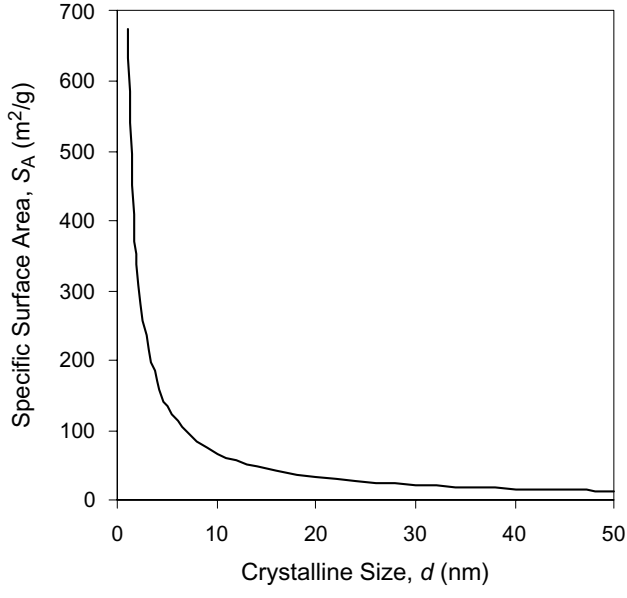

Figure 1.1 Specific surface area as a function of crystalline size of Ni (ρ = 8900 kg/m^3).

(1–10 nm) are reasonable surface areas obtained. It is impossible to apply such small particles in reactors, and therefore support bodies are applied. Catalyst supports are in general porous materials, to allow a high loading of highly dispersed metal particles, whereas the particles of the active phase need to be synthesized in such a way that they are as small as possible.

Despite the observations made above, many authors of papers in catalysis journals seem to ignore the importance of the preparation procedure used for the eventual catalytic results they obtain. The procedure used is usually described in very general terms, and often conditions are used that appear to have no fundamental reasoning, e.g. the used catalyst precursor, calcination conditions, pH of precursor solution (often not mentioned), temperature of solutions, etc. Fortunately, other researchers take the preparation of catalysts seriously and many publications and textbooks exist that discuss the preparation of catalysts on a scientific basis.[1] Of particular note is

the group of Geus (and continued in the group of de Jong) at the Utrecht University in The Netherlands,[1,2] where years of research on the preparation of catalysts has lead to a more scientific basis for catalyst preparation.

Several procedures exist in order to attach the active phase to the support, i.e. to prepare supported catalysts. In the catalyst manufacturing industry, impregnation is usually employed, for practical and economic reasons. Impregnation allows the use of pre-shaped or structured supports. Preparation of catalysts starting from these commercially available supports is attractive because a support with optimal properties can be selected.

From a chemical point of view impregnation and precipitation represent two extreme cases:

- Impregnation is often related to ion-exchange, where the interaction with the support is dominant;
- Precipitation in principle is a crystallization process and can occur in the bulk of the liquid or on a relatively inert surface. Here, particles of active phase can be kept small because the support particles act as crystallization nuclei for the active phase precursor.

In this chapter the most common techniques for preparation of supported metal catalysts will be discussed, including impregnation, co-precipitation, homogeneous deposition precipitation, and precipitation at constant pH. In addition, recently introduced novel technologies involving organic functionalization of supports in combination with deposition of surfactant functionalized metal particles,[3] as well as photodeposition, usually applied in the rapidly emerging field of photocatalysis,[4,5] will be discussed. In principle, these techniques can all be used to attach the active phase to supports, some preferably in the form of a powder, others in the form of a pre-shaped body. First, a general description of the techniques will be presented. Then, the techniques are illustrated by specific examples of the preparation of metallic catalysts. In view of the expertise of the authors of this chapter, Pt, Au, and Ag as the active metal phases will be emphasized. The last two examples are focused on the

production of propene oxide and, as a consequence, they refer to an unresolved research issue. Furthermore, for Au catalysis we have included potential applications in photocatalytic conversions.[6]

1.2 General Description of Preparation Methods

1.2.1 *Impregnation*

Impregnation is a preparation technique in which a solution of the precursor of the active phase is brought into contact with the support. Two methodologies exist. In dry impregnation, also referred to as "pore volume impregnation", just enough liquid (solution of the precursors) is used to fill the pore volume of the support. In wet impregnation the support is dipped into an excess quantity of solution containing the precursor(s) of the active phase. Wet impregnation is sometimes also called impregnation in excess of solution (IES).[7] In dry impregnation the solubility of the catalyst precursors and the pore volume of the support determine the maximum loading available each time of impregnation. If a high loading is needed, successive impregnations (and heat treatments) may be necessary. When several precursors are present simultaneously in the impregnating solution the impregnation is called "co-impregnation". In the first step of impregnation three processes occur:

- transport of solute to the pore system of the support bodies;
- diffusion of solute within the pore system;
- uptake of solute by the pore wall.

In the case of wet impregnation, a fourth process is operative, *viz.* transport of solute to the outer particle surface. Depending on the process conditions, different profiles of the active phase over the support body will be obtained. For instance, depending on the pH, the interaction with the support can be strong or weak, and even repulsion can exist.

Soluble catalyst precursors are fixed to the support either by reaction, exchange with surface OH groups, and/or by adsorption.

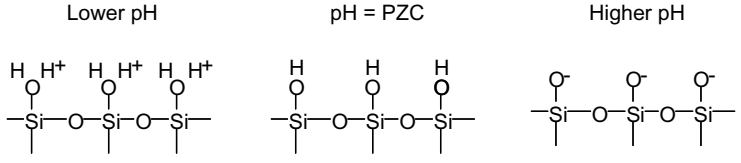

Figure 1.2 Effect of pH on surface charge in silica.

pH	pH < PZC	pH = PZC	pH > PZC
Surface Charge	positive	neutral	negative
Species	MOH_2^+	MOH	MO^-
Adsorption	anions		cations
pH increase	⟶		

Figure 1.3 Relationship between PZC and surface charge.

In the former case, the concentration (density) of surface OH groups, which depend on the pre-treatment of the support, is crucial. In the latter case, the surface charge plays an important role. At a pH value of the so-called Point of Zero Charge (PZC) the surface is electrically neutral. At pH values above PZC, the surface is negatively charged, while at pH values below PZC the surface is positively charged (see Figs. 1.2 and 1.3).

For silica this can be illustrated as follows. At pH = 3 the surface is neutral. In a mildly basic environment H^+ is removed, and, as a result, the surface is negatively charged. In an acid environment the surface will become protonated. If it is intended to deposit anions onto the carrier surface, the preparation should proceed at pH values below the PZC, whereas if cations are to be deposited, a pH value above that of the PZC is preferred (Fig. 1.2). Table 1.1 gives PZC values for alumina, silica, and a mixture of alumina and silica.

It should be mentioned that the exact PZC values not only depend on the chemical nature of the carrier, but also on its history and the method by which it was prepared. Of course, for the solid

Table 1.1 PZC values for alumina, silica, and 10% Al_2O_3 in SiO_2.

Carrier	PZC
Alumina	8–9
Silica	*ca.* 3
10% alumina/silica	*ca.* 5

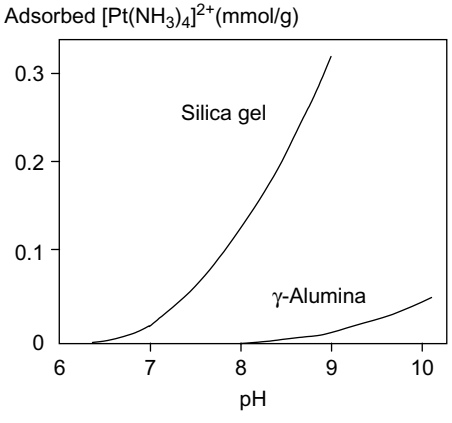

Figure 1.4 Adsorption from solution containing $[Pt(NH_3)_4]^{2+}$ (as chloride) onto silica gel (Davison 70, 370 m^2/g) and γ-alumina (Alcoa F-20, 204 m^2/g) as a function of pH at room temperature.[2]

support, a window of applicable pH exists. At improper pH values (e.g. pH > 12 for alumina), the carrier itself may be dissolved.

It is illustrative to compare the adsorption of $[Pt(NH_3)_4]^{2+}$ cations on alumina and silica and experimental results[2] are shown in Fig. 1.4.

These data show that silica adsorbs the Pt-ions much better than alumina. The explanation is as follows. The Pt is introduced as a positive ion, and the charge of silica and alumina will be different: silica has a negative charge already at pH 6 (PZC of silica is about 3), while the alumina surface at this pH is still positively charged. With an increasing pH the amount of Pt precursor adsorbed on silica increases: the surface contains more and more negative sites for Pt attachment. For alumina, Pt containing cations only start to adsorb

on the surface at pH > 8, while the amount is much less than on silica. Apparently, with silica, a good catalyst can be prepared with $[Pt(NH_3)_4]^{2+}$, while with alumina this appears less feasible. If $PtCl_6^{2-}$ had been chosen as the Pt complex, results would have been the other way round. In conclusion, if ion-exchange phenomena dominate the preparation process, $[Pt(NH_3)_4]^{2+}$ is preferred for the preparation of Pt/SiO_2 catalysts and $PtCl_6^{2-}$ for alumina-based catalysts. It should be mentioned that the presence of Cl^- ions in catalyst formulations is usually undesirable, because it induces metal particle sintering upon calcination, and in several cases poisoning of the catalyst. Extensive washing procedures are needed, which will be further addressed in the case study on the preparation of Au catalysts.[7]

1.2.1.1 *Impregnation profiles on pre-shaped catalyst support bodies*

For impregnated catalysts a completely uniform profile of the active material over the pre-shaped support particle is not always the optimal profile. It is possible to generate profiles on purpose, and in this way to improve the catalyst performance in specific reactions. Figure 1.5 shows four major types of active-phase distribution in catalyst spheres. The grey regions represent the areas impregnated with the active phase. Type *a* is a uniform catalyst while the others have a non-uniform active-phase distribution. They are sometimes referred to as "egg-shell", "egg-white" and "egg-yolk" catalysts, respectively. The optimal profile is determined, among other things, by the reaction kinetics and the mode of catalyst poisoning. For example, an egg-shell catalyst is favorable in the case of a reaction with a positive reaction order, whereas an egg-yolk catalyst is the best choice for reactions with negative orders. When pore-mouth poisoning is dominant it might be attractive to locate the active sites in the interior of the catalyst particles. Another factor is attrition. If attrition is important and if the active phase is expensive (e.g. in the case of precious metals), it might be preferable to place the active phase in the interior of the catalyst particles.[8]

Achieving these distributions can best be discussed by analysis of a practical example. Consider the processes occurring during wet

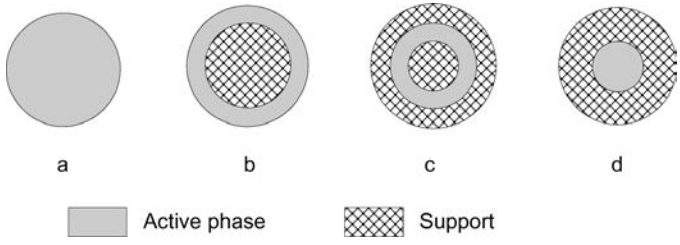

Figure 1.5 Four types of active-phase distribution, (a) uniform, (b) egg-shell, (c) egg-white and (d) egg-yolk.

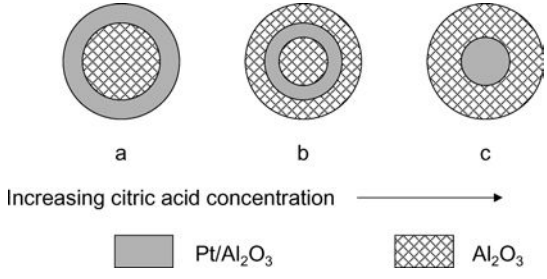

Figure 1.6 The influence of co-adsorbing ions (citrate) on the Pt concentration profile (adsorption of chloroplatinic acid, H_2PtCl_6).

impregnation of alumina using a solution of H_2PtCl_6. As previously discussed, the alumina surface interacts with H_2PtCl_6 by adsorption of $PtCl_6^{2-}$:

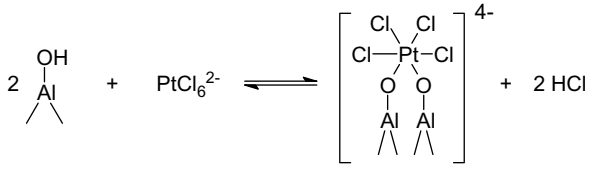

(1.1)

The number of surface sites limits the amount of Pt complexes that can be adsorbed. Typically, Pt-γ-alumina catalysts contain up to 1 wt% Pt. Adsorption is a fast process and in general an egg-shell catalyst will be formed. The addition of a second component to the impregnating solution allows fine-tuning of the catalyst. This is illustrated in Fig. 1.6.

Impregnation of H_2PtCl_6 was carried out in the presence of citric acid, which adsorbs more strongly than H_2PtCl_6 (and HCl). Without the presence of citric acid, an egg-shell type of profile for Pt is obtained (Fig. 1.6(a)). When some citric acid is present, this will be adsorbed on the outer layers of the support body, and the Pt ions will adsorb in a ring at the inside (Fig. 1.6(b)). Higher citric acid concentrations will eventually lead to distribution c. The interaction and profiles obtained using the citrate method, have recently been investigated in detail using magnetic resonance imaging, including spatial distributions within a catalyst support body and the evolution of these distributions in time.[9]

1.2.1.2 *Drying*

The drying step, which follows the impregnation step, also affects the distribution of the active phase. In drying, the solution in the pores will become oversaturated and precipitation takes place. Because of the large surface area, and associated here with the large number of nuclei, a high dispersion can be realized. In principle, rapid evaporation is favorable because it causes rapid super-saturation, and associated with that, a high dispersion. However, if fast drying is achieved by rapid heating of the wet support bodies, boiling phenomena might result in an inhomogeneous distribution. On the other hand, slow drying in combination with well-crystallizing precursor salts, will yield an egg-shell distribution. This is the result of the crystals formed initially at the pore mouths of the support, initiating migration of the impregnation liquid to the outer surface of the support by capillary forces. It has been shown for various catalysts that the use of less well-crystallizing salts gives a more homogeneous distribution of the active phase over the support body.[10] Also the viscosity of the solution plays a role: at higher viscosity the flow rates toward the pore mouth are reduced and a more homogeneous profile results. A related problem arises from the range of pore sizes of the supports. The biggest pores will first empty themselves, the solution accumulating in the smaller pores. A loss of dispersion is the result. Thus, drying is a very critical step and may well determine the quality of the catalyst. Drying in a microwave or freeze-drying is applied occasionally

because these methods usually lead to more uniform distribution of the active phase over the particle, or a structured reactor, as will be discussed in the following section.

1.2.1.3 *Preparation of structured catalysts (monoliths)*

Recently, the use of monolith reactors also in multiphase applications has received much attention.[11–13] They exhibit high rates and high selectivity due to the short diffusion paths. They show interesting hydrodynamic behavior. For instance, under industrial conditions, the flow rates are too high to operate a packed bed counter-currently, but in a structured reactor, tailored design is possible that allows counter-current operation. It is remarkable that for multiphase applications, so-called Taylor flow (the liquid/gas system flows as a train of liquid slugs separated by gas bubbles with a size exceeding the diameter of the channels) is the normal regime.[11–13] An attractive characteristic of this regime is the very high mass transfer from the gas bubble to the liquid.

Synthesis of catalytic monoliths is far from straightforward. Nijhuis *et al.*[14] have provided an overview of preparation procedures for catalytic monoliths. Obtaining a homogeneous metal distribution is often troublesome. Vergunst[14,15] has shown that an appropriate drying method is crucial in this respect. Monolith catalysts were prepared by wet impregnation of an alumina-washcoated cordierite monolith with a solution of $Ni(NO_3)_2 \cdot 6H_2O$. This was achieved by placing the monolith in the impregnation solution for 1 h. Subsequently, the channels were dried. Figure 1.7 shows a schematic representation of the impregnation profiles obtained after drying by different methods, *viz.* using stationary air in an oven (a), flowing air (up flow) (b), a microwave (c), or freeze-drying ((d) and (e)).

The drying method had a profound effect on the impregnation profile. Conventional drying (in an oven with stationary air) produced an increased Ni concentration near the entrance and exit of the monolith. Drying in flowing air shows accumulation of Ni at the point of first contact between gas and solid (the top of the monolith). The reason for these non-uniform profiles is that

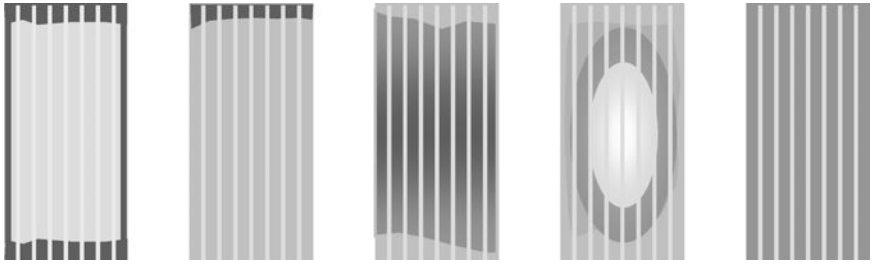

Figure 1.7 Schematic of impregnation profiles obtained after (a) conventional drying; (b) forced-flow drying; (c) microwave drying; (d) freeze-drying (1 h) and (e) freeze-drying (24 h).

during drying, the liquid present in the interior of the monolith migrates outward due to evaporation of the liquid at the external surface. If the Ni has little or no interaction with the support, it will move with the liquid to the exterior, where the liquid evaporates and the Ni precipitates. Microwave drying yields a rather uniform distribution because heat is supplied throughout the support and therefore evaporation of the liquid occurs more homogeneously. The effect of freeze-drying is that the liquid is prevented from flowing to the external surface of the support, thereby also yielding a much more homogeneous distribution of Ni throughout the support. Another method of obtaining a uniform metal profile in the case of monoliths is deposition precipitation, which will be discussed next.

1.2.1.4 *Homogeneous deposition precipitation via pH increase*[1,16,17]

As previously discussed, as a result of the use of impregnation techniques, the active phase of the catalyst can be located at the outside of the particles leading to relatively large crystallites. Furthermore, the combination of high loading and high dispersion is difficult to obtain when impregnation is used, and usually the impregnation procedure has to be repeated to achieve a well-dispersed catalyst with a high loading. An alternative method called "homogeneous deposition precipitation" (HDP)[1,16,17] can be used to obtain uniform

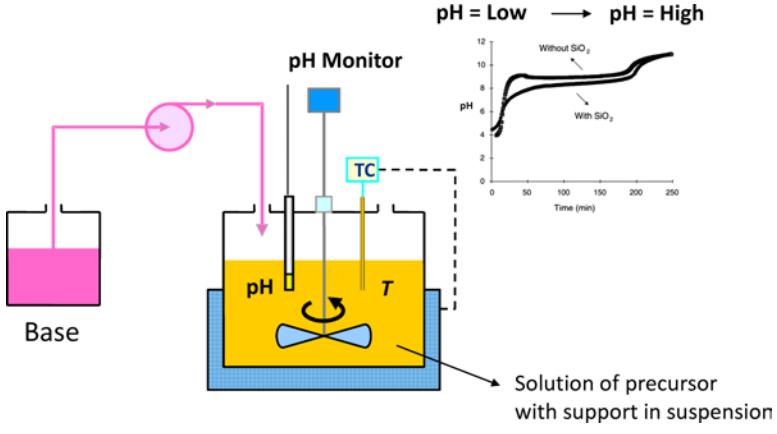

Figure 1.8 Laboratory unit for the preparation of catalysts by HDP.

catalysts. In HDP the support is introduced in the precipitation vessel as a powder. Figure 1.8 illustrates a laboratory unit for the preparation of catalysts by HDP. The pH is slowly increased by injection of a basic NaOH or NH_3 solution in the precipitation vessel. Alternatively, urea can be added to the solution. If the mixture is heated slowly, at 363 K urea starts to decompose:

$$CO(NH_2)_2 + 3\ H_2O \rightarrow CO_2 + 2\ NH_4^+ + 2\ OH^-. \qquad (1.2)$$

Due to this reaction the pH slowly increases.

In the HDP procedure, the desired metal ion deposits in the form of the hydroxide. To obtain a homogeneous distribution, nucleation of the hydroxide must occur uniformly on the surface of the support particles, and not in the bulk solution. To prevent the latter, the suspension must be vigorously stirred and the pH must be adjusted slowly. The large surface of the support particles favors uniform nucleation of a large number of nuclei, and as a consequence, the crystallites formed are very small. With this procedure, highly dispersed catalysts can be prepared with a high metal loading. In Fig. 1.8, a pH curve as a function of base injection is shown. Typically, the maximum in the pH at around 40 min as a function of the amount

of base injected, is indicative of a low interaction between the precipitating compound and the support, and usually indicates that poor catalysts with a low dispersion will be obtained. The explanation is as follows. The pH rises into the super-saturation region of the hydroxide of the desired metal ion. Once the first nuclei have been formed, rapid growth of these first nuclei occurs, consuming large amounts of OH^- ions, causing the pH to drop (the injected amount of base per time cannot compensate for the OH^- consumption). At some point (around 50 min) a steady state is reached in which the OH^- consumption and injection rate are again in equilibrium. On the other hand a smooth rise of the precipitation curve is expected if a strong interaction between the precipitating precursor and the support particles exists, since then metal hydroxide concentration does not enter the super-saturation region, thus preventing the high precipitation rates. In conclusion, monitoring of the pH during the precipitation process yields valuable information on whether highly dispersed catalysts will be obtained or not, especially if precipitation curves both with and without supports can be compared.

1.2.1.5 *(Co)precipitation at constant pH*

This preparation technique is related to homogeneous deposition precipitation, but here the base and the precursor solution are injected simultaneously to the suspension of the catalyst support at a fixed pH. In this way, the interaction of the precipitating compound with the support can be optimized, while at the same time the crystallization of unwanted compounds, such as large crystallites of basic copper nitrate in the case of copper catalysts, can be prevented.[18,19]

Precipitation at constant pH (Fig. 1.9) is also a prerequisite in order to co-precipitate two catalyst components at the same time. This is illustrated for example by the preparation of Pd/La catalysts for methanol decomposition.[20] The preparation procedure and the La_2O_3/Pd weight ratio of these $Pd/La_2O_3/SiO_2$ catalysts (5 wt% Pd) were found to be important for high catalytic activities in methanol decomposition. If the precipitation procedure leads to La_2O_3 deposition in the final step, which is the result of the HDP method,

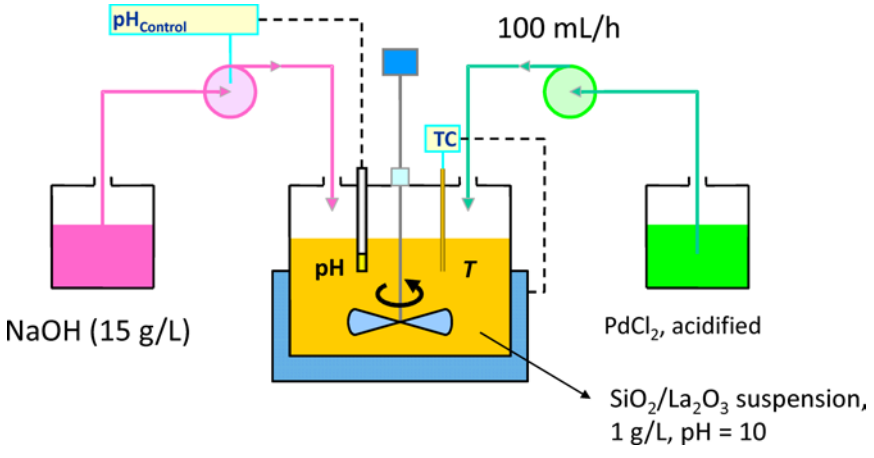

Figure 1.9 Set-up for co-precipitation at constant pH. The pump-speed of the basic solution is adjusted to maintain the pH at the desired value. This set-up was employed for precipitation of $Pd(OH)_2$ onto a La_2O_3/SiO_2 support and the conditions are indicated.[20]

coverage of Pd particles by La_2O_3 patches occurs, which negatively affects the activity. Co-precipitation of La in Pd at fixed pH was found to lead to an optimized interaction of Pd with La_2O_3 and thus to an optimized use of expensive Pd.

Co-precipitation is also applied in the synthesis of hydrotalcite-like precursors (HTlcs) for catalysts e.g. based on Cu-Zn-Al[21], or Co-Al catalysts.[22,23] Synthetic HTlcs, with a general formula $[M^{2+}_{1-x}M^{3+}_{x}(OH)_2][A^{m-}]_{x/m}\cdot nH_2O$, are hydrated hydroxycarbonates of a random lamellar structure. These materials can be visualized as brucite-type octahedral layers, in which M^{3+} cations partially substitute for M^{2+} cations ($x = M^{3+}/M^{2+}+M^{3+}$). The cations are located in the center of the octahedron formed by six hydroxyl groups. The metal-octahedra share edges to form two-dimensional infinite sheets, similar to brucite ($Mg(OH)_2$). The brucite-like layers can stack to build a tri-dimensional network and are linked by various chemical interactions (mainly hydrogen bonding) between the sheets. The positive charge resulting from this substitution is balanced by anions (often carbonate) together with water molecules arranged in interlayers

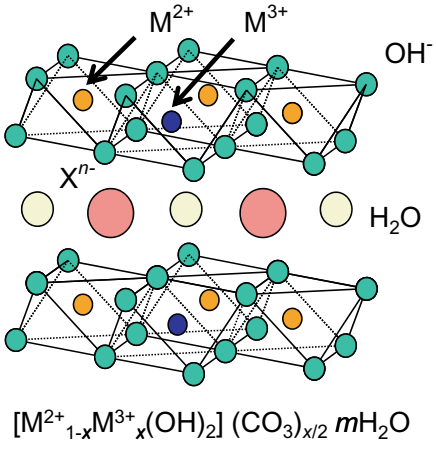

Figure 1.10 Schematic illustration of the structure of hydrotalcite-like compounds.

alternating with the octahedral sheets. The structure, as outlined above, is further illustrated in Fig. 1.10.[23]

Hydrotalcite-like compounds (HTlcs) have attracted much attention in recent years as catalyst precursors and catalyst support. This is due to (i) their ability to accommodate a large variety of bivalent and trivalent cations, (ii) the homogeneous mixture of the cations on an atomic scale, and (iii) the formation of thermostable mixed oxides, often denoted as ex-HTlcs, with high surface area upon decomposition. The first two properties are a result of the precursor while the last property appears to be related to the decomposition mechanism. The transitions in the structural properties of Co-based hydrotalcites upon high temperature treatments have been extensively studied in our group.[23] In the first decomposition step, water is removed from the structure. This transition is followed by dehydroxylation and decarbonation, as well as carbonate reorganization in the interlayer. Thermal treatment in air finally leads to a solid solution of cobalt spinels ($Co(Co,Al)_2O_4$). Mixtures of CoO and $CoAl_2O_4$ are formed upon treatment in inert.

Many papers dealing with applications, and variations in synthesis parameters of hydrotalcite-like compounds can be found in the open

literature, but it is beyond the scope of this chapter to present an overview here. On concluding this paragraph, it should be mentioned that hydrotalcite-like compounds are often used as catalyst precursors in the catalyst industry, because of the properties stated above.

1.2.1.6 *Synthesis by using organic functionalization*

A commonly known disadvantage of the use of homogeneous catalysts and enzymes in the chemicals industry is the difficulty of separating the active catalyst and the product (often also dissolved in the liquid phase). One of the most commonly proposed solutions to overcome this problem is to immobilize the organo-metallic catalyst or enzyme on an inert support, such as silica. It is not within the scope of the present chapter to discuss immobilization extensively. However, it should be mentioned that the immobilization techniques used by the metal-organic community has inspired the use of metal complexes for preparation of heterogeneous catalyst synthesis, in particular to prepare alloys. Examples include the synthesis of Au catalysts,[24,25] and mixed Au-Pt catalysts.[26] Van Gorp[27] prepared combinations of Rh and Cu and Pd and Cu catalysts using organo-metallic compounds. Complexes containing two metals in a fixed ratio, such as $(\text{p-tolyl})_4Cu_2Rh_2$ were used. The advantage of this complex is that it decomposes readily at mild temperatures into the mixed metallic particles, eliminating the necessity of a high temperature hydrogen reduction, which might cause sintering of the small metal particles.

Also pre-functionalization of the support has been applied e.g. in the synthesis of SiO_2 supported Pt catalysts with well defined particle size distributions. Pt nanoparticles with an average size of similar to 3 nm were successfully immobilized on the surface of SiO_2 and functionalized with $-NH_2$ and $-SH$ groups through chemical reduction process using polyvinylpyrrolidone as a stabilizer and different reducing agents.[28]

On concluding this paragraph on immobilization, it should be stated that it is seldom applied in the catalyst industry, because of the high price of the chemicals required, and, if applicable, the air sensitivity of the organo-metallic complexes.

1.2.1.7 *Photodeposition of metals on semiconductor supports*[4,5,29]

When a semiconductor absorbs UV/Vis light of energy greater than the so-called band gap between the highest energy level of the valence band and lowest level of the conduction band, a transition in the electronic state occurs. Both photo-excited electrons and holes are formed. For crystalline semiconductor particles, the transition of an electron from the valence band to the conduction band is followed by migration of photo-excited electrons and holes to the surface. The "holes" are capable of oxidizing a substrate by accepting an electron, and "electrons" able to reduce a (second) substrate. If this substrate is a metal ion, deposition, referred to as photodeposition, can be induced.[30] This has been mainly applied for TiO_2 supported metal particles and for applications in photocatalysis.[31] For example, for Au deposition, in practice a suspension of TiO_2 in $AuCl_4^-$ is exposed to UV light. A hole scavenger, such as methanol, also needs to be present to prevent accumulation of positive charges during the photodeposition procedure.[32] Figure 1.11 demonstrates the principle of the procedure. Interestingly, when the synthesis of Au nanoparticles is analyzed by UV-Vis probes *in situ*, the deposition

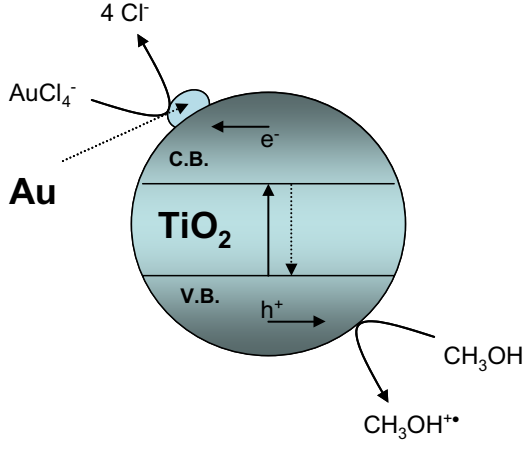

Figure 1.11 Principle of photodeposition of Au particles on the surface of TiO_2 crystals. Oxidation of methanol is required to prevent charge accumulation.

of the particles can be followed by the growth of the surface plasmon band at approximately 540 nm. The obtained particles sizes are in the order of approximately 20 nm, using this methodology, which is still rather large for various applications in heterogeneous catalysis.

A recent example of an advanced form of this methodology is provided by Zhang and coworkers for Ag deposition.[33] Under ambient light illumination, silver nanoparticles on a TiO_2 support were synthesized by a triblock copolymer induced reduction of $Ag(NH_3)_2^+$ ions in ethanol. Conventional chemical reducing agents, thermal treatment, and radiation sources are no longer necessary in this novel approach. This novel ambient light route has been successfully applied to deposit silver nanoclusters on TiO_2 of about 2 nm in size, strongly anchored to the TiO_2 particles with high dispersion. The obtained catalysts were highly active in various photocatalytic applications. The scale of the procedure requires development of photo reactors, while these are usually not available in catalyst manufacturing facilities.

1.2.1.8 *Calcination procedures*

All of the above-described techniques produce a dried solid catalyst, which is usually further treated at elevated temperature in static or flowing air, which is referred to as calcination. It was already discussed that drying is a crucial step in the impregnation preparation procedure, and recent studies have demonstrated that calcination conditions will also largely determine the eventual size distribution of the obtained metal nanoparticles. This will be further addressed in the following case studies.

1.3 Case Studies

In the following, three examples of the effect of the preparation of metal catalysts on the performance in the desired reactions will be discussed. In the first example the very important effect of heat treatment after the impregnation procedure is illustrated by a study on the redox activity of Pt(O) catalysts as a function of heat treatment and particle size.

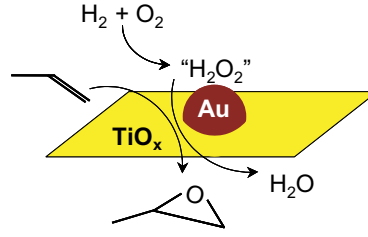

Figure 1.12 Schematic presentation of the reaction of propene with hydrogen and oxygen to yield PO.

In the second example we will focus on preparation methodologies for gold catalysts, and the effect on the performance of gold in selective epoxidation of propene to PO (see reaction scheme in Fig. 1.12).

The commonly proposed mechanism for the reaction is that hydrogen and oxygen recombine on the catalyst surface to yield a peroxy intermediate, which subsequently reacts with propene to yield PO and water.[34,35] Recently, evidence for the formation of this peroxide intermediate was provided,[36,37] suggesting alternative mechanisms are less likely.

In the final example, we will continue with the subject of selective oxidation of propene to PO, but this time using advanced $CaCO_3$ supported Ag catalysts. The focus is directed towards a novel synthesis procedure, in which La incorporation is shown to have a significant effect on the alkali content of the catalyst and thus on the resulting catalyst performance. Although much less significant as the case for the Au catalysts, recent new information on the role of the support and the preparation procedures has appeared in the open literature, and this is briefly addressed.[38–41]

1.3.1 *Impregnation: preparation of Pt catalysts, the effect of the pre-treatment conditions*

Although Pt catalysts have been and are used extensively in various processes, such as hydrogenation/dehydrogenation, and are usually

prepared by impregnation, the procedure is often described in very limited detail. In Section 1.2 various aspects of the preparation of Pt catalysts by impregnation have already been discussed (use of precursors, co-adsorbents, and effect of PZC of the supports). It was mentioned that drying needs to be well controlled in order to obtain a high dispersion. Another experimental condition of great importance is the heating rate chosen for the pre-treatment of the catalyst system. In a paper by the group of de Jong,[10,42] it was reported that a low heating rate (0.2 K/min) is essential in order to obtain small Pt clusters of 13–20 atoms (Pt < 1.1 nm), in the case of zeolite-Y supported catalysts. The beneficial effect of low heating rates is explained by the slow desorption of water and ammonia (in cases where $[Pt(NH_3)_4]^{2+}$ was used as the precursor) from the zeolite in combination with stabilization of the Pt particles by the cavity walls. A higher heating rate of 1 K/min resulted in a bi-model distribution, in which 5 wt% of the Pt was present as particles of 4–9 nm, and 95% as particles of 1–1.2 nm. The importance of these findings can be illustrated by work done in our own group on the behavior of Pt-based catalysts in reduction/oxidation cycles, which is of relevance to NOx decomposition in lean-burn applications.

We have applied our Multi-Track reactor, an advanced TAP-like reactor system,[43] to evaluate the number of redox-active Pt surface sites (Pt_{surf} *redox*) on Pt/Al_2O_3 catalysts as a function of Pt dispersion. The number of Pt_{surf} *redox* sites was compared with the total number of Pt_{surf} sites determined by conventional volumetric CO chemisorption.

1.3.1.1 *Procedures*

A detailed description of the catalyst preparation and the Multi-Track set-up can be found elsewhere.[43] Before performing titration experiments in Multi-Track, the catalyst (1 wt% Pt on Alumina) was subjected to two different pre-treatments:

Pre-treatment procedure M1. After inserting the fresh catalyst into the vacuum system, it was heated up to 573 K at 10 K/min^{-1}. The catalyst

was stabilized for 2 h. This treatment leads to catalyst M1 and was intended to preserve the structure fresh catalyst as much as possible.

Pre-treatment procedure M2. After inserting the reactor into the vacuum system it was heated up to 773 K (10 K/min^{-1}). Subsequently, the catalyst was subjected to H_2 pulses (10^{17} molecules per pulse, 1 pulse/sec) for 1 h. Then, the reactor was cooled to 573 K, and stabilized for 2 h. This treatment results in catalyst M2 and was meant to induce sintering of Pt particles in order to study the influence of the particle size on redox behavior by comparing catalysts M1 and M2.

Following these pre-treatments, titration experiments were performed at temperatures between 473 K and 573 K. Pure hydrogen (10^{17} molecules per pulse) was used to reduce the Pt catalyst. The catalyst is denoted as "completely reduced" when the area under the hydrogen-signal was constant. Pulses of 20 vol.% O_2 in Ar (10^{17} molecules per pulse) were used to re-oxidize the reduced catalyst. The catalyst is denoted "completely oxidized" when the area under the succeeding oxygen-signals is constant.

Figure 1.13 shows a typical result of a titration experiment, and indicates the high sensitivity of the Multi-Track system (responses of one single pulse were detected and calculated to construct the curves shown in Fig. 1.13).

From the area under the curves, the total hydrogen needed for reduction of the Pt surface can be calculated. A remarkable difference in the amount of hydrogen needed to reduce the surface of catalysts M1 and M2 can be observed. By repeating the H_2/O_2 reduction/oxidation cycles, it was confirmed that the hydrogen uptake values were reproducible within ±10%. After the Multi-Track titration experiments, the dispersion of the catalyst was determined in a separate set-up by conventional CO chemisorption. The Pt dispersion as derived from the CO chemisorption experiments was decreased from 0.73 for catalyst M1 to 0.47 for catalyst M2, indicating that the pre-treatment procedure M2 indeed induced sintering of Pt. For catalyst M2, the number of chemisorption sites as determined by CO chemisorption, and the number of surface sites participating in

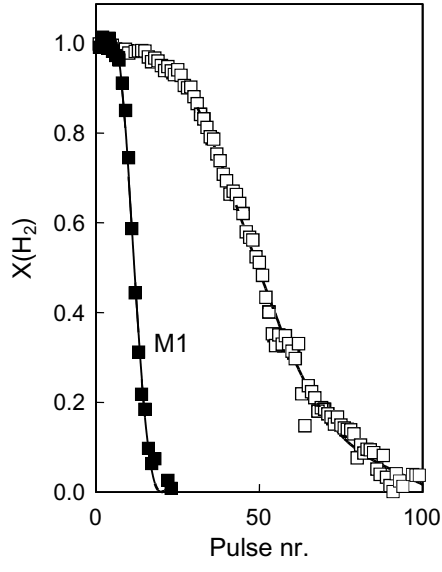

Figure 1.13 Reduction by a train of hydrogen pulses of previously O_2-oxidized Pt catalysts. For pre-treatment conditions of catalysts M1 and M2 see text above.

the H_2/O_2 cycles in the Multi-Track experiments (*Pt_{surf} redox)* are in good agreement. On sample M1, however, only 10% of the *Pt_{surf}* sites as determined from CO chemisorption appear to be involved in the redox cycles.

The discrepancy between the CO chemisorption experiment and the Multi-Track experiment for catalyst M1, can be explained by the large difference in applied H_2 partial pressure in the Multi-Track experiment and in pre-conditioning the catalyst before CO chemisorption. During the H_2 titration procedure in the Multi-Track reactor the partial pressure of hydrogen is extremely low, at least eight orders of magnitude lower than the H_2 partial pressure in the pre-treatment for the CO chemisorption experiment (typically performed with pure H_2, at 553 K, for 2 h). Under Multi-Track conditions, 90% of the surface sites in catalyst M1 are apparently not affected by hydrogen, while these sites are reduced in the hydrogen pre-treatment of the CO chemisorption experiments.

Interestingly, the Multi-Track results appeared very representative for the behavior of the catalysts under realistic deNOx conditions, showing a significant increase in performance after sintering, in agreement with the higher reducibility of catalyst M2 in Multi-Track conditions. Several authors have noticed an influence of the Pt dispersion on the performance of Pt-group catalysts in HC-SCR.[44,45] Burch *et al.*[45] presented an apparent hyperbolic relation between dispersion of the fresh catalyst and turnover frequency (TOF) in HC-SCR over Pt/Al_2O_3 and Pt/SiO_2 catalysts. Catalysts with a large Pt particle size exhibit a higher TOF than those with small size. It was further shown by various research groups that highly dispersed Pt catalysts undergo sintering in HC-SCR, which is proposed to be an NO induced process.[45–47] It should be mentioned that a particle size dependency on activity of Pt catalysts has not only been observed in reactions involving the reduction of NO,[48] but also in many other oxidation reactions. The rates of the oxidation of propene,[49] methane,[44,50–52] benzene,[53,54] and other hydrocarbons,[54] are all increased as a function of increasing Pt particle size, which we suggest, based on our Multi-Track data, is the result of a higher reducibility of the Pt sites involved in the reactions.

In summary, for Pt catalysts prepared by impregnation, various preparation variables can be changed (as indicated in the paragraph discussing impregnation techniques in general), but the most important factor for the eventual particle size/performance of these catalysts is the heat treatment. Heating rate and temperature of pre-conditioning of the Pt catalysts are crucial.

1.3.2 *Precipitation vs. impregnation by ion-exchange: Au precursors and the effect of the method of preparation and selected support on performance in selective epoxidation of propene over Au/TiO_2 catalysts*

Au catalysts have received considerable attention recently because of the extraordinary performance in the low temperature oxidation of CO[55] and high selectivities of over 99% in the direct epoxidation of propylene in the presence of hydrogen. Besides the extraordinary

performance in oxidation of CO and propene, Au catalysts have also been reported to be very effective in promoting photocatalysis.[6,32,56] The preparation procedure was found crucial, in particular in relation to the effect on the OH population of the applied TiO_2 support. In photocatalysis, these OH-groups are essential for activity, in particular for conversion in organic phases. Hugon and coworkers have recently given an overview of impregnation procedures that might lead to improved catalysts.[7] Here, we will further focus on the effect of preparation on the performance in epoxidation reactions.

The first reports of Haruta and coworkers have initiated many ongoing academic studies that focus on the mechanism of the reactions (CO oxidation and propene epoxidation) and the effect of the Au particle size on the activity and selectivity in propene epoxidation, e.g. Refs. 37, 57–63. A peroxide-like intermediate is proposed to selectively react with propylene to yield PO.[37] This was previously illustrated in Fig. 1.12. Industrial interest has also been significant, as patents have appeared recently on improvements of the Au/TiO_2 system, which mainly claim promoters of the catalytic system to reduce hydrogen consumption. The most recent breakthrough was reported by the Haruta group, applying mesoporous structures and methylation of support groups.[60,61] This improvement of the catalyst system enhanced the PO yield to about 10%.

As stated, to obtain Au particles with a high selectivity, and stability, the preparation procedure and support appear to be of crucial importance. Furthermore, the morphology and composition of the support appear also of crucial importance, as is illustrated by the following.

1.3.2.1 *Experimental*

To evaluate the role of the support, the following catalysts were prepared.[64] Degussa P25 (80% anatase, 50 m^2/g), was applied as the TiO_2 support for the 1 wt% Au-catalysts. TS-1 was synthesed either using tetraethyl orthosilicate (TEOS), TPA-OH (tetra-propylammonium hydroxyde, Aldrich) and TBOT (tetrabutylorthotitanate) (Catalyst TS-1a), or SiO_2 particles (Degussa Aerosil) rather than

TEOS, keeping the other ingredients and procedures similar (Catalyst TS-1b). An extensive description of the preparation of the TS-1 supports can be found elsewhere.

$AuCl_3$ was used as the Au source. Incipient wetness impregnation was performed by adding the $AuCl_3$ solution to the appropriate amount of TiO_2 support, followed by drying at 375 K (5 K/min), and calcination at 673 K (5 K/min) for 1 h. In a homogeneous deposition precipitation method (method **HDP-I**), a gradual increase of the pH of an $AuCl_3/TiO_2$ suspension (acidified to pH 3, and a TiO_2 amount of 100 g/L) was brought about by injection of a diluted NH_4OH solution. In a pH-static precipitation method (method **HDP-II**), a solution of $AuCl_3$ was injected at pH 10 (made basic through NH_4OH) into the TiO_2 suspension (100 g/L). After precipitation, the catalysts were filtered, dried at 375 K in static air (5 K/min) and calcined at 673 K (5 K/min) for 1 h, again in static air. A more detailed description of the preparation can be found in Xue *et al.*[48]

1.3.2.2 *Impregnation vs. precipitation*

Catalysts prepared by impregnation were found to be completely inactive in the epoxidation reaction of propene.[65] Figure 1.14 shows a SEM

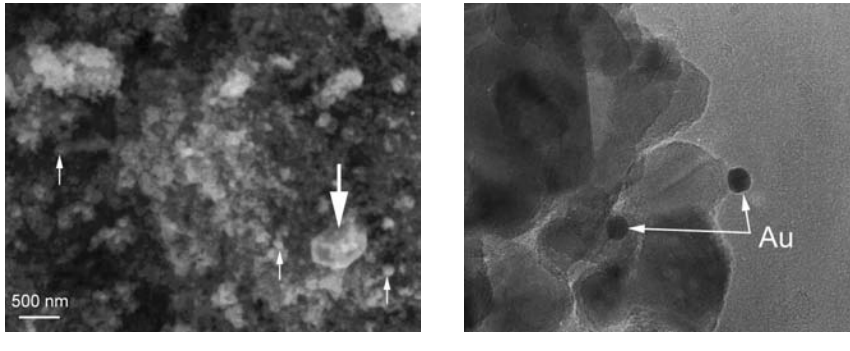

(a) (b)

Figure 1.14 Representative micrographs of the Au/TiO_2 catalysts prepared by impregnation (SEM micrograph, Fig. 1.14(a)) and precipitation (HDP-II, TEM micrograph, Fig. 1.14(b)).

picture of an impregnated Au catalyst on TiO_2, and a TEM picture of a precipitated catalyst using method HDP-II (same TiO_2 support). A ready explanation for the inactivity of the catalysts prepared by the impregnation method is found in the large Au particle diameter, which exceeds 100 nm, and can even be observed by SEM. This gold particle size is very large compared to that of the precipitated catalyst, which can only be observed using TEM. From Fig. 1.13, the Au size for the precipitated catalyst is estimated at 3–10 nm, and particles are homogeneously dispersed throughout the catalyst sample.

1.3.2.3 *Precipitation conditions*

Catalysts prepared by method HDP-I, with an Au loading of 1 wt% or 3 wt%, showed a very high activity for hydrogenation of propylene to propane at 323 K, in agreement with data provided by Haruta.[58] Minor amounts of acetone were also produced. Catalytic activity for the formation of PO from propylene was not found. Haruta reports that the Au particle size strongly affects the reactivity and selectivity in the oxidation of propylene in the presence of hydrogen. Only when the Au particles exceed 2 nm, and are smaller than 10 nm, is the desired conversion to PO achieved. Apparently, catalysts prepared by method HDP-I had particle sizes below 2 nm, independent of the TiO_2 support used, or the speed of base addition. This explains why mainly products of hydrogenation, rather than epoxidation, were obtained. The minor amounts of acetone were most likely formed by reaction of propane and oxygen.

Generally, catalysts prepared by method HDP-II with a TiO_2 "concentration" of 50 g/L (or below), were not catalytically active in the oxidation of propylene below 373 K. This suggests that insufficient nucleation sites were available for the genesis of a highly dispersed system. In agreement with this tentative conclusion, upon calcination Au particles were sintered to sizes larger than 10 nm, thus explaining the low activity (confirmed by TEM analysis, not shown).

When a specific concentration of 100 g/L TiO_2 (anatase) was applied, selective catalysts were formed. Apparently, this support

density is high enough to achieve sufficient interaction between the precipitating Au and the support. This resulted in the particle size distribution shown in Fig. 1.13(b), which appears to induce selective propene epoxidation. Using a feed of 10% propylene, 10% H_2 and 10% O_2 in He with a flow rate of 50 ml/min at 353 K, a propylene conversion of 0.7% was achieved using 250 mg catalyst. The selectivity to PO was 99%. The hydrogen efficiency amounted to an approximate 23%, the other product of hydrogen consumption being water. Some other factors were also investigated. Lowering the pH of the precipitation suspension resulted in a catalyst with a reduced performance. Increasing the Au loading from 1 to 3 wt%, yielded catalysts with significantly decreased activity. In both cases larger Au particles were obtained, explaining the decreased performance.

1.3.2.4 *Support effects*

Many researchers have observed that the Au/TiO_2 catalysts rapidly deactivated, typically within one hour.[64] Deactivation can be prevented, if the TiO_2 is supported on SiO_2, or if TS-1 is used as the support. However, if a silicalite-derived material containing Ti (TS-1) is used as the support material, the preparation method of the support itself appeared to also largely affect the activity. A combined SEM and TEM study was conducted to analyze the various catalysts and to obtain insight into the reasons for the low activity in propylene epoxidation of some catalysts, and the high activity and selectivity of others.

Two synthesis methods were applied to prepare the TS-1 supports (TS-1a and TS-1b). It was found that, after deposition of Au by precipitation method HDP-II, TS-1a was a good catalyst, whereas catalyst TS-1b was totally inactive. In Figs. 1.15(a) and (b), TEM pictures of the Au-TS-1 samples are shown. The morphology of the two samples is quite different. TS-1a consisted of very small crystallites (10 nm), agglomerated to form 150 nm particles, whereas TS-1b consisted of 35 μm crystals. The size of the gold particles in the TS-1a sample with the small crystallites, was estimated to be 3–15 nm, which is not significantly smaller than those observed on the edges

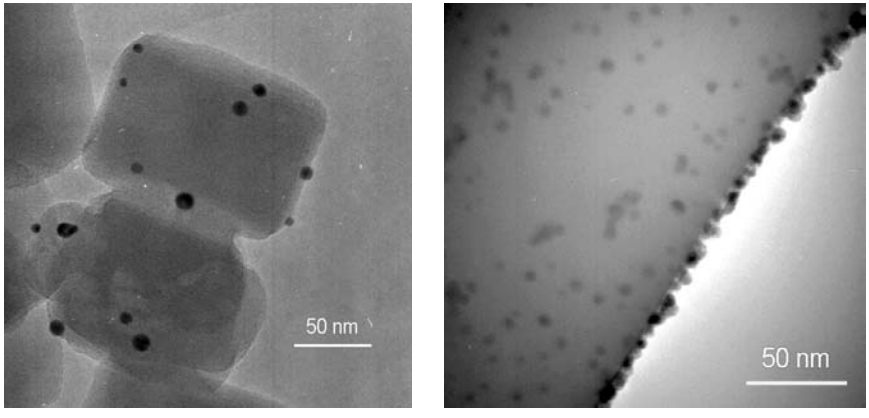

(a) (b)

Figure 1.15 TEM images of Au supported on TS-1a and TS-1b, respectively.

of the large TS-1b crystals. However, Titanium is an essential factor in the activity of dispersed gold catalysts in the epoxidation of propylene. It was therefore hypothesized that, since the Au particles were all located on the outside of the crystals, the Ti-phase is located in the interior of the support containing the large crystals.

Essentially the gold particles only "see" silica moieties, and do not interact with the Ti-phase present. This hypothesis, however, could not be verified experimentally.

Concluding, this example is probably the best to show the dramatic difference between an impregnation procedure, homogeneous deposition precipitation (HDP), and precipitation at constant pH. Impregnated catalysts are usually inactive, HDP leads to very small particles with hydrogenation activity, whereas the use of precipitation at constant pH yields highly selective epoxidation catalysts. Furthermore, the morphology of the TS-1 support was shown to play an important role in obtaining active catalysts. Recently various alternative procedures as compared to the ones described above are available, of which optimized impregnation,[7] use of ligand protected particles,[66] and photodeposition[3,32] appear quite promising.

1.3.3 *Co-precipitation: preparation of advanced $CaCO_3$ supported Ag catalysts*

1.3.3.1 *Introduction*

Direct oxidation of propylene to propylene oxide (PO) with high selectivity and activity is yet to be achieved in heterogeneous catalysis, as was already indicated in the description on the preparation of the Au catalysts. Obviously, the most attractive reaction is the direct oxidation with oxygen, rather than using the previously discussed mixture of oxygen and hydrogen:

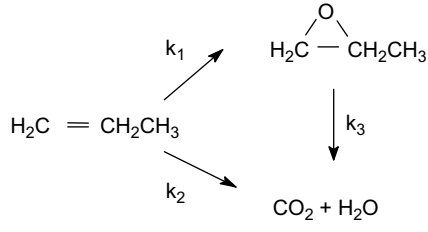

(1.3)

Although epoxidation of ethylene with O_2 over Ag catalysts has been industrially applied for many years, the catalysts used for this process typically show poor selectivity in the epoxidation reaction of propylene, yielding mainly CO_2 and water.

The low selectivity of these catalysts in the oxidation of propylene is often explained by the difference in mechanism for the formation of PO from propene and EO from ethane.[67] In both cases, the reaction involves the interaction of the alkene with an oxygen radical on the Ag surface, yielding an epoxide intermediate.[68] In the case of propene, abstraction of a hydrogen atom of the CH_3 group of the epoxide precursor by reaction with a neighboring oxygen radical on the Ag surface results in the formation of CO_2, rather than PO (reaction pathway k2 is preferred in the above propene epoxidation scheme). Due to the absence of the specific hydrogen (CH_3 group) in the ethylene molecule, high selectivities can be obtained for ethylene.

The selectivity of Ag-based catalysts in propylene oxidation is expected to improve by the preparation of Ag sites without destructive

neighboring oxygen radicals. The formation of these isolated Ag sites might be approached by preparation of very small Ag particles. This might be achieved using catalysts based on zeolites and mesoporous materials,[69,70] sol-gel preparation methods[71,72] or alloying of Ag with e.g. Au.[18] Unfortunately, none of these methods has appeared to be successful in significantly improving PO selectivity in propylene epoxidation. Another approach is based on poisoning of a specific amount of Ag sites with either an alkali metal,[73–75] or gas phase additives, such as NO or alkyl halides,[73,76] which has been successfully used in improving the selectivity of ethylene epoxidation catalysts. Recently the particular use of an alkali carbonate to support the Ag particles in combination with these "poisoning" promoters has been claimed in a Canadian patent by Union Carbide (1,282,772 (1991)). This catalyst does not necessarily contain α-alumina, commonly used in selective ethylene epoxidation catalysts. Besides the alkaline earth metal carbonate (Mg, Sr, Ca, Ba) as the support material, another novel aspect is the specific use of KNO_3, in combination with NO/NO_2 as gas phase additives, to enhance the selectivity for the desired products in alkene epoxidation reactions. Again, poisoning of a specific amount of Ag sites seems to be the reason for the high selectivity of these Ag-based catalysts.

As many as ten patents have been assigned to ARCO Chemical, all describing improvements of the Union Carbide Patent for the epoxidation of propylene. Selectivities as high as 50% have been claimed, in the range of 2–5% conversion, based on a 10% propylene and 5% oxygen feed. Various modifications have been claimed of which the most important one is that also silver catalysts supported on other alkaline earth metal compounds than carbonates are active,[38,41] such as calcium titanate, tribasic calcium phosphate, calcium molybdate, or calcium fluoride, as well as the magnesium and strontium analogues. Such supports provide significantly higher selectivity to the desired epoxide than would be expected from the performance of related materials. Selectivities are lower than those reported in the original Union Carbide patent.

The specific method of preparation of the Ag catalysts is usually impregnation of the carbonate by a solution containing silver ions

and organic complexing agents, such as ethylene diamine, oxalic acid, and ethanol amine.[41] The patent discloses the formation of a slurry, which is spread on a flat surface and roasted to remove organic precursors and reduce the silver. The potassium nitrate is added by impregnation after reduction of the silver precursor to the metallic state, but may also be included in the silver precursor solution. The procedure is rather tedious and involves two different impregnation steps. Recently we have developed precipitation methods (US patent 6,392,066) to obtain active catalysts based on the compositions claimed in the Union Carbide and Arco patents. We have found that the inclusion of lanthanum nitrate, or other rare earth metal nitrates, in the precipitation solution is essential in order to obtain active alkaline earth metal carbonate supported silver catalysts by this preparation procedure. Furthermore, the inclusion of promoting amounts of Cl^- and K^+ or Na^+ in the precipitation solution significantly enhances the selectivity in propylene oxidation.

1.3.3.2 *Precipitation of carbonate supports: experimental*

Precipitated catalysts were prepared by a HDP procedure. Base injection into a precursor solution was performed using the equipment described in Fig. 1.8. The base used consisted of a solution of 60 g/L K_2CO_3, which was injected under vigorous stirring at 5 ml/min in to a 250 ml solution of precursor. A reference catalyst was prepared by using only 5 g $Ca(NO_3)_2 \cdot 4H_2O$ and 2.5 g $AgNO_3$. The pH changed as a function of the amount of base solution injected and the amount of remaining Ag^+ and Ca^{2+} present in the solution. When the precipitation rate equals the rate of base (carbonate) injection, the pH attains a constant value (see Section 1.2). $AgCO_3$ is precipitated before $CaCO_3$ at pH 7, followed by $CaCO_3$ initiating at pH 8.5 and continuing at a steady state level at a pH of 7.5.

The procedure including structural promoters (rare earth metal nitrates), was conducted as follows. A 4 g/L KOH and 46 g/L K_2CO_3 containing base solution was injected at 5 ml/min into a HNO_3 acidified catalyst precursor solution (pH 3) of 2.5 g $AgNO_3$, 5 g

$Ca(NO_3)_2 \cdot 4H_2O$, and 1 g $La(NO_3)_3 \cdot 6\ H_2O$. The precipitation was completed in 50 min and injection of the basic solution was ended at a final pH of 10. Please note that we also changed the composition of the base solution by adding KOH to the K_2CO_3 solution.

The precipitates were filtered (not washed), dried, and calcined at 600 K (heating rate 10 K/min) for only ten minutes, sufficient to reduce the Ag precursor without decomposition of the nitrates incorporated into the catalyst. A yellowish/brown catalyst was obtained.

1.3.3.3 *Results and discussion*

An overview of the effect of the precipitation variables on morphology, chemical composition and performance in selective propene oxidation is given in Table 1.1. The precipitated catalysts without La addition to the solution showed a much lower selectivity than the selectivity of the catalysts prepared by impregnation reported in the Arco patents, which is 40–50% in comparable experimental conditions. At most, a selectivity of 8% was obtained, at 6% propene conversion (see Table 1.2) for these precipitated catalysts.

To modify the morphology of the catalyst system, lanthanum was added to the precipitation solution. As indicated in Table 1.2, this induces K incorporation in the catalyst formulation, whereas the morphology of the silver particles was also affected. However, a high selectivity was still not obtained. Changing the base composition from a K_2CO_3 solution to a mixed KOH/K_2CO_3 solution, did not effect the performance either, although the cubic crystals of $CaCO_3$ were better defined, and the Ag particles were somewhat sintered compared to the preparation using the K_2CO_3 solution without KOH. High selectivities were obtained by using a combination of the KOH/K_2CO_3 basic solution and La in the precursor solution. A selectivity of 31% to PO was obtained, which is close to the performance of the Arco catalysts. Variation of the amount of La affects the obtained selectivity; 7 wt% La gave the best selectivity. Addition of La also slightly enhanced the activity of the catalyst.

Table 1.2 Analytical data for various precipitated $Ag/CaCO_3$ catalysts. The K, La, Ca and Ag quantities were determined by ICP analysis.

Catalyst	Sel.	XRD	SEM	K	La	Ca*	Ag
Base Case	8	Ag $CaCO_3$	*$CaCO_3$*: Cubes and spheres *Ag*: Round particles	0.07	—	64.5	48
Adding La	11	Ag LaO_2CO_3 $CaCO_3$	*$CaCO_3$*: Cubes – less defined, bigger *Ag*: Round, smaller, needle structures	0.38	8.2	54.7	41.3
Adding KOH	9	Ag $CaCO_3$	*$CaCO_3$*: Cubes – very well defined *Ag*: Round particles, sintered	0.07	—	64.5	45
KOH and La addition	31	Ag $CaCO_3$	*$CaCO_3$*: Cubes – less defined, bigger *Ag*: Small round agglomerated particles, web like structure	0.33	8.2	52	40.2

* Percentage given as weight percent $CaCO_3$. The composition usually adds up to 108–112%. This indicates that part of the Ca in the precursor solution precipitated as $Ca(OH)_2$, and is converted to CaO, rather than $CaCO_3$, upon calcination.

The catalysts prepared with La surprisingly contained a higher amount of K than those prepared without La. We suggest that La enhances potassium uptake as the catalyst forms, because part of the La precipitates as a mixed potassium lanthanum carbonate, i.e. $KLa(CO_3)_2$. A similar compound has been reported for sodium in the literature.[77] A second important observation is that the presence of both La and K in the catalyst does not necessarily induce a high selectivity, unless KOH is also employed in the basic K_2CO_3 solution. Omission of KOH from the basic solution results in a similar chemical composition (compare cases two and four in Table 1.2) but a much less selective catalyst. This is most likely a consequence of the precipitation procedure itself. Without KOH in the base, a step-wise precipitation

occurs, in which La (and K) is entirely precipitated first, followed by Ag (as the carbonate), and Ca (as the carbonate). With addition of KOH, a simultaneous precipitation of La (and K) and Ag occurs (indicated by the beige coloring of the precipitate), apparently increasing the interaction between the La (and K) and the Ag. This hypothesis is corroborated by EDAX analysis, which shows that La was always associated with Ag in the catalytic composition if a KOH/K_2CO_3 base composition had been used. Furthermore, SEM analysis showed that only the combination of the two modifications (OH^- addition to the base and the presence of La in the precipitation mixture), causes a unique web-like structure of the silver particles, supported by $CaCO_3$ crystallites that did not show a high degree of ordering. Relatively large $CaCO_3$ clusters formed, that had a less-defined cubic structure than observed in the catalysts prepared without La. These results suggest that a more amorphous structure of $CaCO_3$ leads to higher PO selectivity. The web-like structure of silver in the La-containing catalysts might provide increased surface area for increased activity and an open pore structure of the active sites for increased selectivity.

As a final note on preparation of these advanced catalysts, it should be mentioned that replacing Ca with Ba, and adding Cl to the preparation mixture yields the best catalyst obtained to date. The Ba-containing catalyst shows initial selectivities of up to 58% towards PO. Unfortunately, the selectivity decreased with time on stream and reached a steady state level of about 45% at 3% conversion at 235°C after 3 h. It should be noted that the 45% selectivity found for the Ba-containing catalyst is higher than obtained for the impregnated catalyst. Besides the addition of Cl to the catalyst, the synergy between $BaCO_3$, Ag and $La(OH)CO_3$ also seems to be even better than the synergy between $CaCO_3$, Ag and $La(OH)CO_3$.

1.3.3.4 *Understanding of the function of the components in the catalytic formulation*

Recently progress has been made to optimize the composition of the Ag catalyst. A crucial factor of the incorporation of the K or Na in the catalyst formulation is the effect of this promoter on the particle

size of the Ag clusters. Lambert and coworkers[41] have indicated that an optimized particle size of Ag is in the order of 20–40 nm. These particles are significantly bigger than previously indicated for Au catalysts, and were obtained by applying the impregnation procedures indicated in the patent literature. Also the group of Oyama[38] has demonstrated and confirmed the high performance of these catalyst formulations based on silver, and also indicated that not only the particle size, but also the Ag morphology changes as a function of the preparation conditions. More rough and less well structured Ag particles have been found as a result of a ball milling procedure, which in combination with particle sizes in the order of 400–700 nm provided the most effective catalysts. Also the positive effect of NaCl on the catalyst performance was confirmed.[38] These authors propose that NaCl not only helped increase the dispersion of the silver on the $CaCO_3$ support, but also probably increased the quantity of electrophilic oxygen species favorable for epoxidation.

Very recent literature indicates that Ag clusters of only several tens of atoms, also yield exceptionally high selectivities in epoxidation of alkenes, other than ethane.[78] The preparation of these clusters is currently only possible in very small quantities, and upscaling of the vacuum methodologies is very necessary.[79] Perhaps also atomic layer deposition, recently applied successfully,[80–82] could provide for a solution, in particular if this becomes feasible in a continuous mode of operation.

1.4 General Conclusions on the Preparation of Metal Catalysts

In this chapter, an overview has been presented on the common techniques for the preparation of catalysts in the laboratory. It was by no means meant as being a complete guide to the preparation of metal catalysts, but the authors hope to have given some basic principles, as well as some case studies that provide some new and useful information to the reader, especially those interested in the preparation of Pt, Au and Ag catalysts. Of the preparation techniques mentioned, impregnation is often the easiest to apply, but in the

example of the Au catalysts it was shown that only by precipitation of the precursor at fixed pH were selective catalysts obtained. In the case of the advanced Ag catalysts, the used preparation procedure in the literature (impregnation with organic precursors) could be simplified by precipitation, using promoters that steer the precipitation sequence and capture alkali ions from the solution, incorporating these in the catalysts. We hope to have shown using the example of the Pt catalysts that not only do the conditions for the impregnation or precipitation itself (such as pH of solutions, suspension densities, rate of base addition, stirring of the suspension etc.) have a profound effect on the behavior and structure of the catalysts eventually obtained, but also the applied drying procedures and, even more importantly, the heat treatment. It is the hope of the authors that future publications in the catalysis literature will pay more attention to the preparation procedure used, to allow a better comparison of catalysts in different laboratories, and to obtain improved catalysts for the desired applications.

References

1. J.W. Geus, A.J. Van Dillen, in *Handbook of Heterogeneous Catalysis, Vol. 1*, Eds.: G. Ertl, H. Knötzinger, J. Weitkamp, Wiley-VCH, Weinheim, 1997, 240.
2. J.W. Geus, J.R. van Veen, in *Catalysis, An Integrated Approach to Homogeneous, Heterogeneous, and Industrial Catalysis*, J.A. Moulijn, R.A. van Santen, P.W.N.M. van Leeuwen. Elsevier, Amsterdam, 1999, 467.
3. Z.Y. Zhong, J.Y. Lin, S.P. Teh, J. Teo, F.M. Dautzenberg, *Adv. Funct. Mater.* 2007, **17**, 1402.
4. G. Colon, M. Maicu, M.C. Hidalgo, J.A. Navio, A. Kubacka, M. Fernández-García, *J. Mol. Catal. A: Chem.* 2010, **320**, 14.
5. J. Ohyama, K. Teramura, S. Okupka, S. Yamazoe, K. Kato, T. Shishido, T. Tanaka, *Langmuir* 2010, **26**, 13907.
6. J.T. Carneiro, C.C. Yang, J.A. Moma, J.A. Moulijn, G. Mul, *Catal. Lett.* 2009, **129**, 12.
7. A. Hugon, N. El Kolli, C. Louis, *J. Catal.* 2010, **274**, 239.
8. S.Y. Lee, R. Aris, *Catal. Rev.-Sci. Eng.* 1985, **27**, 207.

9. A.A. Lysova, J.A. Bergwerff, L. Espinosa-Alonso, B.M. Weckhuysen, I.V. Koptyug, *Appl. Catal. A: Gen.* 2010, **374**, 126.
10. A.J. van Dillen, R. Terorde, D.J. Lensveld, J.W. Geus, K.P. de Jong, *J. Catal.* 2003, **216**, 257.
11. A. Cybulski, J.A. Moulijn, *Catal. Rev.-Sci. Eng.* 1994, **36**, 179.
12. A. Cybulski, A. Stankiewicz, R.K.E. Albers, J.A. Moulijn, *Chem. Eng. Sci.* 1999, **54**, 2351.
13. A.K. Heibel, J.J. Heiszwolf, F. Kapteijn, J.A. Moulijn, *Catal. Today* 2001, **69**, 153.
14. T.A. Nijhuis, A.E. Beers, T. Vergunst, I. Hoek, F. Kapteijn, J.A. Moulij, *Catal. Rev.-Sci. Eng.* 2001, **43**, 345.
15. T. Vergunst, M.J.G. Linders, F. Kapteijn, J.A. Moulijn, *Catal. Rev.-Sci. Eng.* 2001, **43**, 291.
16. P. Burattin, M. Che, C. Louis, *J. Phys. Chem. B* 1998, **102**, 2722.
17. J.W. Geus, *Stud. Surf. Sci. Catal.* 1983, **16**, 1.
18. P.V. Geenen, H.J. Boss, G.T. Pott, *J. Catal.* 1982, **77**, 499.
19. C.J.G. Vandergrift, A.Q.M. Boon, A.J.W. Vanveldhuizen, H.G.J. Trommar, J.W. Geus, J.F. Quinson, M. Brun, *Appl. Catal.* 1990, **65**, 225.
20. G. Mul, A.S. Hirschon, *Catal. Today* 2001, **65**, 69.
21. I. Melian-Cabrera, M.L. Granados, J.L.G. Fierro, *Phys. Chem. Chem. Phys.* 2002, **4**, 3122.
22. J. Perez-Ramirez, G. Mul, F. Kapteijn, J.A. Moulijn, *J. Mat. Chem.* 2001, **11**, 2529.
23. J. Perez-Ramirez, G. Mul, J.A. Moulijn, *Vib. Spec.* 2001, **27**, 75.
24. A.P. Kozlova, S. Sugiyama, A.I. Kozlov, K. Asakura, Y. Iwasawa, *J. Catal.* 1998, **176**, 426.
25. H. Liu, A.I. Kozlov, A.P. Kozlova, T. Shido, K. Asakura, Y. Iwasawa, *J. Catal.* 1999, **185**, 252.
26. C. Mihut, B.D. Chandler, M.D. Amiridis, *Catal. Comm.* 2002, **3**, 91.
27. K. van Gorp, PhD Thesis, Utrecht University (1996).
28. C.Y. Kim, C.Y. Jung, J.W. Jung, S.H. Jeong, S.C. Yi, W.J. Kim, *Mater. Res. Bull.* 2010, **45**, 1419.
29. K. Maeda, K. Teramura, D.L. Lu, N. Saito, Y. Inoue, K. Domen, *J. Phys. Chem. C* 2007, **111**, 7554.
30. S.K. Lim, S.K. Lee, S.H. Hwang, H. Kim, *Macromol. Mat. Eng.* 2006, **291**, 1265.

31. J.M. Herrmann, J. Disdier, P. Pichat, *J. Phys. Chem.* 1986, **90**, 6028.
32. M.C. Hidalgo, M. Maicu, J.A. Navio, G. Colon, *J. Phys. Chem. C* 2009, **113**, 12840.
33. L.Z. Zhang, J.C. Yu, H.Y. Yip, K.W. Kwong, A.W. Xu, P.K. Wong, *Langmuir* 2003, **19**, 10372.
34. G. Mul, A. Zwijnenburg, B. van der Linden, M. Makkee, J.A. Moulijn, *J. Catal.* 2001, **201**, 128.
35. A. Ruiz, B. van der Linden, M. Makkee, G. Mul, *J. Catal.* 2009, **266**, 286.
36. J.J. Bravo-Suarez, K.K. Bando, T. Fujitani, S.T. Oyama, *J. Catal.* 2008, **257**, 32.
37. J.J. Bravo-Suarez, K.K. Bando, J.I. Lu, M. Haruta, T. Fujitani, S.T. Oyama, *J. Phys. Chem. C* 2008, **112**, 1115.
38. J.Q. Lu, J.J. Bravo-Suarez, M. Haruta, S.T. Oyama, *Appl. Catal. A: Gen.* 2006, **302**, 283.
39. J.Q. Lu, J.J. Bravo-Suarez, A. Takahashi, M. Haruta, S.T. Oyama, *J. Catal.* 2005, **232**, 85.
40. A. Palermo, A. Husain, M.S. Tikhov, R.M. Lambert, *J. Catal.* 2002, **207**, 331.
41. F.W. Zemichael, A. Palermo, M.S. Tikhov, R.M. Lambert, *Catal. Lett.* 2002, **80**, 93.
42. J. de Graaf, A.J. van Dillen, K.P. de Jong, D.C. Koningsberger, *J. Catal.* 2001, **203**, 307.
43. A.R. Vaccaro, G. Mul, J. Perez-Ramirez, J.A. Moulijn, *Appl. Catal. B: Env.* 2003, **46**, 687.
44. P. Briot, A. Auroux, D. Jones, M. Primet, *Appl. Catal.* 1990, **59**, 141.
45. R. Burch, P.J. Millington, *Catal. Today* 1995, **26**, 185.
46. P. Loof, B. Stenbom, H. Norden, B. Kasemo, *J. Catal.* 1993, **144**, 60.
47. S. Schneider, D. Bazin, G. Meunier, R. Noirot, M. Capelle, F. Garin, G. Maire. *Catal. Lett.* 2001, **71**, 155.
48. E. Xue, K. Seshan, J.R.H. Ross, *Appl. Catal. B: Env.* 1996, **11**, 65.
49. L.M. Carballo, E.E. Wolf, *J. Catal.* 1978, **53**, 366.
50. M.C. Demicheli, L.C. Hoang, J.C. Menezo, J. Barbier, M. Pinabiaucarlie, *Appl. Catal. A: Gen.* 1993, **97**, L11.
51. R.F. Hicks, H.H. Qi, M.L. Young, R.G. Lee, *J. Catal.* 1990, **122**, 280.
52. R.F. Hicks, H.H. Qi, M.L. Young, R.G. Lee, *J. Catal.* 1990, **122**, 295.
53. T.F. Garetto, C.R. Apesteguia, *Appl. Catal. B: Env.* 2001, **32**, 83.

54. A. Monzon, T.F. Garetto, A. Borgna, *Appl. Catal. A: Gen.* 2003, **248**, 279.
55. H.H. Kung, M.C. Kung, C.K. Costello, *J. Catal.* 2003, **216**, 425.
56. J.T. Carneiro, T.J. Savenije, G. Mul, *Phys. Chem. Chem. Phys.* 2009, **11**, 2708.
57. E. Dokou, E.E. Stangland, R.P. Andres, W.N. Delgass, M.A. Barteau, *Catal. Lett.* 2000, **70**, 1.
58. M. Haruta, B.S. Uphade, S. Tsubota, A. Miyamoto, *Res. Chem. Int.* 1998, **24**, 329.
59. T. Hayashi, K. Tanaka, M. Haruta, *Abstr. Pap. Am. Chem. S.* 1996, **211**, 42.
60. C.X. Qi, T. Akita, M. Okumura, M. Haruta, *Appl. Catal. A: Gen.* 2001, **218**, 81.
61. A.K. Sinha, S. Seelan, S. Tsubota, M. Haruta, *Angew. Chem. Int. Ed.* 2004, **43**, 1546.
62. E.E. Stangland, K.B. Stavens, R.P. Andres, W.N. Delgass, *J. Catal.* 2000, **191**, 332.
63. B.S. Uphade, M. Okumura, S. Tsubota, M. Haruta, *Appl. Catal. A: Gen.* 2000, **190**, 43.
64. T.A. Nijhuis, PhD Thesis, Delft University of Technology (1997).
65. T.A. Nijhuis, B.J. Huizinga, M. Makkee, J.A. Moulijn, *Ind. Eng. Chem. Res.* 1999, **38**, 884.
66. O. Lopez-Acevedo, K.A. Kacprzak, J. Akola, H. Hakkinen, *Nat. Chem.* 2010, **2**, 329.
67. S.R. Bare, *J. of Vac. Sci. Techn. A: Vac. Surf. and Films* 1992, **10**, 2336.
68. C.J. Bertole, C.A. Mims, *J. Catal.* 1999, **184**, 224.
69. I. Pastoriza-Santos, D.S. Koktysh, A.A. Mamedov, M. Giersig, N.A. Kotov, L.M. Liz-Marzan, *Langmuir* 2000, **16**, 2731.
70. T. Teranishi, I. Kiyokawa, M. Miyake, *Adv. Mat.* 1998, **10**, 596.
71. W.L. Dai, J.L. Li, Y. Cao, Q. Liu, J.F. Deng, *Catal. Lett.* 2000, **64**, 37.
72. A. Henglein, M. Giersig, *J. Phys. Chem. B* 1999, **103**, 9533.
73. M.V. Badani, M.A. Vannice, *Appl. Catal. A: Gen.* 2000, **204**, 129.
74. S.N. Goncharova, E.A. Paukshtis, B.S. Balzhinimaev, *Appl. Catal. A: Gen.* 1995, **126**, 67.
75. M.R. Salazar, J.D. Kress, A. Redondo, *Surf. Sci.* 2000, **469**, 80.
76. M.A. Al-Juaied, D. Lafarga, A. Varma, *Chem. Eng. Sci.* 2001, **56**, 395.
77. H. Schweer, H. Seidel, *Z. Anorg. Allg. Chem.* 1981, **477**, 196.

78. Y. Lei, F. Mehmood, S. Lee, J. Greeley, B. Lee, S. Seifert, R.E. Winans, J.W. Elam, R.J. Meyer, P.C. Redfern, D. Teschner, R. Schlogl, M.J. Pellin, L.A. Curtiss, S. Vajda, *Science* 2010, **328**, 224.
79. S. Vajda, S. Lee, K. Sell, I. Barke, A. Kleibert, V. von Oeynhausen, K.H. Meiwes-Broer, A.F. Rodriguez, J.W. Elam, M.M. Pellin, B. Lee, S. Seifert, R.E. Winans, *J. Chem. Phys.* 2009, **131**, 121104.
80. S.T. Christensen, H. Feng, J.L. Libera, N. Guo, J.T. Miller, P.C. Stair, J.W. Elam, *Nano Lett.* 2010, **10**, 3047.
81. S.S. Lee, B. Lee, F. Mehmood, S. Seifert, J.A. Libera, J.W. Elam, J. Greeley, P. Zapol, L.A. Curtiss, M.J. Pellin, P.C. Stair, R.E. Winans, S. Vajda, *J. Phys. Chem. C* 2010, **114**, 10342.
82. W. Setthapun, W.D. Williams, S.M. Kim, H. Feng, J.W. Elam, F.A. Rabuffetti, K.R. Poeppelmeier, P.C. Stair, E.A. Stach, F.H. Ribeiro, J.T. Miller, C.L. Marshall, *J. Phys. Chem. C* 2010, **114**, 9758.

CHAPTER 2

DETERMINATION OF DISPERSION AND CRYSTALLITE SIZES FOR SUPPORTED METAL CATALYSTS

J. A. Anderson[1], M. Fernández-García[2] and A. Martínez-Arias[2]

[1]*Surface Chemistry and Catalysis Group, Department of Chemistry, University of Aberdeen, Kings College, Aberdeen, Scotland, UK*

[2]*Instituto de Catálisis y Petroleoquímica, CSIC, C/Marie Curie, Cantoblanco, 28049 Madrid, Spain*

2.1 Introduction

The aim of any dispersion measurement (Dispersion, D) for a supported metal should be to determine the ratio of the number of surface metal atoms (N_s) to the total number of metal atoms (N_t) within the system, i.e.

$$D = N_s/N_t. \tag{2.1}$$

Although more rigorous quantitative descriptions of dispersion can be employed,[1] for the purpose of the present chapter, this will suffice. In general, a measurement of dispersion is obtained either by chemical means whereby the amount of gas (usually carbon monoxide, oxygen or hydrogen) required to complete monolayer coverage is determined, or by physical means whereby an average particle size is found from which the surface/bulk ratio may be determined by making an assumption regarding particle shape. In either case, the

outcome provides a means by which metal surface area may be calculated and thus permit the activity of a group or series of catalysts to be compared on a per site or unit area basis rather than a per gram of metal basis, which given the surface nature of catalysis, allows a more appropriate method of comparison. However, neither method allows discrimination between active/inactive sites or accounts for the fact that a reactant molecule may require more than one metal atom as an adsorption site or require a particular arrangement of metal atom sites, and thus presentation of actual figures for turn-over frequency (activity per unit site) derived following measurement of dispersion should be considered as a method of comparison rather than as a stand-alone value of true significance. Notwithstanding the limitations arising from the use of dispersion derived values to compare activities, the determination of dispersion provides a valuable method by which different preparation methods may be compared in an effort to optimize metal area, and allows the extent of deactivation due to sintering and poisoning to be measured.

2.2 General Considerations

2.2.1 *Physical methods*

Physical methods for size determination are mainly related to the use of X-ray based diffraction, scattering and absorption techniques, microscopy, and magnetic measurements. Physical and chemical methods may be combined, for example in the use of infrared spectroscopy coupled to the use of probe molecules such as CO to determine the fraction of exposed metal atoms. However, as Chapter 4 will deal with characterization of supported metal systems by X-ray absorption and infrared spectroscopies in some detail, they will not be included here.

2.2.1.1 *XRD*

As indicated above, physical methods provide a means by which the dispersion is derived from measurement of particle size. In actual

fact, the value referred to as particle size when obtained by X-ray diffraction, should be termed crystallite size as the particle may contain several crystallites and the parameter being measured is the effective length in the direction of the diffraction vector along which there is coherent diffraction. Additionally, for the case of X-ray diffraction, the value obtained is inherently an average value given that the sample will contain a distribution of particle sizes and the quantity to be determined from the XRD pattern is the line broadening, β, which is related to the particle size D by the Scherrer equation:

$$D = \frac{k\lambda}{\beta \cos \theta} \tag{2.2}$$

where λ is the wavelength of the radiation employed, θ is the Bragg angle and *k* is a constant which depends on the shape of the crystallite. The standard method of obtaining a value for line broadening ($\beta_{1/2}$) involves measurement in radians of the full width of the diffraction line at half maximum (FWHM). However, it is also possible to obtain a value (β_1) by measuring the integral width over the whole reflection intensity and dividing this by the intensity maximum. The value of constant *k* also depends on the method used to determine peak width (and on particle shape) and lies between 0.84 and 0.89 when $\beta_{1/2}$ is used, or between 1.00 and 1.16 when β_1 is employed. Crystallite size is not the only source of line broadening in a difractogram. However, instrumental broadening can be accounted for by measurement of a reference profile (e.g. NaCl or quartz) which involves a sample of crystallite size > slit width. Assuming the profiles have a Gaussian shape, the value β may be obtained from $\beta^2 = \beta_s^2 - \beta_R^2$, where the subscripts S and R refer to the sample and reference peaks, respectively. Additional strain effects on line shape and width must be also considered, as detailed below.

The intensity of the diffracted radiation is related to the square of the atomic number and hence for the case of supported metal catalysts, the lower limit of sensitivity is likely to fall around 0.3 to 0.8 wt% loading. Additionally, once the crystallite size falls below *ca.* 2–4 nm, the diffraction line becomes so broad and

diffuse as to render difficult extraction by subtraction from the background signal due to the support. Background subtraction is a common method of obtaining the XRD pattern of the supported metal component although it is also possible to determine the metal fraction responsible for the peaks due to the latter, by employment of suitably adapted quantitative Rietveld analysis. In the former approach, it is usually necessary to perform appropriate scaling of the signal due to the support pattern until the latter may be correctly superimposed over different wide ranges of the supported catalyst pattern. Although information may be derived from use of a peak due to a single reflection (usually the most intense peak), information may be extracted using the whole diffraction profile by the use of Fourier analysis,[2] although in the case of supported metal catalysts, this is often limited to a few reflections. The advantage of employing Fourier analysis over several diffraction lines is that lattice microstrain analysis is possible by employing the Warren–Averbach method.[3]

$$\ln A\left(L, \frac{1}{d_{hkl}^{\,2}}\right) = \ln[A^{s}(L)] - \frac{2\pi\left\langle \varepsilon^{2}(L)\right\rangle}{d_{hkl}^{\,2}} L^{2} \tag{2.3}$$

The remaining contribution to the instrument corrected Fourier whole transform, A(L), of the peak profile, yields surface weighted average sizes from L-axis intercepts of tangents drawn to the $A^{s}(L)$ transformed profiles,[4] where the latter refers to the Fourier transform due only to size effects. Multiplication of the derived value by 3/2 yields the diameter for a single spherical particle,[4] and may hold for a distribution of differently sized spherical particles.[5] Line broadening analysis and X-ray scattering are both covered in a relevant review chapter concerning X-ray techniques in catalysis,[6] and in a review document dealing with supported catalysts.[7]

2.2.1.2 *X-ray scattering*

In addition to line broadening, metal particle size for a supported metal catalyst may be determined from X-ray scattering techniques

such as Wide Angle X-ray Scattering (WAXS) and Small Angle X-ray Scattering (SAXS). The latter techniques measure particle size whereas line broadening measures crystallite size. This may give rise to differences in information obtained by line broadening and SAXS (or TEM) where multidomain particles are present. Advances in the employment of Anomalous Wide Angle X-ray Scattering (AWAXS) have recently been reviewed.[8] These techniques have received less widespread application than XRD as they are less commonly available. Additionally, both AWAXS and ASAXS require the use of synchrotron sources and reliability of results obtained depend upon the metal under investigation. SAXS is limited to applications where there is a similarity between the scattering characteristics of the support and the supported metal particles, which permits a straightforward subtraction of the former to obtain the required information regarding the metal crystallites. However, this condition is seldom met due to interference effects originating between the metal particles and the pores. Pore maskant methods, involving the use of materials such as CH_2I_2 with similar electron density as the support, may be employed to overcome this effect[9] although application is not straightforward. Compressing the samples at extremely high pressures to collapse the pores has also been applied. An alternative involves the use of ASAXS.[8]

2.2.1.3 *Magnetic measurements*

The magnetic properties of small ferromagnetic particles have been observed to display important size dependence.[10–12] This is useful in obtaining particle size information in catalysts containing a supported ferromagnetic metal (among individual transition metals, Fe, Co, and Ni, although mixtures of these with other metals can also present such a property) or metallic oxide. When the particles are sufficiently small such that the particle magnetic moment can achieve thermal equilibrium in the time of the measurement, the ferromagnetic particles are said to behave as super-paramagnets, i.e. each particle can be considered as a paramagnetic centre with a gigantic magnetic moment (μ). Since the thermal barrier for magnetization relaxation is proportional

to the particle volume, the temperature at which such a state is achieved (so called blocking temperature or T_B) is inversely proportional to the particle size; for instance, for indicative purposes and considering the practical conditions employed in electron spin resonance (ESR) instruments, T_B is estimated as 61 K for 4 nm spherical particles in which the anisotropic magnetic field within the particles is assumed to be exclusively magnetocrystalline.[10,11] Below T_B the magnetization of the particles would depend on their magnetic history. However, above T_B, and assuming a system of non-interacting magnetic dipoles (as it occurs for well dispersed supported metal systems), the magnetization of the super-paramagnetic system (M(H,T)) follows a Langevin law and its susceptibility a Curie function:[10,11]

$$M(H,T) = M_s(T)L(\chi)$$
$$L(\chi) = \coth(\chi) - \chi^{-1}$$
$$\chi = \mu H/kT = M_s(T)VH/kT$$

where $M_s(T)$ is the spontaneous magnetization per unit volume, V the volume of the particles, H the applied external field, k the Boltzmann constant and T the temperature.

On this basis, a representation of the magnetization (that can be obtained in general with magnetometers or can be considered proportional to the ferromagnetic resonance signal obtained in ESR spectrometers) *vs.* temperature yields thermomagnetic curves as a function of the particle volume.[11] From comparison of experimental data with such curves, an estimation of the mean particle size can be obtained. Size distributions can also be obtained by a similar method, by considering the dependence of μ with the particle volume in the corresponding integral form.[12,13]

2.2.1.4 *TEM*

Transmission electron microscopy (TEM) is a powerful and routinely employed technique for the analysis of particle size and morphology in supported metal catalysts. A more thorough description of its uses and applications is provided in Chapter 3,

however for completeness, this overview is included in this chapter. The use of HRTEM, including studies of supported metal and bimetallic catalysts, and the inter-relationship with other techniques for structure determination, has recently been reviewed.[14] As an important difference with X-ray diffraction or scattering techniques or those based on measurement of magnetization (or other spectroscopic techniques that can be employed to obtain estimates of average particle size, such as EXAFS or IR employing probe molecules, as covered in Chapter 3 of this book) the possibility given by TEM of direct observation of individual particles allows size distributions for the supported metal component to be obtained, given that the information obtained can be considered as representative of the examined sample (i.e. that a sufficient number of particles is obtained in the micrographs for giving reliability of the counting statistical analysis; in this respect, the information obtained under low magnification conditions may suffice from a practical point of view).[4] The information provided by TEM is obtained in the form of micrographs (theoretical aspects of TEM imaging can be found elsewhere),[15–19] from which (mainly using those obtained in real space) particle size data are directly extracted either manually or with the use of computer programs. In principle, any of the techniques associated with the analysis of the electron beam transmitted by the sample (either classic bright- or dark-field TEM imaging, analysing essentially the main central or a determinate diffracted beam, respectively, high resolution electron microscopy (HREM) employing usually both the main central and diffracted beams to form the image, or scanning transmission electron microscopy with high angle annular dark-field detection (STEM-HAADF) analysing the inelastically scattered beam at high angles and giving rise to Z-contrast images) can be employed to analyse supported metal characteristics.[4,20–24] In the case of supported metal catalysts essentially constituted by two different phases, differential contrast analysis which depends essentially on the structural and chemical characteristics of each of the phases as well as on general morphological aspects of the sample mainly determines the type and quality of the information

obtained.[4,20] In any case, the usual large differences in atomic numbers between the metal and its support facilitates the identification of small metal particles in the micrographs while determination of particle size from the micrographs does not necessarily require a detailed interpretation of the contrasts obtained in the pictures. Nevertheless, computer simulations might be needed to analyse every specific case and in particular to establish the detection limit of the technique,[20,21] as will be outlined below. Several monographs or review articles are available in the literature containing examples on the use of this technique for particle size or morphology analysis in supported metal systems.[20–22,24]

Despite the invaluable information that can be gained using TEM techniques on the properties of the supported metal component (or the support itself) of this type of system, several inherent characteristics of the technique must be taken into account and controlled in order for proper characterization of the metal particles to be obtained. Thus, interactions of the sample with the electron beam can lead to sample damage as a consequence of effects of charging or melting-sintering-recrystallization of the metallic particles.[4] In this respect, the electrical and thermal properties of the support can play a role in dissipating electrical or thermal energy, thus minimizing such effects.[4] On the other hand, modifications induced in the metallic particles as a consequence of the necessity to expose the catalyst to air in the absence of a controlled atmosphere (or *in situ*) instruments must be also taken into account.

A relevant point in the analysis of particle size by TEM is related to the detection limit of the technique. In the general case, such a limit is both sample and instrument dependent, its most precise determination requiring image simulation of structural models of the supported metal catalyst.[20–22] A complete example of application of this method to HREM images of Rh/CeO_2 systems has been reported by Bernal *et al.*,[21] showing a detection limit for the rhodium particles of about 1 nm in either profile or planar view.[21,25] In general terms, particles larger than 1 nm can be readily detected both by bright- or dark-field electron microscopy although in most favourable cases, a lower limit can be reached as demonstrated by the

successful HREM bright-field imaging of 3-atom clusters of Os on alumina.[20] Nevertheless, general detection of small metallic clusters is most favoured in STEM-HAADF instruments as a consequence of the higher sensitivity to atomic number differences.[22,24]

On the other hand, estimates of the metal dispersion have been achieved by use of HREM.[26] Thus, such parameters can be inferred from the particle size distribution by assuming a certain metal particle geometry (equations relating this to N_s and N_t being available),[27] structure and orientation with respect to the support.[25,26] Application of such an approach becomes extremely useful in cases when such a parameter cannot be readily obtained by chemical methods as a consequence of relatively strong spillover phenomena, such as that which occurs for systems supported on ceria-related materials.[25,26,28]

2.2.2 *Chemical methods*

2.2.2.1 *Chemisorption*

Unlike physical methods, where a direct measurement of metal crystallite size is made, chemisorption methods provide a surface average crystallite size *via* adsorbate-surface metal atom interactions. This may require that certain assumptions are made such as that all surface metal atoms are free from other adsorbates such as coke or other poisons, that the surface metal atoms are all in an appropriate oxidation state (usually zero) and that the adsorption stoichiometry is known and is independent of crystallite size. The assumption regarding the metal being free from coke or other poisons accumulated during use, implies that the accuracy with which chemisorption determines dispersion for a used catalyst may not be as good as for a fresh catalyst and that other physical methods may be more appropriate. Depending on how the measurement is made, for example by static or dynamic means, the strength and kinetics of the adsorption may also be important. Although several, if not all of the above, may be determined, it is clear that chemical methods require much more rigorous control over preparation and pre-treatment than their physical counterparts in order to

avoid inaccurate determination of dispersion or particle size. As the main adsorbate molecules used in determining dispersion (hydrogen, oxygen, carbon monoxide and nitrous oxide) are adsorbed in a known manner over reduced metal surfaces, an important step prior to measuring gas uptake is pre-reduction of the surface. As it is important that this treatment is not so severe as to modify the dispersion of the supported metal catalyst, it is possible that a fraction of the metal remains in an unreduced state. This fraction may be significant, for example low loaded nickel catalysts are often less than 30% reduced.[29] It is therefore important to either confirm that complete reduction is achieved under the selected pre-treatment condition, or to perform an evaluation to determine the percentage reduction. This may be achieved by conducting a TPR (temperature programmed reduction) with calibrated TCD (thermal conductivity detector) signal or an isothermal gravimetric measurement in hydrogen at the selected reduction temperature. It is also possible to determine the reducible fraction by reacting the reduced catalyst with oxygen at a temperature at which bulk, stoichiometric oxide is formed and measuring the oxygen consumed. For example, O_2 uptake at 723 K is assumed to convert Ni to NiO from which the proportion of reduced Ni in the catalyst might be determined.[29] Sample pre-treatment procedures for supported Pt Ni, Cu and Pd catalysts are outlined in a British Standards document.[30]

2.2.2.2 *Choice of method*

The quantity of molecules selectively chemisorbed by the metallic component of the catalyst may be determined by what are commonly described as static (volumetric) or dynamic (flow) methods. The former is performed at reduced pressure and involves allowing the system to reach equilibrium between the adsorbed and gaseous states. The later group of methods, which involves pulsed chemisorption, are generally performed at atmospheric pressure and the equilibrium between adsorbed and gas states is not achieved (or maintained).

Static methods

This is conducted under isothermal conditions and involves dosing gas from a chamber of known volume into a vessel containing the sample which has previously been pre-treated (reduced) and then outgassed under high vacuum conditions. A low pressure of gas from the calibrated vessel is expanded into the vessel containing the catalyst and the system allowed to reach equilibrium. Equilibration time may range from 5 min to 1 h. The number of moles consumed by the metal is measured from the decrease in pressure of the system beyond that due to gas expansion. This measurement is repeated by increasing the pressure of gas admitted to the sample and again allowing equilibrium to be attained. The volume of gas adsorbed by the sample (V_a) at each equilibrium pressure is then plotted (Fig. 2.1) against equilibrium pressure (usually a minimum of five data points) to yield the adsorption isotherm. The plot usually takes the form of a steadily increasing curve terminated by a plateau region during which the sample shows no further increase in uptake despite increased gas pressure. When the isotherm takes this form and conforms to the Langmuir model, the volume of the chemisorbed monolayer (V_m) is determined by extrapolation of the linear region of the isotherm to $P_{eq} = 0$. This procedure, involving deriving V_m by extrapolation of the linear part of the isotherm, may

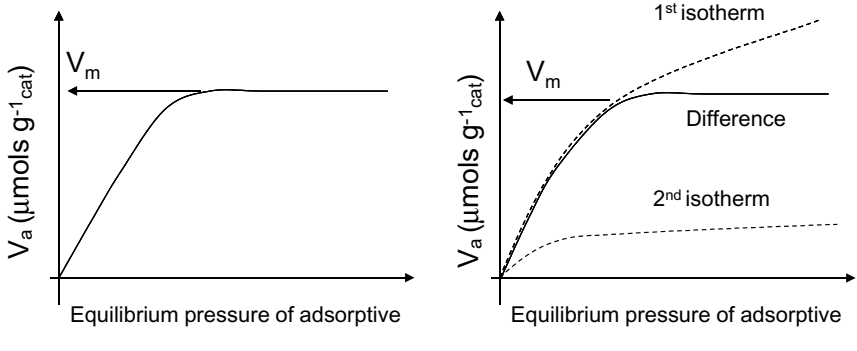

Figure 2.1 Adsorption isotherms where the monolayer is obtained (LHS) directly from the isotherm or (RHS) from application of the double isotherm method.

also be employed when the linear part shows a progressive increase in V_a with increasing P_{eq}. The reason for this progressive rise may be the consequence of progressive removal of a poison which is displaced as the adsorbate pressure is increased. Under these conditions, the isotherm no longer shows such a characteristically sharp "knee". One example of this behaviour[31] is when the catalysts contains Cl^- ions, either due to selection of the catalyst precursor or resulting from the use of Cl containing gases during regeneration treatments of sintered catalyst.

However, the most common reason for the rise in the linear part of the isotherm is the result of weak adsorption resulting either from direct adsorption onto the support or resulting from spillover of the adsorbate onto the support following activation on the metal component of the catalyst. In order to distinguish this "reversible" form of adsorption from the "irreversible" form due to adsorption on the metal, it is common practice to measure a second adsorption isotherm immediately following the measurement of the first isotherm but intervened by a brief period of evacuation at the adsorption temperature. Subtraction of the second isotherm (reversible component) from the first isotherm (total adsorption) provides a measure of the strongly chemisorbed gas (Fig. 2.1). This double isotherm method has received significant criticism[32,33] since the amount of adsorbed gas removed by evacuation is largely a consequence of experimental rather than thermodynamic parameters. For example, the pumping speed and evacuation time are crucial in determining how much "weakly" adsorbed species are removed[32,33] although 30 min is the usually recommended period of evacuation.[30]

As there is a difference between the heat of adsorption of this "weakly" bound adsorbate on the support and the more strongly bound "irreversible" adsorption on the metal, it is possible to determine monolayer capacity of the metal by noting the value of coverage at which the heat of adsorption abruptly decreases to give a constant value.[33] Heats of adsorption may be obtained from isochore type measurements where variations in pressure are measured while varying the temperature after exposing the catalyst to different initial amounts of adsorbate.

Dynamic methods

These are usually more rapid than static methods as it is unnecessary to carry out calibration (e.g. to determine free space) and it is not essential to allow equilibration between gaseous and adsorbed states to occur. Dynamic methods may be the most suitable method for determination of certain metal surface areas, for example the determination of copper metal area by reactive frontal chromatography.[34] In this method, the sample is reduced and then held in a flow of He. To this He is added a low concentration of N_2O while the sample is held at a temperature below that at which bulk oxidation might be expected. The amount of N_2 released prior to N_2O breakthrough is determined by either TCD or mass spectrometer and thus corresponds to the amount of oxygen atoms chemisorbed of the metal surface. Knowing the stoichiometry between surface metal atoms and chemisorbed oxygen atoms allows calculation of metal surface area and thus dispersion and average crystallite size. This method has been most widely used for the determination of copper dispersion, although it has also been applied to supported Ru catalysts.[35] While the use of N_2O decomposition is most commonly applied using a flow of the diluted gas, it may also be employed by exposing the sample to calibrated pulses of N_2O.

Pulse chemisorption (Fig. 2.2) involves exposing the reduced catalyst to a number of pulses of adsorbate gas from a calibrated loop which are passed over the catalyst in a flow of inert carrier at atmospheric pressure. Early studies employed only a single pulse with a recommended volume of *ca.* twice the volume likely to be consumed.[36] The quantity of gas remaining (i.e. not adsorbed) from the pulse is measured by TCD and in a typical experiment the first two or three pulses would be completely consumed while only fractions of the subsequent peaks would be taken up by the sample. Eventually, the area of the peaks detected reaches a constant level indicating that the sample has reached monolayer capacity. The volume of gas adsorbed is calculated from the sum of the areas of peaks fully consumed plus the areas of the partially consumed peaks by equating the area of a peak eluted where no gas was taken up with

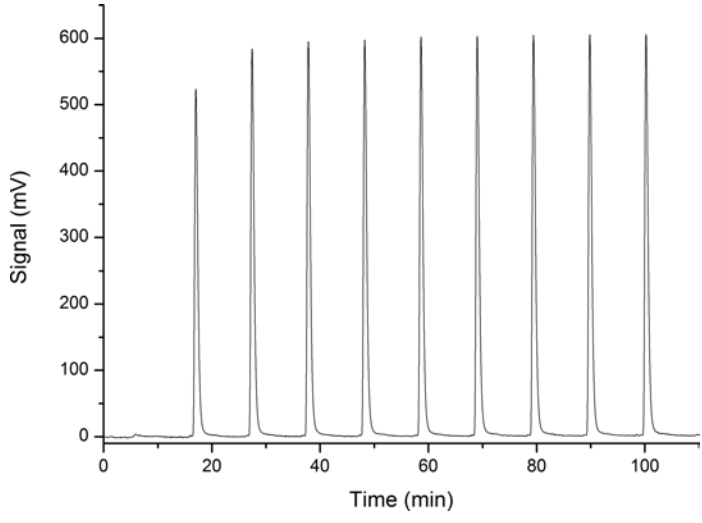

Figure 2.2 Example of pulse chemisorption where 0.285 cm^3 pulses of CO are introduced to the catalyst at 298 K every 10 min and the volume adsorbed is apparent from differences between the peak area of the initial peaks compared to the final (full area) peaks.

the volume of gas involved in each pulse. In actual fact, the area of the peaks eluted once no evidence for further adsorption is apparent are often smaller than those observed for a pulse in the absence of the catalyst. This is a consequence of an amount of weakly adsorbed gas which is released by the sample between pulses, and which results in an equivalent amount of the subsequent pulse being consumed. It is clear that pulse chemisorption measures only the amount of strongly or irreversibly adsorbed gas.

An alternative, dynamic method of determining the number of chemisorbed molecules/atoms, involves performing a measurement during the desorption rather than the adsorption stage. Temperature programmed desorption (TPD) involves measurement of the amount of gas released by the solid following pre-treatment (reduction), adsorption, and then a flushing stage in inert gas to remove weakly held and physisorbed contributions. This method has the advantage of providing details of the heterogeneity of the surface as indicated by the shapes of the profiles and the

proportions of molecules released at a particular temperature. However, high temperature desorption peaks may often be traced to release of gas from the support,[37] for example, hydrogen which was spilled over onto the support during the adsorption process and then released under TPD conditions as a result of re-oxidation of reduced surface sites by water or hydroxyl groups.[38]

2.2.2.3 *Choice of adsorptive*

The decision to use a particular adsorptive gas or procedure to determine the dispersion of a particular supported metal catalyst will involve the requirement to minimise adsorption on the support and on exposed, unreduced ions of the metal, avoid multilayer formation or absorption of the adsorptive and to form an adsorbed monolayer with a well-defined, uniform and known stoichiometric relationship between adsorbate and adsorbent. As this clearly differs from metal to metal, these will be addressed individually below, although common factors exist which may drive the choice of adsorptive irrespective of the metal being examined. For example, a preference for the use of CO over hydrogen as adsorptive is usually based on a concern that a fraction of the consumed hydrogen, particularly in the case of static measurements, may originate from adsorption on the support due to spillover from the metal to the support and involving hydroxyl groups on the latter. This may give rise to considerable overestimation of the H:M ratio, especially where supports involving oxygen storage components such as ceria or ceria-zirconia are concerned.[39,40] This may be overcome by performing the adsorption experiments at *ca.* 195 K rather than 298 K.[39,40] The additional complications of performing the adsorption at temperatures below 298 K to kinetically hinder the spillover process and which might also involve performing double isotherm measurements to determine the contribution from weakly bound species which are promoted under these conditions, means that a single experiment using CO at room temperature may prove to be the more attractive option. In fact, Perrichon *et al.*[40] have shown that for Pt/CeO_2-ZrO_2 catalysts the dispersion values provided by the

double isotherm method at 195 K using hydrogen are consistent with the CO chemisorption values obtained at room temperature where the latter is followed by FTIR spectroscopy which allows adsorption on the support to be distinguished from adsorption on the Pt surface. Although contributions from CO adsorbed on the support are generally neglected, it is known that CO is consumed by oxides such as alumina[41] and titania[42] at 298 K both directly as adsorbed CO at exposed Lewis acid sites in the oxide surface and in the form of carbonates, bicarbonates and formates.

Platinum

These are probably the most widely studied of all supported metal catalysts owing to their widespread use in reforming (see Chapter 6), automotive (see Chapter 8) and fine chemicals (see Chapter 9) applications. Carbon monoxide is often used to determine the dispersion of these catalysts although the appropriateness of assuming that the stoichiometry is equal to 1:1 depends strongly on the metal particle size. Vibrational spectroscopic studies of supported Pt catalyst provide clear evidence that both linear (1:1) and bridged (2:1) forms of carbon monoxide are normally present.[43–45] Less abundant, three-fold bridging sites (3:1) may also be present.[44] However, simple integration of the two main IR bands does not alone provide access to the bridged:linear ratio as the molar absorption coefficients are quite different for the two adsorbed forms, with the former having a value *ca.* ten times lower than the latter. Justification for the use of a 1:1 stoichiometry to calculate dispersion, based on the relatively low intensity of the bridged bound carbonyl is therefore not well founded. Gruber[36] provided an empirical correlation for CO on Pt to account for the change in CO:Pt ratio as a function of dispersion. However, this was based upon observation that the proportion of bridged carbonyls decreases as the dispersion decreases, which is at odds with some suggestions that bridge bonding predominates on large crystallites while linear bonding predominates on highly dispersed Pt.[46] Spectroscopic studies on the other hand, often find a decrease in the bridging : linear ratio following higher temperature reduction,[47] although this may be

attributed to an annealing of the particle surface and a change in morphology[47] rather than implying a change in dispersion.[36] Comparative studies report that although CO and H atoms chemisorb with similar stoichiometry on small Pt crystallites, large Pt crystallites adsorb relatively less of the former[48] which could be interpreted as a change in adsorption stoichiometry at lower dispersion. Rather than a change in stoichiometry at an individual adsorbate-adsorbent level, the reduction in overall CO consumption relative to hydrogen may reflect that the former adsorbate has a greater degree of sensitivity to the particular exposed crystal facets, the proportion of which will be highly dependent on the crystallite size.[49] For example, saturation coverage on the (110), (100) and (111) platinum single crystal faces is reached at CO:Pt values of 1.00:1,[50] 0.77:1,[51] and 0.64:1,[52] respectively, suggesting a reduction in CO adsorption stoichiometry with increasing Pt surface atom coordination. The EUROPT-1 (6.3% Pt/SiO_2) catalyst with a dispersion of *ca.* 60% as determined by TEM, consumed *ca.* 200 μmol g^{-1} H_2[53] but only 185–230 μmol g^{-1} CO[54], the latter consistent with a 1:1 CO:Pt stoichiometry and therefore inferring, that at this level of dispersion, the adsorption stoichiometry for hydrogen is greater than that of CO. However, additional consumption of hydrogen may be accounted for by spillover onto the support although this is more likely to account for greater hydrogen than CO uptakes at high dispersion when the amount of metal support interfaces sites is at its greatest. A further reason why measurements using CO and hydrogen may not correlate involves cases where the pre-treatment conditions fail to achieve complete reduction of the platinum as CO will adsorb on exposed Pt ions[45,55] while this is not expected of hydrogen. The fraction of unreduced Pt is seldom calculated or considered when determining Pt dispersion despite the fact that TPR traces of Pt catalysts, particularly in the presence of chloride, often show reduction features above 773 K.[56]

Assuming that spillover can be either suppressed or accounted for, hydrogen is usually the recommended[9,48] adsorptive for determining Pt dispersion as the H:Pt stoichiometry is well established from combined chemisorption, TEM and X-ray line broadening experiments as being 1:1.[48,57,58] However, there are indications that

at high dispersion, the H:Pt ratio may exceed one. Using isochore measurements, a hydrogen atom to total Pt ratio of 1.28:1 was obtained for the EUROPT-1 reference catalyst.[33] Given that the dispersion of Pt measured by various laboratories using TEM was around 60%[59,60] a $H:Pt_{(t)}$ of 1.28:1 would equate to an adsorption stoichiometry of around 2:1. However, TPD studies using the same catalyst,[53] revealed four states of adsorbed hydrogen including a high temperature desorption state which was assigned to spillover hydrogen on the silica support. When only the latter of the two states assigned to hydrogen on platinum was considered, good correlation was obtained between the dispersion calculated by TEM (60%) and chemisorption (65%). The neglected additional state due to adsorption on Pt which could be desorbed at *ca.* 200 K, was assigned to weak adsorption on low coordination sites which could adsorb more than one H atom or even molecularly adsorb H_2.[53] As these low coordination sites are likely to make a large contribution to the total number of exposed Pt sites on a well-dispersed catalyst,[49] the use of double isotherms and other procedures to allow for this contribution must be considered to avoid overestimation of dispersion where a 1:1 H:Pt stoichiometry is applied.

In the same way in which a H:Pt stoichiometry of 1:1 may be inappropriate at high Pt dispersion,[33] an O:Pt ratio of 1:1 may not be appropriate for determining Pt dispersion where small particles are involved and a value of less than 1 O:Pt should be used.[34,61] However, this finding is not supported by adsorption calorimetric studies of oxygen over Pt/TiO_2 catalysts with loadings between 0.001 to 1.83 wt% which concluded that the O:Pt stoichiometry was 1 for all catalysts.[62] Additionally, any oxygen consumed by the support was molecular compared to the dissociative adsorption on the metal and no spillover was evident. This contrasted with the significant amounts of hydrogen which were spilled over under similar experimental conditions.[38] An O:Pt ratio of 1:1 was found for the EUROPT-1 Pt/SiO_2 catalyst with high (65%) dispersion as determined by TEM,[54] although the outcome of the study conducted by many European laboratories was that oxygen chemisorption did not provide a reliable form of determining Pt dispersion due to its

potential to cause serious surface perturbations of Pt surface atom positions. There is also evidence to suggest that the stoichiometry of oxygen chemisorption on Pt is dependent on the thermal history of the catalyst, possibly reflecting changes from a defective form to an equilibrated form of lower surface free-energy.[48] This may also explain why repeated H_2-O_2 titration leads to enhanced hydrogen uptakes but reduced oxygen consumption.[55]

The use of H_2-O_2 titration is a method of enhancing the sensitivity relative to a standard hydrogen chemisorption measurement which involves the use of hydrogen to titrate a chemisorbed layer of oxygen.[63] The enhanced sensitivity results from an increased hydrogen consumption as the stoichiometry is raised to 3 H:1 Pt:

$$\text{Pt-O} + 1.5\ \text{H}_2 \rightarrow \text{Pt-H} + \text{H}_2\text{O}. \qquad (2.5)$$

Later studies[64] however, found that the stoichiometry of the titration was closer to 4:1 implying that Pt-H_2 species were formed. This difference in the values obtained by different laboratories may have been a consequence of the different dispersions being considered as Wilson and Hall[58] found that the ratio of O_2 chemisorption:H_2 titration ranged from 1:3.8 to about 1:3 for Pt/SiO_2 catalysts, with the latter value obtained for poorer dispersed catalyst as indicated by TEM and X-ray line broadening. However, rather than attributing this to the presence of Pt-H_2 species at high dispersion,[64] they concluded that it was the stoichiometry of the O_2 chemisorption which showed particle size dependence,[58] consistent with the proposal[61] that oxygen uptake on small particles is less than 1 atom per surface Pt.

Palladium

Unlike the case of supported Pt catalysts which show IR spectra of adsorbed CO to exist predominantly in the linear (1:1) form,[43,44] spectra of supported Pd catalysts also show significant contributions from bridged carbonyls.[65–67] Linear carbonyls (*ca.* 2,090 cm^{-1}) may arise due to adsorption on (111) type facets,[65] although for very small particles, a preference for linear carbonyl formation has been

observed.[68] This is consistent with results of a TPD and SSIMS study of Pd particles with mean diameter > 5 Å and < 5 Å which showed that CO on edge sites were adsorbed in the linear mode.[69] The bridged carbonyls reflect Pd:CO ratios of 2:1 and 3:1 and probably arise from adsorption on (100) and (111) type facets on small crystallites, respectively. However, as two-fold bridging sites may also exist at steps and edges on small crystallites, the ratio of linear:bridged sites may be low on small crystallites and show a dependence on dispersion. As the distribution of the different Pd facets varies with crystallite size[49] and the ratio of the maximum number of adsorbed molecules to number of surface Pd atoms differs from one plane to another,[70] a constant CO:Pd stoichiometry across a wide range of dispersions is not expected. Despite this, recent careful studies using X-ray line broadening, TEM, and SAXS to measure crystallite sizes for Pd supported on carbon, alumina and silica report that a Pd/CO stoichiometry of 2 is of general validity independent of the nature of the support or Pd dispersion when measurements are performed using pulse chemisorption.[5,71,72] The same authors had earlier reported that agreement between dispersion measurements obtained by CO chemisorption and SAXS could be obtained when using a Pd/CO chemisorption stoichiometry of 2 except in the case of the most dispersed Pd/SiO_2 catalyst where a stoichiometry of 1.3 was required for agreement with SAXS data.[73] Sheu *et al.*[74] reported that for a particle size of 50 Å the CO/Pd stoichiometry was around 1.9 but fell to about 1.65 for a particle size of 15 Å. The latter value is more consistent with the British Standards recommended value[30] which assumes an equal proportion of linear and bridged (two-fold) species are present and also with the Pd/CO ratio obtained by paramagnetic susceptibility measurements where the magnetisation of 1.5 Pd atoms could be cancelled out by the addition of each CO molecule.[75] This value also provided correlation with particle sizes obtained by TEM for Pd/SiO_2 catalysts[76] whereas a Pd:CO stoichiometry of 1:1 gave good correlation between dispersion and nitrobenzene hydrogenation activity,[77] and other examples of the use of the latter stoichiometry are commonplace.[78] The 2:1 Pd:CO ratio has also been used in

cases of selective deposition of promoters/poisons where a systematic removal of, in this example, on top sites would increase the average adsorption stoichiometry.[79]

In addition to CO adsorption by the support, CO may also be taken up by exposed Pd cations,[80] which may take the form of Pd^{3+}, Pd^{2+}, and Pd^{+66}. The concentration of unreduced palladium is seldom reported.

While the use of CO as adsorbate to determine dispersion suffers from the range of proposed CO:Pd stoichiometries, hydrogen is also a problematic adsorptive in that unless certain precautions are taken, both adsorption and absorption may occur. Exposure of supported Pd catalysts to hydrogen at room temperature leads to the formation of β-Pd-H_x where x decreases as the Pd dispersion increases.[73,81] While Boudart and Hwang[81] found that the solubility of hydrogen dropped to zero only when the dispersion approached 100%, Nandi *et al.*[82] report that the amount of β–hydride formed becomes insignificant for Pd dispersions greater than 30%. Although absorbed hydrogen in the β–hydride phase may be removed by outgassing at room temperature,[81] the procedure normally employed[70,80,83] to measure dispersion involves exposure of the supported Pd catalyst to hydrogen at 343 K to avoid its formation. One report indicates that even at 343 K, β–hydride was formed at hydrogen pressures above 80 Torr and suggested a maximum pressure of 20 Torr.[84] Under these conditions, minimal amounts of α-hydride were formed which overestimated the adsorption capacity of Pd/sepiolite catalyst by only *ca.* 2%. The use of higher temperatures may lead to an underestimation of the Pd surface area.[81] Although Pd is known to absorb hydrogen at low temperature, it has been argued[85] that the high temperature procedure is not essential and it is common to find adsorption temperatures between 298 and 308 K[75,78,85] being employed. Assuming that the formation of bulk hydride can be avoided, there is a general consensus[75,78,83–85] that the ratio of H:Pd equals 1:1 irrespective of the support type or Pd dispersion. A difference between average particle sizes determined by TEM and hydrogen chemisorption has been attributed[83] to polyhydride formation with an H/Pd stoichiometry greater than 1 for particles below 15 Å.

Although the maximum coverage obtainable for oxygen on the (111), (100) and (110) low index single Pd crystal surfaces is less than that for hydrogen or carbon monoxide[70] an O:Pd stoichiometry of 1:1 is often applied.[78,84,85] The use of this stoichiometry may underestimate Pd dispersion on supports where particles are formed with a predominance of (111) and (100) facets.[84] However, most studies involve a comparison of O_2 adsorption uptakes to hydrogen consumption data and thus rely on an assumed H:Pd ratio to determine the O:Pd stoichiometry. Assuming the H:Pd ratio to equal 1:1 then the O:Pd ratio is also equal to 1:1.[85] Concern over the use of oxygen adsorption to determine Pd dispersion is linked to the use of low evacuation temperatures which are employed to prevent sintering but may fail to remove hydrogen retained following pre-treatment. Some of these concerns may be overcome by the use of H_2/O_2 (or O_2/H_2) titration, which also has the advantage of increased gas uptake when dealing with catalysts of low dispersion. These titrations may be expressed as

$$2\ \text{Pd-H} + 1.5\text{O}_2 \rightarrow 2\text{Pd-O} + \text{H}_2\text{O} \qquad (2.6)$$

and

$$\text{Pd-O} + 1.5\ \text{H}_2 \rightarrow \text{Pd-H} + \text{H}_2\text{O}. \qquad (2.7)$$

Consistent with these reaction stoichiometries, titration of a 1%Pd/Al_2O_3 catalyst at 303 K led to the consumption of twice the number of moles of hydrogen as oxygen.[78] Under the same conditions, Pd/MnO_xCeO_2 catalysts showed significantly greater levels of gas adsorption, consistent with the spillover of both oxygen and hydrogen to the support at 303 K.[78] Martín *et al.*,[84] using TEM and WAXS as comparative experimental methods, reported that H_2-O_2 or O_2-H_2 titration gave a reliable estimate of dispersion for Pd/sepiolite catalysts but overestimated dispersion for $Pd/AlPO_4$. A recent study has suggested that Pd dispersion may be obtained by redox titration of adsorbed oxygen by the use of $FeCl_3$ solution.[86] Following the titration of sorbed hydrogen, differences between the amount of $K_2Cr_2O_7$ solution required to titrate the Fe^{2+} formed in the absence and presence of adsorbed oxygen reveal the amount of the latter present on

the supported Pd from which the dispersion may be derived if an assumption is made regarding the O:Pd stoichiometry.[86]

Rhodium

Infrared studies of CO on supported Rh catalysts reveal CO:Rh adsorption stoichiometries of 2:1, 1:1 and 1:2.[87,88] Recent HREELS[89] and density function studies[90] for Rh (111) suggest that CO may also adsorb in three-fold hollow sites on this surface thereby providing an adsorption stoichiometry of 1:3. Linear (1:1) and bridged (1:2) species are commonly found on Rh single crystal[91,92] and supported catalysts[87,88] alike whereas the gem-dicarbonyl species (2:1) are found only for supported crystallites,[87,88] although there is a report of these species on Rh field emitter tips.[93] In addition to the variable adsorption stoichiometry, there is some concern that the use of CO as adsorbate at 300 K may lead to the disruption of Rh–Rh metal bonds in small Rh crystallites[94] leading to the formation of the gem-dicarbonyl species.[95] As this CO induced disruption has been shown to occur even at temperatures well below 298 K,[96] this casts serious doubt upon the use of CO to determine Rh dispersion. Earlier studies had suggested that supported rhodium catalysts which had shown 100% dispersion in accordance with the H:Rh ratios, could display varying CO:Rh ratios, all greater than 1:1, depending upon the number of Rh atoms which composed two-dimensional rafts where only the peripheral atoms could adsorb two CO molecules.[97] Although overall stoichiometries greater than 2 have been reported,[98] for the case of highly dispersed catalysts, it would seem appropriate to use a CO:Rh stoichiometry somewhere between 1 and 2 depending upon the relative fraction of gem-dicarbonyl species present. These may be determined from the published values of the IR molar absorption coefficients.[88,99] Although the adsorption stoichiometry of CO on Rh is not simple and invariant,[98] there are reports that CO may be used as a quantitative adsorption probe using FTIR as the molar absorption coefficients for linear and bridged species do not vary significantly with dispersion.[99] For poorer dispersed catalysts with

larger crystallite size, the surface adsorbate:Rh atom stoichiometry may fall between 1 and 0.5 as the saturation CO coverage occurs at around 0.75 on the (111)[100] and (100)[91,92] crystal faces with the latter showing a considerable fraction of bridged species. Saturation coverage appears to be closer to 1 on the Rh (110) face.[101] CO is also adsorbed on unreduced exposed Rh ions, with oxidation states of III, II and I being assigned to carbonyl species giving IR bands in the 2,136–2,090 cm^{-1} range.[102–104] The proportion of these unreduced sites is seldom calculated, as TPR studies generally show that the rhodium precursor is reduced to the metallic state at reduction temperatures below 400 K.[105,106] However a fraction of rhodium may remain unreduced if high temperature oxidation has preceded the reduction treatment[107] or where precursors such as the chloride ion are retained by the support which helps stabilise Rh in a higher oxidation state.[104]

Although hydrogen is commonly employed to yield H:Rh ratios from which reaction turn-over frequencies may be obtained,[108] low loaded dispersed catalysts often show $H:Rh_{(total)}$ ratios greater than 1[98,99,106,107,109] indicating that an adsorption stoichiometry of 1:1 is not appropriate at high Rh dispersions. Experiments conducted using Rh black also showed a surface stoichiometry slightly greater than 1[98] confirming that the cause of high uptake values did not have its origin in spillover effects. While Vis *et al.*[106] suggest that those Rh atoms capable of adsorbing two CO molecules might also adsorb two H atoms, comparative studies where both adsorbates have been used[98,107,109] commonly show greater $CO:Rh_{(total)}$ than $H:Rh_{(total)}$ ratios. A good correlation was obtained however when the dispersion for a series of Rh/SiO_2 catalysts was measured using a hydrogen chemisorption and a quantitative FTIR method using CO.[99] The higher CO:Rh ratios might be understood if disruption of Rh-Rh bonds occurs[94–96] in the presence of this adsorbate at 298 K. Experiments conducted involving cycles of hydrogen–CO–hydrogen uptakes might help to confirm whether CO induced modifications to the Rh crystallites is the origin of the greater CO uptake relative to hydrogen. For catalysts containing larger crystallites, a H:Rh stoichiometry of 1:1 provides a measurement of crystallite size

which is comparable with TEM measurements.[106] Absence of correlation for sintered catalysts has been attributed to a broad and even multimodal particle size distribution where a fraction of the total rhodium goes undetected by physical methods.[98]

Wanke and Dougharty[98] and Yao *et al.*[107] compared oxygen adsorption uptakes with uptakes of CO and hydrogen for a series of supported Rh catalysts. Although earlier studies had shown the surface oxidation stoichiometry to be *ca.* 1,[110] both groups found that the surface adsorption stoichiometry was *ca.* 1.5 corresponding to an oxidation state of Rh^{3+} when the adsorption was performed between 298 and 573 K[107] or 473 and 573 K.[98] There is some concern that exposure to oxygen at such elevated temperatures would lead to the formation of bulk oxide and indeed for low loaded catalysts, the ratio $O:Rh_{(total)}$ approaches 1.5.[107] For poorer dispersed (higher loaded) catalysts, the adsorption stoichiometry fell such that it was no longer consistent with formation of bulk Rh_2O_3 although the uptake was still 50% greater than obtained using hydrogen.[98] While these results could be interpreted as a surface phenomenon where stoichiometric oxide formation is limited to the uppermost exposed Rh atoms, oxygen uptakes on Rh black did not follow the behaviour of sintered alumina supported catalysts but showed uptakes equivalent to 2O:1Rh at 473 and > 5 O:Rh at 573 K.[98]

The uncertainty involving ascribing a specific value to the O:Rh stoichiometry, at least for poorer dispersed catalysts, has implications when employing the hydrogen-oxygen titration method[63] to determine dispersion where a value of x is required in determining the overall reaction stoichiometry:

$$Rh\text{-}O_x + (x + y/2)H_2 \rightarrow Rh\text{-}H_y + xH_2O. \qquad (2.8)$$

At temperatures below 373 K, titration is incomplete,[98,107] whereas above this temperature, and up to 541 K, the value of y is constant (assumed to be unity) and corresponds with values obtained in chemisorption measurements. Above 543 K, the value of y drops off,[107] indicating incomplete hydrogen coverage.

The widespread use of rhodium for use in vehicle emission control (Chapter 8) has led to the use of NO as an adsorbate for the determination of Rh dispersion.[107,111] NO:$Rh_{(total)}$ ratios of up to *ca.* 2:1 have been reported[107,111] suggesting that a surface stoichiometry of up to two is possible. This is consistent with FTIR studies which confirm the presence of gem-dinitrosyl species for highly dispersed catalysts[112] in addition to linear bound species. Bridge bonded NO (NO:Rh = 1:2) is found on the Rh (111) surface,[113] although the presence of sites capable of multiple NO adsorption on this crystal face appears to depend on the presence of co-adsorbates.[113,114] Good correlation between NO:Rh and CO:Rh ratios obtained across a series of Rh catalysts between 0.13 and 9.80 wt% loadings would provide strong evidence that the sites which are capable of CO adsorption are also capable of binding NO molecules. As both adsorbates gave higher ratios than those obtained using hydrogen, and often involve adsorbate:$Rh_{(total)}$ values greater than 1,[107,111] the Rh-Rh disruption concept[94,95] invoked to account for the higher CO uptakes than for hydrogen would have to be extended to NO also. Solymosi *et al.*[115] have confirmed the positive influence of NO on the number of Rh sites capable of multiple adsorbate uptake. In addition to this modifying ability of the adsorbate on the Rh dispersion and its variable adsorption stoichiometry, the use of NO to determine dispersion must be employed with precautions to avoid adsorbate dissociation which is known to occur even at 298 K.[112] Additionally, NO adsorbs readily on most oxide supports[116,117] and so this uptake should be subtracted before presenting NO:$Rh_{(total)}$ values.

Nickel

Unlike the supported noble metals discussed so far, where it is customary, although not always justifiably so, to assume that all of the metal is present in its reduced state following pre-treatment in hydrogen, for base metal catalysts such as supported Ni, it is quite common to find a fraction present in an unreduced state.[29] This is not confined to alumina and the consequence of Ni aluminate formation,[118] but is also common for silica[119] and silicate[120] supported

catalysts. This unreduced nickel may be present as a separate phase[29] or as an interfacial layer between the support and the reduced metal particle[121] and thus may or may not be exposed to the adsorptive gas. It is recommended that metal dispersion and crystallite size estimates should include a correction for this unreduced fraction of nickel and in particular in cases where the adsorptive (e.g. hydrogen) is adsorbed to a relatively limited extent on this phase compared to the metal. Although CO is adsorbed at exposed unreduced Ni^{2+} centres as indicated by the detection of an IR absorption band at *ca.* 2,200 cm^{-1},[29,120] there is some concern that the exact adsorption stoichiometry is uncertain and that the amount adsorbed on the exposed Ni^{2+} is relatively small compared to that on the metal.[29] Anderson *et al.*[120] report a linear correlation between the amount of unreduced Ni in Ni/sepiolite catalysts prepared by impregnation and the integrated intensity of the IR absorption band at 2,200 cm^{-1} suggesting the presence of a two-dimensional unreduced Ni phase with a fixed CO : Ni^{2+} stoichiometry.

The CO : Ni ratio for the reduced metal fraction is known from IR studies to range from 1:3 to 4:1. In the latter case, $Ni(CO)_4$ is characterised by an IR absorption band at 2,057 cm^{-1} and its formation may be avoided[29] by exposing the adsorptive to the catalyst at 273 instead of 298 K. Even if the formation of this gaseous nickel tetracarbonyl can be avoided, the overall surface stoichiometry is unlikely to be straightforward given that even the simplest IR spectra for CO on supported Ni catalyst reveal at least two features at *ca.* 2,055 and 1,925 cm^{-1} due to linear (1:1) and bridged (1:2) forms of adsorption, respectively.[122–124] These frequencies are similar to those found on the Ni (100) surface.[125,126] The IR spectra obtained for supported catalysts frequently contain more than two features[120,127] and an additional feature appearing at *ca.* 1,900 cm^{-1} is consistent with the frequency of the two-fold bridging site on Ni (111).[128] Bands between 1,850–1,800 cm^{-1} suggest three-fold bridging sites which may be present on the Ni (111) face.[127] Bands in the range 2,090–2,065 cm^{-1} are also assigned to $Ni(CO)_2$ and $Ni(CO)_3$ species.[129] Small, unannealed particles may exhibit a band around 2,086 cm^{-1}.[127] The relative proportion of these features varies with the particle size and annealing temperature[127]

and this is reflected in the change in CO:Ni surface ratios which range from 1.9 for d = 4.4 nm, to 0.8 for d = 6.3 nm to 0.55 for d = 2000 nm.[29] These results indicate that $Ni(CO)_2$ species dominate at high dispersion whereas Ni_2CO species are most abundant at low dispersion. Clearly this complex stoichiometry suggests that CO should not be used to measure Ni surface areas although it has been suggested that it may be used to study particle size effects and metal support interactions.[29]

Although magnetic measurements are often used to determine dispersion of supported Ni catalysts,[119,130,131] with the advantage of being able to obtain both the percentage reduction and the mean crystallite size of the chemical methods, hydrogen is the most commonly-used adsorbate for the determination of nickel dispersion/surface area,[29,120,132] although this involves the need for a separate measurement of the extent of reduction[118,120] and the assumption that the adsorptive is not consumed by exposed Ni ions.[29] A surface stoichiometry of 1 H:1 Ni is generally employed in calculating dispersion[118,120,132] although there is some concern that although this may be widely applicable (Ni loadings 3–23 wt%, dispersions between 15–50%) it may not be valid for lower loaded samples.[29] Poor correlation between the crystallite sizes measured by TEM and XRD and those derived from hydrogen uptakes and high CO/H adsorption ratios for low loaded Ni/Al_2O_3 and Ni/SiO_2 catalysts led the authors to believe that SMSI effects were present as found for Ni/TiO_2.[29] This strong metal support interaction has been confirmed when employing alumina,[118] silica[131,133,134] and silicate based catalysts.[120]

Although oxygen as an adsorptive is often used when characterising Ni catalysts, this is usually employed with the reduced catalyst at elevated temperature (700–725 K) where the stoichiometric formation of NiO under these conditions allows the fraction of reducible Ni to be determined.[29,118] However, as exposure of reduced Ni surfaces to oxygen at room temperature leads to oxygen incorporation into the Ni crystal lattice of Ni powders and even at 195 K, O:Ni ratios of *ca.* two can be obtained,[135] this molecule has found limited applicability in determining Ni dispersion.

Copper

Catalysts containing Cu are commonly employed in the petrochemicals industry in processes such as methanol synthesis and the low temperature water gas shift reaction and as such, the measurement of Cu dispersion has received significant attention. However, in common with Ag and Au, weak adsorption of the commonly used adsorbates, CO and hydrogen, leads to a requirement for alternative procedures for these supported catalysts. Weak adsorption of CO at Cu^0 sites leads to the need for high adsorptive pressures to ensure complete coverage and renders inadequate dynamic techniques such as pulse chemisorption, which allow large proportions of the adsorbed gas to be released between pulses. This weak adsorption is emphasised by the need to employ CO pressures of up to 13 kPa[136] or adsorption temperatures down to 77 K[137] to attain the maximum intensity of the IR band at *ca.* 2,100 cm^{-1} for supported Cu catalysts. Although low temperatures or high pressures may be required to ensure complete surface coverage, the mode of adsorption of CO on supported catalysts is predominantly linear and thus a straightforward 1:1 stoichiometry may be assumed. Only on the Cu(111) face are two-fold and three-fold bridging of CO commonly observed.[138] A further complication, however, is that CO is adsorbed indiscriminately on exposed Cu^{2+} and Cu^+ ions as well as Cu^0 and these unreduced copper sites may be present in the surface, as detected spectroscopically by CO adsorption,[136,137] even when other techniques suggest complete sample reduction.[137,139]

Hydrogen is also weakly adsorbed on Cu surfaces and negligible uptake is reported at ambient temperature and moderate pressures on the low index (100), (111) and (110) planes.[140] Enhanced adsorption occurs on higher index Cu planes[140] and its presence on the Cu component of an industrial $Cu/ZnO/Al_2O_3$ catalyst confirmed by the use of solid state NMR.[141] This hydrogen is readily desorbed at 298 K from polycrystalline[142] and supported[143,144] Cu catalysts, and the coincidence of this peak with that from the support alone have lead to criticism[144] of hydrogen TPD as a potential technique[143] for the determination of metal surface area in Cu catalysts.

The difficulties involved with the use of CO or hydrogen to measure Cu surface areas[145] has led to the use of molecules, namely oxygen and nitrous oxide, which are dissociatively chemisorbed on the reduced Cu surface. As both of these adsorptives leave an adsorbed layer of oxygen atoms, it is essential that the adsorption is performed under conditions in which oxidation is limited to the top layer copper atoms only. The reaction stoichiometry using N_2O assumes:

$$N_2O_{(g)} + 2Cu_{(s)} \rightarrow N_{2(g)} + Cu\text{-}O\text{-}Cu_{(s)}. \quad (2.9)$$

The amount of exposed Cu may therefore be calculated by static methods, by measuring the fraction of N_2 in the final gas mixture,[146,147] or using a pulse method to determine the consumption of N_2O,[148] or in a flow method (reactive frontal chromatography) where the breakthrough time for the detection of N_2 is measured.[34] A check on the amount of oxygen deposited may be made by titrating the adsorbed layer with CO and measuring the amount of CO_2 evolved.[34] N_2O is exposed to the copper catalyst at temperatures between 293 and 363 K.[34,137,146] There is a concern, however, that at the lowest temperature N_2O decomposition may not occur over the whole of the copper surface,[147] thereby underestimating the dispersion, or at the highest temperature, bulk oxidation occurs, thus overestimating the dispersion. A recent study has shown that bulk oxidation may begin even at room temperature[149] thereby casting a doubt[150] on the use of this adsorptive under any experimental condition. However, Jensen *et al.*[151] have recently shown that the relative contributions due to surface and bulk oxidation by N_2O can be distinguished under appropriate gas flow conditions from the shape of the TCD signal for N_2 with a long tail on the latter arising due to the diffusion limited bulk oxidation process. A recent study has reverted to recommending the use of oxygen chemisorption, although rather than employing a lengthy, time consuming double isotherm method at 78 K,[152] a pulse method using 5%O_2 in He at 143 K was employed.[150] An earlier report had recommended 123 K as an appropriate temperature for conducting the adsorption experiment.[153] Only at temperatures above 150 K was evidence found for bulk oxidation.[150] An O : Cu stoichiometry of 0.43 : 1

was obtained by combining the gas uptake data with crystallite size measurements determined using XRD-WAXS and this was interpreted as indicating a stoichiometry of 0.5 with *ca.* 15% of the surface Cu atoms remaining unoccupied.[150] This stoichiometry is consistent with the half-monolayer coverage or 5×10^{14} O atoms cm^{-2} commonly used in calculating Cu surface area.[34,147]

Bimetallics

One of the most straightforward cases for the use of chemisorption in bimetallic systems is where only one component of the system chemisorbs the adsorbate gas. For example, the proportion of group VIII metal exposed in bimetallic clusters with group 1b (or 11) metals can be determined by hydrogen chemisorption since this gas is not significantly adsorbed by 1b metals. Ru-Cu and Os-Cu samples have been analysed on this basis since copper atoms in the surfaces of these clusters do not adsorb hydrogen.[154] Similarly, O_2-H_2 titration may be used by assuming that the O_2 which is weakly adsorbed on the group 1b metal will be desorbed during evacuation prior to H_2 titration.[155] Similarly, the use of the dynamic pulse method for chemisorption[156] ensures that only strongly adsorbed species are retained by the catalyst. The use of selective chemisorption for analysis of platinum containing alloys (with Re, Ir, Ru) has been reviewed by Charcosset.[157] Pt-Re/Al_2O_3 can be analysed by O_2 chemisorption at 298 K which gives the total Pt and Re surface atoms. Since oxygen chemisorbed on Pt can be reduced by hydrogen at 298 K, a second oxygen titration permits estimation of the number of Re atoms by difference.[157,158] It is possible that the applicability of this method may be limited to cases where no alloying has occurred as platinum interaction with Re may result in oxygen on Re being reduced at 298 K.[158] The dispersion of Pt in Pt-Re/Al_2O_3 catalysts, where alloying was confirmed by XANES,[159] has been obtained by hydrogen chemisorption at 298 K[159,160] on the basis that the adsorptive is selectivity adsorbed by Pt under these conditions.[161]

Although there are reports involving the use of hydrogen alone,[162] the surface composition of supported Pt-Ru bimetallic

catalysts are more commonly measured using a selective titration method.[163–165] The titration stoichiometry of the reaction between chemisorbed oxygen and gaseous CO is different for the two metals: the ratio of surface metal/O_2/CO/CO_2 is 1/0.5/2/1 for Pt and 1/1/1/0.3 on Ru.[165] These ratios are independent of surface composition and the concentration of Ru and Pt in the surface can be calculated from the equations:

$$Vo_2 = ½(Pt)_s + (Ru)_s \quad (2.10)$$

$$Vco = 2(Pt)_s + (Ru)_s \quad (2.11)$$

where Vo_2 is the volume of chemisorbed O_2 and Vco is the volume of CO required to titrate a monolayer of O_2.[165] For Rh-Ru/SiO_2 catalysts this technique has also been applied[166] using the metal/O_2/CO ratios of 1/1/1 for Ru and 1/0.5/1.75 for Rh. A method for determining metal dispersion in bimetallic Pt-Sn/Al_2O_3 has been reported which involves the use of both hydrogen and oxygen as adsorptive gases and which allows the fractions of unalloyed Pt, alloyed Pt, and alloyed Sn to be determined.[167] Limitations of selective chemisorption and titration exist due to the possibility of induced segregation, which might change the relative adsorption stoichiometry of each component and thus over or underestimate the dispersion. Additionally, static measurements may include interference due to weakly chemisorbed species.

References

1. W. Romanowski, in *Highly Dispersed Metals,* Ellis Horwood Ltd, Chichester, 1983, 13.
2. B.E. Warren, *Prog. Met. Phys.* 1959, **8**, 147.
3. B.E. Warren, B.L. Averbach, *J. Appl. Phys.* 1952, **23**, 497.
4. R.J. Matyi, L.H. Schwartz, J.B. Butt, *Catal. Rev.* 1987, **29**, 41.
5. G. Fagherazzi, P. Canton, P. Riello, N. Pernicone, F. Pinna, M. Battagliarin, *Langmuir* 2000, **16**, 4539.
6. P. Gallezot, in *Catalysis: Science and Technology*, Eds.: J.R. Anderson, M. Boudart, Springer-Verlag, Berlin, 1984, 221.

7. J. Pielaszek, *X-Ray diffractometry in supported catalyst studies*, Polska Akademia Nauk, Warsaw, 1995.
8. D. Bazin, L. Guczi, J. Lynch, *Appl. Catal.* 2002, **226**, 87.
9. T.E. White, P.W. Kirkin, R.W. Gould, H. Heinemann, *J. Catal.* 1972, **25**, 407.
10. J.I. Gittleman, B. Abeles, S. Bozowski, *Phys. Rev. B* 1974, **9**, 3891.
11. L. Bonneviot, M. Che, D. Olivier, G.A. Martin, E. Freund, *J. Phys. Chem.* 1986, **90**, 2112.
12. M. Respaud, J.M. Broto, H. Rakoto, A.R. Fert, L. Thomas, B. Barbara, M. Verelst, E. Snoeck, P. Lecante, A. Mosset, J. Osuna, T. Ould Ely, C. Amiens, B. Chaudret, *Phys. Rev. B* 1998, **57**, 2925.
13. C. Estournès, T. Lutz, J. Happich, T. Quaranta, P. Wissler, J.L. Guille, *J. Magn. Magn. Mater.* 1997, **173**, 83.
14. J.M. Thomas, P.A. Midgley, *Chem. Commun.* 2004, 1253.
15. D.B. Williams, C.B. Carter, *Transmission Electron Microscopy*, Plenum Press, New York 1996.
16. L. Reimer, *Transmission Electron Microscopy* 4th Edition, Springer Series in Optical Sciences, Vol. 36, Springer, Berlin, 1997.
17. J.C.H. Spence, *Mater. Sci. Eng. R* 1999, **26**, 1.
18. M.J. Yacamán, G. Díaz, A. Gómez, *Catal. Today* 1995, **23**, 161.
19. Z.L. Wang, *J. Phys. Chem. B* 2000, **104**, 1153.
20. A.K. Datye, D.J. Smith, *Catal. Rev.* 1992, **34**, 129 and references therein.
21. S. Bernal, F.J. Botana, J.J. Calvino, C. López-Cartes, J.A. Pérez-Omil, J.M. Rodríguez-Izquierdo, *Ultramicroscopy* 1998, **72**, 135.
22. M.J. Yacamán, J.A. Ascencio, S. Tehuacanero, M. Marín, *Top. Catal.* 2002, **18**, 167.
23. K. Sun, J. Liu, N.K. Nag, N.D. Browning, *J. Phys. Chem. B* 2002, **106**, 12239.
24. A.K. Datye, *J. Catal.* 2003, **216**, 144.
25. S. Bernal, J.J. Calvino, M.A. Cauqui, J.A. Pérez Omil, J.M. Pintado, J.M. Rodríguez-Izquierdo, *Appl. Catal. B: Env.* 1998, **16**, 127.
26. S. Bernal, J.J. Calvino, J.M. Gatica, C. López-Cartes, J.M. Pintado, in *Catalysis by Ceria and Related Compounds*, Ed.: A. Trovarelli, Imperial College Press, London, 2002, 85.
27. R. Van Hardeveld, F. Hartog, *Surf. Sci.* 1969, **15**, 189.

28. J.M. Gatica, R.T. Baker, P. Fornasiero, S. Bernal, J. Kašpar, *J. Phys. Chem. B* 2001, **105**, 1191.
29. C.H. Bartholomew, R.B. Panell, *J. Catal.* 1980, **65**, 390.
30. BS 4359 1994. *Determination of the specific surface area of powders. Part 4 Recommendations for methods of determination of metal surface area using gas adsorption techniques.*
31. F. Caballero, J.A. Anderson, unpublished results.
32. A. Guerrero-Ruiz, *React. Kinet. Catal. Lett.* 1993, **49**, 53.
33. C. Hubert, A. Frennet, *Catal. Today* 1993, **17**, 469.
34. G.C. Chinchin, C.M. Hay, H.D. Vandervell, K.C. Waugh, *J. Catal.* 1987, **103**, 79.
35. H. Berndt, U. Muller, *Appl. Catal.* 1999, **180**, 63.
36. H.L. Gruber, *Anal. Chem.* 1962, **34**, 1828.
37. P. Ferreira-Aparicio, A. Guerrero-Ruiz, I. Rodriguez-Ramos, *J. Chem. Soc. Faraday Trans.* 1997, **93**, 3563.
38. H. Ehwald, U. Leibnitz, *Catal. Letts.* 1996, **38**, 149.
39. N. Hickey, P. Fornasiero, J. Kašpar, J.M. Gatica, S. Bernal, *J. Catal.* 2001, **200**, 181.
40. V. Perrichon, L. Retailleau, P. Bazin, M. Daturi, J.C. Lavalley, *Appl. Catal. A: Gen.* 2004, **260**, 1.
41. N.D. Parkyns, *J. Chem. Soc. A* 1967, 1910.
42. K. Tanaka, J.M. White, *J. Phys. Chem.* 1982, **86**, 4708.
43. J.A.Anderson, C.H. Rochester, *J. Chem. Soc. Faraday Trans.* 1991, **87**, 1479.
44. C. De La Cruz, N. Sheppard, *Spectrochim. Acta* 1994, **50**, 271.
45. J.A. Anderson, *Catal. Letts.* 1992, **13**, 363.
46. T.A. Dorling, R.L. Moss, *J. Catal.* 1967, **7**, 378.
47. J.A. Anderson, F. Solymosi, *J. Chem. Soc. Faraday Trans.* 1991, **87**, 3435.
48. J. Freel, *J. Catal.* 1972, **25**, 149.
49. R. Van Hardeveld, F. Hartog, *Surf. Sci.* 1969, **15**, 189.
50. T. E. Jackson, J.A. Davies, D.P. Jackson, W.N. Unertl, P.R. Norton, *Surf. Sci.* 1982, **120**, 389.
51. P.R. Norton, J.A. Davies, D.K. Creber, C.W. Sitter, T.E. Jackson, *Surf. Sci.* 1981, **108**, 205.
52. P.R. Norton, J.A. Davies, T.E. Jackman, *Surf. Sci.* 1982, **122**, L593.
53. A. Frennet, P.B. Wells, *Appl. Catal.* 1985, **18**, 243.

54. P.B. Wells, *Appl. Catal.* 1985, **18**, 259.
55. E. Kikuchi, P.C. Flynn, S.E. Wanke, *J. Catal.* 1974, **34**, 132.
56. J.A. Anderson, M.G.V. Mordente, C.H. Rochester, *J. Chem. Soc. Faraday Trans.* 1991, **87**, 1479.
57. L. Spenadel, M. Boudart, *J. Phys. Chem.* 1960, **64**, 205.
58. G.R. Wilson, W.K. Hall, *J. Catal.* 1972, **24**, 306.
59. G.C. Bond, P.B. Wells, *Appl. Catal.* 1985**, 18**, 221.
60. G.C. Bond, P.B. Wells, *Appl. Catal.* 1985, **18**, 225.
61. R.A. Dalla Betta, M. Boudart, *Proc. 5th Int. Cong. Catal.* 1972, 1329.
62. D. Uner, N.A. Tapan, I. Ozen, M. Uner, *Appl. Catal.* 2003, **251**, 225.
63. J.F. Benson, M. Boudart, *J. Catal.* 1965, **4**, 704.
64. D.E. Mears, R.C. Hansford, *J. Catal.* 1967, **9**, 125.
65. A. Palazov, G. Kadinov, Ch. Bonev, D. Shopov, *J. Catal.* 1982, **74**, 44.
66. D. Tessier, A. Rakai, F. Bozon-Verduraz, *J. Chem. Soc. Faraday Trans.* 1992, **88**, 741.
67. M. Fernández-García, J.A. Anderson, G.L. Haller, *J. Phys. Chem.* 1996, **100**, 16247.
68. G. Gubitosa, A. Berton, M. Camia, N. Pernicone, in *Preparation of Catalysts III*, Eds.: G. Poncelot, P. Grange, P.A. Jacobs, Elsevier, Amsterdam, 1983, 431.
69. E. Gillet, S. Channakhone, V. Matolin, M. Gillet, *Surf. Sci.* 1985, **152**, 603.
70. A. Corma, M.A. Martín, J. Perez-Pariente, *Surf. Sci. Letts.* 1984, **136**, L31.
71. P. Canton, G. Fagherazzi, M. Battagliarin, F. Menegazzo, F. Pinna, N. Pernicone, *Langmuir* 2002, **18**, 6530.
72. P. Canton, F. Menegazzo, S. Polizzi, F. Pinna, N. Pernicone, R. Riello, G. Fagherazzi, *Catal. Letts.* 2003, **88**, 141.
73. G. Fagherazzi, A. Benedetti, S. Polizzi, A. Di Mario, F. Pinna, M. Signoretto, N. Pernicone, *Catal. Letts.* 1995, **32**, 293.
74. L.L Sheu, Z. Karpinski, W.M.H. Sachtler, *J. Phys. Chem.* 1989, **93**, 4890.
75. J.P. Candy, V. Perrichon, *J. Catal.* 1984, **89**, 93.
76. A. Beck, A. Hováth, A. Szucs, Z. Schay, Z.E. Hováth, Z. Zsoldos, I. Décány, L. Guczi, *Catal. Letts.* 2000, **65**, 33.
77. N.K. Nag, *Catal. Letts.* 1994, **24**, 37.
78. M. Machida, D. Kurogi, T. Kijima, *J. Phys. Chem. B* 2003, **107**, 196.

79. J.A. Anderson, J. Mellor, R.P.K. Wells, *J. Catal.* 2009, **261**, 208.
80. W. Juszczyk, Z. Karpiński, I. Ratajcykova, Z. Stanastuk, J. Zieliński, L.L. Sheu, W.M.H. Sachtler, *J. Catal.* 1989, **120**, 68.
81. M. Boudart, H.S. Hwang, *J. Catal.* 1975, **39**, 44.
82. R.R. Nandi, J.B. Georgopoulos, J.B. Cohen, J.B. Butt, R.D. Burwell Jr., *J. Catal.* 1982, **77**, 421.
83. M.A. Aramedía, V. Borau, C. Jiménez, J.M. Marina, A. Moreno, *Colloids and Surfaces A* 1996, **106**, 161.
84. M.A. Martín, J.A. Pajares, L. Gonzalez-Trejuca, *J. Catal.* 1985, **95**, 540.
85. G. Prelazzi, M. Cerboni, G. Leofanti, *J. Catal.* 1990, **181**, 73.
86. S. Szabó, F. Nagy, J. Gyimesi, *Appl. Catal.* 2002, **238**, 273.
87. A.W. Yang, C.W. Garland, *J. Phys. Chem.* 1957, **61**, 1504.
88. R.R. Cavanagh, J.T. Yates Jr., *J. Chem. Phys.* 1981, **74**, 4150.
89. D. Curulla, R. Linke, A. Clotet, J.M. Ricard, J.W. Niemantsverdriet, *Chem. Phys. Letts.* 2002, **354**, 503.
90. D. Curulla, R. Linke, A. Clotet, J.M. Ricard, J.W. Niemantsverdriet, *Phys. Chem. Chem. Phys.* 2002, **4**, 5372.
91. L.-W.H. Leung, J.-W. Hu, D.W. Goodman, *J. Chem. Phys.* 1990, **93**, 8328.
92. A.M. de Jong, J.W. Niemantsverdriet, *J. Chem. Phys.* 1994, **101**, 10126.
93. N. Kruse, *J. Vac. Sci. Technol.* 1990, **8**, 3432.
94. H.F.J. van't Blik, J.B.A.D. Van Zon, T. Huizinga, J.C. Vis, D.C. Koningsberger, R. Prins, *J. Phys. Chem.* 1983, **87**, 2264.
95. F. Solymosi, M. Pásztor, *J. Phys. Chem.* 1985, **89**, 4789.
96. F. Solymosi, H. Knozinger, *J. Chem. Soc. Faraday Trans.* 1990, **86**, 389.
97. D.J.C. Yates, L.L. Murrel, E.B. Prestridge, *J. Catal.* 1979, **57**, 41.
98. S.E. Wanke, N.A. Dougharty, *J. Catal.* 1972, **24**, 367.
99. P.B. Rasband, W.C. Hecker, *J. Catal.* 1993, **139**, 551.
100. P.A. Thiel, E.D. Williams, J.T. Yates Jr., W.H. Weinberg, *Surf. Sci.* 1979, **84**, 54
101. R.A. Marbrow, R.M. Lambert, *Surf. Sci.* 1977, **67**, 489.
102. C.A. Rice, S.D. Worley, C.W. Curtis, J.A. Guin, A.R. Tarrier, *J. Chem. Phys.* 1981, **74**, 6487.
103. J.P. Wey, W.C. Neely, S.D. Worley, *J. Catal.* 1992, **134**, 378.
104. D.I. Kondariides, Z. Zhang, X.E. Verykios, *J. Catal.* 1998, **176**, 536.
105. A.E. Newkirk, D.W. McKee, *J. Catal.* 1968, **11**, 370.

106. J.C. Vis, H.F.J. van't Blik, T. Huizinga, J. van Grondelle R. Prins, *J. Catal.* 1985, **95**, 333.
107. H.C. Yao, S. Japar, M. Shelef, *J. Catal.* 1977, **50**, 407.
108. G.M. Nuñez, A.R. Patrignani, A.J. Rouco, *J. Catal.* 1986, **98**, 554.
109. E.A. Hyde, C.H. Rochester, *J. Chem. Soc. Faraday Trans.* 1 1983, 79, 2405.
110. A.L. Sverdlova, G.L. Rabinovich, G.I. Tysovskii, T.A. Slovkhotova, V.M. Evgrashin, *Russ. J. Phys. Chem.* 1975, **49**, 1179.
111. B. Harrison, J.F. Heffer, F. King, in *Proc. 7th Int. Cong. Catal.* 1980, B2-1.
112. E.A. Hyde, R. Rudham, C.H. Rochester, *J. Chem. Soc. Faraday Trans.* 1984, **80**, 531.
113. T.W. Root, G.B. Fischer, L.D. Schmidt, *J. Chem. Phys.* 1986, **85**, 4687.
114. T.W. Root, G.B. Fischer, L.D. Schmidt, *J. Chem. Phys.* 1986, **85**, 4679.
115. F. Solymosi, T. Bánsági, E. Novák, *J. Catal.* 1988, **112**, 183.
116. N.D. Parkyns, in *Proc. 5th Inter. Cong. Catal.* North Holland, Amsterdam, 1973, Ed.: J.T. Hightower, 255.
117. T.J. Dines, C.H. Rochester, A.M. Ward, *J. Chem. Soc. Faraday Trans.* 1991, **87**, 643.
118. S. Narayanan, K. Uma, *J. Chem. Soc. Faraday Trans.* 1 1985, **81**, 2733.
119. J.T. Richardson, R.J. Dubus, *J. Catal.* 1978, **54**, 207.
120. J.A. Anderson, L. Daza, J.L.G. Fierro, M.T. Rodrigo, *J. Chem. Soc. Faraday Trans.* 1993, **89**, 3651.
121. J.W.E. Coenen, *Ind. Eng. Chem. Fund.* 1986, **25**, 43.
122. C.E. O'Neil, D.J.C. Yates, *J. Phys. Chem.* 1961, **65**, 901.
123. R.P. Eischens, S.A. Francis, W.A. Pliskin, *J. Phys. Chem.* 1956, **60**, 194.
124. W.L. van Dijk, J.A. Groeneweger, V. Ponec, *J. Catal.* 1976, **45**, 277.
125. S. Andersson, *Solid State Commun.* 1977, **21**, 75.
126. N. Vasquez Jr., A. Muscat, R.J. Madix, *Surf. Sci.* 1994, **301**, 83.
127. K. Coulter, X. Xu, D.W. Goodman, *J. Phys. Chem.* 1994, **98**, 1245.
128. J.C. Bertolini, G. Dalmai-Imelik, J. Rousseau, *Surf. Sci.* 1977, **68**, 539.
129. C.H. Rochester, R.J. Terrel, *J. Chem. Soc. Faraday Trans.* 1 1977, **73**, 609.
130. J.T. Richardson, J.G. Crump, *J. Catal.* 1979, **57**, 417.
131. R. Fréty, L. Tournayan, M. Primet, G. Bergeret, M. Guenin, J.B. Baumgartner, A. Borgna, *J. Chem. Soc. Faraday Trans.* 1993, **89**, 3313.

132. J.L. Carter, J.A. Cusumano, J.T. Sinfelt, *J. Phys. Chem.* 1966, **70**, 2257.
133. L. Zhang, J. Lin, Y. Chen, *J. Chem. Soc. Faraday Trans.* 1992, **88**, 2075.
134. T. Ueckert, R. Lamber, N.I. Jaeger, U. Schubert, *Appl. Catal. A: Gen.* 1997, **155**, 75.
135. J. Müller, *J. Catal.* 1966, **6**, 50.
136. G.J. Millar, C.H. Rochester, K.C. Waugh, *J. Chem. Soc. Faraday Trans.* 1991, **87**, 1467.
137. G. Ghiotti, F. Boccuzzi, *Catal. Rev.* 1987, **29**, 151.
138. M.A. Chester, S.F. Parker, R. Raval, *Surf. Sci.* 1986, **165**, 179.
139. F. Coloma, F. Marquez, C.H. Rochester, J.A. Anderson, *Phys. Chem. Chem. Phys.* 2000, **2**, 5320.
140. J. Pritchard, T. Catterick, R.K. Gupta, *Surf. Sci.* 1975, **53**, 1.
141. P.R. Dennison, K.J. Packer, M.S. Spencer, *J. Chem. Soc. Faraday Trans. 1* 1989, **85**, 3537.
142. K.C. Waugh, *Catal. Today* 1992, **15**, 51.
143. M. Muhler, L.P. Nielson, E. Tornqvist, B.S. Clausen, H. Topsøe, *Catal. Letts.* 1992, **14**, 241.
144. S. Bailey, K.C. Waugh, *Catal. Letts.* 1993, **17**, 371.
145. J.H. Sinfelt, W.F. Taylor, D.J.C. Yates, *J. Phys. Chem.* 1965, **69**, 95.
146. R.M. Dell, F.S. Stone, P.F. Tiley, *Trans. Faraday Soc.* 1953, **49**, 195.
147. J.J.F. Scholten, J.A. Konvalinka, *Trans. Faraday Soc.* 1969, **65**, 2465.
148. B. Dvoŕák, J. Pašel, *J. Catal.* 1970, **18**, 108.
149. S. Sato, R. Takahashi, T. Sodesawa, K. Yuma, Y. Obata, *J. Catal.* 2000, **196**, 195.
150. N. Pernicone, T. Fantinel, C. Baldan, P. Riello, F. Pinna, *Appl. Catal. A: Gen.* 2003, **240**, 199.
151. J.R. Jensen, T. Johannessen, H. Livbjerg, *Appl. Catal. A: Gen.* 2004, **266**, 117.
152. G.E. Parris, K. Klier, *J. Catal* 1986, **97**, 374.
153. G. Petrini, F. Montino, A. Bossi, F. Garbassi, in *Preparation of Catalysts, III*, Eds.: G. Poncelet, P. Grange and P.A. Jacobs, Elsevier, Amsterdam 1983, 735.
154. J.H. Sinfelt, *J. Catal.* 1973, **29**, 308.
155. R.D. Gonzalez, *Appl. Surf. Sci.* 1984, **19**, 181.
156. J. Sárkány, R.D. Gonzalez, *J. Catal.* 1982, **76**, 75.
157. H. Charcosset, *Int. Chem. Eng.* 1983, **23**, 187.

158. R.L. Moss, in *Specialist Periodical Report — Catalysis,* Vol. 4, RSC, London, 1981, 31.
159. M. Fernández-García, F.K. Chong, J.A. Anderson, C.H. Rochester, G.L. Haller, *J. Catal.* 1999, **182**, 199.
160. F.K. Chong, J.A. Anderson, C.H. Rochester, *J. Catal.* 2000, **190**, 327.
161. C. Bolivar, H. Charcosset, R. Frety, M. Primet, L. Tournayan, C. Betizeau, G. Leclercq, R. Maurel, *J. Catal.* 1976, **45**, 163.
162. J.R. González-Velasco, M.A. Gutiérrez-Ortiz, J.A. González-Marcos, P. Pranmda, P. Stetenpohl, *J. Catal,* 1990, **187**, 24.
163. H. Miura, T. Suzuki, Y. Ushikubo, K. Sugiyama, T. Matsuda, R.D. Gonzalez, *J. Catal.* 1984, **85**, 331.
164. H. Miura, H. Taguchi, K. Sugiyama, T. Matsuda, R.D. Gonzalez, *J. Catal.* 1990, **124**, 194.
165. H. Miura, R.D. Gonzalez, *J. Catal.* 1982, **74**, 216.
166. M.M. McClory, R.D. Gonzalez, *J. Phys. Chem.* 1986, **90**, 628.
167. D. Rajeshwer, A.G. Basrur, D.T. Gokak, K.R. Krishnamurthy, *J. Catal.* 1994, **150**, 135.

This page intentionally left blank

CHAPTER 3

IMAGING AND MICROANALYSIS OF SUPPORTED METAL CATALYSTS IN THE ANALYTICAL ELECTRON MICROSCOPE

Andrew A. Herzing[1] and Christopher J. Kiely[2]

[1]*National Institute of Standards and Technology Surface and Microanalysis Science Division, 100 Bureau Drive, Stop 8371 Gaithersburg, MD 20899–8371, USA*

[2]*Department of Materials Science and Engineering, Lehigh University, 5 East Packer Avenue, Bethlehem, PA 18015–3195, USA*

3.1 Introduction

The modern transmission electron microscope (TEM) is a powerful instrument for analyzing the structure and composition of nanoscopic volumes of material. It should be considered as an essential tool in the growing armory of characterization techniques available for studying supported metal catalysts. The TEM offers the possibility of studying the *crystallography* of the material by electron diffraction and its *structure and morphology via* a wide array of available imaging modes. In addition, it is possible to determine local *composition* of the material by either X-ray energy dispersive spectroscopy (XEDS) or electron energy loss spectroscopy (EELS).

In this chapter, we will only present a very basic introduction to some of the most important techniques available in these versatile instruments for the study of supported metal catalyst particles. Our intention here is not to present an exhaustive review, but rather to simply illustrate, by way of some examples, the types of information

that can be reliably obtained from supported metal particles. For those readers who are interested in the detailed construction or underlying physical principles pertaining to the TEM or scanning transmission electron microscope (STEM), there are a number of excellent reference texts available.[1–4] We will also draw attention to some of the pitfalls that can occur in TEM/STEM analyses and would like to stress at the outset that electron microscopy results should always be considered in conjunction with data obtained from other characterization techniques (e.g. infrared and Raman spectroscopies, XRD, XPS, EXAFS, TGA, ICP and BET measurements).

3.2 Electron-Specimen Interactions

For examination by transmission electron microscopy, the sample must be transparent to the high energy (typically 80 keV to 300 keV) incident electrons produced by the electron gun. For a powdered catalyst material this usually means that the sample is dispersed onto a commercially available lacey or holey carbon film that is supported on a metal mesh TEM grid. This dispersion can either be achieved by simply dipping the grid into the dry powder and tapping off the loose residue, or by grinding the catalyst powder in a suitable solvent and allowing a single drop of the resulting suspension to dry on the carbon film. Some catalyst powder adheres to the grid by Van der Waals attraction and the most useful areas for analysis can be found where an agglomerate of the catalyst powder overhangs a hole in the carbon support film.

Since the specimen is thin compared to the mean free path of the incident electrons, most will not interact at all with the constituent atoms of the sample but will simply pass undeflected through the material. However, provided the sample is crystalline, some fraction of the incident electrons will be scattered from crystal planes within the material by Bragg diffraction, and give rise to characteristic spots or rings in an electron diffraction pattern. These diffracted electrons lose little or none of their incident energy in such Bragg scattering events and are said to be *elastically* scattered.

Occasionally some of the incident high energy electrons will transfer some fraction of their kinetic energy to atoms of the sample and are said to *inelastically* scattered. Monitoring the resulting energy dispersion of the transmitted electrons forms the basis of the electron energy loss spectroscopy (EELS) technique used for compositional analysis. In conjunction with this, in response to such inelastic collisions, atoms within the specimen may also emit X-ray photons which can be collected and analyzed in the X-ray energy dispersive spectroscopy (XEDS) technique.

In the TEM mode, a selected area of the specimen is illuminated by a static parallel beam of electrons. If the sample being examined is a single crystal, then a characteristic spot diffraction pattern such as that shown in Fig. 3.1(a) will be generated if the crystal lattice is aligned along a high symmetry direction with respect to the incident beam. For powdered polycrystalline catalyst materials, the incident beam of parallel electrons usually encounters numerous crystals which have random orientations within the field of view. The resultant polycrystalline electron diffraction pattern then consists of a series of concentric diffraction rings such as that shown in Fig. 3.1(b). Each ring corresponds to a characteristic family of diffracting planes within the crystal structure, whose interplanar spacing, d, can be calculated using the relation:

$$d = \frac{L\lambda}{r} \tag{3.1}$$

where r is the experimentally measured ring radius, λ is the electron wavelength and L is the camera length (defined as the effective distance from the back focal plane of the objective lens to the viewing plane). The latter two parameters can easily be determined and calibrated for the electron microscope. The sequence of interplanar spacings determined in this manner can then often be used to identify the crystal structure under investigation by matching the spacings and relative intensities of the rings to those of known standard materials. It should be noted however that a practical limitation of this ring diffraction technique is related to the individual crystallite size

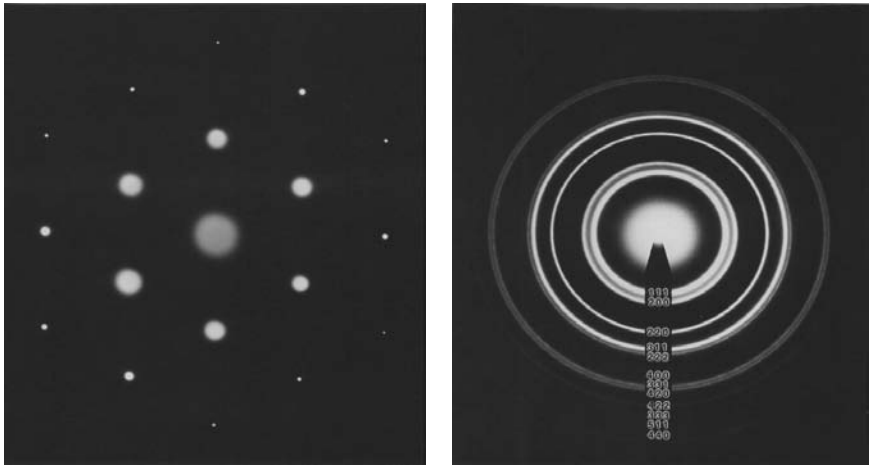

(a) (b)

Figure 3.1 (a) A spot diffraction pattern from a single crystal of gold; (b) A ring diffraction pattern from polycrystalline gold particles supported on amorphous carbon.

of the particulate material. As the particle size approaches nanoscale dimensions, the diffraction ring itself becomes broader and fainter, until eventually the ring becomes hard to distinguish from the diffuse background signal. For metal nanoparticles on amorphous supports (e.g. activated C or SiO_2) the sharp ring diffraction pattern will be generated by the crystalline metal nanoparticles only. For the situation where the metal nanoparticles are sitting on a crystalline metal oxide support (e.g. TiO_2, CeO_2), the resultant diffraction pattern will be a superposition of the two separate ring patterns generated by the metal and metal oxide components of the catalyst which then need to be deconvoluted during indexing of the diffraction pattern.

3.3 Imaging Supported Metal Particles in the TEM

The diffraction pattern, where the electrons are effectively sorted into the directions in which they are traveling upon emerging from

the back surface of the specimen, is actually generated in the back focal plane of the objective lens of the electron microscope. If a suitably-sized objective aperture is inserted into this plane, it is possible to selectively allow only the undiffracted beam, or alternatively a specific diffracted beam, to progress down the TEM column to form the final image as shown schematically in Fig. 3.2. If only the transmitted beam of undeflected electrons is allowed to contribute to the image, then a *bright field (BF)* micrograph is generated in which the material under investigation shows a dark contrast against a bright background (Fig. 3.2(a)), since all scattering events locally subtract intensity from the resulting image. Conversely, if a single diffracted beam (or even a small arc of a polycrystalline diffraction ring) is selected by the objective aperture, then a *dark field* (*DF*) micrograph

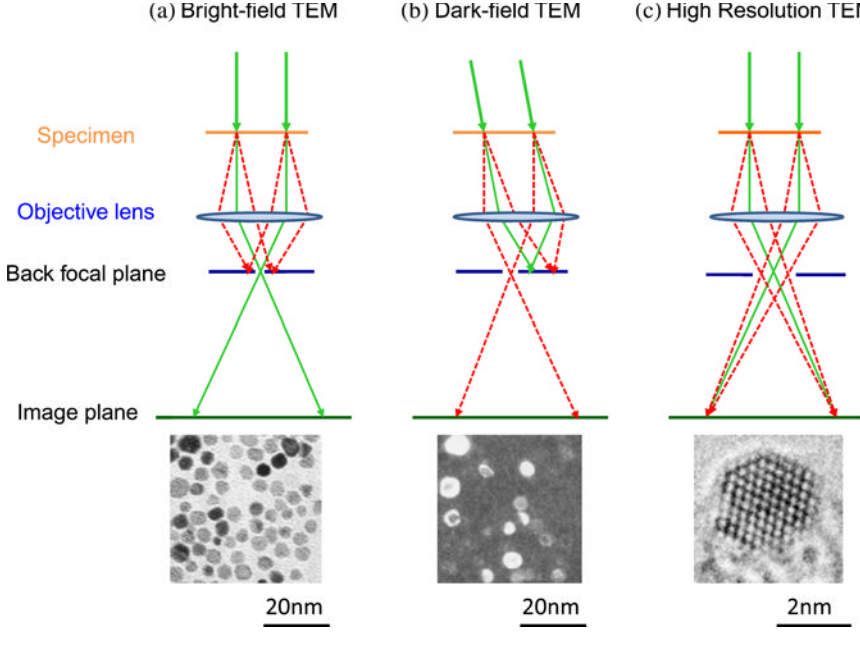

Figure 3.2 Schematic ray diagrams illustrating the (a) BF-TEM, (b) DF-TEM, and (c) HREM image modes used in a transmission electron microscope. The inset images show example micrographs of each type of Pt particles supported on amorphous carbon.

is formed in which the strongly diffracting particles appear bright against a dark background (Fig. 3.2(b)). A third option, as illustrated in Fig. 3.2(c), is to use a large objective aperture which allows both the undiffracted and some subset of the diffracted beams to contribute to the final image. Under these conditions, it is possible to generate a high resolution (HREM) *lattice* image in which appropriately oriented crystalline regions of the specimen can exhibit a characteristic set of periodic lattice fringes which are related to the atomic structure of the material. In the context of supported metal catalysts, all three of these TEM imaging modes can be used to gain useful information about the size distribution and morphology of both the metal nanoparticles and the support materials.

The three commonly encountered contrast mechanisms in TEM imaging are: (i) *mass-thickness contrast* which occurs due to greater absorption or scattering of incident electrons from denser or thicker parts of the specimen; (ii) *diffraction contrast* where crystalline regions of different orientation exhibit different contrast due to the orientational dependence of Bragg diffraction; and (iii) *phase contrast* where phase-shifted waves from the undiffracted and diffracted beams are allowed to interfere and generate lattice fringes.

At low magnification, the bright-field (BF) and dark-field (DF) imaging modes are commonly used, and, to a certain extent, are complementary to each other. In the BF-TEM image shown in Fig. 3.2(a), the Pt metal particles supported on a flat amorphous carbon film show a combination of mass-thickness and diffraction contrast. All the particles in the field of view are visible against the low-mass amorphous carbon background by virtue of mass-thickness contrast, but those which are especially dark have an extra contribution from diffraction contrast as these are oriented in such a way so as to give rise to strong Bragg scattering. In the corresponding DF-TEM image (Fig. 3.2(b)) only a subset of the metal particles show up brightly against the dark background, i.e. only those which are diffracting electrons into the specific limited arc of the diffraction ring that is allowed to pass through the objective aperture. Hence, the DF-TEM technique, although giving rise to high contrast images which can be useful for discerning the size and shape of supported metal

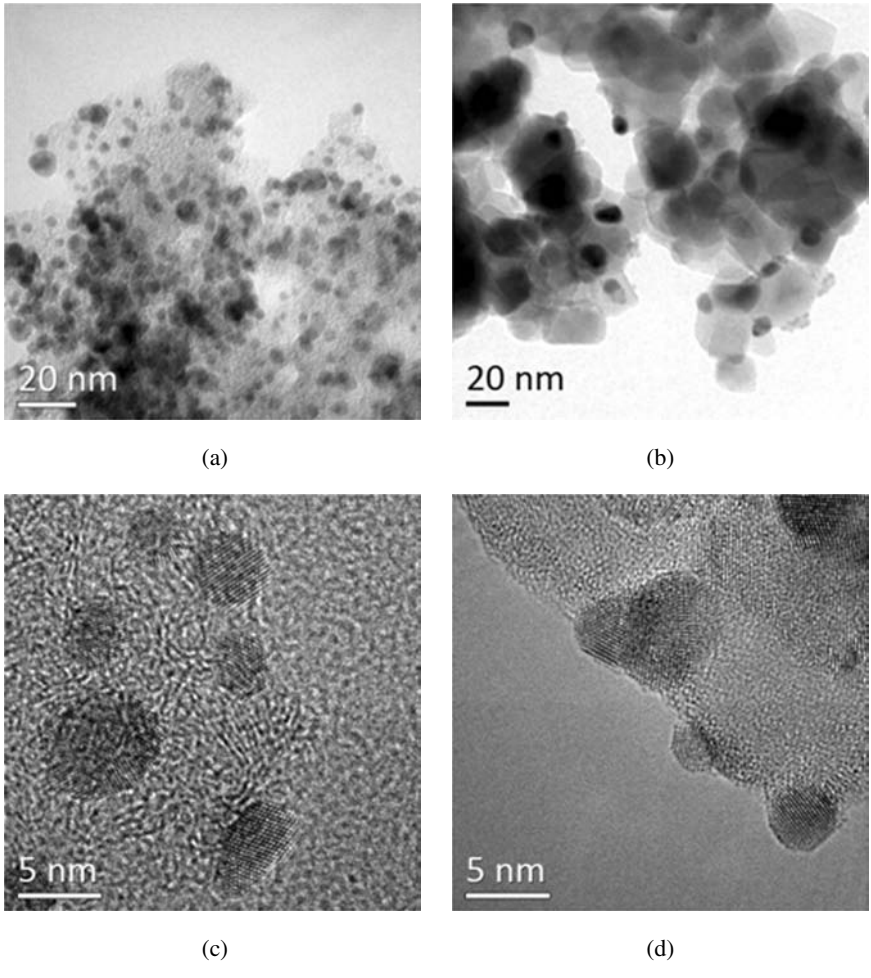

Figure 3.3 (a) BF-TEM image of AuPd/activated carbon; (b) BF-TEM image of AuPd/TiO_2; (c) phase contrast image of AuPd/activated carbon; and (d) phase contrast image of AuPd/TiO_2. *(Courtesy of R. Tiruvalam, Lehigh University, USA).*

particles, is not especially appropriate for detailed particle counting measurements, as all particles not specifically oriented to produce diffracted intensity in the angular range subtended by the objective aperture will be invisible. Figures 3.3(a) and (b) show BF-TEM images of AuPd alloy nanoparticles resting on activated carbon and

TiO_2 supports respectively, which nicely illustrates the "masking" effect that a crystalline support material can have on the visibility of metal nanoparticles. The AuPd particles on those TiO_2 support grains that are strongly diffracting and/or relatively thick are not clearly visible and sometimes cannot even be discerned. In contrast, all the AuPd particles are more obvious against the activated carbon support, since there is no strong diffraction contrast component from the amorphous background material.

Phase contrast or lattice images are encountered when working at higher magnifications in a TEM, provided that the instrument is equipped with electron optics capable of attaining a sufficient level of image resolution. This technique involves allowing several diffracted beams, as well as the undiffracted beam, to pass through the objective aperture to contribute to the final image. Such images are deliberately taken at a slightly underfocused objective lens setting (known as Scherzer defocus) to create an optimum phase shift between the undiffracted and diffracted beams, which in turn maximizes the interference contrast giving rise to strong "lattice" fringes. These fringes, which have the same periodicities as the diffracting planes in the crystal, are superimposed on the slightly out of focus image of the sample. When several sets of lattice fringes overlap, the crossed fringe pattern often has the appearance of an "atomic" structure as shown in Figs 3.3(c) and (d) for AuPd particles supported on activated C and TiO_2, respectively. It is very important to recognize that the lattice image is merely a complex interference pattern which, in some special circumstances, can resemble the atomic structure of the material. We are *not* forming direct images of the projected atomic structure *via* the phase contrast method, and therefore cannot arbitrarily assign the bright or dark dots in the lattice images to be the atomic columns or channels in the crystal structure. Nevertheless, it is safe to measure the spacings and intersection angles of the sets of lattice fringes from such phase contrast images, and directly relate them to the planar spacings and interplanar angles of the crystalline material.

On crystalline supports, the most useful phase contrast information can usually be extracted from metal particles which are

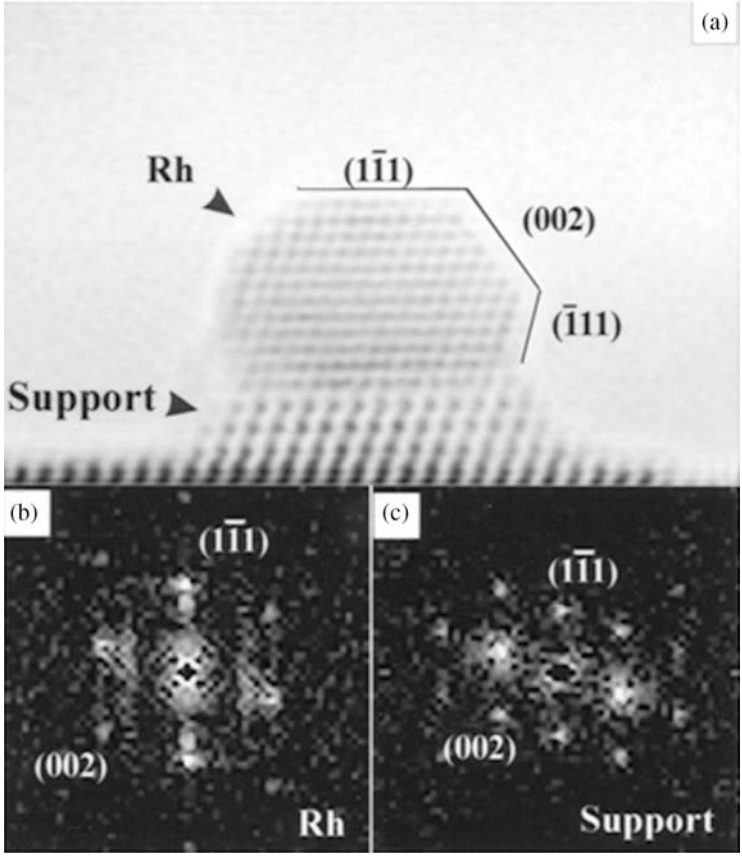

Figure 3.4 (a) Phase contrast image of a Rh particle supported on CeO_2 viewed in profile view; (b) and (c) are the fast Fourier transforms (FFTs) obtained from the Rh particle and CeO_2 support respectively, showing that they have an epitaxial orientation relationship and a lattice mismatch. *(Courtesy of J.J. Calvino, University of Cadiz, Spain).*[7]

imaged in profile. This is because the particle-support interface is viewed "edge-on" in this case so that the two structures do not spatially overlap in the image. By way of example, a profile image of a Rh particle on a CeO_2 support is presented in Fig. 3.4(a), in which specific {111} and {200}-type crystal planes can be indentified and the surface termination planes of the metal particle are

clearly delineated.[5,6] A useful trick that can be carried out on such images is to use a standard image processing package to generate the fast Fourier transforms (FFTs) from the lattice fringe patterns in the metal particle and oxide support regions separately, as shown in Figs 3.4(b) and (c) respectively. The FFTs generated can be thought of (to a crude first approximation) as the local diffraction pattern from each area, in which the spot positions yield the interplanar spacings and the angles between pairs of spots correspond to interplanar angles. In the case of the Rh/CeO_2 example in Fig. 3.4, this allows one to deduce the epitaxial orientation relationship that exists between the metal particle and oxide support.

Such profile lattice images have also been tremendously useful in visualizing situations where strong metal support interactions (SMSIs) occur, in which the supporting oxide migrates over the metal particle surface during use, effectively burying it under a thin oxide "skin". Lattice images have also proven to be highly effective in numerous studies of particle shape, surface facet and step structures, internal defect structures, phase identification, and particle/support epitaxy.[7,8]

In order to interpret the rich detail contained in such profile lattice images at a deeper level, for example to determine the relative atom positions at the metal/support interface, it is necessary to resort to detailed image simulations of these lattice images. Bernal *et al.* have been particularly active in this area and have developed a specialized program called "Rhodius" which can be used for constructing crystallographic models of metal particles which have specific sizes, shapes and epitaxial orientations on oxide supports.[6] These tailored particle/support models can then be used as the "input data" for commercial image simulation packages such as JEMS.[†,9,10] These programs perform standard Multislice or Bloch wave image simulations[11] using conditions that are appropriate for the model/configuration of electron microscope used and the specific acquisition conditions of the image. For example, Figs 3.5(a) and (b) respectively show a raw experimental image and the corresponding simulated

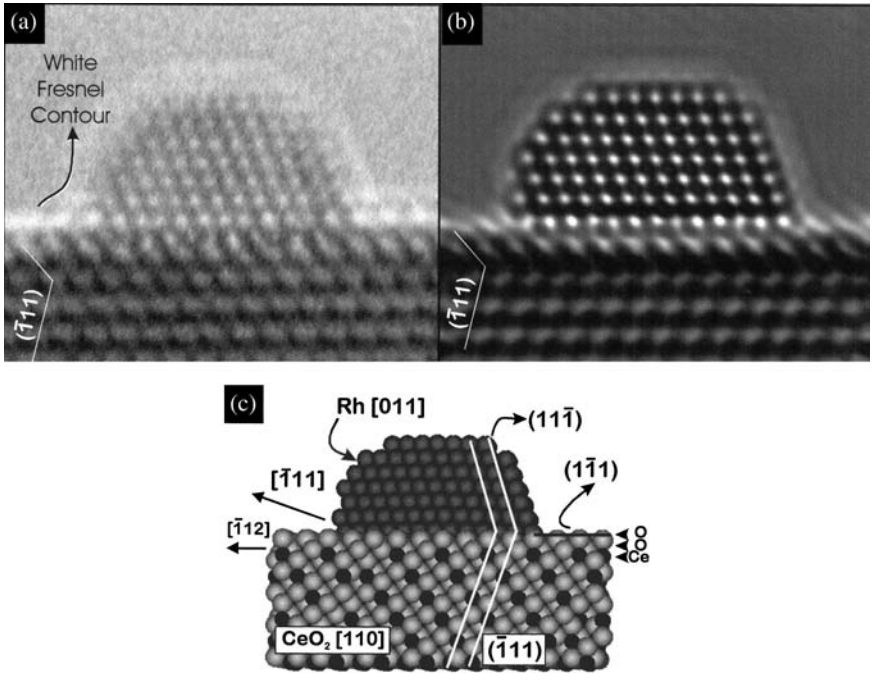

Figure 3.5 (a) Experimental phase contrast image of an epitaxial Rh particle on CeO_2; (b) The matching simulated image of the same particle using the model structure shown in (c). *(Courtesy of J.J. Calvino, University of Cadiz Spain).*[6]

image of a Rh particle on a CeO_2 support, that were generated from a Rh/CeO_2 supercell model structure generated by the Rhodius program. Such comparisons between experimental and simulated images are particularly useful when one is trying to distinguish between competing model structures of metal nanoparticles on oxide supports. More recently, a technique involving the acquisition of a through-focal series of aberration-corrected HREM images combined with exit-wave restoration techniques has been use by Gontard *et al.* to create detailed structural models of individual Pt particles showing surface defect sites.[12]

Some further complexities of lattice image interpretation are graphically illustrated in Fig. 3.6 where profile images of a Rh/CeO_2

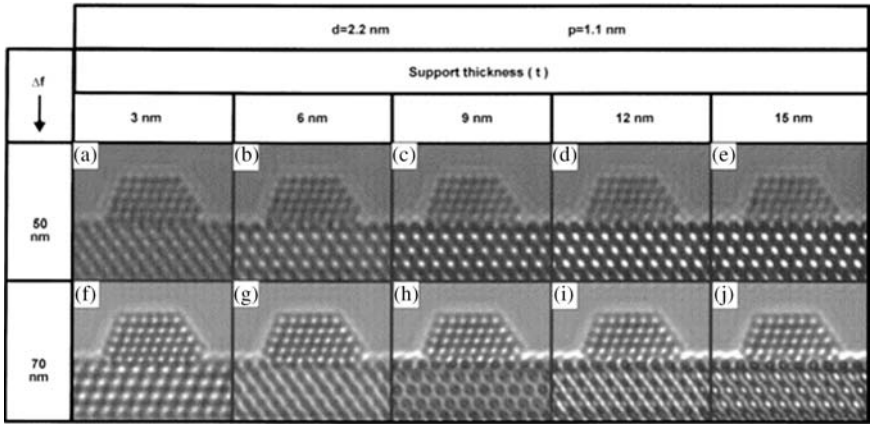

Figure 3.6 A montage of simulated phase contrast images of Rh/CeO_2 for two different defocus values and five different CeO_2 support thicknesses. *(Courtesy of J.J. Calvino, University of Cadiz, Spain).*[6]

particle are simulated for a systematic series of support thicknesses at two different microscope defocus settings.[6] The strong variations observed in the lattice fringe structure (across a row in the montage) for the CeO_2 support shows that the image features are highly dependent on sample thickness. By comparing pairs of images in specific columns in Fig. 3.6, it is also clear that the image details show a strong dependency on the microscope defocus setting used during image acquisition. Hence great care should be taken not to *over-interpret* the details in such lattice images unless one knows details of the sample thickness/acquisition parameters and are prepared to take them into account through image simulation methods. It is also very reasonable to ask the question, "What is the smallest metal particle that can be seen in profile on a metal oxide support by phase contrast imaging?" Bernal *et al.* have also addressed this particular question by carrying out image simulations at different defocus settings of metal clusters containing (1, 10, 28, 45 and 133) Rh atoms on CeO_2 supports as shown in Fig. 3.7.[6] The larger clusters (28 Rh atoms and above) are clearly discernable in profile, but the smaller ones are not; therefore, supported sub-nanometer diameter metal particles and atomically dispersed metal species will probably not be detected in

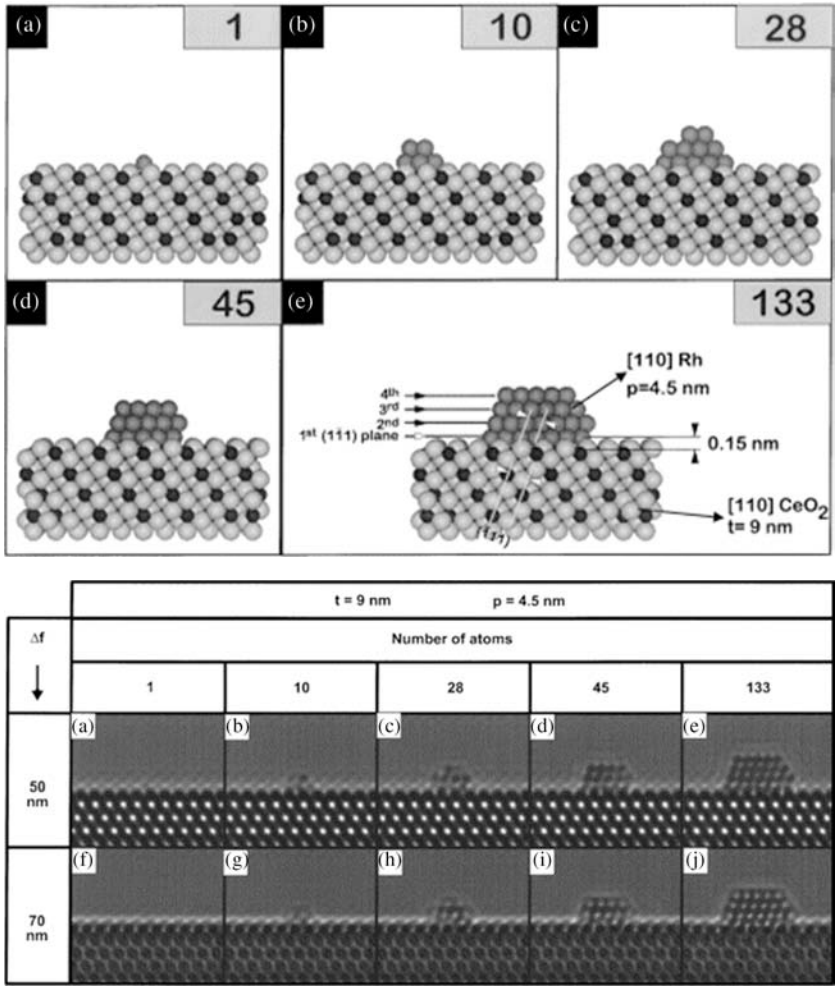

Figure 3.7 (Above) A montage of model Rh/CeO_2 structures for five different Rh cluster sizes. (Below) Corresponding simulated phase contrast images for two different defocus values for the model structures. *(Courtesy of J.J. Calvino, University of Cadiz, Spain).*[6]

conventional high resolution electron microscopy (HREM) lattice images. Hence it is important to recognize that the absence of these ultra-small metallic species in HREM images does not necessarily mean that they are not present!

3.4 Imaging Supported Metal Nanoparticles in the STEM

The scanning transmission electron microscope (STEM) allows us to overcome some of the limitations encountered in BF-TEM, DF-TEM and HREM images.[13] In the STEM, an image is formed by focusing the electron probe into a fine spot that is scanned over the sample in a raster similar to that in a scanning electron microscope (SEM). The transmitted signals can either be collected on a line-of-sight bright-field (BF) detector, or on an offset annular dark-field (ADF) or high-angle annular-dark field (HAADF) detector as shown schematically in Fig. 3.8(a). The signals from these detectors are then amplified and used to modulate the signal on a television screen which is scanned synchronously with the spot position on the specimen. The obtainable resolution in STEM mode primarily depends on the dimensions of the incident electron probe. With the recent availability of brighter, more coherent, electron sources and sophisticated aberration-corrected lens systems,[14] it is now possible to form an electron probe that is less than 100 pm in diameter and which can reveal atomically resolved structural (and chemical) information on the sample.[15]

In STEM-BF mode, the image is formed by electrons scattered less than 10 mrad from the optic axis and can resemble rather noisy HREM phase contrast images. In the STEM-DF mode, an annular detector gathers electrons scattered into an annulus around the beam. The ADF detector typically has inner and outer annular radii of 10 mrad and 50 mrad respectively, and captures all Bragg diffracted electrons with this angular range irrespective of the scattering direction. What really sets the STEM apart for imaging supported metal catalyst systems is the availability of the HAADF detector (inner radius 50 mrad — outer radius 200 mrad) which collects incoherently scattered electrons that are generated by the coulombic interaction of the passing electrons with the atomic nuclei of the sample. Since very few electrons get Bragg scattered out further than 50 mrad, the HAADF images do not show diffraction contrast, but instead they do exhibit strong atomic number (Z) contrast.[16,17] The Rutherford scattering cross-section in this high

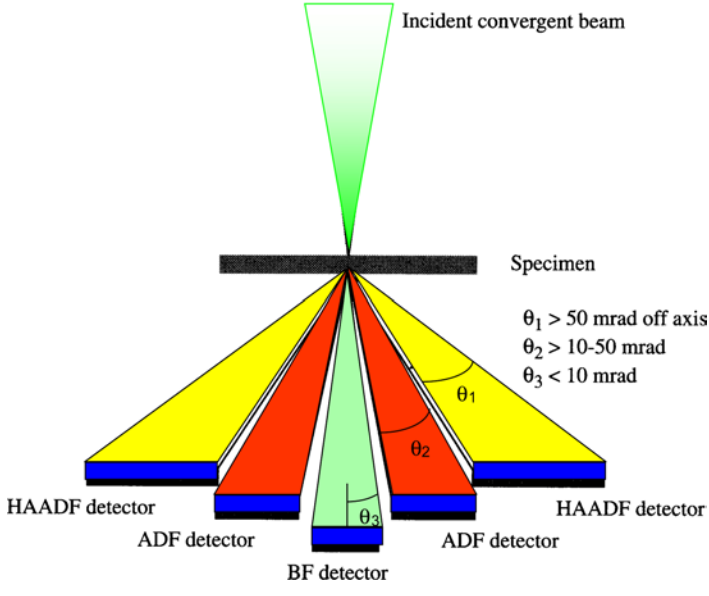

(a)

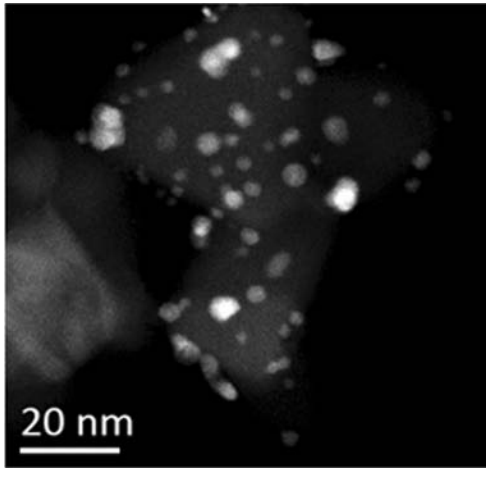

(b)

Figure 3.8 (a) A schematic diagram of the probe/sample/detector arrangement of a scanning transmission electron microscope (STEM); (b) A STEM-HAADF image of AuPd alloy particles supported on activated carbon. *(Micrograph courtesy of R. Tiruvalam, Lehigh University, USA).*

angular range is approximately proportional to the square of the atomic number, so regions with a higher atomic number appear brighter in the HAADF image. Figure 3.8(b) shows an HAADF image of AuPd nanoparticles which show very strong *Z*-contrast against the much lower mass carbon support. This HAADF imaging mode is an excellent choice for measuring metal particle size distributions on oxide or carbon supports. Furthermore, sequential HAADF images of supported metal particles do not show any diffraction contrast effects as the relative angle between the incident beam and particles is varied by tilting the specimen. Hence systematic HAADF image sequences of a sample taken at 1° to 2° tilt intervals can be combined to create a three-dimensional reconstruction of the particle distribution. This technique is known as *electron tomography*,[18–20] and allows the spatial distribution of metal particles to be determined on the surface of dense oxide support, or within the internal pore structure of a mesoporous (e.g., zeolitic) type support.

In STEM instruments that are equipped with an aberration corrector, it is now routinely possible to generate an electron probe that is in the order of 100 pm in diameter. If this probe is used to acquire STEM-HAADF images, it becomes possible to generate HAADF images of appropriately oriented metal nanoparticles with atomic resolution. As an example of this, several images of cyclically twinned gold nanoparticles, taken using the BF-TEM, HREM and STEM-HAADF imaging techniques, are presented in Fig. 3.9. The BF-TEM image (Fig. 3.9(a)) shows a decahedral gold particle comprised of five tetrahedral sub-units, with two of them oriented in strongly diffracting conditions which are easily distinguishable by diffraction contrast. In the HREM image (Fig. 3.9(b)) the gold particle is clearly visible against the characteristic speckle contrast of the amorphous carbon support film, and the lattice fringe pattern highlights the five internal twin interfaces. The bright spots in the STEM-HAADF *Z*-contrast image of the five-fold twinned gold particle in Fig. 3.9(c) can be directly related to the positions of the atomic columns and their intensity is related to the projected number of gold atoms in each column. The amorphous carbon support

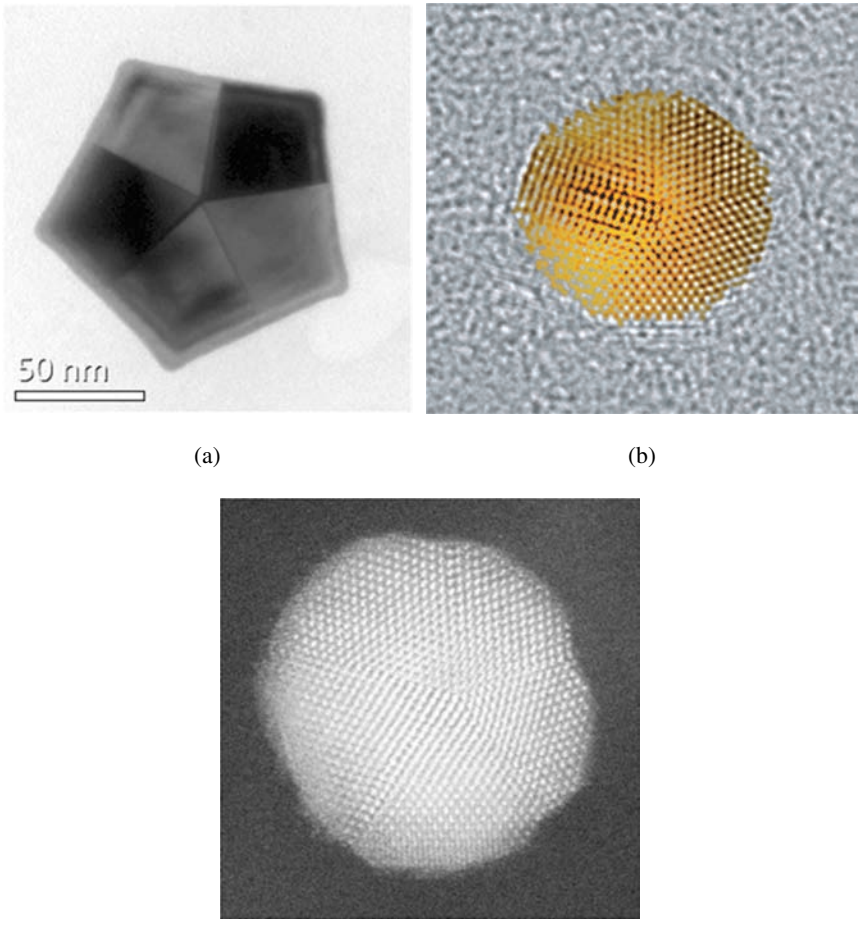

Figure 3.9 (a) BF-TEM diffraction contrast images, (b) HREM phase contrast image, and (c) aberration-corrected STEM-HAADF image of cyclically twinned gold nanoparticles supported on amorphous carbon. *(Micrographs A and C courtesy of R. Tiruvalam, Lehigh University, USA. Micrograph B courtesy of A. Burrows, Lehigh University, USA).*

film is virtually invisible in this image due its low atomic mass in comparison with the gold.

The *Z*-contrast, inherent to STEM-HAADF images, can also yield additional information on supported metal alloy particles.

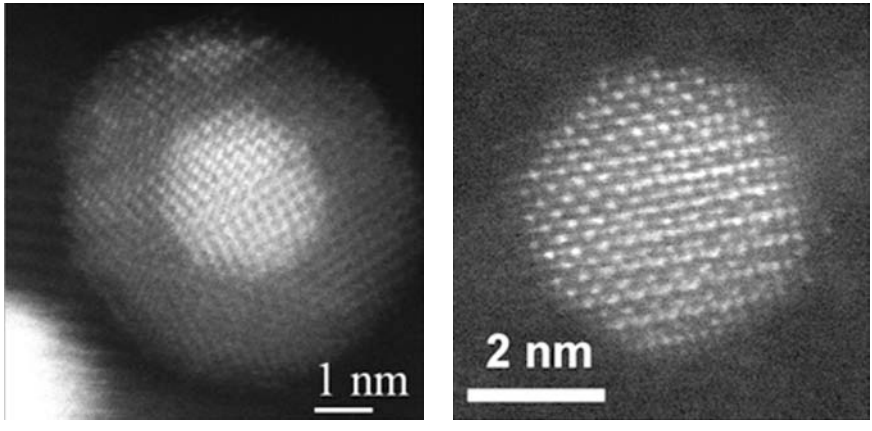

(a) (b)

Figure 3.10 Aberration-corrected STEM-HAADF *Z*-contrast images of (a) an AuPd core-shell nanoparticle, and (b) an FePt ordered alloy particle.[22] *(Micrograph A courtesy of R. Tiruvalam, Lehigh University, USA. Micrograph B courtesy of J. Wittig, Vanderbilt University, Tennessee, USA).*

For example, Fig. 3.10(a) shows an HAADF image of a 7 nm diameter bimetallic AuPd alloy particle which has a gold-rich core and a palladium-rich shell.[21] The core and shell morphology can easily be distinguished in this micrograph by virtue of the large atomic mass difference between Au ($Z = 79$) and Pd ($Z = 46$) which give rise to a bright core and a much fainter shell region. The FePt nanoparticle shown at atomic resolution in Fig. 3.10(b) is an example of an ordered alloy structure in which the two elemental species occupy well defined sub-lattices. This HAADF image from Wittig *et al.* was taken along a crystal projection in which the atomic columns contain either Pt or Fe atoms (but not both).[22] Hence the Fe ($Z = 26$) atomic columns appear considerably dimmer than the bright Pt ($Z = 78$) columns in this image.

Another extremely important feature of aberration-corrected STEM-HAADF imaging of supported metal catalyst systems, is that sub-nm clusters and even atomically dispersed metal atoms become visible provided there is a reasonable *Z*-contrast between the metal

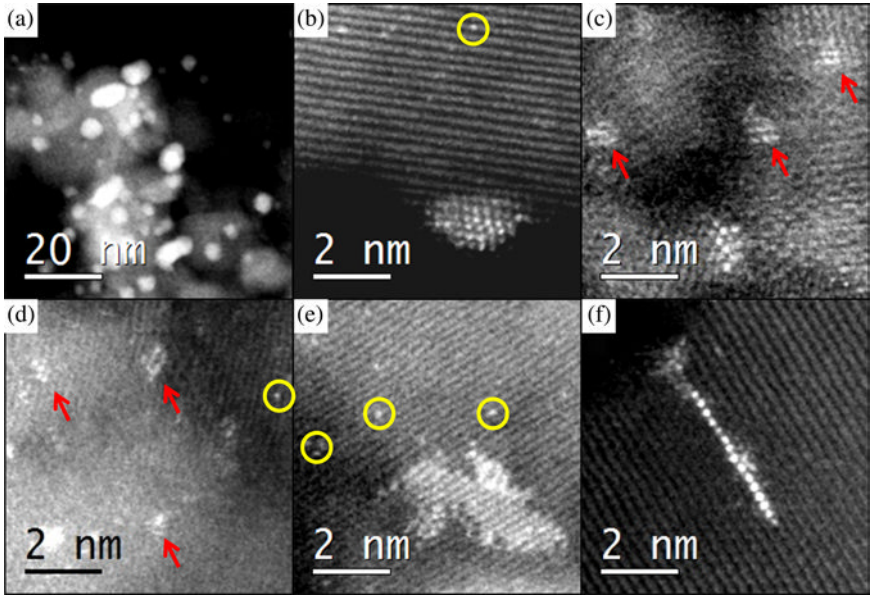

Figure 3.11 Aberration-corrected STEM-HAADF *Z*-contrast images showing the various Au species co-existing on the ZnO support; (a), (b) three-dimensional Au nanoparticles; (c) sub-nm Au clusters (white arrows); (d) sub-nm Au clusters and isolated Au atoms (white circles); (e) ordered monolayer Au rafts and isolated Au atoms, and (f) linear stripes of Au. *(Micrographs courtesy of Q. He, Lehigh University, USA).*[27]

and the support.[23–26] For example, Fig. 3.11 from He *et al.* shows the wide variety of Au species that can *co-exist* on a ZnO support when the metal component is introduced onto the support by a simple deposition precipitation route.[27] In addition to gold nanoparticles which are a few nm in size, a number of other structures can be observed, including sub-nm clusters (containing less than ten atoms), extended monolayer rafts of Au, a dispersion of Au atoms, and linear assemblies of Au atoms presumably at step edges. Conventional HREM lattice images only show the presence of Au nanoparticles that are greater than 1 nm in size, so in this case the STEM-HAADF image is providing an invaluable and much more representative view of *all* the potentially catalytically active metallic species that are present.

3.5 Other Technical Developments

Heating stage holders are also available for use within the TEM/STEM to study the thermal stability of metal nanoparticles on oxide supports. For example, Fig. 3.12 shows a sequence on STEM-HAADF of some AuPd nanoparticles that are coalescing under the influence of *in situ* heating within the vacuum environment of the microscope. Such *in situ* heating studies can shed light on the mechanisms of particle sintering (i.e., coarsening *vs.* Ostwald ripening) and allow informed strategies to be developed for modifying the support in order to improve the adhesion of the metal nanoparticles and hence increase the catalyst stability and lifetime.

Environmental cell transmission electron microscopy (ETEM), whereby catalysts are viewed real-time under a gaseous environment at reaction temperature, continues to be of fundamental interest to the catalysis community because it offers the possibility of examining

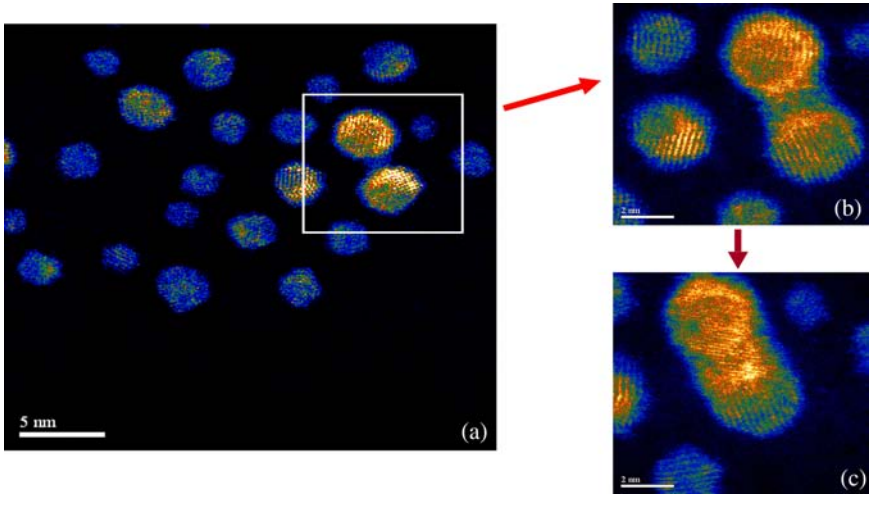

Figure 3.12 Aberration-corrected STEM-HAADF images showing the various stages of sintering of a pair of Au-Pd nanoparticles supported on amorphous carbon. (a) Initial image shows a number of bimetallic nanoparticles with atomic resolution. (b) and (c) Subsequent images acquired from the same area show particle migration and sintering occur over time under electron irradiation. *(Micrographs courtesy of R. Tiruvalam, Lehigh University, USA).*

catalysts under conditions that are closer to their normal operating conditions. The subject of ETEM is beyond the scope of this current article, but the interested reader is referred to some excellent reviews by Gai *et al.*[4,28]

3.6 Analytical Electron Microscopy (AEM) for Catalyst Research

So far, we have seen how the various scattering mechanisms undergone by incident electrons within a thin specimen can be utilized to reveal atomic- and nanoscale detail relating to the structure and morphology of supported metal catalysts. In a modern configuration of the TEM commonly known as an analytical electron microscope (AEM), a number of elemental, chemical, and electronically sensitive spectroscopic signals can also be generated and collected, often at or near atomic resolution. Generally, the AEM consists of a high resolution scanned probe TEM (STEM) that is equipped with X-ray energy dispersive and electron energy-loss spectrometers (XEDS and EELS, respectively). The XEDS signals can be acquired, along with the STEM-HAADF image signal, either separately or simultaneously, allowing sensitivity to a broad range of the technologically relevant elements of the periodic table. In the following section, we will discuss the nature of these electron-specimen interactions, and the way in which the resulting signals are collected, interpreted, and quantified.

3.7 The Origin of Microanalytical Signals

The majority of the signals utilized for imaging of catalyst materials are based on elastic processes such as diffraction and high-angle Rutherford-like scattering in which the incident electron undergoes a directional change but transfers little or no energy to the specimen. In contrast, the XEDS and EELS signals, which we are now going to consider, are based solely on inelastic events that result when the incident electron undergoes little in the way of directional change, but does transfer some definite amount of energy to the specimen.

There are a number of mechanisms by which inelastic electron scattering can occur, all of which will contribute to the intensity observed in the EELS spectrum. However, for the present purposes, we will mainly focus on the case where the impinging high energy electrons in the TEM ionize atoms within the specimen *via* the ejection of an inner-shell electron from the nucleus. The energy transfer required for these ionization processes are highly specific to the identity of the excited atom and, as such, form the basis for elemental and chemical analysis *via* EELS spectroscopy.

Once inner-shell ionization of an atom has occurred, relaxation can occur when a higher energy electron in the atom falls down into the vacated, lower energy state. This process requires the release of energy, which can occur in a number of ways including the radiative emission of X-ray photons or Auger electrons. Since the energy of an emitted X-ray photon is equal to the difference between the two electron energy levels involved, this too, like the ionization process itself, contains element-specific information and forms the basis for XEDS spectroscopy. The likelihood that a given ionization event will result in the emission of an X-ray photon is given by the fluorescence yield which, for K-shell photon emission, approximately follows an inverse relationship with Z^4, where Z is the atomic number. Therefore, the detection of light elements is more difficult, since the relaxation of ionized atoms is dominated by the Auger process rather than X-ray emission. This problem is exacerbated by the fact that conventional XEDS detectors exhibit a reduced detection efficiency for lower energy photons. For these reasons, microanalysis of light elements by the EELS technique is far more efficient than XEDS.

The spectral information necessary for qualitative and quantitative analysis in the AEM can be acquired in a variety of ways. The most straightforward of these involves positioning the beam over a region of interest in the specimen and simply collecting the total counts of either X-ray photons or energy-loss electrons from the area illuminated by the electron beam. This approach generally has the advantage of producing spectra with a high signal-to-noise ratio, since a relatively large area of the specimen is being analyzed with a

fairly high-current electron probe. However, the resulting spectral information represents the total signal collected from the entire area of the specimen that is being illuminated by the beam, which is typically several nm^2 or even μm^2 in size. Thus, any fluctuations in composition over this analytical region will not be resolved.

In contrast, current technology also allows for the acquisition of spatially resolved spectroscopic signals *via hyperspectral* imaging. This can be accomplished in one of two ways. The first, carried out in STEM mode, involves acquiring an entire spectrum in a serial fashion from a spatial array of pixels.[29,30] This approach is commonly utilized to produce STEM-XEDS or STEM-EELS spectrum image datasets. Alternatively, in TEM mode, a suite of images may be acquired sequentially over an entire energy range, and this is the preferred approach in energy-filtered (EF)-TEM analysis. It should be noted that the result of all of these analytical techniques (STEM-XEDS, STEM-EELS, EF-TEM) is a three-dimensional datacube, two dimensions of which represent the *x*- and *y*-spatial coordinates while the third dimension corresponds to the energy channels of the spectral signal. Thus, the data generated from both the spectrum-wise (XEDS, EELS) and image-wise (EF-TEM) acquisitions are functionally the same, in that they represent two different methods of filling the three-dimensional data-space. However, it should be noted that, in practice, the data obtained by each approach differs in some important ways, and the suitability of one method over the other for a particular experiment must be judged on the individual merits of each.

3.8 X-ray Energy Dispersive Spectroscopy (XEDS) of Supported Metal Catalysts

A typical XEDS spectrum generated from a supported metal catalyst powder specimen is presented in Fig. 3.13(a). In this case, the catalyst consisted of an Al_2O_3 support that was co-impregnated with Au and Pd *via* an incipient wetness method, and exhibits the elemental peaks characteristic of Au (9.71 keV and 2.12 keV), Pd (2.84 keV), Al (1.49 keV) and, O (0.52 keV). In addition to these elemental

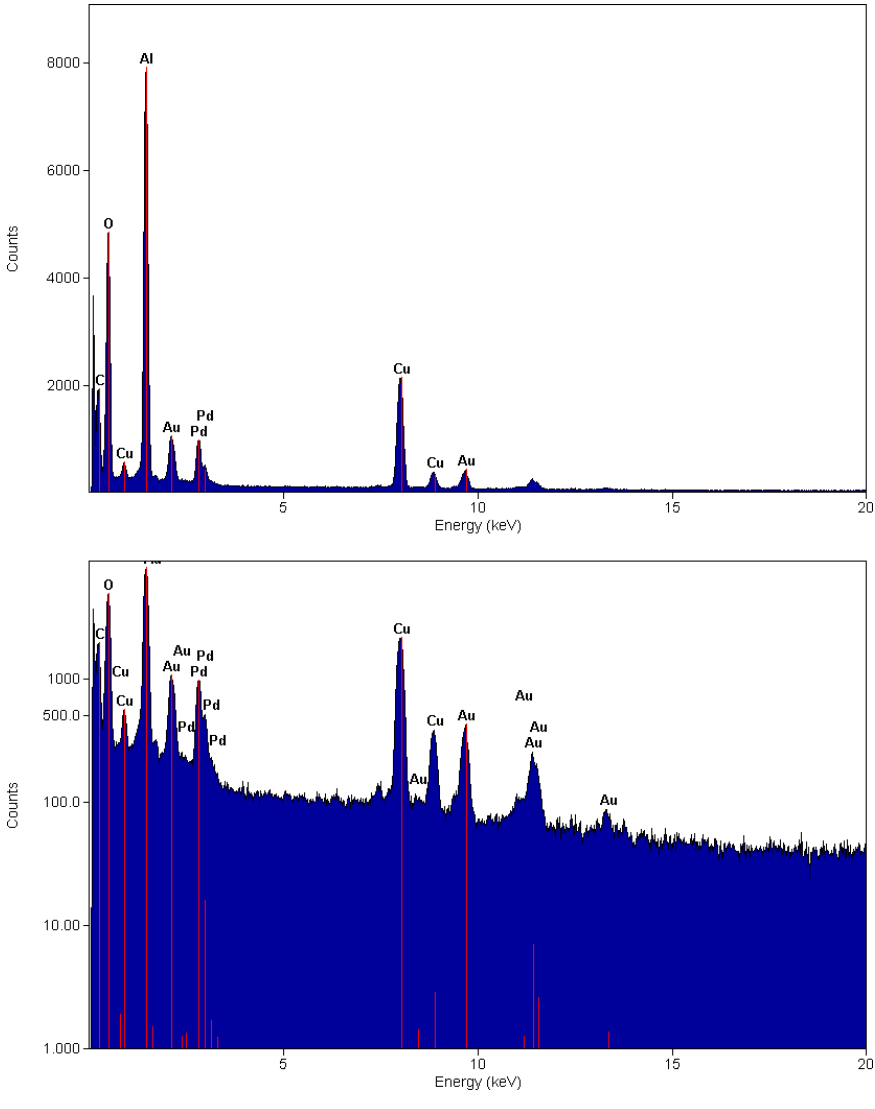

Figure 3.13 Typical XEDS spectrum collected from a supported metal catalyst (Au-Pd/Al_2O_3) shown with (top) a linear y-axis and (bottom) a logarithmic y-axis in order to emphasize the background signal.

peaks, there is a continuum background level of radiation that exists under and between the characteristic peaks. This background is mostly due to the Bremmstrahlung or "braking radiation", which occurs as the high energy incident electrons lose some energy due to deceleration by the Coulombic fields exerted by the atomic nuclei. This background can be emphasized by using a logarithmic intensity scale as shown in Fig. 3.13(b). It can be seen that, at higher energies, the background continuum radiation exhibits a logarithmic decay, and an apparent sharp fall-off of background signal also occurs at low energy due to inefficiencies of the XEDS detector at low X-ray photon energies.

With the exception of a few artifacts, most of which are easily identified, qualitative analysis of such XEDS spectra is straightforward since the energies of the characteristic X-rays are well known. The most common errors associated with qualitative XEDS compositional analysis arise due to the limited energy resolution (typically 150 eV) and sometimes poor energy calibration of the detector involved.[31] This can lead to erroneous identification of an X-ray peak due to the spectral overlap of similar energy peaks exhibited by two or more elements. A common example of this occurs for the case of Pb and S, which exhibit characteristic X-rays at 2.364 keV and 2.307 keV, respectively. If the microanalyst is unaware of such overlaps, the wrong elemental assignation could easily be made when identifying peaks in the resulting spectra. To avoid such errors, a careful calibration of the energy scale should be performed in order to determine which of the two elements is present. However, in situations where both elements may co-exist in a sample, it can sometimes be impossible to determine whether or not both elements are present, since the tail of the more abundant element will hide the less intense peak of the minor element. Other spectral artifacts that can lead to errors in qualitative analysis include sum, system, and escape peaks, and these have been described elsewhere.[31] An example of a system peak artifact is contained in the spectra shown in Fig. 3.13, in which the peak at 8.04 keV suggests that the catalyst material contains a sizable amount of Cu. However, this signal is purely an artifact which originates from

the interaction of high energy back-scattered electrons with the Cu mesh grid used to support the amorphous carbon film carrying the catalyst specimen. Another common artifact encountered in AEM-based XEDS spectra are sum peaks, in which two photons arrive at the detector nearly simultaneously and are counted as a single event at an energy corresponding to the sum of the two peaks. A final common artifact is known as an escape peak, which can occur when an incoming photon strikes the Si-based detector and fluoresces a Si-K_α X-ray (1.74 keV). Some of these secondary photons will "escape" from the detector, resulting in a peak located at energy 1.74 keV lower than the true energy of the incoming photon. These types or artifacts can be a source of error in assessing XEDS spectra acquired in the AEM, and so the analyst must be very wary of their possible presence.

Once a thorough qualitative analysis has been done, the analyst may then wish to quantify the various elemental constituents that have been identified. However, great care must be taken to avoid the many pitfalls that can plague this type of quantitative analysis. For a comprehensive discussion of the proper approach to quantitative analysis, see, for example, Joy *et al.*[32], and Williams and Carter[1], and the many references therein.

In general, the first step in the XEDS quantification process involves the removal of the contribution of the background from integrated signal intensity under each of the peaks of interest. In the case of intermediate or high energy peaks, this is rather easily done since the background can be approximated to a linear decay: however, much more care is necessary when analyzing low energy peaks due to the non-uniform shape of the background in this region of the spectrum.

Once background removal has been accomplished, the ratio of the integrated intensity of the two characteristic X-ray peaks can then be used to calculate the mass fractions of each element using the Cliff–Lorimer relationship[33]:

$$\frac{I_a}{I_b} = k\frac{C_a}{C_b}. \tag{3.2}$$

In this equation, C represents the concentration, by mass, of element a or b, whereas I is the integrated intensity of the associated peaks, and k is a constant that depends strongly on the specific instrumental and experimental parameters employed as well as on the identity of the two elements. In most cases, the Cliff–Lorimer factor k is determined by the analysis of standard samples of known composition in the same instrument using similar experimental conditions to those employed while analyzing the unknown specimen. So-called standardless quantification algorithms are also available, where, instead of being experimentally determined, the k values are generated either from first-principles calculations or by fitting to a database of reference spectra acquired on a different instrument. However, this latter approach can be fraught with errors and the analyst should take the time to verify the validity of their performance before accepting the results.[34]

These quantitative approaches were developed to analyze individual spectra, but they are equally suited to the analysis of spatially resolved XEDS hyperspectral image datasets as well. STEM-XEDS is a particularly powerful technique, since it results in high spatial resolution concentration maps of the various elements analyzed. However, care must be taken, since specimens with complex geometries, such as the rough surfaces typically encountered in supported metal catalysts, can lead to errors when performing quantitative data analysis.

An excellent example of the application of quantitative XEDS analysis in catalyst research can be found in the work of Lyman and colleagues.[35–39] In these studies, the composition of supported bimetallic precious metal particles was determined by collecting an entire XEDS spectrum while scanning the probe over individual particles and calculating their composition based on the intensities of the characteristic X-ray peaks of the two metals. This process was repeated for several hundred particles in order to generate statistically relevant data, and the results were used to produce a scatter plot of composition *vs.* particle size. Figure 3.14 shows the data from one such study on the Pt-Rh/Al_2O_3 catalyst system.[38] Figure 3.14(a) shows a particle size composition plot, which clearly reveals two

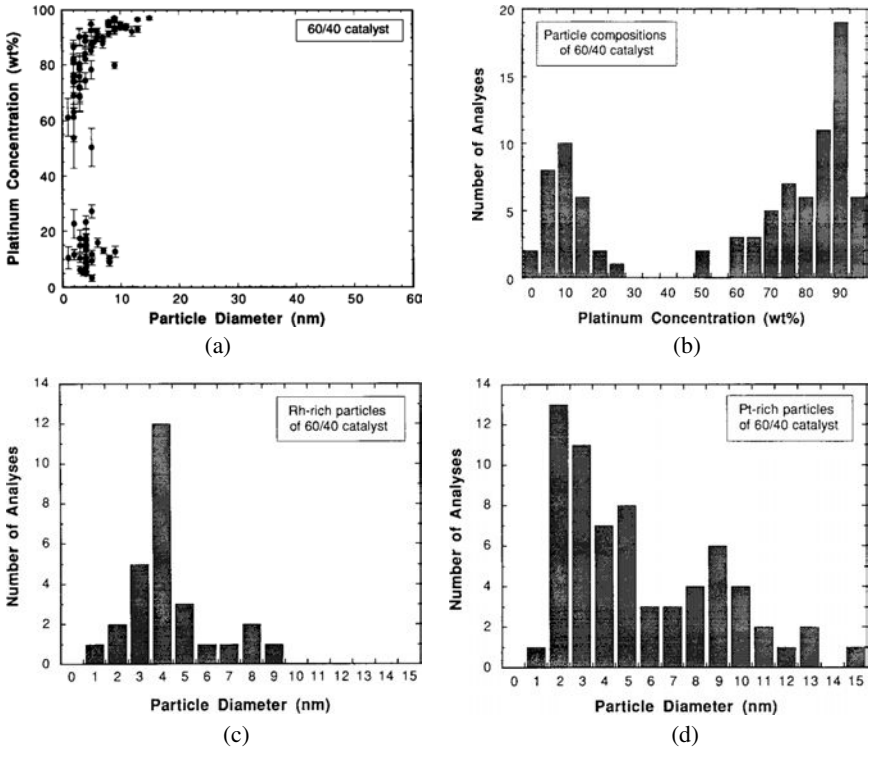

Figure 3.14 Results obtained from AEM analysis of a Pt-Rh/Al_2O_3 NO_x reduction catalyst (mass fraction of Pt and Rh: 0.61 and 0.40, respectively) obtained by Lyman *et al.*[35–39] A plot of particle composition *vs.* size (a), a histogram showing the number of particles analyzed of a given composition (b), and histograms showing the size distribution of Rh-rich and Pt-rich particles ((c) and (d), respectively).

distinct regions of compositional space occupied by the particles in the catalyst, one of which is Rh-rich and the other Pt-rich. The authors attributed this observation to the miscibility gap present in the Pt-Rh equilibrium phase diagram, which was consistent with the thermal history of the catalysts. The data in the particle size composition plot can also be represented as a histogram of the number of particles *vs.* particle composition (Fig. 3.14(b)). Finally, the data may then be extracted in such a way as to produce a pair of histograms, shown in (Fig. 3.14(c) and (d)), which describe the size

distributions of the two characteristic particle compositions (i.e. Rh-rich and Pt-rich) within the catalyst. This manner of presenting the data is far more informative than a traditional particle size distribution, in that the latter contains no compositional information. These studies were the first to demonstrate that AEM analysis was the only technique capable of combining sufficient spatial resolution with analytical sensitivity in such a way as to allow the identification of compositional heterogeneities within populations of small particles that can dramatically affect the resulting catalyst performance.

While the previous example shows the utility of analyzing the "bulk" composition of individual particles, the development of hyperspectral imaging techniques (see Friel and Lyman[40] for a review) has now made it possible to study the compositional fluctuations within individual particles as well. As described in several publications by the Lehigh group,[41–45] by acquiring hyperspectral images and applying suitable statistical processing algorithms such as principal component analysis (PCA), the spatial distribution of the elements within individual bimetallic nanoparticles can be studied as a function of heat treatment conditions or synthesis routes. For example, Fig. 3.15 shows the spatial distribution of Au and Pd in a single bimetallic particle supported on TiO_2. As indicated by the enhancement of the Pd signal at the perimeter of the particle, it is apparent that there is a significant enrichment of Pd at the particle surface relative to the interior, resulting in an Au-rich core surrounded by a Pd-rich shell. Data of this sort are especially valuable, because the *chemical* and *structural* nature of the particle surface can dominate the catalytic performance, and proper characterization of both aspects is a necessity for developing structure-property relations to aid catalyst design. Other surface-sensitive spectroscopic techniques such as X-ray photoelectron spectroscopy (XPS) and low energy ion scattering (LEIS) can also aid in determining the surface composition of catalyst particles, however, only as a representative average over a large ensemble of particles. The analysis of XPS or LEIS data is complicated by the fact that, in a "real" catalyst system, the composition can vary from particle to particle, as well as within individual particles, and this makes the high spatial resolution

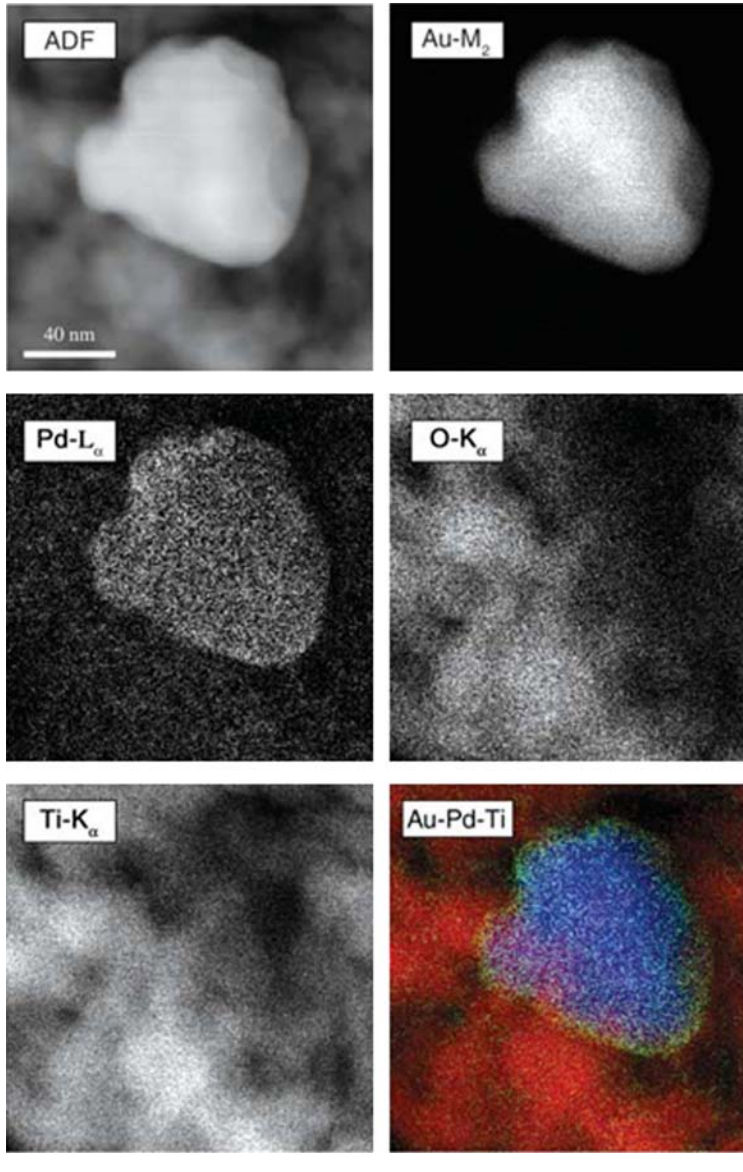

Figure 3.15 Application of hyperspectral imaging to individual particles in supported metal catalysts. Annular dark-field image (top left) acquired from an Au-Pd/TiO_2 catalyst and the corresponding XEDS elemental maps: Au-M (top left), Pd-L (middle left), O-K (middle right), and Ti-K (bottom left). Also shown is a color overlay of the Ti (red), Pd (green), and Au (blue) signals.[27]

mapping afforded by the AEM an excellent complement to "bulk" techniques. These hyperspectral imaging techniques have also been employed to track the segregation behavior of bimetallic nanoparticles as a function of heat treatment,[43] to analyze the particle size dependence of composition by mapping large ensembles of bimetallic alloy particles,[44] and to spatially map a minor metallic constituent in a bimetallic catalyst in the presence of peak overlaps.[44]

3.9 Core-Loss Electron Energy Loss Spectroscopy (EELS) of Supported Metal Catalysts

While XEDS in the AEM has seen a wider application than EELS thus far in the field of supported metal catalysts, there are some cases where the latter technique is superior and can provide unique and valuable compositional information from these materials.[46,47] As mentioned previously, the detection of light elements by XEDS is highly problematic due to the tendency of such species to emit Auger electrons instead of X-rays in response to ionization events caused by the electron beam, and because of detector inefficiencies in the low energy range. In contrast, EELS is capable of detecting characteristic inelastic scattering events regardless of the subsequent relaxation process that follows, and the detection efficiency for light elements is reasonably high.

In addition, the spatial distribution of the inelastically scattered electrons carries a strong forward-bias such that the majority of the signal can be collected by the on-axis post-specimen EELS spectrometer commonly employed in the AEM. This makes EELS a far more efficient technique in terms of signal collection than XEDS, where the detector samples only a tiny fraction ($< 1\%$) of the emitted X-ray photons. An energy resolution of less than 1 eV in the EELS spectrum is readily achievable in most commonly available instrumentation; a value that is far superior to the ≈150 eV spectral resolution of XEDS. Finally, and perhaps most uniquely, with careful analysis, the EELS spectrum can also yield information related to the electronic structure and inter-atomic bonding present in the specimen, both of which are not detectable with the XEDS technique.

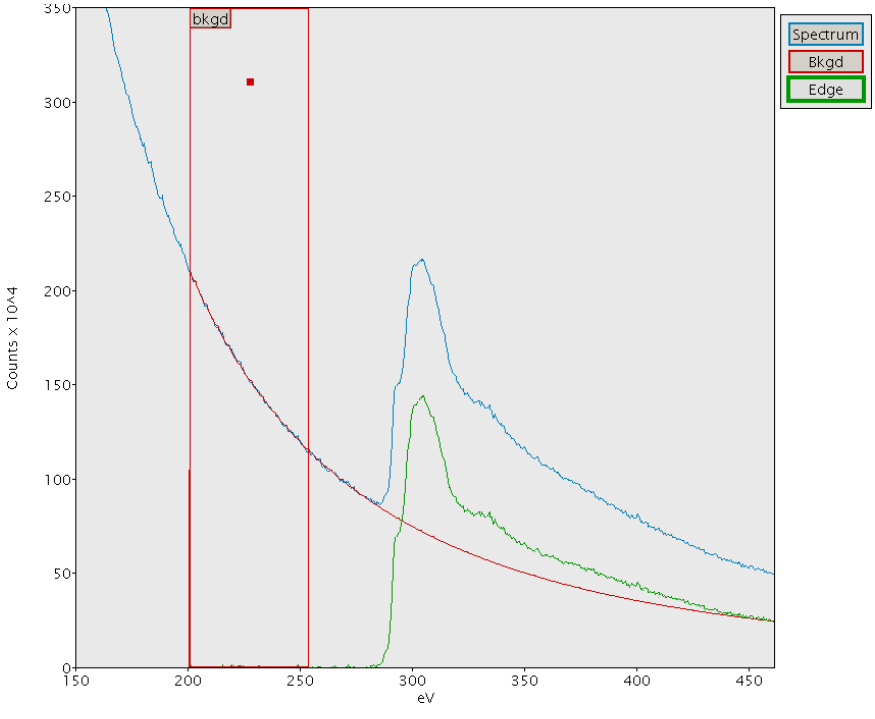

Figure 3.16 Typical EELS spectrum collected from a carbon supported catalyst specimen. The raw spectrum (blue) consists of a strong C-K edge superimposed on a decaying background signal (red). The signal (green) must be carefully extracted by proper modeling of the pre-edge background signal prior to analyzing the data.

The analysis of EELS data needs to be more rigorous than that of XEDS, mostly due to the less uniform structure of the background signal in the EELS spectrum which can significantly complicate even qualitative analysis of the data. A typical EELS spectrum collected from a carbon support material is shown in Fig. 3.16. The spectrum is seen to consist of a strong C-K edge at 283.8 eV energy loss, that is superimposed on a decaying background (shown in red). The pre-edge background can usually be fitted to an equation of the type:

$$I = AE^{-r} \tag{3.3}$$

where ***I*** is the intensity in energy channel ***E***, while ***A*** and ***r*** are curve-fit parameters. Once the background has been modeled, it can be stripped from the raw spectrum, resulting in a more faithful representation of the elemental signature (shown in green).

The background in an EELS spectrum arises from a number of factors, including the excitation of valence electrons to the vacuum level and the presence of extended tails from lower energy features. While the former contribution can be reliably modeled for most intermediate (> 50 eV loss) and high energy loss features, the contribution of the latter can be particularly difficult to remove, especially in a complex system containing many elemental constituents. In addition, the non-uniformity of the background makes it difficult to quickly assess, on a semi-quantitative basis, the relative concentrations of each element. Finally, the thickness of the specimen is of much greater importance in EELS analysis, with very thin samples being preferred, as multiple scattering events in thicker samples can lead to improper data analysis.

Once a careful treatment of the raw signal has been carried out, the composition of, for example, a two-component system containing elements *A* and *B* can be determined *via* the relation:

$$\frac{N_A}{N_B} = \frac{I_K^A \sigma_K^B}{I_K^B \sigma_K^A}. \tag{3.4}$$

In this equation, N is the number of atoms present in the analytical volume, I_K is the intensity above background of the relevant K edges, and σ_K is the partial ionization cross-section. This relationship applies specifically to K edges, but similar expressions have been derived for L and M edges. This equation is analogous to that discussed previously for XEDS quantification, in that the concentration of the two elements is related directly to the ratio of the intensities adjusted by a sensitivity factor, which, in this case is the ratio of the two partial ionization cross-sections (σ).

As demonstrated by Sun *et al*,[48] EELS can be particularly informative when applied to supported metal catalysts. In their work, point spectra were acquired from various positions on a Pd-Cu

nanoparticle supported on γ-Al_2O_3, in an effort to characterize any chemical heterogeneities that existed within the bimetallic. Two examples of this type of analysis are reproduced in Fig. 3.17. In the first case, all three spectra were collected from a ≈3 nm particle: one from the center and two from either side. While the Pd M edge (334.7 eV energy loss) is clearly present in all three, the Cu L edge (931 eV) is only present in the spectrum acquired from the particle center. Since the EELS signal results from the transmission of the electron beam through the bulk of the particle, the absence of Cu signal at the particle perimeter suggested that surface enrichment in Pd had occurred. When this technique was applied to similar Pd-Cu particles after a high-temperature reduction treatment, Cu and Pd were detected at all of the analytical points. The authors were able to use this information and spectral analyses of a larger range of particles to track the microstructural evolution of the various metal particle types formed during catalyst synthesis and subsequent heat treatment.

While the previous study was carried out in STEM mode by collecting spectra from individual points by focusing the electron probe at specific locations, if the AEM is equipped with an imaging energy filter, the energy-loss signal can be acquired in an image-wise fashion from a large specimen area illuminated by a broad, parallel beam in energy-filtered EF-TEM mode. To do this, a portion of the energy-loss signal is selected *via* a slit which is inserted in the dispersion plane of the EELS spectrometer, and only those electrons falling in this range are re-combined to form an image, which represents the spatial distribution of the energy-loss events.[49] EF-TEM has also been successfully applied to the study of heterogeneous catalysts, even though the complex shape of supported metal catalysts can complicate the interpretation of such data due to local variations in specimen thickness as one traverses across the diameter of a support particle.

An elegant solution to this problem was reported by Crozier and McCartney,[50] wherein the authors prepared a TEM specimen by the ultramicrotomy sectioning of an Al_2O_3-supported Ni-Cu-Cr catalyst embedded in a resin matrix. In so doing, the morphological characteristics of the specimen were preserved, while it was also

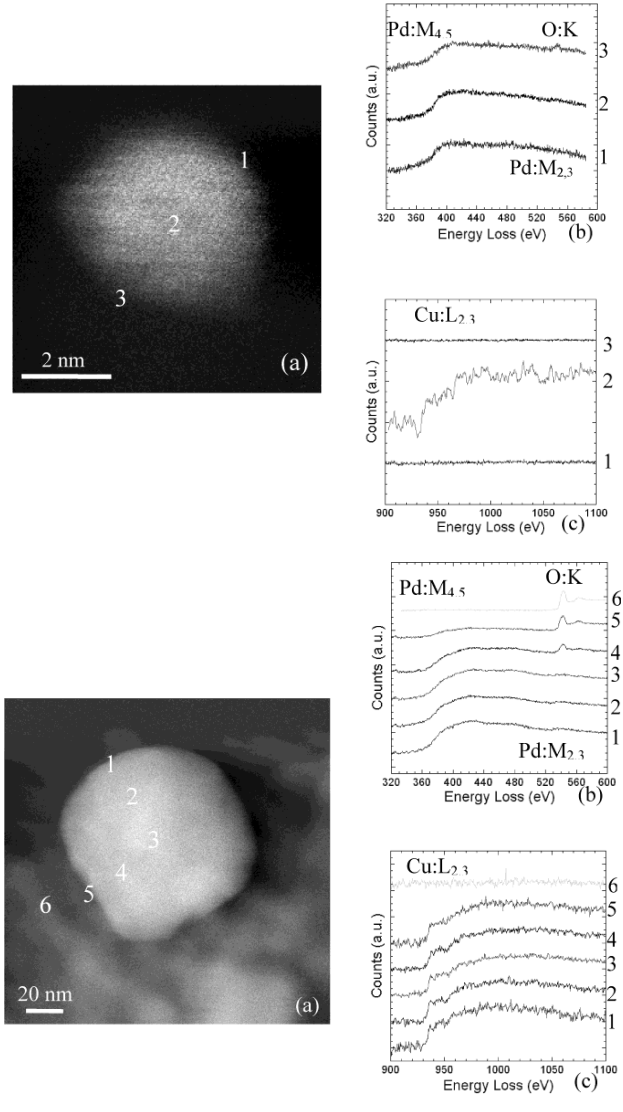

Figure 3.17 The application of core-loss EELS spectroscopy to a catalyst system consisting of γ-Al_2O_3 supported Pd-Cu bimetallic particles. The results depict the EELS response collected at several points near and within a core-shell particle exhibiting surface enrichment of Pd (top), as exhibited by the consistent Pd signal (b) from all three points and the lack of Cu signal (c) near the perimeter. Also shown are similar results collected from a more homogeneous particle (bottom), where the Pd (b) and Cu (c) signals are more consistent from all of the analytical regions.[48]

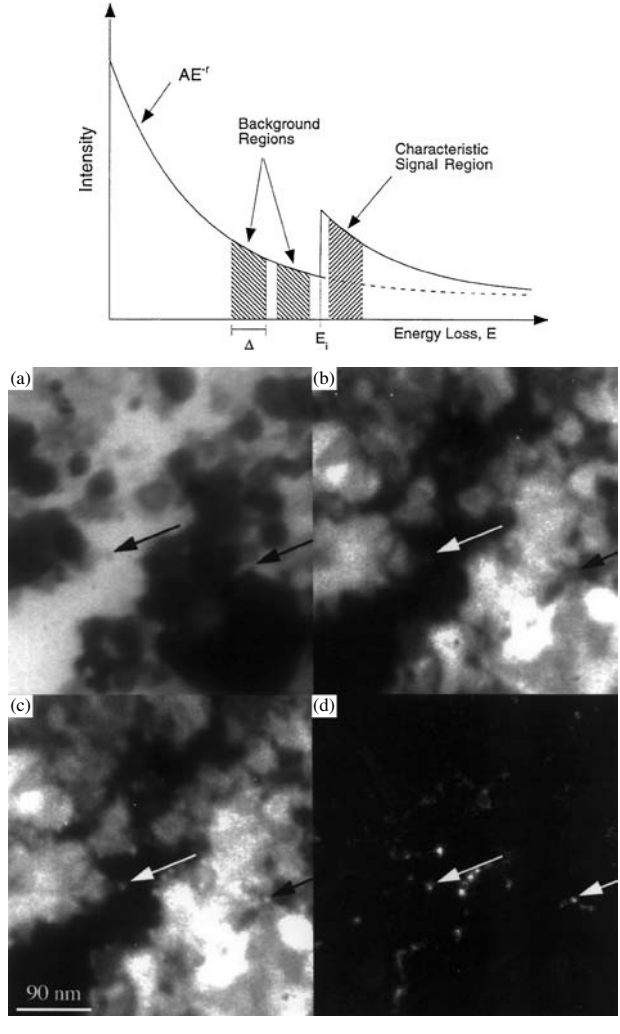

Figure 3.18 Results presented by Crozier and McCartney (1996)[50] wherein EF-TEM core-loss mapping was performed on an Al_2O_3-supported NiCuCr catalyst. A schematic plot shows the energy-loss regions used to collect the signal and to model the background contributions (top). The zero-loss filtered BF image of a particular area of interest (a) is shown, along with one of the images extracted from the Cr-L pre-edge background region (b). Also shown are the raw and background subtracted image from the characteristic signal region ((c) and (d)) respectively) for the Cr-L edge. Arrows point out the region in each image associated with two Cr-rich particles, as revealed by the background subtracted elemental map (d).

rendered uniformly thin for EF-TEM analysis. Elemental mapping was then carried out *via* the three-window method,[47] whereby two images are collected from energy ranges preceding the energy-loss edge of the given elements and a third from the post-edge region (see Fig. 3.18). The first two windows are used to compute a background model with which to then correct the raw image signal collected in the third window. The result is a two-dimensional elemental map, which can then be quantitatively related to the concentration of the given element at each image pixel. The results of this analysis for the Cr-L edge (574 eV) are presented in Fig. 3.18, which contains the zero-loss filtered BF-TEM image of the specimen area being analyzed (a), one of the two pre-edge background images (b), the raw post-edge image (c), and the background-corrected elemental maps (d). Arrows are present to emphasize the location in each image of two Cr-rich particles, as revealed by the background-corrected map (d). The power of this technique is evident in two respects. Firstly, the elemental maps reveal the distribution of the metallic constituents in a directly interpretable fashion. In contrast, while the broad structural features are easily visible in the BF-TEM image, the similarity in atomic number and structures adopted by the three elements present (Ni, Cu, and Cr), makes any further interpretation of the data difficult. Secondly, it is extremely important to compare the stark difference in the raw post-edge image with the background subtracted map, which demonstrates the necessity of carefully removing the background contributions prior to analyzing the images produced in the core-loss EF-TEM signal.

3.10 Summary

It should now be evident that the modern AEM offers an incomparable level of versatility for the characterization of supported metal catalysts. The sheer variety of imaging and spectroscopic signals, all of which can be spatially resolved at, or near, the atomic-level, affords the catalyst chemist the opportunity to locally probe a host of catalytically relevant features within a catalyst sample. Recent

advances in three-dimensional structural and chemical imaging, as well as the ability to carry out *in situ* analyses under realistic temperatures and pressures, are further widening the scope of catalysis applications in which the AEM can play a characterization role. When used in concert with other surface and bulk analytical techniques, AEM can provide vital information pertaining to the nature of the active species within a catalyst and increase our understanding of the structural and compositional factors that control catalytic performance.

† — Certain commercial equipment, instruments, or materials are identified in this document. Such identification does not imply recommendation or endorsement by the National Institute of Standards and Technology, nor does it imply that the products identified are necessarily the best available for the purpose.

References

1. D.B. Williams, C. Barry Carter (Eds.), *Transmission Electron Microscopy: A Textbook for Materials Science*, 2nd Edition, Springer, New York, 2009.
2. P.J. Goodhew, J. Humphreys, R. Beanland (Eds.), *Electron microscopy and analysis*, 3rd Edition, Taylor and Francis, London, 2001.
3. A.I. Kirkland, J.L. Hutchison (Eds.), *Nanocharacterisation*, Royal Society of Chemistry, London, 2007.
4. P.L. Gai, E.D. Boyes (Eds.), *Electron microscopy in heterogeneous catalysis*, IoP Publishing, London, 2003.
5. R.T. Baker, S. Bernal, J.J. Calvino, J.A. Pérez-Omil, C. López-Cartes, in *Nanotechnology in Catalysis, Volume 2*, Eds.: B. Zhou, S. Hermans, G.A. Somorjai, Kluwer Academic/Plenum Press, New York, 2003, 403.
6. S. Bernal, F.J. Botana, J.J. Calvino, C. Lopes-Cartes, J.A. Perez-Omil, J.M. Rodriguez-Izquiredo, *Ultramicroscopy* 1998, **72**, 135.
7. S. Bernal, R.T. Baker, A. Burrows, J.J. Calvino, C.J. Kiely, C. Lopes-Cartes, J.A. Perez-Omil, Rodriguez-Izquierdo, *Surf. Interface. Anal.* 2000, **29**, 411.
8. S. Bernal, J.J. Calvino, M.A. Cauqui, J.M. Gatica, C.L. Cartes, J.A. Perez-Omil, J.M. Pintado, *Catal. Today* 2003, **77**, 385.

9. P. Stadelmann, *Ultramicroscopy* 1987, **21,** 131.
10. P. Stadelmann, JEMS Java Electron Microscopy Software; Available from: http://cimewww.epfl.ch/people/stadelmann/jemsWebSite/jems.htmlhttp://cimewww.epfl.ch/people/stadelmann/jemsWebSite/jems.html. Accessed on 1 August 2010.
11. E.J. Kirkland, *Advanced computing in electron microscopy*. Plenum Press, New York, 1998.
12. L.C. Gontard, L.-Y. Chang, C.U.D Hetherington, A.I. Kirkland, D. Ozkaya, R.E. Dunin-Borkowski, *Angew. Chem. Int. Ed.* 2007, **46,** 3683.
13. J. Liu, *Microscopy and Microanalysis* 2004, **10**, 55.
14. O.L. Krivanek, N. Dellby, A.R. Lupini, *Ultramicroscopy* 1999, **78**, 1.
15. M. Varela, A.R. Lupini, K. van Benthem, A.Y. Borisevich, M.F. Chisholm, N. Shibata, E. Abe, S.J. Pennycook, *Annual Review of Material Research* 2005, **35**, 539.
16. S.J. Pennycook, L.A. Boatner, *Nature* 1988, **336**, 565.
17. S.J. Pennycook, *Ultramicroscopy* 1989, **30**, 58.
18. P.A. Midgley, M. Weyland, J.M. Thomas, B.F.G. Johnson, *Chem. Commun.* 2001, **10**, 907.
19. M. Weyland, P.A. Midgley, in *Nanocharacterization*, Eds.: A.I. Kirkland, J.L. Hutchison, Royal Society of Chemistry, London, 2007, 184.
20. H. Friedrich, P.E. de Jongh, A.J. Verkleij, K.P. de Jong, *Chem. Rev.* 2009, **109**, 1613.
21. C.J. Kiely**,** *Nature Materials* 2010, **9**, 296.
22. J.W. Wittig, J. Bentley, L.F. Allard, M.S. Wellons, C. Lukehart, *Microscopy and Microanalysis* 2008, **14,** 216
23. P.D. Nellist, S.J. Pennycook, *Science* 1996, **274**, 413.
24. K. Sohlberg, S. Rashkeev, A.Y. Borisevich, S.J. Pennycook, S.T. Pantelides, *Chem. Phys. Chem.* 2004, **5**, 1893.
25. S. Wang, A.Y. Borisevich, S.A. Rashkeev, M.V. Glazoff, K. Sohlberg, S.J. Pennycook, S.T. Pantelides, *Nat. Mat.* 2004, **3**, 143.
26. A.A. Herzing, C.J. Kiely, A.F. Carley, P. Landon, G.J. Hutchings, *Science* 2008, **321**, 1331.
27. Q. He, J.K. Edwards, G.J. Hutchings, C.J. Kiely, *Microscopy and Microanalysis* 2010, **16**, 1188.
28. P.L. Gai, in *Nanocharacterization*, Eds.: A.I. Kirkland, J.L. Hutchison, Royal Society of Chemistry, London, 2007, 268.

29. J.A. Hunt, D.B. Williams, *Ultramicroscopy* 1991, **38**, 47.
30. C. Jeanguillaume, C. Colliex, *Ultramicroscopy* 1989, **28**, 252.
31. J.I. Goldstein, D.E. Newbury, P. Echlin, D. Joy, A. Romig, C.E. Lyman, C.E. Fiori, E. Lifshin (Eds.), *Scanning electron microscopy and X-ray microanalysis*, 2nd Edition, Plenum Press, New York, 1981.
32. D.C. Joy, A.D. Romig, J.I. Goldstein (Eds.), *Principles of analytical electron microscopy*, 2nd Edition, Plenum, New York, 1986.
33. G. Cliff, G.W. Lorimer, *J. Microsc.* 1975, **103**, 203.
34. D.E. Newbury, *Microscopy and Microanalysis* 1999, **4**, 585.
35. L. Bednarova, C.E. Lyman, E. Rytter, A. Holmen, *J. Catal.* 2002, **211**, 335.
36. Z. Hu, F.M. Allen, C.Z. Wan, R.M. Heck, J.J. Steger, R.E. Lakis, C.E. Lyman, *J. Catal.* 1998, **174**, 13.
37. R.E. Lakis, C.E. Lyman, H.G. Stenger, *J. Catal.* 1995, **154**, 261.
38. C.E. Lyman, R.E. Lakis, H.G. Stenger, *Ultramicroscopy* 1995, **58**, 25.
39. C.E. Lyman, R.E. Lakis, H.G. Stenger, B. Totdal, R. Prestvik, *Mikrochimica Acta.* 2000, **132**, 301.
40. J.J. Friel, C.E. Lyman, *Microscopy and Microanalysis* 2006, **12**, 2.
41. J.K. Edwards, B.E. Solsona, P. Landon, A.F. Carley, A. Herzing, C.J. Kiely, G.J. Hutchings, *J. Catal.* 2005, **236**, 69.
42. D.I. Enache, J.K. Edwards, P. Landon, B. Solsana-Espriu, A.F. Carley, A. Herzing, M. Watanabe, C.J. Kiely, D.W. Knight, G.J. Hutchings, *Science* 2006, **311**, 362.
43. A.A. Herzing, A. F. Carley, J.K. Edwards, G.J. Hutchings, C.J. Kiely, *Chem. Mater.* 2008, **20**, 1492.
44. A.A. Herzing, M. Watanabe, J.K. Edwards, M. Conte, Z. Tang, G.J. Hutchings, C.J. Kiely, *Faraday Discussions* 2008, **138**, 337.
45. J.K. Edwards, B. Solsona, P. Landon, A.F. Carley, A. Herzing, M. Watanabe, C. Kiely, G.J. Hutchings, *J. Mater. Chem.* 2005, **15**, 4595.
46. R. Brydson, *Electron Energy Loss Spectroscopy*, Bios Scientific Publishers, Oxford, 2001.
47. R.F. Egerton, *Electron Energy Loss Spectroscopy in the Electron Microscope*, 2nd Edition, Plenum, New York, 1996.
48. K. Sun, J. Liu, N.K. Nag, N.D. Browning, *J. Phys. Chem. B* 2002, **106**, 12239.
49. L. Reimer, *Energy-Filtered Transmission Electron Microscopy*, Springer, New York, 1995.
50. P.A. Crozier, M.R. McCartney, *J. Catal.* 1996, **163**, 245.

CHAPTER 4

CHARACTERIZATION OF SUPPORTED METAL CATALYSTS BY SPECTROSCOPIC TECHNIQUES

M. Fernández-García[1] and J. A. Anderson[2]

[1]*Instituto de Catálisis y Petroleoquímica, CSIC, C/Marie Curie, 28049 Madrid, Spain*

[2]*Surface Chemistry and Catalysis Group, Department of Chemistry, University of Aberdeen, Kings College, Scotland, UK*

4.1 Introduction

It is impossible to present, in a single chapter, an exact theory concerning the structural and electronic properties of metals and alloys as well as present the theoretical background of the spectroscopies used to establish the structural and electronic basis of metal catalysts. As an indication of the volume of data concerning such aspects, we refer to the text by Ponec and Bond which collects some of the most significant data[1] and to the fact that the catalysis of Pd-supported systems has been subjected to a complete series of reviews.[2] Rather than a complete compilation of experimental results, we will pursue an approach which, in the first instance, tries to briefly synthesizse the main guidelines recently employed in interpreting the geometrical and electronic properties of mono- and bimetallic catalysts. Subsequently, the chapter attemps to provide a glimpse of the effect that nanostructure and the support will have on the metallic component of the catalyst. Thus, in the second part of this chapter, we will review the theoretical basis of spectroscopic

techniques employed for *in situ* characterization of metallic systems and present examples from relevant studies. Four main groups of techniques will be envisaged; the first group is related to the use of X-ray absorption/emission techniques, the second considers new "time-resolved" and "total scattering" approaches to the X-ray diffraction, the third concerns vibrational techniques, and the fourth includes the use of photoelectron spectroscopy under relevant, environmental conditions. Emphasis has been placed on selecting representative data of real "*in situ*" characterization, meaning that analysis of the systems has been performed under the appropriate atmosphere and at the temperature and pressure required by its industrial application. A final part of the review will briefly cover other, non-*in situ* work of interest, mainly related to the use of magnetic resonance spectroscopy.

4.2 Main Properties of Monometallic Systems

Metals used in catalysts are mainly of the transition series which display face centered cubic (fcc) bulk structure with the exception (at room temperature) of Co, Ru, Re (hexagonal centered primitive, hcp) and Fe (body centered cubic, bcc). The need for high surface area, as catalysis is essentially a surface phenomenon, requires the dispersion of the metal component on a support and thus the formation of metal entities with limited size and number of atoms (typically below 100). Metallic nanostructures or clusters, may display cuboctahedra or Wolf polyhedra particles morphologies derived from the fcc structure.[3] In essence, the high surface to bulk number of atoms present in a cluster are such that surface energy and stress contributions to the total energy are not negligible and induce significant structural changes with respect to the bulk. In fact, surface stress acts to displace atoms from the equilibrium positions which they normally occupy in bulk materials.[4] In addition, it is well known that clusters can present icosahedra or decahedra structures which do not match with known bulk structures.[5] The latter two structures are characterised by five-fold symmetry axes and have been observed for Au,[6,7] Ag[8] and Cu[9] clusters containing 150 or

less atoms. Such structures appear for clusters with specific numbers of atoms, called magic numbers and their formation is dominated by kinetic rather than thermodynamic factors.[10,11] As shown by previous experience, the interaction with the support can also play a role; although this will induce changes in atomic positions, bulk-like fcc structure will usually hold, but a strong influence in shape can be expected when the M–O bond strength is similar to the M–M. In such cases, rather than spherical morphologies, planar particles can be formed, as shown in Fig. 4.1 for the case of Pd particles supported in a LTL-Zeolite.[12] Studies of metal growth in model systems, using single crystals as supports, have been reviewed in the literature[13,14] but the energetics of the metal support interface is so dependent on the effect of local order or impurities present in real carriers that more work is required in order to construct a bridge between model and real systems. A final point to mention concerning this brief overview on structural properties of monometallic systems would take into account that metal catalysts are analysed in the presence of a gaseous atmosphere and potentially hydrogen is chemisorbed during the reduction process. This usually produces changes in the M–M bond distance and influences electronic properties.[15]

Electronic properties of transition metals can be described by a simplified model, which, essentially, considers a narrow d sub-band

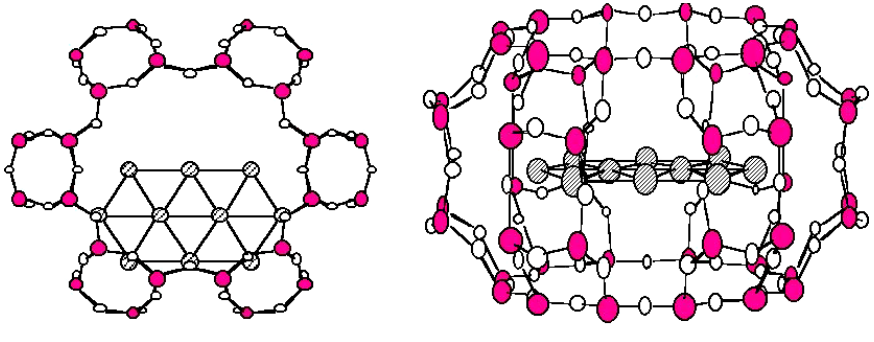

Figure 4.1 Metal-L-Zeolite interface. (a) Viewed perpendicular to the c-axis of the L-Zeolite channel. (b) Viewed along the c-axis of the L-Zeolite channel.[12]

having a somewhat localised, atomic-like nature, while the sp subband is wider and mostly delocalised.[1] The Fermi level has a major contribution to the density of states from the d band in most typical active phases, such as those including noble metals. The limited size of clusters produces the so-called quantum or size confinement effects. These essentially arise from the presence of discrete, atomic-like electronic states. From the solid state point of view, the electronic states of clusters can be considered as being a superposition of bulk-like states with concomitant increases in oscillator strength.[14] This separation of the states is visible in the valence band of metallic clusters synthesised by physical methods[3] but is obscured in supported metals by the effect of the polydispersity. The usually broad and asymmetric particle size distribution present in supported systems produces the broadening of the valence band although a measurable size effect can be detected in core levels. The so-called surface core-level shift is a well-established phenomenon which can be directly associated with the electronic modification suffered by the metal at the surface.[16] That is to say that it is an initial state effect, derived by changes in the electronic structure of surface atoms. The separation of electronic levels has profound implications in metal properties as it drives the metal-insulator transition.[3,17] Although not well defined in general for all metals, the cut-off point for metallic character is believed to take place for clusters of transition metals around/below 150 atoms.[17] This happens concomitantly with changes in the nature of the Fermi edge; for example, Pd has an atomic average electronic configuration of $d^{10}s^{0}$ for clusters below four atoms while larger clusters display a $d^{9.9}s^{0.1}$ average electronic configuration. Alkali metals may however maintain bulk-like properties to a significantly large extent.[18,19] The effect of the support is, as mentioned, of importance. As detailed previously, clusters located in regular positions of support are mainly affected by Pauli repulsion with the oxygen anions and concomitant polarization of the metal electron cloud.[1] This produces a redistribution of electronic charge which is actively investigated by using XPS.[20] Defective sites, such as steps or edges, produce some moderate charge transfer between the basic oxygen ions and the metal

particle. As mentioned above, another aspect to consider when characterizing metal particles is the presence of adsorbed hydrogen atoms which modify metal–metal (M–M) bonds and sp/d hybridization.[15,21]

4.3 Main Properties of Bimetallic Systems

The term bimetallic was introduced by Sinfelt to account for the fact that a catalyst may contain a multitude of phases containing the active metallic components.[22] Of these many phases, a characteristic is the binary alloy. The term alloy can describe a broad range of situations from well-defined phases or solid solutions to surface alloys in cases where bulk alloys are not thermodynamically favoured but a clearly defined surface local arrangement is obtained. Note that the novel core-shell bimetallic structures are included in this catch-all term. An historical overview of the properties of alloys in connection with catalysis has been published by Ponec.[23] At present, a broadly agreed view accepts that alloy components can be "chemically" recognised and, therefore, supports a somewhat "localised" interpretation of the alloy nature and properties. Obviously, a "delocalised" view loses most of its meaning in the case of clusters due to its finite dimensions.

Simple thermodynamic considerations indicate that the surface composition of an alloy would differ strongly from that of the bulk. This is a phenomenon driven primarily by the difference in binding energy between the A–B heterometallic bond and the A–A, B–B homometallic bonds.[24] In general, surface segregation depends on a range of parameters including bond strengths, atomic sizes, enthapies of sublimation and surface energies, temperature, exposed surface plane, and particle size. Analysis of surface composition is usually performed in terms of the broken-bond or regular solution models.[1] Although no satisfactory theory can account for all of the above mentioned parameters,[1] Mezey developed a theory known as the modern thermodynamics, calculated at the interface properties[25] which, after some refinements, displays good agreement with extended alloys, including face-sensitive

composition.[26] Nowadays, the effect of a limited size is mainly introduced by Monte Carlo simulations[1] but essentially it is believed that the lower the coordination particle site, the greater the tendency for segregation. The effect of size is not confined to the surface. Nanostructured alloy particles show phase diagrams very different from those of bulk materials.[27] The influence of the support on surface composition is also of importance but has been scarcely investigated. Contrarily, significant effort has been put in to understanding the effects of absorbates.[28] Simple tests of the adsorbate (X) effects are based on the relative strength of the A-X and B-X bonds. However, kinetic factors seem to play a major role in the extent of adsorbate induced segregation; depending on the reaction temperature, diffusion of atoms at the surface can allow a new adsorbate induced equilibrium surface composition. This is illustrated in Fig. 4.2 which displays CO adsorption on a $Pd_{0.75}Cu_{0.25}$ nanostructured alloy particle at both room temperature and at 573 K.[29] The drastic enrichment in Pd at the particle surface is clearly evidenced by the growth of the bridge contribution at *ca.* 1850 cm^{-1} and the frequency change of the on-top carbonyl (*ca.* 1950 cm^{-1}). This Pd-rich surface is stable when the temperature is returned to ambient.

The use of bimetallic catalysts is a direct consequence of the improved catalytic performance with respect to monometallic systems.[1] The "localised" view mentioned above crystallises in a theory which supports such improved performance in the so-called geometric or ensemble, and electronic or ligand, type of effects. Ensemble effects are interpreted in such a manner that the surface sites available to a reactant molecule can be defined by the nature (A or B) and number of the first coordination metal shell. Note that although catalysis is an essentially surface phenomenon, a three-fold hcp site present in an fcc surface has subsurface atoms as nearest neighbours. This has been analysed in a general manner by Rodriguez *et al.*[30] On the other hand, it can be also be argued that the mechanism by which molecules involved in the rate limiting step (or prior to this step) have multiple bonds with the surface may limit the usefulness of this concept. This is closely related to

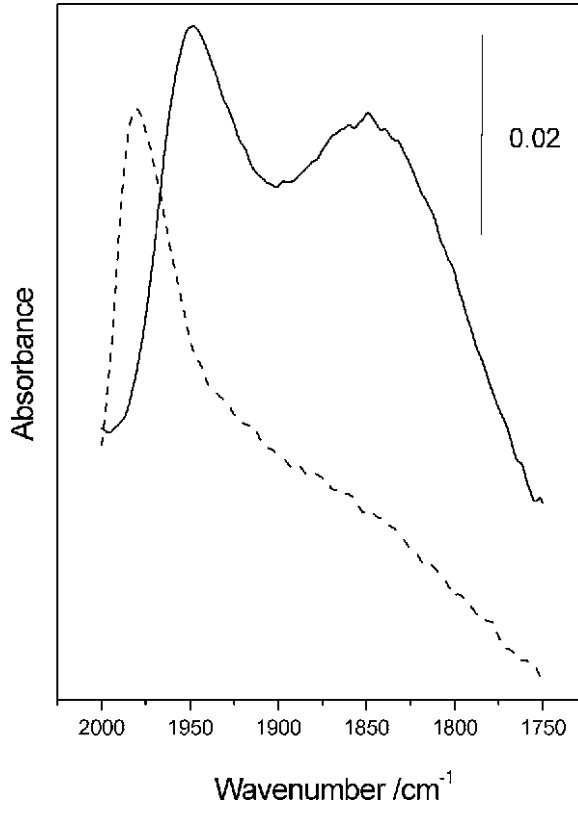

Figure 4.2 FTIR spectra of the carbonyl region for a $Pd_{0.75}Cu_{0.25}$ nanostructured alloy after CO adsorption at room temperature (dashed line) and at 573 K (solid line).[29]

the surface-sensitive or insensitive character of a reaction and will be further analysed in following chapters. In any case, it can be safely mentioned that the tridimensional (not exclusively surface) ensemble will be constituted by a limited (typically lower than ten) number of atoms. However, most papers claim the existence of synergism between alloy components related in a somewhat obscure way to a ligand or electronic effect.[1,30] The existence of an electronic interaction between alloy components has been deduced mainly on the basis of IR characterization using CO as a probe

molecule and by XPS measurements, but data from these spectroscopies cannot be adequately interpreted without the help of theoretical calculations. This can be emphasised by continuing with the Pd-Cu alloy example. Nanosized Pd-Cu bimetallic catalysts[30–33] can form Pd-Cu solid solutions over a broad range of compositions, at least in the Pd : Cu = 0.5–2.0 range.[31] As occurs with Pd-Cu extended alloys, XPS data for these solid solutions display positive/negative shifts of the Pd/Cu core-level binding energies with respect to the appropriate monometallic reference system.[18] A simplistic interpretation of the XPS shift based upon a simple charge transfer model would indicate an electron flow from Pd to Cu. The first principle analysis of the heterometallic bond gives a more complex interpretation, with a Cu(4sp) $\rightarrow$ Pd(5sp) charge transfer and a strong internal Pd d $\rightarrow$ sp re-hybridization as the main contributions. The theoretical analysis unequivocally shows the XPS shift is dominated by the Pd polarization and, therefore, does not provide any information concerning charge transfer. The example sheds some light onto the fact that the heterometallic bond is formed through non-bonding (Pauli repulsion) and bonding (polarization, charge transfer and correlation) contributions and all of these may influence the experimental observations. Limiting the interpretation of the heterometallic bond to the charge transfer process is obviously erroneous and frequently drives to misleading conclusions. CO is used as a probe molecule and its C-O stretching frequency followed by infrared spectroscopy. In the case of Pd-Cu cluster alloys, a moderate to low blue shift is detected with respect to the appropriate monometallic Pd reference. This result is at odds with the red shift expected on the basis of a purely geometric (ensemble) dilution of Pd effect by Cu and thus provides a strong indication for the presence of electronic effects in this system.[18] The detailed interpretation of the shift in the CO stretching frequency was supported by theoretical calculations, which showed that it is dominated by the correlation contribution to the adsorbate-alloy bond.[33] This again indicates that the observable parameter, the C-O stretching frequency, is not directly related to a charge flow process between the alloy constituents.

4.4 *In situ* Characterization

4.4.1 *X-ray absorption and emission spectroscopies*

X-ray absorption and, more recently, emission techniques are customarily used to analyse the local structure of materials. More concretely, the X-ray absorption fine structure (XAFS) acronym refers to the oscillatory structure observed in the absorption coefficient ($\mu(E)$) just above or close to the absorption edge of an element constituting the sample. X-ray absorption spectroscopies are, essentially, synchrotron-based techniques and measure the absorption coefficient as a function of the X-ray energy $E = h\omega$. A typical absorption spectrum ($\mu(E)$ *vs.* E) shows three general features. The first one is an overall decrease in $\sigma(E)$ with increasing energy which, sometimes, also contains well-defined peaks at specific energies called pre-edge transitions. The second is the presence of the edge, which roughly resembles a step function with a sharp rise at the corresponding edge energy and reflects the ionisation of an inner-shell (or core) electron of the element under study. The third component appears just above the edge and corresponds to the oscillatory structure that can be roughly described as a periodical function, progressively damped as it evolves from the edge energy. Being absorption techniques, XAFS spectroscopies are element-specific. On the other hand, the deep penetration of X-rays into matter means that they provide information over the whole system, becoming surface-sensitive only by employing specific detection schemes which will be briefly discussed below.

The XAFS spectrum, $\chi(E)$, is defined as the normalised oscillatory structure of the X-ray absorption, e.g. $\chi(E) = (\mu(E) - \mu_0(E)/\mu_0(E))$, where $\mu_0(E)$ is the smooth varying atomic-like background absorption. Essentially, the XAFS spectrum implicates the quantum-mechanical transition from an inner, atomic-like core orbital electron to an unoccupied, bound (pre-edge transition) or unbound, free-like continuum level. The oscillatory structure therefore reflects the unoccupied part of the electronic bands/structure of the system in the presence of a core-hole.[34–38] Note that this differs from the initial, ground state by physical effects induced by the fact that the

core-hole is not infinitely long lived but must decay as a function of time and distance from the photo-absorbing atom.[34–38] The latter point is worthwhile stressing here as their short range order characteristic makes these techniques particularly suitable for the analysis of nano-structured materials which, frequently, do not possess or present strongly disturbed long range order.

Historically, it was controversial to recognise the local nature of the XAFS techniques (see Lytle for a recent discussion)[39] but now the theoretical description of the techniques is reasonably well settled.[36,37] The absorption of X-ray by matter is described in many text books.[40] The treatment of the radiation as an electric field without practical spatial variation on a molecular/local scale and eliminating magnetic parts leads to the Fermi Golden Rule for the X-ray cross-section:

$$\mu(E) = K[\langle \phi_f / e \bullet \overline{r} / \phi_i \rangle]^2 \delta_{Ef-Ei+hy}. \tag{4.1}$$

The intensity of the absorption process is then proportional to the square of the transition matrix element connecting the initial (ϕ_i) and final (ϕ_f) states times, a delta function which ensures that it satisfies the conservation of energy theorem. The elimination of the spatial dependence of the electric field corresponds to a series expansion of its $e^{2\pi z/\lambda}$ dependence up to the first term (linear dependence in r — Eq. (4.1); this yields the dipole approximation of the interaction energy between the atom electronic cloud and the X-ray radiation field. Better approximations will include quadrupole and octupole terms and so forth. However, except in a few cases, some of them detailed here, the dipole approximation gives a quantitative analysis of the XANES shape and EXAFS oscillations.

An important approximation is to assume that the matrix element can be rewritten into a single-electron matrix element. This is based on the sudden approximation which allows the transition element in Eq. (4.1) to be rearranged in terms of an overlap term of the N-1 "inactive" electrons, which is roughly independent of

energy, and the mentioned single-electron matrix element connecting wave-functions of the unbound and inner-core electrons.[41] The validity of the sudden approximation depends primarily on the photo-excited electron kinetic energy and has been subjected to many studies.[35,37,38] All electron rearrangements (inter-atomic and mainly extra-atomic relaxation of valence electrons) in response to the core-hole creation are thus neglected and the series of delta functions corresponding to different final states identifies with the local density of states (ρ)[42] and the corresponding X-ray absorption cross-section becomes:

$$\mu(E) = K[\langle \varphi_f / e \bullet \bar{r} / \varphi_i \rangle]^2 \rho \tag{4.2}$$

where $\varphi_{i,f}$ correspond to the previously mentioned initial and final mono-electronic wave-functions. The dipole matrix element dictates that the local density of states has an orbital moment that differs by one from the core state ($\Delta L = \pm 1$) while the spin is conserved ($\Delta S = 0$). If the electric quadrupole radiation is considered, the selection rule changes and becomes ($\Delta L = 0, \pm 2$; $\Delta S = 0; \pm 1, \pm 2$).

There are two XAFS techniques; X-ray absorption near edge spectroscopy (XANES) and extended X-ray absorption fine structure (EXAFS). They differ in the energy of the final electronic state sampled, which is limited to a maximum of about 40–50 eV for XANES and above that point for EXAFS (Fig. 4.3). Intuitively, it is obvious that pure electronic information (e.g. chemical bonding information) is only enclosed in the low-lying extended states and is thus confined to the XANES region. This will be discussed below. On the other hand, at high energy in the continuum of electrons participating in EXAFS, the effect of neighbouring atoms becomes small and electron state approximates to spherical waves that are simply scattered by such atoms. The information extracted is thus of geometrical local character.

As a general rule, Eqs (4.1) and (4.2) can be solved by using modern quantum-mechanical methods. Two general approaches are discerned. The first one involves *ab-initio* or DFT methods to

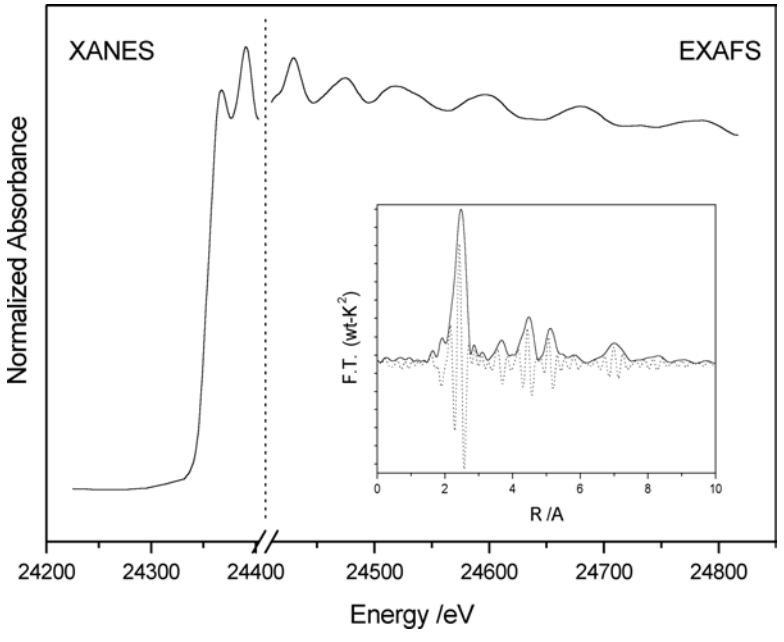

Figure 4.3 Pd K edge XAFS spectrum of a Pd foil. Inset; Fourier Transform of the EXAFS signal.

calculate the initial and final wave-functions of the electronic transition. The second reformulates the Schrödinger equation in terms of the scattering theory and allows one to write the absorption equation as a correlation function. This latter is particularly useful for EXAFS analysis of nano-structured materials as they can be treated as clusters for calculations which, in turn, can be performed in steps of growing size, showing the effect of introducing different coordination spheres. Detailed accounts for the multiple-scattering EXAFS theory can be found in Natoli[43] and Rehr and Albers[44]. Using this theoretical framework the EXAFS formulae can be written as:

$$\chi(E) = S_0^2 \sum_i \frac{N_i F(k)}{k R_i^2} e^{-2R/\lambda(k)} e^{-2DW} \sin(2kR + \phi(k)). \qquad (4.3)$$

This was originally proposed by Sayer *et al.*,[45] based in a single-scattering formalism but can be generalised to represent the contribution of N equivalent multiple-scattering contributions of path-length 2R.[44] It can therefore be considered as the standard EXAFS formula, providing a convenient parameterization for fitting the local structure around the absorbing atoms. The dependence of the oscillatory structure on inter-atomic distance and energy is reflected in the sin(2kR) term. The decay of the wave due to the mean free path or lifetime (including intrinsic core-hole and extrinsic inelastic losses) is enclosed in the exponential $2R/\lambda$, which is largely responsible for the relatively short range probed by EXAFS in a material. As recognised in earlier studies,[45] the sinusoidal nature of the EXAFS phenomenon allows a Fourier analysis of the signal (inset in Fig. 4.3), yielding key information to provide initial guesses for the fitting parameters. In fact, for each shell contributing to the EXAFS signal, we may have (*vide infra*) a peak in the Fourier Transform spectrum. The strength of the interfering waves depends on the type and number (N) of neighbouring atoms through the back-scattering amplitude (F(k)) which largely dictates the magnitude of the signal. The phase function (ϕ(k)) reflects the quantum-mechanical wave-like nature of back-scattering which depends on both the absorber and the scattering atom properties and accounts for the difference between the measured and geometrical inter-atomic distances (which is typically *ca.* 0.3–0.4 Å for low atomic number (Z) back-scatterers and lower for the rest of the atoms) displayed in the Fourier Transform.[35,37,39]

Another important factor is the Debye–Waller factor e^{-DW}. This accounts for thermal and static disorder effects concerning the movement/position of atoms around their equilibrium/averaged position. A point to stress is that the nature of this term is different to the counterpart term in XRD.[46] Since vibrations increase with temperature, EXAFS spectra are usually acquired at low temperature (below 100 K) in order to maximise information. Spectra at different temperatures may, on the other hand, allow decouple thermal and static contributions to DW. The DW term smears the sharp interference pattern of the sinusoidal term and cuts off EXAFS at sufficiently

large energy beyond *ca.* 20 A^{-1}. It is important to stress that the DW factor is in fact a complex mathematical function and has a natural cumulative expansion in powers of k. The amplitude of the e^{-DW} factor contains even moments $DW(k) = 2C_2k^2 - (2/3)C_4k^4 + ...$ while odd moments contribute to the EXAFS phase $\phi(k) = 2c_1k-(4/3)C_3k^3+....$[47] While the fitting of bulk systems makes use of up to the squared term of the k-series expansion, the point is that the k^3 behaviour is important for "disordered" systems; as surface atoms have a less symmetric environment with respect to bulk ones and correspond to a significant part in nano-structured materials, the cumulative expansion needs to be considered in analysing EXAFS data. The third cumulative expression would mainly correct distance values, which are systematically shortened by the standard (second order) equation. Correction of coordination numbers (a Debye–Waller term) would require the use of the fourth cumulative expression. Although the importance of the anharmonic pair bond potential has been discussed previously for nanosized metal particles,[48,49] it appears that very small particles (less than *ca.* 50 atoms) may display a Gaussian/harmonic potential up to moderate temperatures (573 K).[50] It should be mentioned here that almost the complete set of data reviewed does not take into account the corrections of the cumulative expansion to quantitative estimations of particle size, morphology and M-M distances.

Comprehensive EXAFS reviews on catalysis have been recently published.[51,52] These encompass studies concerning surface mediated electrochemical processes and catalytic solids under environmental conditions. The first set of studies examined the local structural changes in the metal occurring in tandem with redox processes under voltage control.[53–57] Recent work in this area examines the stability of bimetallic Pt-Ru electrodes and their performance in the hydrogen oxidation reaction in the presence of CO[58,59] or direct methanol fuel cells.[60] Studies reviewed involving supported metal catalysts concern, in the first place, the reduction process[61–63] while other studies[64] also consider the oxidation process and reduction under inert gases. All of these studies make an attempt to understand the relevance of the metal support interface

and the kinetic parameters of the reduction in the final average particle size and distribution[61,62,64] some of these being specific to bimetallic systems.[61,63] Additional studies consider the stability upon reduction-oxidation cycles in several systems including Cu[65] and Pd[66] on ceria matrixes/supports and Pd on perovskites.[67] The analysis of reduction and/or oxidation steps is usually completed by studying the low temperature (*ca.* 100 K) EXAFS spectrum after completing the corresponding process, in order to obtain detailed information concerning average particle size and morphology. Details on the use of EXAFS coordination numbers for the first three metal-metal shells for size/morphology analysis of fcc clusters can be found in Xia *et al.*,[11] Jentys,[68] and Agostini *et al.*[69] Closely related works follow the decarbonylation process of Ru or Mo mono and bimetallic carbonyls to yield metallic particles.[70,71] Activation treatments other than reduction mainly concern the sulfidation of Ni-Mo catalysts,[72,73] Rh nanoparticles,[74] or Pd-Pt bimetallic catalysts,[75,76] analyzing the intermediates and final products of the process, and sulphur tolerance of precious metals as well as the effect of some chelating agents.[72–76]

Fewer EXAFS works have been devoted to the study of catalytic systems under reaction conditions due, as already said, to inherent limitations of the technique at high, working temperatures characteristic of catalytic reactions. Among these, a majority include studies of Cu/ZnO (Cu/SiO_2) in methanol synthesis.[77,78] The solid state physics of the active copper phase in methanol synthesis is a rather intriguing problem which has not achieved consensus concerning the oxidation state and the hosting of the Cu phase characteristics. The EXAFS works mentioned above elucidated mainly the importance of the metallic state in the reaction. Similarly, the metallic state has been shown to be of importance in the water gas shift reaction (WGS) in Cu,[79] Au,[80] and bimetallic Pd-Cu[81] systems supported on ceria. The importance of ceria vacancies on the activation of water and of the metal (and more precisely, of the metal at support boundaries) for CO activation appear as key elements for this reaction. The bimetallic Pd-Cu work analyses the modulation of Pd behaviour by effect of the alloy with the base

metal due to the fact that such bimetallic formulation appears to force the exclusive presence of Pd-Cu neighbours at first coordination distance. Additional EXAFS studies concern hydrocarbon activation (ethene dehydrogenation) reactions.[82] Finally, Baiker's group[83,84] has analysed Pd samples in the oxidation of alcohols in the presence of oxygen in the liquid phase. In the liquid phase, the oxidation state of the active Pd metal and the Bi promoter under reaction conditions have been proved to be metallic, suggesting that the catalytic role of the promoter goes through an ensemble effect restricted, in this case, to the surface of the active phase. Other liquid phase EXAFS studies analyse metal evolution of Pd-homogeneous catalysts in the Suzuki–Miyaura reaction.[85]

XANES spectroscopy probes the electronic state of an absorbing atom of the X-ray radiation. The two XAFS techniques are sensitive to local order, making them particularly suitable for analysing nanostructured materials, but differ in the fact that XANES is essentially not affected by thermal effects and in the absence of vibronic or specific (non-frequent) cases of spin-orbit coupling, the recording temperature does not affect the XANES shape.[35–37,86] This spectroscopy provides information concerning the local order around the absorber atom, independently of the pressure and temperature, making it highly suitable for *in situ* studies. In metallic systems, the electronic transitions visible in a XANES K edge or L_{III} edge have been assigned by Sham.[87] The effect of the nanostructure can be analysed with the help of theoretical calculations.[88,89] Nanostructure can influence the presence/absence of XANES peaks (called continuum resonances, CRs, in the language of solid state physics), their intensity, and energy position. For spherical or cuboctahedral cluster, the Pt L_{III} edge ($2p_{3/2} \rightarrow 5d_{3/2,5/2}$ transition; s final state contribution is rather small) XANES spectrum shows the disappearance of the CR at *ca.* 11580 eV for clusters with less than 20 atoms.[88] Trends on the Au XANES spectrum *vs.* size were also analysed with the help of theoretical calculations.[90] For Cu K edge ($1s \rightarrow 4p$ transition), clusters with less than 15 atoms display a single CR at *ca.* 8985 eV, where larger clusters or bulk metal display two distinctive CRs.[89] Such differences can be explained in terms of the scattering

theory, as the different CRs are dominated by contributions corresponding to different coordination shells of the clusters, their absence in the smaller clusters indicating the dominant contribution of third or higher shells. Alternatively, they show the d/sp charge redistribution effects mentioned in previous sections of this chapter. In any case, this phenomenon clearly indicates that the XANES shape is highly sensitive to size and shape of clusters containing 25–30 atoms.

Nonetheless, the intensity of the CRs is also sensitive to size but in a larger range of sizes. Before commenting, it should be noted that the absorption edge reflects the final state density of unoccupied states, presenting significant differences with the corresponding property of the ground state.[35,37] This limits the use of CR intensity for d/sp occupation analysis as a function of size as the presence of the core-hole must be considered.[86] The use of appropriate, well-known reference systems allows this inconvenience to be solved in the majority of cases (see below). The nanostructure produces the broadening of CRs with respect to well-crystallised materials. The reason for this can be understood in terms of the f-rule.[91] This rule implies that the total absorption is a constant independent of the nature of the final state. Disorder, therefore, inherent to metal clusters, broadens the spectrum without altering the overall intensity.[88,89] Additional broadening of CRs comes from the interaction with the support (the Pauli repulsion and metal polarization spread electronic levels in the range of a few eV)[88] and adsorbates (typically hydrogen chemisorbed after reduction).[21] These factors, together with the inherent size distribution, mean that the fine electronic details may be lost in the XANES spectrum. However, as indicated above for the case of Pd, a d-count variation is expected at and near the Fermi region in going from the atom to the metal. Although possibly restricted to very small clusters,[18] this would be visible in the White line (first CR) of the L_{III} edge. These size-limited clusters are, however, of great interest in catalysis. The use of X-ray detection schemes based upon fluorescence emission channels of semi-core levels will improve experimental energy resolution and would allow (*vide supra*) a careful study of XANES shape,

helping in the analysis of electronic details.[92] We will briefly discuss this at the end of this section.

The CR energy position depends on both geometric and electronic factors.[35,86] Geometrical factors are summarised in the so-called $1/R^2$ rule, which states that the quantity $\Delta E/R^2$ is a constant for each CR, where ΔE refers to the energy difference with the zero kinetic energy and R is the first M-M distance. Although the paper by Kizler[93] indicates limitations in its applicability, the rule can be safely used when adequate reference systems are at hand. This occurs when reference and sample systems have similar scattering geometry; in our case, for example, the rule can be applied to the study of alloy distances with the help of a monometallic reference system of similar particle size while maintaining the same (fcc, bcc or other) structure.[31] In Fig. 4.4 Cu K edge XANES spectra are compared for two nanosized (20–25 atoms) $Pd_{50}Cu_{50}$ and Cu clusters. The CR are labelled with the initial (1s) and final states of the transition. Note that the selection rule implies $\Delta L = \pm 1$ and that final states labelled with s, d, f character indicate a $l = 1$ projection from electronic wave-functions of neighbouring (not the absorber) atoms. The $1/R^2$ rule can be applied to the $1s \rightarrow 4f$ transition as it is the more energetic and thus less influenced by chemical bonding (electronic effects). An energy difference of 7.6 eV indicates an increase of about 10% in terms of inter-atomic distance in the alloy, a fact compatible with the atomic alloy composition and with Vergard's rule.[31]

The application of XANES to the characterization of catalysts in real *in situ* conditions has recently been reviewed[86] and so here we will concentrate on more recent contributions. *In situ* analysis of the calcination step for impregnated catalysts[94] or the evolution of Pd oxide[95] at high temperature has been published. The latter shows the PdO to Pd decomposition process at around 1123 K on heating while PdO is formed at about 953 K during cooling, thus providing evidence for a hysteresis cycle characteristic of the decomposition process. The reduction of metal supported catalysts has been frequently followed by XANES and examples can be found for Cu,[96] Ni,[97–99], Rh,[100] Ir,[101], Rh,[102] Pd,[103] and Pt[104] monometallic systems and

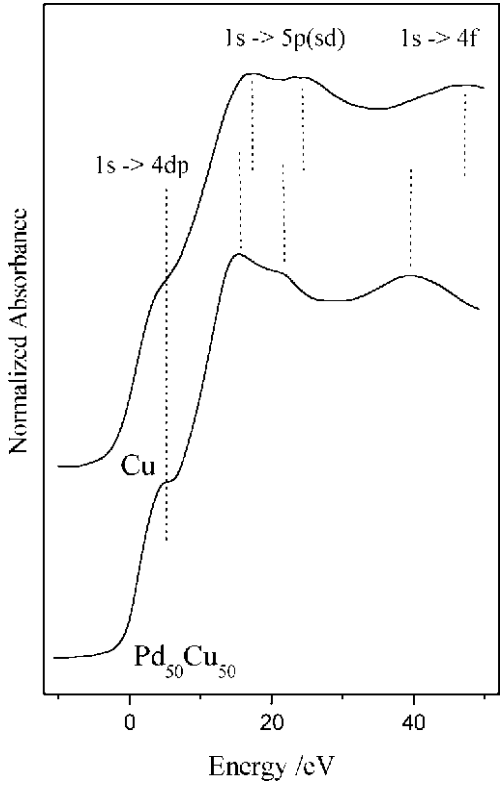

Figure 4.4 Cu K edge XANES spectra of Cu and $Pd_{0.50}Cu_{0.50}$ nanoparticles. The pre-edge and post-edge transitions are labelled by their initial and final electronic states.[31,86]

bimetallic systems containing Ru with Cu[105] and Co,[106] Pd with Cu,[31,107] Ag,[108] Au,[109–111] and Sn,[112] Pt with Ni,[113] Co,[106] Mo,[114] Re,[115–117] Sn,[118] and Ge,[63,119] and, finally, Ir with Re.[120] A compendium of the degree of interaction between components of bimetallic catalysts is available.[86] Essentially, the reduction process of metallic catalysts is governed by both thermodynamic and kinetics factors. For bimetallic systems, contact between both components can be present even in the oxidised state[31] or favoured by the presence of an intermediate, mobile species.[117] As already mentioned, the resulting alloy can be present in the whole particle or restricted to the surface. Kinetic

factors are rather difficult to determine with precision but are evidenced when comparing silica and alumina-supported systems, a higher probability of alloying being found using silica due, among other things, to the greater mobility of zero-valent species.[118] Tracking the reduction processes by XANES is mainly obscured by the fact that several phases can contribute to a XANES spectrum under specific conditions (atmosphere, T, P). This can be worked out by subjecting data to statistical methods of analysis over the series of XANES spectra taken during a treatment. The method, called Principal Component Analysis (PCA), assumes that the absorbance in a series of spectra can be modelled as a linear sum of individual contributions; the chemical species containing the absorbing atom (called factors), plus noise.[121] The outcome of the analysis gives XANES spectra corresponding to the factors and corresponding concentration profiles. The latter are shown in Fig. 4.5 for two Rh-Cu/Al_2O_3 catalysts with different Rh : Cu atomic ratios.[105] The identification of the chemical species allows one to conclude that Rh is present initially as the stable single oxide Rh_2O_3 nanoparticle while copper is present as copper aluminates. The Rh_2O_3-like phase is reduced to the single Rh chemical phase but copper aluminates display strong variation in the onset temperature, the reduction profile and the presence of the Cu(I) intermediate, indicating a stronger interaction of Rh with the alumina surface. Bulk copper aluminates are formed by the alumina solution during the impregnation step while, depending on the Rh : Cu ratio, surface copper aluminate is also formed. When the alumina surface has enough area to form a strong interaction with both metals (presence of surface copper aluminate), co-reduction of Rh(III) and surface Cu(II) aluminate occurs with subsequent formation of an alloy phase.

Other activation treatments have followed the oxychlorination of Pt-Re,[116,117,122,123] which gives evidence for the existence of a mobile partially oxidised Re intermediate during the alloying process. The presence of chlorine ions, besides maintaining an appropriate level of acidity in the alumina, appears to affect the resulting zero-valent particles *via* a preferential interaction with Re,

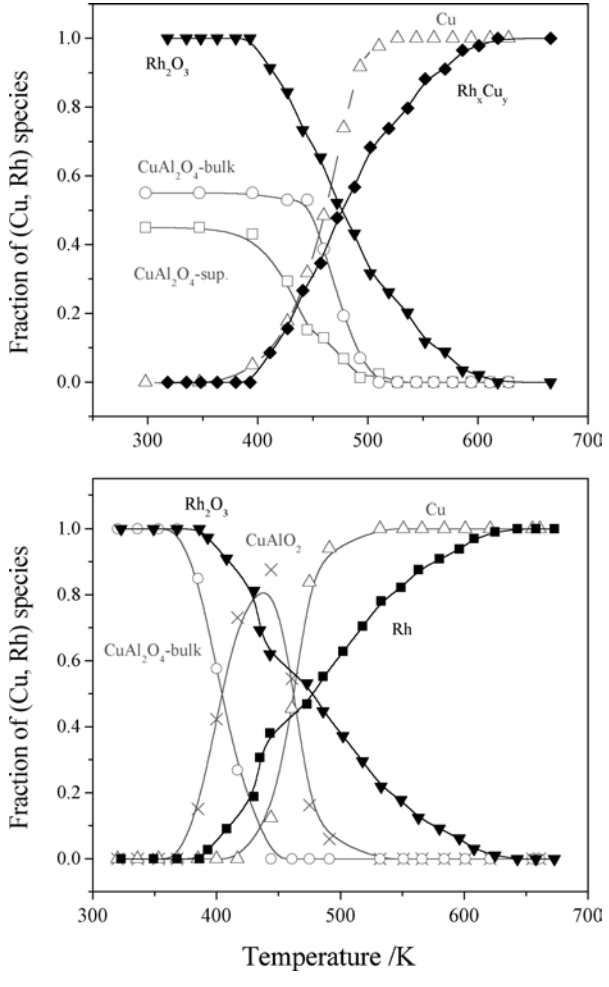

Figure 4.5 Cu (grey line) and Rh (black line) concentration profiles following a temperature-programmed run under hydrogen for two Rh-Cu bimetallic catalysts: Rh : Cu = 0.14 : 1.0 (top), 0.43 : 1.0 (bottom).[105]

which seems to be at the surface to a larger extent than in the absence of chlorine.[117] Sulfidation of Co-Mo,[124,125] Ni-Mo,[72,73] and Mo carbides[126] or metallic Pd-Pt[75,76] systems has also been analysed, showing the different temperature regions and the mutual influence of the metals in the case of bimetallic systems. Finally,

activation treatments with NO_2 of $Pt/Ba/Al_2O_3$ catalysts have been followed in order to interpret the use of Ba containing matrixes as traps for NOx species and their subsequent reduction[127,128] or the effect of S-poisoning on the trapping capabilities of these systems.[129]

The NO elimination reactions constitute, probably, the main subject of XANES studies of supported catalysts under reaction conditions. Starting with the simplest CO+NO and $CO+NO+O_2$ stoichiometric mixtures, works on Cu,[130,131] Rh,[102] Pd,[132–134] Pd-Cu,[135] Pd-Cr,[136–138] and Pd-Ni[138] have all been reported. The existence of a redox mechanism is suggested in all cases. For copper, independent of the initial Cu(II) phase (aggregates or ions), a Cu(I) containing phase is involved in the rate determining step. Larger aggregates, which are not stabilised by interaction with the support, may however proceed to a further state of reduction, leading to Cu(0), mostly inactive due to the severe sintering under reaction conditions.[130] Novel studies try to analyse these reactions in the context of three-way catalysts and the redox processes occurring upon cycling, lambda oscillations characteristic of the elimination of pollutant using three-way catalysts.[139–141] These last studies showed significant differences with those considering average, stoichiometric mixtures which are particularly important in relation to the handling of CO.[139,141] The presence of metallic, Cu(0) species was also observed in segregated clusters appearing from Cu-Mg hydrotalcites under $NO+C_3H_6$.[142] The stability and reaction with NO has also been studied for Cu-exchanged zeolites.[143] In the case of Pd mono- and bimetallic samples, three-way ceria containing catalysts have been analysed.[132–138] NO oxidised Pd and Ce components while CO reduced both. At the onset of light-off of NO reduction, Pd is typically in the metallic state in the presence of oxygen, although an effect of particle size on the average Pd oxidation state must be considered. The presence of hydrocarbons in the reaction mixture ($CO+C_3H_6+NO+O_2$) induces significant changes in the behaviour of both Ce and Pd.[144] In Fig. 4.6(a) the concentration profiles of Pd containing species during a light-off test are presented for three systems supported on Al_2O_3, $CeZrO_4$, and $(Ce,Zr)O_x/Al_2O_3$. In the presence of the $CeZrO_4$ bulk oxide, Pd yields Pd(0) *via* an intermediate in the

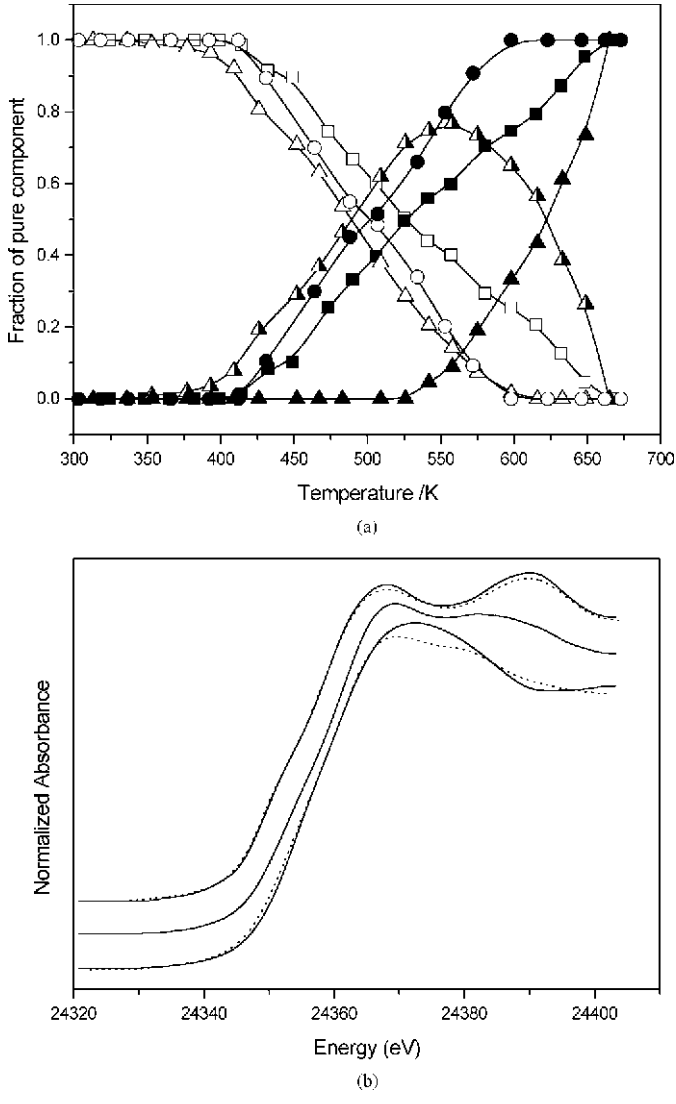

Figure 4.6 (a) Pd concentration profiles for a temperature-programmed run under a C_3H_6+CO+NO+O_2 stoichiometric mixture of Pd/Al_2O_3 (circles), $Pd/CeZrO_4$ (triangles), and $Pd/(Ce,Zr)O_x/Al_2O_3$ (squares). Initial species (open symbols), intermediate species (half-filled symbols), and final species (filled symbols). (b) XANES spectra of Pd chemical species detected along the same temperature-programmed run for the $Pd/CeZrO_4$ sample; lower, initial; middle, intermediate; upper, final species. Dashed lines, PdO and Pd reference XANES spectra.[144]

reduction process but is reduced directly over the other supports. Figure 4.6(b) shows the XANES spectra for the Pd containing species detected for $Pd/CeZrO_4$, which allows identification of the intermediate as a Pd(I)-like oxycarbide phase. This phase has a significant influence on the catalytic properties.[144] A similar conclusion in terms of the key importance of Pd-carbide phases on dynamic, lambda oscillation situations has been also recently uncovered.[139,141] Cu,[145,146] Rh,[147] Pd,[147,148] Ag,[149] and Co-supported[147] catalyst performance in the selective catalytic reduction (SCR) of NOx with hydrocarbons in the presence of water and excess oxygen has been examined in the light of metal K- (Pt L_{III}–) XANES data. With the exception of Co and, possibly, Pt, the latest work in this field indicates that the complete reaction mixture maintains the active phase in a fully oxidised state. Only in the case of high loadings are reduction of the active phases and poor activity observed. This indicates that ions or size-limited clusters of such metals are stabilised by interaction with the support while larger clusters suffer reduction and are highly active for the combustion of the hydrocarbon, thus lowering the SCR activity.

An interesting new use of the XANES spectroscopy considers the analysis of catalytic beds in a space-resolved way. Using microsized beams it is possible to analyse the redox behaviour of a metal along the reactor space coordinate(s). Such an approach has been mainly used to investigate Pd-based catalysts in methane partial oxidation or combustion reactions.[150,151] These works unveil a clear relationship between the oxidation state of the metal and the light-off temperature of the reactions as well as with the oscillation behaviour observed for specific oxygen to hydrocarbon ratios. Other catalytic reactions studied by XANES under *in situ* conditions involve CO hydrogenation,[29] CO preferential oxidation in presence of hydrogen,[152] water gas shift,[79–81] dry reforming of methane,[101,153,154] hydrocarbon hydrogenolysis,[155] methanol oxidation,[156] and the selective oxidation of n-butane.[157,158] Preferential CO oxidation is carried out with Cu on ceria catalysts and XANES is able to indicate the key role played by Cu(I) species in the reaction rate limiting step.[152] Supported Ir[101] and Rh[153,154] systems have been tested in the

dry reforming of methane with results showing the existence of a redox mechanism by which the active metal is reduced by the hydrocarbon and oxidised by CO_2. In the case of Ir, analysis of the particle size indicates that the smaller clusters appear to be more sensitive to oxidation and thus less active in the reaction. The neopentane hydrogenolysis work has focused on the role of hydrogen and shows that the metal-hydrogen bond is a key parameter in interpreting catalytic activity.[155] In the case of methanol oxidation, a XANES study of the O K edge clearly identifies the active oxygen species for both partial and total oxidation reactions.[156] The n-butane selective oxidation studies indicate that V(V) is involved as the kinetically significant species, although the local order around this atom seems rather important. It would appear that the active centre is surrounded by V(IV) species.[157,158]

A brief final comment should be added concerning X-ray emission spectroscopy. The physical basis of X-ray emission is more complex than the absorption one,[92,159] but in the context of catalysis, its application is mainly restricted to the obtention of high resolution XANES spectra, not limited by the core-hole broadening effect of the electron excited. This implies the measurement with high energy resolution (using secondary monochromators) of specific radiative decay paths. As an example of use within the field of catalysis, we mention that this approach has been used to attempt to distinguish CO absorption site (e.g. on-top, bride, or three-fold) on nanosized Pt clusters supported on alumina,[160] methane partial oxidation with Pd catalysts,[150] or CO oxidation with Pt.[161]

4.4.2 *Novel diffraction approaches*

The use of synchrotron radiation sources, e.g. the selection of the excitation wavelength in a broad range, together with parallel-data collection detectors has opened the study of real catalytic systems upon reaction conditions. Metal-based catalytic systems commonly require, however, the detection of low loading active species on-top of dominant signals coming from the support or other components

and time-resolution around/below the second to track chemical changes at *operando* conditions. Although the technique opens an unlimited number of possibilities concerning anomalous scattering (to exalt specific diffraction contributions), total scattering (to analysed simultaneously local and long range order), or high energy excitation (to limit absorption and subsequent fluorescence from the sample), its use in catalysts has been mostly oriented to analyse other than metal-based catalysts where active phases are typically above a few percent of weight.[162,163] In spite of such limitations, some studies of noble metal three-way catalysts may serve as a fine example of the potential of the technique to solve time-dependent or fast phenomena occurring under reaction conditions and involving nanometer size phases.[141,164] In Fig. 4.7 the behaviour of two Pd samples in a CO/NO cycling treatment is presented. Both systems contain Pd particles below 3 nm (around 1.5 nm in the smallest case) which behaved in a cyclic way mimicking the gas phase changes, and displayed significant changes of diffracting plane distances, indicating the modulated variation of the crystalline lattice by inclusion of alien species. This occurs in the presence of CO and by concomitant formation of a Pd-carbide phase, while in the presence of NO such a phase disappears.

Another approach that is gaining acceptance in the catalysis world is the use of total scattering formalisms and, particularly, the analysis of the nanoscale structural order from the atomic pair distribution function (PDF).[165,166] Although this approach has a long history, the advent of synchrotron and novel detectors has provided a powerful tool to analyse nanoscale. The PDF method can yield precise short and long range structural and size information provided that special care is applied to the measurement and handling of data. The atomic PDF, G(g), is defined as:

$$G(r) = 4\pi\rho\,[\rho(r) - \rho_0], \tag{4.4}$$

where $\rho(r)$ is the atom-pair density, ρ_0 is the average atomic number density and r is the radial distance. The PDF yields the probability of finding pairs of atoms separated by a distance r. It is obtained by a

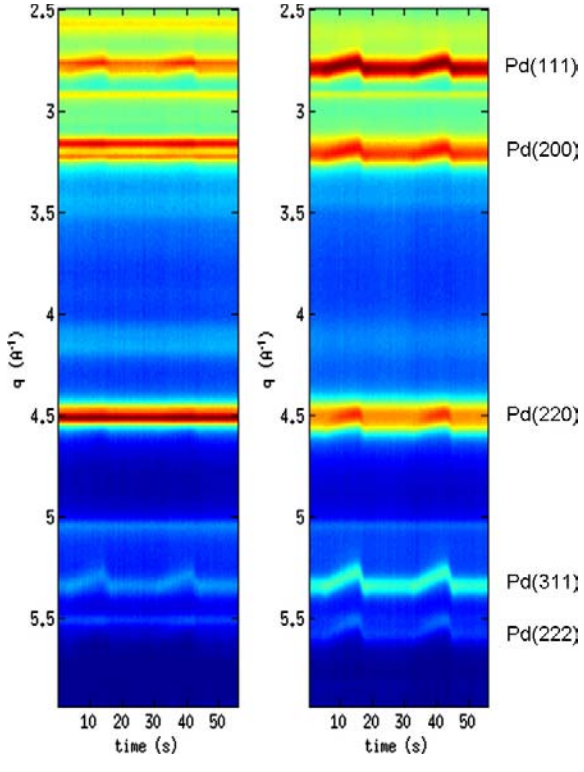

Figure 4.7 XRD patterns of 2 (left) and 4 (right) wt% Pd-Al_2O_3 systems upon a cycling CO/NO treatment at 673 K.

sine Fourier transformation of the reciprocal space total scattering structure function S(Q), according to:

$$G(r) = \frac{2}{\pi}\int_0^{\infty} Q\,(S\,(Q)-1)\sin Q\,r\;dQ, \tag{4.5}$$

where S(Q) is the corrected, normalised, diffracted intensity from the sample and Q is the magnitude of the scattering vector ($4\,\pi\,\sin\varphi/\lambda$). Data corrections account for extraneous contributions (sample mounts, sample fluorescence, Compton scattering, and multiple scattering) and aberrations as detector dead-time and

absorption. Finally the flux is normalised by incident flux and number of atoms. The main weakness of the technique is the low sensitivity to particle shape in the nanometer range, a weakness shared with X-ray absorption/emission spectroscopies and which requires additional input from other techniques, like SAXS, to be fully solved.

In the context of metal-based catalysts, the PDF-XRD methodology has been applied to study the structural details, both at short and long range, of monometallic, as Pt[167] or Ag,[168] and bimetallic, such as Pt-Ru[169] or Fe-Pd,[170] materials, giving important details. For example, compositional information concerning local enrichment and "unexpected" (local) structure distortions, long range details concerning structure (core-shell or other particle arrangements), and lattice parameter information. Other studies analyse the formation of metal nanostructures during either the calcination of dried precursor samples or the reduction of calcined catalysts using the differential-PDF technique in order to get rid of the dominant support contributions.[171,172] Calcination occurs with partial loss of metal-Cl coming from chloride precursors up to a critical point where Pt-Pt correlation appear and grows exponentially. The Pt local order appears to be strongly influenced by the exact calcination treatment parameters. Reduction of the calcined particles takes place with loss of coherence of Pt-O distances including oxygen atoms of the support and takes place in two steps, forming first small nuclei (<1 nm) at low reduction temperatures and then agglomerating into ensembles on many small particles.

4.4.3 *Vibrational spectroscopy*

Vibrational spectroscopies are particularly useful for the analysis of the adsorbed layers on metallic particles. Among them, infrared spectroscopy is of widespread use and provides a powerful tool in the study of metal-based catalysts under reaction conditions. Under the

$$\Psi_V = \prod_k^{3n-6} \Psi(Q_k);\ E = \sum_k^{3n-6} (n+1/2)\ h\nu_k \quad n = 0,\ 1,\ 2,\ \ldots. \qquad (4.6)$$

approximation of vibrational and rotational coordinate separation, the vibrational wave-function Ψ_V is a function of the internal coordinates (Q_k) and is a solution of the vibrational Hamiltonian. Assuming a quadratic approximation of the potential energy in terms of the internal coordinates, then: the solution of the vibrational problem Ψ_V is expressed as a product of harmonic oscillator functions $\Psi(Q_k)$ and the energy is a simple sum of the corresponding term, where every Q_k has an associated quantum number n(k) and normal frequency ν_k. Note that 3n-6 (or 5) are the degrees of freedom for gaseous molecules while 3n are those for an adsorbed molecule in which translation and rotation are observed as frustrated modes. The energy levels for which all quantum numbers are zero except one, which has a unity value, are called fundamental vibrations. When only one normal mode is excited with $n > 1$, this is called an overtone and when two or more quantum numbers have non-zero values, the resulting level is called a combination. The effect of the energy potential terms higher than second (terms called anharmonic for obvious reasons) is mostly concentrated in changing the energy of overtone and combination levels by introducing energy correction terms of the $(n + 1/2)(m + 1/2)\ F(\nu_{k;}\ \nu_l)$ type in Eq. (4.6). This essentially lowers the energy of the vibration levels and reduces the energy difference between levels to a greater extent as the energy is increased.[173]

Under the dipole approximation of the molecule radiation field interaction (see previous section), the coefficient of absorption under vibrational excitation between initial and final vibrational states is given by:

$$B_{if} = \frac{8\pi^3}{3\hbar^2}\left\langle \left|(\mu_x)_{ij}\right|^2 + \left|(\mu_y)_{ij}\right|^2 + \left|(\mu_z)_{ij}\right|^2 \right\rangle;\ (\mu_x)_{ij} = \int \Psi^*_f\, \mu_x\, \Psi_i\, d\tau \quad (4.7)$$

where Ψ^*_f is the complex conjugate of the wave-function of the final state, and μ_x is the x component of the dipole moment. If all dipole integrals are zero, the transition is forbidden. The selection rules indicate that non-vanishing elements occur when only one quantum number changes by one unit.

In catalysis, infrared spectroscopy is mainly employed for characterisation of the adlayer produced by the reactants under reaction conditions. A classical approach to vibrational properties of adsorbed molecules is described by Willis *et al.*[174] Vibrational techniques excite molecule vibrations through long range electromagnetic fields. Representing the vibrating adsorbed molecule as an oscillating dipole, the image charge produced at the metal causes an important effect described by the "metal-surface rule". For reflection-absorption, this imposes the restriction that only the vibrations giving dipole changes perpendicular to the metal surface will absorb radiation strongly.[175] This follows from the fact that dipole moments parallel to the surface create an image dipole moment in the contrary direction. The summation becomes a quadrupole with a much weaker scattering cross-section. Greenler *et al.*[176] also showed that this selection rule applies to infrared spectra of adsorbed species on metal particles but only in cases where a particle a size larger than 2 nm exists; below this cut-off point the rule is expected to be relaxed. For transmission-absorption spectra, the rule is however completely reversed; i.e. only the vibrations giving dipole changes parallel to the metal surface will absorb radiation.[177] Nevertheless, unless the particle is very thin, the major part of the radiation transmitted as a whole in a catalyst will not have been transmitted through the metal particles but will have been reflected by the metal surface particles and then transmitted through the relatively transparent oxide support. Therefore, we can expect that metal catalysts obey the metal-surface rule for reflected radiation. Identification of adsorbed species nature and local geometry should be thus carried out considering the implications of this rule.

Another point in interpreting infrared spectra of adsorbed layers is the coupling interaction between adsorbates. This primarily depends on the nature of the adsorbate-adsorbent bond. For CO this bond is mainly covalent-dative,[178] while for NO it is mostly ionic.[179] Thus, the CO molecule can be classically represented by a dipole while the NO is a point charge of –1 unity located at the <r> expectation value of the $2\pi^*$ orbitals. When interacting with the electromagnetic field, this gives very different energy operators for

molecule-molecule and molecule-image charge interactions. The adlayer interactions have been extensively studied in the case of dipole coupling.[1] Briefly speaking, the potential energy term in normal coordinates (Q_k) of the dipoles, their dipole moments μ_k and intermolecular distances R_{ij} is, in matrix form:

$$2V = Q'\lambda\, Q + \mu' S(I + \alpha\, S)^{-1}\mu \tag{4.8}$$

where,

$$S_{ij} = \begin{cases} R_{ij}^{-3} + (R_{ij}^2 + 4d)^{-3/2} + 12d^2\,(R_{ij}^2 + 4d^2)^{-5/2} & i \mp j \\ -\dfrac{1}{4}\, d^3 & i = j \end{cases}$$

and $\lambda_i = 4\,\pi^2\, c^2\, \Omega_i^2$ (Ω the isolated wavenumber of the isolated absorbed molecule, called the singleton), I is the N × N identity matrix, α_e the polarizability tensor, and d the distance between the centre of the dipole and the classical image plane. The R^{-3} term corresponds to the classical pair-wise dipole-dipole interaction, called interactions through space, while other terms accounts for the influence of the metal, treated as a classical conductor, including electron polarization (called as a whole interaction through the solid).[174] Numerical solution of Eq. 4.8 (e.g. the Hamiltonian including 4.8) for the case where all adsorbed molecules are identical indicates two observable effects in the infrared spectrum; a shift of the absorption band to higher frequency with respect to the isolated molecule, and a reduction of the effective (apparent) molar absorption coefficient as the number of molecules interacting increases. A third effect, however, is also observed when the adlayer contains more than one species having different singleton frequencies. There is a characteristic transfer of intensity for the band due to the lower frequency species to the higher counterpart. The magnitude of the intensity shift depends on the dynamic dipole of the adlayer. For CO, coupling effects are small/negligible for species exhibiting singleton frequencies separated by more than 100/200 cm^{-1}. A typical

case in supported catalysts is the formation of islands under reaction conditions where the centre and perimeter molecules have very similar singleton frequencies but different adsorbate-adsorbate interactions, giving rise to a broad absorption band (which only in specific conditions can be split in two bands) with an apparent decreased intensity in the low frequency region, which appears as a pronounced tail. The variety of situations produced in stepped surfaces and the use of isotopically labelled CO to analyse the frequency shift have been reviewed by Hollins.[180]

The main drawback of infrared spectroscopy can be interference from the gas phase and bulk contributions (for example of supporting oxides) which results in the loss of information in several key regions of the spectrum. To overcome this, the sum frequency generation (SFG) technique has been developed. The principle of SFG is governed by second order non-linear optics.[181,182] IR-vis SFG is now actively used to investigate supported metal catalysts due to its inherent surface specificity.[183,184] To acquire a SFG vibrational spectrum of adsorbed molecules on a metal surface, two laser pulses are spatially and temporally overlapped in the sample. One input beam is in the visible range at fixed frequency (ω_V) while the second is tuneable in the mid-infrared (ω_I) to probe the vibrational modes. By tuning the infrared beam and monitoring the intensity of the SFG output, the vibrational spectrum is acquired by plotting the SFG intensity as a function of infrared beam frequency. The input beam mixing induces a non-linear polarisation on the material which to second order, P^2, is:

$$\vec{P}^2 = \bar{\mathrm{X}}_s^2 \{\vec{E}(\omega_I) \bullet \vec{E}(\omega_V)\}; \bar{\mathrm{X}}_s^2 = \sum_q \frac{A_{R(q)}}{\omega_I - \omega_q + i\Gamma_q} + A_{NR}\, e^{i\phi} \qquad (4.9)$$

being X_s^2 the surface non-linear susceptibility and E the corresponding electrical field. The trigonometric dependence of the fields ($\cos(\omega t)$) implies the possibility of generation of an oscillating dipole at the sum (SFG) and difference (DFG) of ω_I and ω_V. The intensity of the SFG signal is proportional to $(X_s^2)^2$ and the intensity

of the infrared and visible electric fields. X_s^2 has two components Eq. (4.7), a resonant X_R^2 (the first term of the sum in the equation, with $A_{R(q)}$ the amplitude, ω_q the frequency, and the damping constant, Γ) for the q-th vibrationally resonant mode, but the surface itself may also contribute through a non-resonant background X_{NR}^2 which, fortunately, is usually invariant.[185] The resonant condition ($\omega_I = \omega_q$) is thus reached by tuning the infrared beam over the corresponding frequency, thus giving a maximum value of X_s^2, the polarisability and intensity of the SFG output. $A_{R(q)}$ includes the number of adsorbate molecules and the product of infrared Eq. (4.9) and Raman dipole moments. Therefore, in order for a vibrational mode to be SFG active, it must simultaneously satisfy both infrared and Raman selection rules. This implies that SFG is not allowed in media with inversion symmetry under the dipole approximation we have been working on. SFG is frequently carried out with ppp (p-perpendicular for the two input and one output beams) geometry as yields maximum intensity, but ssp (s-parallel) is also used in testing the adsorbate geometry on the surface.

One point to mention is that SFG is not fully independent of the gaseous environment. At pressures above 1 Torr, a significant energy-dependent infrared absorption occurs *via* vibrational and rotational excitation of gas phase molecules. Since the intensity of the SFG depends on the input infrared beam intensity, gas pressure indirectly influences the outcome of SFG. To compensate for such an effect, several strategies have been proposed.[145] Another point is that the SFG phenomenon depends on both infrared and Raman absorption coefficients and therefore correlation of band intensity with adsorbate concentration is not straightforward.

While IR-based techniques can be considered as a whole as the most widely available tool used for analysis of catalytic samples, it is apparent that its use under real, *in situ* conditions is not as widely employed as might be expected. The use of SFG is even more scarce with regard to real catalysts.[186] A detailed review of the use of infrared in catalysts up to 2001 has been published by Ryczkowky.[187] More recent, *in situ*-type of studies involve the preparation of catalysts,[188] the presence of poisons during the preparation step,[189] or

studies following catalytic reactions[190] and analysis of the adsorbed phase under reactions conditions. Most of the latter concern CO oxidation and NO reduction in the presence of other oxidant/reductant molecules. Noble metals of the Pt group (Pt, Pd, and Rh) are typically used for such reactions due, mainly, to their high turnover frequencies and, in the case of Pt and Rh, to their reasonable resistance to some poisons (such as SO_2) present in the inlet feeds of industrial applications such as car exhaust emission treatment (see Chapter 10). The most simple and widely studied reaction is the oxidation of CO by oxygen. *In situ* FTIR spectroscopy was used to follow simultaneously the frequency of the band due to adsorbed CO and the intensity of the gas phase CO_2 band during the oxidation of CO with oxygen over a wide range of O_2 : CO ratios using a Pt/Al_2O_3 catalyst.[191,192] It was found that the linear carbonyl band was progressively shifted to lower frequencies and then remained constant (at 2064 cm^{-1}) during a linear temperature-programmed ramp (Fig. 4.8). The study of such an effect as a function of the particle size has been reported for Pd.[193]

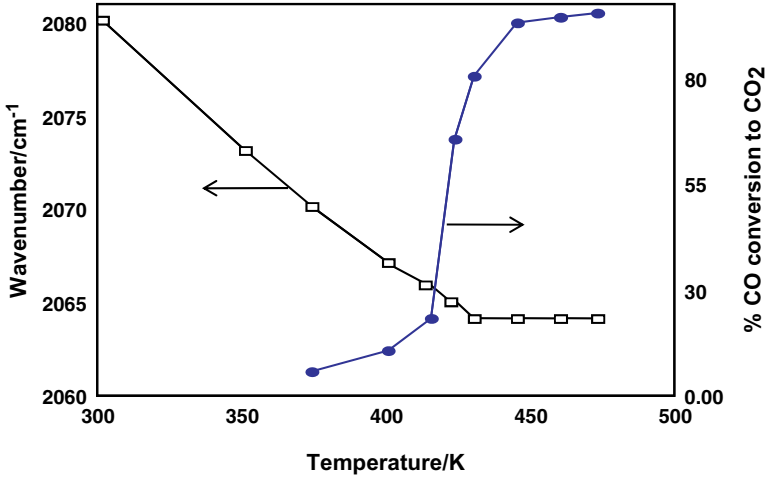

Figure 4.8 Shift in wavenumber for the linear carbonyl species and CO conversion for a Pt/Al_2O_3 catalyst during a temperature-programmed run under $CO+O_2$ (net-oxidising conditions).[191]

These and previous studies were in agreement with the belief that the CO oxidation reaction is essentially structure insensitive and thus independent of particle size, but IRAS studies using model Pd catalysts were able to show in fact that such reaction displays a weak structure sensitivity.[194] When the temperature-ramp (light-off) experiment was repeated using different O_2 : CO ratios, a relationship was observed between the temperature at which this invariance in the carbonyl stretching frequency was initiated, and attainment of *ca.* 80% CO to CO_2 conversion (Fig. 4.9).

Results were interpreted[191] in terms of the formation of islands of CO molecules where the island size was dictated by the number of Pt atoms in a terrace-type ensemble on the metal crystallite. Consistent with this interpretation, re-reduction of the sample, which is known to produce smoother particles with fewer steps and edges and more extended terraces, led to a shift in the frequency at which this invariance was observed (2076 cm^{-1}) and also a change in the % CO conversion which was achieved at the corresponding temperature (Fig. 4.10).[152] This methodology was then applied to a supported Pt-Rh catalyst, where it was shown that the ensembles

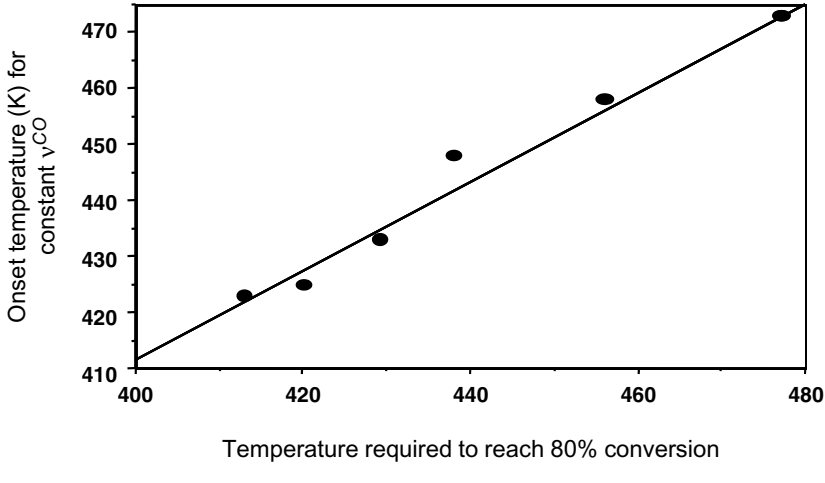

Figure 4.9 Relationship between the onset temperatures for constant νCO and the temperature required to attain 80% CO conversion for 1%Pt/Al_2O_3 over a range of CO/O_2 ratios.[191]

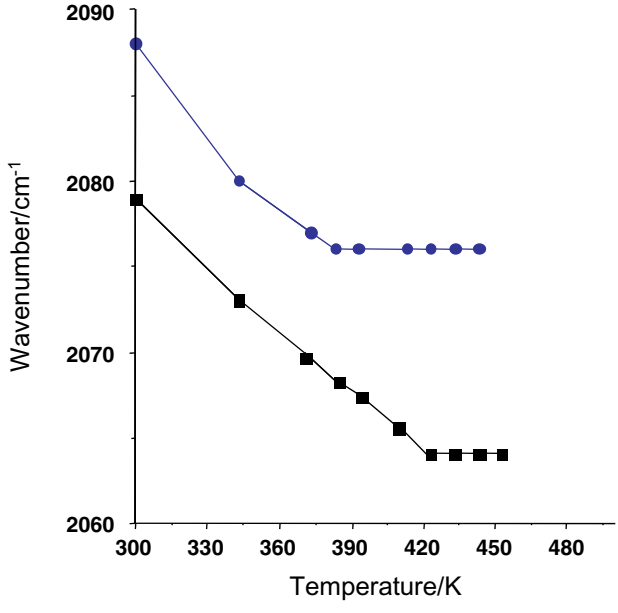

Figure 4.10 Shift in the linear CO band as a function of reaction temperature during CO oxidation (1%CO, 16% O_2) over a fresh (squares) and a re-reduced (circles) 1%Pt/Al_2O_3 catalyst.[192]

containing only Pt atoms were eliminated after a cycle of reaction-reduction-reaction due to incorporation of Rh from the previously highly dispersed Rh phase in to the PtRh crystallites.[195]

NO reduction using CO was also analysed in this context.[196] In this reaction as well as for stoichiometric CO + NO + O_2 mixtures[132–138,193,197] the main question arises as to which is the rate limiting step, which in some cases is believed to be the NO dissociation[193,198] while in other (possibly more frequent) cases seems to be related to the N-coupling steps.[196] Both elementary steps need a cluster of noble metal atoms and thus NO reduction processes are generally structure sensitive and size dependent.[132–138,193,195,198] The rate of these two steps and the performance of the catalyst under reaction conditions seems closely connected with the availability of noble metal reduced (zero-valent) sites, the formation of which are strongly inhibited at the surface of the metal by the presence of

NO.[134,193,196,198] In fact, the use of oxygen or nitrogen oxide as oxidant for the CO oxidation process in complex CO + NO + O_2 mixtures depends critically on the particle size through the average surface chemical state reached and corresponding influence in the co-adsorption/activation and (NO) dissociation elemental processes.[134,193,196,198] As previously mentioned in Section 4.4.1, some recent studies used a multitechnique approach including vibrational techniques to analyse Pd-based three-way catalysts upon cycling CO/(NO+O_2) conditions observing significant differences in the behaviour of the noble metal with respect to the one displayed upon an averaging, stoichiometric mixture.[140,141,164] In fact, the size-sensitivity expected for NO-elimination reactions seems essentially lost in cycling conditions. NOx storage and subsequent reduction with CO, hydrocarbons, or H_2 is also a field of interest for FTIR studies.[127,128,199] Pt/BaO/Al_2O_3 are used to store nitrogen oxides under lean conditions, releasing and reducing NOx under subsequent, short periodic excursions to stoichiometric or rich conditions. Efficient storage requires the presence of Pt in order to oxidise NO to NO_2 while this molecule interacts with alumina and baria components where it is stored mainly in the form of nitrites/nitrates.[127,128,199–201] Although bulk phase Ba nitrate may or may not form under reaction conditions,[128] the system efficiently removes NO coming from exhaust gases under oxidising conditions and produces N_2 under the stoichiometric or rich conditions. More complex effects can be observed when treated with mixtures representing car exhaust gases. When a CO + C_3H_6 + NO + O_2 model mixture is used, the presence of the hydrocarbon may strongly influence the state of the metal and the response to the gaseous atmosphere.[144]

DRIFTS spectra are shown for a light-off test using these two Pd/(Ce,Zr)O_x/Al_2O_3 and Pd/$CeZrO_4$ catalysts (Fig. 4.11). The corresponding XANES spectra for the two samples under similar conditions are displayed in Fig. 4.6. In essence, the data illustrates that not only the metal properties (type, size, shape, etc.) but also its interaction with the support play a significant role in this type of reaction. DRIFTS data display the presence of different Pd oxidation states at the surface under the reactive mixture; the CO molecule (of

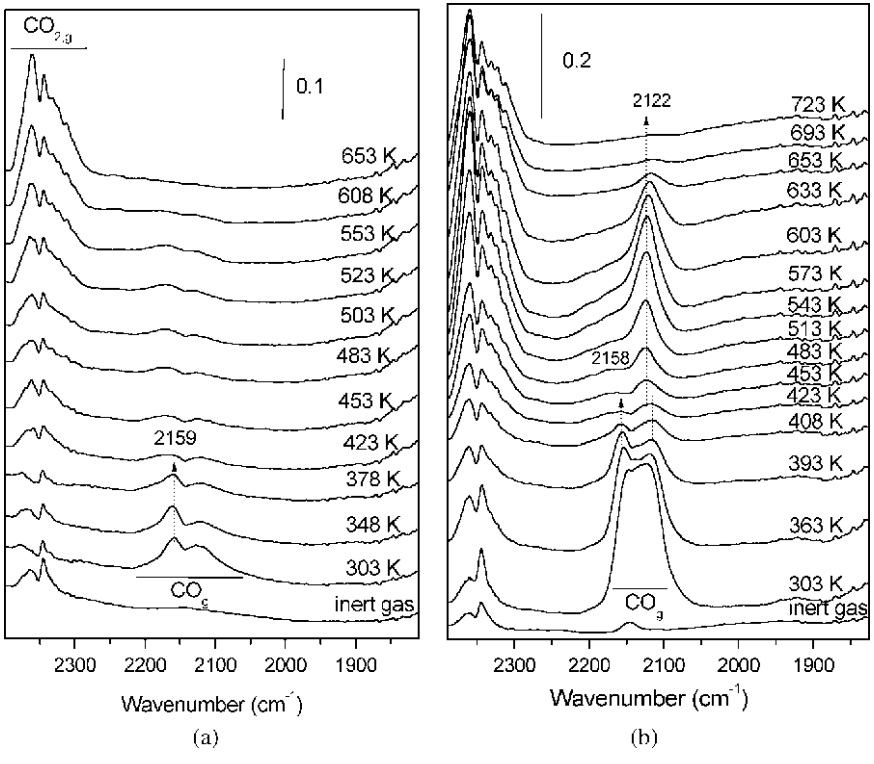

Figure 4.11 DRIFTS spectra for Pd/(Ce,Zr)O_x/Al_2O_3 (a) and Pd/$CeZrO_4$ (b) samples during a temperature-programmed run under a C_3H_6+CO+NO+O_2 stoichiometric mixture.[144]

the mixture or produced by the incomplete combustion of the hydrocarbon) can be used as a probe, indicating that Pd is in a Pd(I)-like state (υCO at 2122 cm^{-1}) when supported in the pure mixed oxide (Fig. 4.11b) while in the mixed (Ce,Zr)O_x/Al_2O_3 support this chemical state is absent (Fig. 4.11a). Combined with results from the XANES study, this indicates the stabilization of a Pd(I)-like oxycarbide phase which strongly reduces the hydrocarbon light-off temperature, thus having a big impact on the catalytic properties.

Other reactions analysed by FTIR techniques are typically CO hydrogenation,[29] and methanol synthesis,[202] while more recently ATR (attenuated total reflection) has been employed for the study

of the solid-liquid interface of catalytic interest.[203–205] Using the latter, it was shown that CO_2 hydrogenation over Pt/Al_2O_3 and using cyclohexane as solvent occurs *via* a carbonate-like species which reacts with hydrogen probably at the metal support interface.[205] Also, in recent dates, polarised-modulation reflection-absorption spectroscopy (PM-IRRAS) has been used to separate gas phase contributions from adsorbed molecules. This approach has been utilised to follow the partial oxidation of organic molecules[206] or NOx storage materials.[207] Finally, we can highlight the study of noble metal nanoparticles suspended in ionic liquids for liquid phase hydrogenation reactions.[208]

To end this section, the use of Raman spectroscopy for metal-based catalysts should be mentioned. Although the use of Surface-Enhanced Raman Scattering (SERS) has been shown to be useful for the study of polycrystalline noble and transition metals, the study of real, nanosized catalysts under *in situ* conditions awaits extended implementation.[209]

4.4.4 *Valence and core photoelectron spectroscopies*

The roots of core and valence level photoemission can be traced back to the famous article of Einstein explaining the photoelectric effect.[210] In this work he postulated the quantum hypothesis for absorption of radiation by the fundamental equation:

$$E_k = h\omega - \xi \tag{4.10}$$

where E_k is the maximum kinetic energy of the photoemitted electron, $h\omega$ is the exciting radiation energy and ξ is the so-called binding energy, the energy required to release the electron. Nowadays, an additional term is added to Eq. (4.10) to take into account the system "work function" (a catch-all term whose precise value depends on both sample and spectrometer).[211] The photoemission and Auger electrons correspond to the two dominant (electronic) de-excitation channels of the solid after the absorption of the radiation; the predominance of one of these depends on the

core electron orbital moment and the atomic number of the element to be ionised.[211] The discovery, during early days of X-ray photoemission spectroscopy (XPS) that non-equivalent atoms, either by symmetry or oxidation state of the same element in a solid gave rise to core-level peaks with different binding energies opened up the use of this technique for chemical analysis.[211,212]

Much effort has focused on the interpretation of core-level energies, or, alternatively, on core-level shifts with respect to well-defined references.[211,213] A core-level energy difference or shift is fundamentally a difference in energy between the final states of the photoemission process, i.e. the energy difference between electronic states in presence of the core-hole left by the absorption of radiation. A typical task for analysis is to unveil if the energy difference encountered in the final state is a property related to the initial ground state contribution or cannot be accounted for by it, thus then being attributed to a final state phenomenon. This last contribution comprises two terms, the intra- and inter-atomic relaxation of the internal/valence electron densities in response to the presence of the core-hole.[211–213] A point to stress is the fact that this description of the photoemission process concentrated, for simplicity's sake, the discussion on electronic charge distribution. In addition, if enough experimental resolution is available, the excitation of internal other than electronic (such as vibrational) modes of the system after being core ionised (as part of the de-excitation process) must be considered in order to explain the XPS shape and energy position.[214] In metals, additional information can be obtained by the line shape. XP spectra shapes for metals often exhibit an asymmetry, skewed to higher binding energies, due to creation of low energy electron-hole pairs concurrently to core ionization in the case of nanosized metals.[211,213] This occurs with the involvement of the rather free valence electrons of the metal and thus provides information about them. In the case of nanosized systems, it is clear that the mobility of such valence electrons is related to size by quantum confinement effects. On the other hand, such a skewing of the XPS line shape is generally known as the Doniach–Sunjic line shape and must be corrected for in order to obtain accurate values of the core-level binding energy.[213]

The study of supported metals by XPS can be affected by sample charging, incomplete screening, reference levels, etc. due to the poor conductivity of supports, although several experimental approaches, amongst which a flood gun is typical, minimise such potential adverse effects.[211,213] Essentially, a cluster has surface and internal (volume or bulk-like from the point of view of the first coordination number) atoms, which experimentally display different core-level shifts. Such an effect is also detected in extended surfaces and typically called the surface core-level shift (SCLF).[211,213] Theoretical studies indicate that the SCLF is an initial state effect, and is therefore related to the chemical properties of the atoms,[16,18,215,216] although some recent results disagree with this view.[217] Taking an average value of the core-level shifts for a metal cluster, this observable would be affected by the previously mentioned surface to volume effect as well as an indirect effect of the substrate either through its influence on the cluster shape and also by influencing the polarization of the metal electronic cloud in the presence of the core-hole (a final state effect).[213,215]

In addition to the theoretically-grounded initial *vs.* final state framework to interpret core-level binding energy shifts, more simple analysis called the equivalent-core approximation[218] or the analysis of Auger parameters using Wagner plots[20,219] have been implemented. The first is based on the fact that a core-level binding energy shift between two different chemical environments is directly related to the difference between two environments in energy associated with replacing element Z (atomic number) to be ionised by Z + 1. The second is electrostatic in nature and obviates exchange-energy terms and allows the determination of final state effect contributions to the core-level binding energy shifts by using both the main XPS and Auger peak information. Both allow the simple extraction of information but at the cost of having strong limitations in terms of the interpretation due to limitations in their application.[20,213,218,219]

XPS is routinely employed for supported metal catalysts and results reported in numerous papers each year. However, the vast majority of these studies are conducted at low pressure (below 10^{-7} Torr). The

difference between this and those characteristic of catalytic reactions, typically one atmosphere or above, corresponds to the so-called "pressure gap." There is increasing evidence from XAFS and infrared SFG (see above) that such a pressure gap strongly influences the catalytic behaviour of samples and, in some cases, the chemical state, thus limiting the usefulness of this type of data. Nevertheless, the recent development of adequate methodologies which allow operation of XPS equipment under "realistic" pressures opens up a new field of study.[220,221] Two approaches have been reported in the literature; the first is the use of a detector adapted by using a differentially pumped electrostatic lens system, to work under millibar pressure[220] while the second uses highly collimated, highly intense and energy controlled molecular beams to produce a high coverage of the reactant molecules at metal surfaces but maintaining a working pressure around 5×10^{-6} Torr.[221] It should be noted that the first implementation is a real "*in situ*" method while the second may still have some residual effects of the "pressure gap". In any case, it should be mentioned that the use of XPS under conditions typical of catalytic processes can have additional complications beyond temperature and pressure. In fact, high temperature produces significant influence on the XP spectrum line shape of metal substrates due to important contributions from photoemission events involving simultaneous excitation of and/or absorption of phonons.[222] On the other hand, a similar physical phenomenon occurs for adsorbate molecules, with the presence of replicas of the main peak associated with vibrational excitation of internal modes of the molecule adsorbed on the surface.[222] For absorbates, an additional fact is that the ionisation cross-section is modified by an energy-dependent final state effect of the substrate electronic cloud,[213,223] thus further complicating analysis of the relative populations of the adsorbates. In spite of these problems, useful information can be obtained. A recent review summarised all these points for metal surfaces.[224] More catalytic studies concern a study of the CO + NO reaction over Rh, using *in situ* XPS indicates that the surface of the metal is mainly populated by NO at reaction temperatures and uncovers details about the local ordering of the adsorbates at the metal surface.[225] Similarly, analysis of the surface and bulk Pt of a $Pt_{50}Rh_{50}$ alloy

under $O_2 + H_2$ reaction conditions has been pursued by taking advantage of the large Pt-SCLS (0.69 eV). In this case, it has been shown that the alloy responds to oxygen lean/rich conditions by changing the chemical composition of the subsurface, leading to Pt enrichment under oxygen-deficient conditions, but the absence of such changes at the surface layer was noted.[221] Other catalytic studies analysed the Pd sintering behaviour upon CO contact,[226] the H_2/D_2 exchange reaction on Pt surfaces,[227] or the CO oxidation on Au nanoparticles supported on silica or titania.[228]

4.4.5 *Other techniques*

Nuclear magnetic resonance (NMR) is the remaining spectroscopy which is often used to analyse metallic properties of catalytic systems.[229,230] Although chemical shifts depend on the local electronic environment of the resonating nucleus, making the technique ideally suited to study supported metals, it has limited accessibility in terms of *in situ* studies under reaction conditions, limiting its applicability in the context of this review. ^{1}H and ^{13}CO probe molecules are typically used to analyse surface properties and dispersion in monometallic systems as well as the (surface) composition in bimetallic systems.[229,231] Note however that experimental results using probe molecules are typically interpreted on the basis of the low/fast exchange model and assuming that NMR sensitivity to local (electronic) structure can be approached exclusively to first neighbour distance, discarding the effect of second and subsequent neighbours. Both simplifications limit the use of the technique to a semi-quantitative level.[229,231] A somewhat special case is that of Pt-based catalysts, where the use of ^{195}Pt as well as double resonance experiments (like ^{195}Pt-^{13}CO) allow a detailed analysis of local electronic density as a function of size as well as the interaction of the probe molecule with the metal surface. The surface composition of Pt-containing alloys[229] as well as the effect of alkali doping (^{23}Na-^{13}CO double resonance) on Pt catalysts[232] has also been investigated. The studies using metal resonating nucleus have been performed to a lesser extent in the case of other metals, but results using ^{103}Rh and ^{61}Ni have been recently

reviewed.[229] Lately, RMN imaging of catalytic materials may add some interesting structural clues to understand phenomena occurring during the lifetime of the catalyst.[230] The use of optical spectroscopies and, particularly, the analysis of Plasmon resonances to study metal particle size and shape is also of interest, although the coupling of intra- and inter-particle effects makes the application to inherently inhomogeneous catalytic materials difficult.[233]

To complete this chapter, we would like to mention that recent monographs have reviewed the use of *in-situ* spectroscopies for monitoring heterogeneously catalysed reaction under supercritical conditions, although very few studies in this field have been devoted to the study of the fluid-solid interface.[234] The use of a multitechnique approach in order to maximise information under real, *in-situ* conditions has also been reviewed recently.[141,163,235,236] The combined use of powerful spectroscopies with simultaneous on-line analysis of the catalytic activity of the sample will become more widespread in application allowing an interpretation of catalytic behaviour in terms of the physico-chemical properties of the solid. The next frontier in spectroscopic characterisation of metal catalysts will consist of time-dependent analysis of the gas/liquid-solid interface, particularly with a view to analyse short-lived intermediates during catalysed reactions and with the aim to determine the response of the catalyst surface and relate these responses to the physico-chemical properties of the solid.

Acknowledgements

The authors thank CICYT for funding CTQ2010–14872/BQU. The contributions of Drs. A. Kubacka, A. Iglesias-Juez, A. Martínez-Arias, M.A. Newton, M. di Michiel, I. Rodríguez-Ramos, A. Guerrero-Ruiz, J.C. Conesa, and J. Soria are gratefully acknowledged.

References

1. V. Ponec, G.C. Bond, *Catalysis by Metals and Alloys*, Elsevier, Amsterdam, 1996.
2. See articles in *J. Mol. Catal. A: Chem.* 2001, **173**.

3. C. Binns, *Surf. Sci. Rep.* 2001, **44**, 1.
4. R.C. Cammarata, K. Sieradzki, *Phys. Rev. Lett.* 1989, **17**, 2005.
5. T.P. Martin, *Phys. Rep.* 1996, **273**, 199.
6. C.L. Cleveland, W.D. Luedtka, U. Landman, *Phys. Rev. Lett.* 1998, **81**, 2036.
7. L.D. Marks, *Rep. Prog. Phys.* 1994, **57**, 603.
8. D. Reinhard, B.D. Hall, P. Berthoud, S. Valkealdhti, R. Monot, *Phys. Rev. Lett.* 1997, **79**, 1459.
9. W. de Heer, *Rev. Mod. Phys.* 1993, **65**, 611.
10. F. Balleto, C. Mottet, R. Ferrando, *Phys. Rev. Lett.* 2000, **84**, 5544.
11. Y. Xia, Y. Xiong, B. Lim, S.E. Skabalak, *Angew. Chem. Int. Ed.* 2009, **48**, 60.
12. P. Menacherry, M. Fernández-García, G.L. Haller, *J. Catal.* 1997, **166**, 75.
13. H.J. Freund, M. Baumer, H. Kuhlenbeck, *Adv. Catal.* 2000, **45**, 333.
14. P. Moriarty, *Rep. Prog. Phys.* 2001, **64**, 287.
15. D.C. Koningsberger, F.B.M. van Zon, M. Vaarkamp, A. Munoz-Paez, *Synchrotron Radiat. Tech. Appl.* 1996, **2**, 257.
16. P.S. Bagus, C.R. Brundle, G. Pacchioni, F. Parmigiani, *Surf. Sci. Rep.* 1993, **19**, 265.
17. A.D. Yoffe, *Rep. Prog. Phys.* 1993, **42**, 173.
18. M. Fernández-García, J.C. Conesa, A. Clotet, J.M. Ricart, N. López, F. Illas, *J. Phys. Chem. B* 1998, **102**, 141.
19. J.M. van Ruitenbeek, in *Metal Clusters on Surface Structure, Quantum Properties*, Ed.: K.H. Meiwes-Broer, Phys. Chem. Series, Springer-Verlag, Heidelberg, 2000, 175.
20. G. Morreti, *J. Electron. Rel. Phen.* 1998, **95**, 95.
21. A.L. Ankudinov, J.J. Rehr, J. Low, S.R. Bare, *Phys. Rev. Lett.* 2001, **86**, 1642.
22. J.H. Sinfelt, *Bimetallic Catalysts Discoveries, Concepts, and Applications*, Wiley, New York, 1983.
23. V. Ponec, *Appl. Catal. A* 2001, **222**, 31.
24. G.A. Somorjai, *Introduction to Surface Chemistry and Catalysis*, Wiley, New York, 1994, chp. 3.
25. L.Z. Mezey, J. Giber, *Surf. Sci.* 1990, **234**, 210.
26. P. Weigend, B. Jelinek, W. Hoffer, P. Vage, *Surf. Sci.* 1994, **301**, 306.
27. J.H. Sinfelt, *Science* 1977, **195**, 641.
28. C.J. Baddely, in *The Chemical Physics of Solid Surfaces Volume 10: Surface Alloys and Alloy Surfaces*, Ed.: DP Woodruff, Elsevier, 2002, 495.

29. J.A. Anderson, M. Fernández-García, G.L. Haller, *J. Catal.* 1996, **164**, 477.
30. J.A. Rodríguez, D.W. Goodman, *Science* 1992, **257**, 897.
31. M. Fernández-García, J.A. Anderson, G.L. Haller, *J. Phys. Chem. B* 1996, **100**, 16247.
32. J.A. Rodríguez, *Surf. Sci. Rep.* 1996, **24**, 223.
33. F. Illas, N. López, J.M. Ricart, A. Clotet, M. Fernández-García, J.C. Conesa, *J. Phys. Chem. B* 1998, **102**, 8017.
34. J.C. Fuggle, J.E. Inglesfield, *Unoccupied Electronic States*, Springer-Verlag, Berlin, 1992.
35. D.C. Konnigsberger, R. Prins (Eds.), *X-ray Absorption*, Wiley, New York, 1987.
36. See articles in *Chem. Rev.* 2001, 101.
37. J.J. Rehr, J.C Albers, *Rev. Modern Phys.* 2000, **72**, 621.
38. W.G. Egelhoff, *Surf. Sci. Rep.* 1987, **6**, 253.
39. F.W. Lytle, *Synchrotron Rad.* 1999, **6**, 123.
40. I.N. Levine, *Molecular Spectroscopy*, Wiley, New York, 1975.
41. T. Aberg, *Phys. Rev.* 1967, **16**, 14201.
42. J.E. Muller, O. Jepen, O.K. Andersen, J.W. Wilkins, *Phys. Rev. Lett.* 1978, **40**, 720.
43. C.R. Natoli, M. Benfatto, S. Doniach, *Phys. Rev. B* 1986, **34**, 4682.
44. J.J. Rehr, R.C. Albers, *Phys. Rev. B* 1996, **41**, 8139.
45. D.E. Sayers, E.A. Stern, F.W. Lytle, *Phys. Rev. Lett.* 1971, **21**, 1204.
46. A.V. Poiarkova, J.J. Rehr, *Phys. Rev. B* 1999, **59**, 948.
47. G. Bunker, *Nucl. Instrum. Methods Phys. Res.* 1983, **207**, 437.
48. B.S. Clausen**,** L. Grabaek, H. Topsoe, L.B. Hansen, P. Stolze, J.K. Norskov, *J. Catal.* 1993, **141**, 368.
49. E. Brus, J.T. Miller, A.J. Kropf, J.A. van Brokhoven, *Phys. Chem. Chem. Phys.* 2006, **8**, 3248.
50. G.E. van Dorssen, D.C. Knoningsberger, *Phys. Chem. Chem. Phys.* 2003, **5**, 3549.
51. M.A. Newton, A.J. Dent, J. Evans, *Chem. Soc. Rev.* 2002, **31**, 83.
52. M.A. Newton, *Chem. Soc. Rev.* 2010, **37**, 2644.
53. G. Guay, G. Tourillon, E. Dartyge, A. Fontaine, J. McBean, K.I. Pandya, W.E. O´Grady, *J. Electroanal. Chem.* 1991, **305**, 83.

54. P.A. Allen, S.D. Covalson, M.S. Wilson, S. Gottesfeld, I.D. Raistrick, J. Valerio, M. Lorato, *J. Electroanal. Chem.* 1995, **384**, 99.
55. D. Hecht, R. Frahm, H.H. Strehbow, *J. Phys. Chem.* 1996, **100**, 10831.
56. A.N. Mansour, C.A. Melendes, J. Wong, *J. Electrochem. Soc.* 1998, **145**, 1121.
57. R.J. Mathew, A.E. Russel, *Top. Catal.* 2000, **10**, 231.
58. G.A. Camara, M.J. Giz, V.A. Peganin, E.A. Ticianelli, *J. Electroanal. Chem.* 2002, **537**, 21.
59. A.S. Arisco, *J. Electrochem. Soc.* 2002, **47**, 3723.
60. S. Stoupin, E.H. Chung, S. Chattopadhyay, C.U. Segre, E.S. Smotkin, *J. Phys. Chem. B* 2006, **110**, 9932.
61. F. Cimini, R. Prins, *J. Phys. Chem. B* 1997, **101**, 5277.
62. S.G. Fiddy, M.A. Newton, A.J. Dent, G. Salvini, J.M. Corker, S. Turin, T. Campbell, J. Evans, *Chem. Commun.* 1999, 831.
63. S.G. Fiddy, M.A. Newton, T. Campbell, J.M. Corker, A.J. Dent, I. Harvey, G. Salvini, S. Turin, J. Evans, *Chem. Commun.* 2001, 445.
64. M.K. Oudenhuijen, P.J. Kooyman, B. Tappel, J.A. van Bokhaven, D.C. Koningsberger, *J. Catal.* 2002, **205**, 135.
65. X. Wang, J.A. Rodríguez, J.C. Hanson, D. Gamarra, A. Martínez-Arias, M. Fernández-García, *J. Phys. Chem. B* 2005, **109**, 16595.
66. Y. Nagai, N. Takagi, Y. Ikeda, K. Damae, G. Guillera, S. Pascarelli, M.A. Newton, H. Shinjoh, S. Matsumoto, *Angew. Chem. Int. Ed.* 2008, **47**, 9803
67. H. Tanaka, M. Uenishi, M. Taneguchi, I. Tan, K. Narita, M. Kimura, K. Kaneko, *Catal. Today* 2006, **117**, 321.
68. A. Jentys, *Phys. Chem. Chem. Phys.* 1999, **1**, 4059.
69. G. Agostini, R. Pellegrini, G. Leofantin, L. Bertinetti, S. Bertarione, E. Groppo. A. Zecchina, C. Lamberti, *J. Phys. Chem. C* 2009 **113**, 10485.
70. G. Sankar, J.M. Thomas, *Top. Catal.* 1999, **8**, 1.
71. Y. Iwasawa, *J. Catal.* 2003, **216**, 165.
72. R. Cattaneo, T. Weber, T. Shido, R. Prins, *J. Catal.* 2000, **191**, 225.
73. B.S. Clausen, H. Topsoe, R. Frahm, *Adv. Catal.* 1998, **42**,315
74. M.A. Newton, A.J. Dent, S. Diaz-Moreno, S.G. Fiddy, B. Jyotha, J. Evans, *Chem. Commun.* 2003, 1906.
75. T. Matsui, M. Harada, K.K. Bando, M. Toba, Y. Yoshimura, *Appl. Catal. A* 2005, **290**, 73.

76. F. Bernardi, M.C.M. Alves, A. Traverse, D.O. Silva, C.W. Scheeren, J. Dupont, J. Morais, *J. Phys. Chem. C* 2009, **113**, 3909.
77. G. Meitner, E. Iglesias, *Catal. Today* 1999, **53**, 433.
78. J.D. Grunwaldt, A.M. Molenbroek, N.Y. Topose, H. Topose, B.S. Clausen, *J. Catal.* 2000, **194**, 402.
79. X. Wang, J.A. Rodríguez, J.C. Hanson, D. Gamarra, A. Martínez-Arias, M. Fernández-García, *J. Phys. Chem. B* 2006, **110**, 428.
80. W. Deng, A.I. Frenkel, R. Si, M. Flytzani-Stephanopoulos, *J. Phys. Chem. C* 2008, **112**, 12834.
81. E.B. Fox, S. Velu, M.H. Engelhard, Y.H. Chin, J.T. Miller, J. Kropf, C. Song, *J. Catal.* 2008, **260**, 358.
82. E. Brus, D.E. Ramaker, J.A. van Brokhoven, *J. Am. Chem. Soc.* 2007, **129**, 8094.
83. J.D. Grunwaldt, C. Keresszegi, T. Mallat, A. Baiker, *J. Catal.* 2003, **213**, 291.
84. C. Keresszegi, J.D. Grunwaldt, T. Mallat, A. Baiker, *Chem. Commun.* 2003, 2304.
85. P.J. Ellis, I.J.S. Fairlamb, S.F.J. Hackett, K. Wilson, A. Flec, *Angew. Chem. Int. Ed.* 2010, **49**, 1820.
86. M. Fernández-García, *Catal. Rev.* 2002, **44**, 59.
87. T.K. Sham, *Phys. Rev. B* 1985, **31**, 1888.
88. A.L. Ankudinov, J.J. Rehr, J.J. Low, S.R. Bare, *J. Chem. Phys.* 2002, **116**, 1911.
89. D. Bazin, J.J. Rehr, *J. Phys. Chem. B* 2004, **107**, 12398.
90. H.M. Chen, R.S. Liu, K. Asakura, L.-Y. Jang, J.-F. Lee, *J. Phys. Chem. C* 2007, **111**, 18550.
91. M. Altarelli, D.L. Dexter, H.H. Nussenzverg, *Phys. Rev. B* 1972, **6**, 4502.
92. F.M.F. de Groot, *Top. Catal.* 2000, **10**, 179.
93. P. Kizler, *Phys. Lett. A* 1992, **172**, 66.
94. E. Dartyge, A. Fontained, A. Juvha, D. Sayer (Eds.), *EXAFS and Near Edge Structure*, Springer, Berlin, 1984, 472.
95. S.J. Cho, S.K. Kay, *J. Phys. Chem. B* 2000, **104**, 8124.
96. M. Fernández-García, I. Rodríguez-Ramos, P. Ferreira-Aparicio, A. Guerrero-Ruiz, *J. Catal.* 1998, **178**, 253.
97. A. Jentys, G.L. Haller, J.A. Lercher, *J. Phys. Chem.* 1992, **96**, 1234.

98. S.R. Bare, F.S. Modica, A.Z. Ringwelski, *J. Synchrotron Rad.* 1999, **6**, 436.
99. J.A. Rodríguez, J.C. Hanson, A.I. Frenkel, J.Y. Kim, M. Pérez, *J. Am. Chem. Soc.* 2002, **124**, 346.
100. P. Ferreira-Aparicio, B. Bachiller-Baeza, I. Rodríguez-Ramos, A. Guerrero-Ruiz, M. Fernández-García, *Catal. Lett.* 1997, **49**, 163.
101. J.D. Grunwaldt, P. Kappen, L. Basini, B.S. Clausen, *Catal. Lett.* 2002, **78**, 13.
102. A. Suzuki, Y. Ineda, A. Yamaguchi, T. Chihera, M. Yuasa, M. Nomura, Y. Iwasawa, *Angew. Chem. Int. Ed.* 2003, **42**, 4795.
103. M.W. Tew, J.T. Miller, J.A. van Brokhoven, *J. Phys. Chem. C* 2009, **113**, 15140.
104. J.H. Bitter, K. Seshan, J.A. Lercher, *Top. Catal.* 2000, **10**, 295**.**
105. M. Fernández-García, A. Martínez-Arias, I. Rodríguez-Ramos, P. Ferreira-Aparicio, A. Guerrero-Ruiz, *Langmuir* 1999, **15**, 5215.
106. M. Meng, P.-Y. Lin, Y.-L. Fu, *Catal. Lett.* 1997, **48**, 364.
107. A. Adelman, W. Shieber, H. Vinek, A. Jentys, *Catal. Lett.* 2000, **69**, 11.
108. D.C. Huang, K.H. Chong, W.F. Pong, P.K. Tseng, K.J. Hung, W.F. Huang, *Catal. Lett.* 1998, **53**, 155.
109. R.J. Davis, M.J. Boudart, *J. Phys. Chem.* 1994, **98**, 5471.
110. J.W. Cowes, P. Meechan, *Physica* 1995, **208/209**, 665.
111. S.N. Reifsnyder, H.H. Lamb, *J. Phys. Chem. B* 1999, **103**, 321.
112. S.H. Choi, J.S. Lee, *J. Catal.* 2000, **193**, 176.
113. A.S. Bommannaver, P.A. Musitano, M.J. Machacan, *Surf. Sci.* 1985, **156**, 426.
114. S.H. Choi, J.S. Lee, *J. Catal.* 1997, **167**, 364.
115. F. Hilbrig, C. Mitchell, G.L. Haller, *J. Phys. Chem.* 1992, **96**, 9893.
116. C.G. Michell, W.E. Brambrick, R.H. Ebel, G. Larsen, G.L. Haller, *J. Catal.* 1995, **182**, 199.
117. M. Fernández-García, F.K. Chong, J.A. Anderson, C.H. Rochester, *J. Catal.* 1999, **182**, 199.
118. G. Meitzner, G.H. Via, F.W. Lytle, S.C. Fung, J.H. Sinfelt, *J. Phys. Chem.* 1988, **92**, 2925.
119. A. Borgna, T.F. Garreto, C.R. Apesteguía, B. Morawek, *Appl. Catal. A: Gen* 1999, **182**, 189.

120. M.S. Nasher, D.M. Somerville, P.D. Lane, D.L. Alder, J.R. Sharpley, R.G. Nuzzo, *J. Am. Chem. Soc.* 1996, **118**, 12964.
121. M. Fernández-García, C. Márquez, G.L. Haller, *J. Phys. Chem.* 1995, **99**, 12565.
122. C.G. Michell, W.E. Brambrick, R.H. Ebel, *Fuel Proc. Technol.* 1993, **35**, 159.
123. D. Bazin, H. Dexpert, J. Lineh, J.P. Bournouville, *J. Synchrotron Rad.* 1999, **6**, 465**.**
124. S.A.M. Bowens, F.B.M. van Zon, M.P. van der Kraan, V.H.J. de Beer, J.A.R. van Veen, D.C. Koningsberger, *J. Phys. Chem.* 1994, **146**, 375.
125. R.G. Lelived, A.J. van Dillen, J.W. Geus, D.C. Koningsberger, *J. Catal.* 1997, **171**, 115.
126. J.A. Rodríguez, J. Drovak, T. Jirsak, *J. Phys. Chem. B* 2000, **104**, 11515.
127. J.A. Anderson, M. Fernández-García, *Trans. Inst. Chem. Eng.* 2000, **78A**, 935.
128. J.A. Anderson, B. Bachiller-Baeza, M. Fernández-García, *Phys. Chem. Chem. Phys.* 2003, **5**, 4418.
129. J.A. Anderson, Z. Liu, M. Fernández-García, *Catal. Today* 2006, **113**, 25.
130. Y. Okamoto, T. Kubota, H. Gotoh, Y. Ohto, H. Aritani, T. Tanaka, S. Yoshida, *J. Chem. Soc. Faraday Trans.* 1998, **94**, 3743.
131. M. Fernández-García, C. Márquez-Alvarez, I. Rodríguez-Ramos, A. Guerrero-Ruiz, G.L- Haller, *J. Phys. Chem.* 1995, **99**, 16380.
132. J.H. Holles, R.J. Davis, *J. Phys. Chem. B* 2000, **104**, 9653.
133. A. Martínez-Arias, M. Fernández-García, A. Iglesias-Juez, A.B. Hungría, J.A. Anderson, J.C. Conesa, J. Soria, *Appl. Catal. B: Env.* 2001, **31**, 51.
134. M. Fernández-García, A. Iglesias-Juez, A. Martínez-Arias, A.B. Hungría, J.A. Anderson, J.C. Conesa, J. Soria, *J. Catal.* 2004, **221**, 148.
135. A.B. Hungría, A. Iglesias-Juez, A. Martínez-Arias, M. Fernández-García, J.A. Anderson, J.C. Conesa, J. Soria, *J. Catal.* 2002, **206**, 281.
136. M. Fernández-García, A. Martínez-Arias, A. Iglesias-Juez, A.B. Hungría, J.A. Anderson, J.C. Conesa, J. Soria, *J. Catal.* 2003, **214**, 220.
137. A. Iglesias-Juez, A.B. Hungría, A. Martínez-Arias, M. Fernández-García, J.A. Anderson, J.C. Conesa, J. Soria, *Appl. Catal. A: Gen.* 2004, **259**, 207.

138. A. Iglesias-Juez, A.B. Hungría, A. Martínez-Arias, J.A. Anderson, M. Fernández-García, *Catal. Today* 2009, **143**, 295.
139. A. Iglesias-Juez, A. Martínez-Arias, M.A. Newton, S.G. Fiddy, M. Fernández-García, *Chem. Commun.* 2005, 4092.
140. M.A. Newton, C. Belver, A. Martínez-Arias, M. Fernández-García, *Angew. Chem. Int. Ed.* 2007, **46**, 8629.
141. M.A. Newton, M. Di Michel, A. Kubacka, M. Fernández-García, *J. Am. Chem. Soc.* 2010, **132**, 4540.
142. I.J. Shannon, F. Rey, G. Sankar, J.M. Thomas, T. Maschmeyer, A.W. Waller, A.E. Palomares, A. Corma, A.J. Dent, G.N. Graves, *J. Chem. Soc. Faraday Trans.* 1996, **92**, 4331.
143. F.X. Llabrés i Xamena, P. Fisicaro, G. Berlie, A. Zecchina, G. Turnes Palomino, C. Prestipino, S. Bordiga, E. Giamello, C. Lamberti, *J. Phys. Chem. B* 2003, **107**, 7036.
144. M. Fernández-García, A. Iglesias-Juez, A. Martínez-Arias, A.B. Hungría, J.A. Anderson, J.C. Conesa, J. Soria, *J. Catal.* 2004, **221**, 594.
145. D.-J. Liu, H.J. Robota, *Appl. Catal. B: Env.* 1994, **4**, 1551.
146. C. Márquez-Alvarez, I. Rodríguez-Ramos, A. Guerrero-Ruiz, G.L. Haller, M. Fernández-García, *J. Am. Chem. Soc.* 1997, **119**, 2905.
147. A. Jentys, W.S. Shieber, H. Vinek, *Catal. Lett.* 1997, **47**, 193.
148. A. Ali, W. Alvarez, C.J. Lougham, D.E. Resasco, *Appl. Catal. A* 1997, **14**, 13.
149. A. Iglesias-Juez, A.B. Hungría, A. Martínez-Arias, A. Fuerte, M. Fernández-García, J.A. Anderson, J.C. Conesa, J. Soria, *J. Catal.* 2003, **217**, 310.
150. B. Kimmerle, J.D. Grunwaldt, A. Baiker, P. Glatzel, P. Boyle, S. Stephen, C.G. Shroeder, *J. Phys. Chem. C* 2009, **113**, 3037.
151 B. Kimmerle, A. Baiker, J.-D. Grunwaldt, *Phys. Chem. Chem. Phys.* 2010, **12**, 2288.
152 D. Gamarra, C. Belver, M. Fernández-García, A. Martínez-Arias, *J. Am. Chem. Soc.* 2007, **129**, 12064.
153. J.D. Grundwaldt, L. Basini, B.J. Clausen, *J. Catal.* 2001, **200**, 231.
154. P. Ferreira-Aparicio, M. Fernández-García, I. Rodríguez-Ramos, A. Guerrero-Ruiz, *J. Catal.* 2000, **190**, 296.
155. D.C. Konongsberger, M.K. Oudenhuijzen, J. de Graaf, J.A. van Bokhoven, D.E. Ramaker, *J. Catal.* 2003, **216**, 178.

156. A. Knop-Gerike, M. Havecker, T. Schedel-Niedrig, R. Schlogl, *Top. Catal.* 2001, **15**, 27.
157. G.W. Coulson, S.R. Bare, H.H. Kung, K. Birkeland, G.K. Bethke, R. Harlow, N. Herron, P.L. Lee, *Science* 1997, **275**, 191.
158. K. Birkeland, S.M. Babitz, G.K. Bethke, H.H. Kung, G.W. Coulson, S.R. Bare, *J. Phys. Chem. B* 1997, **101**, 6895.
159. F. de Groot, *Chem. Rev.* 2001, **101**, 1779.
160. P. Glatzel, J. Sing, K.O. Krashina, J.A. van Brokhoven, *J. Am. Chem. Soc.* 2010, **132**, 2555.
161. J. Singh, E.M.C. Alayon, M. Tromp, O.V. Safonova, P. Glatzel, M. Nachtegaal, R. Frahm, J.A. Van Bokhoven, *Angew. Chem. Int. Ed.* 2008, **47**, 9260.
162. P. Norby, J.C. Hanson, *Catal. Today* 1998, **39**, 301.
163. S. Nikitenko, A.M. Beale, A.M.J. Van Der Eerden, S.D.M. Jacques, O. Leynaud, M.G. O'Brien, D. Detollenaere, W. Bras, *J. Synchr. Rad.* 2008, **15**, 632.
164. A. Kubacka, A. Martínez-Arias, M. Fernández-García, M. Di Michiel, M.A. Newton, *J. Catal.* 2010, **270**, 275.
165. T. Egami, S.J.L. Billinge, *Underneath the Bragg Peaks: Structural Analysis of Complex Materials*, Pergamon Press, Oxford, 2003.
166. S.J.L. Billinge *J. Solid State Chem.* 2008, **181**, 1695.
167. M.M. Martínez-Iñesta, R.F. Lobo, *J. Phys. Chem. C* 2007, **111**, 8573.
168. W. Dmowski, H. Yin, S. Sai, S.H. Overbury, T. Egami, *J. Phys. Chem. C* 2010, 114, 6983.
169. S. Agayoglu, P. Zavalij, B. Eichhorn, Q. Wang, A.I. Frenkel, P. Chupas, *ACS Nano* 2009, **3**, 3127.
170. V. Petkov, T. Ohta, Y. Hou, Y. Ren, *J. Phys. Chem. C* 2007, **111**, 714.
171. P.J. Chupas, K.W. Chapman, G. Jennings, P.L. Lee, C.P. Crey, *J. Am. Chem. Soc.* 2007, **129**, 13822.
172. P.J. Chupas, K.W. Chapman, H. Chen, C.P. Crey, *Catal. Today* 2009, **145**, 213.
173. E.B. Wilson, J.C. Decius, R.C. Cross, *Molecular Vibrations*, Dover, New York.
174. R.F. Willis, N.A. Lucas, G.H. Mohan, in *The Chemical Physics of Solid Surfaces and Heterogeneous Catalysts Volume 2*, Eds.: D.A. King, D.P. Woodruff, Elsevier, Amsterdam, 1983, chp. 2.

175. R.G. Greenler, *J. Chem. Phys.* 1966, **44**, 310.
176. R.G. Greenler, D.R. Snider, D. Witt, R.S. Sorbello, *Surf. Sci.* 1982, **118**, 415.
177. M. Ito, W. Suetaka, *J. Phys. Chem.* 1975, **79**, 1190.
178. P.S. Bagus, F. Illas, *Phys. Rev. B* 1990, **42**, 10852.
179. F. Illas, J.M. Ricart, M. Fernández-García, *J. Chem. Phys.* 1996, **104**, 5647.
180. P. Hollins, *Surf. Sci. Rep.* 1992, **16**, 51.
181. Y.R. Shen, *Surf. Sci.* 1994, **299/300**, 551**.**
182. C.D. Bazin, *J. Chem. Soc. Faraday Trans.* 1995, **91**, 1281.
183. G.A. Somorjay, K.R. McCrea, *Adv. Catal.* 2000, **45**, 385.
184. G. Rupprechter, *Phys. Chem. Chem. Phys.* 2001, **3**, 4621.
185. K.Y. Kung, P. Chen, F. Wei, G. Rupprechter, Y.R. Shen, G.A. Somorjay, *Rev. Sci. Instrum.* 2001, **72**, 1806.
186. G. Ruppretcher, C. Weilech, *J. Phys. Condens. Matter* 2008, **20**, 184019.
187. J. Ryczkowky, *Catal. Today* 2001, **68**, 263.
188. J. Guzman, B.C. Gates, *Langmuir* 2003, **19**, 3897.
189. F.J. Gracia, J.T. Miller, A.J. Kroft, E.E. Wolf, *J. Catal.* 2002, **209**, 341.
190. H. Igarashi, T. Fujino, Y. Zhu, H. Uvhida, M. Watanabe, *Phys. Chem. Chem. Phys.* 2001, **3**, 306.
191. J.A. Anderson, *J. Chem. Soc. Faraday Trans.* 1992, **88**, 1197.
192. J.A. Anderson, *Catal. Letts.* 1992, **13**, 363.
193. A. Martínez-Arias, A.B. Hungría, M. Fernández-García, A. Iglesias-Juez, J.A. Anderson, J.C. Conesa, *J. Catal.* 2004, **221**, 85.
194. J. Libuda, I. Meusel, J. Hoffman, J. Hartmann, L. Piccolo, C.R. Henry, H.J. Freund, *J. Chem. Phys.* 2001, **114**, 4669.
195. J. A. Anderson, *J. Catal.* 1993, **142**, 153.
196. J.L. Freysz, J. Saussey, J.C. Lavalley, P. Bourges, *J. Catal.* 2001, **197**, 131.
197. M. Yang, M. Shen, J. Wang, M. Zhao, W. Wang, *J. Phys. Chem. C* 2009, **113**, 12778.
198. M. Fernández-García, A. Iglesias-Juez, A. Martínez-Arias, A.B. Hungría, J.A. Anderson, J.C. Conesa, J. Soria, *J. Catal.* 1999, **187**, 474.
199. Ch. Sedlmair, K. Shesan, A. Jentys, J.A. Lercher, *J. Catal.* 2003, **214**, 308.
200. A. Desikumastuli, T. Staudt, H. Gronbeck, J. Liduda, *J. Catal.* 2008, **260**, 315.

201. F. Viñes, A. Desikumastuli, T. Staudt, H. Gronbeck, J. Liduda, K.M. Neymann, *J. Phys. Chem. C* 2008, **112**, 16539.
202. J. Hoffmann, S. Schauermann, V. Johanek, J. Hartmann, J. Libuda, *J. Catal.* 2003, **213**, 176.
203. I. Ortiz-Hernández, C.T. Williams, *Langmuir* 2003, **19**, 2956.
204. T. Burgi, R. Wirz, A. Baiker, *J. Phys. Chem. B* 2003, **107**, 6774.
205. D. Ferri, T. Burgi, A. Baiker, *Phys. Chem. Chem. Phys.* 2002, **4**, 2667.
206. D.M. Meier, A. Urakawa, A. Baiker, *J. Phys. Chem. C* 2009, **113**, 21849.
207. N. Maeda, A. Urakawa, A. Baiker, *J. Phys. Chem. Lett.* 2010, **1**, 54.
208. F. Jutz, J.M. Anderson, A. Baiker, *J. Catal.* 2009, **268**, 356.
209. Z.-Q. Tian, B. Ren, D.-Y. Wu, *J. Phys. Chem. B* 2002, **106**, 9463.
210. A. Einstein, *Ann. Phys. Leipzig* 1905, **17**, 132.
211. D. Briggs, M.P. Seah, *Practical Surface Analysis by Auger and X-ray Photoelectron Spectroscopy,* Wiley, New York, 1983.
212. K. Siegbahn, C. Nordling, A. Fahlman, H. Nordberg, K. Hamrin, J. Hedman, G. Johansson, T. Bergmark, S.E. Karlsson, J. Lindgren, B. Lindberg, *Electron Spectroscopy for Chemical Analysis,* Almquist and Wiksells, Stockholm, 1967.
213. W.F. Egelhoff, *Surf. Sci. Rep.* 1987, **6**, 253.
214. J.N. Andersen, T. Balasubramanian, L.I. Johansson, R. Nyholm, *Phys. Rev. Lett.* 2001, **86**, 4398.
215. F. Parmigiani, E. Kay, P.S. Bagus, C.J. Nelin, *J. Elec. Relat. Phenom.* 1985, **36**, 257.
216. S. Lizzit, A. Baraldi, A. Groso, K. Reuter, M.V. Ganduglia-Pirovano, C. Stampft, M. Scheffler, M. Stichler, C. Keller, W. Wurth, D. Menzel, *Phys. Rev. B* 2001, **63**, 205419, 1–14.
217. A. Stierle, C. Tieg, H. Dosch, V. Formoso, E. Lungren, J.N. Andersen, *Surf. Sci.* 2003, **529**, L263.
218. H.P. Hjalmarson, H. Buttner, J.D. Dow, *Phys. Rev. B.* 1981, **24**, 6010.
219. D.Q. Yang, E. Sacher, *Appl. Surf. Sci.* 2002, **195**, 187.
220. D.F. Ogletree, H. Bluhm, G. Lebedev, C.S. Fadley, Z. Hussain, M. Salmeron, *Rev. Sci. Inst.* 2002, **73**, 3872.
221. A. Baraldi, G. Comelli, S. Lizzit, M. Kiskinova, G. Paolucci, *Surf. Sci. Rep.* 2003, **49**, 169.
222. Ch. Sondergaard, Ph. Hofmann, Ch. Sultz, M.S. Moreno, J.E. Gayone, M.A. Vicente Alvarez, G. Zampieri, S. Lizzit, A. Baraldi, *Phys. Rev. B* 2001, **63**, 233102.

223. M.S. Smedh, A. Beutler, T. Ramsvik, R. Nyholm, M. Borg, J.N. Andersen, R. Duschek, M. Sock, F.P. Netzer, M.G. Ramsey, *Surf. Sci.* 2001, **491**, 99.
224. H. Bluhm, M. Havecker, A. Knop-Gerike, M. Kiskinova, R. Schogl, M. Salmeron, *MRS Bull.* 2007, **32**, 1022.
225. F.G. Requejo, E. Hebenstreit, D.F. Oglatree, M. Salmeron, *J. Catal.* 2006, **226**, 83.
226. F. Tao, S. Day, L.W. Wang, Z. Liu, D.R. Butcher, H. Bluhm, M. Salmeron, G.A. Somojai, *Science* 2010, **327**, 850.
227. M. Montano, K. Bratlic, M. Salmeron, G.A. Somorjai, *J. Am. Chem. Soc.* 2006, **128**, 13229.
228. T. Herranz, X. Deng, A. Cabot, P. Alivisatos, Z. Liu, G. Soler-Illa, M. Salmeron, *Catal. Today* 2009, **143**, 158.
229. J.J. Van der Klink, *Adv. Catal.* 2000, **44**, 1.
230. A.A. Lysova, J.A. Bergwerff, L. Espinosa-Alonso, B.M. Weckhuysen, I.V. Koptyug, *Catal. Today* 2010, **374**, 126.
231. L. Yang, *Curr. Top. Catal.* 1999, **2**, 59.
232. J.A. Norcross, C.P. Slitcher, J.H. Sinfelt, *Catal. Today* 1999, **53**, 343.
233. C. Noguez, *J. Phys. Chem. C* 2007, **111**, 3806.
234. J.D. Grunwaldt, R. Wandeler, A. Baiker, *Catal. Rev.* 2003, **45**, 1.
235. A. Bruckner, *Catal. Rev.* 2003, **45**, 97.
236. M.G. Obrien, A.M. Beale, S. Jacques, M. Di Michiel, B.M. Weckhyusen, *ChemCatChem.* 2009, **1**, 99.

This page intentionally left blank

CHAPTER 5

SUPPORTED METAL CATALYSTS FOR FINE CHEMICALS SYNTHESIS

R.P.K. Wells and J.A. Anderson

Surface Chemistry and Catalysis Group, Department of Chemistry, University of Aberdeen, Kings College, Aberdeen, Scotland, UK

5.1 Introduction

Catalysis provides by far the most efficient technology whereby rates of chemical reactions are accelerated to levels that make the large-scale production of fine chemicals in industry financially viable. The principal task of the catalyst is to provide the necessary control mechanisms by which the appropriate thermodynamic product is prevented from being formed, the required high-value 'fine chemical', often being an intermediate along the pathway to the thermodynamically stable product. Hence, control of selectivity is vital to the success of any fine chemical process. As environmental controls become ever more stringent, selectivity increases in importance even beyond activity. Shortfalls in selectivity result in poor use of raw materials and the need to either identify markets for the by-products, incurring increased costs due to expensive and time-consuming separation procedures, or to dispose of the by-products as waste. Reduced activity can be compensated for by plant design and the use of more efficient reactor technology, however this is a subject in its own right[1] and will not be dealt with here.

This chapter does not aim to deal with all aspects of fine chemical catalysis, merely to bring to the reader's attention the principal

strategies involved, using three broad reaction types as examples; selective hydrogenation, selective oxidation and enantioselective reactions. By choosing specific examples of each class of reaction the factors influencing selectivity and routes that can be used to affect it will be illustrated.

5.2 Selective Hydrogenation over Supported Metal Catalysts

5.2.1 *Overview*

The importance of selective hydrogenation in fine chemicals can best be represented by way of example. Figure 5.1 shows the two stereoisomers of linalool which is employed as a scent in *ca.* 70% of cleaning agents and perfumed hygiene products including soaps, detergents, shampoos and lotions. It also finds use as a chemical intermediate. Although it is found in nature as a terpene alcohol in flowers and spices, its widespread use in fine chemicals means that it is manufactured industrially. This process involves reacting 2-methyl-2-hepten-6-one with acetylene (a base-catalysed ethynylation) to dehydrolinalool. This means a final stage, selective hydrogenation whereby linalool is produced *via* hydrogenation of the triple bond to leave the terminal = CH_2 unit.[2]

Clearly varied aspects of 'selectivity' are required to ensure production of the desired final product. The hydrogenation reaction must proceed selectively to avoid overhydrogenation to produce a terminal — CH_3 group *via* consecutive hydrogenation reaction, targets the appropriate part of the molecules to avoid hydrogenating the internal C = C bond during any concurrent reaction and proceeds with

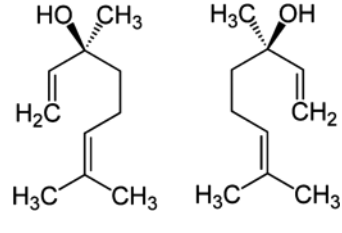

Figure 5.1 Representations of the two stereoisomers of linalool.

appropriate chemoselectivity to avoid hydrogenation of the alcohol functional group. While many laboratories may work directly on such complex molecules, (a list of some of the industrially relevant cases where carbon–carbon multiple bond hydrogenation is involved is listed in Chen *et al.*[3]) others often adopt a strategy which involves the use of model reagents and focus on issues of either avoiding overhydrogenation (concurrent reaction-based selectivity) or chemoselectivity (consecutive reaction-based selectivity). The latter has been the subject of a recent review.[4] In terms of partial or semi-hydrogenation, there is abundant literature on liquid phase hydrogenation of both internal[5–7] and terminal[7,8] and functionalised[9,10] alkynes. Factors affecting selectivity in the hydrogenation of molecules containing more than one carbon–carbon double bond are reviewed in the following section (Section 5.2.2). In the case of alkyne hydrogenation, a key target is to ensure prevention of overhydrogenation to provide the alkane, but also to avoid isomerisation. In the case of internal alkynes, this means suppression of routes which lead to geometric isomerisation and which convert the desired, and predominantly produced, cis-alkene into the more thermodynamically favoured trans-alkene. While geometric isomers are not produced by semi-hydrogenation of terminal alkynes, the alkene product may undergo isomerisation *via* double bond-shift to produce the 2-alkene.[11] During the initial stages of reaction, selectivity to the favoured alkene product is high as a consequence of the favoured adsorption of alkyne relative to alkene. However, as the alkyne is consumed, selectivity is diminished. Traditionally this was managed by selecting a solution-based modifier such as quinoline with an adsorption enthalpy lying between those of the alkyne and alkene which minimise adsorption of the latter. This is part of the basis on which the Lindlar[12] catalyst operates. Recent studies in the area of liquid phase partial hydrogenation of alkynes have focused on the structure sensitivity,[6,8] role of subsurface hydrogen (hydride),[6,13] carbon (carbide),[13,14] selection of the support[5] and the use of surface modifiers.[7] Studies comparing the relative roles of Bi and Pb, suggest that the propensity for terminal alkenes to isomerise (double bond-shift) may be suppressed by elimination of step and edge sites while cis-trans isomerisation is facilitated at open terrace

sites, and these ensembles should be broken up to reduce the rate at which internal alkenes are consumed.

5.2.2 *Hydrogenation of buta-1,3-diene over non-modified metal catalysts*

The hydrogenation of buta-1,3-diene, CH_2=CH-CH=CH_2 is one of the simplest hydrogenation reactions in which selective control can yield differing products. The molecule itself is made up of two identical unsaturated functions, and hydrogenation yields a mixture of three n-butenes, but-1-ene, *cis*- and *trans*-but-2-ene and the fully hydrogenated product butane. Conventional wisdom suggested that but-1-ene was the initial product of the reaction, whose isomerisation yielded the two but-2-ene isomers, with any butane being explained by product readsorption followed by further hydrogenation. However, D-tracer experiments of the reaction over alumina supported metals such as Fe, Co, Ni, Cu[15] and Pd[16] in a static reactor yielded a completely different mechanism (Fig. 5.2).

All these metals exhibited high selectivity (97–100%) for butene formation. Also, the deuterium distribution within each butene was

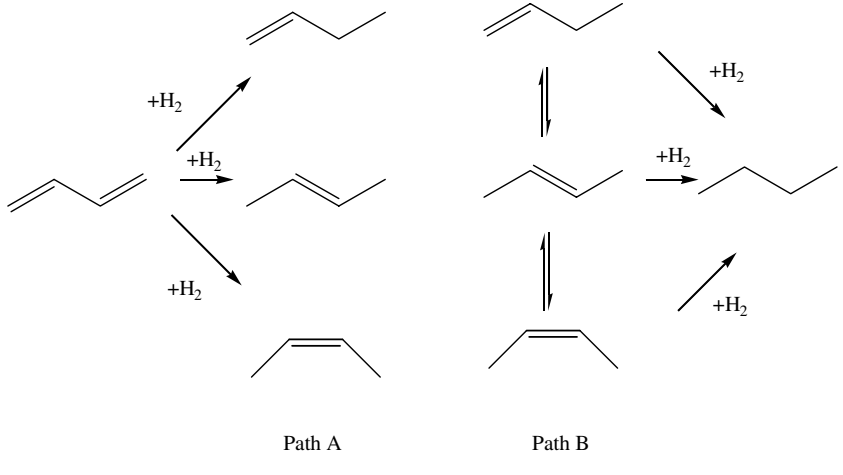

Figure 5.2 Schematic indicating the separate stages of the hydrogenation of buta-1,3-diene.

similar and the butene composition was independent of deuterium pressure. Butene isomerisation would be expected to yield products with redistributed deuterium content, hence it was concluded that all three butenes were primary products of the reaction. These experiments indicated that the reaction proceeded according to path (a). As the strongly adsorbed butadiene is removed to the point at which it no longer dominates the active sites on the surface, the initial product butene is readsorbed and further hydrogenated to butane in the second step (path (b)). At this stage there is a competition between butene isomerisation and further hydrogenation to yield butane and hence the product composition shifts towards the thermodynamic equilibrium (*trans*-but-2-ene > *cis*-but-2-ene > but-1-ene) as the butene is removed. This isomerisation however only occurs in the second stage of the process. This provides a useful example of the first requirement for the attainment of selectivity in multistep processes, being that the reactant adsorption should be sufficiently strong to exclude readsorption of the required product and hence prevent subsequent reaction.

Product compositions from butadiene hydrogenation vary greatly depending on the catalyst utilised. Some examples and associated references are detailed in Table 5.1.

The mechanism for the reaction over alumina supported Co and Ni catalysts based on the deuterium tracer studies is believed to be one in which the adsorbed diene and adsorbed hydrogen are in dynamic equilibrium with σ- and σ-π-bonded half-hydrogenated species, resulting in the wide distribution of deuterium in the observed butanes (Fig. 5.3).

In the subsequent rate determining steps hydrogen atom addition to the σ-adsorbed butenyl gives the but-1-ene isomer whereas the addition of hydrogen to the σ-π-adsorbed butenyl occurs *via* a π-allylic transition state. In process B, butadiene molecules can be adsorbed either in the *transoid* or *cisoid* conformation, the former yielding but-1-ene and *trans*-but-2-ene by 1 : 2 and 1 : 4 addition respectively and the latter yielding but-1-ene and *cis*-but-2-ene by the same mechanism. Hence if the required product is the alk-1-ene, then the catalyst of choice would be one with an electronic

Table 5.1 Butene distributions obtained after the hydrogenation of butadiene over various metal catalysts.

Catalyst	Temp/ °C	Conv/ %	Butenes/% But-1-ene	*Trans*-b-2-ene	*Cis*-b-2-ene	Ref
10% Cu/alumina	60	20	87	6	7	16
5% Pd/alumina	0	50	65	33	2	17
10% Co/alumina	100	10	82	11	7	18
Ni powder	100	10	62	25	13	19
Ni film	0	20	66	25	9	19
Ni film/S, θ = 0.70	90	20	32	57	11	19
Ni film/S, θ = 1.00	90	15	23	68	12	19
Mn film	20	20	86	10	4	19
V film	0	10	50	28	22	20
Zr film	0	5	40	45	15	20

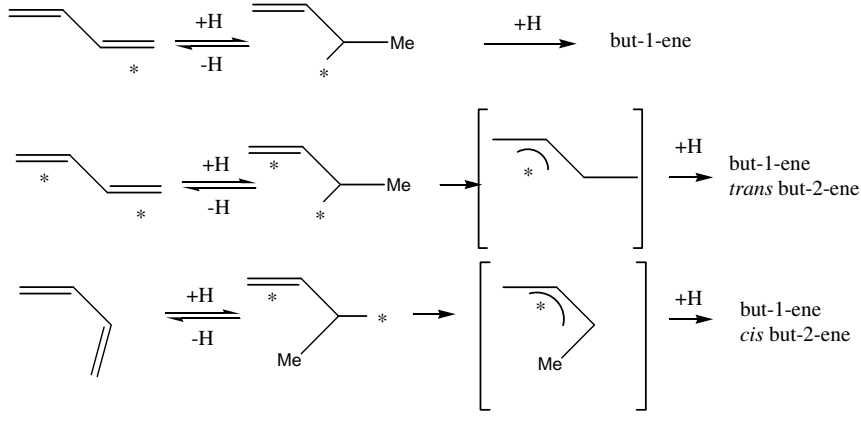

Figure 5.3 Simplified mechanism for the hydrogenation of buta-1,3-diene over metals other than Pd.

structure that does not readily form a π-ally complex in the transition state. For example Cu produces 87% but-1-ene (Table 5.1), its nearly full *d*-shell restricting the formation of the π-ally complex. For Co, Ni, Cu, Mn, V and Zr very little selectivity is observed between the two but-2-ene isomers, hence it was concluded that the

interconversion between the *cisoid* and *transoid* forms of the adsorbed butadiene and/or the σ-π-adsorbed half-hydrogenated species was facile. In contrast to this, with Pd, although 65% of the butene yield is but-1-ene, the ratio of *trans* : *cis* but-2-ene is 16.[16] Values of the *cis : trans* ratio up to 20 have been recorded, hence in this situation, although process A still occurs, the but-2-ene formation process must be different.

The rotation of gas phase butadiene molecules about the central carbon–carbon bond in the gas phase is restricted, and at any one instant there is an excess of molecules whose geometry approximates to the *transoid* conformation rather than to the *cisoid*. The *transoid* : *cisoid* ratio has been determined experimentally to be between 10 and 20 : 1 at room temperature.[20] It would be expected that if the conformation in the gas phase was frozen on adsorption, then the subsequent 1,4 addition would yield a high *trans* : *cis* ratio in the but-2-ene. Palladium is well known to be exceptionally good at forming π-allylic compounds with unsaturated hydrocarbons and hence the observed selectivity can be explained by assuming that the butadiene molecules adsorb directly as two conformationally distinct π-allylic states (Fig. 5.4) which, because of the mode of bonding, cannot interconvert. The high *trans* : *cis* ratio in the product therefore directly mirror the high ratios in the gas phase and the observation of decreasing *trans* : *cis* ratio with increasing temperature can also be explained.

Butadiene hydrogenation has been studied over most transition metals in the form of evaporated thin films[19,20] and also over

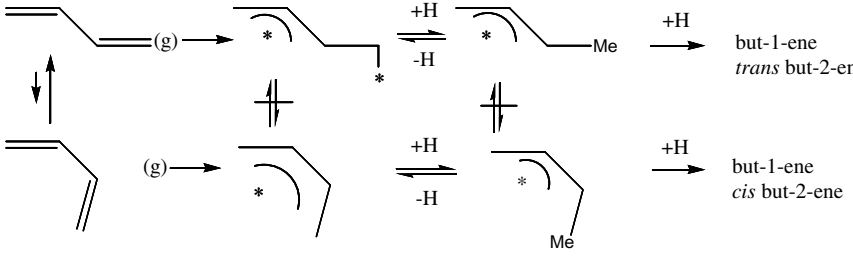

Figure 5.4 Mechanism of but-2-ene formation over Pd.

UHV-grown model catalysts[21,22] which allow comparison between model and impregnated catalysts. Hence the mechanisms described can be considered to be reasonably widely applicable. A point that can be gleaned from the evaporated film experiments is that the yield of but-1-ene increases with Pauling electronegativity of the metal.[20] This correlation was shown to apply for all three transition series. Again, this can be rationalised by the above mechanisms in that but-1-ene yield is determined by the electronic structure of the metal because as the *d*-band is filled, so the likelihood of forming π-allylic transition state is reduced. The use of model catalysts such as $Pd/Al_2O_3/NiAl(110)$ allows determination of the relative population of specific surface sites and hence permits calculations of rates per type of surface site (i.e. site specific TOFs) although normalisation for particles with sizes below 3 nm is difficult due to the absence of well-developed and defined facets.[23] Studies of initial hydrogenation rates suggest that TOF increases with mean particle size. However, when the TOF is normalised for the number of Pd-atoms in the (111) facets, at least for particles of mean diameter greater than 4 nm, the TOF becomes constant and consistent with the rate obtained over single crystal Pd(111), suggesting that these are the active sites.[21,22] For particles smaller than 4 nm, the activity approaches the value predicted for Pd(110), which is five times greater than over Pd(111).[22]

5.2.3 *The Hydrogenation of buta-1,3-diene over modified metal catalysts*

Early work involving some alumina supported Co and Ni catalysts gave unexpectedly low but-1-ene yields together with high *trans : cis*-but-2-ene ratios, and it was eventually discovered that the unexpected yields were a result of sulphur contamination which had migrated from the impure alumina support during catalyst preparation.[18] Once this effect was recognised it quickly became apparent that the electronegative elements adjacent to sulphur in the periodic table such as P, As, Se, Br and Cl all had similar effects on the selectivity of Co or Ni. Similarly, the effect of group V triphenyl

compounds on the selective hydrogenation of isoprene over Pd has been identified.[24] A quantitative investigation was carried out[19] by exposing metal films to progressive doses of hydrogen sulphide which underwent dissociative adsorption at 293 K depositing sulphur and liberating molecular hydrogen. Butadiene hydrogenation was studied as a function of sulphur coverage and the reaction mechanism was shown to move progressively from predominantly 1 : 2 addition to being predominantly 1 : 4 addition, the result being an increase in the *trans : cis* ratio of the evolved but-2-ene (some example data is given in Table 5.1). In terms of the mechanisms discussed earlier, the effect of the sulphur was to move the mechanism away from processes A and B in Fig. 5.4 and move towards process C in Fig. 5.3, with process A becoming poisoned. This effect was explained by the adsorption of sulphur resulting in the molecules adjacent becoming polarised, giving $M^{\delta+}$ sites, which stabilised the half-hydrogenated states as π-allylic intermediates, thereby enhancing the 1 : 4 addition.[25]

To summarise, for butadiene hydrogenation over metal catalysts, the selectivity for but-1-ene formation is governed by the electronegativity of the catalyst. Hence, selectivity may be affected either by tailoring the supported metal and/or by the addition of promoter species. If electronegative promoters are utilised, these function by generating positively polarised adsorption sites that favour *trans*-isomer formation, by 1 : 4 addition. It is important to note that if yield of but-1-ene is plotted relative to the *trans* : *cis* ratio of but-2-ene the data points for evaporated films (upon which much of the systematic research has been done), alumina supported metals *and* promoted metal catalysts fall on the same curve indicating the universality of the proposed mechanism.[26]

5.2.4 *Hydrogenation of α,β-unsaturated aldehydes over non-modified metal catalysts*

Unsaturated aldehydes contain two different functional groups (Fig. 5.5), providing great challenges if selective hydrogenation of one group only is required.[27]

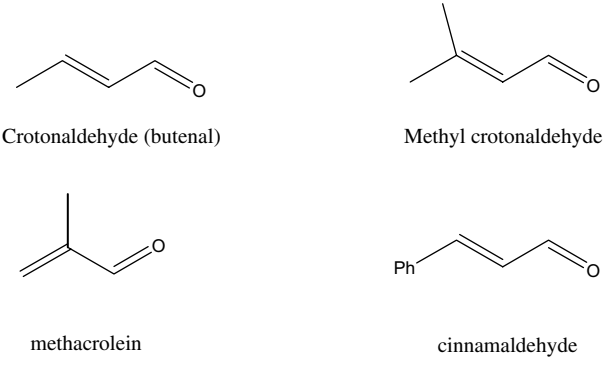

Figure 5.5 Some examples of α,β-unsaturated aldehydes.

When a compound contains both a carbon–carbon double bond as well as a carbon–oxygen double bond, the thermodynamics of the system favours the reduction of the former. For example for crotonaldehyde ($CH_3CH=CHCH=O$) hydrogenation, the free energy change for conversion to butyraldehyde (CH_3H_7CHO), crotyl alcohol ($CH_3CH=CHCH_2OH$) and *n*-butanol at 273 K are −71, −31 and −105 kJ mol^{-1} respectively. Therefore crotonaldehyde conversion over non-modified supported metal catalysts usually yields saturated butyraldehyde as the initial product, with butanol as either a primary or secondary product.

As is all too commonly the case in fine chemical synthesis, the industrially required product is the α,β-unsaturated alcohol, these being of major use as intermediates in the formation of perfumes, flavourings and pharmaceuticals.[28] As expected, Cu and Ni yield only butyraldehyde and butanol, although surprisingly a Cu-Ni alloy results in a selectivity of 54% crotyl alcohol.[29] Platinum alone yields butyraldehyde selectively at 433 K, but the addition of iron results in the formation of crotyl alcohol.[30,31] The use of liquid phase reactors has a significant effect on the selectivities observed in the reaction. For example, high selectivities to crotyl alcohol are observed for Ru, Re and Os on several supports, with Os/ZnO giving a reported selectivity of 97%.[32] However, certainly in the case of Ru when similar catalysts were utilised in the vapour phase, although initial selectivities to crotyl alcohol were observed, selectivity decayed rapidly with time on stream.[33]

5.2.5 *The hydrogenation of α,β-unsaturated aldehydes over modified metal catalysts*

The promotion of Pt by the addition of Fe[30,31] was followed by a further report indicating that a similar promotion was observed with Cu/chromia.[34] These results were a forerunner for many systematic and detailed studies on promoted supported metal catalysts, resulting in some remarkably successful systems.

Broadly speaking, the most successful catalytic systems have been achieved by use of supported metal catalysts modified using one of two distinct strategies: (a) the addition of an electropositive additive or (b) an electronegative additive, which by its action on the adsorbate yields positive centres in the active phase. The principal for both routes is the formation of bonds between the aldehydic O-atom and the positive centre, resulting in electron depletion in the adjacent C-atom, and thereby its activation towards H-atom addition.

The effect on selectivity and activity for the hydrogenation of 3-methyl crotonaldehyde using Pt/SiO_2 modified with cations from successive groups in the periodic table was studied by Ponec *et al.*[35,36] The most effective promoter was found to be Fe and Sn both of which raised the selectivity to the unsaturated alcohol from 21% to about 80%. Interestingly, this increase in selectivity was also accompanied by a substantial rate enhancement from 2.0 to 12.7 $\mu mol\ s^{-1}\ (g\ cat)^{-1}$ in the case of Pt : Sn prepared with a 4 : 1 ratio. Similar selectivity and activity enhancement were reported by Vannice and Sen for crotonaldehyde hydrogenation over Pt/TiO_2 in the vapour phase using a H_2 : aldehyde ratio of 22.7 : 1.[37] Under both low temperature reduction and high temperature reduction (SMSI) conditions, crotyl alcohol was formed, the best yield being 37% over the latter at low conversion. IR studies show the progressive loss in specific sites as the SMSI state is induced by higher temperature reduction of Pt/TiO_2.[38,39] By contrast Pt supported on SiO_2, Al_2O_3 or merely in its powder form all showed no selectivity to the unsaturated alcohol, forming only butyraldehyde under the same conditions. The increase in selectivity caused by the TiO_2 was rationalised by the presence of Ti^{3+} or Ti^{2+} ions or oxygen vacancies

coordinating the oxygen atom of the carbonyl group, thereby activating the adjacent C-atom for H-addition. The combined effects of addition of a promoter metal and a reducible oxide support have been studied by Sepúlveda-Escribano and coworkers.[40–41]

The fact that Pt has a high alkene hydrogenation capability has lead to a considerable amount of research being undertaken on a less active metal, Cu. This, combined with the ability of sulphur to promote the formation of unsaturated alcohol by the formation of δ^+ sites on the active surface as described earlier, lead to an in-depth study by Hutchings and Rochester[42–43] involving Cu and Pd and later extended to Au.[44,45] Some important points are illustrated in Table 5.2.

The most important point to remember when considering vapour phase reaction data is that irrespective of the presence of promoters on the copper catalyst the product distributions vary considerably with time on stream. For example the first three entries in Table 5.2 show the drastic decrease in production of butanol over the first 60 minutes of reaction together with the corresponding increase in butyraldehyde. Selectivity towards crotyl alcohol however remains constant. On sulfidation of the Cu/Al_2O_3 catalyst by thiophene, a much enhanced selectivity of 58% after 30 minutes to the unsaturated alcohol was observed. As with the non-promoted catalyst, the initial large production of butanol is replaced by butyraldehyde but also with some high molecular weight products formed by aldol condensation. The nature of the copper sites on the catalyst surface was probed by infrared spectroscopy.[46] The shift in the adsorbed CO band frequency on addition of thiophene led to the deduction that four types of adsorption sites were present at the catalyst surface: (i) Cu^0, (ii) Cu^+ in a matrix of Cu^+, (iii) Cu^+ in a matrix of Cu^{2+} and (iv) Cu^{2+}. Similar studies involving the hydrogenation of butyraldehyde and crotyl alcohol showed that isomerisation of the alcohol to the aldehyde and its dehydrogenation back to the reactant occurred at a measurable rate. Hence a reaction pathway was proposed (Fig. 5.6), with curve fitting providing the values of the pseudo first order rate constants shown.

Table 5.2 Reaction products observed in the vapour phase hydrogenation of crotonaldehyde over various supported metal catalysts. (Reaction conditions: H_2 : crotonaldehyde = 14 : 1, Pressure = 1 bar).

					Products/%			
Catalyst	Promoter[a]	Temp/K	TOS[b]/min	Conv[c]/%	Butyraldehyde	Crotyl alcohol	Butanol	Others[d]
Cu/Al_2O_3	—	353	5	17	39	9	51	1
Cu/Al_2O_3	—	353	5	8	59	10	27	5
Cu/Al_2O_3	—	353	60–180	5	89	10	0	1
$S\text{-}Cu/Al_2O_3$	Th-2	353	5	19	9	32	48	11
$S\text{-}Cu/Al_2O_3$	Th-2	353	15	10	15	40	27	18
$S\text{-}Cu/Al_2O_3$	Th-2	353	30	5	20	58	16	6
$S\text{-}Cu/Al_2O_3$	Th-2	353	180	3	25	37	0	38
Cu/Al_2O_3	—	373	60	16	87	9	0	4
$S\text{-}Cu/Al_2O_3$	Th-1	373	60	4	42	38	0	20
$S\text{-}Cu/Al_2O_3$	Th-2	373	60	4	23	56	0	21
Cu/SiO_2	—	383	40	59	15	64	20	1
3 : 1 $Cu\text{-}Pd/SiO_2$	—	383	40	35	10	64	25	1
Pd/SiO_2	—	383	40	42	27	0	73	
$S\text{-}Cu/SiO_2$	Th-1	383	40	37	22	70	7	1
$S\text{-}3 : 1Cu\text{-}Pd/SiO_2$	Th-1	383	40	39	29	0	65	6
$S\text{-}Pd/SiO_2$	Th-1	383	40	45	20	0	80	

[a] Th = thiophene dosed onto catalyst at 483 K, number indicates dosage/μL

[b] TOS = time on stream/min

[c] Conv = conversion/%

[d] For Cu others are aldol condensation products, for Cu-Pd others are but-1-ene and butane

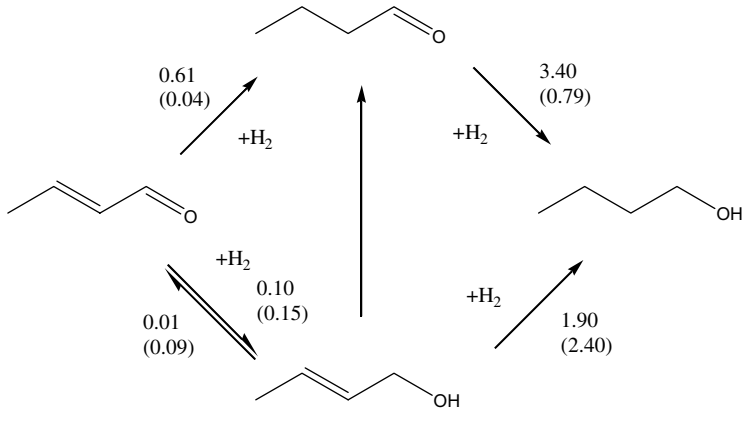

Figure 5.6 Reaction network and rate coefficients for crotonaldehyde conversion over Cu/Al_2O_3 at 373 K. Rate coefficients in brackets represent reaction over sulfided Cu/Al_2O_3.

The kinetic analysis provides a fascinating insight into the detailed reaction mechanism. The rates of formation and removal of butyraldehyde are reduced by the presence of sulphur, but more surprisingly the rate of crotyl alcohol hydrogenation to butanol is *increased*. Hence the enhanced selectivity to crotyl alcohol exhibited by the sulphur-modified catalysts can only be explained by a combination of the poisoning of the pathway *via* butyraldehyde and its enhanced rate of formation. The ratio of sulphur atoms to copper atoms in the active surface was calculated to be about 0.002 : 1.000. This ratio is far too low for the outcomes of sulphur modification to be described as steric, rather the effects were attributed to newly formed Cu^+-S sites, these being responsible for the activation of the carbonyl group on reactant adsorption, the selectivity variation therefore being electronic in origin.

All these reactions occurring over supported metal catalysts utilise the full range of metal crystal faces normally present on microcrystalline metals. A theoretical study by Delbecq and Sautet[47] showed that the adsorption geometries of acrolein, crotonaldehyde and 3-methyl crotonaldehyde differed depending onto which face they were adsorbing. Pt(111) yielded di-σ adsorption, whilst Pt(100)

and Pt(110) yield planer-η_4 and π_{CC} forms respectively. Hence an interesting challenge is to devise methods of preparing face specific catalysts for use in such reactions, such routes are already being proposed in the field of enantioselective fine chemical catalysis.

5.3 Selective Oxidation

The development of clean selective oxidation routes is a significant challenge to the fine chemical and pharmaceutical industries.[48,49] The use of stoichiometric inorganic reagents is decreasing but remains widespread. Ever tightening environmental legislation is driving the development of new environmentally benign methods. In many cases, homogeneous catalysis provides the necessary solutions, but at an industrial scale the usual deficiencies are evident, these being corrosion, plating of reactor walls, handling, recovery and reuse. The use of heterogeneous catalysts in conjunction with air or hydrogen peroxide can provide a viable alternative.[50–52] However significant drawbacks include poisoning by the strongly adsorbed by-products[53] or commonly the formation of an inactive surface oxide layer.[54]

5.3.1 *Supported platinum-group metals*

Pt group metals can activate alcohols and molecular oxygen under close to ambient conditions, producing the corresponding carbonyl or carboxylic acids in high yields. Enhanced selectivity and activity has been obtained by the use of bi- and multimetallic catalysts.[55–57] However, as was the case with selective hydrogenation, the optimum catalysts developed to date have involved a combination of supported metals and selectivity promoters. The most commonly used catalysts consist of either Pt or Pd as the active metal combined with Bi or Pb as promoters, commonly on carbon or alumina supports. Other promoters reported include Cd,[58] Co,[58] Cu,[59] Se,[60] Ce,[60,61] Te,[62] Sn,[63] Au[63,64] and Ru.[63,65,66] The catalysts can be prepared by simultaneous deposition and reduction of the metal precursors onto a suitable support.[60] However, more commonly, preparation involves a

two step route in which the promoter is deposited onto a supported Pt or Pd catalyst with subsequent reduction. Also demonstrated is a variation on this route whereby the promoter metal salt is added to the slurry containing the supported Pt group catalyst, and the promoter ion is reduced to metal by the alcohol reactant in the initial stages of the reaction.[59,67] Such catalysts can produce very significant changes in both selectivity and activity of oxidation reactions. Figure 5.7 shows the reaction pathway by which propylene glycol can be oxidised to yield pyruvic acid. Oxidation can proceed through two pathways, one *via* hydroxyacetone, the second *via* lactic acid. Pinxt *et al.*[68] showed that the addition of Pb and Bi enhanced the oxidation of lactic acid resulting in higher yields of pyruvic acid. The addition of Sn lead to high selectivities for both hydroxyacetone and pyruvic acid, this was ascribed to the formation of a Sn-diol complex, in which the Sn was in the Sn(IV) state.

The state of the bi- or multimetallic catalyst is important as segregated single metal sites yield reduced selectivity. These may be formed either by single metal agglomerations on the surface or multilayer adsorption of the secondary component on the initial supported metal catalyst.[52] It has been shown that selectivities and activities may be influenced by the presence of organic modifiers such as amines[68,69] or phosphines.[70,71] Mallat *et al.* described a systematic study[70] for the partial oxidation of L-sorbose with molecular oxygen over Pt/C and Pt/Al_2O_3 catalysts, modified with trace

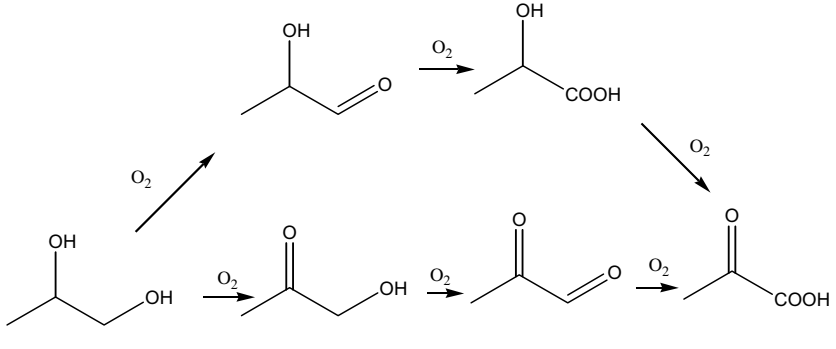

Figure 5.7 Reaction scheme for the oxidation of propylene glycol.

amounts of amines and phosphines. In general, the higher the modifier : Pt ratio, the greater the resulting selectivity to 2-keto-L-gulonic acid. This was accompanied by a corresponding reduction in reaction rate. Increases in selectivity from 40% with an unmodified catalyst up to 81% were recorded. By monitoring the catalyst potential during the reaction, the oxidation state of the Pt was shown to decrease with promotion, indicating that some side reactions leading to catalyst poisons were suppressed.

A particular advantage of these catalyst systems is their ability to function in aqueous media, making them attractive for environmentally sustainable processes. Where non-water soluble reactants are involved the use of organic solvents can still be avoided by the use of water-detergent solvent systems.[72,73] For example, Mallat *et al.* demonstrated the selective oxidation of cinnamyl alcohol to cinnamaldehyde over Bi-Pt/Al_2O_3 catalysts with air in an aqueous solution containing equal masses of Li_2CO_3 and dodecylbenzene-sulfonic acid sodium salt detergent. Selectivities up to 98.5% were observed together with a ten-fold increase in activity.[73] Other solvent systems have been demonstrated, including ionic liquids[74] and supercritical CO_2.[75–78]

5.3.2 *Supported gold and silver*

In recent years the unexpected observation of highly active Au as a low temperature CO oxidation catalyst[79,80] has initiated extensive research activity into the use of supported gold for liquid phase oxidation reactions. In general, the adsorption characteristics and catalytic properties of Au depend crucially on particle size, which can be controlled by the preparation method and the support.[81–86] The crucial question involving gold catalysis which as yet has not been fully answered is the concept of why Au nanoparticles exhibit such radically different behaviour than bulk Au.[87–90] Further details of preparation methodologies are given in Chapter 1 and details regarding use of Au catalyst are provided in Chapter 6.

The current range of applications for which supported gold catalysts can be used cannot currently be described as broad, although

much progress has been made in recent years. Under mild conditions supported gold catalysts appear to require the presence of a strongly basic aqueous medium. For example, Hutchings *et al.* studied the oxidation of glycerol over supported Pt, Pd and Au catalysts and have shown that 100% selectivity to glyceric acid can be obtained under certain circumstances using Au catalysts.[91–93] The reaction pathway for glycerol oxidation, shown in Fig. 5.8, is complex and a considerable challenge exists if high selectivities to glyceric acid are to be obtained.

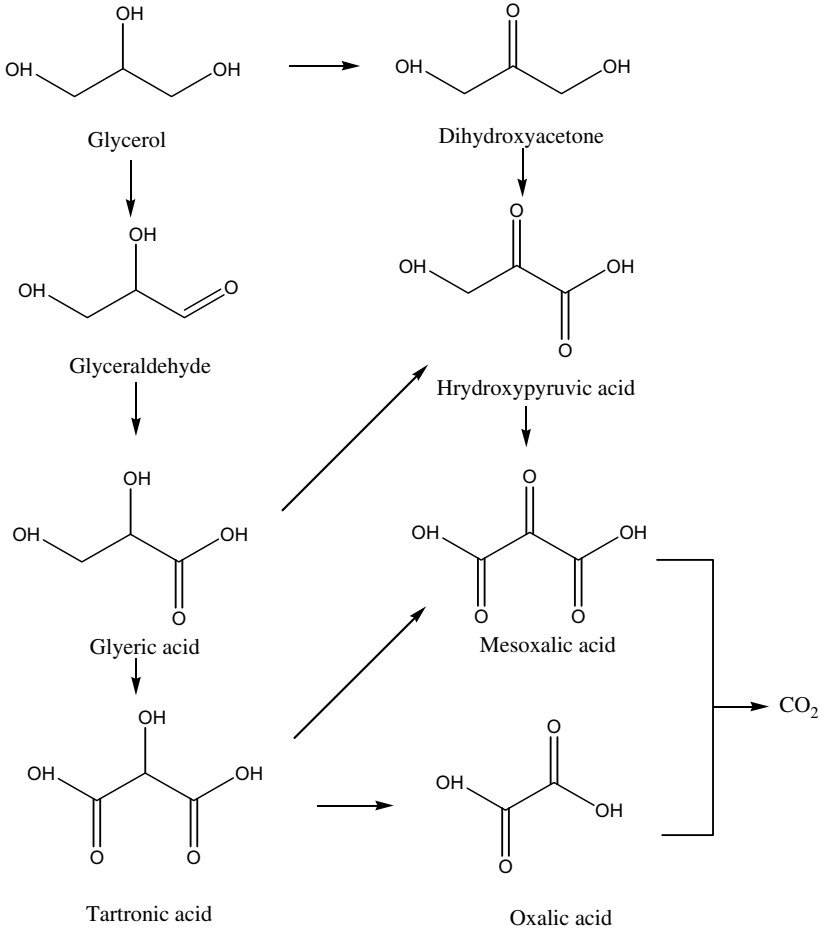

Figure 5.8 Reaction scheme for the oxidation of glycerol.

Supported Pt and Pd were shown to yield some selectivity in batch conditions using air as oxidant, but the principal products were the unwanted single carbon species such as CO_2, HCHO and HCOOH. Under these conditions, supported Au catalysts were totally inactive. Using pure oxygen and 3 bar pressure Au became active, and the formation of C_1 by-products was eliminated when NaOH was added. Using 1 wt% Au supported on either graphite or activated carbon, 100% selectivity to glyceric acid was readily achieved. It was concluded that in the absence of base, the initial dehydrogenation of glycerol, *via* hydrogen abstraction is not possible for the Au catalyst, unlike Pt or Pd. In the presence of base, the H^+ is readily abstracted from one of the primary hydroxy groups of glycerol, forming the glycerate anion, thereby overcoming the rate limiting step of the alternative reaction pathway.

Unfortunately, this requirement for the presence of aqueous base may well represent a strong limitation to the use of supported gold catalysts, as various base-catalysed side reactions such as keto-enol tautomerism or oxidative decarbonylation could diminish selectivities.

Supported silver catalysts are relatively commonly used in gas phase oxidations of alcohols.[94,95] Benzyl alcohol can be selectively oxidised to benzaldehyde using a 0.6% Ag/pumice catalyst[96] with 100% selectivity, although its activity is less than a similar Pd material. However, a mixed Pd-Ag/pumice bimetallic increases the activity whilst retaining the 100% selectivity to benzaldehyde. The authors of this study concluded that the role of the Pd was to activate the substrate whereas the highly dispersed silver particles served to activate the oxygen. Hence the mechanism was one of cooperation between the Ag^0 and Pd^0 sites; the alloy phase, detected by EXAFS, was not considered to play an important role.

5.3.3 *Catalyst deactivation*

The most common problem associated with supported metal catalysts for use in oxidation reactions is the 'overoxidation' of the active sites. For example the rate of oxidation is far higher on reduced

metal sites than on the oxidised surface.[97,98] This provides an interesting chemical engineering challenge in that the reactor must be operated in an oxygen transport-limited mode. For example, in a batch reactor, the rate of alcohol dehydrogenation decreases with time, due to the reduction in the concentration of reactant meaning the ratio of oxygen to active reacting site is increasing. Hence, the oxygen pressure should be decreased with reaction time or an external stimulus such as the increase of temperature should be applied in order to speed up the reaction of the remaining material.[99,100]

The formation of strongly adsorbed by-products is another major difficulty. Possible contaminants include condensation and oligomerisation products of carbonyl species and the decomposition of alcohol species to yield CO and adsorbed hydrocarbon. Numerous examples of such deactivation scenarios exist giving a genuine challenge to both the catalyst chemist and the chemical engineer to produce systems which minimise these problems.

Both the examples dealt with above can be considered reversible. However, sintering of the active metal particles and leaching of the same into solution are both irreversible. Sintering usually requires elevated temperatures, although if chelating agents are present the active phase may be subjected to the process of Ostwald ripening.[101] Leaching is encouraged by the presence of acidic or basic media and the presence of complexing agents, and great care must be taken to ensure that the reactivity being measured in a reaction is in fact due to the presence of the heterogeneous catalyst and not to minute quantities of dissolved metal in solution acting as a homogeneous catalyst. All these deactivation processes complicate the use of supported metals for oxidation reactions, however it also provides a significant challenge for the chemist and engineer to design catalyst systems in which the support, active metal, promoter species and reactor combine to give efficient oxidation systems.

5.4 Enantioselective Reactions

The concept of controlling not just the selectivity of a particular reaction, but also the enantioselectivity, provides perhaps the greatest

challenge for the catalyst chemist. However, the concept of enantiocontrol is not just an academic curiosity but a central issue to the modern fine chemicals industry. Pharmaceuticals and vitamins,[102–104] agrochemicals,[105] flavours and fragrances[106–108] are increasingly produced as enantiomerically pure compounds. The primary driver for these advances has been either the superiority of single enantiomers or because legislation has demanded the evaluation of both enantiomers of a biologically active compound before its approval.

The first report of enantioselective catalysis over metal catalysts was made in 1939 by Lipkin and Stewart who showed that hydrocinchonine β-methylcinnamate could be hydrogenated in ethanol over an Adams Pt catalyst to yield β-phenylbutyric acid which exhibited an optical rotation of 8%.[109] Some 20 years later Akabori and coworkers reported that Pd supported on silk-fibroin was enantioselective for compounds containing both C=N and C=C functionalities, yielding optical yields as high as 66%, although the origin of the enantioselectivity in these systems has never been clear.[110] A further 20 years later Orito and coworkers reported that conventional supported Pt catalysts could be made enantioselective by the adsorption of naturally occurring materials such as the cinchona alkaloids cinchonidine and cinchonine.[111–113] The reactions studied were the hydrogenations of α-keto esters, such as methyl pyruvate, MeCOCOOMe, and ethyl benzoylformate, PhCOCOOEt. Optical yields up to 80% were reported at room temperature, using standard catalysts, common solvents and elevated hydrogen pressure. These papers lead to an explosion of interest in the subject and several excellent reviews are available.[114–122]

5.4.1 *Enantioselective hydrogenation of activated ketones over supported platinum*

The general structures of the cinchona alkaloids are shown in Fig. 5.9.

These molecules contain an aromatic quinoline ring system and a saturated quinuclidine ring system separated by the carbon numbered C_9. Chiral centres are present at C_3, C_4, C_8 and C_9, of which C_8 and C_9 have the S- and R- configuration respectively in cinchonidine

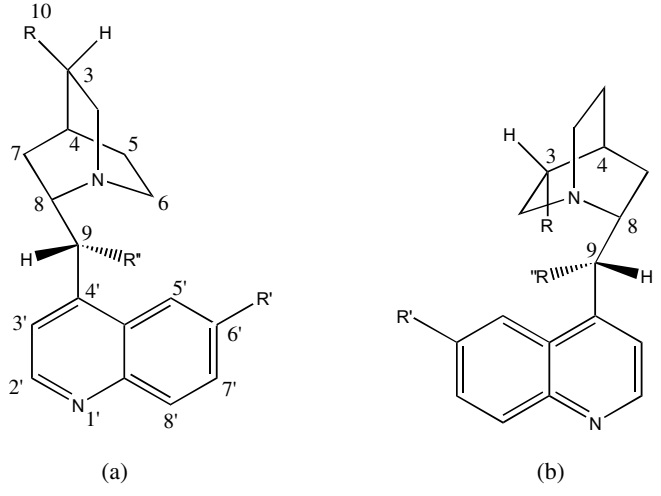

Figure 5.9 Structures of the cinchona alkaoids:

(a) cinchonidine (CD), cinchonine (CN): R = C_2H_3 R′ = H R″ = OH
(b) quinine (QN), quinidine (CD): R = C_2H_3 R′ = OMe R″ = OH
dihydroderivatives (e.g. DHCD): R = C_2H_5
O-methyl derivatives (e.g. O-MeDHCD): R″ = OMe

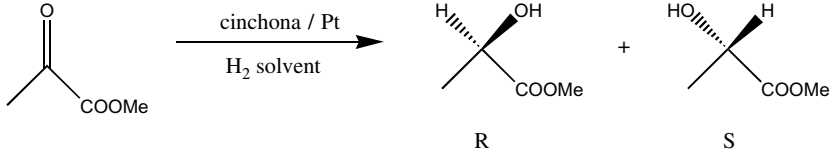

Figure 5.10 Enantioselective hydrogenation of activated ketones.

and in quinine, but the R- and S- configuration respectively in cinchonine and quinidine. Thus cinchonidine and cinchonine are related as 'near enantiomers' and their enantiodirecting effects are indeed in opposite senses. Simple derivatives have been investigated, the most important being the 10,11-dihydroalkaloids, compounds in which the substituent at C_9 has been varied, and compounds in which the quinuclidine-N-atom has been quaternised.

Hydrogenation of alkyl pyruvates (Fig. 5.10) to their corresponding lactates has received considerable attention both from a

theoretical and experimental standpoint. Some example results are shown in Table 5.3. Enantioselectivity in these systems is measured in terms of enantiomeric excess (ee) which is defined as ([R] – [S]) / ([R] + [S]).

Clearly modifiers having the cinchonidine configuration S- at C_8 and R- at C_9 yield an enantiomeric excess in favour of the R-product, whereas modifiers having the cinchonine configuration R- at C_8 and S- at C_9 give the S-product in excess. High enantioselectivity (ee = 60 to 80%) is achieved by use of the natural alkaloids as modifiers of reactions at elevated hydrogen pressure and ambient temperature without system optimisation (entries 1–8, Table 5.3). The 10,11-dihydroderivatives provide slightly higher enantioselectivities (entries 5,7,8). To make comparisons valid, most reactions presented in Table 5.3 were conducted in ethanolic solution. However, reactions occur in a variety of solvents, enantiomeric excess being reduced by use of solvents of high dielectric constant. Thus, by use of cinchonidine as modifier, Baiker, Blaser and coworkers have observed enantioselectivities of 79.9–81.4% in solvents of low dielectric constant (cyclohexane, ε = 2.02; toluene, 2.38; tetrahydrofuran, 7.6; dichloromethane, 9.08), lower values of 75.0–78.0% in alkanols, (pentanol, ε = 13.9; ethanol, 24.3; methanol, 33.6) and inferior values of 54.1% in water (ε = 80.4) and of 48.0% in formamide (ε = 109).[129] The exception to this general rule is that carboxylic acid solvents tend to give higher enantioselectivities than predicted from their polarity.[127] For example, ethyl pyruvate hydrogenation in acetic acid, using dihydrocinchonidine-modified Pt gave ee = 88% and dihydro-O-methyl-cinchonidine provided ee = 95% (entry 12). Acetic acid may also be used to advantage as a co-solvent, for example with toluene.[127] By comparison, the use of bases as solvents is severely disadvantageous (entry 13). Data from the group of Hutchings have shown that the reaction proceeds enantioselectively in the absence of solvent,[134] albeit with a reduction in ee, the maximum being 43% occurring for methylpyruvate hydrogenation over a 2.5% Pt/SiO_2 catalyst. The efficiency of cinchonidine, cinchonine and their dihydro derivatives as modifiers is diminished above 315 K.[130] A synthetic alkaloid resembling cinchonidine but in which C_9

Table 5.3 Representative values of the enantiomeric excess (ee) observed in the hydrogenation of methyl pyruvate (MePy) and of ethyl pyruvate (EtPy) catalysed by cinchona-modified Pt/silica or Pt/ alumina[a].

	Modifier[b]							
Entry		R	R′	R″	Reactant	Solvent	ee/%	Ref
1	CD	C_2H_3	H	OH	MePy	Ethanol	64-77(R)	127
2	CD	C_2H_3	H	OH	EtPy	Ethanol	76(R)	128
3	CN	C_2H_3	H	OH	EtPy	Ethanol	56(S)	128
4	QN	C_2H_3	OMe	OH	MePy	Ethanol	61(R)	120
5	DHQN	C_2H_5	OMe	OH	MePy	Ethanol	65(R)	128
6	QD	C_2H_3	OMe	OH	MePy	Ethanol	55(S)	129
7	DHCD	C_2H_5	H	OH	MePy	Ethanol	80(R)	130
8	DHCD	C_2H_5	H	OH	EtPy	Ethanol	82(R)	131
9	O-MeDHCD	C_2H_5	H	OMe	EtPy	Ethanol	82(R)	131
10	O-MeDHCD	C_2H_5	H	OMe	EtPy	Toluene	88(R)	131
11	O-MeDHCD	C_2H_5	H	OMe	EtPy	Propionic acid	91(R)	131
12	O-MeDHCD	C_2H_5	H	OMe	EtPy	Acetic acid	95(R)	131
13	O-MeDHCD	C_2H_5	H	OMe	EtPy	Triethylamine	3(R)	131
14	O-AcDHCD	C_2H_5	H	OAc	MePy	Ethanol	44(R)	120
15	O-AcDHCD	C_2H_5	H	OAc	EtPy	Ethanol	20(R)	128
16	Deoxy-CD	C_2H_3	H	H	EtPy	Ethanol	40(R)	128
17	Epiquinidine	C_2H_3	OMe	H	MePy	Ethanol	0	120, 132
18	Benzyl(CD)Cl	C_2H_3	H	OH	EtPy	Ethanol	0	128,104
19	Benzyl(CD)Cl	C_2H_3	H	OH	MePy	Ethanol	2(R)	120

[a] Reactions conducted at *ca.* 293 K and analysed at high conversions. 10 bar pressure, catalysts pre-modified before admission to reactor.[120,127,129] 70 to 100 bar pressure, catalysts not pre-modified, modifier added to reactor with reactant.[128,131]

[b] Modifier structures and nomenclatures are defined in Fig. 5.9.

was not chiral gave enantioselective reaction but with a reduced enantiomeric excess (entry 16). Epiquinidine, in which both C_8 and C_9 have the R-configuration, is not an effective modifier (entry 17). Modification of cinchona alkaloids by quaternisation at the quinuclidine-N-atom, e.g. by conversion to benzyl cinchonidinium chloride, substantially destroys enantioselectivity (entries 18 and 19). However, hydrocinchonidine sulphate, in which the quinuclidine-N is simply protonated, behaves as cinchonidine.[129] The dependence or otherwise of enantiomeric excess on conversion and hydrogen pressure may vary with the procedure used for catalyst preparation and modification (see below). When modification is carried out separate to the reactor there may be little variation with conversion[130] whereas, with *in situ* modification, in which the modifier is simply added to the reaction vessel with the catalyst and reactant, enantioselectivities tend to be low initially, rise steeply over the first 20% of conversion[135–138] and remain fairly steady thereafter.[133,138] 5′,6′,7′,8′,10,11-Hexahydrocinchonidine, a modifier having a partially hydrogenated quinoline ring, gave an initial enantiomeric excess of 45% which decayed steadily to 23% at 80% conversion.[138]

High performances have been reported for modified Pt catalysts over several different supports including silica, alumina and carbon[120,131,139,140] or deposited in the mesopores of MCM-41.[141] The dependence of enantiomeric excess on catalyst preparation procedure and Pt particle size has been studied[138,141] as has the wider matter of particle morphology,[123] but a detailed performance/structure correlation has yet to be established. Very small Pt particles (*ca.* 0.7 nm in diameter) do not promote enantioselectivity,[142] particles of average size, 1.8 nm particles, such as are present in the 6.3% Pt/silica reference catalyst EUROPT-1 provide average enantioselectivities, and the sintering of this particular catalyst so that the mean Pt particle size was increased to 4 nm improved the enantiomeric excess to 80%;[123] this concurs with the general conclusions of a wider study.[139] Modification of catalyst grain size by use of ultrasonication may also lead to an improvement in enantioselectivity.[143] By contrast, the highest enantiomeric excess yet reported for pyruvate

ester hydrogenation of 97.5% has been achieved by use of a polyvinylpyrollidone-stabilised Pt colloid having a narrow particle size distribution centred at 1.4 nm.[144] A colloid having a mean particle size of 1.8 nm gave ee = 81.4% in ethanol (a Pt particle size and ee closely similar to those provided by the 6.3% Pt/silica, EUROPT-1) and this performance was improved to ee = 95.9% by use of acetic acid as solvent. Exceptional performance (ee = 91.3%) was retained when the 1.4 nm colloidal particles were deposited onto alumina to provide a supported catalyst. This suggests that optimum Pt particle configuration is not simply determined by size and that other factors contribute to optimum performance; for example, the polyvinylpyrollidone protecting agent may control Pt particle morphology in some appropriate manner or it may restrict the available Pt surface and thereby reduce the number of unmodified sites which catalyse racemic reaction.

Other families of prochiral ketones have been investigated including alkane diones,[145] and in general these give much reduced enantioselectivity, although the effect of kinetic resolution in the second stage of reaction (conversion to alkane diol) results in a significant increase in ee for the remaining hydroxyketone.[146]

Considerable debate has taken place over the years regarding the mechanism of enantioselective hydrogenation. Pyruvate ester undergoes slow hydrogenation to racemic product at an alkaloid-free Pt surface, the reaction being zero order in ester and first order in hydrogen, indicating strong adsorption of ester and relatively weak adsorption of hydrogen. These kinetic parameters are retained in the presence of alkaloid, with small deviations depending on the solvent used,[147,148] but more importantly, rates are greatly enhanced and the reaction becomes enantioselective. Molecules of pyruvate ester may adsorb by either of their enantiofaces, as shown in Fig. 5.11; hydrogenation of enantioface A gives R-lactate as product whereas enantioface B gives S-product.

Enantioselectivity may arise by the operation of either thermodynamic or kinetic factors. If competitive adsorption of ester as configurations A and B occurs at enantioselective sites cognate to adsorbed alkaloid with free energy changes $\Delta G^{O}_{ads,A}$ and $\Delta G^{O}_{ads,B}$

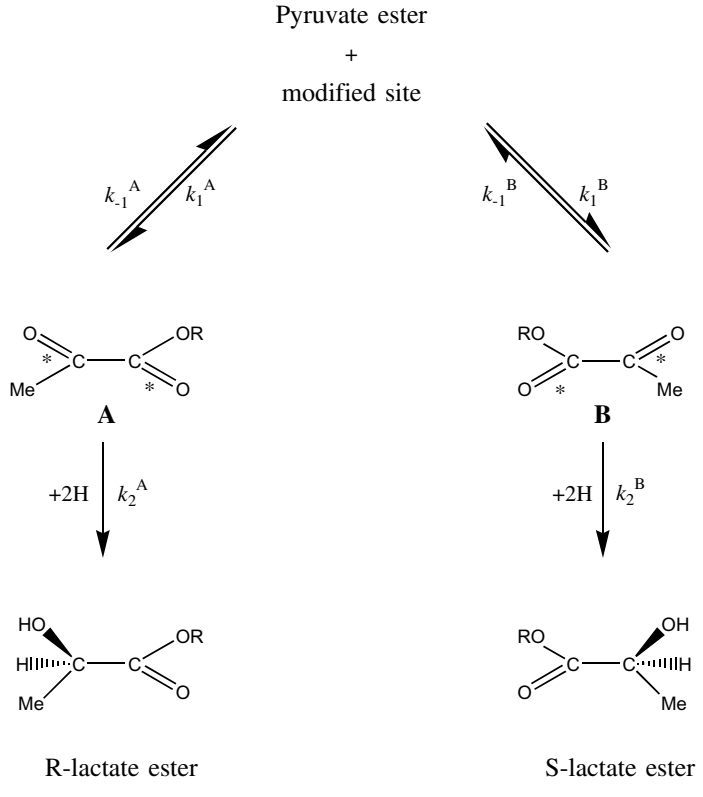

Figure 5.11 Reaction scheme showing the adsorption of pyruvate ester adsorbed by its two enantiofaces and the consequences of hydrogenation.

respectively, then, provided adsorption equilibrium is achieved, the relative surface coverages θ_A/θ_B will be a direct function of $\exp(-\delta\Delta G^{O}_{ads}/RT)$, where $\delta\Delta G^{O}_{ads}$ is the difference in the free energies of adsorption of the ester in configurations A and B. Because of the exponential form of this expression, a chiral environment that distinguishes only modestly between A and B in terms of free energies of adsorption will provide a high value of the ratio $\Delta\theta_A/\theta_B$. If no kinetic factor operates, i.e. if $k_2^{A} = k_2^{B}$, then the enantiomeric excess is thermodynamically determined, [R-lactate]/[S-lactate] = θ_A/θ_B, and enantioselectivity is attributable to *selective enantioface adsorption*. There is, of course, the possibility that molecules adsorbed by the

less stable enantioface may exhibit a higher inherent activity ($k_2^A \neq k_2^B$) in which case a kinetic factor also influences enantiomeric excess. Baiker and Blaser[124] describe a classic example of kinetic control in homogeneous catalysis in which the major enantiomer product is formed from the minority enantiofacial form of the reactant. Mathematical procedures for consideration of kinetic factors as applied to metal-catalysed enantioselective reactions have been described.[149–151] For the present case, where modifier and reactant are strongly adsorbed and achieve substantial surface coverages, semi-quantitative modelling of the thermodynamic factor can provide an estimate of the relative concentrations of the surface coverages of the two enantiofacial forms of the adsorbed reactant, and thereby a firm indication of the sense of the enantioselectivity that would be achieved if there were no kinetic factor operating. If the sense of the enantioselectivity is thus correctly predicted the procedure is of value, and the contribution of kinetic factors may be discernible from variations of enantiomeric excess with experimental variables. If the observed sense of the enantioselectivity is the reverse of that predicted then there is a *prima facie* case for the predominance of kinetic effects. Modelling of selective enantioface adsorption can only be partial at the present time; although the interactions of pyruvate ester molecules with cinchona alkaloids in their various low energy conformations can be determined with some accuracy (Fig. 5.12), the interactions with the metal surface cannot.

Consequently, the available methodology involves (i) determining the (repulsive) interactions as pyruvate molecules dock with alkaloid molecules in 1 : 1 arrangements and (ii) assuming that relatively the same energy situations pertain in the adsorbed state. Following this procedure, the docking of pyruvate ester molecules with the open-3 conformation of, say, cinchonidine, leads to the two geometrical situations shown in Fig. 5.13.[97,152]

The interaction energies are measured at the unique configurations such that, were the molecules adsorbed at a Pt(111) surface, the aromatic rings of the alkaloid and the carbonyl groups of the reactant would be located directly over surface Pt-atoms. Under

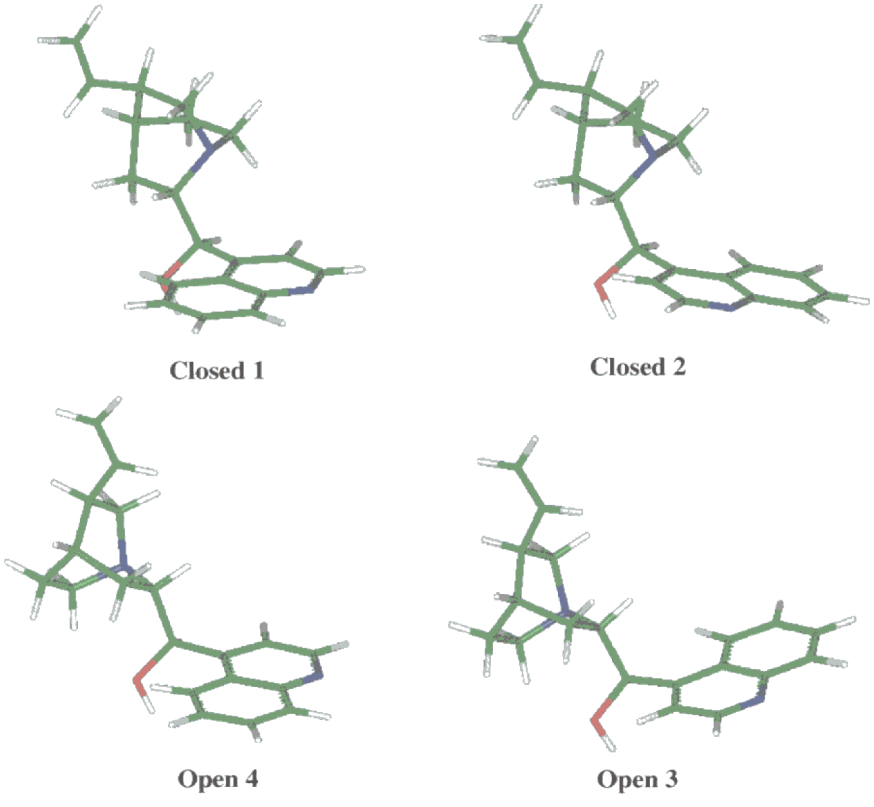

Figure 5.12 Calculated lowest energy conformations of cinchonidine.

these conditions, the cinchonidine : pyruvate ester interactions are less severe for enantioface A than for enantioface B; the free energy of adsorption of A is therefore expected to exceed that of B, and selective enantioface adsorption will occur with $\theta_A > \theta_B$ leading to enantioselectivity in favour of R-lactate. This concurs with observation (Table 5.3). No conditions for selective enantioface adsorption of pyruvate are evident for 1 : 1 interactions with alkaloid in the closed conformations. Analogous calculations for interactions between pyruvate ester and cinchonine identify less severe interactions for enantioface B than for enantioface A, leading to a predicted enantiomeric excess in favour of S-lactate ester, again in agreement with experiment.

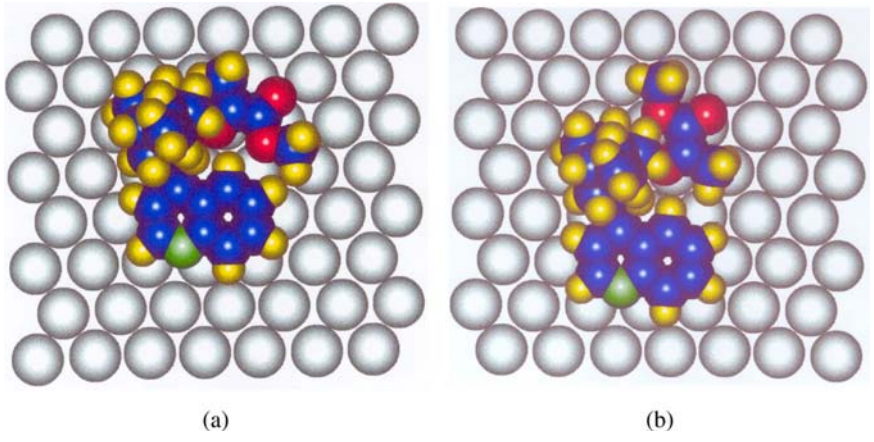

Figure 5.13 Methyl pyruvate adsorbed by each of its enantiofaces at the enantioselective site adjacent to cinchonidine adsorbed in the open-3 conformation. On hydrogenation (a) gives R-lactate and (b) gives S-lactate.

5.4.2 *Enantioselective hydrogenation over other supported metals*

Supported palladium shows modest activity for pyruvate ester hydrogenation. The first report by Blaser and coworkers indicated that enantioselectivity over cinchonidine-modified Pd/C was low and favoured S-lactate[153] — the reverse of the situation over Pt. Closer examination showed that reaction over conventionally supported Pd differed in every important particular from the corresponding Pt-catalysed reaction.[123,154] Rate enhancement was no longer apparent, indeed rate decreased in the presence of modifier. Over supported platinum the reaction proceeded *via* first order kinetics with respect to hydrogen, whereas over palladium the order was half-order and unlike Pt, there was no solvent sensitivity, indeed there was a significantly reduced number of solvents in which the reaction would proceed at all. Most importantly, reaction with deuterium gave product exchanged at the methyl group adjacent to the α-keto group, i.e. the product was $CX_3CX(OX)COOCH_3$ (where X = H or D),[154] whereas over Pt the participation of deuterium was limited to addition giving $CH_3CX(OX)COOCH_3$.[130] These differences are consistent with pyruvate undergoing dissociative adsorption by H-atom loss from the

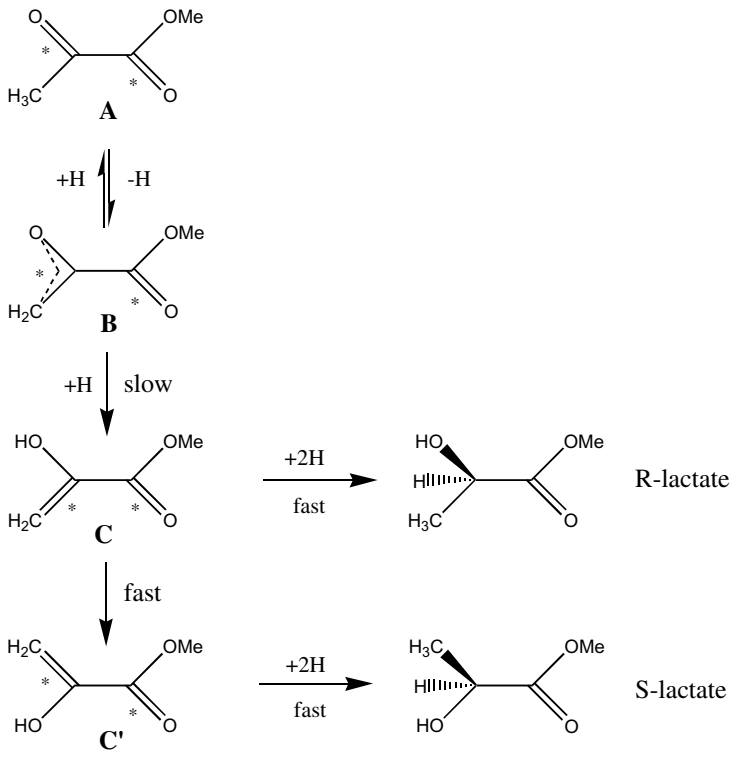

Figure 5.14 Mechanism for the enantioselective hydrogenation of pyruvate ester over palladium.

methyl group followed by re-hydrogenation to give the enol in a rate determining step (Fig. 5.14).

The process then becomes one of carbon–carbon double bond hydrogenation, a process for which Pd is well known to have high activity. Fast conversion of the enol to lactate, by conversion of intermediate C to D (Fig. 5.14), would provide an enantioselectivity in the product that is determined by any selective enantioface adsorption of pyruvate ester on Pd. If the characteristics of adsorption on Pd follow that on Pt, then enantioselectivity in favour of R-lactate would be expected with cinchonidine, and the reverse with cinchonine. However, the observed reversed enantioselectivity can be simply interpreted if it is supposed that the latent intramolecular repulsion

between the >C=C< and >C=O functions in adsorbed species C can be released by rotation about the carbon–carbon single bond to give adsorbed species C′ which gives S-lactate on hydrogenation. This mechanism then interprets the major experimental observations. First, there is no enhanced rate because the intermediate formed from pyruvate involved in the rate determining step (B) does not contain an –OH group that can participate in hydrogen bonding with the quinuclidine-N-atom. Second, the half-order in hydrogen is consistent with the rate determining step involving the addition of one hydrogen atom (assuming that dissociative hydrogen adsorption under these conditions obeys the Langmuir equation). A study highlighting the hydrogen pressure effects on enantioselectivity has been published.[155] Third, solvent specificity may indicate that enolisation occurs more effectively in one solvent than another. The low enantioselectivities normally observed (e.g. 15%[154]) are attributable to the greater contribution of racemic (unmodified) sites to product formation that necessarily follows the absence of rate enhancement at enantioselective (modified) sites, and also to the sensitivity imparted to the mechanism by the possible conversion of intermediates C and C′. Indeed, reactions giving low enantioselectivities in favour of R-product over cinchonidine-modified Pd/alumina have recently been reported,[156] and swings in the sense of the enantioselectivity have been obtained by variation of the ester group.

Platinum and palladium dominate the enantioselective catalysis scene as far as alkaloid modifiers are concerned. Of the other platinum-group metals, Ir follows Pt in cinchona-modified pyruvate ester hydrogenation,[157] the fact that Rh can hydrogenolyse alkaloids adsorbed at its surface[158] makes it unlikely to function successfully and Ru tends to be too easily oxidised by adventitious oxygen in these reactions.

5.5 Conclusions

Supported metal catalysts clearly have a major role to play in the fine chemicals industry. With the continued growth of environmental legislation further increasing the challenge to increase the

selectivity of chemical reactions and coupled to this, the need for such reactions to take place in more benign (but often chemically more complex) media such as aqueous rather than organic solvents,[159] the challenge for the catalytic chemist is immense. This contribution has touched on only a few examples of selectivity and fine chemical catalysis but it is hoped that the reader will have been encouraged to investigate further this fascinating challenge.

References

1. P.L. Mills, R.V. Chaudhari, *Catal. Today* 1997, **37**, 367.
2. C.S. Sell (Ed.), *The Chemistry of Fragrances*, 2nd Edition, RSC, London, 2006, 60.
3. B. Chen, U. Dingerdissen, J.G.E. Krauter, H.G.J. Lansink Rotgerink, K. Möbus, D.J. Ostgard, P. Panster, T.H. Riermeirer, S. Seebald, T. Tacke, H. Trauthwein, *Appl. Catal. A: Gen.* 2005, **280**, 17.
4. P. Mäki-Arvela, J. Hájek, T. Salmi, D. Yu Murzin, *Appl. Catal. A*: *Gen.* 2005, **292**, 1.
5. G. Alvez-Manoli, T.J. Pinnavaia, Z. Zhang, D.K. Lee, K. Marín-Astorga, P. Rodriguez, F. Imbert, P. Reyes, N. Marín-Astorga, *Appl. Catal. A*: *Gen.* 2010, **387**, 26.
6. A. Mastalir, Z. Király, F. Berger, *Appl. Catal. A*: *Gen.* 2004, **269**, 161.
7. J. A. Anderson, J. Mellor, R.P.K. Wells, *J. Catal.* 2009, **261**, 208.
8. N. Semagina, A. Renken, L. Kiwi-Minsker, *J. Phys. Chem.* 2007, **111**, 13933.
9. T.A. Nijhuis, G. Van Koten, J.A. Moulijn, *Appl. Catal. A*: *Gen.* 2003, **238**, 259.
10. T.A. Nijhuis, G. Van Koten, F. Kapteijn, J.A. Moulijn, *Catal. Today* 2003, **79–80**, 315.
11. G.C. Bond, P.B. Wells, *Advances in Catalysis,* Vol. 15, Academic Press, New York, 1964, 91.
12. H. Lindlar, *Helv. Chim. Acta.* 1952, **35**, 446.
13. D. Teschner, J. Borosodi, A. Wootsch, Z. Révay, M. Hävecker, A. Knop-Gericke, S.D. Jackson, R. Schlogl, *Science* 2008, **320**, 86.
14. E. M. Vass, M. Hävecker, S. Zafeiratos, D. Teschner, A. Knop-Gericke, R. Schlogl, *J. Phys. Condens. Matter* 2008, **20**, 184016.

15. J.J. Phillipson, P.B. Wells, G.R. Wilson, *J. Chem. Soc. A* 1969, 1351.
16. A.J. Bates, Z.K. Leszczynski, J.J. Phillipson, P.B. Wells, G.R. Wilson, *J. Chem. Soc. A* 1970, 2435.
17. G.C. Bond, G. Webb, P.B. Wells, M.W. Winterbottom, *J. Chem. Soc. A* 1965, 3218.
18. M. George, R.B. Moyes, D. Ramanarao, P.B. Wells, *J. Catal.* 1978, **52**, 486.
19. A.G. Burden, J. Grant, J. Martos, R.B. Moyes, P.B. Wells, *Discussions of the Faraday Soc.* 1981, **72**, 95.
20. R.B. Moyes, P.B. Wells, J. Grant, N.Y. Salman, *Appl. Catal. A*: *Gen.* 2002, **229**, 251.
21. J. Silvestre-Alvaro, G. Rupprechter, H.-J. Freund, *Chem. Commun.* 2006, 80.
22. J. Silvestre-Alvaro, G. Rupprechter, H.-J. Freund, *J. Catal.* 2006, **58**, 240.
23. G. Rupprechter in *Model Systems in Catalysis*, Ed.: R. Rioux, Springer, New York, 2010, 319.
24. Y. Fujii, J.C. Bailar Jr., *J. Catal.* 1978, **52**, 342.
25. L.B. Smith, J.L. Massingil, *J. Am. Chem. Soc.* 1961, **83**, 4301.
26. P.B. Wells, A.J. Bates, *J. Chem. Soc. A* 1968, 3064.
27. P. Gallezot, D. Richard, *Catal. Rev.* 1998, **40**, 81.
28. K. Bauer, D. Garbe, in *Ullmann's Encyclopedia of Industrial Chemistry*, 3rd Edition, VCH, New York, 1988, **A11**, 141.
29. H. Noller, W.M. Lin, *J. Catal.* 1984, **85**, 25.
30. J. Simonik, P. Beranek, *Coll. Czech. Chem. Commun.* 1972, **37**, 353.
31. J. Simonik, P. Beranek, *J. Catal.* 1972, **24**, 348.
32. D.V. Sokolskii, A.K. Zharmagambetova, N.V. Anisilmova, A. Ualikhanova, *Dokl. Akad. Nauk. SSR* 1983, **273**, 151.
33. B. Coq, F. Figueras, P. Geneste, C. Moreau, P. Moreau, M. Warawdekar, *J. Mol. Catal.* 1993, **78**, 211.
34. R. Hubault, M. Daage, J.P. Bonnelle, *Appl. Catal.* 1986, **22**, 231.
35. T.B.L.W. Marinelli, J.H. Vleeming, V. Ponec, *Proc. 10th Int. Cong. Catal.* 1993, **B**, 1211.
36. T.B.L.W. Marinelli, S. Nabuurs, V. Ponec, *J. Catal.* 1995, **151**, 431.
37. M.A. Vannice, B. Sen, *J. Catal.* 1989, **115**, 65.

38. F. Coloma, J.M. Coronado, C.H. Rochester, J.A. Anderson, *Catal. Letts.* 1998, **51**, 155.
39. J. Ruiz-Martínez, A. Sepúlveda-Escribano J.A. Anderson, F. Rodríguez-Reinoso, *Phys. Chem. Chem. Phys.* 2009, **11**, 917.
40. J. Ruiz-Martínez, A. Sepúlveda-Escribano, J.A. Anderson, F. Rodríguez-Reinoso, *Catal. Today* 2007, **123**, 235.
41. J. Silvestre-Albero, A. Sepulveda-Escribano, F. Rodriguez-Reinoso, J. A. Anderson, *J. Catal.* 2004, **223**, 179.
42. J. Silvestre-Albero, A. Sepulveda-Escribano, F. Rodriguez-Reinoso, J. A. Anderson, *Phys. Chem. Chem. Phys.* 2003, **5**, 208.
43. G.J. Hutchings, F. King, I.P. Okoye, C.H. Rochester, *Appl. Catal. A* 1992, L7.
44. M.B. Padley, C.H. Rochester, G.J. Hutchings, F. King, *J. Catal.* 1994, **148**, 438.
45. G.J. Hutchings, F. King, I.P. Okoye, M.B. Padley, C.H. Rochester, *J. Catal.* 1994, **148**, 453.
46. G.J. Hutchings, F. King, I.P. Okoye, M.B. Padley, C.H. Rochester, *J. Catal.* 1994, **148**, 464.
47. S.S. Ashour, J.E. Baillie, C.H. Rochester, J. Thomson, G.J. Hutchings, *J. Mol. Catal. A* 1997, **123**, 65.
48. J.E. Baillie, G.J. Hutchings, H.A. Abdullah, J.A. Anderson, C.H. Rochester, *Phys. Chem. Chem. Phys.* 2000, **2**, 283.
49. J.E. Bailie, G.J. Hutchings, *Chem. Comm.* 1999, **21**, 2151.
50. F. Coloma, B. Bachiller-Baeza, C.H. Rochester, J.A. Anderson, *PCCP* 2001, **3**, 4817.
51. F. Delbecq, P. Sautet, *J. Catal.* 1995, **152**, 217.
52. R.A. Sheldon, J. Dakka, *Catal. Today* 1994, **19**, 215.
53. R.A. Sheldon, I.C.E. Arends, A. Dijksman, *Catal. Today* 2000, **57**, 157.
54. K. G. Griffin, P. Johnston, S. Bennett, S. Kaliq, in *Catalysis of Organic Reactions*, Ed., D.G. Morrell, Marcel Dekker, New York, 2002, 169.
55. R. Anderson, K. G. Griffin, P. Johnston, P. L. Alsters, *Adv. Synth. Catal.* 2003, **345**, 517.
56. T. Mallat, A. Baiker, *Appl. Catal.* 1991, **79**, 41.
57. T. Mallat, A. Baiker, *Chem. Rev.* 2004, **104**, 3037.
58. M. Besson, F. Lahmer, P. Gallezot, P. Feurtes, G. Flèche, *J. Catal.* 1995, **152**, 116.

59. M. Besson, P. Gallezot, *Catal. Today* 2000 **57**, 127.
60. P. Gallezot, *Catal. Today* 1997, **37**, 405.
61. T. Mallat, A. Baiker, *Catal. Today* 1994, **19**, 247.
62. M. Hronec, Z. Cvengrosova, J. Tulejy, J. Ilavsky, *Stud. Surf. Sci. Catal.* 1990, **55**, 169.
63. M. Akada, S. Nakano, T. Sugiyama, K. Ichitoh, H. Nakao, M. Akita, Y. Moro-oka, *Bull. Chem. Soc. Jpn.* 1996, **66**, 1511.
64. H. Kimura, A. Kimura, I. Kokubo, T. Wakisaka, Y. Mitsuda, *Appl. Catal. A*: *Gen.* 1993, **95**, 143.
65. R. Oi, S. Takenaka, *Chem. Lett.* 1988, 1115.
66. H. Hayashi, S. Sugiyama, N. Shigemoto, K. Miyaura, S. Tsujino, K. Kawashiro, S. Uemura, *Catal. Lett.* 1993, **19**, 369.
67. T. Mallat, Z. Bodnar, A. Baiker, O. Greis, H. Strübig, A. Reller, *J. Catal.* 1993, **142**, 237.
68. H. Pinxt, B.F.M. Kuster, G.B. Marin, *Appl. Catal. A*: *Gen.* 2000, **191**, 45.
69. M. Besson, G. Fleche, P. Fuertes, P. Gallezot, F. Lahmer, *Recl. Trav. Chim. Pays-Bas* 1996, **115**, 217.
70. S. Hermans, M. Devillers, *Appl. Catal. A*: *Gen.* 2002, **235**, 253.
71. H.E.J. Hendrix, B.F.M. Kuster, G.B. Martin, *Carbohydr. Res.* 1990, **204**, 121.
72. C. Bronnimann, T. Mallat, A. Baiker, *Chem. Commun.*1995, 1377.
73. C. Bronnimann, Z. Bodnar, R. Aeschimann, T. Mallat, A. Baiker, *J. Catal.* 1996, **161**, 720.
74. T. Mallat, C. Bronnimann, A. Baiker, *Appl. Catal. A*: *Gen.* 1997, **149**, 103.
75. T. Mallat, C. Bronnimann, A. Baiker, *J. Mol. Catal.* 1997, **117**, 425.
76. T. Mallat, Z. Bodnar, A. Baiker, *Stud. Surf. Sci. Catal.* 1993, **78**, 377.
77. T. Mallat, Z. Bodnar, P. Hug, A. Baiker, *J. Catal.* 1995, **153**, 131.
78. K.R. Seddon, A. Stark, *Green Chem.* 2002, **4**, 119.
79. G. Jenzer, T. Mallat, A. Baiker, *Catal. Lett.* 2001, **73**, 5.
80. A.M. Steele, J. Zhu, S.C. Tsang, *Catal. Lett.,* 2001, **73**, 9.
81. G. Jenzer, M.S. Schneider, R. Wandeler, T. Mallat, A. Baiker, *J. Catal.,* 2001, **199**, 141.
82. R. Glaser, R. Jos, J. Williardt, *Top. Catal.* 2003, **22**, 31.
83. M. Haruta, *Catal. Today* 1997, **36**, 153.
84. G.C. Bond, D.T. Thompson, *Catal. Rev. Sci. Eng.* 1999, **41**, 319.
85. M. Haruta, M. Date, *Appl. Catal. A*: *Gen.* 2001, **222**, 427.

86. S. Biella, F. Porta, L. Prati, M. Rossi, *Catal. Lett.* 2003, **90**, 23.
87. F. Porta, M. Rossi, *J. Mol. Catal. A*: *Chem.* 2003, **204**, 553.
88. J.D. Grunwaldt, C. Keiner, C. Wogerbauer, A. Baiker, *J. Catal.* 1999, **181**, 223.
89. Q. Xu, K.C.C. Kharas, K.A. Datye, *Catal. Lett.* 2003, **85**, 229.
90. C. Bianchi, F. Porta, L. Prati, M. Rossi, *Top. Catal.* 2000, **13**, 231.
91. M. Valden, X. Lai, D.W. Goodman, *Science* 1998, **281**, 1647.
92. S. Golunski, R. Rajaram, N. Hodge, G.J. Hutchings, C.J. Keily, *Catal. Today* 2002, **72**, 107.
93. M. Okumura, Y. Kitagawa, M. Haruta, K. Yamaguchi, *Chem. Phys. Lett.* 2001, **346**, 163.
94. P. Claus, A. Bruckner, C. Mohr, H. Hofmeister, *J. Am. Chem. Soc.* 2002, **122**, 11430.
95. S. Cerrettin, P. McMorn, P. Johnstone, K. Griffin, G.J. Hutchings, *Chem. Commun.* 2002, 696.
96. S. Cerrettin, P. McMorn, P. Johnstone, K. Griffin, C.J. Kiely, G.J. Hutchings, *Phys. Chem. Chem. Phys.* 2003, **5**, 1329.
97. S. Carrettin, P. McMorn, P. Johnston, K. Griffin, C.J. Kiely, G.A. Attard, G.J. Hutchings, *Top. Catal.* 2004, **27**, 131.
98. W.F. Holderich, *Catal. Today* 2000, **62**, 115.
99. G.A. Voronova, O.V. Vodyankina, V.N. Belousova, E.V. Bezrukov, L.N. Kurina, *Kinet. Catal.* 2003, **44**, 652.
100. L.F. Liotta, A.M. Venezia, G. Deganello, A. Longo, A. Martorana, Z. Schay, L. Guczi, *Catal. Today* 2001, **66**, 271.
101. J.M.H. Dirkx, H.S. Van der Baan, *J. Catal.* 1981, **67**, 1.
102. J.M.H. Dirkx, H.S. Van der Baan, *J. Catal.* 1981, **67**, 14.
103. L. Jelemensky, B.F.M. Kustner, G.B. Marin, *Ind. Eng. Chem. Res.* 1997, **36**, 3065.
104. J.H.J. Kluytmans, B.G.M. van Wachem, B.F.M. Kuster, J.C. Schouten, *Ind. Eng. Chem. Res.* 2003, **42**, 4174.
105. M. Besson, P. Galezot, *Catal. Today* 2003, **81**, 547.
106. S.C. Stinson, *Chem. & Eng. News* 20 October, 1997, 38.
107. S.C. Stinson, *Chem. & Eng. News* 21 September, 1998, 83.
108. S.C. Stinson, *Chem. & Eng. News* 22 November, 1999, 57.
109. G.M. Ramos, H.U. Blaser, in *Pesticide Chemistry and Bioscience*, Eds.: G.T. Brooks, T. Roberts RSC, Cambridge, 1999, 33.

110. R. Nyori, *Chemtech* 1992, **22**, 366.
111. E. Polastro, *Chiral Reactions in Heterogeneous Catalysis*, Plenum Press, New York, 1995, 5.
112. D. Pauluth, A.E.F. Wachter, in *Chirality in Industry II*, Eds.: A.N. Collins, G.N. Sheldrake, J. Crosby Wiley, New York, 1997, 263.
113. D. Lipkin, T.D. Stewart, *J. Am.Chem. Soc.* 1939, **61**, 3295.
114. S. Akabori, S. Sakurai, Y. Izumi, Y. Fujii, *Nature* 1956, **178**, 323.
115. Y. Orito, S. Imai, S. Niwa, in *Collected Papers of the 43rd Catalyst Forum,* Japan, 1978, 30.
116. Y. Orito, S. Imai, S. Niwa, *Nippon Kagaku Kaishi* 1979, 1118.
117. Y. Orito, S. Imai, S. Niwa, *Nippon Kagaku Kaishi* 1980, 670.
118. H-U. Blaser, M. Müller, *Studs. Surf. Sci. Catal.* 1991, **59**, 73.
119. H-U. Blaser, *Tetrahedron Asymm.* 1991, **2**, 843.
120. G. Webb, P.B. Wells, *Catal. Today* 1992, **12**, 319.
121. A. Baiker, *J. Mol. Catal. A*: *Chem.* 1997, **115**, 473.
122. H-U. Blaser, H.P. Jalett, M. Muller, M. Studer, *Catal. Today* 1997, **37**, 441.
123. P.B. Wells, A.G. Wilkinson, *Top. Catal.* 1998, **5**, 39.
124. A. Baiker, H-U. Blaser, in *Handbook of Heterogeneous Catalysis*. Eds.: G. Ertl, H. Knozinger, J. Weitkamp, Wiley-VCH, Weinheim, 1997, **5**, 2422.
125. P.B. Wells in R.P.K. Wells, in *Chiral Catalysts Immobilisation and Recycling* Eds.: D. de Vos, I.F.J. Vankelcom, P.A. Jacobs, Wiley-VCH, Weinheim, 2000, 123.
126. H.U. Blaser, F. Spindler, M. Studer, *Appl. Catal. A*: *Gen.* 2001, **221**, 119.
127. I.M. Sutherland, A. Ibbotson, R.B. Moyes, P.B. Wells, *J. Catal.* 1990, **125**, 77.
128. H-U. Blaser, H.P. Jalett, D.M.. Monti, A. Baiker, J.T. Wehrli, *Stud. Surf. Sci. Catal.* 1991, **67**, 147.
129. P.A. Meheux, P.B. Wells, unpublished work.
130. P.A. Meheux, A. Ibbotson, P.B. Wells, *J. Catal.* 1991, **128**, 387.
131. H-U. Blaser, H.P. Jalett, J. Wiehl, *J. Mol. Catal.* 1991, **68**, 215.
132. P.B. Wells, K.E. Simons, J.A. Slipszenko, S.P. Griffiths, D.F. Ewing, *J. Mol. Catal. A*: *Chem.* 1999, **146**, 159.
133. J.T. Wehrli, A. Baiker, D.M. Monti, H-U. Blaser, H.P. Jalett, *J. Mol. Catal.* 1989, **57**, 245.

134. M. Von Arx, N.F. Dummer, R.P.K. Wells, S.H. Taylor, P.B. Wells, D.J. Willock, G.J. Hutchings, *Chem. Commun.* 2003, 1926.
135. U.K. Singh, R.N. Landau, Y. Sun, C. LeBlond, D.G. Blackmond, S.K. Tanielyan, R.L. Augustine, *J. Catal.* 1995, **154**, 91.
136. J. Wang, Y. Sun, C. LeBlond, R.N. Landau, D.G. Blackmond, *J. Catal.* 1996, **161**, 759.
137. J.L. Margitfalvi, P. Marti, A. Baiker, L. Botz, O. Sticher, *Catal. Lett.* 1990, **6**, 281.
138. X. Li, R.P.K. Wells, P.B. Wells, G.J. Hutchings, *J. Catal.* 2004, **221**, 653.
139. X. Li, R.P.K. Wells, P.B. Wells, G.J. Hutchings, *Catal. Lett.* 2003, **89**, 163.
140. J.T.Wehrli, A.Baiker, D.M. Monti, H-U. Blaser, *J. Mol. Catal.* 1990, **61**, 207.
141. T.J. Hall, J.E. Halder, G.J. Hutchings, R.L. Jenkins, P. Johnston, P. McMorn, P.B. Wells, R.P.K. Wells, *Top. Catal.* 2000, **11**, 351.
142. S.D. Jackson, M.B.T. Keegan, G.D. McLellan, P.A. Meheux, R.B. Moyes, G. Webb, P.B. Wells, R. Whyman, J. Willis, in *Preparation and Characterisation of Catalysts V,* Eds.: G. Poncelet, P.A. Jacobs, P. Grange, B. Delmon, Elsevier, Amsterdam, 1991, 135.
143. B. Torok, K. Felfoldi, G. Szakonyi, K. Balazsik, M. Bartok, *Catal. Lett.* 1998, **52**, 81.
144. X. Zuo, H. Liu, M. Liu, *Tetrahedron Lett.* 1998, **39**, 1941.
145. X. Li, N. Dummer, R. Jenkins, R.P.K. Wells, P.B. Wells, D.J. Willock, S.H. Taylor, P. Johnstone, G.J. Hutchings, *Catal. Lett.* 2004, **96**, 147.
146. J.A. Slipszenko, S.P. Griffiths, P. Johnston, K.E. Simons, W.A.H. Vermeer, P.B. Wells, *J. Catal.* 1998, **179**, 267.
147. A. Gamez, J.U. Kohler, J.S. Bradley, *Catal. Lett.* 1998, **55**, 73.
148. C.R. Landis, J. Halpern, *J. Am. Chem. Soc.* 1987, **109**, 1746.
149. M. Boudart, G. Djega-Mariadassau, *Catal. Rev.* 1994, **29**, 7.
150. J. Wang, C. LeBlond, C.F. Orella, Y. Sun, J.S. Bradley, D.G. Blackmond, in *Heterogeneous Catalysis and Fine Chemicals IV,* Eds.: H.-U. Blaser, A. Baiker, R. Prins, Elsevier, Amsterdam, 1997, 183.
151. Y. Sun, R.N. Landau, J. Wang, C. LeBlond, D.G. Blackmond, *J. Am. Chem. Soc.* 1996, **118**, 1438.
152. K.E. Simons, P.A. Meheux, S.P. Griffiths, I.M. Sutherland, P. Johnston, P.B. Wells, A.F. Carley, M.K. Rajumon, M.W. Roberts, A. Ibbotson, *Recl. Trav. Chim. Pays-Bas* 1994, **113**, 465.

153. H.-U. Blaser, H.P. Jalett, D.M. Monti, J.F. Reber, J.T. Wehrli, *Stud. Surf. Sci. Catal.* 1988, **41**, 153.
154. T.J. Hall, P. Johnston, W.A.H. Vermeer, S.R. Watson, P.B. Wells, *Stud. Surf. Sci. Catal.* 1996, **101**, 221.
155. Y. Sun, R.N. Landau, J. Wang, C. LeBlond, D.G. Blackmond, *J. Am. Chem. Soc.* 1996, **118**, 1348.
156. P.J. Collier, T.J. Hall, J.A. Iggo, P. Johnston, J.A. Slipszenko, P.B. Wells, R. Whyman, *Chem. Commun.* 1998, 1451.
157. K.E. Simons, A. Ibbotson, P. Johnston, H. Plum, P.B. Wells, *J. Catal.* 1994, **150**, 321.
158. G. Bond, P.B. Wells, *J. Catal.* 1994, **150**, 329.
159. J.A. Anderson, A. Athawale, F.E. Imrie, F.-M. McKenna, D. Molyneux, M. Shand, R.P.K. Wells, *J. Catal.* 2010, **270**, 9–15.

CHAPTER 6

SUPPORTED GOLD IN CO OXIDATION, THE WATER-GAS SHIFT, AND DeSOx REACTIONS

Jose A. Rodriguez

Chemistry Department, Brookhaven National Laboratory, Upton, NY 11973, USA

6.1 Introduction

Bulk metallic gold typically exhibits a very low chemical and catalytic activity.[1,2] Among the transition metals, gold is by far the least reactive and is often referred to as the "coinage metal". The low reactivity of metallic Au is a consequence of combining a deep-lying valence 5d band and very diffuse valence 6s,p orbitals.[3,4] In the last 15 years, gold has become the subject of a lot of attention due to its unusual catalytic properties when dispersed on oxide[1a,5–27] and carbide supports.[28–33] The Au/TiO_2 system is particularly interesting.[6,12–18,21,23,26,27] Gold particles supported on titania are active catalysts for the low temperature oxidation of CO. This phenomenon was originally discovered by Haruta and coworkers in the early 1990s,[6] and has been corroborated by many subsequent studies.[2,7,8,17,23,25] The exact catalytic activity of the Au/TiO_2 system depends on the method of preparation and the dispersion of the metal on the support,[6–8,23] but in general Au particles with sizes between 2 and 4 nm display a catalytic activity for CO oxidation much larger than that of bulk metallic gold. New preparation methods aim for the synthesis of very small Au particles (< 2 nm) with an extremely high catalytic activity.[23]

The Au/TiO_2 systems lose catalytic activity over time as a consequence of the sintering of the Au particles.[6,23] The smaller the initial size of the particles, the more dramatic the negative effects of sintering. In the case of Au nanoparticles dispersed on TiC, the interactions of the admetal with the carbide substrate are stronger than typical interactions with oxides,[29,30] and the Au/TiC system is an excellent catalyst for CO oxidation.[28,32,33]

Au particles supported on reducible oxides such as titania or ceria are also efficient catalysts for the water-gas shift, the destruction of sulfur dioxide (DeSOx processes), the complete oxidation of methane, the selective or partial oxidation of propene, the hydrogenation of CO and olefins, and the reduction of NO with hydrocarbons.[1a,6,7,9,21,22,26,27] Depending on the conditions, Au/TiO_2 and Au/CeO are useful catalysts for the destruction of the three major contaminants produced during the combustion of fossil-derived fuels: CO, NO and SO_2.[1a,6,21] Several models have been proposed for explaining the activation of supported gold:[6,8,15–17,21,27,29] from special electronic properties resulting from the limited size of the active gold particles (usually less than 10 nm),[6,8,17,27,29] to the effects of metal support interactions (i.e. charge transfer between gold and the oxide or carbide).[13,16,21,26,29,30] In principle, the active sites for the catalytic reactions could be located only on the supported Au particles or on the perimeter of the gold oxide interface.[6,8,10,14,21,30–32] The $Au/TiO_2(110)$ and Au/TiC(001) surfaces appear as ideal and well-defined systems to examine some of these hypothesis in a controlled manner.[8,10,12–16,21,29–32] On the other hand, there is a clear need to characterize the active phases of the powder catalysts under reaction conditions.[26,34–37]

6.2 Oxidation of CO on Supported Gold Nanoparticles

High surface area Au/TiO_2 catalysts are very efficient for the low temperature oxidation of CO.[6,8,23,36,37] $Au^{\delta+}$, Au, and $Au^{\delta-}$ species have been proposed as the active species for the oxidation of CO.[1a,26,36,37] In any case, a strong contact between the Au nanoparticles and oxide support is indispensable for high catalytic activity because the

periphery sites probably carry out the oxidation of CO.[38] Studies of FTIR indicate that CO and O_2 adsorb on different sites of the catalyst surface.[36] As mentioned above, the average particle size of gold has a strong effect on the performance of powder catalysts.[6,8,18,19,23] The morphology of the oxide support substantially affects the dispersion of gold and catalytic activity.[7,37,39]

The bottom trace in Fig. 6.1 shows the catalytic activity of $Au/TiO_2(110)$ surfaces as a function of gold coverage.[7] Images of scanning tunneling microscopy (STM) indicate that Au grows on $TiO_2(110)$ forming three-dimensional nanoparticles, mainly located at defect sites and steps of the oxide substrate.[7,8] The size of the Au nanoparticles increases with Au coverage. On $TiO_2(110)$, there is a marked size effect on the catalytic activity,[7,8] with Au clusters in the range of 3.5 nm exhibiting the maximum

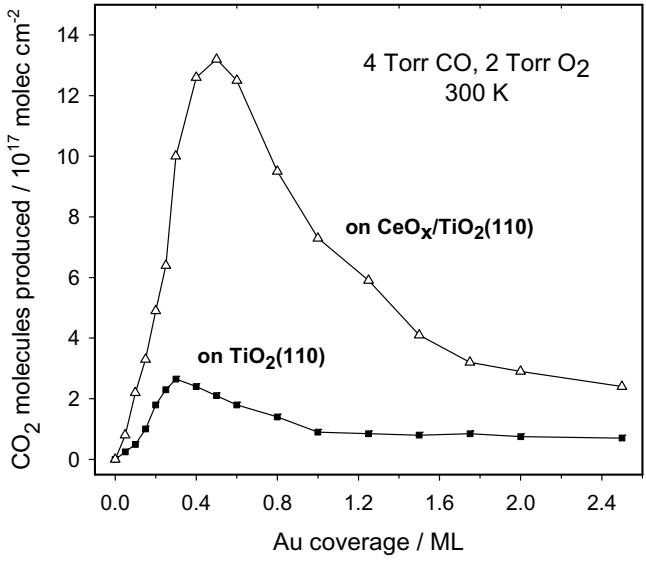

Figure 6.1 CO oxidation activity of $Au/TiO_2(110)$ as a function of Au coverage.[7] The area of $TiO_2(110)$ covered by CeO_x was ~16% of the clean substrate. The reported values for the production of CO_2 were obtained after exposing the catalysts to 4 Torr of CO and 2 Torr of O_2 at 300 K for 5 min. The number of CO_2 molecules produced is normalized by the sample surface area.

reactivity.[8] For this size, most of the particles have a band gap of 0.2 to 0.6 V according to scanning tunneling spectroscopy. Particles with a larger band gap (>1 V) display a lower reactivity, and particles with metallic character (band gap ≈0 V) are the least active. Thus, there is a correlation between the electronic and chemical properties of the supported Au nanoparticles.[8] Studies of STM indicate that exposure to CO has no effect on the morphology of the $Au/TiO_2(110)$ surface.[8] On the other hand, significant morphological changes occur after exposure to O_2 or CO : O_2 mixtures. In these cases, the Au cluster density is greatly reduced as a result of sintering.[8] The $Au/TiO_2(110)$ surfaces exhibit an exceptionally high reactivity towards O_2 at 300 K that promotes the sintering of the Au nanocrystallites.[8,20] This sintering eventually leads to a decrease in the CO oxidation activity of the $Au/TiO_2(110)$ systems.[8]

The nature of the interactions between Au and $TiO_2(110)$ has been examined in several theoretical studies.[13,15–17,21,27] In agreement with experimental observations, density functional (DF) calculations show weak bonding interactions between Au atoms and stoichiometric $TiO_2(110)$. Au–Au bonds are stronger than Au–TiO_2 bonds, which explains the formation of mostly three-dimensional particles. The results of STM and DF calculations show that Au adatoms prefer to interact with the O-vacancy sites present on the oxide support.[7,8,16,17,21,27] The theoretical studies[16,21] and photoemission measurements[13,21] indicate that the Au atoms bonded to these sites receive some electron density from the oxide substrate. As we will discuss below, a transfer of electrons from the titania support to atoms in the Au nanoparticles could help to explain the high catalytic activity of Au/TiO_2.[8,13,16]

The addition of a second oxide to the titania surface produces new nucleation sites for Au and improves the dispersion of the admetal.[7,37–39] In the $CeO_x/TiO_2(110)$ systems, the Ce cations adopt a structural geometry (Fig. 6.2A) and an oxidation state (+3) which are quite different from those seen in bulk ceria or for ceria nanoparticles deposited on metal substrates.[7] On $TiO_2(110)$, one has Ce_2O_3 dimers that join forming wire-like structures on the terraces of the titania substrate.[7,40]

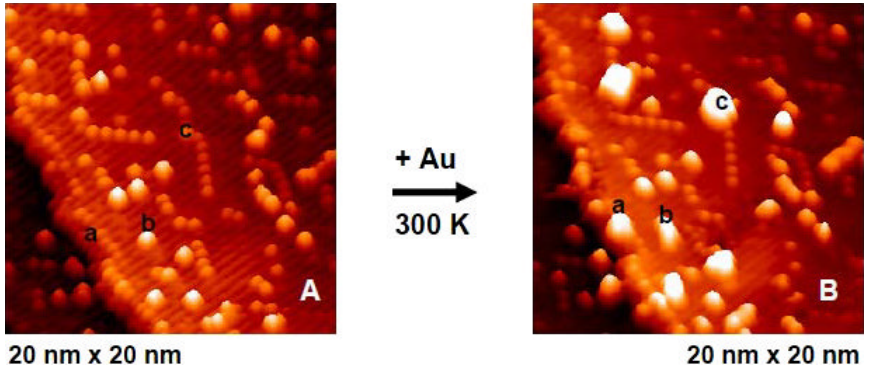

Figure 6.2 (A) STM image of an CeO_x/TiO_2 (110) surface.[7] (B) STM image for an $Au/CeO_x/TiO_2$ (110) surface.[7] The gold was deposited on the same area shown in "A" at ≈300 K.

These wire-like structures contain sites which are very effective for anchoring gold nanoparticles (see Fig. 6.2B). On $CeO_x/TiO_2(110)$ surfaces, the dispersion of Au nanoparticles is substantially larger than seen on a pure $TiO_2(110)$ surface where Au mainly binds to the steps.[7,8]

Figure 6.1 compares the activity of $Au/TiO_2(110)$ and $Au/CeO_x/TiO_2(110)$ for the oxidation of CO.[7] In all cases, $Au/CeO_x/TiO_2(110)$ is a much better catalyst for the oxidation of CO than $Au/TiO_2(110)$. If the maximum catalytic activities seen in Fig. 6.1 are normalized by the number of Au atoms present on the oxide supports,[7] one can estimate turnover frequencies (TOFs) for CO oxidation of 2.1 molecules $site^{-1}$ s^{-1} for $Au/TiO_2(110)$ and 6.2 molecules $site^{-1}$ s^{-1} for $Au/CeO_x/TiO_2(110)$. These should be taken as lower limits for the TOFs because the calculation overestimates the number of exposed Au active sites.[7] The relatively high dispersion of Au (Fig. 6.2B) could be responsible for the superior activity of $Au/CeO_x/TiO_2(110)$ during the oxidation of CO at room temperature.

DF calculations have been used to study the CO oxidation process on an isolated (i.e. non-supported) Au_{10} cluster.[17] Two different reaction paths were considered: one where O_2 dissociates and one where adsorbed O_2 reacts directly with adsorbed CO. Both

reactions were found to be extremely facile on the Au_{10} particle, with reaction barriers of less that 0.4 eV indicating that the CO oxidation reaction should be possible well below room temperature.[17] This is contrary to the behavior found for an Au(111) surface. The small Au_{10} cluster offers special geometrical configurations (corner and edge sites) that cannot be found on the extended surface.[17] The size and shape of the Au particle are important parameters together with its fluxionality that allows the adsorption and activation of O_2.[25] Also the electronic structure of the Au atoms in the cluster is different from that of the Au atoms at the surface of a large crystal. The DF results show that an isolated Au nanoparticle could catalyze the oxidation of CO. However, the rate for this reaction is enhanced by interactions with the oxide, which can participate directly in the reaction[17,18,25] or modify the chemical properties of Au.[17,41] DF calculations indicate that the active sites for CO oxidation on Au/MgO(100) involve low-coordinated Au atoms and Mg cations.[18] The oxide stabilizes a peroxo-like intermediate, $CO{\bullet}O_2$, and then the oxidation reaction proceeds in the metal/oxide interface.[18] Such a reaction pathway is consistent with studies for Au/TiO_2 high surface area catalysts,[6,38] which show that a strong contact between the Au nanoparticles and oxide support is indispensable for high catalytic activity because the periphery sites probably carry out the oxidation of CO.

A very important issue is the adsorption and dissociation of O_2 on the Au/oxide systems since this seems to be a necessary step in total and partial oxidation reactions.[17,18,41] Can isolated Au nanoparticles dissociate O_2? Is the Au/oxide interface necessary for the cleavage of O–O bonds? Calculations based on density functional theory have been carried out for a series of unsupported Au nanoparticles as well as for extended systems containing low-coordinated sites.[42] Strong adsorption of molecular oxygen on Au nanoparticles is a necessary but not sufficient condition for O_2 dissociation.[42] For reasonably large Au cubo-octahedral nanoparticles, there is a common pathway for O_2 dissociation on nanoparticles which involves a particular configuration of adsorption sites and a critical particle size.[42] If these conditions are not satisfied, the

oxidation of CO on gold/oxide systems probably follows a mechanism in which the cleavage of the O–O bond in molecular oxygen is facilitated by interactions with the CO molecule (i.e. O–O••C–O → O + CO_2).[17,18,41]

There is a general desire to find supports which can activate gold up to the point that this metal easily dissociates O_2. The reactivity of Au nanoparticles supported on TiC(001) towards O_2 dissociation is much larger than that of similar nanoparticles supported either on TiO_2(110) or MgO(001) surfaces.[32] Photoemission results (Fig. 6.3) indicate that at 150 K, O_2 adsorbs molecularly on the supported gold nanoparticles, and upon heating to temperatures above 200 K the O_2 → 2O reaction takes place with migration of atomic oxygen to the TiC(001) substrate.[32] Au nanoparticles

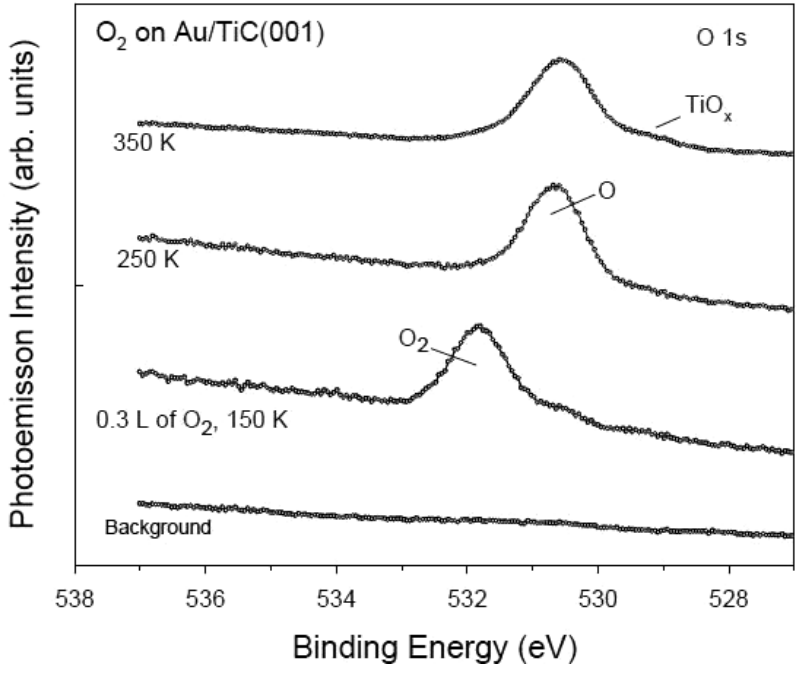

Figure 6.3 O 1s core-level photoemission spectra taken after adorbing O_2 on Au nanoparticles supported on TiC(001).[32] Oxygen was dosed at 150 K, and then the sample was heated to 250 and 350 K.

dispersed on TiC films or TiC(001) can oxidize carbon monoxide at temperatures below 200 K.[28,32,33] A polarization of charge seen for Au atoms on TiC(001)[29,30] facilitates bonding of the admetal with O_2 (Fig. 6.3) and helps to explain chemical activity that Au/TiC exhibits for the oxidation of CO.[32]

6.3 Water-Gas Shift Reaction on Supported Gold Nanoparticles

The water-gas shift reaction (WGS, $CO + H_2O \rightarrow H_2 + CO_2$) is critical for providing clean hydrogen.[24,34] Common industrial catalysts for the WGS (mixtures of Fe-Cr or Zn-Al-Cu oxides) are pyrophoric and normally require lengthy and complex activation steps before usage.[34] Recent works report that Au nanoparticles supported on oxides such as CeO_2 and TiO_2 are very efficient catalysts for the WGS reaction.[24,34,35] This is remarkable since neither bulk Au nor bulk ceria and titania are known as WGS catalysts. Results of density-functional calculations point to a very high barrier for the dissociation of H_2O on Au(111) or Au(100),[43] which leads to negligible activity for the WGS process. Even gold nanoparticles cannot dissociate water and catalyze the WGS.[43] Furthermore, surfaces and nanoparticles of copper are by far much better catalysts for the WGS than surfaces and nanoparticles of gold.[43] Thus, how can Au/CeO_2 catalysts be much more active than conventional Cu/ZnO catalysts?[24]

Originally, it was suggested that the active phase in Au-CeO_2 catalysts are AuO_x nanoparticles or more specifically cationic $Au^{\delta+}$ species. Subsequently, the chemical state of gold during the WGS was determined by means of *in situ* time-resolved X-ray absorption near-edge spectroscopy (XANES).[34,35] Figure 6.4 displays Au L_3 edge XANES spectra collected at room temperature for fresh catalysts with an Au content of 0.5 wt% (dashed trace) or 2.4 wt% (solid traces).[35] The line shape of these two spectra is very similar and shows a clear feature at ≈2.5 eV above the edge that is not seen for metallic gold and is characteristic of gold oxides.[34,35] The intensity of

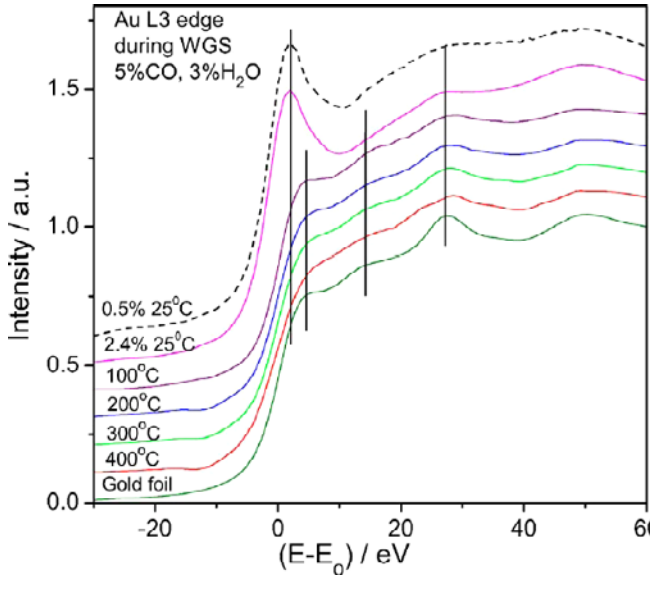

Figure 6.4 Au L_3 edge XANES spectra collected *in situ* during the WGS reaction over a 2.4 wt% Au–CeO_2 catalyst. The spectra for a fresh 0.5 wt% Au–CeO_2 catalyst, dashed trace, and a gold foil are included for comparison. The vertical line indicates the main features for AuO_x *vs.* metallic Au.[35]

this peak is higher than that observed for Au_2O and closer to that seen in Au_2O_3.[34] Once the 2.4 wt% Au-CeO_2 catalyst was exposed to a mixture of CO/H_2O at elevated temperatures, the XANES features for gold oxide disappeared.

At temperatures above 200°C, when significant WGS activity was detected,[35] the line shape of the Au L_3 edge resembled that of pure gold. The XANES spectra in Fig. 6.4 were obtained under a reaction mixture of 5% CO and 3% H_2O in He (total flow ≈10 ml/min).[35]

Similar results were found when using a 1% CO and 3% H_2O in He reaction mixture. Thus, the *in situ* time-resolved XAS data indicate that cationic $Au^{\delta+}$ species cannot be the key sites responsible for the WGS activity, because they do not exist under reaction conditions.[35] An identical finding has been reported for $AuO_x/Ce_{1-x}Zr_xO_{2-y}$ powder catalysts.[34] In these catalysts, the active phase

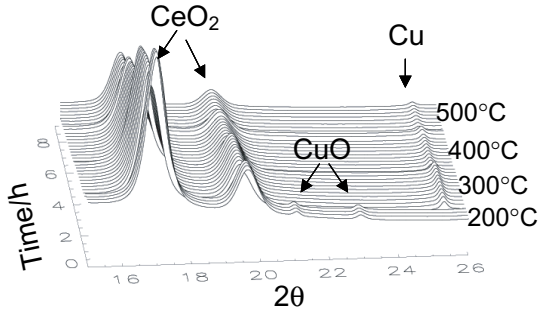

Figure 6.5 Time-resolved X-ray diffraction patterns collected *in situ* during the WGS reaction over a 5% CuO-CeO_2 catalyst.[44] The transformation of CuO into Cu occurs near 200°C before significant activity for the production of H_2 was observed.[44]

consisted of small Au aggregates (<2 nm in size) dispersed on partially reduced ceria ($CeO_{1.94}$-$CeO_{1.98}$).[34,35]

The active phase of CuO-CeO_2 WGS catalysts was also investigated.[44] The results of *in situ* time-resolved XRD (Fig. 6.5) and XAS (not shown) point to a complete reduction of the CuO to metallic Cu before the catalysts become active for the WGS.[44] This reduction of the CuO is consistent with the behavior observed for CuO/ZnO catalysts and other Cu-based catalysts.[34,45,46] As in the case of AuO_x-CeO_2, the active phase of CuO-CeO_2 catalysts contains nanoparticles of the noble metal disperse d on a partially reduced ceria support. The same is valid for Pt-CeO_2 and Pd-CeO_2 catalysts.

Although pure ceria is a very poor WGS catalyst, the properties of this oxide were found to be crucial for the observed activity of the Au-CeO_2 nanocatalysts.[24,34] Several studies dealing with metal/oxide powder catalysts and the WGS indicate that the oxide plays a direct role in the reaction, but because of the complex nature of these systems,[24,34,47] there is no agreement on its role. The kinetics of the WGS reaction have been investigated in detail on model catalysts generated by vapor-depositing nanoparticles of gold on $CeO_2(111)$,[35,48] $ZnO(000\bar{1})$,[48] $TiO_2(110)$[27] and polycrystalline MoO_2.[49] On these oxide

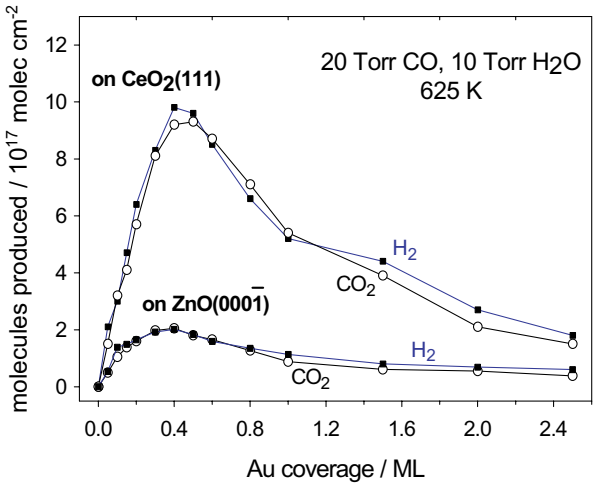

Figure 6.6 WGS activity of model $Au/CeO_2(111)$ and $Au/ZnO(000\bar{1})$ catalysts as a function of gold coverage. Each surface was exposed to a mixture of 20 Torr of CO and 10 Torr of H_2O at 625 K for 5 mins. Steady state was reached 2–3 mins after introducing the gases in the batch reactor.[48]

substrates, gold grows, forming three-dimensional particles.[8,48,50] Figure 6.6 displays the behavior of the $Au/CeO_2(111)$ and $Au/ZnO(000\bar{1})$ catalysts as a function of gold coverage.[48] $CeO_2(111)$ and $ZnO(000\bar{1})$ are both O terminated surfaces. These oxide supports are inactive as catalysts for the WGS reaction. In Fig. 6.6, the catalytic activity of the metal/oxide systems initially increases when Au is added, reaching a maximum at ≈0.4–0.5 monolayer (ML).

Above these coverages, the overall catalytic activity decreases. Similar trends have been observed for the WGS on $Au/TiO_2(110)$[7,27] and Au/MoO_2.[49] STM images show that the particle size of Au on $CeO_2(111)$, $ZnO(000\bar{1})$ or $TiO_2(110)$ raises above 4 nm and continuously grows when the admetal coverage is increased beyond 0.5 ML.[8,48,50] The trends in Fig. 6.6 probably reflect changes in the size of the gold particles: high catalytic activity is seen for small gold particles (size < 4 nm), and it decreases as the particle size increases. Although the optimum WGS activity in Fig. 6.6 is for admetal coverages of 0.4–0.5 ML, metal/oxide catalysts with gold coverages near

1 ML are still substantially more active than Au(111) or polycrystalline gold, surfaces which are not catalytically active.[8,48]

The gold atoms in the $Au/CeO_2(111)$ and $Au/ZnO(000\bar{1})$ catalysts were probably not oxidized during the WGS process.[48] After reaction, XPS showed Au 4f positions that were almost identical to those seen upon deposition of gold on the oxides and very different from those typically seen for AuO_x species.[35,48] Post-reaction surface analysis also showed the presence of formate- and/or carbonate-like groups on the surface of the catalysts. Possible reaction paths for the formation of these groups are discussed in the work by Burch.[34] It is not completely clear if they are key intermediates in the WGS process or simple spectators.[27,48]

Figure 6.7 compares the WGS activity of 0.5 ML of Au and Cu deposited on $CeO_2(111)$ and $ZnO(000\bar{1})$ with the corresponding activity of Au(111) and Cu(100).[48] The WGS activity seen for Cu(100) is in between that detected for Cu(111) and Cu(110).[45,51,52] The deposition of Cu nanoparticles on $ZnO(000\bar{1})$ produces a

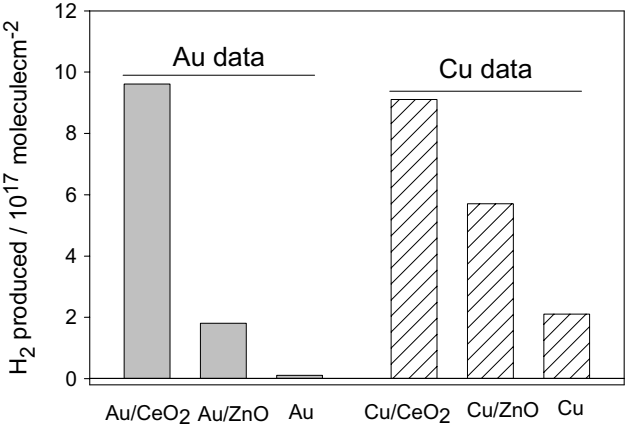

Figure 6.7 Amounts of H_2 produced during the WGS reaction on 0.5 ML of gold or copper deposited on $CeO_2(111)$ and $ZnO(000\bar{1})$. For comparison are also included the activities of Au(111) and Cu(100). The catalysts were exposed to a mixture of 20 Torr of CO and 10 Torr of H_2O at 625 K for 5 mins in a batch reactor.[48]

catalyst that is clearly more active than the pure extended Cu surfaces.[48] An even better catalyst is obtained when the Cu nanoparticles are supported on $CeO_2(111)$. The $Au/ZnO(000\bar{1})$ system displayed a catalytic activity worse than that of $Cu/ZnO(000\bar{1})$. On the other hand, $Au/CeO_2(111)$ is an excellent catalyst with an activity similar to that of $Cu/CeO_2(111)$.[48] The nature of the support plays a key role in the activation of the gold nanoparticles. Zinc oxide is frequently used in industrial Cu-ZnO WGS catalysts.[34] However, the $Au/ZnO(000\bar{1})$ system displays low WGS activity when compared to $Au/CeO_2(111)$,[48] Au/MoO_2[49] or $Au/TiO_2(110)$.[27]

The ceria, molybdena and titania contain a substantial number of O vacancies and metal cations that are not fully oxidized under WGS reaction conditions and may participate directly in important steps of the process.[27,48,49] This is not the case for $Au/ZnO(000\bar{1})$.[48]

In situ measurements of time-resolved XRD and XAS indicate that the ceria support in powder Au-CeO_2[35] and Cu-CeO_2[53] catalysts participates directly in the WGS reaction. Figure 6.8 shows the lattice parameters for ceria determined from (111) diffraction peaks of time-resolved XRD patterns for 2.4 wt% Au–CeO_2 under different

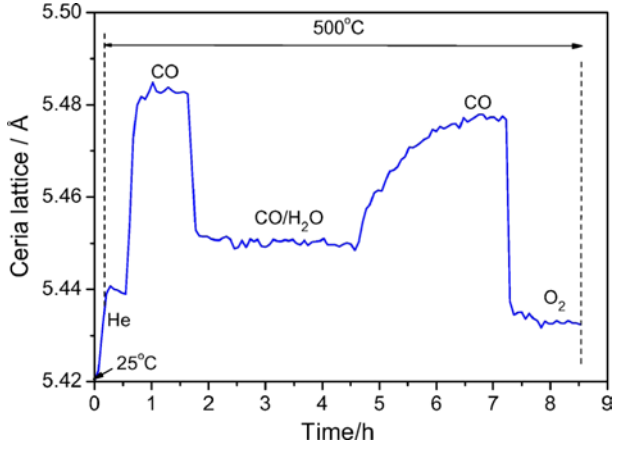

Figure 6.8 Ceria lattice parameters determined from time-resolved XRD patterns for a 2.4 wt% Au-CeO_2 catalyst under different gases at 500°C: pure He, 5% CO in He, 5% CO and 3% H_2O in He, again 5% CO in He, and finally 5% O_2 in He.[35]

gases at 500°C.[35] The sample was first heated from 25 to 500°C in He, producing an increase of ≈0.02 Å in the ceria lattice due to thermal expansion. The oxide lattice varied significantly after exposure to CO, ≈0.04 Å increase as a consequence of the formation of O vacancies and Ce^{3+}, or H_2O, ≈0.03 Å decrease probably as a result of the decomposition of this adsorbate on the O vacancies.[35] Under a mixture of CO/H_2O, O vacancies were formed that could be removed only upon exposure to O_2.[35]

Similar trends are seen for ceria during the reduction/oxidation of Cu-CeO_2 catalysts.[53]

For explaining the role of the oxide in Au-based WGS catalysts, one must understand well the catalytic process on pure gold systems.[49] Figure 6.9 shows the calculated energy profile for the WGS on periodic Au(100) and Cu(100) surfaces.[43] Copper surfaces are the typical benchmark for studies of the WGS on metal surfaces.[45,51,52] On Cu(100), the first and the most energy consuming

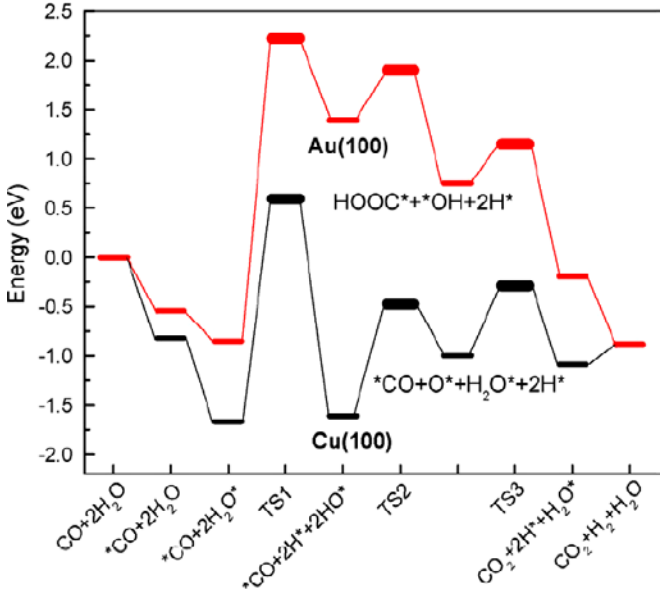

Figure 6.9 DFT calculated reaction profile for the WGS on Cu(100) and Au(100).[43,48]

step, or rate limiting step, is water dissociation with a ΔE_3 of +0.39 eV and a barrier (ΔEa_3) of +1.13 eV. The cleavage of the first O–H bond is also the rate limiting step on a Cu(110) surface.[45] In contrast, the dissociation of adsorbed OH and the formation of CO_2 are more facile. All the adsorbates bond more weakly on Au(100) than on Cu(100). Consequently, the rate limiting dissociation of H_2O on Au(100) is even more endothermic (ΔE_3 = +0.74 eV) and the corresponding barrier is also higher (ΔEa_3 = +1.53 eV).[43] These DFT results are in agreement with experimental measurements, which show that Cu is a good WGS catalyst while Au is an extremely poor one.[45,48]

The results in Fig. 6.9 indicate that gold will be an excellent WGS catalyst if in some way it is helped with the dissociation of water.[43] Assuming that OH can be formed on Au(100) or Au(111), subsequent steps for the WGS process should occur readily on the gold substrate.[43] Indeed, experimental and theoretical studies have shown that water dissociates on O/Au(111) yielding hydroxyls which react with CO to produce CO_2 and hydrogen.[12]

One can obtain a stable catalyst for the WGS by adding CeO_x nanoparticles to Au(111).[11] On an inverse oxide/metal catalyst, the reactants can interact with defect sites of the oxide nanoparticles, metal sites, and the metal/oxide interface.[53] Figure 6.10 shows a STM image obtained after depositing ceria nanoparticles on Au(111).[54] There is a random distribution of the ceria nanoparticles on the terraces of the gold substrate which maintains its characteristic herringbone reconstruction. The particles occupy specific sites with respect to the dislocation ridges of the reconstruction.[54] The initial oxidation state of the Ce cations in the ceria nanoparticles was +4 and many of them were reduced to Ce^{3+} upon exposure to the reactants of the WGS.[11,55]

Figure 6.11 displays an Arrhenius plot for the WGS activity of a CeO_x/Au(111) surface in which 20% of the gold substrate was covered by ceria.[55] For comparison we also include results obtained for the WGS on Cu(100),[48] Cu(111)[55] and Cu/ZnO(000$\bar{1}$)[48] surfaces. The results in Fig. 6.11 indicate that the inverse CeO_x/Au(111) catalyst exhibits a larger WGS activity than those of copper surfaces or

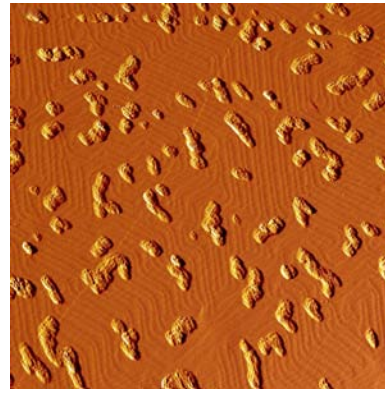

Figure 6.10 STM image for the deposition of ceria nanoparticles on Au(111), 200 nm × 200 nm.[54]

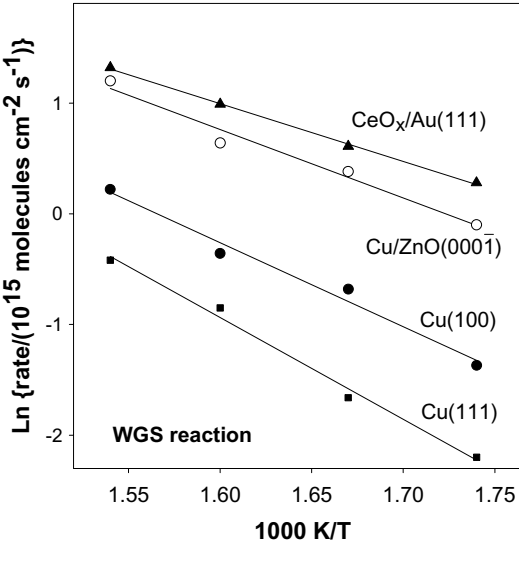

Figure 6.11 Arrhenius plot for the WGS reaction rate on Cu(111),[55] Cu(100),[48] Cu/ZnO(000$\bar{1}$),[48] and on an Au(111) surface approximately 20% covered by ceria.[11,55] The data were acquired with a pressure of 20 Torr of CO and 10 Torr of H_2O and temperatures of 575, 600, 625 and 650 K.[11,55]

even Cu nanoparticles dispersed on a $ZnO(000\bar{1})$ substrate. On Cu(111) and Cu(100), the apparent activation energies for the WGS are 18.1 and 15.2 kcal/mol, respectively.[48,55] The apparent activation energy decreases to 12.4 kcal/mol on $Cu/ZnO(000\bar{1})$[48] and 10.3 kcal/mol on $CeO_x/Au(111)$.[55] In the inverse $CeO_x/Au(111)$ catalyst, the gold surface gains activity due to the active participation of the oxide in the dissociation of water.[11,55] One probably has a bifunctional catalyst in which the oxide helps to break the O–H bonds and the subsequent steps of the reaction occur at the oxide/gold interface.[11,55]

Post-reaction characterization of the inverse $CeO_x/Au(111)$ catalyst with XPS pointed to a $Ce^{4+} \rightarrow Ce^{3+}$ transformation and identified a C 1s feature at 289–290 eV corresponding to either HCOO or CO_3 species on the $CeO_x/Au(111)$ surface.[11,55] The mechanism for the WGS in $CeO_x/Au(111)$ is assumed to undergo the following pathway:[11]

$$\begin{aligned} CO &\rightarrow CO\ (a) \\ H_2O &\rightarrow H_2O\ (a) \\ H_2O\ (a) &\rightarrow OH\ (a) + H\ (a) \\ CO\ (a) + OH\ (a) &\rightarrow HCO_x\ (a) \\ HCO_x\ (a) &\rightarrow CO_2 + H\ (a) \\ 2H\ (a) &\rightarrow H_2 \end{aligned} \qquad (6.1)$$

A stable HCO_x intermediate species must precede the formation of H_2 and CO_2. It has been proposed that the key intermediate species for the WGS reaction is either a *formate* (HCOO) or a *carbonate* (CO_3).[34] Recent theoretical calculations also suggest the possibility of a *carboxylate* (HOCO) intermediate.[11,27,51] These species have different coordination modes and different lifetimes on the surface of the catalyst. Adsorption of HCOOH and CO_2 was used to create HCOO and CO_3 groups on $CeO_x/Au(111)$ surfaces.[55] $HCOO_{ads}$ appeared to have greater stability than $CO_{3,ads}$ with desorption temperatures up to 600 K while CO_3 only survived on the surface up to 300 K. Both species could be valid intermediates for the WGS because the reaction temperatures in Fig. 6.11 are elevated

(575–650 K).[55] On the CeO_x/Au(111) catalysts, the presence of Ce^{+3} led to the dissociation of H_2O to give OH groups.[11,55] The adsorption of CO on these systems led to the formation of carbonates and formates but no clear signal was found for a carboxylate (HOCO) intermediate.[55] Thus, the carboxylate intermediate seen in DFT calculations[11,27,51] is experimentally elusive and difficult to detect.[55] The low thermal stability of the carboxylate makes it an ideal transient species for the WGS[11,27,51] and it may only be present under steady state conditions. *In situ* diffuse reflectance FT-IR has been used to study the mechanism of the WGS reaction over a 2% Pt-CeO_2 catalyst.[56] The data clearly showed that the formates as seen by FT-IR were essentially spectator species at 433 K, while formates were possible main reaction intermediates at 493 K or higher temperatures.[56] This is consistent with the patterns of stability seen for formates on CeO_x/Au(111), because at temperatures below 500 K formate species are too stable to be viable intermediates for the WGS.[55] They may actually poison active sites of the catalyst surface.[55,56]

The studies described above indicate that highly active WGS catalysts are bifunctional with the metal and oxide catalyzing different parts of the reaction. To optimize the performance of these systems one must enhance the participation of the metal and oxide phases in the catalytic process. In catalysts with a conventional metal/oxide configuration, one enhances the reactivity of the metal but this usually covers the defect sites of the oxide (nucleation centers for the metal particles) which have chemical activity. This is not the case in an inverse oxide/metal catalyst, Fig. 6.10, which enhances the participation of the oxide in the catalytic reaction.[11,55] In the quest to optimize the reactivity of the metal and oxide phases, perhaps the most complex and promising configuration is a mixed-metal oxide array in which nanoparticles of a metal and an oxide can interact with the reactants.[7,40] Extremely active WGS catalysts have been found after co-adsorbing nanoparticles of gold and ceria on a TiO_2(110) substrate.[7]

Figure 6.2 illustrates the unique morphology of Au/CeO_x/TiO_2(110) surfaces.[7] The dispersion of the Au on the surface is substantially larger than for Au/TiO_2(110)[8] and one has nanoparticles

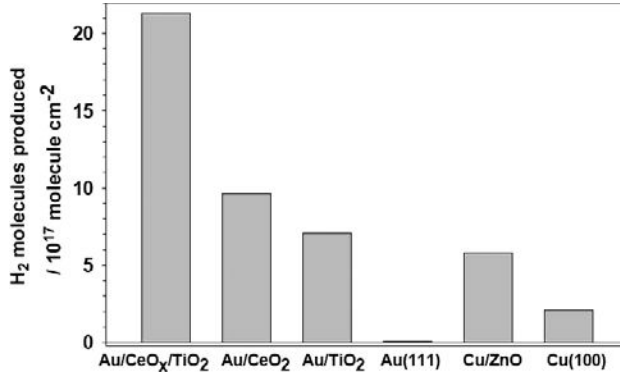

Figure 6.12 Comparison of the water-gas shift activity of Cu(100), Au(111), and 0.5 ML of Au supported on $TiO_2(110)$[27] $CeO_2(111)$[48] or CeO_x/TiO_2 (110).[7] Data for 0.5 ML of Cu on $ZnO(000\bar{1})$ are also included.[48] The reported values for the production of H_2 were obtained after exposing the catalysts to 20 Torr of CO and 10 Torr of H_2O at 625 K for 5 mins.[7,27,48]

of the admetal and ceria in close contact. Figure 6.12 compares the WGS activity of a series of metal/oxide catalysts. Au/CeO_2[48] and Au/TiO_2[27] are better catalysts than the commercial Cu/ZnO catalyst,[48] but they do not come close to matching the activity of $Au/CeO_x/TiO_2(110)$.[7] The large dispersion of gold on $CeO_x/TiO_2(110)$, Fig. 6.2, should lead to a high catalytic activity. The Ce^{3+} sites present in $CeO_x/TiO_2(110)$ easily dissociate water[40] but, upon exposure to CO, highly stable HCO_x species were formed on the oxide surface and there was no production of H_2 or CO_2 gas.[7,40] In $Au/CeO_x/TiO_2(110)$, one has a bifunctional catalyst: the adsorption and dissociation of water takes place on the oxide, CO adsorbs on the gold nanoparticles, and all subsequent reaction steps occur at oxide/metal interfaces.

The results in Fig. 6.12 illustrate the tremendous impact that an optimization of the chemical properties of gold and ceria can have on the activity of a WGS catalyst.[7,40] $CeO_x/Pt(111)$ is also an excellent support for Cu and Pt nanoparticles.[40] This has been verified in experiments with high surface area powder $Pt/CeO_x/TiO_2$ catalysts[57] which in many aspects show a behavior similar to that seen for

$Pt/CeO_x/TiO_2(110)$ surfaces.[40] These systems take advantage of the complex interactions that occur in mixed-metal oxide at the nanometer level.[7,40,57]

6.4 Decomposition of SO_2 on Supported Gold Nanoparticles

Surfaces of metallic gold interact very weakly with SO_2 and the molecule desorbs intact at temperatures below 200 K.[21] Titania is the most common catalyst used in the chemical industry and oil refineries for the removal of SO_2 through the Claus reaction: $SO_2 + 2H_2S \rightarrow 2H_2O + 3S_{solid}$.[58,59] The main product of the adsorption of SO_2 on stoichiometric $TiO_2(110)$ are SO_3 and SO_4 species.[21,60] A substantial concentration of O vacancies on the oxide surface is necessary to induce the decomposition of SO_2 at high temperatures (>400 K). In contrast, $Au/TiO_2(110)$ surfaces fully dissociate SO_2 at room temperature.[21] Figure 6.13 shows S 2p photoemission spectra for the adsorption of SO_2 on $TiO_2(110)$ and $Au/TiO_2(110)$ at 300 K. The S 2p spectra indicate that upon adsorption of SO_2 on $Au/TiO_2(110)$, SO_4 and atomic S (produced by the full dissociation of SO_2) co-exist on the surface. For the systems in Fig. 6.13, the larger the Au coverage on titania (0.05 → 0.5 ML range), the bigger the amount of atomic S deposited. This trend points to a direct involvement of gold in the dissociation of SO_2. A large shift in the corresponding Au 4f core level spectra also supports this idea.[21] Results of DFT calculations indicate that Au and TiO_2 work in a cooperative way during the dissociation of S–O bonds.[21] How important is the participation of the oxide in the destruction of SO_2?

Figure 6.14 compares S 2p areas measured for atomic S after dosing the same amount of SO_2 to $Au/TiO_2(110)$ and Au/MgO(100) surfaces at 300 K.[21,61,62] Neither $TiO_2(110)$ nor MgO(100) are able to dissociate SO_2 on their own.[21,61]

On both oxide supports the largest activity for the full dissociation of SO_2 is found in systems that contain Au coverages smaller than 1 ML when the average diameter of the nanoparticles is below 5 nm.[21,62]

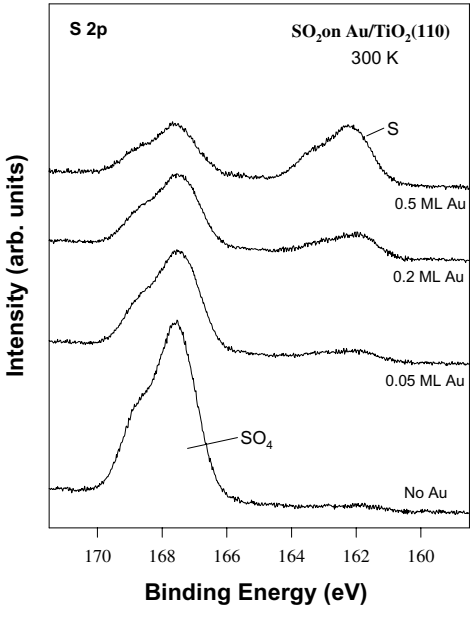

Figure 6.13 S 2 p spectra for the adsorption of SO_2 on $TiO_2(110)$ and on $Au/TiO_2(110)$ surfaces with Au coverages of 0.05, 0.2, and 0.5 ML.[21]

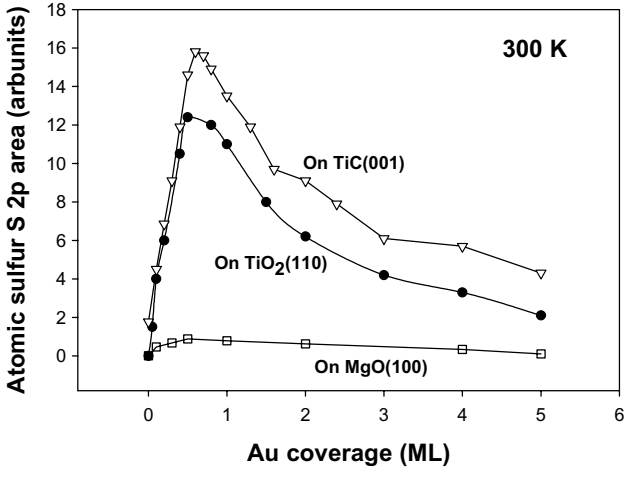

Figure 6.14 S 2p areas measured for atomic S after dosing SO_2 (5L) to Au/TiC(001), $Au/TiO_2(110)$, and Au/MgO(001) surfaces at 300 K.[21,30,62]

Clearly the $Au/TiO_2(110)$ systems are much more chemically active than the Au/MgO(100) systems. SO_2 adsorbs on Au/MgO(100) at 100 K and the molecule mainly desorbs upon heating to 300 K.[61,62] Catalytic tests also show that Au/TiO_2 is much more active than Au/MgO for the Claus reaction or the reduction of SO_2 with CO.[21,59] These data indicate that titania either plays a direct active role in the dissociation of SO_2 or modifies the chemical properties of the supported Au nanoparticles.

DF calculations have been used to examine the adsorption of SO_2 on Au(100) and a series of clusters: Au_6, Au_8, Au_{14}, and Au_{29}.[30,62] Very weak bonding interactions were observed on the extended Au surface with adsorption energies smaller than 0.15 eV. On the other hand, the corner atoms in the Au clusters were able to interact reasonably well with SO_2, giving adsorption energies of 0.43–0.65 eV.[62] However, none of the isolated clusters was able to dissociate the SO_2 molecule. The DF calculations indicate that such a process is very endothermic on Au_6, Au_8, and Au_{14}.[62] For example, the adsorption of SO_2 on the Au_{14} particle is an exothermic process but, upon heating, the molecule should desorb instead of dissociating.[62] Thus, the chemistry seen experimentally for SO_2 on Au/MgO(100) adsorption of the molecule at 100 K and desorption upon heating to 300 K, seems to reflect mainly the intrinsic reactivity of Au nanoparticles with the oxide support playing only a minor role.[61,62]

Variations in the strength of metal $\leftrightarrow$ support interactions are probably the key to the large difference in chemical activity seen in Fig. 6.14 for Au/MgO and Au/TiO_2. During the preparation of the active $Au/TiO_2(110)$ surfaces, the system is annealed to temperatures as high as 700–750 K to induce the formation of O vacancies and migration of bulk defects to the surface of the oxide.[21] Au particles like to interact with O vacancies[13,16,17,21,27] and on these adsorption sites an oxide $\rightarrow$ gold charge transfer has been predicted from theoretical studies[13,16,21] and XPS measurements.[8,13,21] The active $Au/TiO_2(110)$ surfaces combine Au atoms electronically perturbed and an oxide substrate with a significant amount of defects. Both factors probably contribute to the high activity of these surfaces for the dissociation of sulfur dioxide.[21] DF calculations for

SO_2/Au/TiO_2(110) systems show several bonding conformations in which Au and O-vacancy sites work in a cooperative way to dissociate the SO_2 molecule.[21] Thus, the active sites should be at the Au-TiO_2 interface. In the case of MgO(100), the formation of O vacancies is a highly endothermic and difficult process.[61,62] In the Au/MgO(100) surfaces, a negligible number of O vacancies is expected and this probably leads to a low activity for the dissociation of SO_2.

Figure 6.15 shows S 2p spectra collected after dosing SO_2 at 300 K to clean TiC(001) and a carbide surface pre-covered with 0.2 ML of Au.[30] On TiC(001) some dissociative chemisorption, SO_2(gas) → S(ads) + 2O(ads), occurs and a typical doublet for adsorbed atomic sulfur is seen from 161–163.5 eV.[30] In general terms, TiC(001) can be classified as a poor DeSOx system. Although Au(111) and polycrystalline gold interact weakly with SO_2, after depositing Au nanoparticles on TiC(001) there is a drastic increase in the reactivity of the system. The S 2p spectrum recorded after dosing SO_2 to Au/TiC(001) shows a clear enhancement in the uptake of sulfur with respect to clean TiC(001). Even more importantly, photoemission results indicate that there is a full dissociation of SO_2

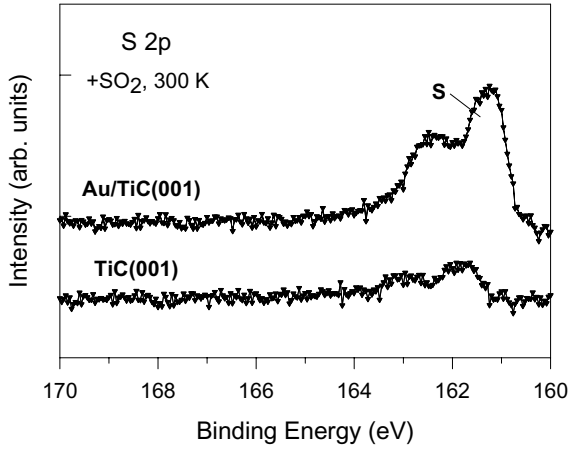

Figure 6.15 S 2p spectra collected after dosing SO_2 at 300 K to TiC(001) and to a surface pre-covered with 0.2 ML of gold.[30]

on Au/TiC(001) at 150 K,[30] while only chemisorbed SO_2 is observed on TiC(001) at the same temperature.

The photoemission data reveals that Au/TiC(001) is a much better DeSOx system than either Au/MgO(100) or Au/TiO_2(110).[30] Au particles dispersed on MgO(100) are able to perform the oxidation of CO[18,19] and bind SO_2 stronger than extended surfaces of gold,[61] but the Au/MgO(100) system is not able to dissociate the SO_2 molecule.[61,62] In the case of Au particles supported on TiO_2(001), SO_2 adsorbs molecularly at 150 K and dissociates upon heating to room temperature.[21] Au/TiC(001) is able to break both S–O bonds at a temperature as low as 150 K.[30] Figure 6.14 compares the amount of atomic sulfur adsorbed after exposing Au/MgO(100),[61] Au/TiO_2(110),[21] and Au/TiC(001)[30] to 5L of SO_2 at 300 K. Au/TiC(001) displays a higher DeSOx activity than Au/TiO_2(110) even at big Au loads. Images of STM for Au/TiC(001) point to a very high DeSOx activity when the average particle height is smaller than 0.5 nm.[30] The DeSOx activity of Au/TiC(001) decreases substantially when the particle height goes above 1 nm at Au coverages higher than 1 ML. Small Au clusters are essential for a high DeSOx activity.[30]

Figure 6.16 shows the calculated adsorption energy for SO_2 on clean TiC(001) and on carbide surfaces with Au atoms, Au_4 or Au_{13} clusters, an Au wire, and a flat Au monolayer.[30] All the Au/TiC(001) surfaces bond SO_2 stronger than clean TiC(001) or the corresponding isolated Au system. Spontaneous dissociation was observed when the SO_2 was set at gold/carbide interfaces. Thus, supported Au atoms, Au_4, Au_{13}, and an Au wire worked in a cooperative way with the carbide and dissociated S–O bonds. Photoemission results for the SO_2/Au/TiC(001) system also indicate the direct participation of Au, Ti and C sites in S–O bond cleavage.[30] In Fig. 6.16, an ideal flat monolayer of gold bonded to TiC(001) adsorbs SO_2 much more strongly than Au(111) or Au(100), but it is not able to dissociate the adsorbate due to the lack of a gold/carbide interface. The DF calculations corroborate that the size of the Au particle has a drastic effect on the reactivity of the system. Supported Au_{29} displayed a much lower DeSOx activity than supported Au_4 or Au_{13} and no dissociation of SO_2 was observed.[30] The effects of the

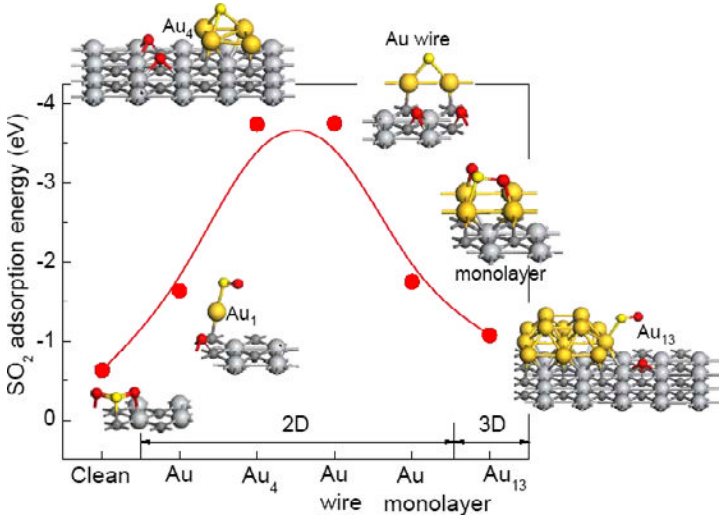

Figure 6.16 Calculated adsorption energies and bonding configurations for SO_2 on TiC(001) and Au/TiC(001).[30] Au atoms, Au_4, and Au_{13} clusters, an Au wire, and a flat Au monolayer were deposited on TiC(001).

Au ↔ TiC(001) interactions were significant only when one had small Au particles.[29,30]

Theoretical calculations indicate that Au atoms supported on ZrC(001) and TaC(001) undergo a charge polarization larger than that seen on TiC(001),[63] making the Au/ZrC(001) and Au/TaC(001) excellent candidates for DeSOx processes.[64–66] Cu also can be added to TiC(001) to facilitate S–O bond cleavage,[65–68] but the copper ↔ carbide interactions are not as strong as the gold ↔ carbide interactions.[69]

6.5 Conclusion

Gold nanoparticles supported on oxides and carbides show a high activity in many catalytic processes not seen for bulk metallic gold. Quantum-effects related to the small size of the particles could be responsible for the enhancement in catalytic activity with respect to bulk gold. The edge and corner sites of a gold nanoparticle have

distinctive electronic properties and can bond well with adsorbates like CO, O_2, and SO_2. They can even perform the catalytic oxidation of CO, but for more demanding reactions (WGS, DeSOx) it is becoming more and more clear that interactions between the gold nanoparticles and the oxide or carbide support can play a very important role in determining chemical activity.

Acknowledgement

The author would like to thank J. Evans, D.W. Goodman, J. Hanson, J. Hrbek, F. Illas, P. Liu, A. Maiti, M. Pérez, and J.F. Sanz for many thought-provoking conversations about the behavior of supported gold nanoparticles. This research was supported by the US Department of Energy, Division of Chemical Sciences.

References

1. a) G.C. Bond, C. Louis, D.T. Thompson, *Catalysis by Gold*, Imperial College Press, London, 2006. b) G.A. Somorjai, *Introduction to Surface Chemistry and Catalysis,* Wiley, New York, 1994.
2. F.A. Cotton, G. Wilkinson, C.A. Murillo, M. Bochmann, *Advanced Inorganic Chemistry*, 6th Edition, Wiley, New York, 2000.
3. J.A. Rodriguez, M. Kuhn, *Surf. Sci.* 1995, **330**, L657.
4. B. Hammer, J.K. Nørskov, *Nature* 1995, **376**, 238.
5. J. Huang, T. Akita, J. Faye, T. Fujitani, T. Takei, M. Haruta, *Angew. Chem. Int. Ed.* 2009, **48**, 7862.
6. M. Haruta, *Catal. Today* 1997, **36**, 153.
7. J.B. Park, J.B. Graciani, J. Evans, D. Stacchiola, S. Ma, P. Liu, A. Nambu, J.F. Sanz, J. Hrbek, J.A. Rodriguez, *Proc. of the National Academy of Science (PNAS)*, 2009, **106**, 4975.
8. M. Valden, X. Lai, D.W. Goodman, *Science* 1998, **281**, 1647.
9. J. Jia, K. Haraki, J.N. Kondo, K. Domen, K. Tamaru, *J. Phys. Chem. B* 2000, **104**, 11153.
10. M.S. Chen, D.W. Goodman, *Science* 2004, **306**, 252.
11. J.A. Rodriguez, S. Ma, P. Liu, J. Hrbek, J. Evans, M. Pérez, *Science* 2007, **318**, 1757.

12. T.S. Kim, J. Gong, R.A. Ojifinni, J.M. White, C.B. Mullins, *J. Am. Chem. Soc.* 2006, **128**, 6282.
13. Z. Yang, R. Wu, D.W. Goodman, *Phys. Rev. B* 2000, **61**, 14066.
14. S.C. Parker, A.W. Grant, V.A. Bondzie, C.T. Campbell, *Surf. Sci.* 1999, **441**, 10.
15. L. Giordano, G. Pacchioni, T. Bredow, J. Fernández-Sanz, *Surf. Sci.* 2001, **471**, 21.
16. A. Vijay, G. Mills, H.J.J. Metiu, *Chem. Phys.* 2003, **118**, 6536.
17. I.N. Remediakis, N. Lopez, J. Nørskov, *Angew. Chem. Int. Ed.* 2005, **44**, 1824.
18. L.M. Molina, B. Hammer, *Phys. Rev. Lett.* 2003, **90**, 206102.
19. A. Sanchez, S. Abbet, U. Heiz, W.D. Schneider, H. Hakkinen, R.N. Barnett, U. Landman, *J. Phys. Chem. A* 1999, **103**, 9573.
20. C.T. Campbell, *Curr. Opin. Solid State Mater. Sci.* 1998, **3**, 439.
21. J.A. Rodriguez, G. Liu, T. Jirsak, J. Hrbek, Z. Chang, J. Dvorak, A. Maiti, *J. Am. Chem. Soc.* 2002, **124**, 5242.
22. M. Okumura, T. Akita, M. Haruta, *Catal. Today* 2002, **74**(3–4), 265.
23. B. Schumacher, V. Plzak, M. Kinne, R.J. Behm, *Catal. Letters* 2003, **89**, 109.
24. Q. Fu, H. Saltsburg, M. Flytzani-Stephanopoulos, *Science* 2003, **301**, 985.
25. H. Häkkinen, S. Abbet, A. Sanchez, U. Heiz, U. Landman, *Angew. Chem. Int. Ed.* 2003, **42**, 1297.
26. J. Guzman, B.C. Gates, *Angew. Chem. Int. Ed.* 2003, **42**, 690.
27. J.A. Rodriguez, J. Evans, J. Graciani, J.-B. Park, P. Liu, J. Hrbek, J.F. Sanz, *J. Phys. Chem. C* 2009, **113**, 7364.
28. L.K. Ono, D. Sudfeld, B. Roldan Cuenya, *Surf. Sci.* 2006, **600**, 5041.
29. J.A. Rodriguez, F. Viñes, F. Illas, P. Liu, Y. Takahashi, K.J. Nakamura, *Chem. Phys.* 2007, **127**, 211102.
30. J.A. Rodriguez, P. Liu, F. Viñes, F. Illas, Y. Takahashi, K.J. Nakamura, *Angew. Chem. Int. Ed.* 2008, **47**, 6685.
31. J.A. Rodriguez, P. Liu, F. Viñes, F. Illas, Y. Takahashi, K.J. Nakamura, *J. Am. Chem. Soc.* 2009, **131**, 8592.
32. J.A. Rodriguez, L. Feria, T. Jirsak, Y. Takahashi, K. Nakamura, F. Illas, *J. Am. Chem. Soc.* 2010, **132**, 3177.
33. L.K. Ono, B. Roldan Cuenya, *Catal. Lett.* 2007, **113**, 86.

34. R.B. Burch, *Phys. Chem. Chem. Phys.* 2006, **8**, 5483.
35. X. Wang, J.A. Rodriguez, J.C. Hanson, M. Perez, J. Evans, *J. Chem. Phys.* 2005, **123**, 221101.
36. B.K. Chang, B.W. Jang, S. Dai, S.H. Overbury, *J. Catal.* 2005, **236**, 392.
37. S.N. Rashkeev, A.R. Lupini, S.H. Overbury, S.J. Pennycook, S.T. Pantelides, *Physical Review B* 2007, **76**, 035438.
38. M. Haruta, *Cattech* 2002, **6**, 102.
39. V. Schwartz, D.R. Mullins, W. Yan, H. Zhu, S. Dai, S.H. Overbury, *J. Chem. Phys. C* 2007, **111**, 17322.
40. J.B. Park, J.B. Graciani, J. Evans, D. Stacchiola, S. Senanayake, L. Barrio, P. Liu, J.F. Sanz, J. Hrbek, J.A. Rodriguez, *J. Am. Chem. Soc.* 2010, **132**, 356.
41. N. Cruz-Hernandez, J.F. Sanz, J.A. Rodriguez, *J. Am. Chem. Soc.* 2006, **128**, 15600.
42. A. Roldan, S. Gonzalez, J.M. Ricart, F. Illas, *ChemPhysChem* 2009, **10**, 348.
43. P. Liu, J.A. Rodriguez, *J. Chem. Phys.* 2007, **126**, 164705.
44. X. Wang, J.A. Rodriguez, J.C. Hanson, D. Gamarra, A. Martínez-Arias, M.J. Fernández-García, J. *Phys. Chem. B* 2006, **110**, 428.
45. J. Nakamura, J.M. Campbell, C.T.J. Campbell, *J. Chem. Soc. Faraday Trans.* 1990, **86**, 2725.
46. J.A. Rodriguez, P. Liu, X. Wang, W. Wen, J. Hanson, J. Hrbek, M. Pérez, J. Evans, *Catal. Today* 2009, **143**, 45.
47. P. Panagiotopoulou, A. Christodoulakis, D.I. Kondarides, S. Boghosian, *J. Catal.* 2006, **240**, 114.
48. J.A. Rodriguez, P. Liu, J. Hrbek, J. Evans, M. Perez, *Angew. Chem. Int. Ed.* 2007, **46**, 1329.
49. J.A. Rodriguez, P. Liu, J. Hrbek, M. Pérez, J. Evans, *J. Mol. Catal. A: Chem.* 2008, **281**, 59.
50. J.B. Park, S.F. Conner, D.A. Chen, *J. Phys. Chem. C* 2008, **112**, 5490.
51. A.A. Gokhale, J. Dumesic, M. Mavrikakis, *J. Am. Chem. Soc.* 2008, **130**, 1402.
52. J.L.C. Fajín, F. Illas, J.R.B. Gomes, *J. Chem. Phys.* 2009, **130**, 224702.
53. J.A. Rodriguez, J.A. Hrbek, *Surf. Sci.* 2010, **604**, 241.
54. S. Ma, J.A. Rodriguez, J. Hrbek, *Surf. Sci.* 2008, **602**, 3272.
55. S. Senanayake, D. Stacchiola, J. Evans, M. Estrella, L. Barrio, M. Perez, J. Hrbek, J.A. Rodriguez, *J. Catal.* 2010, **271**, 392.

56. F.C. Meunier, D. Tibiletti, A. Goguet, S. Shekhtman, C. Hardacre, R. Burch, *Catal. Today* 2007, **126**, 143.
57. I.D. Gonzalez, R.M. Navarro, W. Wen, N. Marinkovic, J.A. Rodriguez, F. Rosa, J.L.G. Fierro, *Catal. Today* 2010, **149**, 372.
58. A. Piéplu, O. Saur, J.-C. Lavalley, O. Legendre, C. Nédez, *Catal. Rev.* 1998, **40**, 409.
59. J. Evans, H. Lee, in *Topics in Environmental Catalysis*, Ed.: S.V. Rao, Interscience, New York, 2001, 187.
60. D.I. Sayago, P. Serrano, O. Böhme, A. Goldoni, G. Paolucci, E. Roman, J.A. Martín-Gago, *Phys. Rev. B* 2001, **64**(20), 205402.
61. J.A. Rodriguez, M. Pérez, T. Jirsak, J. Evans, J. Hrbek, L. González, *Chem. Phys. Lett.* 2003, **378**, 526.
62. J.A. Rodriguez, P. Liu, M. Pérez, G. Liu, J. Hrbek, *J. Phys. Chem. A* 2010, **114**, 3802.
63. E. Florez, L. Feria, F. Viñes, J.A. Rodriguez, F. Illas, *J. Phys. Chem. C* 2009, **113**, 19994.
64. J.A. Rodriguez, P. Liu, Y. Takahashi, K. Nakamura, F. Viñes, F. Illas, *Top. Catal.* 2010, **53**, 393.
65. A. Tshope, W. Liu, M. Flytzani-Stephanopoulos, J.Y. Ying, *J. Catal.* 1995, **157**, 42.
66. M. Polcik, L. Wilde, J. Haase, B. Brena, D. Cocco, G. Comelli, G. Paolucci, *Phys. Rev. B* 1996, **53**, 13720.
67. J.A Rodriguez, J.M. Ricart, A. Clotet, F. Illas, *J. Chem. Phys.* 2002, **116**, 4698.
68. A.R. Alemozafar, X.-C. Guo, R.J. Madix, *J. Chem. Phys.* 2002, **116**, 4698.
69. T. Gómez, E. Florez, J.A. Rodriguez, F. Illas, *J. Phys. Chem. C* 2010, 114, 1622.

This page intentionally left blank

CHAPTER 7

RECENT PROGRESS IN SUPPORTED METAL-CATALYSED C1 CHEMISTRY

A. Guerrero-Ruiz[1,2] and I. Rodríguez-Ramos[2,3]

[1]*Dpto. Química Inorgánica y Técnica. Fac. Ciencias. UNED, Senda del Rey 9, 28040 Madrid, Spain*

[2]*Unidad Asociada Grupo de Diseño y Aplicación de Catalizadores Heterogéneos UNED-ICP(CSIC), Madrid, Spain*

[3]*Instituto de Catálisis y Petroleoquímica, CSIC, C/Marie Curie, Cantoblanco, 28049 Madrid, Spain*

7.1 Introduction

The C1 chemistry concept aims to define a group of reactions that, starting from compounds with a single carbon atom, lead to the formation of chemicals with higher value from the economic point of view, with greater potential application or utilities, and with increased chemical reactivity for use as intermediates. These ideas, initially applied to the Fischer–Tropsch process in Germany during the first decades of the 20th century, emerged after the petroleum crisis in 1975 and were applied to hydrocarbon production from synthesis gas ($CO + H_2$). The manufacture of methanol and higher alcohols from CO and H_2 was also an early development. During the 1980s, a major research drive involved the synthesis of chemicals from natural gas, of which, coupling and partial oxidation of methane were the most widely studied processes. Additionally, the transformation of methanol to hydrocarbons over zeolite catalysts became a topic of great interest. More recently, the number of

reactions involving CO_2 have increased, largely as a consequence of its known contribution to the greenhouse effect, that is, use in formation of intermediates for the chemical industry such as acid or lactone synthesis, and large-scale production of energy-rich compounds (methanol, hydrocarbon, synthesis gas, etc). Many of these and other reactions involving C1 substances take place in the presence of heterogeneous catalysts. Moreover, many excellent reviews have independently treated each of these subjects. Based on the well-established and revised scientific literature, we will introduce examples to illustrate more recent progress in the different reactions which are included in the C1 chemistry concept. From an academic point of view, we will emphasise the surface chemistry reactions involved in the different heterogeneous-catalysed processes (surface intermediates, active sites, etc.). With regard to industrial applications of these new reactions, we will distinguish between currently implemented technologies and the more promising trends for the future.

Before beginning to review recent progress in C1 chemistry, it is worthwhile defining some of the concepts which will be covered in this chapter. If C1 chemistry is widely understood as the group of chemical reactions that use compounds with a single carbon atom in their formula (for example CH_4, CO, CH_3OH,…), to obtain various products (long-chain hydrocarbons, methanol, formaldehyde,…), we should introduce our first restriction within this definition. That is, only processes giving rise to higher quality compounds (constructive chemistry) will be analysed. Thus, a better quality product has higher molecular weight and/or a larger chemical reactivity than that of the reactant. The transformation of synthesis gas ($CO + H_2$) to hydrocarbons is obviously constructive, because from a low molecular weight molecule, CO organic products (paraffins, olefins, etc.) with much wider application in further synthesis processes and with higher chemical complexity are produced. Even the transformation of CH_4 into CO is assumed as an upgrading, considering the higher reactivity of CO in comparison with CH_4. However, the combustion of CH_4 ($+O_2$) to CO_2 is not considered here as a constructive C1 chemistry reaction. The lower

reactivity of CO_2 and H_2O in comparison with the consumed CH_4 should be taken into account in this case. A thorough review on catalytic combustion of methane over Pd catalysts can be found in Ciuparu *et al.*[1] The latter line of reasoning can also be applied to the transformation of methanol (or methane) to hydrogen, due to the higher chemical richness of the reactant CH_3OH (or CH_4) molecule compared with the resulting H_2 ($+CO_2$) product. Furthermore, these conversions, currently of great interest in the general framework of hydrogen fuel cell technologies, will be treated in another chapter of this book. The application of CH_3OH in direct methanol fuel cells will also not be analysed, because it is a chemically destructive process. In short, we will review a series of heterogeneous-catalysed reactions which, starting from different C1 compounds (CO, CO_2, CH_4, CH_3OH, HCOH), lead to useful chemical intermediate products. Thus, the main processes which will be considered here are:

- Fischer–Tropsch synthesis.
- Methanol and higher alcohol production from syngas.
- Hydrogenation reactions and other possibilities aimed at re-using CO_2.
- Hydroformylation of olefins with synthesis gas.
- CH_4 dimerisation and oligomerisation.
- CH_4 reforming to syngas and partial oxidation products.
- CH_3OH to hydrocarbons and to other intermediate compounds.

These different reactions are displayed in Scheme 7.1, where M indicates those heterogeneous-catalysed processes involving supported metals.

Due to the abundance and the nature of the primary compounds involved in these reactions, C1 chemistry has become a major area of research interest. CH_4 (main component of natural gas) may be considered as a raw material for the next decades to produce various organic intermediates (chemicals, liquid fuels), as well as a principal source of energy. CO_2 is the largest by-product emitted to the atmosphere and holds the main responsibility for the green house effect. For

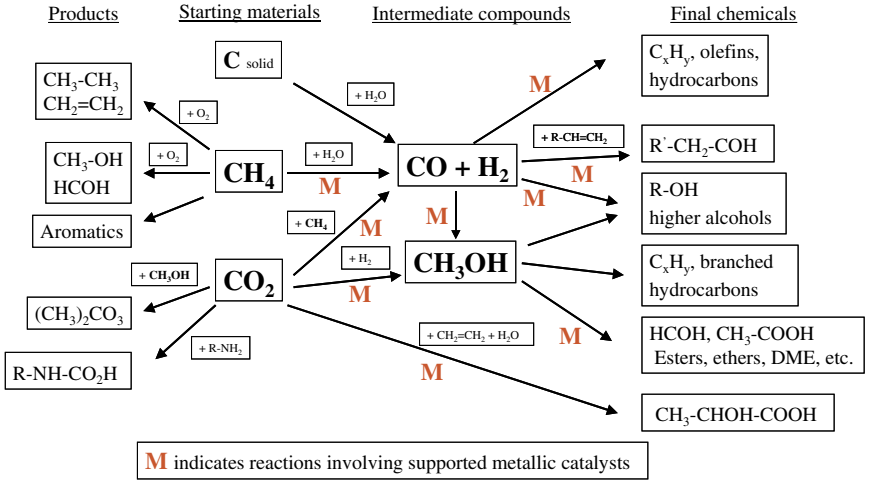

Scheme 7.1 Routes to higher value products from C1 reagents.

this latter reason, its reutilisation is strongly desirable. CH_3OH is a synthetic compound that allows numerous chemical transformations of great interest in the production of intermediates for the chemicals industry. Also CO (or CO + H_2 mixture, usually called synthesis gas or syngas), although it is a product obtained from raw materials, is considered as a route for transforming coal or natural gas into chemicals or non-petroleum derived fuels.

Finally, only reactions performed over supported metallic catalysts will be the object of this review, and we will emphasise surface chemistry mechanistic aspects as well as recent technological innovations (membrane systems, supercritical media, new materials, microchannel technologies, etc.).

7.2 Fischer–Tropsch Synthesis

The synthesis of hydrocarbons from CO hydrogenation over transition metals is a major source of organic synthetic chemicals and fuels. The Fischer–Tropsch (FT) reaction, which is directed to the production of hydrocarbons from syngas, implies the polymerisation of $–CH_x$ entities and carbon-carbon bond formation is required.

It should be stressed that supported iron and cobalt-based catalysts are the only ones applied in industrial plants. In fact the earlier Sasol reactors operated using iron catalysts while the more recent plants utilise cobalt.[2,3] The historical achievements in the FT reaction have been revised on several occasions; see for instance the reviews by Vannice,[4] Schulz[5] and the special issue of *Catalysis Today*[6] devoted to FT. Also, a synopsis of the main recent industrial developments has been presented by Adesina.[7] Furthermore, it is worth noting the issue of *Topics in Catalysis*[8] where different aspects of the reaction mechanism, surface reconstruction of active surfaces, improved reactors and optimisation of catalyst preparations have been treated by various specialists, scientists and engineers.

The FT synthesis may be formulated as:

$$nCO + nH_2 \rightarrow (-CH_2-)_n + nH_2O. \qquad (7.1)$$

Various elementary surface steps are involved in this reaction:

- CO chemisorptions;
- Splitting of C–O bond;
- Dissociative chemisorption of H_2;
- Reaction of two H atoms with one O atom to yield H_2O;
- Desorption of H_2O;
- Reaction of two H atoms with one C atom to yield $-CH_2$ intermediates;
- Formation of C–C bond;
- Readsorption and further reaction of intermediates (i.e. chain termination);
- Desorption of hydrocarbon products.

An initial question in this complex reaction mechanism, which has been extensively investigated, is whether CO dissociates into C and O species prior to the formation of monomer CH_x intermediates or, alternatively, whether the CO bond remains without splitting and inserts, forming intermediate species containing oxygen. At present the polymerisation (chain prolongation) step seems to

occur through $-CH_2-$ units. However, the CO insertion is not ruled out because alcohols can be produced under FT reaction conditions (see below), and because the addition of oxygenated compounds into the FT feed stream (including labelled molecules) shows their insertion into product molecules.[5] Perhaps in the case of Fe catalysts (also for Co and Ni), CO dissociation and surface carbon formation is clearer and CH_2 are the common accepted monomer species in the FT pathway mechanism. However, for Cu, Rh or Pd, which are mainly catalysts for methanol and higher alcohols synthesis, the CO insertion mechanism should be reconsidered. Some new contributions, particularly using isotopically labelled molecules, have been performed. Using Carbon-13 labelled C_2-vinyl probes and Rh, Ru, Co and Fe as catalysts, Maitlis *et al.*[9] concluded, in agreement with previous work, that the key species in the reaction are surface methylenes, which are polymerised. However, the $^{13}C_2$-incorporation data favours alkenyl intermediates coupling with surface methylenes and an alkenyl mechanism for FT polymerisation rather than the alkyl intermediates in the alkyl mechanism, which was previously proposed.[10] In the alkenyl mechanism, instead of chain growth being ended by β-elimination (as in the Brady–Pettit model), the termination step is now the reaction of the surface alkenyl with surface hydrogen, giving the 1-alkene directly and accounting for α-olefin formation as primary products. Two more aspects are raised in this contribution: oxygenates such as ethanol are produced, especially over Rh, but no mechanistic interpretation is given; and significant differences in the cleavage of the vinyl probes is found depending on the metal catalyst. This latter observation that different reaction pathways are possible on different metal surfaces, is also mentioned by Davis.[11] While oxygenate intermediates participate in the FT synthesis over Fe catalysts, alcohols and CO_2 are inert on the Co surface. Also, Fe carbide is a clear intermediate on Fe catalysts while these species are not well documented for Co.[11] In a comparative study of the CO activation pathways on Fe and Co surfaces[12] it is concluded that direct CO dissociation routes are minor contributors towards monomer formation on Fe, and may become favoured at high temperatures on alkali promoted catalysts, but not on Co

catalysts, which remove oxygen as water because of the preponderance of H-assisted CO dissociation routes. Evidence from density functional theory calculations on Co (0001) indicates that the main reaction pathway for the Fischer–Tropsch process is not a carbide mechanism[13] and that the propagation cycle may include a CO insertion into surface RCH groups.[14] In connection with this latter aspect of the C1 + C1 intermediates coupling and chain propagation to form long hydrocarbons, another density functional study[15] on Co (0001) demonstrated that CH_3 + C and CH_2 + CH_2 steps are major C1 + C1 coupling pathways in FT synthesis on Co, and that CH + CH coupling on terraces also may contribute under certain conditions. Calculations of C2 + C1 and C3 + C1 coupling suggest that RCH_2 + C and RCH + CH_2 are the most important pathways in the polymerisation reaction.

The vinyl mechanism during FT over Rh catalysts has been considered in another tracer study involving co-feeding Carbon-13 ethylene.[16] It should also be mentioned that FT reaction is very sensitive to reaction conditions, and for instance, selectivity can be directed by simply changing the reaction temperature.[17,18] Even more difficult is to make the assumption of a given FT mechanism when the catalyst morphology is modified during the reaction, and when real feedstocks containing sulphur are processed.[18]

Water generated by the process may also play an important role by altering the relative concentration of reactive molecules at the catalyst surface, *via* the water-gas shift reaction ($CO + H_2O \leftrightarrow CO_2 + H_2$). Moreover, its ability as an oxidising reactant of the transition metal catalysts can modify the intrinsic catalytic properties of a metallic surface during the hydrogenation and/or during the polymerisation steps. In this way, the role of water in the FT process has been addressed in different research papers. Thus, it has been observed that under the hydrothermal conditions created by high conversion FT reaction, a silica-supported Co catalyst becomes a mixed oxide with a needle-like morphology which causes catalyst deactivation.[19] By reduction at high temperature of this cobalt-silica mixed oxide, small metallic cobalt particles are formed and the catalyst is regenerated. However, on Co/SiO_2 model catalysts it has

been clearly shown that oxidation of the metal particles with water under FT reaction conditions is difficult and is size-dependent.[20,21] In addition, on carbon nanofibre-supported cobalt the sintering of the metal was evidenced, which was associated with the presence of water.[22] Three deactivation mechanisms of cobalt FT catalysts have been identified and related with the presence of water: sintering of the metallic active phase, carbon deposition and surface reconstruction, but fortunately all of them can be reversed by adequate regeneration treatments.[23] Furthermore in order to avoid these deactivation processes a number of noble metals can be added to the Co catalysts as promoters, such as Re,[24] Ru[25] or Pt,[26] all of them seem to modify secondary reactions, for example, the hydrogenation of carbon intermediates giving place to long hydrocarbons and/or filamentous carbon. The addition of these promoters seems to have less influence on the degree of reduction of Co or on the nanoparticles sintering, although the effects on the reconstruction of catalyst surfaces are a challenging topic to be studied. For these latter investigations *in situ* techniques are offering some advantages. Thus, during a study of promotion impact of alkali metals on the carburisation rates of Fe/Si catalysts by X-ray absorption spectroscopy,[27] it is revealed that the presence of the alkali promoter leads to an increase in the CO dissociative adsorption rate, and consequently in the catalysts carburisation rate. This promotion does significantly alter the carbide distribution in the catalyst.

Following on with the water effects in FT, transient carbon isotope experiments carried out over supported and unsupported Co catalysts indicate that water vapour increases the amount of monomeric and active surface carbon species under steady state reaction conditions.[28] This effect of water is attributed to an acceleration of the rate of CO dissociation, and as a main consequence, it induces a shift in the FT selectivity, lower methane selectivity and formation of higher molecular weight products. The impact of the water produced at high conversion level in the case of alkali promoted iron catalysts is also attributed to the water-gas shift reaction. It appears that the relative rates of the FT and WGS reactions are responsible for the drop in CO conversion to hydrocarbons. At high

conversion levels, the hydrogen production by WGS reaction seems to be the rate limiting factor in the FT synthesis over these catalysts; therefore the secondary water-gas shift process becomes the rate controlling step.[29] In an investigation of the effects of water on the FT synthesis catalysed by cobalt catalysts, it is observed that the water increases CO conversion rates and the selectivity to olefins and to higher hydrocarbons. Assuming that these effects can reflect modification in the density of CO intermediates or in the number and reactivity of the surface Co atoms, kinetic isotope studies (H_2O and D_2O) and *in situ* infrared spectroscopy analysis were performed.[30] Based on the absence of significant differences in both types of studies, the authors concluded that reactive carbon species are present as a minority, but are kinetically relevant intermediates for FT reaction. These may be formed during the FT reaction and are responsible for the macroscopically observed effects of water. The effect of water on the catalytic properties of silica-supported cobalt during FT synthesis, either produced as a reaction product or added in varying amounts into the feed gas, has been identified in a continuous stirred tank reactor (CSTR).[31] It is concluded that water increases CO conversion, when small amounts of water are added, and does not have significant effect on the catalyst deactivation. On the other hand, when larger amounts of water are fed continuously, severe deactivation results under these reaction conditions. The addition of water during FT synthesis over a supported Ru catalyst, as in the cases of Fe and Co, led to a significant increase in the reaction rates and a significant modification in the process selectivity, with lower methane selectivity and improved chain growth.[32] Mechanistically, in addition to methylene chain growth, another route for long hydrocarbon formation is postulated by considering a combination of adjacent alkyl chains to form paraffins ('reverse hydrogenolysis'). As a conclusion, it appears that water plays a crucial role as a moderator in the kinetic regime of the FT-catalysed reaction because a narrow product distribution is obtained. At this point, it is worth noting that water has been identified as a very effective agent in removing carbon deposits from metal surfaces, for instance in the case of Fe/ZrO_2 or $Fe/K/ZrO_2$ catalysts.[33] If, as these

latter authors indicate, a $H_2 + H_2O$ atmosphere is able to reduce the catalysts only to divalent iron, at temperatures close to that of the FT synthesis, a potential role of water in the restructuring of the metallic catalytic particles could be speculated on, as well as in modifying the oxidation states of the catalytic sites under real FT conditions. As for the current industrial catalysts, the activities of the active ingredients Fe and/or Co for water-gas shift reaction ($CO + H_2O \rightarrow CO_2 + H_2$) are clearly different. Thus, Fe catalysts are more active in WGS than the Co ones.[34] This makes preferable the iron catalysts when used in FT operation conditions with H_2-deficient feeds,[35] because achieving high conversion of a H_2 poor syngas, both high WGS and high FT activities, is required,[34] and this is not possible with Co catalysts. On the other hand, from a technological point of view, the specific catalytic properties have to be adapted to new and more complex compositions of syngas. So, instead of the current $CO + H_2$ mixtures produced by steam reforming of methane or from gasification of coal, new feedstocks can be used to obtain syngas such as biomass[36] or other carbonaceous wastes (main differences lie on the general compositions of feeds and in particular of the H_2/CO ratios). Also, the appropriate selection of the FT catalyst allows operation with typical bio-syngas feedstock[36] (H_2, CO, CO_2 and CH_4) either directly or combining FT process with carbon dioxide reforming of methane.[37]

On the basis that FT synthesis is a polymerisation reaction, some authors realise that olefins can suffer secondary reactions, and consequently product distributions can be modified.[38] A general overview about the likely secondary reactions involved (hydrogenation, isomerisation, reinsertion or hydrogenolysis) has been revised.[39] Readsorption of olefins can lead to initiation of chain growth processes, with subsequent modification of the product distribution. Secondary hydrogenation of α-olefins may also occur, and depending on the catalysts and of the reaction conditions, these can affect the olefin to paraffin ratio. For this group of authors, kinetic expressions and selectivity models should account for these secondary reactions.[38,39] Puskas and Hurlbut[40] presented an opposing point of view. For these authors, a multiplicity of chain

growth probability is the only reasonable cause of deviations from the Anderson–Schulz–Flory distributions in the FT reaction (particularly in the range of products with more than six carbon atoms in the molecule). This idea is also supported by experimental evidence in relation to the product distributions obtained over Fe and Co catalysts, when reactant partial pressures are varied, or when 1-alkenes (or ethene) are co-fed.[41] While for Co catalysts modification of product distributions by secondary chain growth of readsorbed alkenes is observed, for Fe, secondary reaction is negligible. Two superimposed Anderson–Schulz–Flory distributions for both Fe and Co catalysts can fit the product distributions. These authors conclude that superimposed distributions with different chain growth probabilities are merely the result of different chain growth mechanisms (or secondary reactions mainly involving olefins). Probably differences in the type and state of the catalytic surface as well as in the range of analysed products make it difficult to compare the product distributions achieved in various laboratories. In this line, changes in the surface composition under FT reaction conditions should be considered as dynamic processes[42] leading to nucleation of certain surface sites (iron carbides, in the case of Fe) whose nature is independent of that of the particle core. The generation of active domains located at surface layers, where reactant diffusion is shorter, can lead to kinetically different catalytic surfaces. Although FT catalysts are complex materials containing the catalyst support and structural and reduction promoters, in addition to the active metal itself, fortunately, at present, we have methods to probe catalyst structures with atomic-scale resolution.[43] However, fundamental understanding of the dynamic chemistry of the metal-carbon-oxygen system is still a developing field.[44] Interestingly, application of Steady-State Isotopic Transient Kinetic Analysis (SSITKA) has made determining the origin of cobalt particles size effects in FT catalysis possible.[45] So it was found that the lower surface-specific activities (or Turn-over Frequencies, TOF) obtained for small cobalt particles (<6 nm) is caused by a remarkable increase in the residence time of CH_x intermediates coupled with a decrease of their intermediate coverage. Also the

higher methane selectivity of small Co particles obtained under FT conditions has been brought about by the higher coverage with hydrogen detected on the surface of smaller Co crystallites. In short, static characterisation methods are available (*ex situ*) while dynamic (*in situ* or *operando*) techniques need to be improved, but in the near future new insights from the application of the latter are expected. As a representative example the application of *in situ* X-ray absorption spectroscopy/wide angle X-ray scattering allows information to be obtained about the local environment of iron catalysts submitted to FT conditions,[46] evidencing a transformation of the supported catalysts from amorphous iron (II) silicate (in the reduced state) to at least two iron carbides after FT pre-treatment.

Among the many published papers in this area during recent years, we aim to highlight those that introduce new ideas or concepts which mainly concern the design of the supported metal catalysts. This is based on the evidence that H_2 and CO chemisorption, and their subsequent dissociations, exhibit structure-sensitive character.[47] Most of the relevant aspects related with the FT industrial applications or with operational parameters (reaction temperature, pressure and CO/H_2 ratio which are fundamental factors affecting product distribution and kinetics) can be found in the existing published literature.[7,48] The effects of Strong Metal Support Interactions (SMSI) on FT reactions and the potential application of new bimetallic catalysts will be emphasised. In a careful study of the FT kinetic on a well-characterised Co/TiO_2 catalyst using a differential fixed bed reactor,[49] it is corroborated that turnover frequencies and rate constants are in good agreement with those previously reported for other Co catalysts, when the data are normalised to the same conditions of temperature and partial pressure of the reactants. However, on cobalt particles supported on γ-aluminas with varying acidic properties, it is found that the acidity of support affects both the reducibility of metallic precursors and the FT product selectivity.[50] Perhaps in this latter case a complementary characterisation of the used catalysts and an analysis of the data on the basis of metallic surface areas would be desirable in order to further the conclusions of this paper. In more complex

systems, i.e. Co-Rh/Nb_2O_5,[51] even if the catalysts are well characterised, an unequivocal correlation amongst the obtained reaction variables (product distribution, reaction rates, etc.) and the metal surface area is quite difficult to achieve. It should be noted that the state of the active surface of bimetallic-supported catalysts is not just metallic but rather a complex composition with chemisorbed entities containing carbon and oxygen atoms. This should be deduced when the pre-treatment gas (CO or H_2 as reductants) is sufficient to modify reaction rates of a Ru-Co/TiO_2 catalyst.[52] The importance of the addition of small amounts of Ru to Co catalysts in order to increase the turn-over rates has been also pointed out,[53] in addition to the support effects.

Aiming at addressing the product distribution, several attempts have been performed using catalysts supported on zeolites. In the earliest studies of FT, using zeolites for instance with microporous ZSM5,[54] these were treated as metal supports which would modify catalytic selectivity by applying the intrinsic 'acidic' and the 'shape-selective' properties of these materials, as in bifunctional catalysis. The dependencies of hydrocarbon product distributions in FT reaction over iron catalysts and physical mixtures of iron-zeolite (HZSM-5) have been evaluated under different reaction conditions.[55] Zeolite presence increased secondary reactions, including cracking of heavier products and light olefins oligomerisation, while product distribution at high space velocity was comparable for iron-HZSM5 and iron catalysts, so the role of the zeolite declined under these reaction conditions. Many publications concern mainly mesoporous silica and Co catalysts.[56–58] In these cases the importance is pointed out of the reducibility of the metal precursors, the influence of the support on the metal dispersion and the shift in the hydrocarbon selectivity. Smaller pores present in MCM-41 lead to a decrease in the size of the Co nanoparticles and to their diminished reducibility under hydrogen. Also, these Co particles are less active in FT and their selectivity to methane increases, the latter being related to their lower reducibility. Comparison of performance in FT[59] of cobalt catalysts, supported on mesoporous molecular sieves (MCM-41 and SBA-15) with

different pore diameters and prepared with high metal loadings (10–20%) by different methods (exchanging template ion and impregnations with Co acetate or Co nitrate), revealed that the acetate precursor gives place to less reducible, almost inactive, Co silicates. Aiming to obtain gasoline-range branched hydrocarbons, hybrid catalysts comprising Co/SiO_2 (FT catalyst) and acidic medium-pore zeolites were comparatively tested.[60] Not only modifications in the selectivity were evidenced but also depletion in the acid activity of the zeolites with the time on stream due to the accumulation of carbonaceous deposits. Regeneration of the spent zeolites is not trivial,[60] which represents a serious obstacle for the possible commercialisation of these catalysts. Also the metallic precursors[58,61] and promoters[62–64] are key parameters in the final performance of these systems.

Recently a facile and efficient preparation route for the fabrication of a FT catalyst based on iron oxides and carbon nanospheres has been reported. The catalyst, which exhibits remarkable stability and selectivity in the FT process,[65] consists of highly dispersed iron oxide nanoparticles, generated by hydrothermal treatment of a glucose solution containing iron nitrate at mild temperature, embedded in carbon spheres. The high catalytic performance is attributed to the confinement effect of carbonaceous matter on the embedded nanoparticles. Thus, the surrounding carbonaceous matter facilitates the formation of iron carbides, which is beneficial for the longer hydrocarbon formation, and also these iron carbides particles do not suffer aggregation during reaction. Throughout time many studies have been devoted to carbon supported FT catalysts.[66] Activated carbon offers an excellent opportunity to improve the effect of promoters due to the lower metal support interactions. So cobalt supported on an activated carbon and promoted by La_2O_3 (15%Co-0.5%La/AC) presents a high activity and an improved selectivity to alcohols formation.[67] These features were attributed to the high dispersion of Co and the appropriate Co^{2+}/Co^0 ratio along with the improved interaction of Co and La_2O_3. In the same line carbon nanofibres have been studied as supports for Co particles, either promoted by manganese oxide[68] or non-promoted ones.[69,70] The

manganese promotion effect was successfully studied without interference of support effects and it was related with the retard in the cobalt particles reduction.[68] In addition, the use of an inert support as carbon nanofibres, makes possible a careful inspection of the intrinsic metal particle size effects on the performance in FT synthesis.[70]

Another interesting approach to achieving improved catalysts for FT synthesis is the use of carbon nanotubes as support materials for metallic particles.[71] Carbon nanotubes distinguish themselves from other carbon materials in that they have graphene layers with semi-conducting or metallic characteristics and a well-defined tubular morphology. Many recent studies use carbon nanotubes, generally multiwall ones, as support for different metals such as Fe,[72,73] Co,[74] Fe-Co[75] or Ru.[76] In all cases some shifts in FT selectivity or improvement in the stabilities (reduced sintering) are evidenced. Also, potassium-promoted iron catalysts supported on carbon nanotubes have been evaluated in FT process[77] with the consequent modifications in the olefins and higher hydrocarbons selectivities. But a major insight in this field can be envisioned if the metallic particles are localised selectively inside or outside the nanotubes,[78,79] because while interior graphene surfaces are expected to be electron-deficient, exterior surfaces should be electron-enriched. The main conclusion from these confinement studies was that iron inside carbon nanotubes exhibits improved catalytic performances. For example FT activities are increased when iron is confined within carbon nanotube tubular channels and the yield to longer hydrocarbons is twice that over the outside iron catalyst.[78] Once the effects of iron particle size were excluded as a crucial factor in modifying catalytic performance, it was proposed that modified redox properties of the confined iron catalysts (for example reducibility) may play a more important role in justifying the modifications of FT catalytic properties.

From the applied catalysis point of view, the reactor operations media and the catalyst engineering can be modulated to improve the FT yield to a given range of products. A recent review of the reactors utilised for the FT processes and their historical developments may be illustrative.[80] A comparison of a series of

$Ru/Co/ZrO_2$-Al_sO_3 FT catalysts in fixed bed and slurry reactors[81] demonstrated that, in both types of reactors, the catalytic properties can be related to the metallic particle structures and surface catalyst evolutions, but in the slurry reactor the pore size distribution of the support seems to be a key parameter due to mass-transfer limitations of heavy hydrocarbon products. Several of the more recent contributions to the field of FT are related to the use of supercritical media. Among the advantages that supercritical fluids introduce are: modification of the reaction environment by changing the pressure, elimination of transport limitations and integration of reaction and separation steps. In a study of FT using a Co catalyst and hexane as supercritical solvent, a marked effect on the hydrocarbon product distribution has been detected, which shifted toward higher carbon number products and also improved the yield of olefins.[82] Similar effects have been observed over a Co/Al_2O_3 catalyst using a supercritical fluid mixture of n-pentane/n-hexane.[83] The interpretation of these findings is rationalised in terms of the faster diffusion of the wax products, which results in lower residence times in the catalyst pores thereby decreasing the probability of readsorption and secondary reactions. Also using supercritical n-pentane, it has been noted that direct wax synthesis can be performed at relatively low temperatures (473 K), and when small amounts of 1-olefins are added to the stream, the CO conversion is enhanced and wax production is also improved.[84,85] In a critical and comprehensive review[86] of the researches carried out on FT synthesis in supercritical media, it is remarked that some discrepancies exist in the results published up to now, so some future assessments will be essential. But it is also concluded that the olefin content in supercritical media exceeds those in other reaction media, which can be interpreted as due to a more efficient extraction and transport of the primary FT products out of the catalyst particles. Also the better stability of the catalysts in supercritical reaction operations is related to a more uniform temperature distribution inside this reactor and to the mentioned easier desorption of heavy hydrocarbons (intermediated strongly adsorbed at the catalyst surface). Despite the numerous studies that have examined FT reaction in supercritical

media,[86,87] the development of this technology has not yet moved beyond laboratory scale, and it is considered also that this development can be specially suitable for small-scale gas to liquid plants because supercritical fluids overcome limitations of the slurry and multitubular reactors.

From the FT chemical engineering point of view some improvements can be achieved using monolithic catalysts, based on both cordierite ceramics[88] or washcoated metallic structures.[89] In the first case a $CoRe/Al_2O_3$ catalyst was incorporated on a commercial square channel cordierite monolith[88] resulting in selectivity shifts to larger amounts of olefins than alkanes in the produced hydrocarbons, when the washcoated catalyst layer is thinner than 50 micrometres. Furthermore, when cobalt-based catalysts are coated onto metallic structured supports with different geometries,[89] the structured catalysts maintain the activity and the selectivity of the original powdered catalysts, which boosts the advantages of operating with a monolithic reactor configuration. On the other hand membrane reactor designs can be useful for FT processes considering that semi-permeable hydrogen-selective distributors allow control of the H_2 : CO ratio along the catalyst bed,[90] and also that membranes of an extractor-type can improve the FT performance by selective removing of the H_2O by-product[91] by means of hydrophilic membranes.[92] Hydrophilic membranes and microporous zeolite membranes outperform amorphous and polymer membranes, offering high permselectivities and H_2O fluxes at temperatures close to the FT conditions. It should be noted that the H_2O extraction membranes should produce very different effects when used with iron or cobalt catalysts. The reason is the abovementioned higher activity of Fe for WGS compared to Co, consequently these membranes can find niches of application with Co catalysts.[92] But up to now no experimental details on their application have been reported; most of the publications in this area report modelling based on theoretical analysis.

In the same way as applied catalytic technologies, novel microreactors constituted by microchannels can be considered[93] (Fig. 7.1). These microchannel reactors can allow an increase in the yield of

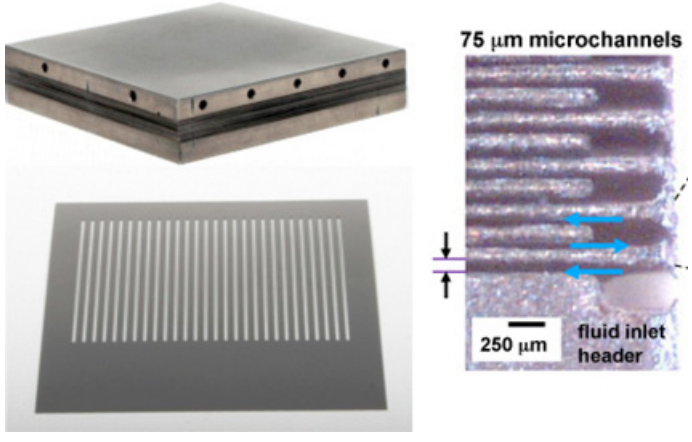

Figure 7.1 Illustrative photographs of a microchannel dispositive.

FT products and a reduction of the reactor size by up to 90%. Heat transfer and fluid dynamic and mixing properties are some of the expected improvements with these reactors. Experimentally, conventional straight microchannel configurations have been compared with zigzag-shaped microchannels,[94] and the obtained results were consistent with the fluidic simulation and the stochastic modelling results. Computational studies of heat transfer in a microchannel reactor for low-temperature FT synthesis[95] conclude that phenomena such as liquid superheat are not significant due to the improved heat transfer inside these reactors which is a consideration relevant for the application of these reactors. Finally it should be noted that FT should be considered as only one of the three steps in the conversion of natural gas into liquids, the other two being syngas generation and hydroprocessing.[96] However, new concepts such as the combination of methane steam reforming and FT synthesis, in order to convert methane directly to hydrocarbons, have been explored.[97] The idea seems to be operative at 573 K, using Ru and Co catalysts, but very low conversions are achieved.[97] Thus higher performance catalysts will have to be developed and the combination with alternative reaction conditions (such as supercritical fluids, membrane technologies, etc.) merits consideration.

7.3 Methanol Production and Higher Alcohols from Syngas

Commercially, methanol has been produced from syngas, mainly containing CO and H_2 along with a small amount of CO_2, for many years (from 1923, by BASF). The major advance in methanol synthesis occurred in 1966 when ICI introduced a lower pressure process based on a very active copper/zinc oxide/alumina catalyst.[98] Over the years, several reviews have concentrated on the process of methanol production from hydrogen and carbon monoxide in the presence of Cu-Zn containing catalysts.[99,100] As a result of the importance of methanol as an energy carrier and feedstock in numerous chemical syntheses, there has been a great deal of research carried out in recent years to elucidate the reaction mechanism and the role of active sites involved in these catalysts, in addition to developing the most efficient catalyst for the methanol synthesis. Recent progress in innovation, optimisation of the reaction conditions, reaction mechanism, and performance of copper-based catalysts for methanol synthesis *via* hydrogenation of CO and CO_2 have been discussed by Liu *et al.*[101] The mechanism of methanol synthesis from syngas over Cu-Zn containing catalysts has been comprehensively reviewed by Ostrovskii.[102] During the past decade, CO_2 hydrogenation rather than CO hydrogenation has emerged as the dominant research topic concerning production of methanol over Cu-Zn containing catalysts. It is assumed that the process proceeds under a wide range of conditions according to the following gross-mechanism:

$$CO + H_2O = CO_2 + H_2 \quad (7.2)$$

$$CO_2 + 3H_2 = CH_3OH + H_2O. \quad (7.3)$$

Such mechanism has been postulated mainly on the basis of isotope-labelling studies.[103–105] Methanol is formed from CO_2 that is produced during the water-gas shift reaction. Under normal operating conditions, carbon dioxide is added to the feed gas. There appears to be a limit to the amount of CO_2 that can be present in the feed,[106] since water produced during methanol synthesis from

a CO_2-rich feed ($CO_2/CO/H_2$) accelerated the crystallisation of Cu and ZnO contained in a Cu/ZnO-based catalyst leading to deactivation of the catalyst. However, the catalyst was only slightly deactivated during methanol synthesis from a CO-rich feed containing a higher concentration of CO, because only a small amount of water was produced during reaction, and no significant crystallisation of Cu and ZnO occurred.

Surface species on Cu-based catalysts have been actively studied in recent years by various methods, including *in situ* methods. Nevertheless, information obtained on the role of various surface species is still controversial. Most authors consider surface formate on copper to play a key role in methanol synthesis.[107–111] However, Fisher and Bell[112] consider a mechanism for methanol synthesis on Cu/ZrO_2 catalysts in which formate species are formed on zirconia and undergo hydrogenation with atomic hydrogen supplied through spillover from copper. However, some authors[113,114] consider surface formaldehyde to be the most important species. At present, surface carbonate seem to become more prominent in the mind of many scientists as the initial surface species to undergo hydrogenation.[115–117] This step is often considered as the rate controlling step.[117]

The nature of the outer layer of the Cu-Zn-based catalysts and the role of the different active sites are still a topic of investigation. Metallic copper is implicated as being the dominant oxidation state of the metal during the reaction. However, the presence of Cu^+ is also important as a small amount of oxygen increases the reaction rate.[103,118] Shen *et al.*[119] found on ceria-supported copper catalyst that in spite of the reductive reaction atmosphere, metallic copper particles on cerium oxide were oxidised during reaction and the catalyst was activated. The formation of the copper oxide species was considered indispensable for the onset of high catalytic activity. Synergy between Cu and ZnO in the catalysis of methanol synthesis has been suggested and the nature of this synergy has been interpreted in many different ways. Spencer[120,121] suggested that synergy arises from H spillover from ZnO to metallic copper, while Schilke *et al.*[122] proposed for the case of Cu/SiO_2-Zr catalyst, that after CO_2 adsorption

over ZrO_2 as HCOO-Zr and HCO_3-Zr, the latter species are hydrogenated by atomic hydrogen generated over metallic Cu, i.e hydrogen diffusion occurred in the opposite direction. The same group[123] concluded on the basis of H/D experiments, that the rate of hydrogen spillover from Cu is more than an order of magnitude higher than the rate of methanol formation, and, hence, not a rate limiting step in the synthesis of methanol over Cu/ZrO_2.

Additional beneficial effects of ZnO in Cu-Zn-containing catalysts include the maintenance of some copper in the 1+ oxidation state. It appears that upon reduction ZnOx moieties are created which migrate onto the surface of Cu particles and stabilise Cu^+.[124] It has also been suggested that the copper metal-zinc oxide interface is one of the active sites for methanol formation. Strong oxide-metal interaction maintains a well-dispersed copper which maximises the oxide-metal interface area where the reaction occurs.[125] At present, new preparation routes are being applied in order to synthesise novel Cu/ZnO catalysts aimed at enhancing the Cu-ZnO interface area. In particular, the deposition precipitation of copper onto high specific surface area zinc oxide particles and the chemical vapour deposition of diethyl zinc have appeared to be effective techniques, leading to catalysts with high catalytic activity in methanol synthesis.[126] Combinatorial tools have also been applied to optimise Cu-Zn containing catalysts for methanol synthesis. Design of experiment combined with a neutral network was shown to be useful when determining the optimum catalyst composition.[127,128]

Various promoters have been introduced to the copper-based catalysts aimed at improving its performance or stability in methanol synthesis. Elements such as B, Ga, Co and Mg have been added without achieving significant improvement.[129–131] Chen *et al.*[132] reported that doping with trivalent metal ions such as Al^{3+}, Sc^{3+} and Cr^{3+} could promote the formation of monovalent cationic defects on the surface of ZnO, which might accelerate both the enrichment and stabilisation of Cu^+ on the surface during reaction. Chromia in a copper catalyst could prevent the rearrangement of Cu sites and improve the active surface of the catalyst.[133] Zirconium oxide has also been studied as a promoter and a support[123,134,135] for the methanol

synthesis catalysts due to its special structure and stability. However, the activity of methanol formation using zirconia as a support is slightly lower than that of zinc oxide as support. Using ZnO with especial morphologies (nanowires and nanotubes) as support of electrodeposited Cu,[136] an increased selectivity towards higher alcohols (C2–C4) from syngas was found, but the general yield to alcohols was low because of the excessive CH_4 and CO_2 formation. Promotion by manganese of this Cu-ZnO system gave a novel high selectivity catalyst, where the formation of CH_4 and CO_2 are reduced, maximising the selectivity to higher alcohols.

Although there appear to be limited opportunities to develop a more efficient catalyst for methanol synthesis without copper in the composition, palladium on several basic oxide supports, including La_2O_3[137] and CeO_2[138,139] has been studied because it appears as a more robust and sulphur tolerant active component.[140] It is clear that the catalytic properties of Pd for methanol synthesis are quite sensitive to the nature of the support, the palladium particle size and the metal precursor. Shen *et al.*[139] found that the Pd precursor, or more specifically its anion, has an effect on the final palladium particles, and therefore affected the interaction between Pd and ceria, which gave rise to differences in the reaction behaviour. It was proposed that during methanol synthesis, the structure of the Pd ceria interaction shifts from small Pd clusters supported on ceria to sintered large Pd particles dispersed on a mass of ceria. This structural change is responsible for the catalyst deactivation. They also studied[141] the influence of the support (Al_2O_3, SiO_2, TiO_2 and ZrO_2) on the activity and selectivity of Pd in the CO hydrogenation reaction. Both the activity and the selectivity of the catalysts were strongly affected by the nature of the support. Only Pd/SiO_2 and Pd/ZrO_2 produced methanol as a major product. The higher CO conversions obtained over Pd/ZrO_2 and Pd/TiO_2 were attributed to the presence of cationic palladium species formed as a result of metal support interaction. Ali and Goodwin[142] using steady-state isotopic transient kinetic analysis (SSITCA) explored differences in the catalytic behaviour of Pd resulting from the use of different supports with different acidities. Palladium on acidic supports

produced significant amounts of methane along with methanol. SSITCA results showed that the nature of the support only slightly influenced the intrinsic activity of sites producing methane and methanol. However, the number of surface intermediates leading to methane and methanol were significantly affected by the support. It was concluded that the impact of the support on the reaction rate was determined by its effect on the concentration of active sites/intermediates on Pd.

The mechanism of methanol synthesis from syngas over Pd catalysts has been studied with Ca-doped Pd catalysts supported on silica.[143] It was found that basic metal oxides are needed to give a Pd catalyst with high activity for methanol formation. The authors proposed that the Ca-doped Pd/SiO_2 catalysts acted as a bifunctional catalyst in the methanol synthesis reaction. Sites on the metal oxide are responsible for the formation of the formate species, and Pd activates hydrogen for the subsequent hydrogenation steps. In contrast to Cu/ZnO, the methanol activity of this $Ca/Pd/SiO_2$ catalyst increased with increasing CO content in a $CO–CO_2–H_2$ mixture. For this reason it was assumed that CO rather than CO_2 was the main carbon source for methanol. It is suggested that high CO partial pressures may inhibit the reverse water-gas shift reaction, the decomposition of the formate species in water and CO and thus favour the hydrogenation of formate to methanol.

The conversion of syngas to methanol is limited by the thermodynamic equilibrium at the temperatures required by current catalysts. The process is limited to low conversion per pass which implies a large recycle of unconverted gas. The reaction is also exothermic and, consequently, requires significant cooling. The recycle and cooling requirements increase the production cost and an increase of the one-pass conversion would be desirable. Recently, various schemes for one-pass conversion have been conceived. A short review of recent technological improvements in methanol synthesis has been made by Lange.[144] One approach is based on the use of a membrane reactor, as a substitute for the traditional reactor, aimed at increasing the production by pushing the conversion by selective separation of products. Different types of membranes are

being developed such as, Li-Nafion membranes,[145] silica/alumina composite membranes[146] and zeolite membranes.[147] Another methodology to improve the catalysed synthesis of methanol, is the application of new reaction conditions such as the use of supercritical fluids as reaction medium.[148,149] In one example using supercritical 2-butanol it was found that this not only facilitated heat and product removal, but also promoted the methanol conversion from syngas. It is claimed that this is one method of overcoming thermodynamic limitations.

Over the last few years, considerable effort has been made in understanding the mechanism of higher alcohol synthesis from syngas and to developing a higher alcohol synthesis catalyst which is as selective as the Cu-based methanol synthesis catalyst. This is a consequence of the fact that the resultant alcohols can be used directly as fuels, as an additive to increase the octane number of traditional fuels and as an important basic material in the chemicals industry. Recent review articles[150–152] have discussed the mechanism and kinetics of higher alcohol synthesis from syngas over various catalytic systems. Catalysts for this transformation fall into one of the following broad types: alkali-modified methanol synthesis catalysts,[152,153] rhodium-based catalysts which are selective towards C_2 oxygenates,[154] molybdenum sulphide-based catalysts[155,156] and copper and alkali-modified Fischer–Tropsch catalysts.[151,157,158]

Copper-based methanol synthesis catalysts promoted by alkalis form principally C_2-C_4 alcohols in addition to methanol from syngas. The dominant alcohol in the mixture is methanol, while the second most abundant alcohol is branched isobutanol. It has been shown by isotopic labelling studies with copper-based, zinc oxide containing catalysts[152] that higher alcohols are formed by a unique carbon-chain growth mechanism, referred to as oxygen retention reversal aldol condensation. However, the formation of the first C–C bond to give ethanol remains the least understood step in this reaction sequence. Results with Cs-Cu/ZnO/Al_2O_3 catalysts suggest that ethanol is formed *via* methanol condensation steps,[159] but over $Cu_{0.5}Mg_5CeO_x$ catalysts a path where CO operates directly is preferred.[153] It has been shown that over these latter materials, the aldol

condensation reaction involves a metal-base bifunctional mechanism.[160] Condensation steps occur on basis sites, but Cu sites appear to be required in order to remove hydrogen from the surface and to increase the rate of the initial C–H bond activation steps. Kinetic studies have shown[153,161] that the dominant factor in guiding the product selectivity is the relative reaction rate of each C–C bond formation step, the C_1 to C_2 step being the rate determining step in forming higher alcohols from syngas. Moreover, it was noted that for higher alcohol synthesis, the initial synthesis gas is essentially free of CO_2, and the H_2/CO molar ratio is ≤1. Elevated levels of CO_2 tend to inhibit the synthesis of higher alcohols.

Among the group VIII metals, Rh is unique in its ability to predominantly catalyse the formation of C_2 oxygenates (ethanol and acetaldehyde) from syngas when promoted by certain reducible metal oxides.[154,162] In recent years, studies[163–166] have been performed which confirm previous results that established the strong influence of promoters and supports on the activity and selectivity of Rh catalysts. Hydrocarbons are mostly formed on Rh supported on SiO_2 and Al_2O_3, but Rh on ZrO_2, TiO_2, CeO_2, MnO or La_2O_3 is a particularly effective catalyst for the formation of ethanol. In a similar manner, Rh/SiO_2 promoted by Mn, Fe, Li or Nb shows a high efficiency for the synthesis of C_2 oxygenates. However, the function of these metal oxides as supports or promoters and the ethanol formation mechanism are still a subject of debate. In particular, there is disagreement over the exact nature of the intermediates for the synthesis of C_2 oxygenates. Some reports, based on IR and labelling experiments, suggested that ethanol and acetaldehyde are formed through the same intermediate,[167,168] either surface acetate or acyl species. More recently, several workers[169–171] have proposed that acetaldehyde and ethanol are derived from different intermediates. Wang *et al.*[170] reported that ethanol is formed by direct hydrogenation of a tilted form of adsorbed CO molecules, followed by CH_2 insertion into the surface CH_2-O species and a subsequent hydrogenation step. Acetaldehyde is formed through CO insertion into the surface CH_3-Rh species, followed by hydrogenation. The role of the

promoter[164,170] was correlated with the formation of the tilted form of adsorbed CO which requires both the Rh and the promoter ions to generate this particular form of adsorbed CO. However, acetaldehyde formation was found to be independent of the presence of the promoter, since direct CO insertion requires only isolated Rh atoms.

Alcohol synthesis over Fischer–Tropsch catalysts modified by copper and alkalis have been intensively investigated, especially those based on cobalt initially developed by IFP.[172] These investigations are aimed at developing catalysts with improved selectivity towards alcohols against the parallel reaction to produce hydrocarbons.[158,173] These catalysts produce linear primary alcohols and linear hydrocarbons, both types of products following a Schulz–Flory type distribution.[172] Earlier studies[172,174] reported that the chain growth probability factor α of hydrocarbons is equal to that of alcohols and that higher CO partial pressures favour higher alcohols. More recently for a K-Co-Cu-Zn-Al catalyst, Boz[157] showed that the chain growth probability factor of higher alcohols was independent of conversion, whereas that of the hydrocarbons was dependent on conversion. At high CO conversions both alcohols and hydrocarbons have the same chain growth probability factor. It was postulated that at low conversions, there are two different active sites with two distinct chain growth probability factors, while at high conversions, alcohols and hydrocarbons are produced on the same active site. Evidently, the nature of active sites changes depending upon reaction conditions. The active sites for alcohol production have been associated with Cu–Co sites in intimate contact, i.e. Cu–Co alloy sites.[175] It was shown that the role of Cu–Co alloy consisted in the formation of cobalt carbide that was able to activate CO associatively to produce oxygenates. In an attempt to shed some light on the mechanism of promoter action, Co promoted by Cu[176] or by Mo-K[177] have been supported on carbon nanotubes. In the first case[176] an increase of the concentration of catalytically active Co species at the catalyst surfaces, CoO(OH), is related with the selective formation of higher alcohols. Additionally carbon nanotubes act as a reservoir of H adspecies retained in the functioning catalyst.

The high surface concentration of these surface species interact with CO_2 from the feed gas, producing an inhibition of the water-gas shift side-reaction.[176] In the second case[177] it is proposed that two catalytical species ($CoO(OH)/Co_3O_4$ and Mo^{4+}) synergistically perform the formation of C2+ alcohols.

Finally, it should be noted that different reaction engineering approaches are being investigated to further increase the activities and selectivities of higher alcohol synthesis. Two reviews of these approaches have been published by Herman[152] and Subramani and Gangwal.[178] In this later article it is remarked that the linear homologation of C1 to C2 alcohols is the bottleneck in the synthesis of higher alcohols. Methanol homologation by co-feeding methanol, formaldehyde, etc., along with syngas over a suitable modified catalyst composition, appears to be a promising approach.[178] Thus a number of studies have been conducted under low temperature methanol synthesis conditions.[179] Low temperature synthesis is carried out in a liquid medium, and these conditions permit the reactor to be operated under different media, for instance different long-chain alcohols, co-feeding CO_2, using various modified heterogeneous catalysts and under supercritical environments.[179] As representative examples of these researches the alkali promotion of a Cu/MgO catalyst used under low temperature methanol synthesis (433 K) by Fujimoto *et al.*[180,181]can be mentioned. In these cases ethanol was the liquid media of the reaction and the main conclusion is that formate species are essential intermediates stabilised as alkali formates by reaction with the promoters. When n-butanol is used as solvent for the low-temperature methanol synthesis (443–463 K) and a sol-gel prepared Cu/ZnO is the catalyst,[182] it has been concluded that the large surface area and homogeneous element distribution in the Cu-ZnO particles are key parameters to obtain the maximum of catalytic performance. In relation to the presence of steam (<10%) in the feed an increase in catalytic activity and stability in methanol from syngas over a $CuZnOAl_2O_3$ catalyst has been demonstrated.[183] But this study is conducted under typical methanol synthesis reaction conditions, since the water solvent seems not to be appropriate

for low-temperature methanol synthesis, probably because water is unable to stabilise formate species. Additionally, separation of methanol and ethanol from the syngas can help to overcome thermodynamic equilibrium limitations and to improve the yield of the process. In this way ceramic membranes have been tested in the range of temperatures of the low-temperature methanol synthesis.[184] Experimental and mathematical modelling have also evidenced that the presence of water contributes to reducing the permeance of hydrogen or carbon dioxide, which resulted in higher separation factors.

Technologically the evaluation of catalysts under realistic conditions is relevant. Thus in a detailed study of the effect of H_2S in the syngas feed over alkali promoted cobalt-molybdenum sulphide catalysts,[185] it is raised that the presence of hydrogen sulphide lowers the alcohol selectivity enhancing the hydrocarbon formation, even if the production of higher alcohols is enhanced at adequate H_2S concentration levels.

7.4 Hydrogenation Reactions and Other Possibilities Aimed to Re-use CO_2

As remarked above, CO_2 can be considered as a co-reactant in the synthesis of methanol and alcohols or as a by-product of the FT reaction (since it is produced in the concomitant water-gas shift reaction: $CO + H_2O \rightarrow O_2 + H_2$). Thus, CO_2 should be considered in the surface reactions taking place in such processes. However, considering the restrictions placed on the C1 chemistry definition above, only chemically constructive reactions will be analysed. Therefore, we will not consider the hydrogenation of CO_2 to CH_4,[186] as it does not yield improved compounds. Even though the pathways involved in CO_2 hydrogenation are different from those of the FT reaction, with lower deactivation rates in the former case.[187] On the other hand, given the recognition of the greenhouse effect produced by the enormous quantities of carbon dioxide released into the atmosphere, the need to reutilise this CO_2 has become a significant challenge. Many catalysed processes have been considered in

order to derive useful products from CO_2. Some of these reactions involve heterogeneous metallic catalysts, such as for instance:

- Hydrocarbon synthesis, applying indirect processes and hybrid catalysts[188,189] (first methanol is formed, then transformed to lower paraffins and olefins), either directly[190,191] or using two-stage reactors;[189]
- Synthesis of acetic acid;[192]
- Methyl amines synthesis from $H_2/CO_2/NH_3$;[193]
- Electrochemical reduction to CO and HCOOH over Fe or Ni catalysts supported on activated carbon fibres;[194]
- Interaction of CO_2 with olefins to yield oxygen containing organic compounds.[195,196]

In a further example of the hydrogenation of CO_2 over composite catalysts, for instance Cu-Zn-chromite and HY zeolite,[197] it has been demonstrated that this combination of methanol synthesis and methanol-to-gasoline catalysts enables the direct formation of ethylene and propylene. The influence of the addition of alkaline metals, of the reaction temperature and of the space velocity on the production of alkenes shows that alkanes are obtained by hydrogenation of the corresponding alkenes.

As one possible method of processing large amounts of CO_2, the dry reforming of methane process has been proposed ($CO_2 + CH_4 \rightarrow 2CO + 2H_2$). Many investigations are continuously appearing in the literature for this reaction and significant progress has been made from the scientific point of view, developing improved catalysts, as well as obtaining a more detailed understanding of the reaction mechanism. Major reviews of this reaction such as that of Bradford and Vannice[198] should be consulted and a special issue of *Applied Catalysis A* has been devoted to catalytic conversion of CO_2.[199] The development of new improved catalysts has been focused on four specific aspects: the intrinsic activity of the metallic phases, their stability towards carbon deposition, the type of support most suitable for improving catalytic performance and the addition of promoters. Many metals have been tested for this

reaction,[200,201] among which noble metals are known to be very active and resistant towards carbon deactivation, especially Ru and Rh.[202,203] The activities of these metals have been systematically compared in terms of turn-over numbers. It has also been shown that, depending on the support, a metal may exhibit different activities when calculated on the basis of exposed surface sites.[198,204,205] Many support materials have been studied, with a variation in the extent to which this interacts with the metal component. Thus, silica[206] and alumina[207] have been largely studied along with 'inert' supports such as carbonaceous materials.[208] Other more reactive support oxides such as TiO_2,[209] La_2O_3,[210] MgO[200] and CeO_2[211] have also been evaluated. More recently the application of high temperature stable oxides such as ZrO_2[212] (or mixed oxides ZrO_2–CeO2[213]), have been investigated because of the high reaction temperatures required in the process. Also, some promoters have been added to the catalyst formulation, amongst these basic oxides (MgO[214,215] or CaO[216]) and high oxygen mobility oxides (CeO_2[217]) have received attention. Based on a comparison of all these systems, some conclusions have been obtained concerning the reaction mechanism and the important role of supports and promoters in this reaction. The resistance to coke formation, i.e. deactivation rate, can be modified as a function of the catalyst support.[211] Basic supports or basic promoter surface sites where the CO_2 can be activated as bicarbonate or carbonates inhibit carbon formation by the Boudouard reaction on the metal. Additionally, a bifunctional mechanism has been considered in which hydroxyl groups of the support or promoter, that are regenerated by the water produced by secondary reactions, may participate in several reaction steps.[218] Studies using isotopically labelled molecules[214,219] and steady-state isotopic transient kinetic analysis (SSITCA)[207,220] have allowed researchers to conclude that the reaction of CO_2 with CH_4 to yield syngas occurs *via* a mechanism with multiple reaction steps. This multiplicity of surface reactions which depend on the catalytic materials used as well as on the choice of reaction conditions, accounts for the observed effects of the support, promoter, nature of active phases,

etc., on the catalytic behaviour observed (activities, selectivities, stabilities, accumulated carbon species).

From the industrial application point of view regarding the CO_2 reforming of methane, further developments are required before a generalisation of processes such as CALCOR[221] takes place. At the laboratory scale the possibility of using membrane reactors to displace the thermodynamic equilibrium of the dry reforming reaction deserve mention. The application of membranes to separate hydrogen from the reaction zone is expected to enable the attainment of higher conversion at lower operational temperatures.[222] Most of the studies involving membrane reactors in reforming reactions have been devoted to the classical steam reforming[223,224] ($CH_4 + H_2O \Leftrightarrow CO + 3H_2$), but some have involved the CO_2 plus CH_4 reaction.[225–227] Based on our own experiences,[228] significant progress is still required, both in the design of more efficient membranes and in the understanding of the secondary effects that hydrogen separation introduces in to the various surface reactions involved in the overall process.

Among the catalysed reaction aimed at using CO_2 in the synthesis of organic products, those which apply metallic catalysts include reactions with olefins. A nice example is the reaction between CO_2, ethylene and water to yield 2-hydroxypropanoic acid (lactic acid).[229,230] In this particular case, careful selection of the bimetallic supported catalyst (Pt-Sn/SiO_2) and complementary characterisation of the catalyst together with the study of the reaction mechanism, have permitted interesting new insight of the surface reaction steps involved and to propose a general reaction scheme for this process. The relationship between the formation of lactic acid and the adsorption properties indicated that carbonylic surface species, which interact with hydroxyl groups of the support, are able to generate acetaldehyde.[230] The latter would appear to be a key intermediate in the process. However, no new reports have appeared considering the application of metallic heterogeneous catalysts for this group of synthetic reactions involving CO_2 and olefins. Another interesting approach is the use of CO_2 as a reactant and solvent in supercritical conditions. This methodology has

been useful in the hydrogenation of CO_2 to formic acid,[231] and in the production of ethylene carbonate from ethylene oxide.[232] Until now, these methods have been largely restricted to homogeneous catalysts.

The necessity to find technological methods to recycle carbon dioxide has been regarded as an opportunity to improve several industrial processes, as well as to develop new ones or to modify others.[233] These methodologies have to be complementary to carbon dioxide sequestration and storage ones. In fact metal supported catalysts can be useful in different chemical reactions such as production of higher alcohols re-using CO_2, but in general these reactions should not be hydrogen demanding and the application of renewable energy sources is desired (for instance combining catalysts and solar energy). Thus, hydrogenations and reverse water-gas shift reactions are less interesting than alcohols production or than hydrocarbon reactions (mainly methane dry reforming) to yield syngas. Also, the production of hydrocarbons, either directly co-feeding CO_2 with the syngas over FT catalysts or a two-stage approach methanol production followed by a methanol to olefins stage (see below in Section 7.7), has attracted quite a lot of attention. For the first case, a FT route where $(CO_2 + CO)/H_2$ mixtures are used as reactant, a number of studies over cobalt[234] and iron[235] catalysts have revealed significant differences in catalytic behaviour. While in the case of Co catalysts the CO_2 hydrogenation is slow in the presence of CO and the typical selectivities of FT (long hydrocarbons) turn to methane in the case of CO_2 reactant, however with a promoted $Fe(K,Cu)/Al_2O_3$ catalyst the same hydrocarbon products are obtained in CO_2 and CO hydrogenation. The different behaviour in Fe and Co catalysts was explained by a different inhibition of the methane formation and product desorption as a prerequisite for chain growth. In the case of promoted iron catalyst the carbide formation and the alkali coverage of the surface enhanced the selectivity to higher hydrocarbons. A technical possibility to improve the CO_2 + FT catalysts is to incorporate a membrane permeoselective to water in the reaction zone.[236] The conversion of CO_2 to long-chain hydrocarbons *via* CO_2 shift and FT reaction can be

enhanced by *in situ* H_2O removal through an integrated ceramic membrane.

7.5 Hydroformylation of Olefins with Synthesis Gas

The reaction of 1-olefins with syngas yielding an aldehyde with one more carbon atom than the reactant olefin ($R - CH = CH_2 + CO + H_2 \rightarrow R' - CH_2 - COH$) is an example of C1 chemistry synthesis which is typically catalysed by homogeneous organo-metallic catalysts. Hydroformylation processes are practised for the production of aldehyde compounds, which are used as precursors of surfactants and plasticisers. One of the major issues in this area is to make heterogeneous catalysts from organo-metallic compounds, anchoring or supporting them on (or into) various solid materials (dendrimers, silica, zeolites, etc.). Among the more recent contributions to this subject, those dealing with aspects such as: new support materials and preparation methods, encapsulation of active phases in microporous or mesoporous structures or application of modifiers to drive the reaction selectivity should be noted.

Different supports, such as inorganic and polymer carriers, have been used for the active metals that catalyse hydroformylation synthesis.[237,238] Leaching of the active component from the support has been observed in many cases, this being a major problem for the heterogeneous supported metal catalyst application. This leaching has been demonstrated for Rh on SiO_2–Al_2O_3,[239] for silica anchored Rh or Pd species prepared by sol-gel method[240] as well as for Co and Rh on SiO_2 and activated carbon, respectively.[237] In the case of activated carbon supports when anchoring Rh complexes, the re-usability of the catalysts has been reported if a petroleum coke-based activated carbon is selected as support.[241] Also a decreased stability has been evidenced, and catalytic performance for immobilised complex of Rh on activated carbon, if water is present in the solvent.[242] Several alternatives have been proposed to overcome the problem of loss of active phase during hydroformylation reaction with heterogeneous catalysts. For instance, no leaching of the active phase was observed[243] for Rh supported on inorganic oxides, including

pillared clays, and the activity and selectivity in the hydroformylation of 1,1-diarylethenes and vinylnaphthalene was found comparable to that of homogeneous Rh catalysts. Other possibilities are the immobilisation of metallic complexes on polymer support[244] or on dendrimers[245] or on dendrimerised silica-coated nanoparticles.[246] In these latter cases, dendritic catalysts potentially combine the advantages of homogenous and heterogeneous catalysts, because they can be separated from the reaction media by nano-filtration. Encapsulation and anchoring of organo-metallic compounds within microporous and mesoporous zeolite supports have been demonstrated as useful methods of obtaining highly active and recyclable catalysts,[247] without the problem of leaching of the metal.

Sol-gel preparation methods offer the possibility of entrapment of the metallic complex. This method has been used for bimetallic Rh-Pd[248] and Rh-Co[249] systems, with silica employed as the support material. The metallic nanoparticles in these catalysts are very efficient, but their interaction with CO can eventually give rise to catalytically inactive metal carbonyls. Similarly Au/Co_3O_4 catalysts with improved catalytic performance in the olefins hydroformylation were prepared.[250] The effects of a series of potential supports (SiO_2, ZSM-5, Al_2O_3 and multiwalled carbon nanotubes) on the catalytic activity of a ruthenium carbonyl polymer have been investigated.[251] It was found that the larger activities, even compared with the unsupported polymer, are obtained with the multiwall carbon nanotubes. This support effect needs further investigation to understand whether it is due to a confinement effect or a modification of electronic properties associated with this special carbon material. Also, the gas phase deposition of $Co(acac)_3$ on silica can provide highly active and selective catalysts, with adequate durability under ethylene hydroformylation reaction.[252] However, it should be considered that the performance of heterogeneous catalysts, in comparison with homogeneous organo-metallics, is very limited when comparing the selectivity for hydroformylation of more complex olefins. For this reason, the use of surface modifiers in large excess is required to enhance the formation of a desired product. Rh carbonyl complexes supported on MCM-41 zeolite only are able

to yield (with good activity and selectivity) cyclohexane carboxaldehyde when the MCM-41 is previously functionalised with amine ligand groups.[253] Other zeolitic structures, SBA-15 and SBA-15 with dendritic structures (ex-polyamidoamine) grown on the surface, have been evaluated as support of Rh complex.[254–257] These types of supports with larger-pore and ordered pore structures have been claimed to bring promotional effects in term of catalytic activities, and in general catalysts based on these supports are claimed as highly selective and as recyclables. On the other hand, the beneficial combination of polyamidoamine dendrimers and nanoalumina support has been shown with a Wilkinson's catalyst in the styrene hydroformylation.[258] Apart from the classical modification of both homogeneous and heterogeneous catalysts by phosphine ligands,[259] alkali promoted, Mn-modified or H_2S-treated metal catalysts also show improved activity and selectivity in ethylene hydroformylation.[260] The optimisation of the aldehyde production, has been related to the attainment of an appropriate balance between CO dissociation, CO insertion and hydrogenation activities over the catalytically active surface sites.[260] More demanding, and much more interesting, is the potential modification of Rh particles by chiral diphosphines to produce chiral aldehydes.[239,261] Some improvements in the optical yields are produced with this system, but catalytic activity is decreased in the presence of the diphosphines and chiral selectivity disappears for the re-used catalysts.

As an interesting technical approach, the use of supercritical fluids in the catalysed hydroformylation reaction should be considered. Bearing in mind that current technologies based on aqueous phases as solvents introduce restrictions due to the low solubility of olefins in water, the use of supercritical CO_2 as a reaction media has been proposed.[262] Novel heterogeneous catalysts have been developed, with optimal fluid-solid interactions, in particular aimed at improving the reaction selectivity and avoiding metal leaching. Amongst these, Rh supported on activated carbon, which is soluble in supercritical CO_2, has been shown to be poorly selective in the hydroformylation of propene to butanal,[263] but highly selective and recyclable for the hexane hydrofromylation when supported on a

polymer.[264] Thus we can conclude that more effort must be applied to the development of this promising area where significant achievements might be attained.

7.6 Catalysed Reactions Involving CH_4

Of the different reactions which employ methane as a reactant, those that lead to formation of syngas by steam or dry reforming and partial oxidation should be mentioned, and these can be considered as indirect methods for the use of natural gas.[265] Direct methods include reactions such as dimerisation, oligomerisation and partial oxidation to methanol or formaldehyde. Steam reforming is a mature technology widely used to generate syngas for use in methanol and petrochemical plants. The dry (CO_2) reforming reaction has been discussed in Section 7.4 of this chapter. Some discrepancies appear in relation to the catalysed partial oxidation of CH_4 by metal-supported catalysts. While some authors claim that the direct partial oxidation, without intermediate formation of CO_2 and H_2O, can take place over Ru/TiO_2,[266] isotopic studies using $^{18}O_2$ and $C^{18}O_2$ over Ru/SiO_2 and Ru/Al_2O_3 catalysts indicated that the partial oxidation of methane reaction follows an indirect pathway, i.e. total oxidation of methane yielding water and carbon dioxide, followed by a steam and/or dry reforming of the unconverted methane to syngas.[267] Evidences of the two step mechanism have been also reported from a series of $Pt/CeZrO_2/Al_2O_3$ catalysts,[268] where the effects of different noble metal loadings were studied. On the other hand, the poisoning effect on Rh catalysts by sulphur compounds has been investigated[269] showing that the steam reforming reaction path to the syngas production is selectively inhibited, independently of the used monolithic support materials (La_2O_3–Al_2O_3 or SiO_2– Al_2O_3). For this methane partial oxidation reaction, some features can be drawn from recent researches concerning the role of the support materials. For example in a work about Ni and Ni-Au catalysts supported over MgO-Al_2O_3 mixed oxides[270] it is evidenced that formation of a $MgAl_2O_4$ spinel, without excess of MgO, provides the highest activity and stability. Also, the modification of Al_2O_3

support by mechanical incorporation of aluminium nitride (AlN) gives place to an improved performance of Ni catalysts: activities, selectivities and absence of carbon deposition.[271] The higher thermal conductivity and stability of materials with AlN incorporated contribute to reduction of nickel precursors at lower temperatures and allow a better and stable dispersion of the metal particles. It is worth noting that catalytic partial oxidation requires the use of nearly pure O_2, and consequently the need for separation of oxygen from air, and the manipulation of the CH_4/O_2 reactant mixture is relatively dangerous. Futhermore, the large quantities of heat evolved during the reaction in certain zones of the catalytic bed is an added problem.[265] To overcome the problems associated with conventional thermal heating methods, it has been proposed to apply plasma technologies[272] (e.g. dielectric-barrier discharge, corona, gliding arc or microwave plasma), in particular post-plasma catalysis (with the catalyst downstream of the reactor) with Fe_2O_3 catalyst gives place to a selectivity toward methanol 36% higher than a non-catalytics system,[273] at a catalyst temperature as low as 150°C.

On the other hand, the oxidative coupling reaction of CH_4 in the presence of O_2, even when performed in membrane-type reactors,[274] is mainly catalysed by metal oxide catalysts.[265] Also oligomerisation, aromatisation and the partial oxidation to methanol or formaldehyde apply non-metallic heterogeneous catalysts (i.e. zeolites, supported metal oxides[275] or heterogenized metal-complexes).[276] The reader is therefore directed to some excellent reviews on these subjects.[277,278] At this point it is perhaps relevant to introduce the formation of carbon nanofibers or nanotubes from methane, these being catalysed by metal nanoparticles, but at the moment this is not considered as a C1 chemistry reaction. Again we direct the attention of the reader to some reviews on this type of process.[279,280]

7.7 CH_3OH to Hydrocarbons and to Other Intermediate Compounds

Methanol is a key compound in C1 chemistry because it allows the conversion of raw materials, from which it is produced, into more

valuable organic chemicals. However the main application of heterogeneous catalysts for the activation of CH_3OH is related to their transformation into hydrocarbons. For these technologies, the catalytic reactions are based on the acid-base properties of surfaces, and the catalytic materials consist of zeolites (ZSM-5, etc.). These are well-established technologies and as a state-of-the-art review, that of Stöcker[281] should be mentioned.

From the point of view of methanol activation by metallic particles, the particular surface properties of copper, which are related to the oxidation state of Cu ions, should be emphasised. Thus, methanol is usually dehydrogenated into methyl formate over supported copper catalysts.[282,283] Over Cu/SiO_2 the reaction exhibits a structure-sensitive character,[284] and by infrared spectroscopy it was determined that adsorbed formaldehyde can react with adsorbed methoxy groups to form methyl formate.[285] Using a Raney Copper[286] it has been shown that methanol dehydrogenation produces primarily formaldehyde, and methyl formate, the main reaction product, seems to be formed by formaldehyde dimerisation. Recently, mesoporous MCM-41 silica has been used to modify the state of copper by controlling the preparation method,[287] and the role of these Cu species in the methanol dehydrogenation reaction has been evaluated. In a comparative study of different supported metal catalysts[288] (and alloys[289]) the decarbonylation of aldehyde species into CO and H_2 has been related to the metallic state of Pd and Pt; while on the supported Pt and Pd alloy phases, aldehyde species were stabilised and an increase in the methyl formate selectivity was observed. Membrane technology was also applied to the dehydrogenation of methanol to yield methyl formate in order to separate hydrogen from the reaction zone and to enable the attainment of higher conversions at lower reaction temperatures. The diffusion of hydrogen through a Pd-Ru membrane placed inside a reactor with a copper containing catalyst was studied.[290] It was found that under the conditions of the methanol dehydrogenation reaction, the membrane was not poisoned with carbon monoxide even at the high concentrations employed, whereas the same reactant rapidly deactivated the membrane at points where the reaction did not occur, which was

interpreted as a consequence of the displacement of adsorbed species from the alloy surface.

Another reaction of significance involving methanol is the direct synthesis of dimethyl carbonate (DMC) by carbonylation of methanol with CO which offers a potentially green chemical replacement for phosgene which is used for polymer production and other processes. The direct synthesis of dimethyl carbonate has been pursued over a variety of carbon supported cuprous chloride catalysts, but these catalysts deactivate due to loss of chloride and as such require reactivation by drying and contact with gaseous HCl. King *et al.*[291,292] discovered that the chloride is not necessary to catalyse the reaction, and a solid catalyst prepared by supporting cuprous ions on a zeolite using a solid state ion exchange method yielded good productivity and selectivity for DMC synthesis with little sign of catalyst deactivation. To elucidate the mechanism of reaction over Cu^+ ion exchanged into an X-zeolite,[293] a steady state kinetic study was performed and the surface species present during reaction were followed by *in situ* FTIR. The study provided insight into the important effect that water has on this system.

Comparatively the synthesis of long-chain oxygenated from methanol has attracted relatively low attention because very low selectivity was obtained in previous work,[294] but more recent studies, using decomposed hydrotalcite (MgO/Al_2O_3 mixed oxides) and ZnO promoted Cu as catalysts, concluded that a mixture of alcohols, ketones, aldehydes, esters and ethers, with two to nine carbon atoms (79% of the total oxygenates products) can be obtained.[295] In addition, in this study it is proposed that the first C–C carbon bond formation goes *via* formyl and formaldehyde intermediates.

Homogeneous Rh catalysed methanol carbonylation is an efficient route that exhibits high acetic acid productivity and yields,[296] and this technology until now has been practised commercially by virtually all major acetic acid manufacturers. Inherent to the homogeneous system, however, are drawbacks related to limitations in catalyst solubility and the loss of expensive Rh metal due to precipitation during the separation stages. Accordingly, immobilisation of the Rh complex on a support has been the subject of considerable investigation. Chiyoda

and UOP[297] have jointly developed an improved methanol carbonylation process for the production of acetic acid based on a heterogeneous Rh catalyst system. The heterogeneous catalyst consists of Rh complexed to a novel poly-vinyl pyridine resin, which has a high tolerance to elevated temperatures and pressures.[298] Catalyst stability has been demonstrated in both single-pass and continuous-recycle pilot plants testing under process conditions, low water content, and no Rh or resin makeup. The catalyst exhibited no deactivation after continuous operation for more than 7000 h.

As concluding remarks for this section and of this review chapter, it is clear that very well-established technologies based on metal-supported catalysts for Fischer–Tropsch and for methanol synthesis processes exist, along with very promising research areas, such as hydroformylation and methanol dehydrogenation reactions. For the latter reactions, more research is desirable and the development of new heterogeneous catalysts which are able to control the selectivity in these reactions should be viewed as a desirable scientific challenge. New technologies, such as reactions under supercritical media and the application of membranes for performing C1 chemistry processes are very promising at present. Additionally, many of the ideas introduced in recent years and defined by the Green Chemistry concepts, might be introduced into areas of progress for C1 Chemistry. In this line the recycling and reutilisation of carbon dioxide reactant in C1 processes is a big challenge for the early decades of the 21st century.

References

1. D. Ciuparu, M.R. Lyubovsky, E. Altman, L.D. Pfefferle, A. Datye, *Catal. Rev.* 2002, **44**, 593.
2. A.Y. Kodakov, W. Chu, P. Fongarland, *Chem. Rev.* 2007, **107**, 1692.
3. A.K. Dalai, B.H. Davis, *Appl. Catal. A: Gen.* 2008, **348**, 1.
4. M.A. Vannice, *Catal. Rev.* 1976, **14**, 153.
5. H. Schulz, *Appl. Catal. A: Gen.* 1999, **186**, 3.
6. E. van Steen (Ed.) *Catal. Today* 2002, **71**, IS 3–4.
7. A.A. Adesina, *Appl. Catal. A: Gen.* 1996, **138**, 345.

8. H. Schulz, (Ed.) *Top. Catal.* 2003, **26**, IS 1–4.
9. P.M. Maitlis, R. Quyoum, R. Long, M.L. Turner, *Appl. Catal. A: Gen.* 1999, **186**, 363.
10. R.C. Brady III, R. Petit, *J. Am. Chem. Soc.* 1981, **103**, 1287.
11. B.H. Davis, *Fuel Process. Techn.* 2001, **71**, 157.
12. M. Ojeda, R. Nabar, A.U. Nilekar, A. Ishikawa, M. Mavrikakis, E. Iglesia, *J. Catal.* 2010, **272**, 287.
13. O.R. Inderwildi, S.J. Jenkins, D.A. King, *J. Phys. Chem. C* 2008, **112**, 1305.
14. M. Zhuo, K.F. Tan, A. Borgna, M. Saeys, *J. Phys. Chem. C* 2009, **113**, 8357.
15. J. Cheng, X.-Q. Gong, P. Hu, C.M. Lok, P. Ellis, S. French, *J. Catal.* 2008, **254**, 285.
16. B.C. Shi, B.H. David, *Catal. Today* 2000, **58**, 255.
17. A.P. Steynberg, R.L. Espinoza, B. Jager, A.C. Vosloo, *Appl. Catal. A: Gen.* 1999, **186**, 13.
18. A.P. Steynberg, R.L. Espinoza, B. Jager, A.C. Vosloo, *Appl. Catal. A: Gen.* 1999, **186**, 41.
19. G. Kiss, C.E. Kliewer, G.J. DeMartin, C.C. Culross, J.E. Baumgartner, *J. Catal.* 2003, **217**, 127.
20. A.M. Saib, A. Borgna, J. van Loosdrecht, P.J. van Berge, J.W. Geus, J.W. Niemantsverdriet, *J. Catal.* 2006, **239**, 326.
21. A.M. Saib, A. Borgna, J. van Loosdrecht, P.J. van Berge, J.W. Niemantsverdriet, *J. Phys. Chem. B* 2006, **110**, 8657.
22. G.L. Bezemer, T.J. Remans, A.P. van Bavel, I. Dugulan, *J. Am. Chem. Soc.* 2010, **132**, 8540.
23. A.M. Saib, D.J. Moodley, I.M. Ciobica, M.M. Hauman, B.H. Sigwebela, C.J. Weststrate, J.W. Niemantsverdriet, J. van Loosdrecht, *Catal. Today* 2010, **154**, 271.
24. S. Storsaeter, O. Borg, E.A. Blekkan, A. Holmen, *J. Catal.* 2005, **231**, 405.
25. J.W. Bae, S.M. Kim, S.-J. Park, P.S.S. Prasad, Y.-J. lee, K.-W. Jun, *Ind. Eng. Chem. Res.* 2009, **48**, 3228.
26. E.L. Viljoen, E. van Steen, *Catal. Lett.* 2009, **133**, 8.
27. M.C. Ribeiro, G. Jacobs, B.H. Davis, D.C. Cronauer, A.J. Kropf, C.L. Marshall, *J. Phys. Chem. C* 2010, **114**, 7895.

28. C.J. Bertole, C.A. Mims, G. Kiss, *J. Catal.* 2002, **210**, 84.
29. W. Ngantsoue-Hoc, Y.Q. Zhang, R.J. O'Brien, M.S. Luo, B.H. Davis, *Appl. Catal. A: Gen.* 2002, **236**, 77.
30. S. Krishnamoorthy, M. Tu, M.P. Ojeda, D. Pinna, E. Iglesia, *J. Catal.* 2002, **211**, 422.
31. J.L. Li, G. Jacobs, T. Das, Y.Q. Zhang, B.H. Davis, *Appl. Catal A: Gen.* 2002, **236**, 67.
32. M. Claeys, E. Van Steen, *Catal. Today* 2002, **71**, 419.
33. F.R. van den Berg, M.W.J. Craje, A.M. van der Kraan, J.W. Geus, *Appl. Catal. A: Gen.* 2003, **251**, 347.
34. S. Logdberg, D. Tristantini, O. Borg, L. Ilver, B. Gevert, S. Jaras, E.D. Blekkan, A. Holmen, *Appl. Catal. B: Env.* 2009, **89**, 167.
35. O.O. James, A.M. Mesubi, T.C. Ako, S. Maity, *Fuel Process. Techn.* 2010, **91**, 136.
36. K.-W. Jun, H.-S. Roh, K.-S. Kim, J.-S. Ryu, K.-W. Lee, *Appl. Catal. A: Gen.* 2004, **259**, 221.
37. K.-S. Ha, J.W. Bae, K.-J. Woo, K.-W. Jun, *Environ. Sci. Technol.* 2010, **44**, 1412.
38. H. Schulz, M. Claeys, *Appl. Catal. A: Gen.* 1999, **186**, 91.
39. G.P. Van der Laan, A.A.C.M. Beenackers, *Catal. Rev.* 1999, **41**, 255.
40. I. Puskas, R.S. Hurlbut, *Catal. Today* 2003, **84**, 99.
41. Y. Liu, C. Graffmann and J. Gaube, *Appl. Catal. A: Gen.* 1999, **186**, 109.
42. S.Z. Li, W.P. Ding, G.D. Meitzner, E. Iglesia, *J. Phys. Chem. B* 2002, **106**, 85.
43. J.L. Casci, C.M. Lok, M.D. Shannon, *Catal. Today* 2009, **145**, 38.
44. E. de Smit, B.M. Weckhuysen, *Chem. Soc. Rev.* 2008, **37**, 2758.
45. J.P. den Brejen, P.B. Radstake, G.L. Bezemer, J.H. Bitter, V. Froseth, A. Holmen, K.P. de Jong, *J. Am. Chem. Soc.* 2009, **131**, 7197.
46. E. de Smit, A.M. Beale, S. Nikitenko, B.M. Weckhuysen, *J. Catal.* 2009, **262**, 244.
47. Y. Borodko, G.A. Somorjai, *Appl. Catal. A: Gen.* 1999, **186**, 355.
48. M.E. Dry, *Catal. Today* 1990, **6**, 183.
49. R. Zennaro, M Tagliabue, C.H. Bartholomew, *Catal. Today* 2000, **58**, 309.

50. J.L. Zhang, J.A. Chen, J. Ren, Y.W. Li, Y.H. Sun, *Fuel* 2003, **82**, 581.
51. A. Frydman, D.G. Castner, C.T. Campbell, M. Schmall, *J. Catal.* 1999, **188**, 1.
52. J.L. Li, L.G. Xu, R. Keogh, B. Davis, *Catal. Lett.* 2000, **70**, 127.
53. E. Iglesia, *Appl. Catal. A: Gen.* 1997, **161**, 59.
54. G. Calleja, A. de Lucas, R. van Grieken, J.L. Peña, A. Guerrero-Ruiz, J.L.G. Fierro, *Catal. Lett.* 1993, **18**, 65.
55. A.N. Pour, Y. Zamani, A. Tavasoli, S.M.K. Shahri, S.A. Taheri, *Fuel* 2008, **87**, 2004.
56. A.Y. Khodakov, A. Griboval-Constant, R. Bechara, V.L. Zholobenko, *J. Catal.* 2002, **206**, 230.
57. A.Y. Khodakov, R. Bechara, A. Griboval-Constant, *Appl. Catal. A: Gen.* 2003, **254**, 273.
58. A. Martinez, C. Lopez, F. Marquez, I. Diaz, *J. Catal.* 2003, **220**, 486.
59. Y. Ohtsuka, Y. Takahashi, M. Noguchi, T. Arai, S. Takasaki, N. Ysubouchi, Y. Wang, *Catal. Today* 2004, **89**, 419.
60. A. Martinez, S. Valencia, R. Murciano, H.S. Cerqueira, A.F. Costa, E.F.S. Aguiar, *Appl. Catal. A: Gen.* 2008, **346**, 117.
61. J. Panpranot, S. Kaewkun, P. Praserthdam, J.G Goodwin, *Catal. Lett.* 2003, **91**, 95.
62. J. Panpranot, J.G. Goodwin, A. Sayari, *Catal. Today* 2002, **77**, 269.
63. M. Johns, P. Landon, T. Alderson, G.J. Hutchings, *Chem. Commun.* 2001, 2454.
64. Y. Yang, H.-W. Xiang, Y.-Y. Xu, L. Bai, Y.-W. Li, *Appl Catal. A: Gen.* 2004, **266**, 181.
65. G. Yu, B. Sun, Y. Pei, S. Xie, S. Yan, M. Qiao, K. Fan, X. Zhang, B. Zong, *J. Am. Chem. Soc.* 2010, **132**, 935.
66. L.R. Radovic, F. Rodriguez-Reinoso, *Chem. Phys. Carbon* 1997, **25**, 243.
67. G. Jiao, Y. Ding, H. Zhu, X. Li, J. Li, R. Lin, W. Dong, L. Gong, Y. Pei, Y. Lu, *Appl. Catal. A: Gen.* 2009, **364**, 137.
68. G.L. Bezemer, P.B. Radstake, U. Falke, H. Oosterbeek, H.P.C.E. Kuipers, A.J. van Dillen, K.P. de Jong, *J. Catal.* 2006, **237**, 152.
69. G.L. Bezemer, P.B. Radstake, V. Koot, A.J. van Dillen, J.W. Geus, K.P. de Jong, *J. Catal.* 2006, **237**, 291.

70. G.L. Bezemer, J.H. Bitter, H.P.C.E. Kuipers, H. Oosterbeek, J.E. Holewijn, F. Kaptein, A.J. van Dillen, K.P. de Jong, *J. Am. Chem. Soc.* 2006, **128**, 3956.
71. E. Van Steen, F.F. Prinsloo, *Catal. Today* 2002, **71**, 327.
72. R.M.M. Abbaslou, A. Tavasoli, A.K. Dalai, *Appl. Catal. A: Gen.* 2009, **355**, 33.
73. R.M.M. Abbaslou, A. Tavasoli, J. Soltan, A.K. Dalai, *Appl. Catal. A: Gen.* 2009, **367**, 47.
74. M. Trepanier, A.K. Dalai, N. Abatzoglou, *Appl. Catal. A: Gen.* 2010, **374**, 79.
75. A. Tavasoli, M. Trepanier, R.M.M. Abbaslou, A.K. Dalai, N. Abatzoglou, *Fuel Process. Techn.* 2009, **90**, 1486.
76. J.C. Kang, S.L. Zhang, Q.H. Zhang, Y. Wang, *Angew. Chem. Int. Ed.* 2009, **48**, 2565.
77. M.C. Bahome, L.J. Jewell, D. Hildebrandt, D. Glasser, N.J. Coville, *Appl. Catal. A: Gen.* 2005, **287**, 60.
78. W. Chen, Z. Fan, X. Pan, X. Bao, *J. Am. Chem. Soc.* 2008, **130**, 9414.
79. R.M.M. Abbaslou, J. Soltan, A.K. Dalai, *Appl. Catal. A: Gen.* 2010, **379**, 129.
80. B.H. Davis, *Top. Catal.* 2005, **32**, 143.
81. S.-J. Park, J.-W. Bae, J.-H. Oh, K.V.R. Chary, P.S.S. Prasad, K.-W. Jun, Y.-W. Rhee, *J. Mol. Catal. A: Chem.* 2009, **298**, 81.
82. X.W. Huang, C.B. Robert, *Fuel Process. Techn.* 2003, **83**, 81.
83. G. Jacobs, K. Chaudhari, D. Sparks, Y.Q. Zhang, B.C. Shi, R. Spicer, T.K. Das, J.L. Li, B.H. Davis, *Fuel* 2003, **82**, 1251.
84. N. Tsubaki, K. Yoshii, K. Fujimoto, *J. Catal.* 2002, **207**, 371.
85. K. Fujimoto, L. Fan, K. Yoskii, *Top. Catal.* 1995, **2**, 259.
86. R.M.M. Abbaslou, J.S.S. Mohammadzadeh, A.K. Dalai, *Fuel Process. Techn.* 2009, **90**, 849.
87. N.O. Elbashir, D.B. Bukur, E. Durham, C.R. Roberts, *AIChE J.* 2010, **56**, 997.
88. F. Kapteijn, R.M. de Deugd, J.A. Moulijn, *Catal. Today* 2005, **105**, 350.
89. C.G. Visconti, E. Tronconi, L. Lierri, G. Groppi, P. Forzatti, C. Cristiani, R. Zennaro, S. Rossini, *Appl. Catal. A: Gen.* 2009, **370**, 93.

90. A.A. Khassin, *NATO Science Series II: Mathematics, Physics, Chemistry* 2005, **191**, 249–271.
91. F.A.N. Fernandes, *J. Nat. Gas Chem.* 2007, **16**, 107.
92. M.P. Rohde, G. Schaub, S. Khajavi, J.C. Jansen, F. Kapteijn, *Micropor. Mesopor. Mat.* 2008, **115**, 123.
93. I. Aartun, H.J. Venvik, A. Holmen, P. Pfeifer, O. Gorke, K. Schubert, *Catal. Today* 2005, **110**, 98.
94. L. Yu, R. Nassar, J. Fang, D. Kuila, K. Varahramyan, *Chem. Eng. Commun.* 2008, **195**, 745.
95. G. Arzamendi, P.M. Dieguez, M. Montes, J.A. Odriozola, E.F. Sousa-Aguiar, L.M. Gandia, *Chem. Eng. J.* 2010, **160**, 915.
96. A.C. Vosloo, *Fuel Process. Techn.* 2001, **71**, 149.
97. M. Johns, P. Collier, M.S. Spencer, T. Alderson, G.J. Hutchings, *Catal. Lett.* 2003, **90**, 187.
98. C.N. Satterfield, *Heterogeneous Catalysis in Industrial Practice*, 2nd Edition, McGraw-Hill, New York, 1991.
99. H.H. Kung, *Catal. Rev.* 1980, **22**, 235.
100. K. Klier, *Adv. Catal.* 1982, **31**, 243.
101. X.-M. Liu, G.Q. Lu, Z.-F. Yan, J. Beltramini, *Ind. Eng. Chem. Res.* 2003, **42**, 6518.
102. V.E. Ostrovskii, *Catal. Today* 2002, **77**, 141.
103. B. Sakakini, J. Tabatabaei, M.J. Watson, K.C. Waugh, F.W. Zeicael, *Faraday Discussion* 1996, **105**, 369.
104. G.C. Chinchen, K. Mansfield, M.S. Spencer, *ChemTech.* 1990, 692.
105. A. Ya. Rozovskii, G.I. Lin, *Top. Catal.* 2003, **22**, 137.
106. J.G. Wu, M. Saito, M. Takeuchi, T. Watanabe, *Appl. Catal. A: Gen.* 2001, **218,** 235.
107. N. Nomura, T. Tagawa, S. Goto, *Appl. Catal. A: Gen.* 1998, **166**, 321.
108. Sh. Fujita, M. Usui, H. Ito, N. Takezava, *J. Catal.* 1995, **157**, 403.
109. J.T. Li, W.D. Zhang, L.Z. Gao, P.Y. Gu, K.Q. Sha, H.L. Wan, *Appl. Catal. A: Gen.* 1997, **165**, 411.
110. I. Nakamura, H. Nakano, T. Fujitani, T. Uchijima, J. Nakamura, *Surf. Sci.* 1998, **404**, 92.
111. Q. Sun, C.W. Liu, W. Pan, Q.M. Zhu, J.F. Deng, *Appl. Catal. A: Gen.* 1998, **171**, 301.
112. I.A. Fisher, A.T. Bell, *J. Catal.* 1998, **178**, 153.

113. E.E. Ortelli, J.M. Weigel, A. Wokaun, *Catal. Lett.* 1998, **54**, 41.
114. J. Weigel, C. Frohlich, A. Baiker, A. Wokaum, *Appl. Catal. A: Gen.* 1996, **29**, 140.
115. M. Kilo, J. Weigel, A. Wokaun, R.A. Koeppel, A. Stoeckli, A. Baiker, *J. Mol. Catal. A: Chem.* 1997, **126**, 169.
116. H.Y. Chen, L. Chen, J. Lin, K.L. Tan, J. Li, *J. Phys. Chem. B* 1998, **102**, 1994.
117. F. Lepeltier, P. Chaumette, J. Saussey, M.M. Bettahar, J.C. Lavalley, *J. Mol. Catal. A: Chem.* 1998, **132**, 91.
118. W.P.A. Jansen, J. Beckers, J.C. Van der Heuvel, A.W.D. Van der Gon, A. Bliek, H.H. Brongersma, *J. Catal.* 2002, **210**, 229.
119. W.J. Shen, Y. Ichihashi, Y. Matsumura, *Catal. Lett.* 2002, **83**, 33.
120. M.S. Spencer, *Catal. Lett.* 1998, **50**, 37.
121. M.S. Spencer, *Top. Catal.* 1999, **8**, 259.
122. T.C. Schilke, I.A. Fisher, A.T. Bell, *J. Catal.* 1999, **184**, 144.
123. K.D. Jung, A.T. Bell, *J. Catal.* 2000, **193**, 207.
124. Y. Kanai, T. Watanabe, T. Fujitani, M. Saito, J. Nakamura, T. Uchijima, *J. Catal.* 1996, **160**, 65.
125. J.C. Frost, *Nature* 1988, **334**, 577.
126. M. Kurtz, N. Bauer, C. Buscher, H. Wilmer, O. Hinrichsen, R. Becker, S. Rabe, K. Merz, M. Driess, R.A. Fischer, M. Muhler, *Catal. Lett.* 2004, **92**, 49.
127. K. Omata, M. Hashimoto, Y. Watanabe, T. Umegaki, M. Yamada, *J. Jpn. Petrol. Inst.* 2003, **46**, 383.
128. K. Omata, Y. Watanabe, M. Hashimoto, T. Umegaki, M. Yamada, *J. Jpn. Petrol. Inst.* 2003, **46**, 387.
129. B.J. Liaw, Y.Z. Chen, *Appl. Catal. A: Gen.* 2001, **206**, 245.
130. M. Kilo, J. Weigel, A. Wokaun, R.A. Koepepel, A. Stoeckli, A. Baiker, *J. Mol. Catal. A: Chem.* 1997, **126**, 169.
131. J. Toyir, P.R. de la Piscina, J.L.G. Fierro, N. Homs, *Appl. Catal. B: Env.* 2001, **29**, 207.
132. H.B. Chen, D.W. Liao, L.J. Yu, Y.J. Lin, H.B. Zhang, K.R. Tsai, *Appl. Surf. Sci.* 1999, **147**, 85.
133. I. Ma, M.S. Wainwright, *Appl. Catal. A: Gen.* 1999, **187**, 89.
134. J.Y. Liu, J.L. Shi, D.H. He, *Appl. Catal. A: Gen.* 2001, **218**, 113.
135. K.T. Jung, A.T. Bell, *Catal. Lett.* 2002, **80**, 63.

136. M. Gupta, J.J. Spivey, *Catal. Today* 2009, **147**, 126.
137. Yu A. Ryndin, R.F. Hicks, A.T. Bell, Yu, I. Yermakov, *J. Catal.* 1981, **70**, 287.
138. W.J. Shen, Y. Ichihashi, H. Ando, M. Okumura, M. Haruta, Y. Matsumura, *Appl. Catal. A: Gen.* 2001, **217**, 165.
139. W.J. Shen, A. Kobayashi, Y. Ichihashi, Y. Matsumura, M. Haruta, *Catal. Lett.* 2001, **73**, 161.
140. M.N. Berube, B. Sung, M.A. Vannice, *Appl. Catal.* 1987, **31**, 133.
141. W.J. Shen, M. Okumura, Y. Matsumura, *Appl. Catal. A: Gen.* 2001, **213**, 225.
142. S.H. Ali, J.G. Goodwin Jr., *J. Catal.* 1998, **176**, 3.
143. A. Gotti, R. Prins, *J. Catal.* 1998, **175**, 302.
144. J.-P. Lange, *Catal. Today* 2001, **64**, 3.
145. R.P.W.J. Struis, S. Stucki, M. Wiedorn, *J. Membr. Sci.* 1996, **113**, 93.
146. B. Sea, K.H. Lee, *React. Kinet. Catal. Lett.* 2003, **80**, 33.
147. G. Barbieri, G. Mariagliano, G. Goléeme, E. Drioli, *Chem. Eng. J.* 2002, **85**, 53.
148. P. Reubroycharoen, Y. Yoneyama, T. Vitidsant, N. Tsubaki, *Fuel* 2003, **82**, 2255.
149. P. Reubroycharoen, T. Vitidsant, K. Asami, Y. Yoneyama, N. Tsubaki, *Catal. Commun.* 2003, **4**, 461.
150. P. Forzatti, E. Tronconi, I. Pasquon, *Catal. Rev.* 1991, **33**, 109.
151. J.A. Dalmon, P. Chaumette, C. Mirodatos, *Catal. Today* 1992, **15**, 101.
152. R.G. Herman, *Catal. Today* 2000, **55**, 233.
153. A.M. Hilmen, M.T. Xu, M.J.L. Gines, E. Iglesia, *Appl. Catal. A: Gen.* 1998, **169**, 355.
154. T. Fukushima, M. Ichikawa, S. Matsushita, T. Tanaka, T. Saito, *J. Chem. Soc. Chem. Commun.* 1985, 1209.
155. Z.R. Li, Y.L. Fu, J. Bao, M. Jiang, T.D. Hu, T. Liu, Y.N. Xie, *Appl. Catal. A: Gen.* 2001, **220**, 21.
156. Z.R. Li, Y.L. Fu, M. Jiang, T.D. Hu, T. Liu, Y.N. Xie, *J. Catal.* 2001, **199**, 155.
157. I. Boz, *Catal. Lett.* 2003, **87**, 187.
158. N. Zhao, R. Xu, W. Wei, Y.H. Sun, *React. Kinet. Catal. Lett.* 2002, **75**, 297.
159. K. Klier, A. Beretta, Q. Sun, O.C. Feely, R.G. Herman, *Catal. Today* 1997, **36**, 3.

160. M.J.L. Gines, E. Iglesia, *J. Catal.* 1998, **176**, 155.
161. K.J. Smith, C.-W. Young, R.G. Herman, K. Klier, *Ind. Eng. Chem. Res.* 1991, **30**, 61.
162. M. Ichikawa, T. Fukushima, K. Shikakura, *Proc. 8th Int. Congr. Catal.* 1984, **2**, 69.
163. Y. Wang, J. Li, W. Mi, *React. Kinet. Catal. Lett.* 2002, **76**, 141.
164. H. Ma, Z. Yuan, Y. Wang, X. Bao, *Surf. Interface Anal.* 2001, **32**, 224.
165. H.M. Yin, Y.J. Ding, H.Y. Luo, L. Yan, T. Wang, L.W. Lin, *Energ. Fuel* 2003, **17**, 1401.
166. S.I. Ito, T. Fujimori, K. Nagaashima, K. Yuzaki, K. Unimori, *Catal. Today* 2000, **57**, 247.
167. L.M. Tau, R. Robinson, R.D. Ross, B.H. Davis, *J. Catal.* 1987, **105**, 335.
168. H. Orita, S. Naito, K. Tamaru, *J. Chem. Soc. Chem. Commun.* 1984, 150.
169. S.D. Jackson, B.J. Branddreth, D. Winstanbey, *J. Catal.* 1987, **106**, 464.
170. M. Bowker, *Catal. Today* 1992, **15**, 77.
171. Y. Wang, H. Luo, D. Liang, X. Bao, *J. Catal.* 2000, **196**, 46.
172. Ph. Courty, D. Durand, E. Freund, A. Sugier, *J. Mol. Catal.* 1982, **17**, 241.
173. A.D. Aquino, A.J.G. Cobo, *Catal. Today* 2001, **65**, 209.
174. X. Xiaoding, E.B.M. Doesburg, J.J.F. Scholten, *Catal. Today* 1987, **2**, 125.
175. G.G. Volkova, T.M. Yurieva, L.M. Plyasova, M.I. Naumova, V.I. Zaikovskii, *J. Mol. Catal. A: Chem.* 2000, **158,** 389.
176. X. Dong, X.-L. Liang, H.-Y. Li, G.-D. Lin, P. Zhang, H.-B. Zhang, *Catal. Today* 2009, **147**, 158.
177. X.-M. Wu, Y.-Y. Guo, G.-D. Lin, P. Zhang, X. Dong, H.-B. Zhang, *Appl Catal. A: Gen.* 2008, **340**, 87.
178. X. Subramani, S.K. Gangwal, *Energy Fuel* 2008, **22**, 814.
179. B. Xu, R. Yang, F. Meng, P. Reubroycharoen, T. Vitidsant, Y. Zhang, Y. Yoneyama, N. Tsubaki, *Catal. Surv. Asia* 2009, **13**, 147.
180. B. Hu, K. Fujimoto, *Appl. Catal. B: Env.* 2010, **95**, 208.
181. B. Hu, Y. Yamaguchi, K. Fujimoto, *Catal. Commun.* 2009, **10**, 1620.
182. J. Bao, Z. Li, Y. Zhang, N. Tsubaki, *Catal. Commun.* 2009, **9**, 913.

183. Y. Luan, H. Xu, C. Yu, W. Li, S. Hou, *Catal. Lett.* 2008, **125**, 271.
184. L. Sandstrom, J. Lindmark, J. Hedlund, *J. Membr. Sci.* 2010, **360**, 265.
185. J.M. Christensen, P.M. Mortensen, R. Trane, P.A. Jensen, A.D. Jensen, *Appl. Catal. A: Gen.* 2009, **366**, 29.
186. T. Inui, M. Funabiki, Y. Takegami, *J. Chem. Soc. Faraday I* 1980, **76**, 2237.
187. Y.Q. Zhang, G.G. Jacobs, D.S. Sparks, M.E. Dry, B. Davis, *Catal. Today* 2002, **71**, 411.
188. M. Fujiwara, R. Kieffer, H. Ando, Y. Souma, *Appl. Catal. A: Gen.* 1995, **121**, 113.
189. T. Inui, *Catal. Today* 1996, **29**, 329.
190. Y. Kou, Z. Suo, J. Niu, W. Zhang, H. Wang, *Catal. Lett.* 1995, **35**, 271.
191. R.A. Fiato, E. Iglesia, G.W. Rice, S.L. Soled, in *Advances in Chemical Conversions for Mitigating Carbon Dioxide*, Eds.: T. Inui, M. Anpo, K. Izui, S. Yanagida, T. Yamaguchi, Elsevier, Amsterdam, 1998, 339.
192. N. Ikehara, K. Hara, A. Satsuma, T. Hattori, Y. Murakami, *Chem. Lett.* 1994, 263.
193. S.V. Greding, R.A. Koeppel, A. Baiker, *J. Chem. Soc. Chem. Commun.* 1995, 73.
194. A. Fujishima, D.A. Tryk, T.N. Rao, in *Advances in Chemical Conversions for Mitigating Carbon Dioxide*, Eds.: T. Inui, M. Anpo, K. Izui, S. Yanagida, T. Yamaguchi, Elsevier, Amsterdam, 1998, 31.
195. G.D. Zakumbaeva, L.B. Shapovalova, I.A. Shlygina, in *Advances in Chemical Conversions for Mitigating Carbon Dioxide*, Eds.: T. Inui, M. Anpo, K. Izui, S. Yanagida, T. Yamaguchi, Elsevier, Amsterdam, 1998, 171.
196. A. Maroto, I. Rodríguez-Ramos, A. Guerrero-Ruiz, J. Llorca, P.R. de la Piscina, N. Homs, *Appl. Organom. Chem.* 2000, **14**, 783.
197. Y. Souma, M. Fujiwara, R. Kieffer, H. Ando, Q. Xu, in *Advances in Chemical Conversions for Mitigating Carbon Dioxide*, Eds.: T. Inui, M. Anpo, K. Izui, S. Yanagida, T. Yamaguchi, Elsevier, Amsterdam, 1998, 327.
198. M.C.J. Bradford, M.A. Vannice, *Catal. Rev.* 1999, **41**, 1.
199. L. Guczi, A. Erdohelyi, J. Rostrup-Nielsen (Eds.) *Appl. Catal. A: Gen.* 2003, **255**, IS 1.
200. J.R. Rostrup-Nielsen, J.-H. Bak-hansen, *J. Catal.* 1993, **144**, 38.
201. H. Papp, P. Schuler, Q. Zhang, *Top. Catal.* 1996, **3**, 299.

202. J.S.H.Q. Perera, J.W. Couves, G. Sankar, J.M. Thomas, *Catal. Lett.* 1991, **11**, 219.
203. P.D.F. Vernon, M.L.H. Green, A.K. Cheetham, A.T. Aschcroft, *Catal. Today* 1992, **13**, 417.
204. Z.L. Zhang, V.A. Tsipouriari, A.M. Festathiou, X.E. Verykios, *J. Catal.* 1996, **158**, 51.
205. J.H. Bitter, K. Seshan, J.A. Lercher, *J. Catal.* 1976, **171**, 279.
206. P. Ferreira-Aparicio, A. Guerrero-Ruiz, I. Rodríguez-Ramos, *Appl. Catal. A: Gen.* 1998, **170**, 177.
207. X.E. Verykios, *Appl. Catal. A: Gen.* 2003, **255**, 101.
208. A. Guerrero-Ruiz, I. Rodríguez-Ramos, A. Sepúlveda-Escribano, *Chem. Commun.* 1993, 487.
209. K. Nagaoka, K. Takanabe, K. Aika, *Appl. Catal. A: Gen.* 2003, **255**, 13.
210. A.M. Efstathiou, A. Kladi, V.A. Tsipouriari, X.E. Verykios, *J. Catal.* 1996, **158**, 64.
211. M.M.V.M. Souza, M. Schmal, *Catal. Lett.* 2003, **91**, 11.
212. F.B. Noroña, A. Shamsi, C. Taylor, E.C. Fendley, S. Stagg-Williams, D.E. Resasco, *Catal. Lett.* 2003, **90**, 13.
213. S. Menad, P. Ferreira-Aparicio, O. Cherifi, A. Guerrero-Ruiz, I. Rodríguez-Ramos, *Catal. Lett.* 2003, **89**, 63.
214. Y. Schuurman, C. Mirodatos, P. Ferreira-Aparicio, I. Rodríguez-Ramos, A. Guerrero-Ruiz, *Catal. Lett.* 2000, **66**, 33.
215. Z.W. Liu, H. S. Roh, K.W. Jun, H.S. Potdar, M. Ji, *J. Ind. Eng. Chem.* 2003, **9**, 576.
216. H.S. Roh, Z.W. Liu, H.S. Potdar, J.W. Kim, K.W. Jun, *J. Ind. Eng. Chem.* 2003, **9**, 762.
217. H.S. Roh, K.W. Jun, S.E. Park, *Appl. Catal. A: Gen.* 2003, **251**, 275.
218. P. Ferreira-Aparicio, I. Rodríguez-Ramos, J.A. Anderson, Guerrero-Ruiz, *Appl. Catal. A: Gen.* 2000, **202**, 183.
219. P. Ferreira-Aparicio, C. Marquez-Alvarez, I. Rodríguez-Ramos, Y. Schuurman, A. Guerrero-Ruiz, C. Mirodatos, *J. Catal.* 1999, **184**, 202.
220. H.M. Swaan, V.C.H. Kroll, G.A. Martín, C. Mirodatos, *Catal. Today* 1994, **21**, 571.
221. S. Teuner, *Hydroc. Process.* 1987, **66**, 52.
222. N.J. Armor, *J. Membr. Sci.* 1998, **147**, 217.
223. J. Xu, G.F. Froment, *AIChE J.* 1989, **35**, 88.

224. J.R. Grace, X. Li, J. Lim, *Catal. Today* 2001, **64**, 141.
225. A.K. Prahbu, S.T. Oyama, *J. Membr. Sci.* 2000, **176**, 233.
226. A.K. Prahbu, R. Radhakrishnan, S.T. Oyama, *Appl. Catal. A: Gen.* 1999, **183**, 241.
227. B.S. Liu, C.T. Au, *Catal. Lett.* 2001, **77**, 67.
228. P. Ferreira-Aparicio, I. Rodríguez-Ramos, Guerrero-Ruiz, *Appl. Catal. A: Gen.* 2002, **237**, 239.
229. J. Llorca, P. Ramizez de la Piscina, J.L.G. Fierro, J. Sales, N. Homs, *J. Mol. Catal. A: Gen.* 1997, **118**, 101.
230. J. Llorca, N. Homs, J. Sales, P. Ramizez de la Piscina, *J. Catal.* 2001, **197**, 220.
231. P.G. Jessop, T. Ikariya, R. Noyari, *Nature* 1994, **368**, 231.
232. X.B. Lu, X.J. Feng, R. He, *Appl. Catal. A: Gen.* 2002, **234**, 25.
233. G. Centi, S. Perathoner, *Catal. Today* 2009, **148**, 191.
234. Y. Zhang, G. Jacobs, D.E. Sparks, M.E. Dry, B.H. Davis, *Catal. Today* 2002, **71**, 411.
235. T. Riedel, M. Claeys, H. Schulz, G. Schaub, S.-S. Nam, K.-W. Jun, M.-J. Choi, G. Kishan, K.-W. Lee, *Appl. Catal. A: Gen.* 1999, **186**, 201.
236. M.P. Rohde, D. Unruh, G. Schaub, *Ind. Eng. Chem. Res.* 2005, **44**, 49653.
237. T.A. Kainulainen, M.K. Niemelä, A.O.I. Krause, *J. Mol. Catal. A: Chem.* 1997, **122**, 39.
238. M. Tada, K. Motokura, Y. Iwasawa, *Top. Catal.* 2008, **48**, 32.
239. J.M. Coronado, F. Coloma, J.A. Anderson, *J. Mol. Catal. A: Chem.* 2000 **154**, 143.
240. L. Balzano, D. Cauzzi, C. Mucchino, G. Predieri, A. Tiripicchio, *J. Mol. Catal. A: Chem.* 2003, **204**, 737.
241. Z. Ma, X. Liu, G. Yang, C. Liu, *Fuel Process. Techn.* 2009, **90**, 1241.
242. C. Disser, C. Muennich, G. Luft, *Appl. Catal. A: Gen.* 2005, **296**, 201.
243. M. Lenarda, R. Ganzerla, L. Riatto, L. Storaro, *J. Mol. Catal. A: Chem.* 2002, **187**, 129.
244. N. Yoneda, Y. Nakagawa, T. Mimami, *Catal. Today* 1997, **36**, 357.
245. J.N.H. Reek, D. De Groot, G.E. Oosterom, P.C.J. Kamer, P.W.N.M. van Leewen, *Comptes Rendus Chimie* 2003, **6**, 1061.
246. R. Abu-Reziq, H. Alper, D. Wang, M.L. Post, *J. Am. Chem. Soc.* 2006, **128**, 5279.

247. K. Mukhopadhyay, A.B. Mandale, R.V. Chaudhari, *Chem. Mater.* 2003, **15**, 1766.
248. R. Abu-Reziq, D. Avnir, I. Miloslavski, H. Schumann, J. Blum, *J. Mol. Catal. A: Chem.* 2002, **185**, 179.
249. F. Gelman, D. Avnir, H. Schumann, J. Blum, *J. Mol. Catal. A: Chem.* 2001, **171**, 191.
250. X. Liu, B. Hu, K. Fujimoto, M. Haruta, M. Tokunaga, *Appl. Catal. B: Env.* 2009, **92**, 411.
251. L. Oresmaa, M.A. Moreno, M. Jakonen, S. Suvanto, M. Haukka, *Appl. Catal. A: Gen.* 2009, **353**, 113.
252. T.A. Kainulainen, M.K. Niemela, A.O.I. Krause, *Catal. Lett.* 1998, **53**, 97.
253. L. Huang, J.C. Wu, S. Kawi, *J. Mol. Catal. A: Chem.* 2003, **206**, 371.
254. J.A. Bae, K.-C. Song, J.-K. Jeon, Y.S. Ko, Y.-K. Park, J.-H. Yim, *Micropor. Mesopor. Mat.* 2009, **123**, 289.
255. L. Yan, Y.J. Ding, L.W. Lin, H.J. Zhu, H.M. Yin, X.M. Li, Y. Lu, *J. Mol. Catal. A: Chem.* 2009, **300**, 116.
256. P. Li, S. Kawi, *J. Catal.* 2008, **257**, 23.
257. P. Li, S. Kawi, *Catal. Today* 2008, **131**, 61.
258. P. Li, W. Thitsartarn, S. Kawi, *Ind. Eng. Chem. Res.* 2009, **48**, 1824.
259. H.R. Gao, R.J. Angelici, *J. Mol. Catal. A: Chem.* 1999, **145**, 83.
260. S.A. Hedrick, S.S.C. Chuang, A. Pant, A.G. Dastidar, *Catal. Today* 2000, **55**, 247.
261. D. Han, X. Li, H. Zhang, Z. Liu, J. Li, C. Li, *J. Catal.* 2006, **243**, 318.
262. G. Zinder, A. Tadd, M.A. Abraham, *Ind. Eng. Chem. Res.* 2001, **40**, 5317.
263. S. Dharmidhikari, M.A. Abraham, *J. Supercritical Fluids* 2000, **18**, 1.
264. S.-I. Fujita, S. Akihara, S. Fujisawa, M. Arai, *J. Mol. Catal. A: Chem.* 2007, **268**, 244.
265. J.H. Lunsford, *Catal. Today* 2000, **63**, 165.
266. C. Elmasides, D.I. Kondarides, W. Grünert, X. Verykios, *J. Phys. Chem. B* 1999, **103**, 5227.
267. A. Guerrero-Ruiz, P. Ferreira-Aparicio, B. Bachiller-Baeza, I. Rodríguez-Ramos, *Catal. Today* 1998, **46**, 99.
268. F.A. Silva, J.A.C. Ruiz, K.R. de Souza, J.M.C. Bueno, L.V. Mattos, F.B. Noronha, C.E. Hori, *Appl. Catal. A: Gen.* 2009, **364**, 122.

269. S. Cimino, R. Torbati, L. Lisis, G. Russo, *Appl. Catal. A: Gen.* 2009, **360**, 43.
270. T.P. Maniecki, K. Bawolak-Olczak, P. Mierczynski, W. Maniukiewicz, W. K. Jozwiak, *Chem. Eng. J.* 2009, **154**, 142.
271. H. Liu, D. He, *J. Phys. Chem. C* 2010, **114**, 13716.
272. P. Pietruszka, M. Heintze, *Catal. Today* 2004, **90**, 151.
273. L. Chen, X.-W. Zhang, L. Huang, L.-C. Lei, *Chem. Eng. Processing* 2009, **48**, 1333.
274. S.M. Liu, X.Y. Tan, K. Li, R. Hughes, *Catal. Rev.* 2001, **43**, 147.
275. C.A. Guerrero-Fajardo, D. Niznansky, Y. Nguyen, C. Courson, A.-C. Roger, *Catal. Commun.* 2008, **9**, 864.
276. R. Palkovits, C. von Malotki, M. Baumgarten, K. Mullen, C. Baltes, M. Antonietti, P. Kuhn, J. Weber, A. Thomas, F. Schuth, *Chem. Sus. Chem.* 2010, **3**, 277.
277. K.T. Tabata, Y. Teng, T. Takemoto, T. Suzuki, M.A. Banares, M.A. Pena, J.L.G. Fierro, *Catal. Rev.* 2002, **44**, 1.
278. K. Otsuka, Y. Wang, *Appl. Catal. A: Gen.* 2001, **222**, 145.
279. K.P. de Jong, J.W. Geus, *Catal. Rev.* 2000, **42**, 481.
280. T.V. Choudhary, E, Aksoylu, D.W. Goodman, *Catal. Rev.-Sci. Eng.* 2003, **45**, 151.
281. M. Stöcker, *Micropor. Mesopor. Mat.* 1999, **29**, 3.
282. T.P. Minyukova, I.I. Simentsova, A.V. Khasin, N.V. Shtertser, N.A. Baronskaya, A.A. Kassin, T.M. Yurieva, *Appl. Catal. A: Gen.* 2002, **237**, 171.
283. K. Hashimot, N. Toukai, *J. Mol. Catal. A: Chem.* 2002, **186**, 79.
284. E.D. Guerreiro, O.F. Gorriz, G. Larsen, L.A. Arrua, *Appl. Catal. A: Gen.* 2000, **204**, 33.
285. R. Zhang, Y.H. Sun, S.Y. Peng, *Fuel* 2002, **81**, 1619.
286. E.H. Shreiber, M.D. Rodees, G.W. Roberts, *Appl. Catal. A: Env.* 1999, **23**, 9.
287. T. Tsoncheva, T. Venkov, M. Dimitrov, C. Minchev, K. Hadjiivanov, *J. Mol. Catal. A: Chem.* 2004, **209**, 125.
288. N. Iwasa, N. Takezawa, *Top. Catal.* 2003, **22**, 215.
289. N. Iwasa, T. Mayanagi, N. Ogawa, K. Sakata, N. Takezawa, *Catal. Lett.* 1998, **54**, 119.

290. S.V. Gorshkow, G.I. Lin, A.Y. Rozovskii, Y.M. Serov, S.J. Uhm, *Kinetics and Catalysis* 1999, **40**, 93.
291. S.T. King, M.E. Jones, M.M. Olken, US Patent No. 5,391,803, 1995.
292. S.T. King, *J. Catal.* 1996, **161,** 530.
293. S.A. Anderson, T.W. Root, *J. Catal.* 2003, **217**, 396.
294. L. Lietti, E. Tronconi, P. Forzatti, *Appl. Catal.* 1991, **70**, 73.
295. T.C. Hsiao, S.D. Lin, *Catal. Lett.* 2007, **119**, 72.
296. N. Yoneda, S. Kusano, M. Yasui, P. Pujado, S. Wilcher, *Appl. Catal. A: Gen.* 2001, **221**, 253.
297. European Chemical News, 26 May–1 June, 1997.
298. N. Yoneda, T. Minami, J. Weiszmann, B. Spehlmann, *Proceedings of the Third Tokyo Conference on Advanced Catalytic Science and Technology* 1998, 93.

CHAPTER 8

SUPPORTED METALS IN THE PRODUCTION OF HYDROGEN

J.L.G. Fierro, M.A. Peña and M.C. Alvarez-Galvan

Instituto de Catálisis y Petroleoquímica, CSIC, C/Marie Curie, Cantoblanco, 28049 Madrid, Spain

8.1 Introduction

Hydrogen is foreseen to become a major source of a non-polluting, inexhaustible, efficient and cost-attractive energy in the near future. Hydrogen gas is a clean energy vector because the chemical energy stored in the H–H bond is released when it combines with molecular oxygen yielding only water as the reaction product. It is currently produced by the steam reforming of methane, naphtha, heavy oil, methanol and coal.[1–3] Steam methane reforming (SMR) is the largest and most economical process used for the production of hydrogen. Although SMR is a complex process, involving many different catalytic steps, as long as natural gas (or CH_4) and hydrocarbon fuels remain at low or even moderate cost, SMR will continue to be the technology of choice for massive H_2 production. After several decades of improvements in catalyst technology, substantial improvements have been introduced. However, this area remains fertile ground for further improvement. As can be seen in the following sections, important recent approaches to the production of hydrogen involve methane decomposition, partial oxidation and the CO_2 reforming of methane and the reforming of low-molecular weight alcohols such as methanol and ethanol. There are a few relatively complete reviews that address this field.[1–4]

The design of suitable metal catalysts for methane decomposition and for the reforming reactions of hydrocarbons and alcohols remains a classical concern. Much work has been devoted to the design of robust and active catalysts and the development of innovative technologies for reforming reactions within the framework of fuel-cell combustion in power generation units. Current interest in this area can be gauged from the 1,400 plus papers/patents published in the field over the past four years. Although many reviews on this topic are available in the literature, the most recent only address certain catalyst systems individually. The main objective of the present contribution report is to review the various catalysts employed in the production of hydrogen from different H containing sources and to identify the most important aspects involved in the respective catalytic transformations from the wealth of information available in the literature. Greater emphasis will be placed on recent literature addressing reforming catalysts. The catalyst systems used in reforming reactions generally consist of fine metal particles deposited on an appropriate substrate. The large number of permutations and combinations used in catalyst systems for decomposition and/or reforming reactions makes it difficult to categorise them in a systematic way. Further complexity arises because certain components, which are themselves active in other kinds of reactions, such as combustion, coupling, or homologation reactions, may be used as reforming catalysts when subjected to specific activation pre-treatments or to modification with certain additives. In this chapter, a condensed overview of the different options and technologies available for the large-scale production of hydrogen is offered. Since catalysis is the key ingredient in most of the processes involved in hydrogen production, another aim is to describe to readers the role played by heterogeneous metal catalysts in this fascinating and rapidly expanding field.

8.2 Methane Conversion

Natural gas, which mainly consists of methane, is a hydrocarbon feedstock of increasing interest owing to its versatility for the production

of valuable chemicals *via* syngas ($CO + H_2$), as described in Chapter 7 ('Supported Metal-Catalysed C1 Chemistry'). Over the past few years, this kind of technology has been designated GTL (Gas-To-Liquids). The proven reserves are currently higher than those of petroleum, and the existence of methane hydrates in sea-floor sediments should multiply these by a factor of 10,[5] if in fact they become exploitable in the future. Natural gas is a cleaner source than petroleum, and because of its high content in hydrogen, the total CO_2 emitted in any process for the production of chemicals is lower than when carbon is used as a source. Natural gas is, and in the near future will remain, the major feedstock for the production of hydrogen *via* syngas. The transformation of methane, the major component of natural gas, to more valuable products is a very challenging task since methane is extremely difficult to activate. In the methane molecule, consisting of a single C-atom surrounded by four H-atoms (CH_4), the sp^3 hybridization of the atomic orbitals of carbon means that the carbon-hydrogen bonds are very strong. The barrier in converting CH_4 into useful chemicals is that the products are less thermodynamically stable than the CH_4 reactant and hence are further consumed into undesired products, namely carbon oxides. Methane is readily activated by metals from Groups 8, 9 and 10 and is then oxidised to afford syngas ($CO + H_2$) first, and finally hydrogen after CO_2 removal. The most extended method for hydrogen/syngas production from methane is steam reforming (SRM). This will be described in the first part of this section. If the final product is hydrogen, it is necessary to convert CO to $CO_2 + H_2$ by means of the water-gas shift reaction (WGS), and this involves the final emission of CO_2. An alternative to avoid this is the decomposition of methane, which is described in the second part. Finally, catalytic systems active in the partial oxidation of methane (POM) and CO_2 reforming (dry reforming) are described in the final part of this section.

8.2.1 *Steam methane reforming*

Steam methane reforming (SMR) is the conventionally used process for converting natural gas and other hydrocarbons into syngas.[1–3]

SMR has been used for several decades as the chief method for hydrogen production since it was first developed in 1926. Owing to its importance, substantial improvements have been introduced over the years and research into catalysts, reactor materials, fluid dynamics and heat transport still continues. SMR takes place over a nickel catalyst according to the reaction:

$$CH_4 + H_2O \rightarrow CO + 3\ H_2 \qquad \Delta H^{\circ}_{298} = +\ 206\ \text{kJ/mol.} \tag{8.1}$$

The reaction is highly endothermic and favoured at lower pressures. The traditional SMR process essentially consists of feed gas pre-heating and pre-treatment, reforming, high- and low-temperature water-gas shift reactions, CO removal and methanation.

A pre-reformer is incorporated prior to the reformer unit. Since the pre-reformer operates at a much lower temperature (770 K) than in SMR, the steam produced within the reformer provides some of the heat of the endothermic reaction.[2] Pre-reforming has a dramatic effect on the gas stream to be fed into the SMR unit. C_2 and C_3 hydrocarbons are completely removed, while a certain proportion of CH_4 is also converted. A recent review[3] summarises the output of a typical pre-reformer. The catalyst used in pre-reforming contains higher Ni-loadings (above 25% Ni) than conventional SMR catalysts.

As stated above, steam reforming catalysts normally contain nickel. The noble metals from Groups 8, 9 and 10 are also active in the reforming reaction but the costs involved make their use prohibitive. For these systems, catalytic activity depends on the surface area of the metal and their properties are dictated by the severe operating conditions used, such as temperatures in the 700–1250 K range and steam partial pressures of up to 30 bar. In general, the activity of the catalyst is not a limiting factor. Thus, a typical nickel catalyst is characterised by a turn-over frequency (TOF) of *ca.* 0.5 s^{-1} at 723 K, which corresponds to CH_4 conversions of around 10%. The main barrier is the equilibrium conversion, which affords very high conversions only at temperatures above 1170 K. In practice, utilisation of the intrinsic catalytic activity is less than 10% (low effectiveness factor) because the reaction is mass-transfer limited.[1]

For the production of hydrogen (ammonia, refinery purposes, petrochemistry, metallurgy, fuel cells), the carbon monoxide contained in the effluent stream is converted to additional hydrogen in high- and low-temperature shift reactors. The water-gas shift reaction (WGS):

$$CO + H_2O \rightarrow CO_2 + H_2 \qquad \Delta H^{\circ}_{298} = -41 \text{ kJ/mol} \tag{8.2}$$

adjusts the H_2/CO ratio. If hydrogen is the target product, two shift reactors must be employed: a high-temperature shift (HTS) reactor at 670 K with a Fe_2O_3/Cr_2O_3 catalyst is followed by a low-temperature shift (LTS) reactor at 470 K with a Cu/ZnO catalyst (see, e.g. Peña *et al.*[5]). However, if syngas is then converted through downstream processes (methanol, FT synthesis), only the HTS reactor is used. For hydrogen production, pressure swing adsorption (PSA) units can supply a purified H_2 stream with a typical purity of 99.99 vol%. In the PSA units, gases other than hydrogen coming from the reformer are adsorbed at elevated pressure on activated carbon or molecular sieves. These non-H_2 containing gases are desorbed by expanding the adsorber tank to nearly atmospheric pressure and then returned to the reformer reactor as auxiliary fuel.

8.2.1.1 *Carbon formation*

In H_2 production from methane, carbon formation usually takes place in the form of fibres or whiskers, with a small Ni particle at the top of a fibre.[6,7] Carbon formation may lead to the breakdown of the catalyst, and carbon deposits and degraded catalyst may cause partial or complete blockage of the reformer tubes. Uneven flow distribution is responsible for local overheating of the hot tubes. Accordingly, carbon formation must be avoided in tubular reformers. There are two major reactions for carbon formation:

$$2\ CO \rightarrow C + CO_2 \qquad \Delta H^{\circ}_{298} = -172 \text{ kJ/mol} \tag{8.3}$$

$$CH_4 \rightarrow C + 2\ H_2 \qquad \Delta H^{\circ}_{298} = +75 \text{ kJ/mol} \tag{8.4}$$

The tendency to form carbon on the catalyst surface depends on the reaction kinetics, process conditions and reformer design.[1,8] These C-forming reactions are carefully balanced by C-consuming reactions ($C + CO_2 \rightarrow 2\ CO$ and $C + H_2O \rightarrow CO + H_2$), which in turn also depend on the kinetic conditions of the process and the reactor design. At low temperatures, the activated Ni catalyst is covered by a hydrocarbon layer, which slowly degrades to a polymeric film blocking the nickel surface. At high temperatures, ethylene from the pyrolysis of higher hydrocarbons produces pyrolytic coke, which encapsulates the catalyst particles. Whisker carbon is the most common form produced during steam reforming.[1] The whiskers grow with a nickel particle at the end. The mechanism involved in whisker formation includes first the dissociation of adsorbed hydrocarbon or CO on the metal surface, yielding carbon atoms that dissolve within the metal particle. Carbon diffuses through the particle and nucleates into the filament at the rear interface. The nickel crystallites change their original shape into a pear-like structure leaving small fragments of nickel at the top of the whisker. These carbon whiskers have high mechanical strength and the catalyst particles are destroyed when the whiskers hit the pore walls of the substrate.

Nickel carbide is not stable under SMR conditions. As a consequence, carbon nucleates in the form of whiskers after an induction period (t_o), after which the carbon whisker grows at a constant rate:

$$dC_w/dt = k_C\ (t - t_o). \tag{8.5}$$

The growth mechanism appears to be the same, irrespective of the hydrocarbon. However, the resulting morphology depends not only on the metal and particle size but also on the type of hydrocarbon and the reaction temperature. The importance of step sites on the catalyst surface for the nucleation of carbon was recently confirmed by *in situ* investigations employing high resolution transmission electron microscopy; the results indicate the segregation of carbon when the formation of whiskers takes place at specific sites on the nickel surface.[2] The addition of potassium to the nickel catalyst leads to an increase in the induction period (t_o) for CH_4 decomposition, which

implies a retarding effect on the dissociation of CH_4 and hence of carbon nucleation. The particle size of the Ni crystallites has a direct effect on the nucleation of carbon. The initiation of carbon formation is retarded on smaller nickel crystallites, as demonstrated by TGA experiments with two Ni catalysts having the same activity but different metal dispersion.[8] Consistent with this view, Christensen *et al.*[9] report that small nickel crystallites derived from hydrotalcites have a higher resistance to coke formation over conventional NiO/Al_2O_3 catalysts, due to a smaller driving force for carbon diffusion.

The rate of carbon formation is far less on noble metals than on nickel[5] and this behaviour appears to be related to the difficulty found by noble metals of dissolving carbon in bulk.[10] The carbon formed on the surface of noble metals was found to be almost indistinguishable from the catalyst particles. High-resolution TEM images taken from a ruthenium catalyst employed in the SMR reaction revealed a structure in which a few carbon layers were deposited on the surface of the Ru particles.[6] The mechanism by which whiskers grow on the surface of the nickel particles becomes blocked by sulphur poisoning of the catalyst surface. In this specific case, several 'octopus' carbon filaments or whiskers are formed on a given nickel particle. A similar carbon structure has been reported to develop on Ni-Cu alloy catalysts with low nickel contents (20 wt%).[11]

Several different approaches can be followed to minimise coke formation on the metal surface. The first relies on the control of the size of the ensemble.[12] Since the SMR requires the dissociation of methane to form a carbonaceous intermediate, it is argued that coke formation would require an ensemble of surface sites that would be larger than that required for the reforming reaction. That is, the formation of coke requires the polymerisation of monoatomic carbon species, while gasification involves only one of these species. Following this reasoning, it can be inferred that by controlling the number of sites in a given ensemble, it may be possible to minimise coke formation while maintaining the reforming reaction. The basis of ensemble size control lies in the work of Alstrup and Andersen[13] on sulphur adsorption on nickel. Those authors found that the

surface grid of the sulphur atoms did not coincide with the surface grid of the nickel atoms. Adsorption of sulphur on the catalyst surface thus delineates the ensemble of sites, the critical size being reached at sulphur coverages above 0.7. Under these conditions, the rate of the steam reforming reaction is decreased but coke formation is almost eliminated. Although sulphur adsorption is strong, it is partly lost during the reaction. As a result, it is necessary to add small amounts of a sulphur-producing gas to the feed. The second approach to the control of coke formation is the prevention of carbide formation.[14] The electronic structure of carbon is similar to the electronic structure of sulphur and the tetra- and pentavalent p metals (Ge, Sn and Pb or As, Sb and Bi). These elements contain spare p electrons in their outer shell close to a stable s-orbital. Nickel carbide is formed from the interaction of the 2p electrons of carbon with the 3d electrons of nickel. Thus, the tetra- or pentavalent metals would also interact with Ni 3d electrons, thereby limiting the possibility of nickel carbide formation.[14] Alloy formation reduces carbide formation but it is undesirable to lose active sites on the surface of nickel crystallites. However, carbide formation can only be developed on the surface layer and hence an alloy formed at the surface layer would be preferred. Based on these ideas, Trimm[14] studied the effect of small amounts of dopants on the catalytic and coking behaviour of nickel catalysts. The effect of tin on steam reforming was small for Sn levels below 1.75%, while coke formation was significantly reduced even by the addition of 0.5% Sn. It is clear that the addition of small amounts of dopant does substantially reduce coking, while having little influence on the rate of the steam reforming reaction.

8.2.1.2 *Mechanisms*

The tolerance of Ni catalysts to carbon-induced deactivation in hydrocarbon steam reforming and partial oxidation reactions can be significantly improved by impregnating Ni with small amounts of Sn (0.2–1 wt% with respect to Ni for Ni particles with the diameter between 30 and 200 nm).[15–17] Based on DFT calculations, it was

proposed that there are two likely mechanisms associated with the superior performance of Sn/Ni catalysts.[15,16] One mechanism is based on the kinetic control of the chemistry of C-atoms and CH_x on the catalysts surface. This mechanism assumes that the difference in the rates of the oxidation of C-atoms and CH_x fragments and the rates associated with the formation of C–C bonds, which are critical for the development of solid carbon deposits, is significantly higher on Sn/Ni compared to Ni, i.e. the Sn/Ni catalyst is more efficient than Ni in the preferential formation of C–O rather than C–C bonds. The second mechanism assumes that carbon deactivation is governed by the thermodynamic control of the nucleation of carbon at the low coordinated Ni sites. Previous *in situ* transmission TEM studies have demonstrated the importance of the low coordination sites for nucleation and growth of carbon fibres.[18] This mechanism assumes that Sn-atoms displace low-coordinated Ni-atoms, preventing the nucleation of carbon deposits on these sites. Kinetic data for supported Ni and Sn/Ni catalysts were interpreted in terms of the mechanism-based overall rate expressions.

The kinetics of methane steam reforming on supported monometallic Ni catalysts have been studied in some detail.[19,20] Although there have been many controversies, recent theoretical and experimental contributions have shown some consistent results. For example, Bengaard *et al.* utilised a combined theoretical and experimental approach to derive a mechanism for steam reforming of methane on Ni.[8] It was shown that methane steam reforming is a structure-sensitive reaction and that undercoordinated Ni surface sites are more active than close packed Ni sites. It was also demonstrated that the rate limiting step in the process is the activation of C–H bonds of CH_4 molecule. These conclusions are consistent with the recent experimental analysis of methane steam reforming at temperatures of 823–1023 K on Ni/MgO catalysts by Wei and Iglesia.[19] These authors also demonstrated that the forward rate is first order with respect to the methane partial pressure and it does not depend on the partial pressure of water or the reaction products. It was also argued that the rates of carbon filament formation are governed by the chemical activity of C-atoms chemisorbed on

the catalyst surface. Previous contributions have postulated that for lower operating temperatures there is a switch in the rate controlling step from the activation of CH_4 to the formation of CO on the catalyst surface.[21]

In a recent study,[22] a kinetic assessment of methane steam reforming on Sn/Ni/YSZ and Ni/YSZ catalysts was obtained using a combination of kinetic studies, isotopic-labelling experiments and DFT calculations. It was found that the reaction rate on Sn/Ni/YSZ and Ni/YSZ is first order with respect to methane and independent of the water partial pressure.[22] Furthermore, it was established that C–H bond activation of a CH_4 molecule is the rate limiting step in both catalysts. In addition, it was revealed that while on monometallic Ni the active sites are the undercoordinated Ni sites, on Sn/Ni the active sites are more abundant, well-coordinated terrace sites. The observed decrease in carbon deactivation of Sn/Ni was attributed to the Sn-induced lowering in the binding energy of carbon on low-coordinate sites, serving as carbon nucleation centres and to an improved propensity of Sn/Ni to oxidise carbon atoms and fragments.

8.2.1.3 *Promoter effects*

Carbon formation can be reduced by adding some promoters to the nickel catalysts. Kinetic experiments have shown that MgO and alkali dissociate steam and then transfer the fragments to the nickel particles through a spillover mechanism.[1] A similar conclusion was derived from isotope-exchange experiments,[23] which demonstrated that the enhanced adsorption of water on magnesia support leading to improved resistance to carbon formation is by nature a dynamic effect. Oxides of the type Ce_2O_3 and La_2O_3 display a similar type of behaviour in the steam reforming reaction[24–28] and also, when these compounds are derived from a perovskite structure[29] in which the lattice oxygen is considered to play an important role in promoting the oxidation of CH_x, fragments adsorbed on metallic nickel.[30] Moreover, it has been also found that Ce promotion over a Ni/Al_2O_3 catalyst increases coke resistance due to the improvement of Ni

dispersion.[31] An intimate contact between Ni and ceria is crucial to reduce the extent of carbon deposition, which critically depends on the catalyst preparation method. No significant carbon deposition has been observed using a low water-to-carbon ratio with a Ni catalyst precoated with ceria, using a sol-gel method.[32] The decrease in the carbon formation on a Pd surface over a $Pd/CeO_2/Al_2O_3$ catalyst for methane steam reforming has been explained in terms of the transfer of O species from ceria to a Pd surface.[33]

In methane steam reforming, the spillover of water probably takes place through OH groups instead of molecular water. In favour of this possibility is a study on Ni/MgO and Ni/TiO_2 catalysts carried out by Bradford and Vannice,[34] who concluded that surface hydroxyl groups, situated on the support surface, react with CH_x fragments adsorbed on the nickel surface. The use of supports that are able to release bulk oxygen, such as yttria-stabilised zirconia and $Ce_xZr_{1-x}O_2$,[35,36] indicates that spillover of lattice oxygen was involved in the reforming reaction.[37] This substrate type could promote dispersion of the nickel species catalysts inhibiting coke formation.[38]

Several recent investigations have described the effect of the catalyst composition on the activation of methane. On looking at the degree of dehydrogenation of CH_x species on various metals, it was observed that x was larger for nickel than for cobalt catalysts, and also larger for magnesia-supported than for silica-supported catalysts.[39] The use of a strong basic support such as La_2O_3 for the nickel phase resulted in a doubly beneficial effect: CH_4 activation increased and at the same time CO_2 adsorption was enhanced.[24] Other investigations demonstrated the retarding effects of molybdenum and tungsten oxides on the rate of coking.[40] Other supports, such as samaria-doped ceria, can increase the resistance towards coke formation. Thus, supported nickel catalyst has better de-coking ability than a gadolinia-doped ceria-supported catalyst in carbon dioxide and steam reforming of methane. An oxygen-transport reaction mechanism for doped ceria-supported Ni catalysts has been proposed to explain the activity behaviours.[41]

Similarly, on the Pt/TiO_2 and Pt/ZrO_2 catalysts used in CO_2 reforming, TiO_x moieties were found to be formed on the platinum

crystallites, with the subsequent suppression of carbon deposition, probably by ensemble control.[42] All these studies shed some light on the improvement of catalyst performance in steam reforming reactions, although additional work is required in order to understand the promoting effects of different oxides and to discern whether or not the promoters decorate the surface of nickel crystallites. The alloying of nickel with copper can also reduce carbon formation,[43] although it is not feasible to reach the required high surface coverage of copper atoms — as occurs with sulphur atoms — to eliminate carbon deposition. The formation of a stable alloy between nickel and tin,[44] and nickel and rhenium,[45] also appears to be responsible for the reduction in carbon formation. Surface modification of Ni with Pd enhances the resistance to Ni oxidation, and it is effective for promotion of the activity and suppression of hot-spot formation.[46] The improvement in the stability and resistance to coke formation in oxidative reforming of methane has also been observed with the addition of Pd on $Ni_{0.2}Mg_{0.8}Al_2O_4$[47] and Pd/$Ni_{0.2}Mg_{0.8}O$,[48,49] where the formation of Pd-Ni alloy was confirmed. A Pt-Ni alloy is also formed by adding Pt.[50–52] It has also been reported that the addition of noble metals (Pt, Pd and Rh) to Ni-alumina and $Ni_{0.2}Mg_{0.8}O$ solid solution catalysts inhibited carbon formation in the oxidative steam reforming of methane under pressure,[53] with Rh being the most effective for the inhibition of carbon deposition.[54] Rhodium maintains Ni species in a reduced state and enhances the methane activation ability.[55] It has also been observed that Ag incorporation to Al_2O_3-supported Ni catalysts enhances the performance for methane reforming as a consequence of the strong modification of the surface properties, related to CO adsorption and higher stability to graphitic carbon deposition. The high stability of the Ag promoted Ni catalysts was attributed to the decrease of Ni ensemble by a geometric effect of Ag, changes of Ni sites involved in the nucleation of the graphite structure, and equilibration of different steps of reaction rate decreasing the monoatomic carbon formation rate.[56] On the other hand, in Ni catalysts supported on Al_2O_3 or $MgAl_2O_4$, the addition of a small amount of Ru appears to facilitate the reduction of such Ni oxides and to decrease the coking propensity of the

catalyst in the steam reforming of CH_4.[57] It was also found that the addition of Co to Ni/ZrO_2 catalysts suppressed carbon formation in the steam reforming of methane (SRM).[58] On the other hand, DFT studies indicate that boron and carbon exhibit similar chemisorption preferences on a Ni catalyst which is proposed to enhance the stability of Ni catalysts by reducing the nucleation of graphene islands from steps, and by reducing the diffusion of carbon to the subsurface sites and subsequently to the bulk Ni.[59]

8.2.2 *Methane decomposition*

The decomposition of methane is an attractive alternative for the production of CO_x-free hydrogen.[60–64] The process requires not only having a metal catalyst able to break the C–H bonds of the methane molecule but also one capable of maintaining high and sustained activity for long time. Methane decomposition (reaction (8.4)) is a moderately endothermic process. The energy required for the production of one mole of H_2 is 45.1 kJ at 1073 K. To achieve this, it is essential that the metal catalyst should remain isolated from the carbon deposit by forming nanometre-sized carbon structures such as tubes, whiskers and fibres. In contrast, if methane decomposition is accompanied by the formation of soot, amorphous or encapsulated carbon on the metal surface, then activity is very low.[65] Since only hydrogen and carbon structures are produced during methane decomposition, product separation is not an issue. Another important advantage of methane decomposition as compared to conventional processes of steam or autothermal processes is the absence of the high- and low-temperature water-gas shift reactions and steps required to remove CO_2. Nickel has the most active catalyst function for the decomposition of methane. However, nickel crystallites larger than *ca.* 80 nm do not yield filaments but instead become covered by a crust that isolates them from the gaseous environment. For this reason, bulk nickel catalysts can be used for the cracking reaction although they rapidly become deactivated by carbon deposits.[66,67] Cobalt catalysts are inappropriate for methane decomposition owing to their lower activity, unreasonable cost and

high toxicity.[67,68] In contrast with cobalt, iron catalysts are inexpensive, non-toxic and resistant to high operation temperatures. This makes them highly attractive for the methane decomposition reaction. In addition, the carbon by-product resulting from the use of iron-based catalysts contains a large proportion of thin-wall nanotubes, which are among the most valuable carbon nanofibres. Carbon formation follows a carbide-cycle mechanism and consists of two steps. The first is the formation of carbon atoms through an intermediate carbide-like compound, and the second involves the topochemical formation of a graphite phase from carbon atoms.

The 'structure-sensitive' character of methane decomposition reaction has been confirmed, as has the importance of the metal dispersion on the catalyst performance over different supported Ni catalysts.[69] TEM analyses of the 'spent' catalysts reveal that both 'filamentous' and 'encapsulating' carbon species were formed under isothermal conditions at 823 K, the latter being responsible for catalyst deactivation.

8.2.2.1 *Nickel catalysts*

Universal Oil Products have developed a process for the production of hydrogen based on methane decomposition.[70] This process employs a 7%Ni/Al_2O_3 catalyst in a fluidised bed reactor-regenerator operated at 1150 K. The reactor exit product consists of *ca.* 94% H_2 the rest being mainly unreacted methane. Another alternative proposed by the United Technologies Corporation[71] involves methane decomposition on a nickel catalyst deposited on glass fibres. At the typical reaction temperature of 1123 K, hydrogen production is accompanied by the formation of a high-density carbon residue, thus requiring less frequent removal of carbon. Ni-doped alumina spherical catalysts were shown to be active and stable in relation to the catalytic decomposition of methane reaction. The analyses indicated the presence of single-walled nanotubes (SWNTs) and multiwalled nanotubes (MWNTs), and the catalytic behaviour and the form of carbon produced were observed to depend on the characteristics of the sites present on the catalyst surface, such as

the formation of $NiAl_2O_4$, and on the operational conditions employed.[72]

Nickel and iron catalysts were employed by Muradov[62] for methane decomposition over a wide range of temperatures. The results showed that catalyst activity drops with the time on-stream, although it can be recovered by an oxidative regeneration, resulting in the production of CO_x in the regeneration step. To circumvent the problem of carbon removal, the active components were supported on a carbon substrate. A recent XPS study showed that a direct relationship exists between the catalytic activity and the amount of defects present on the graphene layers, which strongly suggests that these defects are the main active sites for methane decomposition over carbon catalysts and carbon-supported catalysts.[73] Activated carbon produced from coconut shells displayed the highest activity while graphite exhibited poor performance. These differences were attributed to the structure and size of the carbon crystallites. The use of binary gaseous mixtures of methane with a second hydrocarbon revealed that addition of acetylene enhances the steady state methane decomposition rate. The carbon deposit resulting from acetylene decomposition was found to be more active towards methane decomposition than that resulting from methane alone.

Li *et al.*[74] reported a novel method of obtaining nickel oxide particles with controlled crystalline size and fibrous shape, highly dispersed on *in situ* produced carbon, inhibiting further growth of Ni particles. On the other hand, Ni/CFC (filamentous carbon) catalysts were shown to have sufficient efficiency in low-temperature methane decomposition. Thus, the use of CFC, whose textural properties can be modified by their activation with H_2 or CO_2, opens up the possibility of its application as a support in heterogeneous catalysis.[75] Methane decomposition over Ni-loaded activated carbon (AC) was also investigated. XRD results showed absence of NiO with only Ni metal crystallites formed in the catalyst even if calcined in Ar, which eliminates the inevitable reduction step with other supports. However, the formation of Ni_3C during the process leads to deactivation of the catalysts. Filamentous carbon formation is

observed and interlaced with the deactivated catalyst surface. It is worth mentioning the significant effect of temperature on the catalytic performance of Ni/AC catalysts.[76] Various carbon blacks with different primary particle size were investigated with respect to methane decomposition under atmospheric pressure from 1123 to 1223 K, and it was observed that with decreasing primary particle size (or increasing specific area), the specific activity increased and the activation energy decreased.[77]

Zhang and Amiridis[78] have studied methane cracking over silica-supported metal catalysts to produce CO-free hydrogen. They observed that a 20% CH_4/He mixture reached 35% CH_4 conversion at 823 K, although this conversion progressively decreased with the time on-stream until the catalyst became completely deactivated after approximately 3 h on-stream. Once the deactivated catalyst had been regenerated with steam, the catalyst completely recovered its original activity, and a total of 3.4 moles of H_2 produced per mol of converted CH_4 were obtained. Some clues as to the nature of carbon deposits and their relative reactivity were derived from TEM images. The TEM images revealed that the external graphite skin of the filamentous carbon, which represented roughly 30% of the total carbon deposited, was very refractive to steam regeneration, while the inner-less graphitic carbon was readily removed by steam gasification.

A mixture of Ni^0/NiO, produced by thermal decomposition of nickel acetate, dispersed on either silica[79] or cordierite supports, was found to be catalytically active for the decomposition of methane without the need for any pre-treatment.[80] Other authors[81] used Ni catalysts supported on zirconia to produce H_2 and a high yield of multiwalled carbon nanotubes. Raman spectroscopy suggested that carbon nanotubes formed at temperatures higher that 973 K had more graphite-like structure than those obtained at lower temperatures. They also reported that feed gas containing methane and hydrogen caused slow deactivation of the catalyst, and carbon yield increased with increasing H_2 partial pressure in the feed gas. For a commercial Ni catalyst (65% wt Ni supported on a mixture of silica and alumina) it was found that catalyst deactivation depends on the

operating conditions, so that the higher the temperature and methane flow, the shorter the life of the catalyst. Different characterisation techniques have shown that the deposited carbon appears either as large filaments emerging from Ni particles or as uniform coatings. In both cases, the carbon deposited is highly ordered graphite whose structure does not depend on the operating conditions. Formation of desirable carbon filaments is favoured by operating conditions promoting low rates of methane conversion. On the contrary, operating conditions promoting high decomposition rates enhance coating carbon deposition and shorten catalyst life.[82]

Bonura *et al.*[69] studied several supported Ni catalysts for methane decomposition and found that both 'filamentous' and 'encapsulating' carbon species were formed under isothermal conditions at 823 K, the latter being responsible for catalyst deactivation. They also confirmed the structure-sensitive character of methane decomposition. The efficient use of these catalysts implies a high dispersion of metal phases which can be achieved by controlled segregation of the active phase. Different Ni mixed oxides such as Ni-Al hydrotalcite, Ni-La perovskites and Ni-Al spinels as catalysts precursors allow a high degree of Ni dispersion, of which that derived from hydrotalcite mixed oxide showed the highest activity for H_2 production by methane decomposition.[83]

Different dopants can be used to increase activity and stability. Among them, Cu was found to be a good promoter of Ni catalysts, increasing H_2 production up to concentrations over 80 vol.% in the product gas. The catalysts promote the formation of carbon nanofibres some micrometers long with different diameters, with particular dependency on the presence or absence of copper.[84] Cu has a strong influence on the dispersion of Ni in the catalysts and inhibits NiO from the formation of nickel aluminate even at high calcination temperatures, which facilitates the formation of metallic Ni-phase during the subsequent catalyst reduction step. All catalysts tested promote the formation of very long filaments of carbon a few tens of nanometers in diameter and some micrometers long.[85] The size of metal particles and the carbon filaments as well as the

nanofilament texture depends on the copper content in Ni-Cu-Mg-Al catalysts.[86] Excellent results were also obtained with the Ni-Cu Raney-type system thermally treated *in situ* at 873 K, as a result of incipient alloy formation.[87] The addition of iron to Ni-Cu/Al_2O_3 system leads to the formation of finely dispersed Ni-Cu-Fe alloy particles which makes the catalysts stable and capable of operating at 973–1023 K in CH_4 decomposition to H_2 and carbon nanofibers.[88] It has been also reported that a certain amount of Cu in silica-supported Ni catalysts could enhance CH_4 decomposition activity. This was explained by the H spillover produced by Cu, which considerably enhances the reducibility of Ni^{2+}.[89] Other reports provide evidence that the addition of Cu and K enhance the catalyst dispersion with the increase in Ni-loading, indicating that surface geometry is modified electronically with the formation of different Ni, Cu and K-phases, which consequently, increase the surface reactivity of the catalyst and the carbon nanotubes/H_2 production.[90] By adding K, a marked effect is produced on the product selectivity and reactivity of a Ni : Cu/Al catalyst system, restricting the formation of carbon on the surface and increasing the production of H_2 and C_2-C_3 hydrocarbons.[91]

Promoters such as ceria have been used for H_2 production by CH_4 decomposition. Although the degree of nickel reduction decreased with the addition of cerium, even in low concentration, the addition of cerium brought about a significant increase in stability compared with a Ni/SiO_2 catalyst. Results showed an enhancement of Ni dispersion leading to a better distribution of deposited carbon which increased the lifetime of Ni particles.[92] The morphology as well as the reactivity of the carbon deposits is strongly dependent on the degree of interaction between Ni and ceria, which explains the differences in the catalytic activity of the Ni/CeO_2 catalysts for CH_4 decomposition, and which subsequently depends on the method used to prepare the catalyst. Thus, the Ni/CeO_2 catalyst prepared by co-precipitation exhibited rather strong metal support interactions probably through the formation of Ni-O-Ce solid solution, resulting in much lower H_2 production rate and relatively higher CO production.[93] In general, textural

promoters prevent nickel particles from sintering. The particles of textural promoter introduced between NiO crystallites avoid aggregation during reduction. However, textural promoters should avoid the formation of inter-metallic compounds which are difficult to reduce.[94] MgO has been used as a textural promoter in Ni-supported catalysts, and the importance of the MgO/NiO ratio has been reported. Thus, an increase in this ratio in alumina-based catalysts led to the modification of the size of the crystallites and the appearance of strong adsorption sites on the surface of nickel and enhanced CH_4 decomposition.[95] The activity of a spinel-like Ni-Mg-Al catalyst was also studied, where it was found that addition of MgO increases the activity and stability of the Ni-Al catalysts due to the greater interaction generated between Ni particles and the support, which prevents the formation of large metallic particles.[96] In silica-supported systems, as the Mg-at/Ni-at ratio increases from 0.10 to 2.20 the Ni-Mg-O interaction becomes stronger until the formation of $Ni_xMg_{(1-x)}O$ solid solution arises. The presence of Mg^{2+} ions allows a higher carbon capacity and consequently a higher H_2 productivity.[97]

8.2.2.2 *Diamond-supported transition metals*

A simple, original method explored recently consists of the use of a partially oxidised diamond substrate to which nickel and palladium metals have been incorporated.[65] Oxidised diamond-supported metals from Groups 8, 9 and 10, containing 3 wt% metal and pre-reduced at 873 K, were tested in the CH_4 decomposition reaction at 873 K and the order of activity was as follows: Ni > Pd >> Fe, Co, Ru, Ir, Rh, Pt. Among these catalysts the Ni- and Pd-loaded types afforded a high conversion of methane and a significant H_2 yield,[98] while carbon whisker formation was found with Ni- and Pd-loaded oxidised diamond catalysts. A high rate of methane conversion and high activity was found on the Pd-supported catalyst. In contrast, the diamond-supported Rh catalyst, in which the rhodium function is considered to be highly active for this reaction,[99,100] did not exhibit catalytic activity under the examined reaction conditions.

8.2.2.3 *Cobalt catalysts*

In contrast with nickel catalysts, only a few studies have focused on the decomposition of methane over cobalt catalysts. Wang and Rukenstein[101] investigated carbon formation during methane decomposition at 1173 K over 48 wt% Co-MgO calcined at three different temperatures (773, 1073 and 1173 K). The size and the morphology of the cobalt clusters in the reduced catalysts were strongly affected by the reducibility of the metal oxide precursors and their distribution over the MgO support. Among the three Co containing phases (Co_3O_4, Co_2MgO_4 and (Co,Mg)O), the former pair are present as independent phases, while in the solid solution Co^{2+} ions are highly dispersed in the lattice of MgO. Because the oxygen that interacts with Co^{2+} in the solid also belongs to Mg^{2+}, such Co^{2+} species are difficult to reduce. Indeed, temperatures above 1273 K are required for the complete reduction of the (Co,Mg)O-phase into metallic cobalt. During reduction of the solid solution catalyst, some reduced Co^o-atoms generated fine metal particles, while others located deeper remained in the MgO matrix, either as Co^o or mostly as Co species in low oxidation states. Furthermore the metallic clusters remained partially embedded within the MgO lattice. Consequently, strong interactions between the crystallites generated and the substrate were developed, particularly with the Co-atoms present in the lattice. As a result, the crystallite appeared more extended and probably exhibited an ordered structure, serving as a template for an ordered nucleus for carbon formation. The carbon nucleus formed generated a graphitic filament because the free energy of the graphitic structure is the lowest. By contrast, when the Co^o crystallites were formed from the more reducible Co_3O_4 and Co_2MgO_4 phases which were only present at calcination temperatures below 1073 K, large metal particles were generated and interactions between these were formed. Thus, the carbon deposits tend to coalesce during their growth, hence impeding the formation of fibres but generating shapeless tangled shell-like structures.

Cobalt molybdenum carbide was also found to be active as a catalyst for the methane decomposition for hydrogen production.

Co-Mo catalysts with 25% Co loading carbided at various temperatures were studied at 973 K and atmospheric pressure, and the 700 K-carbided catalyst was found to be the most active for H_2 production.[102] The active species of the cobalt molybdenum carbide catalyst for the CH_4 decomposition is the cobalt molybdenum oxycarbide on the surface that was formed during the carburization.[103] The activity of both Co and Ni catalysts supported on Al_2O_3, modified by the addition of MgO and CeO_2, has been investigated. MgO was used to enhance the reducibility of the metal oxide precursor and CeO_2 was intended to promote CO_x formation in the oxidation step (with O_2 or CO_2), that follows the decomposition, in order to eliminate the deposit. At the chosen conditions (773 K using 5% CH_4/He), Ni was more active and more stable than Co during the CH_4 decomposition step and several CH_4 decomposition-carbon oxidation cycles were completed on the Ni catalyst without significant loss in activity, whereas the Co catalyst deactivated. This behaviour is explained in part by the facile reduction of NiO by CH_4.[104]

8.2.2.4 *Nature of the carbon by-product*

The formation of filamentous carbon deposits on transition metal catalysts (Fe, Co, Ni) and their alloys have been investigated in some detail over the past two decades.[43,105–107] Among them, nickel is the most promising candidate since it forms carbon deposits at temperatures as low as 723–823 K using CH_4, C_2H_6 or CO + H_2 feeds. Carbon fibres are usually produced during these reactions. Typical forms of the carbon produced from CH_4 decomposition on silica-supported Ni catalysts are shown in Fig. 8.1. The pyrolysis of methane at temperatures somewhat lower than 873 K produces fishbone type nanofibres.[108] The Ni metal particles are present at the tip of each carbon fibre, and catalyse methane decomposition as well as growth of the carbon fibres. The edges of the stacking carbon layers are exposed at the walls of the fibres and these layers adopt a turbostratic graphite structure in which the layers of atoms are randomly displaced with respect to each other.[109] The sizes of the nickel particles or the diameter of the carbon fibres range from

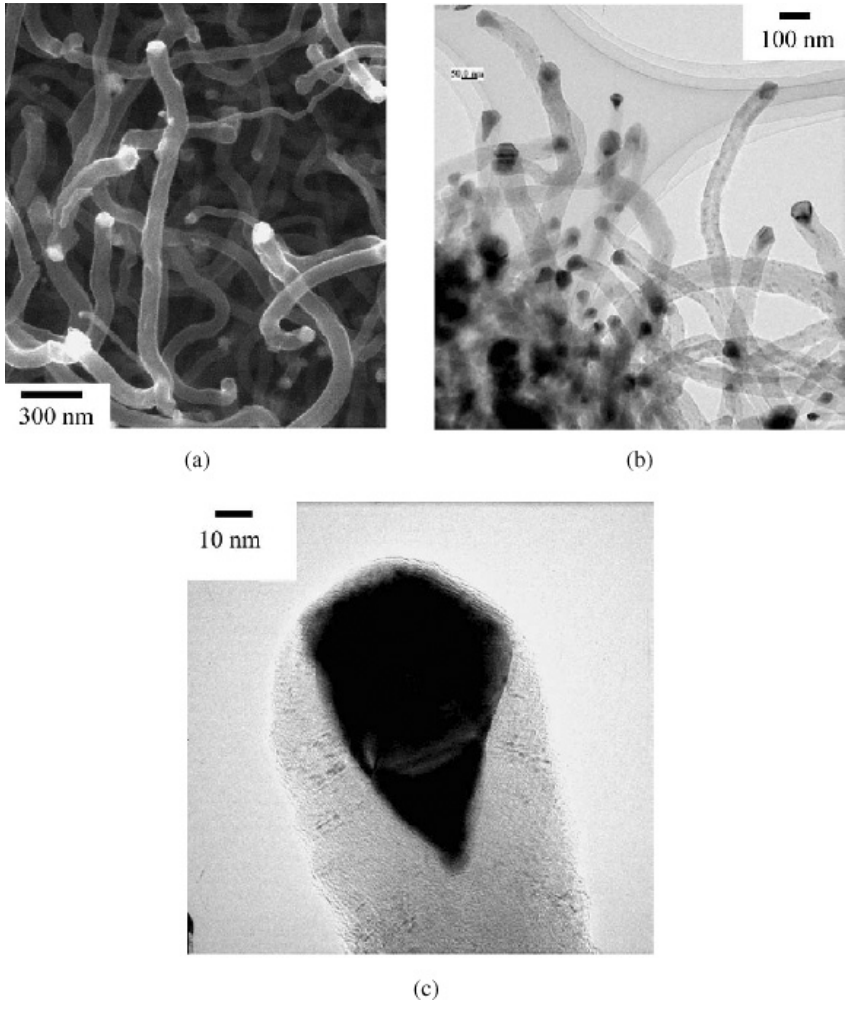

Figure 8.1 SEM and TEM images of carbon nanofibres developed by methane decomposition over Ni/SiO_2 catalyst at 773 K. (a) SEM image for 5 wt% Ni/SiO_2; (b) and (c) TEM images for 40 wt% Ni/SiO_2 catalysts.[116]

ca. 10 to 100 nm. Similar results have been found on alumina-supported Ni, Ni-Ca, Co and Fe catalysts.[110] The catalytic activity of Ni catalysts for CH_4 decomposition was found to be strongly related to the crystalline size of reduced Ni, in unsupported systems, with an

optimum size of about 11 nm being found. An increase up to 26 nm resulted in total deactivation of the catalyst. The Ni crystallites depart from the fibrous structures and gradually aggregate into particles by the dissociation of the deposited carbon. These Ni particles are highly dispersed on the *in situ* produced carbon, which can inhibit the further growth of the Ni particle. As a result, the initial fibrous structure morphology of the metallic Ni could be gradually turned into pear-like shapes.[111]

The results obtained with a catalyst derived from a spinel-like Ni-Mg-Al indicate that the proportion of each type of carbon depends on the operating conditions. In this case, the main carbonaceous products formed over the catalyst surface are carbon herring-bone nanofibres (diameters ≈ 10–35 nm) and amorphous carbon, which causes the catalyst deactivation by encapsulation. The addition of small quantities of hydrogen in the feed produces the cleaning of the catalytic surface and prevents the formation of encapsulating coke, since hydrogen competes with methane for the Ni surface sites. An increase in the reaction temperature favours the formation of both carbon nanofibres and encapsulating coke and, at high reaction temperatures, the catalyst deactivation effect is more important than the nucleation and growth of new nanofibres.[112] In activated carbon (AC)-supported nickel catalysts, the formation of zigzag filamentous carbon with Ni metal on the tip shows that the mechanism of filamentous carbon formation and growth over AC may be the same as that of over Ni catalysts supported on other supports. Temperature has a great effect not only in CH_4 decomposition but also on the formation and characteristics of the filamentous carbon. Thus, the amount of filamentous carbons increased with reaction temperature as well as the carbon tube properties.[113] However, the shapes of the carbon structures appear quite different on Pd-Ni bimetallic catalysts.[114] For a Pd-Ni bimetallic catalyst with a Pd/(Pd + Ni) atomic ratio of 0.5, branched carbon nanofibres with a large variety of diameters ranging from 10 to 300 nm are developed, in contrast with the carbon nanofibres formed on supported nickel catalyst (Fig. 8.2). The carbon structure is not uniform. Several carbon fibers grow on the PdNi-alloyed metal

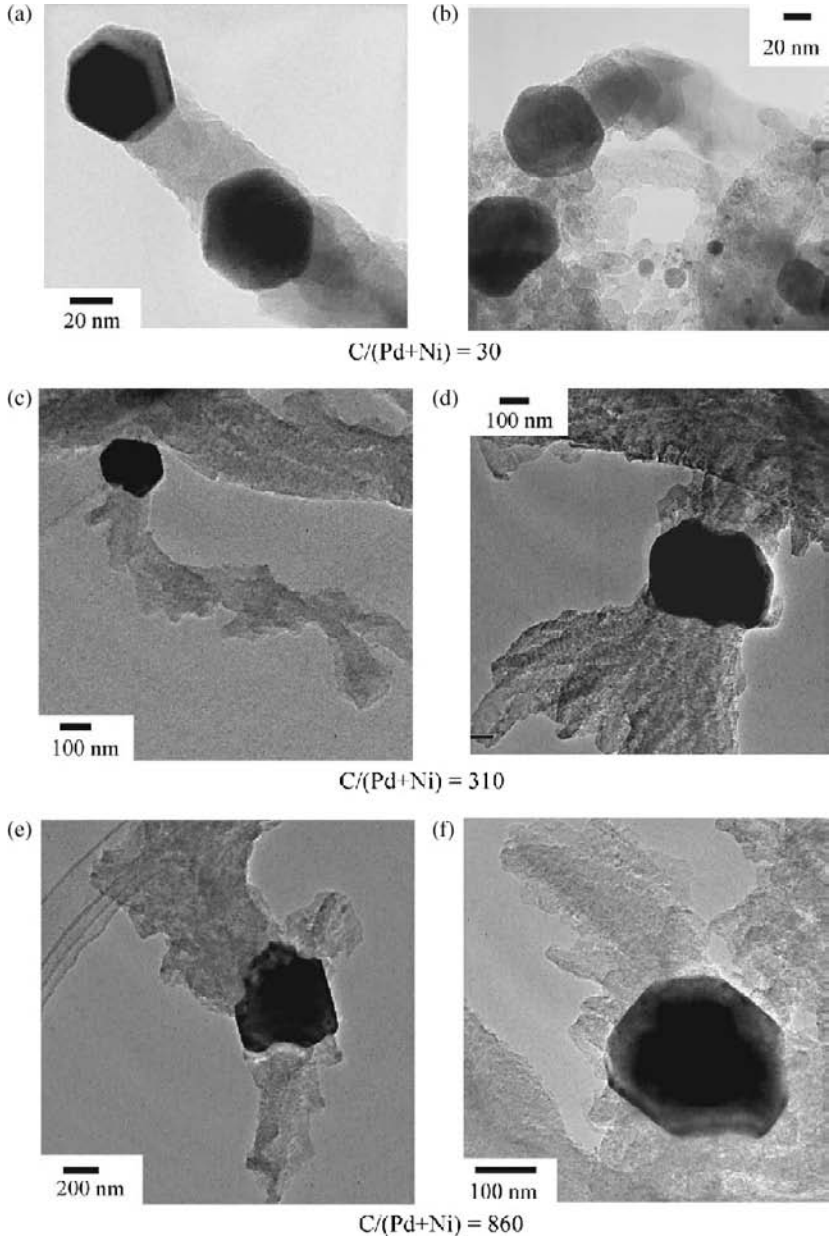

Figure 8.2 TEM images of Pd-Ni/SiO_2 catalyst after methane decomposition at 873 K. Loading of (Pd + Ni) = 10 wt%, molar ratio Pd/(Ni + Pd) = 0.5.[116]

particles, and become entangled with each other and form a coarse texture of the fibres. These carbon structures lead to progressive catalyst deactivation. No changes in the Ni–K edge XANES spectra of a 5wt% Ni/SiO_2 catalyst before and after the catalytic decomposition of methane could be observed under steady state reaction. However, for the deactivated catalyst ($C/Ni \geq 900$) the Ni–K edge XANES spectrum exhibited shoulders at 8332 and 8341 eV and grew in intensity with an increase of the C/Ni ratio.[115] These changes in the XANES spectra of nickel during deactivation could be ascribed to the structural change of nickel particles from Ni metal to a Ni-carbide species. Catalyst deactivation is a complex kinetic process controlled by the decomposition rate of methane into carbon and hydrogen atoms on one side of the Ni particle and the rate of diffusion of carbon and the graphitisation of C-atoms at the other side of the Ni particle. The imbalance among these rates results in catalyst deactivation, presumably *via* the formation of a Ni-carbide species. When the decomposition of CH_4 or the C–H bond cleavage of CH_4 is the rate determining step, no deactivation occurs. Collision of a carbon nanofibre with the active Ni particle on the tip of the carbon fiber and/or coating of the active Ni surface with a carbon layer have been suggested, among others causes, to be responsible for catalyst deactivation. Some structural differences are clearly differentiated when comparing the monometallic Ni catalyst and the bimetallic Pd-Ni system. The Ni–K edge XANES spectrum of the deactivated bimetallic Pd-Ni catalyst virtually coincides with that of the fresh counterpart, indicating that the local structure of the PdNi alloy remains unchanged during CH_4 decomposition. The longer life of the Pd-Ni catalyst for CH_4 decomposition may be ascribed to the PdNi alloy itself, which is resistant to reacting with carbon to form a stable carbide phase.

The carbon nanofibres produced during CH_4 decomposition can be removed by a consecutive gasification process with CO_2, O_2 and H_2O.[116] Gasification by CO_2 of the carbon structures formed on a 5 wt% Ni/TiO_2 catalyst deactivated in the CH_4 decomposition reaction brings about the formation of CO ($CO_2 + C \rightarrow 2\ CO$). The conversion of the carbon nanofibres with CO_2 is highly effective,

since conversion levels higher than 95% are obtained. The process can be repeated for 3–5 cycles. Oxygen and steam, instead of CO_2, are also effective for the gasification of carbon nanofibres produced in CH_4 decomposition on the nickel surface of the same Ni/TiO_2 catalyst. Gasification of carbon fibres with O_2 and H_2O also affords levels above 95% and the process can be repeated over several cycles. The gasification of carbon nanofibres with CO_2, O_2 and H_2O allows the original activity of the Ni/TiO_2 catalysts to be recovered. However, the TOF values of hydrogen formation on Ni/SiO_2 and Ni/Al_2O_3 catalysts do not follow the same trend as the Ni/TiO_2 system. The TOF values for the Ni/SiO_2 catalysts decrease progressively upon increasing the number of reaction-regeneration cycles as a consequence of the increase in particle size of the Ni crystallites during the operation cycle. In contrast, the interaction of Ni species with a TiO_2 substrate is stronger than with SiO_2, preventing the formation of large Ni particles during the repeated cycles. The stronger interaction between Ni and the Al_2O_3 support prevents the formation of Ni metal particles suitable for CH_4 decomposition, resulting in a lower catalytic activity in the first few cycles. However, further decomposition-regeneration cycles lead to the growth of Ni metal particles and hence the TOF values progressively increase.[116]

8.2.2.5 *Theoretical investigation*

The activation energies for the dissociation of the CH_4 molecule and CH_x fragments on metal surfaces were determined by applying the bond-order conversion Morse-potential (BOC-MP) developed by Shustorovich and Baetzold.[117] Using ASED-MO semi-empirical methods and clusters analysis, Anderson and Maloney[118] studied the activation of CH_4 on a Pt(111) surface and calculated an activation barrier of 0.45 eV for CH_4 on a Pt_{10} cluster; see Blomberg *et al.*[119] carried out several theoretical calculations of CH_4 activation over single Rh- and Pd-atoms and found barriers of 0.41 and 1.09 eV, respectively. A somewhat larger barrier (1.17 eV) was found by relativistic effective core potential (RECP) calculations of methane activation on a single O_s-atom.[120]

Methane dissociation on several transition metals (M) (M = Ru, Os, Rh, Ir, Pd, Pt, Cu, Ag, Au) was analysed theoretically by Au *et al.*[121] by simulating the surface with a M_{10} cluster. On the Pt_{10} cluster, the barrier for the first dehydrogenation was estimated to be 0.84 eV. This value was much larger than the ASED-MO value, but reasonably comparable to that obtained with UBI-QEP methodology. The same applies for the Ir_{10} cluster. For the second dehydrogenation step ($CH_{3s} \rightarrow CH_{2s} + H_s$), the values estimated were found to be close to the UBI-QEP data. The dehydrogenation of CH_x to CH_{x-1} fragments was highly endothermic in the gas-phase with D_e values (dissociation energy of the CH_x in the gas-phase) of 4.85, 5.13, 4.93 and 3.72 eV for x = 4, 3, 2 and 1, respectively.[121] On metal surfaces, however, there was significant reduction in the D_e values owing to the development of strong M-CH_{x-1} and M-H bonds. On the Ru surface, the first and second dehydrogenation steps were nearly thermoneutral, while the second and third, and fourth steps were slightly exothermic and endothermic, respectively. On the Rh surface there were one slightly exothermic and two endothermic steps, but in Cu, Ag and Au metals all the steps were found to be rather endothermic. For the whole process, the reaction with the highest activation barrier should be the rate determining step. However, among the transition metals the highest barriers were found to be very similar. Thus, from these results it was not easy to predict the catalytic behaviour.

The summation of the energies for the four discrete steps, which gives the total dissociation energies, was found to be a more realistic measure of the activity of the metal in methane dissociation. The calculations of these sums carried out by Au *et al.*[121] revealed that the total dissociation of methane on Rh is thermodynamically more favoured on Rh than on other transition metals, and the values varied in the order: Rh < Ru < Ir < Os ≈ Pt < Pd. This trend is similar to that obtained by Schmidt *et al.*[122,123] in the partial oxidation of CH_4 to syngas. By contrast, these sums proved to be highly endothermic for the coinage metals. Two causes may be invoked to account for this behaviour. First, the adsorption energy of H-atom on the coinage metals was relatively small when compared with that on the

other transition metals, and secondly, the adsorption of CH_x fragments on the coinage metals increased only weakly from x = 3 to x = 1 and even decreased from x = 1 to x = 0. Therefore, a complete dissociation of CH_4 to surface C_s and H_s is difficult on the coinage metals, in agreement with the experimental observation that these metals are inactive in the partial oxidation reaction.

In addition to the direct dissociation of methane on clean metal surfaces, oxygen-assisted dissociation has also been performed. The dissociation of CH_4 on Rh in the presence of Os was studied by applying the BOC-MO model,[124] where different surface oxygens at on-top, bridge and hollow sites were considered. The BOC-MP calculations revealed that oxygen atoms at on-top sites promote methane dehydrogenation. Because the H-atoms bind more strongly with oxygen at on-top sites than with the clean metal, the CH_4 dissociation reaction in the presence of surface O_s located at on-top sites has lower reaction energies due to hydroxyl formation. This means that oxygen at on-top sites promotes the dehydrogenation of CH_x, in agreement with the BOC-MP predictions.[124] However, the oxygen atoms at hollow locations showed a different behaviour in CH_4 dissociation. Thus, the oxygen at hollow sites increased the adsorption energies of H on Pt and coinage metals, but decreased those on other transition metals. Accordingly, Pt, Cu and Au metals promoted CH_4 dissociation, but no promotion was found on the other metals.

The reaction pathway of C–H bond breaking of methane on clean Pd(111) and O-modified Pd(111) surfaces was investigated by the density functional theory. The calculated results showed that methane favours such a configuration whereby one hydrogen points towards the surface in the on-top site. Methyl is adsorbed on the top site, and hydroxyl, oxygen and hydrogen are all adsorbed on the fcc site. On the clean Pd(111) surface, the activation energy of 0.97 eV is smaller than that of 1.42 eV in the case of oxygen-modified (O-atom acts as a 'spectator') Pd(111) surface, which indicates that the presence of the oxygen atom inhibited C–H bond cleavage. Compared with the case where only the surface O-atom exists, the activation energy decreased from 1.43 to 0.72 eV when the subsurface O-atom

exists. This suggests that subsurface O-atom promotes the activation of methane molecule. On the oxygen-modified Pd(111), the activation energy of the reactions forming methyl and hydrogen and methyl and hydroxyl is 1.42 and 1.43 eV, respectively, which indicates that the reaction possibility is equivalent.[125]

Density functional theory has been also used to examine different transition states for methane dissociation on Ni(111), Pt(111), Ni(100), Pt(100) and Pt(110). In all cases, the minimum energy path for dissociation is over a top site. The barriers are large, 0.66–1.12 eV, and relatively insensitive to the rotational orientation of the (non-reacting) methyl group and the azimuthal orientation of the reactive C–H bond. There is a strong preference on the Pt surfaces for the methyl fragment to bond on the on-top site, while on the Ni surfaces there is a preference for the hollow or bridge sites. Thus, during the dissociation on Pt, only the low mass H-atom needs to significantly move or tunnel, while on Ni, both the dissociating H and the methyl fragment move away from the top site.[126]

8.2.3 *Partial oxidation and dry reforming of methane*

As explained above, steam methane reforming (SMR) is currently the most important industrial process for the production of hydrogen from methane. Considering the current parameters of the energy and commodity chemicals market, it is the most economical method of hydrogen/syngas production. Nevertheless, steam reforming has some unresolved difficulties: (i) it is a highly endothermic process and a huge amount of energy is required. Considering only the balance of the reaction enthalpies, a 20% surplus of methane for burning is necessary to supply the reaction heat. (ii) It is necessary to overheat water up to the reaction temperature (>1073 K) to maintain the H_2O/CH_4 ratio around three times the stoichiometric value in order to avoid carbon deposition. This implies that additional energy must be supplied. (iii) The H_2/CO ratio of the produced syngas is 3 or higher. Since certain important processes using this syngas (methanol synthesis, Fischer–Tropsch process, etc.) require a ratio of 2, it is necessary to use modified SMR reactors (autothermal

reforming ATR, combined reforming CMR),[3,127] or to modify the syngas composition by reverse water-gas shift (WGS).

As a consequence, SMR is a very expensive process (in a methanol synthesis plant, the cost of the reformer is about 60% of the total cost), and only the current price of natural gas, with an uncertain future, can compensate the overall energy demand of the process. In this context, new processes for the production of hydrogen from methane, at lower energy costs, are needed, and the partial oxidation of methane (POM) is an attractive alternative:

$$CH_4 + \tfrac{1}{2}\, O_2 \rightarrow CO + H_2 \qquad \Delta H^{\circ}_{298} = -36 \text{ kJ mol}^{-1}. \tag{8.6}$$

This is an exothermic reaction, and therefore no energy is required (it is produced); there is not water to be overheated, and the stoichiometric H_2/CO ratio of the syngas produced is 2, the optimum value for possible downstream processes. These characteristics, together with increasing interest in highly efficient processes for the production of hydrogen for fuel cells, have led to an extraordinary increase in experimental work related to the development of active and stable catalysts for this reaction over the last 15 years. Despite these research efforts, the industrial application of POM is still limited, mainly owing to the requirement of an oxygen plant (as in the ATR, air-blown is possible, but with additional difficulties[127,128]), and as yet no clearly stable supported metal catalyst is available.

Besides POM, research into another reformer reaction has also been of interest: CO_2 reforming (dry reforming):

$$CH_4 + CO_2 \rightarrow 2\, CO + H_2 \qquad \Delta H^{\circ}_{298} = +247 \text{ kJ mol}^{-1}. \tag{8.7}$$

This reaction does not overcome the energetic problems of SMR, as can be seen from its reaction enthalpy value, but it is interesting in combination with SRM or POM by recycling CO_2 produced in the tail gases of the process. CO_2 is a very efficient energy carrier and its recycling increases the efficiency of the plant. At the same time, the process itself is interesting since CO_2 is a greenhouse gas that, by

means of this reaction, could be incorporated to chemicals through the production of syngas. POM and dry reforming thus have this parallel interest because the active catalysts, the reaction mechanisms, and the deactivation processes have several features in common.[129,130]

A more suitable approach is the combination of the exothermic POM with one of the exothermic reactions (SRM or/and CO_2 reforming) in a similar way to that carried out in ATR. If the reactants ($CH_4 + O_2 + H_2O$ or $CH_4 + O_2 + CO_2$ or $CH_4 + O_2 + H_2O + CO_2$) are combined at the appropriate proportions, the process is autothermal and there are no problems of heat exchange (it is not necessary to release it or provide it). Along these lines, Choudhary *et al.*[131] investigated the activity of a $NiCoMgCeO_x$/zirconia–hafnia catalyst, with unusually high thermal stability, for syngas generation *via* a process that includes the catalytic partial oxidation of methane (CPOM), the oxidative steam reforming of methane (OSRM) and the oxidative CO_2 reforming of methane (OCRM). The catalyst showed excellent activity/selectivity for above reactions. Furthermore, no catalyst deactivation was observed over a period of 20 h. For the OSRM process, the H_2O/CH_4 ratio and the reaction temperature had a strong effect on the product H_2/CO ratio and the heat of the reaction. Depending on the H_2O/CH_4 ratio and reaction temperature, the process could be operated in a mildly exothermic, thermoneutral or mildly endothermic mode. In the OCRM process, the CO_2 conversion was very strongly affected by the reaction temperature.

Temperature gradients and hot spots can be also minimised using a fluidised bed instead of a fixed bed reactor. A series of different-sized Ni catalysts were prepared and used for methane autothermal reforming with CO_2 and O_2 in a fluidised bed reactor. It was found that the activity and stability of Ni catalysts depends strongly on the particle size and the operating space velocity. As the methane decomposition rate slows on larger Ni particles and at higher space velocity, surface Ni will be gradually oxidised by remaining O_2 leading to Ni deactivation.[132] For a Ni/SiO_2 catalyst, a high activity and selectivity was observed for the reaction that

combines CO_2 reforming and partial oxidation of methane to produce syngas. The use of a nickel citrate precursor strengthened interaction between NiO and support to form nickel silicate-like species which could be reduced to produce small crystallites of metallic nickel at high temperatures.[133]

8.2.3.1 *Catalytic mechanism and heat exchange*

The POM reaction has been known from the 1930s, as described by York *et al.* in a recent review,[134] but poorly active catalysts, that require high temperatures and that rapidly become deactivated, were studied initially. Because of the comparative advantages of SRM at that time, the POM reaction was not considered of great importance. However, after an intensive research period during the 1980s, when the oxidative coupling of methane (OCM) was considered to be the future of the natural gas conversion, several research groups noted that, under similar reaction conditions, some catalytic systems yielded large amounts of hydrogen, with no catalyst deactivation.[135] It was also found that very similar catalytic systems were active and stable for CO_2 reforming.[136] Since then, intensive work has been developed regarding the mechanism of the reaction and the parameters required for obtaining a stable catalyst.

The active catalysts for POM and CO_2 reforming are very similar to the supported metals used in SRM. They are all metals from Group 8, 9 and 10 (Ni, Co, Fe, Ru, Rh, Pd, Ir, Pt) and, as in SMR, supported nickel and noble metals catalysts have been the systems most studied. Also, the activity of transition metal carbides (especially Mo) has been considered for CO_2 reforming,[137–139] due to their high coking resistance, although under reaction conditions these systems only seem to be stable at high pressure. Based on equilibrium calculations for the POM reaction, the increase in temperature produces an increase in both conversion and $CO + H_2$ selectivity. In this sense, at atmospheric pressure and 1073 K, the equilibrium predicts a methane conversion higher than 90% and selectivity close to 100% (Fig. 8.3). Increasing pressure has a detrimental effect on the POM reaction. The catalytic systems mentioned have high activity

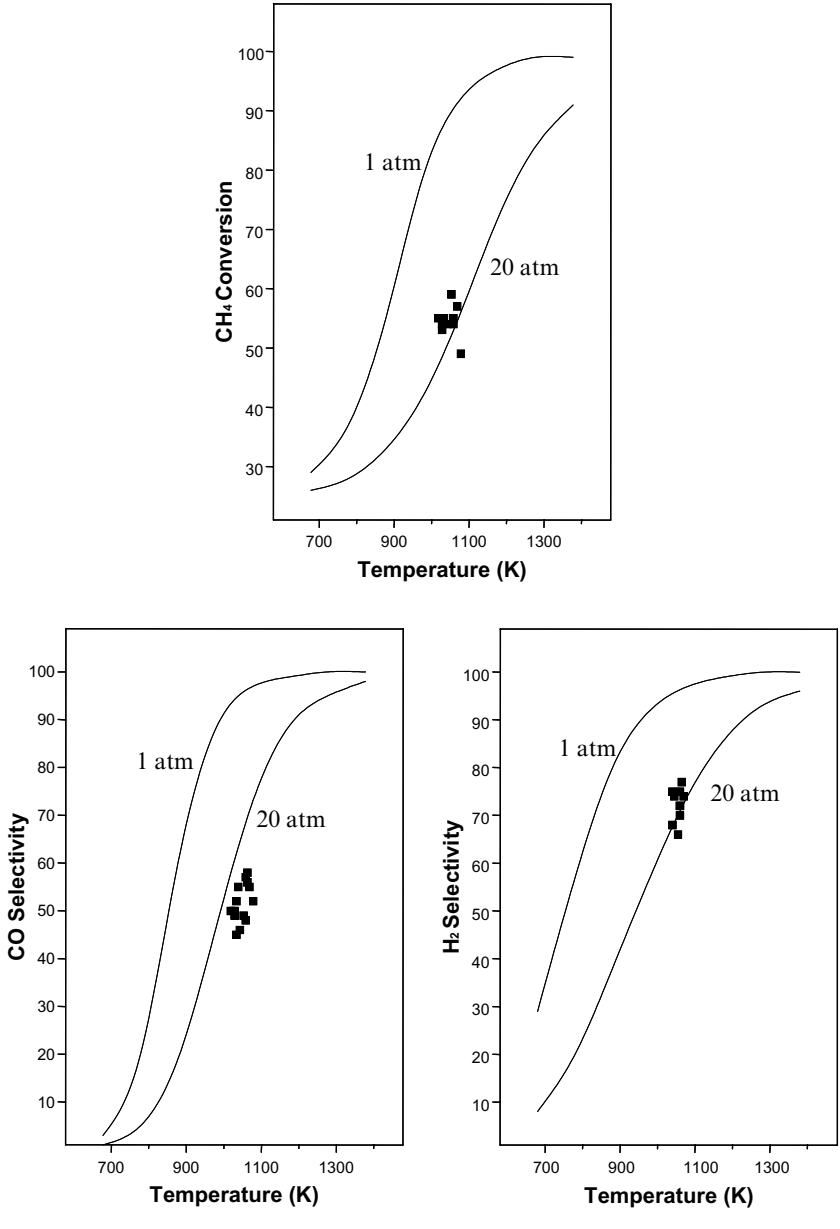

Figure 8.3 Equilibrium calculations for the POM reaction as a function of the temperature, at atmospheric pressure and 20 atm (solid line). Squares correspond to experimental results using nickel-based catalysts.

under these reaction conditions, and they produce the values predicted by the equilibrium. Catalysts for CO_2 reforming are less active, and usually equilibrium values are not obtained.

Since several supported catalytic systems have sufficient activity for the POM reaction, the main topic of research is the stability of the catalysts. There are two main processes for the deactivation of the catalyst: carbon deposition and sintering of the metal. Carbon deposition is due to the process of decomposition of CH_4 and CO (reactions (8.3) and (8.4)). Two different kinds of carbon can be formed in the surface of the catalyst: encapsulated carbon, which covers the metal particle and is the reason for physical-chemical deactivation; and whiskers of carbon, which do not deactivate the particle directly but may produce mechanical plugging of the catalytic bed.

Two mechanisms have been proposed for the POM reaction: (i) The combustion and reforming reactions mechanism (CRR). In this, the methane is combusted in the first part of the catalytic bed, producing CO_2 and H_2O. Along the rest of the bed, and after total oxygen conversion, the remaining methane is converted to $CO + H_2$ by SMR and CO_2 reforming (reaction [2]). (ii) The direct partial oxidation mechanism (DPO). $CO + H_2$ is produced directly from methane by recombination of CH_x and O species at the surface of the catalysts. The development of direct or indirect pathways depends on the concentration of surface oxygen species and the nature of the catalyst. When the concentration of oxygen is low, CO and H_2 are primary products. At high oxygen surface concentrations, CO and H_2 cannot desorb without undergoing further oxidation and CO_2 and H_2O are the main products.

Dissanayake *et al.*[140] showed that the CRR is the working mechanism in Ni/Al_2O_3 catalysts, obtaining almost complete conversion of methane at temperatures higher than 973 K, with a selectivity to $CO + H_2$ of nearly 95%. Analysis of the different phases present in the catalytic bed leads to the conclusion that it is divided into three regions: the first, in contact with the CH_4/O_2 reacting mixture, is a $NiAl_2O_4$ spinel, of moderate activity for methane combustion; the second part is NiO/Al_2O_3, of high activity for methane combustion,

and where the total conversion of oxygen occurs. Finally, the rest of the catalytic bed consisted of Ni/Al_2O_3, active for SRM and CO_2 reforming. The distribution of these different regions is temperature-dependent and is the reason for the observed changes in the behaviour of the catalyst, which is activated in the presence of the reactive mixture at 1023 K, maintains different degrees of activity when the temperature decreases to 773 K, and deactivates at lower temperatures (Fig. 8.4).

The highly exothermic combustion reaction at the top of the catalytic bed produces hot spots in the supported catalysts that increase the problem of deactivation by sintering, but also produce some results concerning activity that are difficult of explain in a first assessment. In this sense, Choudhary *et al.* tested several metal

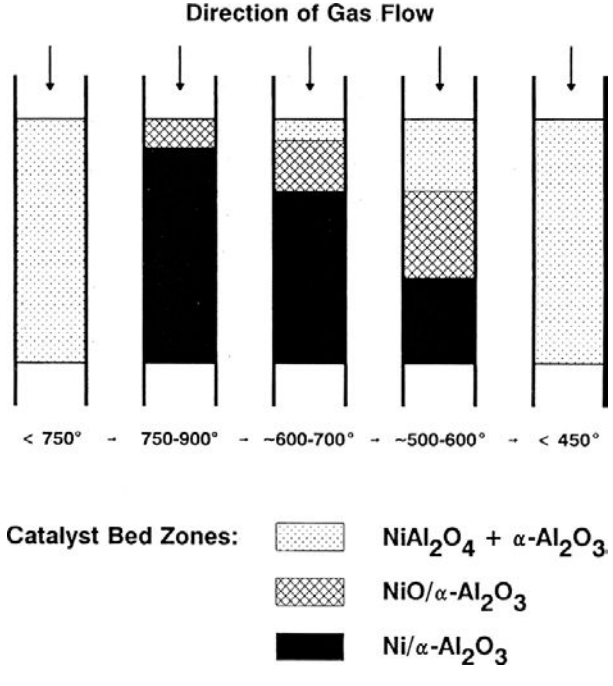

Figure 8.4 Schematic representation of Ni/Al_2O_3 catalyst bed composition during CH_4/O_2 reaction at various temperatures.[140]

supported catalysts such as Co-MgO,[141] Ni-MgO,[142] Ni/Yb_2O_3,[143] and Ni/Al_2O_3[144] with and without pre-reduction at an extremely high space velocity ($5 \cdot 10^5$ $cm^3g^{-1}h^{-1}$). The catalysts were reduced under the reaction conditions at T > 773 K, producing highly dispersed metallic Co or Ni and, after this activation they were still active below 773 K. The methane conversions measured were higher than those of the thermodynamic equilibrium values: at 673 K, 64.6% methane conversion and ≈ 80% H_2 and CO selectivity. Under the same conditions (low temperature), no reforming by CO_2 or H_2O was detected, and the authors concluded that the CRR mechanism is not feasible. The large excess of activity with respect to the equilibrium can be explained in terms of a kinetic control instead of a thermodynamic control. Nevertheless, Dissanayake *et al.*,[145] and Chang and Heinemann[146] demonstrated that this behaviour is due to hot spots in the catalytic bed, which are not detected by the thermocouple (high temperature gradients[147]), although an optical pyrometer indicated that the real temperature in the catalytic bed was higher than 1123 K when the thermocouple indicated a temperature of 723 K. The amount of heat generated was much higher than dissipation through the reactor wall, and the reaction was autosustained (the catalytic bed glowed with the heat source removed for hours). The results correspond to a higher temperature than that indicated by the thermocouple and reported by Choudhary *et al.*, and there is concordance with the equilibrium predictions, as expected. When an industrial reactor is used, the heat exchange problems can be indeed more important. In that case, some engineering solutions, such as the use of fluidised bed reactors, can be applied.[148]

The POM reaction was investigated for supported (ZrO_2, CeO_2–ZrO_2) rhodium catalysts. The activity tests indicated that the indirect reaction mechanism, consisting of methane combustion followed by steam and dry reforming, prevails under the experimental conditions studied.[149] The POM mechanism was investigated on Rh/SiO_2 catalysts using *in situ* FTIR. It was found that CO_2 was formed before CO could be detected when CH_4 and O_2 were introduced over the pre-oxidised Rh/SiO_2 catalyst,

whereas CO was detected before CO_2 was formed over the pre-reduced Rh/SiO_2 catalyst.[150] Similarly, the POM mechanism was studied on supported platinum catalysts by means of temperature-programmed surface reaction analysis.[151,152] The results showed that the POM reaction occurs in two steps on Pt/Al_2O_3, Pt/ZrO_2, Pt/CeO_2 and Pt/CeO_2-ZrO_2 catalysts: combustion of methane followed by H_2O and CO_2 reforming of unreacted methane, since the surface Pt-atoms in these catalysts are initially partially oxidised leading to the formation of full oxidation products, followed by dry and steam reforming. On the other hand, a direct mechanism was observed over Pt/Y_2O_3 catalysts, which is explained by a strong interaction between Pt and Y_2O_3 substrate which caused a moderation in the rates of oxidation and reduction of the metal particle with the formation of a quasi-steady state concentration of metallic sites during reaction conditions. For POM reaction on Pt/ZrO_2-CeO_2-Al_2O_3 catalysts there is strong indication that the reaction proceeds through the two step mechanism.[153] It has also been shown for supported Pt-Ru catalysts that the indirect combustion and reforming mechanism operate in CPO, and that the CPO reaction first yields the maximum amounts of CO_2 and H_2O achievable with the available O_2 according to total combustion.[154]

Besides these results confirming the CRR mechanism, DPO is the active mechanism in other systems. Schmidt and coworkers[155–157] found that POM could be achieved in Pt and Rh monoliths at very high space velocity and low residence times (in the order of ms). Additionally, an increase in the space velocity produces an increase in $CO + H_2$ selectivity. These results are not compatible with the CRR mechanism, but do correctly match the DPO, where C_{ads} and O_{ads} species are formed directly from methane. This does not mean that CRR is the mechanism for nickel catalysts and DPO for noble metals. As will be described below, in some of the examples of metal catalysts used to illustrate this section, the active mechanism is different for different supported metal catalysts, and also changes for the same catalysts when the reaction conditions are modified.

8.2.3.2 *Catalyst supports*

In the search for stable catalysts, the influence of the support has been one of the issues most investigated. The need to support the active metal is evident when supported catalysts are compared with physical mixtures of components.[158] Merely by mixing NiO and Al_2O_3, very low activity is obtained, and this activity increases with time due to the migration of nickel through the alumina phase. Al_2O_3 is the support most widely used owing to its stability at high temperature and under strong reaction conditions and to its commercial availability. However, it is not the most suitable carrier from the point of view of deactivation by sintering and coke deposition and other alternatives have been suggested. Tsipouriari *et al.*[159] compared Ni/Al_2O_3 with Ni/La_2O_3 and found that in the alumina-supported catalysts the deposition of carbon increases with the time on-stream, leading to deactivation. In the lanthana-supported catalyst, carbon is also accumulated, but this carbon deposited on the surface is constant and does not increase with time. The $NiAl_2O_4$-phase, which is difficult to reduce, is not active for the reforming reaction but it is active for carbon formation. Something similar has been described by Barbero *et al.*[160] in different supported Ni catalysts. The better performance of lanthana-supported catalysts is assigned to the formation of a deficient perovskite $LaNiO_{3-\delta}$, that, after reduction, maintains the nickel particles highly dispersed in the La_2O_3 matrix, with stronger resistance to sintering and carbon formation. The same effect is detected when an MgO support is used, due to the formation of a solid solution between nickel and magnesia.[161] Ni/MgO catalysts are more active and even more stable than the parent Ni/La_2O_3 catalysts. The reason for the excellent performance of Ni/MgO catalysts lies in the formation of a cubic (Mg,Ni)O solid solution in which the Ni^{2+} ions are highly stable against reduction even at temperatures as high as 1273 K. Under operation, the small fraction of nickel reduced remains highly dispersed and in close interaction with the basic MgO substrate, this structure being specially suited for syngas production from methane.[162] In contrast, the use of ZrO_2 as a support is not effective,

since its low interaction with nickel produces large metal particles that easily deactivate. The formation of the perovskite-like structure La_2NiO_4, and the formation of small particles of nickel after the reduction of this phase are also the argument used by Luo *et al.*[163] to explain the stability of nickel-lanthanum catalysts supported in zeolite 5A in the CO_2 reforming of methane.

A porous structure of the support also increases the stability of the metal. On comparing α-Al_2O_3 with γ-Al_2O_3, and SiO_2, and MgO of different porosities Lu and Wang[164,165] concluded that porous supports favour metal dispersion and contact between the active sites and reactants, increasing the activity for CO_2 reforming and stability. This is also clear when a commercial γ-Al_2O_3 support was compared with a γ-Al_2O_3 prepared by the sol-gel method.[166] Nickel supported in both aluminas had similar activity, but the stability of the catalyst prepared by sol-gel was higher, and this was explained in terms of the small particle size of the metal, which is below a critical value (10 nm) that is the lowest limit for the formation of carbon on the nickel surface.

The effect of the support has also been investigated in other active metals, and the tendencies are not the same in all cases. Bitter *et al.*[167] found that the trend in stability on supported platinum was $ZrO_2 > TiO_2 > Al_2O_3$. This trend was different in supported nickel, with Al_2O_3-supported nickel being more stable than the corresponding TiO_2-supported catalyst.[158] In the case of Pt, there is no evidence of sintering, and deactivation is produced by blocking of the active centres by carbon. The support, in this case, has a very active role, and for the reducible oxides (TiO_2, ZrO_2) small oxide crystallites decorate the metal particle, producing a better control of carbon formation at this interface. In addition, it has been reported that $Pt/Ce_xZr_{(1-x)}O_2$ catalysts are more active, stable and selective than Pt/CeO_2 and Pt/ZrO_2 catalysts. The higher reducibility and oxygen storage/release capacity of $Pt/Ce_xZr_{(1-x)}O_2$ catalysts promotes the mechanism of continuous removal of carbonaceous deposits from the active sites, which takes place at the metal support interfacial perimeter.[168] Pd supported on ceria-zirconia was found also to be more active and stable than with alumina as support.[169]

For Al_2O_3-, ZrO_2-, CeO_2- and Y_2O_3-supported Pt catalysts, the Pt/CeO_2 system showed the highest stability in the POM reaction due to the higher reducibility and oxygen storage/release capacity which allowed a continuous removal of carbonaceous deposits from the active sites.[170] This reaction has been also studied over Rh supported on Ce oxide with Zr, Gd and La. Results obtained indicate that the type of doped ceria support and its reducibility played an important role in catalyst activity. It was observed that doping CeO_2 with Zr, rather than with La or Gd, causes an enhanced reducibility of Rh/supported ceria catalysts which increases the activity of the system for the production of syngas.[171]

Zhang *et al.*[172] found that the activity for CO_2 reforming in supported Rh catalysts followed the order: YSZ > Al_2O_3 > TiO_2 > SiO_2 > La_2O_3 > MgO, which is directly correlated with the acidity of the support. Deactivation is controlled by other parameters, since in a specific support it decreases when the particle size of Rh increases. Nevertheless, the nature of the support has a stronger influence in the catalytic lifetime, which is low on TiO_2 and MgO within the previously mentioned support series. These latter data contrast with the results for nickel catalysts, where MgO is an excellent catalyst support owing to the formation of the Ni-Mg-O solid solution. The formation of this solid solution is not favoured in the Rh-Mg system. Also, some differences are found in supported Ir catalysts, with an activity trend for the POM in the order TiO_2 > ZrO_2 > Y_2O_3 > MgO > Al_2O_3 > SiO_2.[173] In these systems, SRM does not change with the support, and the trend for POM and CO_2 reforming is the same. Therefore a CRR mechanism can be concluded for these catalysts. Bradford and Vannice[174] studied different CO_2 reforming active metals (Ni, Co, Fe, Rh, Pd, Ir, Pt) supported on TiO_2 and SiO_2. The TOF depended on the d-character of the transition metal, but the activity maximum was different for each support: Rh for TiO_2 and Pt for SiO_2.

Besides the stabilization of the dispersed metal, some supports also participate in the activation of reactants and/or reaction intermediates. In the POM reaction on Rh/Al_2O_3,[175] H_2O is adsorbed on the support, which plays the role of the oxygen source. Also in Ni

and Ru supported in Al_2O_3, a similar effect is produced, due to the formation of hydroxyl groups at the surface of Al_2O_3 that provide oxygen to the active metal sites. In contrast, when these metals are supported on SiO_2, the support does not participate in the reaction mechanism. Some CH_xO species have been found by DRIFTS at the interface of metal-TiO_2[174] during CO_2 reforming, also pointing to the activation of CH_4 and CO_2 in the support. A bifunctional mechanism has been proposed for CO_2 reforming on Rh/Al_2O_3,[176] where CO_2 is activated in the support as a formate intermediate, and CH_4 is activated on the metallic Rh. In this sense, there is an important role for the metal support interfacial zone, where both intermediates should come together. Nevertheless, the addition of inactive copper to this catalyst, which limits diffusion at the Rh-Al_2O_3 interface, reduces stability but does not produce a decrease in the TOF of Rh. This implies that the reaction is not structure-sensitive. This is also found in the case of Rh/SiO_2.[172]

It is also important to consider the use of a sulfating support which minimises the poison of sulphur compounds present in natural gas from adsorbing on or near the active metal sites. Thus, using La_2O_3-Al_2O_3 as a support in Rh-based catalysts, the partial oxidation reaction is much less inhibited than with a less sulphating support such as SiO_2-Al_2O_3, since the support is capable of acting as a sulphur storage reservoir.[177]

8.2.3.3 *Reaction intermediates*

The intermediates formed at the surface of the catalysts, and the way in which they participate in the reaction mechanism, differ depending on the active metal, the support, and the interactions between the two. In nickel supported on Ce-doped ZrO_2, two kinds of sites have been identified,[178] one for the activation of CH_4 and the other for activation of O_2 and/or H_2O. The balance of these sites depends on the nickel loading, and is optimum for 15%, since for this loading the interaction of nickel with the support is sufficient to balance the number of active sites. The formation of carbonates is easy when basic supports are used, and in Ni/La_2O_3

they can be detected by FTIR.[179] In this system, Ni^o, La_2O_3, $La_2O_2CO_3$, NiO and Ni_3C-phases have been identified during POM reaction. The presence of the surface carbide seems to be important for the activity of the catalyst for CO_2 reforming, and in Ni/SiO_2 a carbide-like layer reacts with adsorbed oxygen (due to CO_2 activation) to produce CO.[180] In a parallel manner, this carbide can diffuse through the metallic particles, forming carbon deposits that deactivate the catalysts. In this sense, the carbide provides active sites and deactivation precursors at the same time. Li *et al.*[181] have followed the surface state of Ni/Al_2O_3 by a transient response technique, concluding that if the oxygen is the most abundant surface intermediate, the catalyst is not active, and that a catalyst in the reduced state, covered by adsorbed carbon, is essential for the activation of the reactants. This reduced state of the metal surface as a condition for the activation of the reactants has also been observed in Rh/Al_2O_3 by TAP experiments,[175] since CH_4 is adsorbed dissociatively on the metal and the pre-adsorption of oxygen reduces this activation. Moreover, the degree of oxygen coverage changes the mechanism of reaction: from DPO at low oxygen coverage to CRR at high oxygen coverage.

In CO_2 reforming, CH_4 and CO_2 are activated in different ways, depending on the active metal. Schuurman *et al.*[182] studied Ni and Ru supported on SiO_2 and Al_2O_3 by TAP. CH_4 was activated by decomposition on both metals producing H_2 and adsorbed carbon. However, the behaviour of CO_2 was different on each metal. CO_2 was adsorbed on Ni to produce CO and adsorbed oxygen. O_{ads} and C_{ads} reacted later in a Langmuir–Hinshelwood mechanism to produce CO: this is the rate determining step. Nevertheless, on Ru, CO_2 reacts directly with C_{ads} (Eley–Rideal mechanism) to produce CO. No adsorbed oxygen is present in this case, and the rate determining step is the adsorption of methane. This activation mechanism is slightly different in the system $Ni\text{-}La_2O_3$/Zeolite 5A, studied by Luo *et al.*[163] Isotopic experiments revealed that the deposition of carbon was due to both CH_4 and CO_2 through a disproportionation of the CO produced. When temperature was increased, the contribution of CO_2 to the carbon formation was greater. At the surface of

this catalyst, HCOO seems to be the intermediate, which is formed by activation of CO_2 on H_{ads}, and of CH_4 on O_{ads}.

Methane dissociation requires a reduced metal surface, but at elevated temperatures oxides of the active species may be reduced by direct interaction with methane or from the reaction with H, H_2, C or CO. The comparison of elementary reaction steps on Pt and Rh illustrates that a key factor to produce hydrogen as a primary product is a high activation energy barrier to the formation of OH. A catalytic material and support which does not easily form or stabilise OH species is therefore desirable. Another essential property for the formation of H_2 and CO as primary products is a low surface coverage of intermediates, such that the probability of O-H, OH-H and CO-O interactions is reduced.[183]

8.2.3.4 *Promoting effects*

The stability of catalysts can be improved not only by the use of an appropriate support, but also by doping the supported catalyst with other added metals. In Ni/Al_2O_3, a beneficial effect of the addition of noble metals (Pt-Pd-Ru) has been described.[184] When the catalyst is used in reaction without pre-reduction, the temperature at which the catalyst is activated under reaction conditions by the reduction of nickel (T_S) is lower when a noble metal is included in the composition. Additionally, catalytic activity is higher when Pt and Ru are the promoters. The activity is similar in Ni and Ni-Pd systems, but Pd is the metal that provides a lower T_S. This behaviour can be explained taking into account that hydrogen is homolytically dissociated at the surface of the noble metals, which are in close association with the nickel and the hydrogen atoms thus formed can easily reduce the $NiAl_2O_4$-phase present in the catalyst. Nichio *et al.*[185] promoted Ni/Al_2O_3 by adding a tin organo-metallic complex to the catalyst in the reduced state (metallic Ni). This procedure allows the collection of bimetallic Sn-Ni systems with a good interaction between metals, and, at concentrations of Sn in the 0.01–0.05% range ($Sn/Ni^{surf} < 0.5$), the deposition of carbon upon reaction decreases with no appreciable change in the catalytic

activity. The Sn causes breakage of the Ni ensembles, active for carbon deposition (this is a structure-sensitive reaction), but is not enough to affect the active sites for POM and CO_2 reforming. The effect is similar to that produced in nickel catalysts promoted with potassium in SRM, where K-atoms block step sites at the surface of the Ni, and these are the active sites for carbon formation.[2] Manganese also promotes Ni/Al_2O_3 for CO_2 reforming by decreasing carbon deposition.[186] In this case, Ni particles are partially covered by MnO_x patches, and its role is to promote the adsorption of CO_2, producing a reactive carbonate. This carbonate reacts with the CH_x fragments, preventing coke from being formed from these fragments. Additionally, the MnO_x patches break the Ni ensemble necessary for carbon formation, without reducing the activity of the catalyst. The most typical way of promoting nickel catalysts is by the use of alkaline and alkaline earth metals. Chang *et al.*[187] explained the promotion with K and Ca of Ni/NaZSM-5 zeolite by the formation of surface carbonates, produced by the interaction of CO_2 with the alkaline promoters, which hinder the formation of inactive coke or scavenge carbon from the surface Ni species. In isotopic effect experiments, they also observed that the activation of CH_4 at the nickel surface is not the rate determining step in the DPO mechanism. The rate is determined by the reaction of $O_{ads} + C_{ads}$, as previously shown by Schuurman *et al.*[182] for Al_2O_3- and SiO_2-supported Ni catalysts. The stabilisation of the catalysts by reducing carbon deposition has been also successfully achieved in $Ni/\gamma\text{-}Al_2O_3$ catalysts promoted with Li and La.[188–190]

Zirconia,[191] lanthana,[27] and ceria[149] have been recently reported as promoters of methane reforming reactions. Incorporation of a 5 wt% ZrO_2 to a base Ni/SiO_2 catalyst resulted in excellent performance for the reforming of methane with a $CO_2 + O_2$ mixture in a fluidised bed reactor. A conversion of CH_4 near thermodynamic equilibrium and low H_2/CO ratio ($1 < H_2/CO < 2$) was obtained without catalyst deactivation for 10 h on-stream, in a most energy efficient and safe manner. It has been argued that ZrO_2 could promote the dispersion of Ni on the silica substrate, which has a direct effect on its reduction behaviour, CO_2 adsorption and catalytic

performance.[191] We recently reported the promotional effect of lanthana on the structural and catalytic properties of Pt/La_2O_3-Al_2O_3 catalysts in methane steam reforming and methane partial oxidation reactions.[27] While the La-free Pt/Al_2O_3 catalyst was strongly deactivated during the methane partial oxidation reaction, the La_2O_3 promoted counterpart displayed much better stability. The increase of activity observed during the reaction was ascribed to the ability of the $[LaPt_xO]Pt^0$-like species to promote the gasification of coke. According to this cleaning mechanism, active sites remain accessible to CH_4 molecules.[27] Similarly, ceria doping of supported Rh catalysts resulted in significant improvement of methane conversion and syngas selectivity during the methane partial oxidation, which could be related to higher noble metal dispersion.[149] For the cerium (1 wt%)-doped Pt/Al_2O_3 catalyst, the good activity and stability in the partial oxidation of methane was associated with its higher metal dispersion, higher oxygen storage capacity and larger degree of alumina coverage by the $CeZrO_2$ moiety which make the carbon cleaning mechanism effective.[192]

8.2.3.5 *Perovskite and hydrotalcite precursors*

The use of perovskite oxides as precursors of metal-supported catalysts has been also extensively used. Perovskites are mixed oxides with a general stoichiometry of ABO_3, where A and B can be partially substituted by other metals. One of the early studies on POM was made on $Ln_2Ru_2O_7$ pyrochlores,[135] which are structures related to perovskites. Most of the perovskites studied have a lanthanide and/or alkaline earth metal in the A site, and the active metal in the B site. After reduction, a highly dispersed metal supported in the lanthanide or alkaline earth oxide is obtained. Batiot-Dupeyrat *et al.*[193] have studied CO_2 reforming in the $LaNiO_3$ perovskite precursor, obtaining total conversion of methane and selectivity to CO of 92% at 1073 K. Some formation of carbon was detected, but with no change in activity after 90 pulses of the reacting mixture. Different phases are present in the catalysts depending on the temperature of reaction. At temperatures higher than 1000 K, the

catalyst can be described as Ni/La_2O_3. But at lower temperatures, the La_2NiO_4 spinel is present. The reaction mechanism in this catalyst can be described as an intrafacial cycle, where CO_2 oxidises metallic nickel to produce the La_2NiO_4 spinel, which is successively reduced to Ni^o by CH_4. However, although the use of La_2NiO_4 as a starting material is possible, perovskite as a catalyst precursor is favoured. In this sense, Guo *et al.*[194] showed that the activity of the final catalysts is better if $LaNiO_3$ is used instead of La_2NiO_4. The promoting effect of other metals can be also analysed using perovskites by partial substitution of the active metal. In the $LaNi_xFe_{1-x}O_3$ perovskite, stabilisation of the active phase is produced by Fe, limiting the reversible mobility of Ni from the La_2O_3 matrix to the metallic particles.[195] This avoids the sintering of nickel, controlling the particle size. The best catalyst of this series is $LaNi_{0.3}Fe_{0.7}O_3$, which at 1073 K does not show deactivation after 250 h on-stream. In some cases, the precursor does not have to be a perovskite to obtain an optimum catalyst. In $Ca_{1-x}Sr_xTi_{1-y}Ni_yO_3$,[196] the perovskite structure is only obtained if $y < 0.1$. Nevertheless, the best catalysts are prepared by reduction of a system with values of $x = y = 0.2$. This means that part of the Ni is initially in the form of free NiO, not integrated in the perovskite structure. However, the final active catalyst is mainly $Ni/Ca_{0.8}Sr_{0.2}TiO_3$. This catalytic system works by the CRR mechanism, with the first part of the bed in the original oxidised form. The perovskite can be also used for the preparation of bimetallic catalysts, as in the case of $LaRu_{0.8}Ni_{0.2}O_3$. This system has been studied by Goldwasser *et al.*[197] with partial or total substitution of La by Sm, Nd and/or Ca. These substitutions improve the catalytic activity for CO_2 reforming, since the reduction of the active metals is easier. In all the cases, metal bimetallic particles of a very small particle size (9–17 nm) were obtained. When perovskites are used as precursors, careful consideration should be given to the nature of the interactions of the different metals. As an illustrative example, Lago *et al.*[198] analysed the behaviour of $LnCoO_3$ systems (Ln : La, Pr, Nd, Sm, Gd). In this series, the reduced Gd-Co perovskite had the highest activity for POM, followed by Sm > Nd > Pr. The reduced La-Co perovskite was only active for the combustion of methane. XPS analysis of the

used catalysts revealed that Co is oxidised to form the original $LaCoO_3$ perovskite under the reaction conditions used. In the Nd-Co system, cobalt is partially oxidised, and in Gd-Co and Sm-Co catalysts cobalt remains reduced. TPR analysis of the perovskites reveals that reduction is produced in two steps ($LnCoO_3 \rightarrow LnCoO_{2.5} \rightarrow Co/Ln_2O_3$); that this reduction is reversible, and that the reduction temperature depends on the lanthanide employed. The most stable perovskite, $LaCoO_3$, is harder to reduce and is very easily reversed to the oxidised state, as revealed by TPO experiments. This trend in stability (quantified as Goldschmidt's tolerance factor and the TPO temperature) can be compared with the catalytic activity in Fig. 8.5. It may be concluded that very stable perovskites are not appropriate precursors of metal supported catalysts, since the metallic particles will tend to reverse to the perovskite phase.

The reduced $NdCoO_3$ perovskite-type catalyst (Co dispersed on Nd_2O_3, after a reduction pre-treatment) has been found to be a highly promising catalyst for carbon-free CO_2 reforming combined with steam reforming or partial oxidation of methane to syngas. In the simultaneous CO_2 and steam reforming, the conversion of methane and H_2O and also the H_2/CO product ratio are strongly influenced by the CO_2/H_2O feed ratio. In the simultaneous CO_2 reforming and partial oxidation of methane, the conversion of methane and CO_2, H_2 selectivity and the net heat of reaction are strongly influenced by the process parameters (temperature, space velocity and relative concentration of O_2 in the feed). In both cases, no carbon deposition on the catalyst was observed.[199] The use of a catalyst derived from a double perovskite ($(La_{0.5}Sr_{0.5})_{(2)}\ FeNiO_6$) has also shown very high CH_4 conversion (>99%) and syngas selectivity (>98%) and, most importantly, no coke formation was recorded at reaction temperature of 900°C. Detailed structural characterisation revealed that the presence of a small amount of $SrCO_3$ and of nano-Ni^0 domains (or clusters <5 nm on average) is vital to this extraordinary catalytic performance.[200]

Another type of system that has been applied as a precursor is the example of hydrotalcite-type material. Hydrotalcite can be described as $Mg_6Al_2(OH)_{16}CO_3 \cdot 4H_2O$, and it is structured in Mg–Al–OH

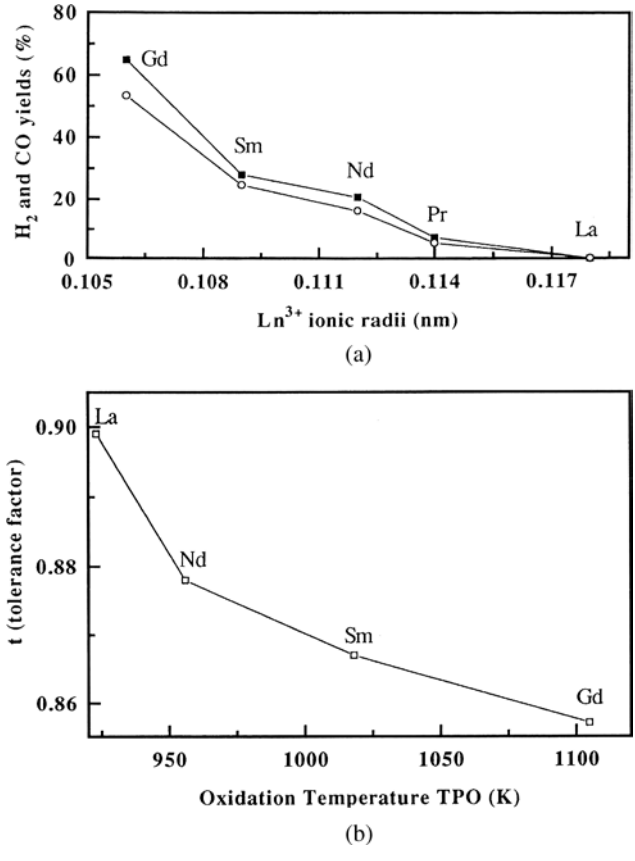

Figure 8.5 Behaviour of $LnCoO_3$ perovskites: (a) H_2 (■) and CO (○) yields from partial oxidation of methane as a function of the lanthanide ionic radii; and (b) Goldschmidt's tolerance factor t and the oxidation temperature obtained from temperature-programmed oxidation experiments.[198]

layers with the carbonate anions and water in the interlayer spaces. Hydrotalcite-derived materials are prepared by partial or total substitution of Mg and/or Al by other metals.[201] After calcination a mixed oxide is obtained, with the characteristic that the original hydrotalcite can be recovered by rehydration. Basile *et al.*[147] and Shishido *et al.*[202] have prepared Ni–Mg–Al hydrotalcites as starting materials of Ni-supported catalysts for POM, obtaining good results with regards activity and stability. Tsyganok *et al.*[203] have also compared

different methods for obtaining the final catalysts from hydrotalcites, when nickel is incorporated to the interlayer space as $[Ni(EDTA)]^{-2}$. The best results (lower carbon deposition and smaller Ni particle size) are obtained when the hydrotalcite is prepared by co-precipitation in presence of the $[Ni(EDTA)]^{-2}$, which is nested between layers.

Ni containing silicate catalysts obtained by decomposition of hydrotalcite-like compounds were also tested in the catalytic partial oxidation of methane. Increasing the silicate load resulted in a decrease of the specific surface area and the Ni dispersion. Moreover, the samples with large silicate content were deactivated by oxidation of metallic nickel particles.[204] Hydrotalcite structure also allows the introduction of promoters, such as halogens. Fluorine-modified Ni-Mg-Al mixed oxides were prepared and tested in the partial oxidation of methane. The results revealed that fluorine was successfully introduced into Ni-Mg-Al mixed oxide *via* the high dispersion of MgF_2. Such catalysts showed a high performance over POM without deactivation even after 120 h at 1023 K. This could be reasonably attributed to the promotion effect of the F^- anions, which improved the homogeneous distribution of nickel and basicity of the catalyst with high resistance to coking and sintering.[205] By repeated 'calcination–reconstruction' cycles, transition metals (Cr, Fe, Co, Ni and Cu) were introduced with ruthenium into layered double hydroxide structure. Preliminary calcination hydrotalcite was shown to markedly affect catalytic behaviour of the derived catalysts and especially their coking capacity. Among all the bimetallic catalysts tested, a $Ru0.1\%–Ni5.0\%/MgAlO_x$ appeared the most attractive for the dry reforming of methane because it demonstrated the highest activity and selectivity to syngas, no induction time when generated *in situ*, a suitable durability and a low coking capacity.[206]

8.3 Alcohol Conversion

8.3.1 *Methanol*

Hydrogen gas has a high fuel density but is difficult to handle. A simple alternative source of hydrogen, despite its substantially lower

energy density, is methanol because this molecule can be decomposed to hydrogen containing mixtures by chemical or physical methods. Among these, catalytic processes including decomposition, steam reforming and oxidative processes remain prominent and are therefore examined in this section.[207]

8.3.1.1 *Methanol decomposition*

Methanol decomposition is an on-site source of H_2 and CO for chemical processes and fuel cells:

$$CH_3OH \rightarrow CO + 2\ H_2 \qquad \Delta H^{\circ}_{298} = +\ 91\ \text{kJ mol}^{-1}. \tag{8.8}$$

The reaction is endothermic and can be performed on metals from Group 10, among which Ni and Pd have been those most widely studied. These metals have been supported on different oxide substrates such as Al_2O_3, TiO_2, SiO_2, CeO_2, ZrO_2 and Pr_2O_3.[208–219]

Among the different metals, palladium seems to be the most effective for methanol decomposition and in the case of Pd supported on CeO_2 it was observed that the decomposition reaction of methanol is sensitive to the metal structure of the catalyst.[219] Usami *et al.*[209] tested a number of metal oxide supported Pd catalysts and found that Pd/CeO_2, Pd/Pr_2O_3 and Pd/ZrO_2 catalysts prepared by a deposition-precipitation procedure were active for the selective decomposition of methanol to H_2 and CO at temperatures below 523 K. It was observed that the interaction of the Pd-phase and the ZrO_2 to a large extent influences the performance of Pd/ZrO_2 catalysts in which smaller metal particles and a stronger contact with the support should be favourable for the decomposition reaction. In particular, the TOF values for methanol decomposition suggested that the CeO_2 and Pr_2O_3 systems are better candidates than ZrO_2 for supporting palladium crystallites on their surface.

In addition, La_2O_3 is a particularly attractive support because it affords high selectivity and specific activity in the methanol synthesis reaction. La_2O_3-modified palladium catalysts have been reported to be very active for the synthesis of methanol from $(CO + H_2)$

mixtures.[220] Like the reverse reaction of methanol synthesis from ($CO + H_2$) gas mixtures, the methanol decomposition reaction was also tested over a series of Pd/SiO_2 catalysts promoted with lanthanum oxide.[221] In keeping with these ideas, La-modified Pd/CeO_2 catalysts were prepared and tested in the reaction of methanol decomposition.[222] The addition of La_2O_3 to a $2\%Pd/CeO_2$ catalyst significantly improved catalytic behaviour in the target reaction. Over the La-modified $2\%Pd/CeO_2$ catalyst, complete conversion of methanol can be achieved at around 548 K, which in turn is nearly 40 K lower than the temperature needed for the $2\%Pd/CeO_2$ catalyst. The TPR profiles showed that the presence of La_2O_3 shifted the reduction temperature of CeO_2 to lower values, while it hindered the reduction of PdO crystallites due to an accelerated diffusion of oxygen at the La_2O_3-CeO_2 interface.

The greater activity of Pd for methanol decomposition reaction was also found by using the steady state isotopic transient kinetic analysis (SSITKA) method over noble metal (Pt, Pd, Rh)/ceria catalysts. Their activity increased in the order Rh < Pt < Pd, while the by-products were (i) methane, carbon dioxide, water, methyl formate and formaldehyde in most cases and (ii) ethylene and propylene, formed only over Rh/CeO_2, at 553 K. SSITKA measurements indicated that two parallel pools exist for the formation of CO (*via* formation and decomposition of formaldehyde and methyl formate). The difference in the activity order of noble metal/ceria catalysts seems to correlate with the surface coverage of active 'carbon containing' species, which followed the same order. The latter implies that a part of these species is formed on the ceria surface or/and metal-ceria interface.[223]

Mechanistic information on the reaction derived from well-defined Pd, Co and PdCo systems revealed that methanol is dehydrogenated to CO even at room temperature by the Pd and Pd-Co catalysts, but high steady state conversion requires temperatures at or above 423 K. Experiments conducted under UHV conditions revealed that CO desorption is the limiting factor at lower temperature. Pure Pd catalysts were found to be more active for methanol decomposition than the bimetallic Co-Pd catalysts.

Although electronic effects in the bimetallic system facilitate desorption of CO at low temperature, this cannot compensate for the lower intrinsic activity of Co sites.[224] Experimental findings imply that edge sites (and other defects) on Pd nanocrystallites exposing mainly (111) facets in supported model catalysts are crucial for catalyst modification *via* deposition of CH_x ($x = 0 - 3$) by-products of methanol decomposition. To explore this problem computationally and to unravel the mechanism of how CH_x species are formed, DFT calculations of C–O bond scission in methanol and various dehydrogenated intermediates (CH_3O, CH_2OH, CH_2O, CHO, CO) deposited on the cubo-octahedron model particle Pd_{79}, were carried out. From the computational results, it was concluded that the decomposition products CH_3 and CH_2 preferentially adsorb at edge sites of nanoparticles. Low-coordinated (edge) sites on Pd nanoparticles accelerate the catalyst contamination by decomposition of CH_x species. In particular, CH_3 and CH_2 products of CH_3O and CH_2OH decomposition were found to occupy preferential positions at the edges of the Pd_{79} nanoparticle. Computational results suggest that CH_3 and CH_2 species undergo fast dehydrogenation to CH and C.[225]

8.3.1.2 *Methanol steam reforming*

Several reactions can be used for the production of hydrogen from methanol. The most widely applied one is probably the steam reforming reaction.

$$CH_3OH + H_2O \rightarrow CO_2 + 3\ H_2 \qquad \Delta H^{o}_{298} = +\ 50\ \text{kJ mol}^{-1} \qquad (8.9)$$

A large variety of catalysts for the steam reforming of methanol which include copper in their composition have been reported.[226–231] Commercial Cu/ZnO water-gas shift and methanol synthesis catalysts[229,230] have also been found to be active for the steam reforming reaction. Microstructural characteristics of the copper phase in Cu/ZnO catalysts depended on the aging time of the precipitate, resulting in changes in reducibility and crystallite size which produced an increase in the catalytic activity. Moreover,

continuous precipitate aging led to decreasing amounts of Zn in the copper clusters of the Cu/ZnO catalysts. The proposed model emphasises the defect-rich state of the homogeneous microstructure of Cu/ZnO catalysts and its implication for the catalytic activity in the steam reforming of methanol.[232]

Shimokawabe *et al.*[231] have also reported that highly active Cu/ZrO_2 could be prepared by impregnation of a ZrO_2 substrate with aqueous solutions of the $[Cu(NH_3)_4(NO_3)_2]$ complex, which is more active than the corresponding Cu/SiO_2 catalysts. Of particular interest is the use of ZrO_2 as a substrate for the copper phases. Highly active Cu/ZrO_2 catalysts have been prepared by a variety of different methods, including impregnation of copper salts onto the ZrO_2 support,[233,234] the precipitation of copper,[233–236] the formation of amorphous aerogels,[237,238] and CuZr alloys.[239] The central idea in all these studies is to maintain the zirconia support in an amorphous state under the calcination and reaction conditions so as to retain a high level of activity. The major drawback of zirconia crystallisation is a dramatic drop in both the copper levels and the specific surface area of the catalysts. A high copper-zirconia interfacial area must be maintained to prevent catalyst deactivation. Tetragonal zirconia can be stabilised by the incorporation of Al_2O_3, Y_2O_3 and La_2O_3 oxides,[240] thus preventing, or at least minimising, its crystallisation.

Breen and Ross[241] found that $Cu/ZnO/ZrO_2$ catalysts are active at temperatures as low as 443 K but they severely deactivate at temperatures above 590 K. However, deactivation is inhibited upon incorporation of Al_2O_3. The deactivation may be explained by considering the transformation of amorphous zirconia into a crystalline metastable tetragonal ZrO_2-phase. It was shown that the temperature of crystallisation of zirconia can be reduced to a considerable extent in the presence of steam,[240] which accelerates crystal growth. The improvement of catalyst stability brought about by Al_2O_3 incorporation comes not only from the increase in the temperature of crystallisation of ZrO_2 but also from the effect of increasing the copper area and the total area of the catalysts. *In situ* bulk structural investigations of a nanostructured Cu/ZrO_2 catalyst under methanol steam reforming conditions revealed small and disordered CuO

particles as the main copper phase present in the precursors. Reduction of the Cu/ZrO_2 catalyst in the feed or re-reduction after oxidation resulted in supported nanoparticles with an increased amount of oxygen in the copper particles, which correlates with the increased activity of the Cu/ZrO_2 catalyst. In contrast to conventional Cu/ZnO catalysts, only a minor degree of microstrain is detected in the active copper phase of Cu/ZrO_2 catalysts. The decreased reducibility of CuO/ZrO_2, the low degree of microstrain and the correlation between the amount of oxygen remaining in the copper particles and catalytic activity, indicate a different metal support interaction compared with Cu/ZnO catalysts.[242]

The effects of ZnO, CeO_2, ZrO_2 and Al_2O_3 on the SRM reaction have been clearly identified. Zirconium oxide promoted the SRM reaction and slightly reduced the concentration of CO, but CeO_2 and Al_2O_3 weakened the SRM reaction. The introduction of ZrO_2 into $CuO/ZnO/Al_2O_3$ (30/60/10, proportions in commercial catalyst) improved the reducibility and stability of the catalyst. The addition of CeO_2 or Al_2O_3 hindered the reducibility of the catalyst and weakened the interaction between CuO and ZnO. Nevertheless, an appropriate amount of Al_2O_3 is needed for the stability and the mechanical strength of the catalysts. The $CuO/ZnO/ZrO_2/Al_2O_3$ (30/40/20/10) and (40/30/20/10) catalysts are good candidates for the SRM, as determined by comparison with the commercial catalyst.[243]

ZnO-supported palladium-based catalysts have been shown in recent years to be both active and selective towards the steam reforming of methanol, although they are still considered to be less active than traditional copper-based catalysts. The activity of PdZn catalysts can be significantly improved by supporting on alumina. It has been shown that the $Pd/ZnO/Al_2O_3$ catalysts have better long-term stability when compared with commercial $Cu/ZnO/Al_2O_3$ catalysts, and that they are also stable under redox cycling. The $Pd/ZnO/Al_2O_3$ catalysts can be easily regenerated by oxidation in air by re-exposure to reaction conditions, while the Cu/ZnO-based catalysts do not recover their activity after oxidation.[244] A novel palladium-based catalyst has been recently

developed for use in a miniature fuel-cell power source for portable applications, incorporating a polymer electrolyte membrane (PEM) fuel cell. Hydrogen, which is the fuel for the cell, is produced in a ceramic microreactor *via* the catalytic reaction of methanol steam reforming. The need for a new catalyst in this application is driven by the limitations of traditional particulate catalysts based on copper oxide, zinc oxide and alumina (Cu–Zn–Al catalysts), which have low thermal stability and high sensitivity towards air and condensing steam. These features result in a declining activity and mechanical integrity of Cu–Zn–Al catalysts under the frequent start-stop conditions typical of the operational mode of the miniature power source. The new Pd-based catalyst has activity and selectivity similar to those of Cu–Zn–Al catalysts, but is more durable and stable under the duty cycle conditions of a portable power source.[245]

The activity and selectivity of ZnO and CeO_2-supported Pd catalysts has been also investigated. The Pd/ZnO catalysts exhibited lower MSR rates but were more selective for the production of CO_2 than the Pd/CeO_2 counterparts. The CH_3OH conversion rates were proportional to the H_2 chemisorption uptake suggesting that the rate determining step was catalysed by Pd. The selectivities are explained based on the reaction pathways and characteristics of the support. The key surface intermediate appeared to be a formate. The ZnO-supported catalysts had a higher density of acidic sites and favoured pathways where the intermediate was converted to CO_2 while the CeO_2-supported catalysts had a higher density of basic sites which favoured the production of CO.[246] The high activity and selectivity of Pd/ZnO catalysts for MSR have been attributed to the formation of PdZn alloy, with formation of large sized PdZn crystallites which exhibit high reactivity and low CO selectivity during methanol steam reforming being found.[247] The effect of ZnO morphology on Pd/ZnO activity for steam reforming of methanol has been studied. The ZnO morphology was varied using different Pd precursors and catalyst preparation methods. The original morphology was preserved using an organic Pd precursor. The catalyst activity, normalised to Pd weight, and for

similarly sized metal particles, strongly depends on ZnO morphology, it being found that the more faceted the ZnO, the higher the catalyst activity and suggesting that this ZnO might be a Zn source for PdZn alloy formation. Furthermore, ZnO might be facilitating one of the intermediate steps in methanol steam reforming.[248] Recently, it has been proposed that the selectivity to carbon dioxide could be controlled through the formation of PdZn surface alloys. A Pd-Zn multilayer alloy (ensembles of PdZn exhibiting a Zn-up/Pd-down corrugation) is CO_2 selective and acts as a bifunctional active site both for water activation and for the conversion of methanol into CO_2.[249]

Besides formulations based on supported Cu and Pd, other catalytic systems have also shown high activities for the steam reforming of methanol. Good activity and selectivity towards hydrogen production have been found for the steam reforming of methanol over a series of copper-manganese spinel oxide catalysts. The results show that formation of the spinel $Cu_xMn_{3-x}O_4$ phase in the oxidised catalysts is responsible for the high activity. Cu-Mn catalysts were found to be superior to CuO-CeO_2 catalysts prepared with the same technique.[250] $CuMn_2O_4$ spinel with a high specific surface area and a tangled structure that apparently resembles the internal surface of the amorphous silica gel show a high catalytic activity, similar to that of the most active catalyst reported in the literature, with the advantage that their stability is enhanced.[251] The higher activity in methanol steam reforming of the spinel-derived catalyst compared with the one derived from the non-spinel system is due to the higher dispersion of Cu metal.[252] Production of hydrogen by the MSR reaction has been successfully achieved over a series of Ni/Al layered double hydroxide catalysts. The presence of potassium and/or sodium cations was found to improve the activity of methanol conversion. The selectivity for CO_2 rather than CO was better with K ions than Na ions, especially at higher temperatures. Methanol steam reforming over a K promoted Ni/Al layered double hydroxide catalyst resulted in better activity and similar stability compared with a commercial Cu catalyst.[253,254]

8.3.1.3 *Partial oxidation of methanol*

Copper-zinc catalysts

Copper-zinc catalysts have been found to be very active for the partial oxidation of methanol.[255]

$$CH_3OH + \tfrac{1}{2}\, O_2 \rightarrow CO_2 + 2\, H_2 \qquad \Delta H^{\circ}_{298} = -192 \text{ kJ mol}^{-1} \qquad (8.10)$$

The partial oxidation reaction started at 488 K and the rates of methanol and oxygen conversion increased strongly with temperature to selectively produce H_2 and CO_2 (Fig. 8.6). The rate of CO formation was very low throughout the temperature range explored (473–498 K) and H_2O formation decreased for temperatures above 488 K. As a general rule, methanol conversion to H_2 and CO_2 increased with the copper content, reaching a maximum with $Cu_{40}Zn_{60}$ catalysts (sub indexes are atomic percentages) and decreasing for higher copper loadings. The $Cu_{40}Zn_{60}$ catalyst with the highest copper metal area was the most active and selective for the partial oxidation of methanol. Unreduced catalysts prior to the reaction displayed very low activity, mainly producing CO_2 and H_2O and only traces of H_2. From the reaction rates and copper areas, TOF values were calculated as a function of the copper content at constant temperature (497 K). It was shown that both the apparent activation energy (E_a) and the TOF were higher for the low-copper catalysts and they decreased slightly, tending to a constant value at Cu-loadings above 50% (atom). The simultaneous variation of E_a and TOF suggests that the enhancement in reactivity is a consequence of a change in the nature of the active sites rather than being induced by a simple spillover type synergy. The activity data in the partial oxidation reaction of methanol to hydrogen and carbon dioxide over Cu/ZnO catalysts obtained with different catalyst compositions and different Cu^o metal surface areas revealed that the reaction depends on the presence of both phases: ZnO and Cu^o. On the other hand, for catalysts with Cu concentrations in the range of 40–60 wt%, the copper metal surface area seems to be the main factor determining the reaction rate.[256]

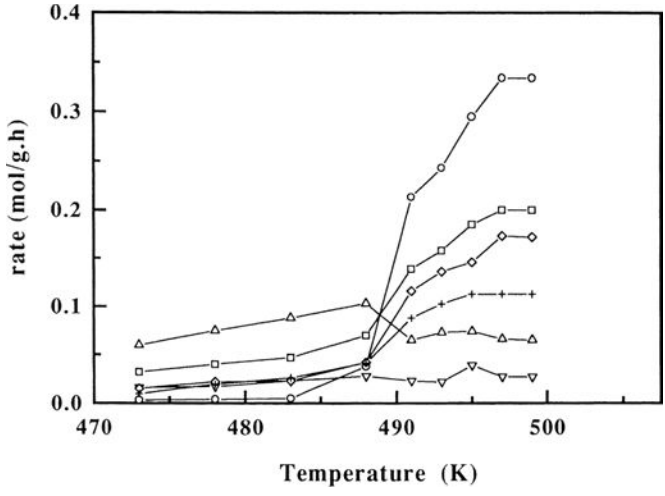

Figure 8.6 Partial oxidation of methanol over the catalyst $Cu_{40}Zn_{60}$. (□), CH_3OH conversion; (+), O_2 conversion; (○), H_2; (◊), CO_2; (Δ), H_2O; (∇), CO.[255]

The O_2/CH_3OH molar ratio in the feed has a strong influence on catalyst performance. As illustrated in Fig. 8.7, the CH_3OH conversion rate and H_2 and CO_2 selectivities increase almost linearly for O_2 partial pressures in the range 0.026–0.055 bar (O_2/CH_3OH ratios = 0.03–0.063).[257] A further increase in the O_2 partial pressure leads to a sharp drop in CH_3OH conversion and almost complete inhibition of H_2 formation, with the simultaneous production of H_2O and CO_2. When returning to lower O_2 partial pressures, the conversion and selectivity to H_2 and CO_2 remain constant and very low, producing a hysteresis curve. In addition, the X-ray diffraction patterns show that a thick layer of copper oxide grows on the surface of copper crystallites when exposed to O_2 pressures above 0.055 bar. These results indicate that metallic Cu^o has low reactivity to methanol and that activity is optimised at intermediate surface coverage by oxygen.

Mechanism studies

Kinetic isotope effects using CH_3OH and CH_3OD show that the O–H bond is at least partially involved in the rate limiting step. TPD

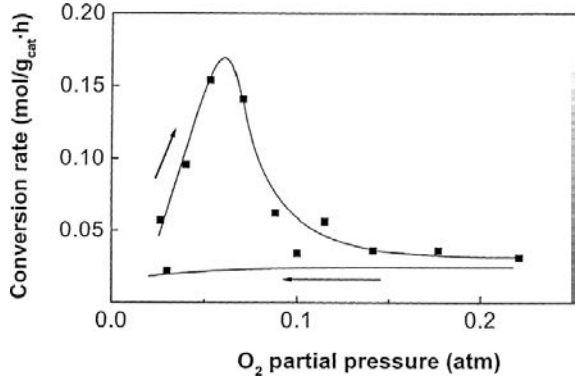

Figure 8.7 Effect of O_2 partial pressure on CH_3OH conversion in the reaction with the $Cu_{40}Zn_{60}$ catalyst at 488 K.[257]

experiments with pure Cu°, pure ZnO and the catalyst Cu/ZnO showed that methanol can be activated by both ZnO and copper. On the ZnO surface, methanol can form intermediates, which, in the presence of copper, might react and desorb more easily, probably *via* a reverse spillover process. The isotopic product distribution of H_2, HD, D_2, H_2O, HDO and D_2O in the temperature-programmed reaction of CH_3OD disclosed a slight enrichment of the products with H, suggesting that during methanol activation on the ZnO some of the D-atoms might be retained by the support.[257] CH_3OH activation *via* O–H bond cleavage occurs easily on metals from Group 8, 9 and 10 at temperatures as low as 100–200 K.[258] Nevertheless, CH_3OH bond activation on copper catalysts requires higher temperatures or the presence of oxygen atoms on the copper surface. It has been proposed that the basic character of O-atoms on copper surfaces facilitates H-transfer from the O–H bond to form a surface methoxy intermediate.[259] The kinetic isotope effect (k_H/k_D = 1.5) observed for CH_3OH conversion[257] can be related to this H-transfer, suggesting that during the CH_3OH oxidation, O–H bond cleavage is at least partially involved in the rate determining step, especially for the water selectivity with $k_H/k_D = 2.0$. However, for H_2 formation (k_H/k_D = 0.9), the rate determining step is related to

C–H bond activation, since the C–O bond does not break during the reaction (no CH_4 formation is observed). These kinetic results obtained for the partial oxidation reaction on Cu/ZnO catalysts agree with those derived for the decomposition and steam reforming reactions of methanol. For these reactions, it has been suggested that a methoxide species is rapidly formed and that the rate determining step is cleavage of the C–H bond to form the H_2CO species.[256,257,259–264]

It has been proposed that oxygen atoms participate in methanol activation by the abstraction of the hydroxyl H-atom to form methoxide and OH_{surf}. This OH_{surf} species rapidly loses H to the surface, regenerating the O surface species.[257] Although all of these reactions occur on the copper surface, ZnO also plays some role in the reaction. The TPD experiments after pre-adsorption of the O_2/CH_3OH mixture on pure ZnO are conclusive to the effect that CH_3OH is partly converted into H_2, CO, CO_2 and H_2CO.[257] Between the two peaks observed in the TPD profiles, the one at low temperature (573 K) for H_2 and CO_2 suggests participation of bulk oxygen, whereas that at slightly higher temperature (590 K) is related to the formation of H_2CO. As stated above, the Cu metal area determines the reaction rate. However, the combination of copper with a certain amount of ZnO seems to be of fundamental importance for the partial oxidation of methanol. Thus, ZnO might also participate in methanol activation and, by a reverse spillover effect, transfer species to the metallic surface for further reaction.

Promoters

The incorporation of small amounts of Al_2O_3 (up to 15% Al at.) to the Cu/ZnO system results in a lower activity, indicating that aluminium has an inhibiting effect for the partial oxidation of methanol. For the catalyst $Cu_{40}Zn_{55}Al_5$, this inhibition is clear at lower temperatures and approaches the activity of the Al-free $Cu_{40}Zn_{60}$ counterpart at temperatures close to 500 K, although other catalysts with higher Al-loadings ($Cu_{40}Zn_{50}Al_{10}$ and $Cu_{40}Zn_{45}Al_{15}$) do not show significant activity in the temperature interval studied.[255] In terms of

stability, the behaviour of $Cu_{40}Zn_{60}$ and $Cu_{40}Zn_{55}Al_5$ catalysts was very different. While the $Cu_{40}Zn_{60}$ catalyst lost 43% of activity, with a less marked drop in the selectivity to H_2 and CO_2, after 110 h on-stream at 503 K, no significant deactivation was observed on the $Cu_{40}Zn_{55}Al_5$ catalyst. The addition of aluminium as Al_2O_3 to the Cu-ZnO favours better dispersion of the copper phase and improves catalyst stability by avoiding the sintering of metal particles.

For both binary Cu-ZnO and ternary Cu-ZnO(Al) systems the reduction pre-treatments govern the structural and morphological characteristics of the catalyst surface.[265] These initial characteristics play a central role in the evolution of the oxidation state and structural morphology during the reaction, since the dynamic behaviour of the catalyst surface is determined by the conditions of the gas atmosphere during the reaction. The temperature dependence of CH_3OH conversion on a $Cu_{55}Zn_{40}Al_5$ catalyst in its oxidised, reduced and air-exposed pre-reduced states during the partial oxidation in an $O_2/CH_3OH = 0.3$ (molar) mixture is shown in Fig. 8.8.[265] All conversion profiles follow a sigmoidal shape, with a dramatic increase in CH_3OH conversion within a narrow temperature range. The reaction starts at 416 K on the reduced sample, whereas this point shifts to 422 and 434 K in the air-exposed and oxidised samples respectively, although conversely, product selectivity is the same in all cases. For a CH_3OH conversion of around 0.6, where oxygen is completely consumed, the slope of the curves changes as a consequence of the overlapping of the decomposition reaction. From the data in Fig. 8.7 it is clear that the oxidised sample becomes reduced during the partial oxidation of methanol and this reduction process leads to surface reconstruction with a higher CH_3OH decomposition capacity than that of the pre-reduced counterparts. These differences are related to changes in the number, but not in the characteristics, of the active sites induced by the different reduction potentials of the reacting gases.

Gold has been used as a promoter in CuO/ZnO catalysts. The Au/CuO/ZnO catalysts are more active and exhibit higher hydrogen selectively with a smaller amount of CO compared to the CuO/ZnO counterparts. The enhanced activity of Au containing catalysts is due to the strong interaction between Au and CuO

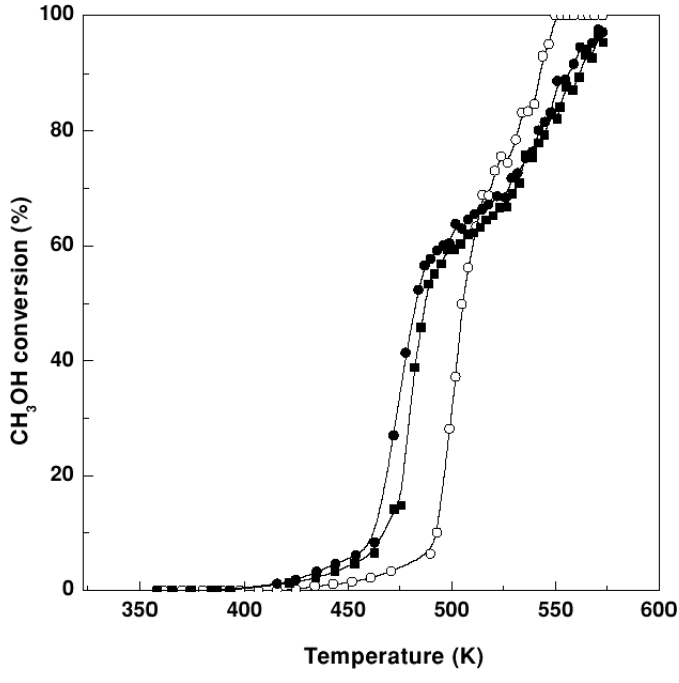

Figure 8.8 Temperature dependence of CH_3OH conversion during temperature-programmed start-up over the $Cu/ZnO/Al_2O_3$ catalyst in different initial states: (○), oxidised; (●), reduced; (■), reduced + air exposed. Atmospheric pressure, feed ratio $O_2/CH_3OH = 0.3$, heating rate = 0.1 K/min.[265]

species.[266] Similarly, incorporation of gold to ZnO/Al_2O_3 catalysts was found to improve the performance for methanol partial oxidation. The activity of the $Au\text{-}Zn/Al_2O_3$ catalysts increased upon increasing the amount of ZnO, and it reached the maximum level when the atomic ratio of Zn to Au was 5 : 1. The main role of ZnO is associated with the progressive formation of smaller Au particles, which provide active oxygen species for oxidation of methanol.[267]

Palladium catalysts

Metals from Groups 8, 9 and 10, and more specifically palladium, are highly active in the partial oxidation of methanol.[268,269] High

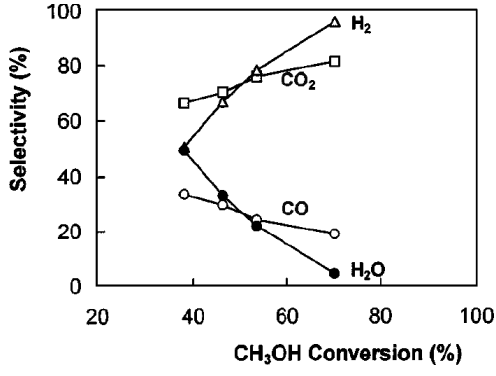

Figure 8.9 Selectivity as a function of CH_3OH conversion for the POM reaction over catalyst 1 wt% Pd/ZnO using feed ratio $O_2/CH_3OH = 0.3$ (molar).[269]

yields to H_2 were obtained on pre-reduced Pd/ZnO catalysts under O_2/CH_3OH feed ratios of 0.3 and 0.5. For the 1 wt% Pd/ZnO catalyst, CH_3OH conversion reached 40–80% within the 503–543 K temperature range. Upon increasing the reaction temperature, CH_3OH conversion increased with a simultaneous increase in H_2 selectivity at the expense of water (Fig. 8.9). Since oxygen was completely consumed, this selectivity trend suggests some contribution of the methanol steam reforming produced by the water by-product. Important structural changes take place at the Pd-ZnO interface during on-stream operation. By using X-ray diffraction, temperature-programmed reduction and X-ray photoelectron spectroscopy techniques, a PdZn alloyed phase could be observed.[154] The reactivity of this alloy is somewhat different from that of small Pd clusters, as illustrated by the behaviour of a 5 wt% Pd/ZnO catalyst, which exhibited a rather high selectivity to HCHO and simultaneous formation of PdZn alloy. It is likely that processes such as CH_3OH decomposition, the inability to oxidise the intermediate HCHO, and the low oxidation rate of CO might be involved in large PdZn alloy particles since CO and HCHO selectivities were much higher for the 5 wt% Pd/ZnO catalyst.

The nature of the support to a large extent determines the performance of the supported catalysts. 1 wt% Pd/ZrO_2 catalysts

exhibited not only oxidation products (H_2 and CO_2) as observed with the parent Cu-ZnO catalysts, but also the decomposition reaction seemed to occur to a greater extent.

Other catalysts

High selective production of hydrogen by partial oxidation of methanol has been achieved over Au/TiO_2 catalysts, it being found that the catalytic activity is strongly dependent on the gold particle size.[270] The catalytic activity of Au/TiO_2 for the POM reaction to produce hydrogen is improved by using the additional support (MO). For these Au/TiO_2-MO_x (M = Fe, Co and Zn) systems, TEM observations showed that the gold particles are stabilised against sintering during calcination and after catalytic tests. The catalytic activity of Au/TiO_2 for the POM reaction to produce hydrogen was improved by using the additional support (MO), probably due to a combination of factors, such as increasing the mobility of the lattice oxygen, maintaining an appropriate oxidation state of the gold particles, and controlling the sintering of gold particles. The most active catalyst was Au/TiO_2-Fe_2O_3. It was suggested that the reaction pathway consists of consecutive methanol combustion, partial oxidation, steam reforming and decomposition reactions.[270]

8.3.1.4 *Autothermal reforming of methanol*

An even more appealing option than the steam reforming and partial oxidation is the combination of these two reactions, providing the possibility of producing hydrogen under almost autothermal conditions.[256,271–275]

$$CH_3OH + (1–2n)\ H_2O + n\ O_2 \rightarrow CO_2 + (3–2n)\ H_2 \quad (0 < n < 0.5). \tag{8.11}$$

Copper-based catalysts also display good performance in combined reforming. In a recent contribution using a Cu-ZnO catalyst, Agrell *et al.*[275] reported that at differential O_2 conversions,

water is produced by combustion of methanol. When oxygen conversion was complete, water production levelled off and H_2 formation was initiated. Then, CH_3OH conversion and H_2 and CO selectivity increased while water selectivity decreased. When ZrO_2 was incorporated to the Cu-ZnO base catalyst, the resulting catalysts were slightly less active than the Cu-ZnO alone. CO formation over these ZrO_2-loaded Cu-ZnO catalysts was less pronounced than in the other catalysts and still lower than in the steam reaction.

The oxidative steam reforming reactions of methanol were also investigated over Cu-ZnO(Al) catalysts derived from hydrotalcite-like precursors.[274] The reaction under $O_2/CH_3OH/H_2O$ = 0,3 : 1 : 1 molar ratios in the feed led to a high activity for CH_3OH conversion and a very high selectivity for H_2 production. All the catalysts exhibited higher CH_3OH conversions than that attained under the conditions of partial oxidation without water. Another interesting result is that CO levels at the exit stream were much lower than in the case of the reaction performed under the condition of pure partial oxidation. Despite the complexity of the mechanism of oxyreforming of methanol, it is likely that the water-gas shift reaction may contribute to the reduction of CO selectivity.

For $Cu/ZnO/Al_2O_3$ catalysts derived from layered double hydroxide precursors, it has been hypothesised that methanol oxidation is catalysed by a Cu oxide present in the first zone of the catalytic bed, where the O_2 concentration is high. The activity of such oxide and, therefore, the kinetics of partial oxidation of methanol can be influenced by the interaction with the other oxides of the dispersing matrix. Some influence of the oxide matrix is present also under SRM conditions.[276] Recently, a kinetic model for oxidative steam reforming of methanol has been developed using the Langmuir–Hinshelwood (LH) approach over a $Cu/ZnO/CeO_2/Al_2O_3$ catalyst. A good agreement was obtained between experimental and model predicted results based on formation of formate from oxymethylene, dissociation of formic acid and formation of adsorbed CO and surface hydroxyls from formate species as the rate

determining steps for methanol partial oxidation, methanol steam reforming and reverse water-gas shift reactions, respectively.[277]

Copper-zinc oxide catalyst/ceramic fibre composites, prepared by a papermaking technique, were used in autothermal reforming (ATR) of methanol to produce hydrogen for fuel cell applications. The performance of the catalyst paper for hydrogen production in the ATR process at 523 K was twice as high as that of commercially available catalyst pellets. The concentration of CO, which acts as a catalytic poison for the Pt anode electrocatalyst of fuel cells, decreased remarkably. Furthermore, the gas generation with catalyst paper was much more stable than with catalyst powder or with pellets, resulting in constant hydrogen production. Such interesting features may be caused by the unique porous structure of paper composites that allows heat and reactants to be supplied effectively onto the catalyst surfaces. In addition, the ATR stability with catalyst paper improved considerably when ZSM-5 zeolite was mixed within the catalyst paper. Therefore, the porous, flexible and easy-to-handle catalyst paper is expected to be a promising catalytic material for enhancing practical performance in the catalytic reforming process.[278]

8.3.2 *Ethanol oxidation*

8.3.2.1 *Ethanol steam reforming*

Hydrogen can be produced by the steam reforming reaction of oxygenated compounds ($C_nH_mO_p$).[279] Among oxygenates, ethanol is particularly suited since it is easily produced from renewable resources. The main advantage of ethanol is its high energy density and ease of handling and the fact that it can be used for the production of hydrogen for fuel cells with applications in mobile and stationary grid-independent power systems. The steam reforming of ethanol for hydrogen production has been demonstrated to be thermodynamically feasible.[279–282] An issue of major relevance is to develop highly active, selective and stable heterogeneous catalysts for the target reaction. The first step of the process involves oxidation of

a fraction of the C_2H_5OH fed into the catalytic reactor to generate the heat required for the steam reforming reaction:

$$C_2H_5OH + 3\ O_2 \rightarrow 3\ H_2O + 2\ CO_2 \qquad (8.12)$$
$$\Delta H^{o}_{298} = -1279\ kJ\ mol^{-1}$$

$$C_2H_5OH + 3\ H_2O \rightarrow 6\ H_2 + 2\ CO_2 \qquad (8.13)$$
$$\Delta\ H^{o}_{298} = +173\ kJ\ mol^{-1}.$$

These two processes must be combined since most catalysts that are active for steam reforming are also active for the combustion reaction. A further water-gas shift reaction step is required to remove the excess of carbon monoxide.

Some studies have been published on the use of Rh/Al_2O_3,[283,284] ZnO,[285] Ni/La_2O_3,[286] potassium promoted Ni/Cu[287] dual bed Pd/C-Ni/Al_2O_3,[288] transition metals (Rh, Pd, Ni, Pt) supported on Al_2O_3 and CeO_2-ZrO_2 substrates,[289] and Co-based catalysts.[290,291] Noble metals supported on metal oxides of the type Al_2O_3, SiO_2, CeO_2, TiO_2 and MgO display high activity in the decomposition of ethanol to CO_x and H_2.[281,283,284,289,292,293] In particular, cerium oxide supported Rh catalysts show a relatively high activity for ethanol decomposition, even in the presence of oxygen.[293] However, the Rh/Al_2O_3 systems appear to be much more active in ethanol reforming reactions.[281,283] It was shown that hydrogen-rich gas mixtures produced upon using Rh/Al_2O_3 catalysts can be considered to be of great interest for molten carbonate fuel-cell applications because they do not involve the production of ethylene or other undesirable products. Under steam reforming conditions, extensive formation of encapsulated carbon was observed, while the addition of oxygen to the reaction stream proved to be very useful since catalyst stability was improved while coke formation was minimised.

The mechanism of the reaction is very complex since several reaction intermediates can be formed. In light of the above studies, it was claimed that the acetaldehyde, formed by ethanol dehydrogenation, is easily decarbonylated to form CH_4 and CO, while the ethylene produced by dehydration was steam-reformed to C_1 (very fast reactions). Rh/CeO_2 catalysts were also found to be highly active

in the autothermal reaction of ethanol and ethanol-water mixtures[294] with residence times below 10 ms. Under these conditions, ethanol conversion exceeded 95% and H_2 selectivity approached 100%. On Pt/CeO_2 catalysts, it has been suggested that the ethanol reforming reaction proceeds through dissociative adsorption at reduced defect sites on ceria (i.e. Ce surface atoms in the Ce^{3+} oxidation state), yielding adsorbed ethoxy species and adsorbed H species, the latter identified to be a type bridging OH group. In the presence of steam, the ethoxy species rapidly undergoes molecular transformation to an adsorbed acetate intermediate by oxidative dehydrogenation.[295]

The metallic function and the acid-base properties of the catalysts used play a central role in the reforming reaction of ethanol. This is illustrated by the $Cu/Ni/K/\gamma\text{-}Al_2O_3$ catalyst, which exhibits acceptable activity, stability and hydrogen selectivity at relatively low temperature (573 K) and atmospheric pressure.[287] In this catalyst, copper is the active agent; nickel promotes C–C bond rupture, increasing hydrogen selectivity and potassium neutralises the acidic sites of the γ-alumina substrate and improves the general performance of the catalyst.

Lanthanum oxide is one of the best support candidates for the metallic function of the ethanol reforming catalysts. It was reported that a Ni/La_2O_3 catalyst, or a $(Ni/La_2O_3)/Al_2O_3$ in pelleted form, exhibited high activity and long-term stability for hydrogen production.[296] The catalytic performance of supported noble metal catalysts was investigated in the temperature range 823–1123 K with respect to the nature of the active metallic phase (Rh, Ru, Pt, Pd), the nature of the support (Al_2O_3, MgO, TiO_2), and the metal loading. For the catalysts with low loadings, Rh was significantly more active and selective toward hydrogen formation as compared to Ru, Pt and Pd which showed a similar behaviour. The $20\%Ni/La_2O_3/Al_2O_3$ catalyst exhibited good stability at 1023 K for on-stream times of over 150 h, with only a small drop in ethanol conversion from 95% to 90%, while hydrogen selectivity remained essentially unchanged.[296] These results indicate the uniqueness of the Ni/La_2O_3 system in terms of its long stability, which is even more pronounced at

relatively low temperatures. The unusual stability of the Ni/La_2O_3 catalyst may be explained by taking into account that a thin overlayer of lanthana is formed on top of the Ni particles following high temperature pre-treatment of the catalyst or exposure to the reaction environment.[179] Under reforming reaction, lanthanum oxide species, which decorate the Ni particles, react with carbon dioxide to form $La_2O_2CO_3$ species, which then react with surface carbon at their periphery, thus cleaning the Ni surface of carbon deposits.

$$La_2O_3 + CO_2 \rightarrow La_2O_2CO_3 \text{ (with C deposit)} \rightarrow La_2O_3 + 2\ CO \qquad (8.14)$$

According to this simple mechanism, the surface carbon at the periphery of the lanthanum oxycarbonate particles is removed, resulting in the observed good stability characteristics of this catalyst. Such a mechanism does not work if Ni is supported on other kinds of support. Klouz *et al.*[297] analysed the nature of carbon deposits on a $Ni\text{-}Cu/SiO_2$ catalyst under reforming conditions. Regardless of the reaction time, the main carbon deposited on the catalyst surface was found to be very sparingly reactive, since it could only be partially hydrogenated even at 1173 K and only reacted with oxygen. Such a low reactivity suggests that this kind of carbon is graphitic and that it accumulates around the metal particles. The poisoning effect of this encapsulating carbon is evident since the catalyst was fully regenerated after burning the carbon and again reducing the catalyst. Catalyst poisoning most likely proceeds as a moving front along the direction of the catalyst bed. Selectivity remained constant for complete ethanol conversion, suggesting that the catalyst bed had been progressively poisoned by carbon. However, the appearance of acetaldehyde when ethanol conversion declined confirms that acetaldehyde may be an intermediate product of ethanol reforming.

Metal/ceria catalysts have received great interest for their reactions involving steam conversion, including CO for low-temperature water-gas shift, and the conversion of chemical carriers of hydrogen, among them methanol and ethanol. The mechanism by which ROH

model reagents are activated on the surface of the Pt/partially reduced ceria catalyst was explored using a combination of reaction testing and infrared spectroscopy.[298] In this particular investigation, the activation and turn-over of ethanol were explored and compared with previous investigations of methanol steam reforming and low-temperature water-gas shift under H_2-rich conditions, where the surface of ceria is in a partially reduced state. Under these conditions, activation of ethanol was found to proceed by dissociative adsorption at reduced defect sites on ceria (i.e., Ce surface atoms in the Ce^{3+} oxidation state), yielding an adsorbed type II ethoxy species and an adsorbed H species, the latter identified to be a type II bridging OH group. In the presence of steam, the ethoxy species rapidly undergoes molecular transformation to an adsorbed acetate intermediate by oxidative dehydrogenation. This is analogous to the conversion of type II methoxy species to formate observed in previous investigations of methanol steam reforming. In addition, although formate then decomposes in steam to CO_2 and H_2 during methanol steam reforming, in an analogous pathway for ethanol steam reforming, the acetate intermediate decomposes in steam to give CO_2 and CH_4. Therefore, further H_2 production requires energy-intensive activation of CH_4, which is not required for methanol conversion over Pt/ceria.[298]

Ceria supported some noble metals such as Ir and Rh-Ni catalysts have also been investigated for steam reforming of ethanol with respect to the nature of the active metals and the catalytic stability. Steam reforming of ethanol over an Ir/CeO_2 catalyst has been studied with regard to the reaction mechanism and the stability of the catalyst. It was found that ethanol dehydrogenation to acetaldehyde was the primary reaction, and acetaldehyde was then decomposed to methane and CO and/or converted to acetone at low temperatures. Methane was further reformed to H_2 and CO, and acetone was directly converted into H_2 and CO_2. The Ir/CeO_2 catalyst displayed rather stable performance in the steam reforming of ethanol at 650°C even with a stoichiometric feed composition of water/ethanol. Long-term stability tests revealed that the Ir/CeO_2 catalyst shows rather stable catalytic performance for 300 h on-stream without

any deactivation. The improvement was attributed to the effective prevention of the sintering of the highly dispersed Ir particles through the strong interaction between Ir and CeO_2 substrate,[298] and to the significant resistance to coke deposition of ceria based on its higher oxygen storage-release capacity (OSC).[299,300] This catalyst has also shown good catalytic behaviour in the oxidative steam reforming of ethanol. The improvement was attributed to the effective prevention of the sintering of the highly dispersed Ir particles through the strong interaction between Ir and CeO_2, and to the significant resistance to coke deposition due to the high OSC of ceria.[301] Rh-Ni/CeO_2 catalysts were studied for hydrogen production by ethanol steam reforming and it was observed that Rh species became highly dispersed when the crystallite size of CeO_2 in the support is small. It has been demonstrated that both ethanol conversion and H_2 selectivity increased and the selectivity for undesirable by-products decreased with increasing Rh metal dispersion. Best catalytic performance was achieved by supporting Ni–Rh bimetallic catalysts on the nanocrystalline CeO_2. The Ni–Rh/CeO_2 catalyst exhibited stable activity and selectivity during on-stream operations at 723 K as well as at 873 K.[302]

A detailed study of the influence of the support over the hydrogen production from ethanol reforming over nickel catalysts modified with Ce, Mg, Zr and La has been developed.[303] The acidity of catalysts containing Mg, Ce, La and Zr additives decreased with respect to that supported on bare Al_2O_3. The trend of metal dispersion followed the order: La_2O_3-Al_2O_3 > MgO-Al_2O_3 > CeO_2-Al_2O_3 > Al_2O_3 > ZrO_2–Al_2O_3. Thus, the higher reforming activity for Mg-modified catalyst respect to bare Al_2O_3 was explained in terms of the lower acidity and better dispersion achieved in the former, while for Ce and Zr-promoted catalysts the improvement in intrinsic activity was ascribed to the enhancement of water adsorption/dissociation on the Ni-Ce and Ni-Zr interfaces developed on these catalysts. On the other hand, the lower intrinsic activity of La-added catalyst was explained in terms of the dilution effect caused by the presence of lanthanum on Ni surfaces. La and Ce additives were found to prevent the formation of carbon filaments on nickel surfaces. The same

research group found an enhancement in the reforming stability of the Ni catalysts with an increase in the lanthanum loading. Catalytic behaviour of Ni/La-Al_2O_3 catalysts in the ethanol steam reforming was found to involve contributions to the activity of the La-Al_2O_3 supports for the ethanol dehydration reaction and the activity of the nickel metallic phase that catalyses both dehydrogenation and C–C bond breaking. Physicochemical characterisation of catalysts revealed that acidity, nickel dispersion and nickel support interaction depend on the La-loading on Al_2O_3. The better reforming stability of catalysts with an increase in La content was explained in terms of the ability of nickel surface and/or La-Ni interactions to prevent the formation of carbon filaments.[304]

Palladium catalysts are substantially more active than the Ni-based catalysts for the steam reforming of ethanol.[305] High activity and selectivity in the reforming reaction were obtained over a commercial alumina supported palladium catalyst. Long-term experiments also revealed good catalyst stability. Hydrogen selectivities of up to 95% were obtained at a temperature of approximately 923 K. It was also observed that for thermodynamic reasons the carbon monoxide concentration exhibited a minimum at a temperature close to 723 K. Furthermore, carbon formation was found to be negligible even for an H_2O/EtOH molar ratio equal to the stoichiometry. By contrast, as the water to ethanol ratio in the feed stream was decreased below the stoichiometric value, the rate of carbon formation was increased, resulting in catalyst deactivation.

Recently, different mixed oxides such as perovskites and spinels have been used as catalysts precursors for hydrogen production by ethanol steam reforming because of the high dispersion of the active phase. $LaFe_yNi_{1-y}O_3$ perovskite-type oxide gave highly dispersed Ni particles. The CH_4 selectivity was sensitive to the particle size of supported Ni, and the smaller nickel particles led to reduced levels of undesired methane. Characterisations of used catalysts indicated that the sintering of nickel particles was not significant even at the high reaction temperature. The $LaFe_yNi_{1-y}O_3$-supported nickel catalysts exhibited very good carbon deposition resistance, which could be ascribed to the highly dispersed Ni particles and the

formation of oxygen vacancies in $LaFe_yNi_{1-y}O_3$ due to the partial substitution of Ni ions for Fe ions.[306] In addition, it has been reported recently that catalysts derived from $LaNiO_3$ perovskite-type oxide precursor are highly active and selective for the production of hydrogen from both steam reforming and oxidative steam reforming reactions of ethanol.[307]

Mg-Al mixed oxide supported nickel catalysts were also found to give superior activity and improved catalyst stability compared to the pure oxide supported nickel catalysts. The improved performance of these catalysts was related to the formation of an $MgAl_2O_4$-phase. This phase exhibited moderate acidic and basic site strength and density compared to the pure oxide supported catalysts which decreased the activity for by-product forming reactions.[308] In a recent work, Ni-based spinel-type oxides, NiB_2O_4 (B = Al, Fe, Mn), were investigated for the ethanol steam reforming reaction. Ethanol conversion over spinel-type oxides without reduction treatment was comparable to that over alumina supported Ni catalysts with reduction. $NiAl_2O_4$ showed extremely stable performance, while the activity of $NiFe_2O_4$ and $NiMn_2O_4$ catalysts was reduced by carbon deposition. Catalyst stability for reforming reaction was closely related to the stability of the nickel metal dispersed on the catalyst surface and the spinel structure.[309]

Recently, mechanistic aspects of ethanol steam reforming on Pt, Ni and PtNi catalysts supported on γ-Al_2O_3 from the analysis of adsorbed species and gas phase products formed, have been reported.[310] DRIFTS-MS analyses of ethanol decomposition and ethanol steam forming reactions show that PtNi and Ni catalysts are more stable than the Pt monometallic catalyst. Ethanol TPD results on Ni, Pt and NiPt catalysts point to ethanol dehydrogenation and acetaldehyde decomposition as the first reaction pathways of ethanol steam reforming. The active sites responsible for the acetaldehyde decomposition are easily deactivated in the first minutes on-stream by carbon deposits. For Ni and PtNi catalysts, a second reaction pathway, consisting of the decomposition of acetate intermediates formed over the surface of alumina support, becomes the main reaction pathway. The greater stability observed for PtNi

catalysts is proposed to be related to a cooperative effect between Pt and Ni activities together with the enhanced ability of Ni to gasify the methyl groups formed by decomposition of acetate species. On the contrary, monometallic catalysts are believed to dehydrogenate these methyl groups forming coke that leads to deactivation of the metal particles.[310]

Cobalt catalysts

Cobalt-based catalysts have also been proposed as appropriate for the reforming reaction. Llorca *et al.*[290] studied the reaction between ethanol and water in the 573–723 K temperature range at atmospheric pressure over supported cobalt catalysts. Co/ZnO, Co/La_2O_3, Co/CeO_2 and Co/Sm_2O_3 catalysts, prepared by impregnation of the corresponding substrates with n-hexane solutions of the $Co_2(CO)_8$ complex, showed a selectivity to hydrogen greater than 60% and above 20% to CO_2. Over these catalysts, the main reactions were the steam reforming of ethanol and the decomposition of ethanol to acetone. Co/La_2O_3, Co/CeO_2 and Co/Sm_2O_3 catalysts exhibited higher conversion levels of ethanol than the respective La_2O_3, CeO_2 and Sm_2O_3 substrates, and the selectivity patterns of the Co-loaded catalysts were also different from those of the oxide supports.[285] The ZnO-supported cobalt catalyst, in which the ZnO substrate (specific area of 100 m^2/g) was prepared by thermal decomposition of Zn-carbonate, exhibited the highest catalytic performance among the series. Using an $EtOH/H_2O = 1/13$ (molar ratio), total conversion of ethanol and the highest values of H_2 and CO_2 were obtained, with no deactivation. Complete EtOH conversion was also attained on the ZnO substrate but the yields of H_2 and CO_2 alone were found to be substantially lower. Decomposition of EtOH into acetone occurs to a large extent on Co/ZnO catalysts. Since this reaction results from consecutive reactions, such as dehydrogenation and aldol condensation, additional experiments indicated that the reforming reaction preferentially takes place at low contact times, while the decomposition of EtOH to acetone *via* aldol condensation of acetaldehyde is suppressed.[305] TEM of the

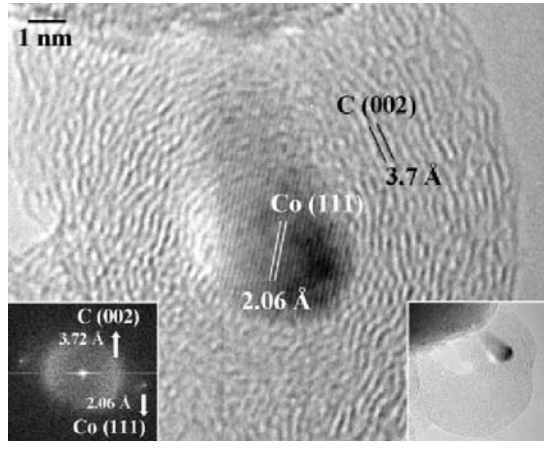

Figure 8.10 Catalyst Co/ZnO after reaction at 873 K. The size distribution of metal cobalt particles ranges from 3–4 nm to 15–30 nm. Small metal cobalt particles are located on ZnO, whereas larger cobalt particles are encapsulated in carbon filaments.[291]

used Co/ZnO catalyst at 873 K revealed[291] the deposition of carbon of graphitic nature, as derived from the C(002) spacing of 3.46 Å, calculated directly from lattice-fringe imaging (Fig. 8.10). In addition, the formation was observed of carbon filaments containing cobalt particles of sizes 15–30 nm, which in turn were much higher than the metallic Co particles in contact with the ZnO surface (*ca.* 3 nm).

The incorporation of sodium (0.06–0.98 wt%) to Co/ZnO catalysts results in a better performance in the reaction of ethanol reforming.[291] The production of hydrogen increased (5–8%) with the Na content under total conversion in the 623–723 K temperature range, and deposition also decreased, as evidenced by HRTEM, XPS and Raman spectroscopy.[291] HRTEM micrographs of the 0.06 wt% Na promoted Co/ZnO catalyst showed the Co^{o} and CoO particles to be surrounded by poorly ordered phases (Fig. 8.11). The high resolution image of one of these particles showed a 3.8 Å spacing for C(002) planes characteristic of poorly graphitised carbon. Analysis of zone (a) indicates the segregation of CoO exhibing (200) planes.

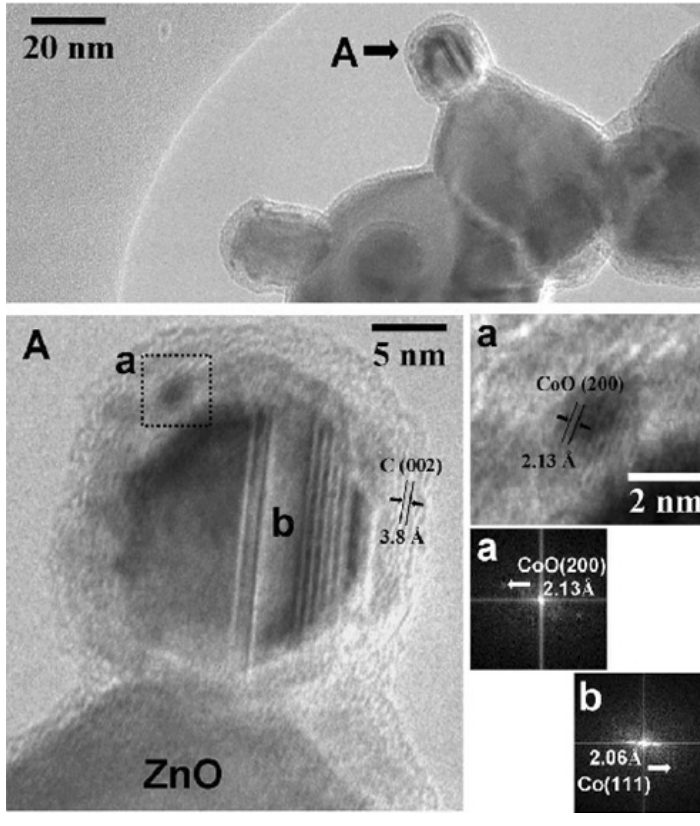

Figure 8.11 High resolution transmission electron microscopy images of catalyst 0.06NaCoZn after steam reforming of ethanol at 723 K, and derived Fourier-transformed patterns.[291]

The Fourier-transformed images in the insets of zones (a) and (b) contain spots corresponding to CoO(200) planes at 2.13 A, and Co(111) planes at 2.06 Å, respectively. The decrease in carbon formation in used catalysts upon increasing Na content was demonstrated by Raman and XPS techniques. The catalyst containing 0.06 and 0.23 wt% Na showed two bands at 1,340 and 1,590 cm^{-1}, which are characteristic of disordered carbon structures.[311] However, the catalyst with higher Na contents showed no bands in this region, indicating that the amount of carbon was below

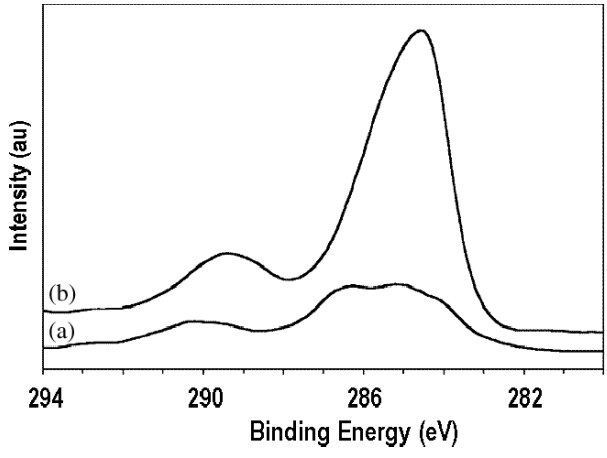

Figure 8.12 XP spectra corresponding to C 1s energy region of catalysts: (a) 0.98NaCoZn; (b) 0.06NaCoZn.[291]

the detection limit. The inhibition of carbon formation with increasing Na contents was also demonstrated by examination of the C 1s core levels of the used catalysts. The C 1s spectra of two representative Na promoted Co/ZnO catalysts (0.06- and 0.98 Na wt%) exhibited four components at 284.3, 284.9, 286.3 and 290.0 eV (Fig. 8.12) associated with graphitic carbon, adsorbed hydrocarbons, species containing C–O bonds and surface carbonate species,[312] respectively. From Fig. 8.11 it is clear that graphitic carbon is much higher for the 0.06Na-CoZn than for the 0.98Na-Co/Zn catalyst.

It has been also reported that the catalytic behaviour of Co catalysts for steam reforming of ethanol is enhanced by promotion with Fe or Mn as a consequence of the effect of these metals on cobalt reducibility. The catalytic activity of Co catalysts supported on ZnO and promoted with Fe and Mn (1%) was compared with that of Ni catalysts supported on La_2O_3-Al_2O_3. The Co catalysts do not promote methane-forming reactions such as ethanol cracking and acetaldehyde decarbonylation, nor do they facilitate the reverse methane steam reforming reaction.[313] The promotion effect of Mn on Co/ZnO catalysts in the steam reforming of ethanol has been studied in coprecipitated catalysts. Alloy particles in Co-Mn/ZnO catalysts prepared by

impregnation are smaller as deduced from HRTEM and exhibit a rapid and higher degree of redox exchange between reduced and oxidised Co as determined from temperature-programmed reduction (TPR) and oxidation pulse experiments with respect to Co-Mn catalysts prepared by coprecipitation, which show a stronger Mn segregation on the surface, as deduced from X-ray photoelectron spectroscopy (XPS). Honeycomb catalysts have been prepared with the best catalytic formulation and are significantly more active and selective than Co/ZnO honeycomb samples.[314]

A synergistic effect of ZrO_2 and CeO_2 in promoting high ethanol conversion while suppressing methanation was observed when $CeZrO_4$ was used as a support for cobalt.

The non-noble metal based 10 wt% $Co/CeZrO_4$ is an efficient catalyst to achieve ethanol conversion of 100% and a hydrogen yield of 82% at 723 K, which is superior to 0.5 wt% Rh/Al_2O_3.[315] In ceria supported catalysts, the results indicated that catalyst deactivation is mostly originated by deposition of various types of carbon on the surface although cobalt sintering could also contribute to the deactivation. The addition of ceria improves the catalytic performance primarily due to the higher oxygen mobility of ceria.[316] Another benefit of ceria is that it stabilises the hcp cobalt structure and, moreover, during the pre-reduction process, the CeO_2 promoter prevents sintering during the transformation of Co_3O_4 to hcp cobalt, which leads to lower CO selectivity and a higher H_2 yield as compared with the unpromoted hcp Co.[317]

The mechanisms of Co/ceria catalyst deactivation during steam reforming, oxidative steam reforming and partial oxidation of ethanol have been recently examined.[318] The nature of carbon deposition and the reaction conditions played critical roles in determining the extent of catalyst deactivation. To shed light on the modes of carbon deposition under different reaction conditions, the mechanisms by which the adsorbed surface species turned over on the catalyst surface were evaluated using diffuse reflectance infrared spectroscopy under reaction conditions and temperature-programmed desorption of adsorbed ethanol. In steam reforming, ethoxy species were converted to acetate and steam promoted forward acetate demethanation. The resulting

methane decomposed on Co metal particles. In this case, carbon diffused through the Co particle, nucleating growth sites for filamentous carbon behind it, with the resulting filaments lifting Co from the support. High H_2O/ethanol ratios and oxygen promoted cleaning of the cobalt surface.[318]

Microchannel catalytic reactors

Packed bed reactors are an inappropriate design when considering the requirements for rapid and frequent power changes in small-scale and mobile hydrogen production systems for portable computers or mobile phones. To fulfil the compact requirements, various types of microstructured reactors have been developed. Among them, the most promising concept considers stacked systems of channelled metallic platelets, coated with active catalyst. Since the characteristic dimensions of the reaction zones are in the sub-millimeter-scale, they are generally referred to as 'microstructured reactors'. Figure 8.13 shows a microreactor (IMM, Mainz) together with one platelet and cross-sectional of a microreactor.[319]

In addition to compactness, microreactors include various advantages: (i) the lower pressure drop compared to classical packed bed reactors since microreactors work under laminar flow conditions; (ii) the rapid mass and heat transfer due to high surface to volume ratio; (iii) the precise control of the process conditions leading to higher product yields; and (iv) the good structural and thermal stability. Indeed, the short characteristic time for radial diffusion in microreactors leads to a narrower residence time distribution of the reaction gases, allowing an optimum contact time between the reactants and the catalyst and avoiding the formation of unwanted by-products. Microstructured reactors also provide built-in safety since a large gas hold-up (reactor volume) is avoided.[320–322] Recently, the catalytic steam reforming of methanol in microchannel reactors has been studied.[323] However, the use of microreactors to produce hydrogen from ethanol is relatively unexplored. Men *et al.*[324] investigated microstructured-based catalysts systems consisting of stainless steel platelets.

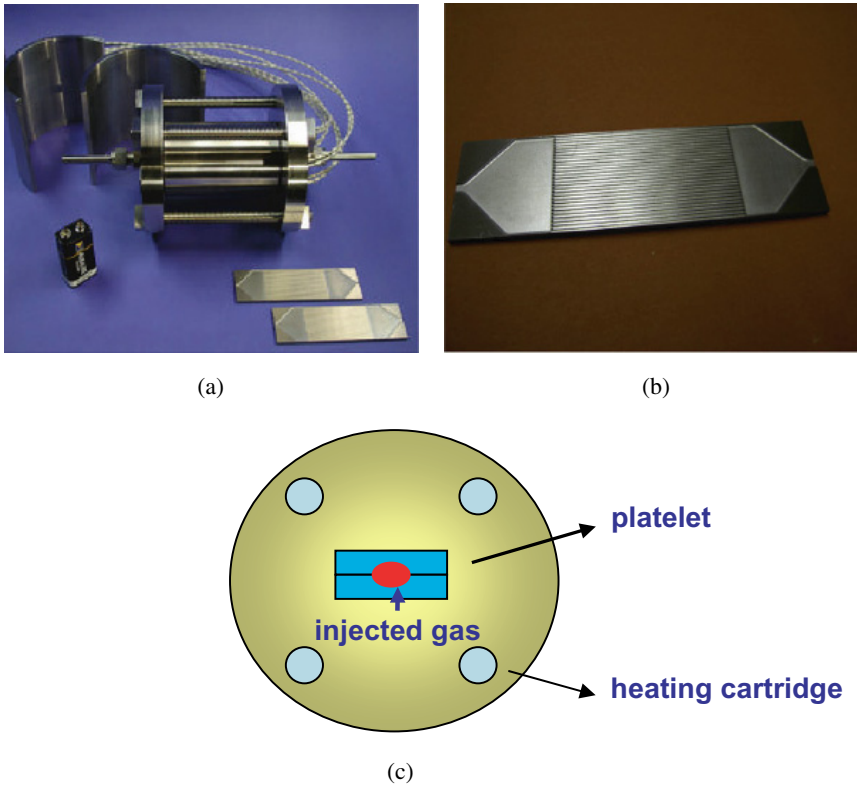

Figure 8.13 Photograph of a microreactor (a), one metallic platelet (b), and the cross-sectional diagram of the microreactor (c).[319]

Llorca *et al.*[325] developed a micro-channel reactor where ethanol steam reforming is performed on one side of the plate while ethanol combustion is performed on the with 14 microchannels. The results revealed that Rh-based catalysts exhibited the highest catalytic activity, when compared to Co and Ni. The Rh-Ni-Ce catalyst was operated for 100 h without any noticeable degradation in activity and selectivity. Full conversion was achieved for the entire period and the H_2 selectivity was 86%. The CO content in reformate remained constant *ca.* 8.2%.

Llorca *et al.*[325] developed a microchannel reactor where ethanol steam reforming is performed on one side of the plate while ethanol

combustion is performed on the other side in order to provide the necessary heat for the endothermic steam reforming reaction. Four different coating methods for depositing the Co/ZnO and $CuMnO_x$ layers on the microchannels were studied in order to guarantee a homogeneous and stable deposition and stability. At 460°C, 3.67 mols of H_2 were produced per mole of ethanol consumed by the system performing both reactions (steam reforming and combustion). The overall efficiency of such a microreactor was 71%. Llorca *et al.*[326] also compared the ethanol steam reforming over a Co_3O_4 catalyst in a conventional monolith reactor and a microchannel reactor. At 500°C, ethanol conversions of 70% and 90% were measured for a monolith reactor and a microreactor, respectively.

Llorca *et al.* have recently developed a micromonolithic support for high-speed catalysis consisting of silicon membranes with millions of parallel microchannels per square centimetre, opening a new and exciting field of research and application. The miniaturised system has been used for the generation of hydrogen through the steam reforming of ethanol, obtaining a very high yield. The microchannels walls were coated with a thin layer of Co_3O_4-ZnO catalyst by a complexation-decomposition method.[326] In a recent publication, new catalysts based on Co_3O_4 coatings prepared inside the channels by *in situ* thermal decomposition of two-dimensional layered cobalt hydroxide salts, showed a remarkable high homogeneity and mechanical stability. The Si-micromonolithic reactor proved extremely promising for hydrogen production for micro fuel-cell operation.[327]

Ethanol steam reforming was very recently studied over a supported Ir/CeO_2 catalyst in a microchannel structured reactor.[328] This catalyst was prepared *via* deposition precipitation[329] by milling the solid to particle size below 5 μm and then dispersing particles into water under vigorous stirring. Methylhydroxyethyl cellulose was added to serve as a binder (mass ratio $Ir/CeO_2 : H_2O = 1 : 4$, binder : $H_2O = 1 : 67$) before the slurry was kept under stirring for 12 h at room temperature. The slurry was injected into the microchannels of the platelets using a syringe and the excess suspension was wiped off with chip knife. The platelets were further dried at ambient

temperature in air for 3 h, before calcination in static air at 400°C for 5 h. The catalyst coating was deposited on the channel walls and showed a remarkably high homogeneity and an excellent adherence to the stainless steel substrate, leading to stable performance during long-term runs. Hydrogen yields exceeding 40 $L_{H2}/g_{cat}\cdot h$ were achieved during testing with partial ethanol conversion of 65% and a residence time in the order of a few milliseconds. This hydrogen productivity was found to be significantly higher than in a comparable conventional fixed bed reactor hence showing promise for hydrogen production in micro fuel-cell applications.

8.4 Conversion of Other Hydrocarbon Feeds

When natural gas is not available, steam reforming of liquid hydrocarbons can be used for the production of hydrogen. This concept applies for the generation of hydrogen for fuel cell applications using jet fuel, gasoline and diesel fractions as primary energy sources.[330] This option is currently an attractive choice for the production of hydrogen since the distribution and supply infrastructure of these fuels is fully developed.[331] Hydrogen generation from gasoline or diesel is one of the critical technologies for the commercialisation of small-scale fuel-cell auxiliary/backup power systems and, therefore, the development of efficient catalysts for this process is needed. For higher hydrocarbons, the catalyst typically contains metals such as Pt, Rh, Ru, Co or Ni deposited over oxide supports, typically lanthanide containing oxides. These can be further promoted or doped with other elements for improved thermal robustness or better activity. With the non-noble metal formulations, such as supported on ion-conducting doped ceria substrates, activities similar to PGM containing catalysts have been reported.

As long-chain hydrocarbons are more reactive than CH_4, the steam reforming reaction of liquid hydrocarbons is less endothermic than CH_4. Since aromatics are more stable than paraffins, their reactivity towards steam approaches that of CH_4. For many years, nickel has been the most suitable metal for the steam reforming of hydrocarbons, because the TOF values for the reaction are very

high. Current steam reforming catalysts are mainly nickel supported on refractory alumina and ceramic magnesium aluminate. These supports provide high crush strength and stability. A simulated diesel mixture (hexadecane + toluene + naphthalene) can be efficiently reformed on Ni/Al_2O_3 catalysts at temperatures of around 923 K in an excess of steam (H_2O/C ratio of 4). At these temperatures, some thermal cracking of the hydrocarbon molecules is unavoidable and carbon deposits occur on the catalyst surface and also on the walls of the reactor. Additionally, gasoline has sulphur concentrations in the 50–250 ppm range, and the concentration of sulphur in diesel grade fuel is higher (up to 0.4%) than that of gasoline. Therefore, coke formation[332] and sulphur poisoning[333] are unavoidable with nickel catalysts. With proper desulphurisation, light diesel can be converted *via* steam reforming into syngas mixtures with no traces of higher hydrocarbons.[3] The pyrolysis reaction follows the thermal cracking mechanism and, to a large extent, operates in situations of strong sulphur poisoning or where the activity of the Ni catalyst is low.

Precious metal (ruthenium, rhodium)-based catalysts have been reported to be more effective catalysts for steam reforming in that they prevent carbon deposition and they have been proposed to replace conventional base metals for steam reforming in fuel-cell applications.[334] The ruthenium-based (Ru/Al_2O_3) catalyst has been used for the steam reforming of hydrocarbons, preventing carbon deposition.[335] Suzuki *et al.*[335] have successfully conducted a long-term (8000 h) test of the steam reforming of desulphurised kerosene ($C_{10}H_{22}$ with <0.1 ppm sulphur) using a Ru/Al_2O_3-CeO_2 catalyst, and they reported that the sulphur resistance was dramatically improved by the addition of CeO_2 to Al_2O_3. When the same catalyst was used for the steam reforming of kerosene (with 30–55 ppm sulphur), the conversion of kerosene was decreased to 85.5% after 25 h on-stream. These results contrast with those obtained with a commercial nickel catalyst during the steam reforming of low sulphur containing kerosene (0.1 ppm sulphur), which showed a drop in kerosene conversion to 72.3% after 24 h on-stream, suggesting that deactivation of the nickel catalyst was predominantly caused by carbon deposition.

Alumina supported Ni and Ni-Pd catalysts have also been used for hydrogen production by the partial oxidation and steam reforming of *n*-octane.[336] The whole process is complex and involves a combination of exothermic partial oxidation and endothermic steam reforming reactions. The highest efficiency could be obtained under the condition of thermoneutrality ($\Delta H = 0$), which made autothermal reforming more popular than steam reforming and partial oxidation. The objective of ATR is to carry out both CPO and SR of hydrocarbon over the same catalyst so that the exothermic reaction and endothermic reaction can be coupled effectively. As a result, the fuel processor based on this technology is less externally energy-intensive, cost effective and response-dynamic. The combination of these reactions can improve the reactor temperature control and reduce the formation of hot spots, avoiding catalyst deactivation by sintering or carbon deposition. All these advantages indicate that ATR could be considered as the technology of choice for small- or medium-scale hydrogen/syngas generators, for providing fuel for fuel cells, especially solid oxide fuel cells.

Experiments were carried out to study the effect of oxygen-to-carbon ratio, water-to-carbon ratio and space velocity on the performance of an autothermal reformer producing hydrogen from synthetic diesel fuel over a 1% Pt/ceria catalyst. It was found that diesel can be reformed to produce hydrogen under adiabatic conditions by heating the feed mixture/ATR reactor to only 673 K in contrast with the previous studies that utilised a temperature above 973 K to achieve similar performance. The temperature profile inside the reactor revealed that the exothermic reactions occur initially, which drive the endothermic reactions down the catalytic bed. The catalyst exhibited good stability for the ATR of synthetic fuel but it is prone to poisoning by S containing fuels.

Ni/γ-Al_2O_3 catalysts displayed good activity at high temperatures and such activity increased with increasing Ni-loadings up to 5.0 wt.%. However, the Ni/γ-Al_2O_3 catalysts rapidly became deactivated. X-ray diffraction of the used catalysts showed that an increase in the particle size of the nickel crystallites was the main reason for the poor stability of the Ni/γ-Al_2O_3 catalysts. In addition, coke

formation during the process was another source of catalyst deactivation. The activity and hydrogen selectivity of Ni-Pd/γ-Al_2O_3 catalysts were significantly higher than the values of the nickel catalyst under the same experimental conditions. The Ni-Pd/γ-Al_2O_3 catalyst displayed stable performance in the reforming reactions of *n*-octane for a period of 500 h on-stream, under molar ratios of $O_2/C_8H_{18} = 1.0$ and $H_2O/C = 3.0$. The amount of coke measured on the Ni-Pd/γ-Al_2O_3 catalyst was 0.16%, which is substantially lower than the amount measured on the Ni/γ-Al_2O_3 catalyst (0.54%) even lasting in the reaction for 60 h. Although no explanation has been offered concerning the role of Pd in minimising coke formation, it may be assumed that a major effect of palladium is its ability to gasify carbon residues under conditions of almost complete oxygen consumption.

Ming *et al.*[337] developed a highly active and stable catalyst for the steam reforming of various hydrocarbons such as *iso*-octane, retail gasoline and hexadecane. A 300 h continuous test revealed that the catalyst shows very stable performance for the steam reforming of *iso*-octane at 1,073 K with a steam/C ratio of 3.6, and that no carbon was deposited during the entire test period. The same catalyst was also tested for the steam reforming of hexadecane (a surrogate of diesel) for 73 h, as well as natural gas for over 150 h continuously, with no deactivation or carbon deposition. The sulphur tolerance of the catalyst was tested using *iso*-octane containing various concentrations of sulphur. There was no catalyst deactivation after a 220 h continuous test using *iso*-octane with 100 ppm sulphur. For comparison, a nickel catalyst (12 wt% Ni/Al_2O_3) was also tested using different levels of sulphur in *iso*-octane. The results indicated that the catalyst has a substantially improved sulphur resistance compared to the nickel catalysts currently used for steam reforming.

The influence of both Ce and La, as thermal stabiliser and activity promoter, respectively, has been studied in alumina supported nickel or platinum catalysts for the oxidative reforming of hexadecane. For both metal catalysts, higher reforming activities were found when active metals were deposited on Ce-La-Al_2O_3 substrate. For Pt-based catalysts, the increase in activity observed for the

catalyst prepared on the Ce-La-modified alumina substrate has been interpreted in terms of the participation of lanthanum in the reaction more than of modifications on coke resistance or dispersion and state of platinum induced by lanthanum.[338] It has been shown that Ni catalysts recorded a greater hydrogen production than Pt for all feeds. The higher activity when decalin is added to the feed stream is attributed to the more labile tertiary carbons of this molecule, and the lower activity for tetralin, to the higher bond dissociation energy of the aromatic C–C and C–H bonds. The characterisation results (by TPR and XPS) revealed a greater active metal-ceria interface in Ni catalysts which may have a role regarding their better catalytic performance and higher intrinsic activity for hydrogen production, as well as the reduced amount of coke deposited.[339] Pt catalysts supported on Al_2O_3 and doped with ceria and/or lanthana were also tested in the oxidative reforming of diesel surrogate with the aim of studying the influence of ceria and lanthana additives over the activity and stability toward hydrogen production for fuel-cell application. The physicochemical characterisation has shown that lanthana inhibits the formation of alpha phase in alumina support and decreases ceria dispersion. Activity results show a better performance with ceria-loaded catalysts, with the Pt/A-C sample being the system that offered higher H_2 yields after 8 h of reaction. This was attributed to the Pt-Ce interaction that may change the electronic properties and/or the dispersion of the active metal phase. Also, the Ce^{3+} form of the Ce^{4+}/Ce^{3+} redox pair enhances the adsorption of oxygen and water molecules, thus increasing the catalytic activity and also decreasing coke deposition over surface active Pt-phases. Stability tests showed that catalysts in which Pt crystallites are deposited on the alumina substrate covered by a lanthana monolayer, give rise to an increase in stability towards H_2 production.[340] The optimisation of the catalyst formulation has been used to scale up the catalyst to be included in the 5 kW diesel reformer, already in use, in order to be integrated with a PEMFC.[341]

Cerium- and nickel-substituted $LaFeO_3$ perovskites have been also investigated as potential low cost coking resistant catalysts for autothermal reforming of a JP-8 fuel surrogate. The high surface

area complex oxides were prepared using aqueous combustion synthesis under fuel-rich conditions. The catalysts exhibited excellent stability during autothermal reforming at 775°C and 1 atm, with near equilibrium hydrogen yield even at high GHSV values (130,000 h^{-1}). The addition of cerium significantly improved coking resistance, which was attributed to improved oxygen ion conductivity, resulting in carbon oxidation on the catalyst surface.[342] Additionally, catalysts derived from lanthanum cobaltite have been reported as being very efficient for the production of hydrogen by diesel oxidative reforming. The Co^0/La_2O_3 derived from $LaCoO_3$ perovskite, and Ru-Co/La_2O_3 catalysts derived from $Ru/LaCoO_3$ prepared by impregnation over the above perovskite, have shown very high hydrogen yields and stability for the oxidative reforming of diesel. Structural and surface analyses revealed that the incorporation of Ru to $LaCoO_3$ produces changes evidenced by a smaller size of the $LaCoO_3$ crystallites and cobalt segregation on the surface. The modifications induced by the addition of Ru directly affect the dispersion and morphology of Co particles developed under the reaction. The characterisation of used samples revealed that enhancement of the cobalt surface concentration and Co-La_2O_3 interactions contribute to the better catalytic stability of the Ru-Co/La_2O_3-derived catalyst.[343] The importance of the element that partially substitutes Co has been emphasised. When Ru is compared with Fe in $LaCo_{1-x}M_xO_3$ (M = Ru or Fe, x = 0.2) precursors, the higher reducibility and metal exposition implies higher reforming activity, as was observed for the Ru containing catalyst.[344] In addition, it was shown that the calcination temperature and precursor type used in the preparation of ZrO_2-supported $LaCoO_3$ catalysts has an important influence on its behaviour for hydrogen production by oxidative reforming of diesel. The use of nitrate precursors and high calcination temperature leads to the formation of $LaCoO_3$ perovskite structures of large particle and crystallite size on ZrO_2 support. On the contrary, the catalyst prepared from acetate precursors and calcined at low temperature showed smaller perovskite crystallite size which resulted in an initial higher and more stable hydrogen production rate for a short-term ageing test.[345]

Recent progress at the Argon National Laboratory indicated that perovskite materials are the most cost-effective catalysts for the autothermal reforming of diesel fuel to hydrogen-rich reformate. For instance, perovskite-type metal oxides with B sites partially exchanged by ruthenium were found to be very active and resistant to sulphur.[346] Ru-loaded lanthanum chromite and aluminite were explored as catalysts for the autothermal reforming of diesel fuel. Dodecane was used as a surrogate fuel. Both catalysts were shown to have high activity toward hydrogen production and good S tolerance when tested with a fuel mixture containing 50 parts per million S in the form of dibenzothiofene.[347] Different lanthanum perovskite oxides ($LaBO_3$, B: Co, Ni, Fe, Cr or Mn) were studied as catalysts for autothermal reforming of liquid hydrocarbon fuels to produce hydrogen for fuel-cell systems, using 2,2,4-trimethylpentane (isooctane) as a surrogate fuel. $LaNiO_3$ and $LaCoO_3$ produced high yields of H_2, but were not structurally stable. The three other binary oxides, $LaCrO_3$, $LaFeO_3$ and $LaMnO_3$, were structurally stable but significantly less active than $LaNiO_3$ and $LaCoO_3$. The effect of substituting La by alkaline earth elements on catalyst performance and stability was also investigated.[348] Finally, $La_{0.8}Sr_{0.2}M_{0.9}Ni_{0.1}O_3$ catalysts (where M = Cr, Mn, or Fe) were tested with a 'benchmark fuel' mixture containing from 0 to 50 ppmw sulphur. These tests showed that using chromium as a stabilising element in $LaNiO_3$ imparts the most sulphur tolerance.[348]

Acronyms

ASED-MO:	Atom Superposition and Electron Delocalisation-Molecular Orbital
ATR:	Autothermal Reforming
BOC-MP:	Bond-Order Conversion-Morse-Potential
CRM:	Combined Reforming of Methane
CRR:	Combustion and Reforming Reactions (mechanism for POM reaction)
DPO:	Direct Partial Oxidation (mechanism for POM reaction)
HRTEM:	High Resolution Transmission Electron Spectroscopy

HTS:	High-Temperature Shift (in WGS)
LTS:	Low-Temperature Shift (in WGS)
OCM:	Oxidative Coupling of Methane
POM:	Partial Oxidation of Methane (some authors use it as Partial Oxidation of Methanol, but not in this chapter)
PSA:	Pressure Swing Adsorption
RECP:	Relativistic Effective Core Potential
SEM:	Scanning Electron Microscopy
SMR:	Steam Methane Reforming
TEM:	Transmission Electron Microscopy
TOF:	Turn-Over Frequency
TPO:	Temperature-Programmed Oxidation
UBI-QEP:	Unity Bond Index-Quadratic Exponential Potential
WGS:	Water-Gas Shift
XANES:	X-ray Absorption Near-Edge Spectroscopy
XPS:	X-ray Photoelectron Spectroscopy
YSZ:	Yttria Stabilised Zirconia

References

1. J.R. Rostrup-Nielsen, in *Catalysis — Science and Technology Vol. 5*, Ed.: J.R. Anderson, M. Boudart, Springer, 1984, 1.
2. J.R. Rostrup-Nielsen, J. Sehested, J.K. Norskov, *Adv. Catal.* 2002, **47**, 65.
3. R.M. Navarro, M.A. Peña, J.L.G. Fierro, *Chem. Rev.* 2007, **107**, 3952.
4. J.N. Armor, *J. Membr. Sci.* 1998, **147**, 217.
5. M.A. Peña, J.P. Gómez, J.L.G. Fierro, *Appl. Catal. A: Gen.* 1996, **144**, 7.
6. J.R. Rostrup-Nielsen, J.H.B. Hansen, *J. Catal.* 1993, **144**, 38.
7. D.L. Trimm, Z.I. Önsan, *Catal. Rev.* 2001, **43**, 31.
8. H.S. Bengaard, J.K. Norskov, J. Sehested, B.S. Clausen, L.P. Nielsen, A.M. Molenbroek, J.R. Rostrup-Nielsen, *J. Catal.* 2002, **209**, 365.
9. K.O. Christensen, D. Chen, R. Lodeng, A. Holmen, *Appl. Catal. A: Gen.* 2006, **314**, 9.

10. L.S. Lobo, D.L. Trimm, *J. Catal.* 1973, **29**, 15.
11. J.R. Rostrup-Nielsen, *J. Catal.* 1984, **85**, 31.
12. J.R. Rostrup-Nielsen, *Stud. Surf. Sci. Catal.* 1991, **68**, 85.
13. I. Alstrup, N.T. Andersen, *J. Catal.* 1987, **104**, 466.
14. D.L. Trimm, *Catal. Today* 1999, **49**, 3.
15. E. Nikolla, A. Holewinski, J. Schwank, S. Linic, *J. Am. Chem. Soc.* 2006, **128**, 11354.
16. E. Nikolla, J. Schwank, S. Linic, *J. Catal.* 2007, **250**, 85.
17. E. Nikolla, J. Schwank, S. Linic, *Catal. Today* 2008, **136**, 243.
18. F. Abild-Pedersen, J.K. Norskov, J.R. Rostrup-Nielsen, J. Sehested, S. Helveg, *Phys. Rev. B* 2006, 73.
19. J.M. Wei, E. Iglesia, *J. Catal.* 2004, **224**, 370.
20. J.W. Snoeck, G.F. Froment, M. Fowles, *Ind. Eng. Chem. Res.* 2002, **41**, 4252.
21. G. Jones, J.G. Jokobsen, S.S. Shim, M.P. Andersson, J. Rossmeisi, F. Abild-Pedersen, T. Bligaard, S. Helveg, B. Hinnemann, J.R. Rostrup-Nielsen, I. Chorkendorff, J. Sehested, J.K. Norskov, *J. Catal.* 2008, **259**, 147.
22. E. Nikolla, J. Schwank, S. Linic, *J. Catal.* 2009, **263**, 220.
23. I. Alstrup, B.S. Clausen, C. Olsen, R.H.H. Smits, J.R. Rostrup-Nielsen, *Stud. Surf. Sci. Catal.* 1998, **119**, 5.
24. Z.L. Zhang, X.E. Verykios, *Catal. Lett.* 1996, **38**, 175.
25. T. Horiuchi, K. Sakuma, T. Fukui, Y. Kubo, T. Osaki, T. Mori, *Appl. Catal. A: Gen.* 1996, **144**, 111.
26. A. Purnomo, S. Gallardo, L. Abella, C. Salim, H. Hinode, *React. Kinet. Catal. Lett.* 2008, **95**, 213.
27. J.C.S. Araujo, D. Zanchet, R. Rinaldi, U. Schuchardt, C.E. Hori, J.L.G. Fierro, J.M.C. Bueno, *Appl. Catal. B: Env.* 2008, **84**, 552.
28. W.H. Cassinelli, L.S.F. Feio, J.C.S. Araujo, C.E. Hori, F.B. Noronha, C.M.P. Marques, J. M.C. Bueno, *Catal. Lett.* **2008**, 120, 86.
29. S.O. Choi, S.H. Moon, *Catal. Today* 2009, **146**, 148.
30. K. Urasaki, Y. Sekine, S. Kawabe, E. Kikuchi, M. Matsukata, *Appl. Catal. A: Gen.* 2005, **286**, 23.
31. K.Y. Koo, H.S. Roh, U.H. Jung, W.L. Yoon, *Catal. Lett.* 2009, **130**, 217.
32. J. Xu, C.M.Y. Yeung, J. Ni, F. Meunier, N. Acerbi, M. Fowles, S.C. Tsang, *Appl. Catal. A: Gen.* 2008, **345**, 119.

33. L.S.F. Feio, C.E. Hori, S. Damyanova, F.B. Noronha, W.H. Cassinelli, C.M.P. Marques, J.M.C. Bueno, *Appl. Catal. A: Gen.* 2007, **316**, 107.
34. M.C.J. Bradford, M.A. Vannice, *Appl. Catal. A: Gen.* 1996, **142**, 97.
35. K. Wang, X.J. Li, S.F. Ji, X.J. Shi, J.J. Tang, *Energy Fuels* 2009, **23**, 25.
36. N. Laosiripojana, S. Assabumrungrat, *Appl. Catal. A: Gen.* 2005, **290**, 200.
37. A.M. Efstathiou, A. Kladi, V.A. Tsipouriari, X.E. Verykios, *J. Catal.* 1996, **158**, 64.
38. H. Wan, X.J. Li, S.F. Ji, B.Y. Huang, K. Wang, C.Y. Li, *J. Nat. Gas Chem.* 2007, **16**, 139.
39. T. Osaki, H. Masuda, T. Horiuchi, T. Mori, *Catal. Lett.* 1995, **34**, 59.
40. T. Borowiecki, A. Golebiowski, B. Stasinska, *Appl. Catal. A: Gen.* 1997, **153**, 141.
41. T.J. Huang, H.J. Lin, T.C. Yu, *Catal. Lett.* 2005, **105**, 239.
42. M.C.J. Bradford, M.A. Vannice, *J. Catal.* 1998, **173**, 157.
43. C.A. Bernardo, I. Alstrup, J.R. Rostrup-Nielsen, *J. Catal.* 1985, **96**, 517.
44. S.M. Stagg, D.E. Resasco, *Stud. Surf. Sci. Catal.* 1997, **111**, 543.
45. J.T. Richardson, J.K. Jung, J. Zhao, *Stud. Surf. Sci. Catal.* 2001, **136**, 203.
46. Y. Mukainakano, B.T. Li, S. Kado, T. Miyazawa, K. Okumura, T. Miyao, S. Naito, K. Kunimori, K. Tomishige, *Appl. Catal. A: Gen.* 2007, **318**, 252.
47. M. Nurunnabi, Y. Mukainakano, S. Kado, T. Miyao, S. Naito, K. Okumura, K. Kunimori, K. Tomishige, *Appl. Catal. A: Gen.* 2007, **325**, 154.
48. M. Nurunnabi, S. Kado, K. Suzuki, K. Fujimoto, K. Kunimori, K. Tomishige, *Catal. Commun.* 2006, **7**, 488.
49. M. Nurunnabi, Y. Mukainakano, S. Kado, T. Miyazawa, K. Okumura, T. Miyao, S. Naito, K. Suzuki, K.I. Fujimoto, K. Kunimori, K. Tomishige, *Appl. Catal. A: Gen.* 2006, **308**, 1.
50. Y. Mukainakano, K. Yoshida, S. Kado, K. Okumura, K. Kunimori, K. Tomishige, *Chem. Eng. Sci.* 2008, **63**, 4891.
51. M. Nurunnabi, B.T. Li, K. Kunimori, K. Suzuki, K. Fujimoto, K. Tomishige, *Catal. Lett.* 2005, **103**, 277.

52. M. Nurunnabi, B.T. Li, K. Kunimori, K. Suzuki, K. Fujimoto, K. Tomishige, *Appl. Catal. A: Gen.* 2005, **292**, 272.
53. K. Tomishige, *J. Japan Pet. Inst.* 2007, **50**, 287.
54. M. Nurunnabi, K. Fujimoto, K. Suzuki, B.T. Li, S. Kado, K. Kunimori, K. Tomishige, *Catal. Commun.* 2006, **7**, 73.
55. M. Nurunnabi, Y. Mukainakano, S. Kado, B.T. Li, K. Kunimori, K. Suzuki, K. Fujimoto, K. Tomishige, *Appl. Catal. A: Gen.* 2006, **299**, 145.
56. N.V. Parizotto, K.O. Rocha, S. Damyanova, F.B. Passos, D. Zanchet, C.M.P. Marques, J.M.C. Bueno, *Appl. Catal. A: Gen.* 2007, **330**, 12.
57. J.H. Jeong, J.W. Lee, D.J. Seo, Y. Seo, W.L. Yoon, D.K. Lee, D.H. Kim, *Appl. Catal. A: Gen.* 2006, **302**, 151.
58. D. Harshini, Y. Kwon, J. Han, S.P. Yoon, S.W. Nam, T.H. Lim, *Kor. J. Chem. Eng.* 2010, **27**, 480.
59. J. Xua, L. Chen, K.F. Tana, A. Borgna, M. Saeys, *J. Catal.* 2009, **261**, 158.
60. M.G. Poirier, C. Sapundzhiev, *Int. J. Hydrogen Energy* 1997, **22**, 429.
61. M. Steinberg, *Int. J. Hydrogen Energy* 1998, **23**, 419.
62. N.Z. Muradov, *Energy Fuels* 1998, **12**, 41.
63. T.V. Choudhary, E. Aksoylu, D.W. Goodman, *Catal. Rev.* 2003, **45**, 151.
64. T.V. Choudhary, C. Sivadinarayana, D.W. Goodman, *Chem. Eng. J.* 2003, **93**, 69.
65. K. Nakagawa, N. Ikenaga, Y.H. Teng, T. Kobayashi, T. Suzuki, *J. Catal.* 1999, **186**, 405.
66. M.S. Kim, N.M. Rodríguez, R.T.K. Baker, *J. Catal.* 1991, **131**, 60.
67. M.A. Ermakova, D.Y. Ermakov, *Catal. Today* 2002, **77**, 225.
68. J. Li, K.J. Smith, *Appl. Catal. A: Gen.* 2008, **349**, 116.
69. G. Bonura, O. Di Blasi, L. Spadaro, F. Arena, F. Frusteri, *Catal. Today* 2006, **116**, 298.
70. K.E. Cox, K.D. Williamson. *Hydrogen: Its Technology and Implications, Vol. 1*, Boca Raton, CRC Press, 1977.
71. G.P. Noyes, US Patent No. 4,836,898, 6 June, 1989.
72. R.M. de Almeida, H.V. Fajardo, D.Z. Mezalira, G.B. Nuernberg, L.K. Noda, L.F.D. Probst, N.L.V. Carreno, *J. Mol. Catal. A: Chem.* 2006, **259**, 328.

73. D.P. Serrano, J.A. Botas, J.L.G. Fierro, R. Guil-Lopez, P. Pizarro, G. Gomez, *Fuel* 2010, **89**, 1241.
74. Y. Li, B.C. Zhang, X.W. Xie, J.L. Liu, Y.D. Xu, W.J. Shen, *J. Catal.* 2006, **238**, 412.
75. R.A. Couttenye, M.H. de Vila, S.L. Suib, *J. Catal.* 2005, **233**, 317.
76. T.V. Reshetenko, L.B. Avdeeva, Z.R. Ismagilov, A.L. Chuvilin, V.B. Fenelonov, *Catal. Today* 2005, **102**, 115.
77. B.H. Ryu, S.Y. Lee, D.H. Lee, G.Y. Han, T.J. Lee, K.J. Yoon, *Catal. Today* 2007, **123**, 303.
78. T.J. Zhang, M.D. Amiridis, *Appl. Catal. A: Gen.* 1998, **167**, 161.
79. A. Venugopal, S.N. Kumar, J. Ashok, D.H. Prasad, V.D. Kumari, K.B.S. Prasad, M. Subrahmanyam, *Int. J. Hydrogen Energy* 2007, **32**, 1782.
80. Z.Q. Bai, H.K. Chen, B.Q. Li, W. Li, *Int. J. Hydrogen Energy* 2007, **32**, 32.
81. Y. Nagayasu, A. Nakayama, S. Kurasawa, S. Iwamoto, E. Yagasaki, M. Inoue, *J. Jpn. Petrol. Inst.* 2005, **48**, 301.
82. I. Suelves, M.J. Lazaro, R. Moliner, B.M. Corbella, J.M. Palacios, *Int. J. Hydrogen Energy* 2005, **30**, 1555.
83. M.E. Rivas, J.L.G. Fierro, R. Guil-Lopez, M.A. Pena, V. La Parola, M.R. Goldwasser, *Catal. Today* 2008, **133**, 367.
84. M.J. Lazaro, Y. Echegoyen, I. Suelves, J.M. Palacios, R. Moliner, *Appl. Catal. A: Gen.* 2007, **329**, 22.
85. Y. Echegoyen, I. Suelves, M.J. Lazaro, R. Moliner, J.M. Palacios, *J. Power Sources* 2007, **169**, 150.
86. A. Monzon, N. Latorre, T. Ubieto, C. Royo, E. Romeo, J. Villacampa, L. Dussault, J.C. Dupin, C. Guimon, M. Montioux, *Catal. Today* 2006, **116**, 264.
87. A.F. Cunha, J.J.M. Orfao, J.L. Figueiredo, *Int. J. Hydrogen Energy* 2009, **34**, 4763.
88. V.V. Chesnokov, A.S. Chichkan, *Int. J. Hydrogen Energy* 2009, **34**, 2979.
89. J. Ashok, P.S. Reddy, G. Raju, M. Subrahmanyam, A. Venugopal, *Energy Fuels* 2009, **23**, 5.
90. S.T. Hussain, M. Mazhar, S. Iqbal, S. Gul, M. Hussain, F. Larachi, *Bull. Kor. Chem. Soc.* 2007, **28**, 1119.
91. S. Hussain, S. Gul, M. Mazhar, D.H. Anjum, F. Larachi, *J. Nat. Gas Chem.* 2008, **17**, 374.

92. O.A. Gonzalez, M.A. Valenzuela, J.A. Wang (Eds.) *Mat. Res. Soc. Symp. Proc.* 2006, **885**, 233.
93. Y. Li, B.C. Zhang, X.L. Tang, Y.D. Xu, W.J. Shen, *Catal. Commun.* 2006, **7**, 380.
94. Y. Echegoyen, I. Suelves, M.J. Lazaro, M.L. Sanjuan, R. Moliner, *Appl. Catal. A: Gen.* 2007, **333**, 229.
95. W. Gac, A. Denis, T. Borowiecki, L. Kepinski, *Appl. Catal. A: Gen.* 2009, **357**, 236.
96. N. Latorre, J.I. Villacampa, T. Ubieto, E. Romeo, C. Royo, A. Borgna, A. Monzon, *Top. Catal.* 2008, **51**, 158.
97. G. Italiano, C. Espro, F. Arena, F. Frusteri, A. Parmaliana, *Catal. Lett.* 2008, **124**, 7.
98. K. Nakagawa, M. Nishitani-Gamo, T. Ando, *Int. J. Hydrogen Energy* 2005, **30**, 201.
99. K. Nakagawa, N.O. Ikenaga, T. Kobayashi, T. Suzuki, *Catal. Today* 2001, **64**, 31.
100. K. Nakagawa, M.A. Yamagishi, H. Nishimoto, N. Ikenaga, T. Suzuki, T. Kobayashi, M. Nishitani-Gamo, T. Ando, *Chem. Mater.* 2003, **15**, 4571.
101. H.Y. Wang, E. Ruckenstein, *Carbon* 2002, **40**, 1911.
102. M. Nagai, H. Kanesugi, *J. Chem. Eng. Jpn.* 2006, **39**, 569.
103. S. Izhar, H. Kanesugi, H. Tominaga, M. Nagai, *Appl. Catal. A: Gen.* 2007, **317**, 82.
104. J. Li, K.J. Smith, *Appl. Catal. A: Gen.* 2008, **349**, 116.
105. M.S. Kim, N.M. Rodríguez, R.T.K. Baker, *J. Catal.* 1992, **134**, 253.
106. N.M. Rodríguez, A. Chambers, R.T.K. Baker, *Langmuir* 1995, **11**, 3862.
107. E. Boelleead, P.K. De Bokx, A.J.H.M. Kock, J.W. Geus, *J. Catal.* 1985, **96**, 481.
108. K.P. de Jong, J.W. Geus, *Catal. Rev.* 2000, **42**, 481.
109. K. Otsuka, H. Ogihara, S. Takenaka, *Carbon* 2003, **41**, 223.
110. K. Murata, M. Inaba, M. Miki, T. Yamaguchi, *React. Kinet. Catal. Lett.* 2005, **85**, 21.
111. Y. Li, B.C. Zhang, X.W. Xie, J.L. Liu, Y.D. Xu, W.J. Shen, *J. Catal.* 2006, **238**, 412.

112. N. Latorre, J.I. Villacampa, T. Ubieto, E. Romeo, C. Royo, A. Borgna, A. Monzon, *Top. Catal.* 2008, **51**, 158.
113. Z.Q. Bai, H.K. Chen, B.Q. Li, W. Li, *Int. J. Hydrogen Energy* 2007, **32**, 32.
114. S. Takenaka, Y. Shigeta, E. Tanabe, K. Otsuka, *J. Catal.* 2003, **220**, 468.
115. S. Takenaka, H. Ogihara, K. Otsuka, *J. Catal.* 2002, **208**, 54.
116. K. Otsuka, S. Takenaka, *Catal. Surv. Asia* 2004, **8**, 77.
117. E. Shustorovich, R.C. Baetzold, *Science* 1985, **227**, 876.
118. A.B. Anderson, J.J. Maloney, *J. Phys. Chem.* 1988, **92**, 809.
119. M.R.A. Blomberg, P.E.M. Siegbahn, U. Nagashima, J. Wennerberg, *J. Am. Chem. Soc.* 1991, **113**, 424.
120. O. Swang, K. Faegri, O. Gropen, *J. Phys. Chem.* 1994, **98**, 3006.
121. C.T. Au, C.F. Ng, M.S. Liao, *J. Catal.* 1999, **185**, 12.
122. P.M. Torniainen, X. Chu, L.D. Schmidt, *J. Catal.* 1994, **146**, 1.
123. S.S. Bharadwaj, L.D. Schmidt, *J. Catal.* 1994, **146**, 11.
124. C.T. Au, H.Y. Wang, *J. Catal.* 1997, **167**, 337.
125. C.Q. Lu, K.C. Ling, G.C. Wang, *Chin. J. Catal.* 2009, **30**, 1269.
126. S. Nave, A.K. Tiwari, B. Jackson, *J. Chem. Phys.* 2010, **132**, 054705.
127. J.R. Rostrup-Nielsen, *Catal. Today* 2000, **63**, 159.
128. D.J. Wilhelm, D.R. Simbeck, A.D. Karp, R.L. Dickenson, *Fuel Process. Technol.* 2001, **71**, 139.
129. S.B. Wang, G.Q.M. Lu, G.J. Millar, *Energy Fuels* 1996, **10**, 896.
130. M.C.J. Bradford, M.A. Vannice, *Catal. Rev.* 1999, **41**, 1.
131. V.R. Choudhary, K.C. Mondal, T.V. Choudhary, *Appl. Catal. A: Gen.* 2006, **306**, 45.
132. Z. Hou, J. Gao, J. Guo, D. Liang, H. Lou, X. Zheng, *J. Catal.* 2007, **250**, 331.
133. S.F. He, Q.S. Jing, W.J. Yu, L.Y. Mo, H. Lou, X.M. Zheng, *Catal. Today* 2009, **148**, 130.
134. A.P.E. York, T.C. Xiao, M.L.H. Green, *Top. Catal.* 2003, **22**, 345.
135. A.T. Ashcroft, A.K. Cheetham, J.S. Foord, M.L.H. Green, C.P. Grey, A.J. Murrell, P.D.F. Vernon, *Nature* 1990, **344**, 319.
136. A.T. Ashcroft, A.K. Cheetham, M.L.H. Green, P.D.F. Vernon, *Nature* 1991, **352**, 225.
137. A.J. Brungs, A.P.E. York, J.B. Claridge, C. Márquez-Álvarez, M.L.H. Green, *Catal. Lett.* 2000, **70**, 117.

138. J.B. Claridge, A.P.E. York, A.J. Brungs, C. Márquez-Álvarez, J. Sloan, S.C. Tsang, M.L.H. Green, *J. Catal.* 1998, **180**, 85.
139. T.C. Xiao, A. Hanif, A.P.E. York, Y. Nishizaka, M.L.H. Green, *Chem. Phys.* 2002, **4**, 4549.
140. D. Dissanayake, M.P. Rosynek, K.C.C. Kharas, J.H. Lunsford, *J. Catal.* 1991, **132**, 117.
141. V.R. Choudhary, S.D. Sansare, A.S. Mamma, *Appl. Catal. A: Gen.* 1992, **90**, L1.
142. V.R. Choudhary, A.S. Mamman, S.D. Sansare, *Angew. Chem. Int. Ed.* 1992, **31**, 1189.
143. V.R. Choudhary, A.M. Rajput, V.H. Rane, *J. Phys. Chem.* 1992, **96**, 8686.
144. V.R. Choudhary, A.M. Rajput, B. Prabhakar, *J. Catal.* 1993, **139**, 326.
145. D. Dissanayake, M.P. Rosynek, J.H. Lunsford, *J. Phys. Chem.* 1993, **97**, 3644.
146. Y.F. Chang, H. Heinemann, *Catal. Lett.* 1993, **21**, 215.
147. F. Basile, L. Basini, M. D'Amore, G. Fornasari, A. Guarinoni, D. Matteuzzi, G. Del Piero, F. Trifirò, A. Vaccari, *J. Catal.* 1998, **173**, 247.
148. A. Santos, M. Menéndez, A. Monzón, J. Santamaría, E.E. Miró, E.A. Lombardo, *J. Catal.* 1996, **158**, 83.
149. S. Eriksson, S. Rojas, M. Boutonnet, J.L.G. Fierro, *Appl. Catal. A: Gen.* 2007, **326**, 8.
150. T. Wu, D. Lin, Y. Wu, X. Zhou, Q. Yan, W. Weng, H. Wan, *J. Nat. Gas Chem.* 2007, **16**, 316.
151. L.V. Mattos, E.R. Oliveira, P.D. Resende, F.B. Noronha, F.B. Passos, *Catal. Today* 2002, **77**, 245.
152. F.B. Passos, E.R. Oliveira, L.V. Mattos, F.B. Noronha, *Catal. Lett.* 2006, **110**, 161.
153. F.A. Silva, J.A.C. Ruiz, K.R. de Souza, J.M.C. Bueno, L.V. Mattos, F.B. Noronha, C.E. Hori, *Appl. Catal. A: Gen.* 2009, **364**, 122.
154. R. Lanza, P. Canu, S.G. Järås, *Appl. Catal. A: Gen.* 2010, **375**, 92.
155. D.A. Hickman, L.D. Schmidt, *J. Catal.* 1992, **136**, 300.
156. D.A. Hickman, L.D. Schmidt, *Science* 1993, **259**, 343.
157. D.A. Goetsch,s L.D. Schmidt, *Science* 1996, **271**, 1560.

158. E. Ruckenstein, Y.H. Hu, *J. Catal.* 1996, **162**, 230.
159. V.A. Tsipouriari, Z. Zhang, X.E. Verykios, *J. Catal.* 1998, **179**, 283.
160. J. Barbero, M.A. Peña, J.M. Campos-Martín, J.L.G. Fierro, P.L. Arias, *Catal. Lett.* 2003, **87**, 211.
161. Y.H. Hu, E. Ruckenstein, *Catal. Rev.-Sci. Eng.* 2002, **44**, 423.
162. J. Requies, M.A. Cabrero, V.L. Barrio, M.B. Guemez, J.F. Cambra, P.L. Arias, F.J. Perez-Alonso, M. Ojeda, M.A. Pena, J.L.G. Fierro, *Appl. Catal. A: Gen.* 2005, **289**, 214.
163. J.Z. Luo, Z.L. Yu, C.F. Ng, C.T. Au, *J. Catal.* 2000, **194**, 198.
164. S.B. Wang, G.Q.M. Lu, *Appl. Catal. B: Env.* 1998, **16**, 269.
165. G.Q.M. Lu, S.B. Wang, *Chemtech* 1999, **29**, 37.
166. S. Tang, L. Ji, J. Lin, H.C. Zeng, K.L. Tan, K. Li, *J. Catal.* 2000, **194**, 424.
167. J.H. Bitter, W. Hally, K. Seshan, J.G. van Ommen, J.A. Lercher, *Catal. Today* 1996, **29**, 349.
168. F.B. Passos, E.R. de Oliveira, L.V. Mattos, F.B. Noronha, *Catal. Today* 2005, **101**, 23.
169. F.L. Shi, M.Q. Shen, Y.A. Fei, J. Wang, D. Weng, *J. Rare Earths* 2007, **25**, 316.
170. F.B. Passos, E.R. Oliveira, L.V. Mattos, F.B. Noronha, *Catal. Lett.* 2006, **110**, 161.
171. M.D. Salazar-Villalpando, D.A. Berry, T.H. Gardner, *Int. J. Hydrogen Energy* 2008, **33**, 2695.
172. Z.L. Zhang, V.A. Tsipouriari, A.M. Efstathiou, X.E. Verykios, *J. Catal.* 1996, **158**, 51.
173. K. Nakagawa, K. Anzai, N. Matsui, N. Ikenaga, T. Suzuki, Y.H. Teng, T. Kobayashi, M. Haruta, *Catal. Lett.* 1998, **51**, 163.
174. M.C.J. Bradford, M.A. Vannice, *Catal. Today* 1999, **50**, 87.
175. D. Wang, O. Dewaele, A.M. de Groote, G.F. Froment, *J. Catal.* 1996, **159**, 418.
176. P. Ferreira-Aparicio, M. Fernández-García, A. Guerrero-Ruiz, I. Rodríguez-Ramos, *J. Catal.* 2000, **190**, 296.
177. R. Torbati, S. Cimino, L. Lisi, G. Russo, *Catal. Lett.* 2009, **127**, 260.
178. W.S. Dong, H.S. Roh, K.W. Jun, S.E. Park, Y.S. Oh, *Appl. Catal. A: Gen.* 2002, **226**, 63.
179. V.A. Tsipouriari, X.E. Verykios, *J. Catal.* 1998, **179**, 292.

180. V.C.H. Kroll, P. Delichure. C. Mirodatos, *Kinet. Catal.* 1996, **37**, 698.
181. C.Y. Li, C.C. Yu, S.K. Shen, *Catal. Lett.* 2000, **67**, 139.
182. Y. Schuurman, C. Márquez-Álvarez, V.C.H. Kroll, C. Mirodatos, *Catal. Today* 1998, **46**, 185.
183. B.C. Enger, R. Lodeng, A. Holmen, *Appl. Catal. A: Gen.* 2008, **346**, 1.
184. V.R. Choudhary, B. Prabhakar, A.M. Rajput, *J. Catal.* 1995, **157**, 752.
185. N. Nichio, M.L. Casella, G.F. Santori, E.N. Ponzi, O.A. Ferretti, *Catal. Today* 2000, **62**, 231.
186. S.H. Seok, S.H. Han, J.S. Lee, *Appl. Catal. A: Gen.* 2001, **215**, 31.
187. J.S. Chang, S.E. Park, J.W. Yoo, J.N. Park, *J. Catal.* 2000, **195**, 1.
188. Q. Miao, G. Xiong, S. Sheng, W. Cui, L. Xu, X. Guo, *Appl. Catal. A: Gen.* 1997, **154**, 17.
189. S.L. Liu, G.X. Xiong, S.S. Sheng, W.S. Yang, *Appl. Catal. A: Gen.* 2000, **198**, 261.
190. R. Ran, G.X. Xiong, W.S. Yang, *J. Mater. Chem.* 2002, **12**, 1854.
191. Q.S. Jing, X.M. Zheng, *Energy* 2006, **31**, 2184.
192. F.A. Silva, D.S. Martinez, J.A.C Ruiz, L.V. Mattos, C.E. Hori, F.B. Noronha, *Appl. Catal. A: Gen.* 2008, **335**, 145.
193. C. Batiot-Dupeyrat, G. Valderrama, A. Meneses, F. Martínez, J. Barrault, J.M. Tatibouet, *Appl. Catal. A: Gen.* 2003, **248**, 143.
194. H.J. Guo, H. Lou, Y.H. Zhu, X.M. Zheng, *Mater. Lett.* 2003, **57**, 4450.
195. H. Provendier, C. Petit, C. Estournes, S. Libs, A. Kiennemann, *Appl. Catal. A: Gen.* 1999, **180**, 163.
196. T. Hayakawa, H. Harihara, A.G. Andersen, K. Suzuki, H. Yasuda, T. Tsunoda, S. Hamakawa, A.P.E. York, Y.S. Yoon, M. Shimizu, K. Takehira, *Appl. Catal. A: Gen.* 1997, **149**, 391.
197. M.R. Goldwasser, M.E. Rivas, E. Pietri, M.J. Pérez-Zurita, M.L. Cubeiro, L. Gingembre, L. Leclercq, G. Leclercq, *Appl. Catal. A: Gen.* 2003, **255**, 45.
198. R. Lago, G. Bini, M.A. Peña, J.L.G. Fierro, *J. Catal.* 1997, **167**, 198.
199. V.R. Choudhary, K.C. Mondal, *Appl. Energy* 2006, **83**, 1024.
200. X. Yin, L. Hong, *Appl. Catal. A: Gen.* 2009, **371**, 153.

201. A. Bhattacharyya, V.W. Chang, D.J. Schumacher, *Appl. Clay Sci.* 1998, **13**, 317.
202. T. Shishido, M. Sukenobu, H. Morioka, M. Kondo, Y. Wang, K. Takaki, K. Takehira, *Appl. Catal. A: Gen.* 2002, **223**, 35.
203. A.I. Tsyganok, T. Tsunoda, S. Hamakawa, K. Suzuki, K. Takehira, T. Hayakawa, *J. Catal.* 2003, **213**, 191.
204. F. Basile, P. Benito, G. Fornasari, D. Gazzoli, I. Pettiti, V. Rosetti, A. Vaccari, *Catal. Today* 2009, **142**, 78.
205. J. Zhang, W. Wei, Y. Sun, *Catal. Lett.* 2010, **135**, 321.
206. A.I. Tsyganok, M. Inaba, T. Tsunoda, K. Uchida, K. Suzuki, K. Takehira, T. Hayakawa, *Appl. Catal. A: Gen.* 2005, **292**, 328.
207. D.R. Palo, R.A. Dagle, J.D. Holladay, *Chem. Rev.* 2007, **107**, 3992.
208. Y. Matsumura, N. Tode, *Chem. Phys.* 2001, **3**, 1284.
209. Y. Usami, K. Kagawa, M. Kawazoe, Y. Matsumura, H. Sakurai, M. Haruta, *Appl. Catal. A: Gen.* 1998, **171**, 123.
210. Y. Matsumura, M. Okumura, Y. Usami, K. Kagawa, H. Yamashita, M. Anpo, M. Haruta, *Catal. Lett.* 1997, **44**, 189.
211. S. Shiizaki, I. Nagashima, Y. Matsumura, M. Haruta, *Catal. Lett.* 1998, **56**, 227.
212. R. Shiozaki, T. Hayakawa, Y.Y. Liu, T. Ishii, M. Kumagai, S. Hamakawa, K. Suzuki, T. Itoh, T. Shishido, K. Takehira, *Catal. Lett.* 1999, **58**, 131.
213. M.P. Kapoor, Y. Ichihashi, K. Kuraoka, W.J. Shen, Y. Matsumura, *Catal. Lett.* 2003, **88**, 83.
214. M.P. Kapoor, Y. Ichihashi, K. Kuraoka, Y. Matsumura, *J. Mol. Catal. A: Chem.* 2003, **198**, 303.
215. W.J. Shen, Y. Matsumura, *Chem. Phys.* 2000, **2**, 1519.
216. Y.Y. Liu, K. Suzuki, S. Hamakawa, T. Hayakawa, K. Murata, T. Ishii, M. Kumagai, *Catal. Lett.* 2000, **66**, 205.
217. Y.Y. Liu, T. Hayakawa, T. Ishii, M. Kumagai, H. Yasuda, K. Suzuki, S. Hamakawa, K. Murata, *Appl. Catal. A: Gen.* 2001, **210**, 301.
218. M. Sasaki, H. Hamada, T. Ito, *Appl. Catal. A: Gen.* 2001, **207**, 191.
219. S. Schauermann, J. Hoffmann, V. Johanek, J. Hartmann, J. Libuda, *Chem. Phys.* 2002, **4**, 3909.
220. A. Gotti, R. Prins, *J. Catal.* 1998, **175**, 302.
221. G. Mul, A.S. Hirschon, *Catal. Today* 2001, **65**, 69.

222. K. Sun, W. Lu, M. Wang, X. Xu, *Appl. Catal. A: Gen.* 2004, **107**, 268.
223. G. Avgouropoulos, *Catal. Commun.* 2009, **10**, 682.
224. H. Borchert, B. Jurgens, T. Nowitzki, P. Behrend, Y. Borchert, V. Zielasek, S. Giorgio, C.R. Henry, M. Baumer, *J. Catal.* 2008, **256**, 24.
225. I.V. Yudanov, A.V. Matveev, K.M. Neyman, N. Rosch, *J. Am. Chem. Soc.* 2008, **130**, 9342.
226. H. Agaras, G. Cerrella, M.A. Laborde, *App. Catal.* 1988, **45**, 53.
227. K. Takahashi, N. Takezawa, H. Kobayashi, *Appl. Catal.* 1982, **2**, 363.
228. K. Takahashi, H. Kobayashi, N. Takezawa, *Chem. Lett.* 1985, 759.
229. J.C. Amphlett, M.J. Evans, R.F. Mann, R.D. Weir, *Can. J. Chem. Eng.* 1985, **63**, 605.
230. C.J. Jiang, D.L. Trimm, M.S. Wainwright, N.W. Cant, *Appl. Catal. A: Gen.* 1993, **93**, 245.
231. M. Shimokawabe, H. Asakawa, N. Takezawa, *Appl. Catal.* 1990, **59**, 45.
232. B.L. Kniep, F. Girgsdies, T. Ressler, *J. Catal.* 2005, **236**, 34.
233. G.J.J. Bartley and R. Burch, *Appl. Catal.* 1988, **43**, 141.
234. R.A. Koeppel, A. Baiker, Ch. Schild, A. Wokaun, *Stud. Surf. Sci. Catal.* 1991, **63**, 59.
235. Y. Nitta, T. Fujimatsu, Y. Okamoto, T. Imanaka, *Catal. Lett.* 1993, **17**, 157.
236. Y. Nitta, O. Suwata, Y. Ikeda, Y. Okamoto, T. Imanaka, *Catal. Lett.* 1994, **26**, 345.
237. D. Bianchi, J.L. Gass, M. Khalfallah, S.J. Teichner, *Appl. Catal. A: Gen.* 1993, **101**, 297.
238. Y. Sun, P.A. Sermon, *Catal. Lett.* 1994, **29**, 361.
239. D. Gasser, A. Baiker, *Appl. Catal.* 1989, **48**, 279.
240. P.D.L. Mercera, J.G. van Ommen, E.B.M. Doesburg, A.J. Burggraaf, J.R.H. Ross, *Appl. Catal.* 1991, **71**, 363.
241. J.P. Breen, J.R.H. Ross, *Catal. Today* 1999, **51**, 521.
242. A. Szizybalski, F. Girgsdies, A. Rabis, Y. Wang, M. Niederberger, T. Ressler, *J. Catal.* 2005, **233**, 297.
243. G. Huang, B.J. Liaw, C.J. Jhang, Y.Z. Chen, *Appl. Catal. A: Gen.* 2009, **358**, 7.
244. T. Conant, A.M. Karim, V. Lebarbier, Y. Wang, F. Girgsdies, R. Schlögl, A. Datye, *J. Catal.* 2008, **257**, 64.

245. O. Ilinich, Y. Liu, C. Castellano, G. Koermer, A. Moini, R. Farrauto, *Plat. Met. Rev.* 2008, **52**, 134.
246. E.S. Ranganathan, S.K, Bej, L.T. Thompson, *Appl. Catal. A: Gen.* 2005, **289**, 153.
247. R.A. Dagle, Y.H. Chin, Y. Wang, *Top. Catal.* 2007, **46**, 358.
248. A.M. Karim, T. Conant, A.K. Datye, *Phys. Chem. Chem. Phys.* 2008, **10**, 5584.
249. C. Rameshan, W. Stadlmayr, C. Weilach, S. Penner, H. Lorenz, M. Havecker, R. Blume, T. Rocha, D. Teschner, A. Knop-Gericke, R. Schlogl, N. Memmel, D. Zemlyanov, G. Rupprechter, B. Klotzer, *Angew. Chem. Int. Ed.* 2010, **49**, 3224.
250. J. Papavasiliou, G. Avgouropoulos, T. Ioannides, *Catal. Commun.* 2005, **6**, 497.
251. G. Marban, T. Valdes-Solis, A.B. Fuertes, *Catal. Lett.* 2007, **118**, 8.
252. T. Fukunaga, N. Ryumon, N. Ichikuni, S. Shimazu, *Catal. Commun.* 2009, **10**, 1800.
253. C.X. Qi, J.C. Amphlett, B.A. Peppley, *J. Power Sources* 2007, **171**, 842.
254. C.X. Qi, J.C. Amphlett, B.A. Peppley, *Catal. Commun.* 2009, **11**, 71.
255. L. Alejo, R. Lago, M.A. Peña, J.L.G. Fierro, *Appl. Catal. A: Gen.* 1997, **162**, 281.
256. J.L.G. Fierro, *Stud. Surf. Sci. Catal.* 2000, **130A**, 177.
257. L.A. Espinosa, R.M. Lago, M.A. Peña, J.L.G. Fierro, *Top. Catal.* 2003, **22**, 245.
258. J.N. Russell, S.M. Gates, J.T. Yates, *Surf. Sci.* 1985, **163**, 516.
259. M. Bowker, R.J. Madix, *Surf. Sci.* 1980, **95**, 190.
260. B.A. Peppley, J.C. Amphlett, L.M. Kearns, R.F. Mann, *Appl. Catal. A: Gen.* 1999, **179**, 21.
261. B.A. Peppley, J.C. Amphlett, L.M. Kearns, R.F. Mann, *Appl. Catal. A: Gen.* 1999, **179**, 31.
262. C.J. Jiang, D.L. Trimm, M.S. Wainwright, N.W. Cant, *Appl. Catal. A: Gen.* 1993, **97**, 145.
263. G.J. Millar, C.H. Rochester, K.C. Waugh, *J. Chem. Soc. Faraday Trans.* 1991, **87**, 2795.
264. M. Mavrikakis, M.A. Barteau, *J. Mol. Catal. A: Chem.* 1998, **131**, 135.
265. R.M. Navarro, M.A. Peña, J.L.G. Fierro, *J. Catal.* 2002, **212**, 112.

266. H.C. Yang, F.W. Chang, L.S. Roselin, *J. Mol. Catal. A: Chem.* 2007, **276**, 184.
267. F.W. Chang, H.Y. Yu, L.S. Roselin, H.C. Yang, *Appl. Catal. A: Gen.* 2005, **290**, 138.
268. M.L. Cubeiro, J.L.G. Fierro, *Appl. Catal. A: Gen.* 1998, **168**, 307.
269. M.L. Cubeiro, J.L.G. Fierro, *J. Catal.* 1998, **179**, 150.
270. F.W. Chang, H.Y. Yu, L.S. Roselin, H.C. Yang, T.C. Ou, *Appl. Catal. A: Gen.* 2006, **302**, 157.
271. S. Velu, K. Suzuki, T. Osaki, *Chem. Commun.* 1999, 2341.
272. T.L. Reitz, P.L. Lee, K.F. Czaplewski, J.C. Lang, K.E. Popp, H.H. Kung, *J. Catal.* 2001, **199**, 193.
273. S. Velu, K. Suzuki, M.P. Kapoor, F. Ohashi, T. Osaki, *Appl. Catal. A: Gen.* 2001, **213**, 47.
274. S. Murcia-Mascarós, R.M. Navarro, L. Gómez-Sainero, U. Costantino, M. Nocchetti, J.L.G. Fierro, *J. Catal.* 2001, **198**, 338.
275. J. Agrell, H. Birgersson, M. Boutonnet, I. Melián-Cabrera, R.M. Navarro, J.L.G. Fierro, *J. Catal.* 2003, **219**, 389.
276. M. Turco, G. Bagnasco, C. Cammarano, P. Senese, U. Costantino, M. Sisani, *Appl. Catal. B: Env.* 2007, **77**, 46.
277. S. Patel, K.K. Pant, *Appl. Catal. A: Gen.* 2009, **356**, 189.
278. H. Koga, S. Fukahori, T. Kitaoka, A. Tomoda, R. Suzuki, H. Wariishi, *Appl. Catal. A: Gen.* 2006, **309**, 26.
279. J.R. Rostrup-Nielsen, *Phys. Chem. Chem. Phys.* 2001, **3**, 283.
280. K. Vasudeva, N. Mitra, P. Umasankar, S.C. Dhingra, *Int. J. Hydrogen Energy* 1996, **21**, 13.
281. S. Cavallaro, S. Freni, *Int. J. Hydrogen Energy* 1996, **21**, 465.
282. I. Fishtik, A. Alexander, R. Datta, D. Geana, *Int. J. Hydrogen Energy* 2000, **25**, 31.
283. S. Freni, *J. Power Sources* 2001, **94**, 14.
284. S. Cavallaro, *Energy Fuels* 2000, **14**, 1195.
285. J. Llorca, P.R. de la Piscina, J. Sales, N. Homs, *Chem. Commun.* 2001, 641.
286. A.N. Fatsikostas, D.I. Kondarides, X.E. Verykios, *Chem. Commun.* 2001, 851.
287. F. Mariño, M. Jobbagy, G. Baronetti, M. Laborde, *Stud. Surf. Sci. Catal.* 2000, **130C**, 2147.

288. V.V. Galvita, G.L. Semin, V.D. Belyaev, V.A. Semikolenov, P. Tsiakaras, V.A. Sobyanin, *Appl. Catal. A: Gen.* 2001, **220**, 123.
289. J.P. Breen, R. Burch, H.M. Coleman, *Appl. Catal. B: Env.* 2002, **39**, 65.
290. J. Llorca, N. Homs, J. Sales, P.R. de la Piscina, *J. Catal.* 2002, **209**, 306.
291. J. Llorca, N. Homs, J. Sales, J.L.G. Fierro, P.R. de la Piscina, *J. Catal.* 2004, **222**, 470.
292. S. Freni, S. Cavallaro, N. Mondello, L. Spadaro, F. Frusteri, *J. Power Sources* 2002, **108**, 53.
293. P.Y. Sheng, A. Yee, G.A. Bowmaker, H. Idriss, *J. Catal.* 2002, **208**, 393.
294. G.A. Deluga, J.R. Salge, L.D. Schmidt, X.E. Verykios, *Science* 2004, **303**, 993.
295. G.A. Jacobs, R.A. Keogh, B.H. Davis, *J. Catal.* 2007, **245**, 326.
296. A.N. Fatsikostas, D.I. Kondarides, X.E. Verykios, *Catal. Today* 2002, **75**, 145.
297. V. Klouz, V. Fierro, P. Denton, H. Katz, J.P. Lisse, S. Bouvot-Mauduit, C. Mirodatos, *J. Power Sources* 2002, **105**, 26.
298. B.C. Zhang, W.J. Cai, Y.D. Li, Y. Xu, W.J. Shen, *Int. J. Hydrogen Energy* 2008, **33**, 4377.
299. B.C. Zhang, X.L. Tang, Y. Li, W.J. Cai, Y.D. Xu, W.J. Shen, *Catal. Commun.* 2006, **7**, 367.
300. B.C. Zhang, X.L. Tang, Y. Li, Y.D. Xu, W.J. Shen, *Int. J. Hydrogen Energy* 2007, **32**, 2367.
301. W. Cai, B. Zhang, Y. Li, Y. Xu, W. Shen, *Catal. Commun.* 2007, **8**, 1588.
302. J. Kugai, V. Subramani, C.S. Song, M.H. Engelhard, Y.H. Chin, *J. Catal.* 2006, **238**, 430.
303. M.C. Sanchez-Sanchez, R.M. Navarro, J.L.G. Fierro, *Int. J. Hydrogen Energy* 2007, **32**, 1462.
304. M.C. Sanchez-Sanchez, R.M. Navarro, J.L.G. Fierro, *Catal. Today* 2007, **129**, 336.
305. A. Goula, S.K. Kontou, P.E. Tsiakaras, *Appl. Catal. A: Gen.* 2004, **49**, 135.
306. S.Q. Chen, Y. Liu, *Int. J. Hydrogen Energy* 2009, **34**, 4735.
307. S.M. de Lima, A.M. da Silva, L.O.O. da Costa, J.M. Assaf, G. Jacobs, B.H. Davis, L.V. Mattos, F.B. Noronha, *Appl. Catal. A: Gen.* 2010, **377**, 181.

308. L.J.I. Coleman, W. Epling, R.R. Hudgins, E. Croiset, *Appl. Catal. A: Gen.* 2009, **363**, 52.
309. H. Muroyama, R. Nakase, T. Matsui, K. Eguchi, *Int. J. Hydrogen Energy* 2010, **35**, 1575.
310. M.C. Sanchez-Sanchez, R.M. Navarro, D.I. Kondarides, X.E. Verykios, J.L.G. Fierro, *J. Phys. Chem. A* 2010, **114**, 3873.
311. P. Lespade, A. Marchand, M. Couzi, F. Cruege, *Carbon* 1984, **22**, 375.
312. S.R. Segal, K.B. Anderson, K.A. Carrado, C.L. Marshall, *Appl. Catal. A: Gen.* 2002, **231**, 215.
313. J.A. Torres, J. Llorca, A. Casanovas, M. Dominguez, J. Salvado, D. Montane, *J. Power Sources* 2007, **169**, 158.
314. A. Casanovas, C. de Leitenburg, A. Trovarelli, J. Llorca, *Chem. Eng. J.* 2009, **154**, 267.
315. S.S.Y. Lin, D.H. Kim, S.Y. Ha, *Catal. Lett.* 2008, **122**, 295.
316. H. Song, U.S. Ozkan, *J. Catal.* 2009, **261**, 66.
317. S.S.Y. Lin, D.H. Kim, S.Y. Ha, *Appl. Catal. A: Gen.* 2009, **355**, 69.
318. S.M. de Lima, A.M. da Silva, L.O.O. da Costa, U.M. Graham, G. Jacobs, B.H. Davis, L.V. Mattos, F.B. Noronha, *J. Catal.* 2009, **268**, 268.
319. W. Cai, F. Wang, A. van Veen, C. Descorme, Y. Schuurman, W. Shen, C. Mirodatos, *Int. J. Hydrogen Energy* 2010, **35**, 1152.
320. L.L. Makarshin, D.V. Andreev, A.G. Gribovskiy, V.N. Parmon, *Int. J. Hydrogen Energy* 2007, **32**, 3864.
321. A. Casanovas, M. Dominguez, C. Ledesma, E. Lopez, J. Llorca, *Catal. Today* 2009, **143**, 32.
322. O. Gorke, P. Pfeifer, K. Schubert, *Appl. Catal. A: Gen.* 2009, **360**, 232.
323. G.W. Chen, S.L. Li, Q. Yuan, *Catal. Today* 2007, **120**, 63.
324. Y. Men, G. Kolb, R. Zapf, V. Hessel, H. Lowe, *Process Saf. Environ. Prot.* 2007, **85**, 413.
325. A. Casanovas, M. Saint-Cerons, F. Griffon, J. Llorca, *Int. J. Hydrogen Energy* 2008, **33**, 1827.
326. J. Llorca, A. Casanovas, T. Trifonov, A. Rodriguez, R. Alcubilla, *J. Catal.* 2008, **255**, 228.
327. A. Casanovas, M. Dominguez, C. Ledesma, E. Lopez, J. Llorca, *Catal. Today* 2009, **143**, 32.
328. W. Cai, F. Wang, A. van Veen, C. Descorme, Y. Schuurman, W. Shen, C. Mirodatos, *Int. J. Hydrogen Energy* 2010, **35**, 1152.

329. W.J. Cai, F.G. Wang, E.S. Zhan, A.C. van Veen, C. Mirodatos, W.J. Shen, *J. Catal.* 2008, **257**, 96.
330. J.R. Rostrup-Nielsen, T. Rostrup-Nielsen, *Cattech* 2002, **6**, 150.
331. D.J. Moon, K. Sreekumar, S.D. Lee, B.G. Lee, H.S. Kim, *Appl. Catal. A: Gen.* 2001, **215**, 1.
332. D.L. Trimm, *Catal. Today* 1997, **37**, 233.
333. C.H. Bartholomew, *Appl. Catal. A: Gen.* 2001, **212**, 17.
334. W.P. Teagan, *Proc. 22nd Int. Precious Metals Conference*, Toronto, Canada, 1998.
335. T. Suzuki, H. Iwanami, T. Yoshinari, *Int. J. Hydrogen Energy* 2000, **25**, 119.
336. J.C. Zhang, Y.H. Wang, R.Y. Ma, D.Y. Wu, *Appl. Catal. A: Gen.* 2003, **243**, 251.
337. Q.M. Ming, T. Healey, L. Allen, P. Irving, *Catal. Today* 2002, **77**, 51.
338. R.M. Navarro, M.C. Alvarez-Galvan, F. Rosa, J.L.G. Fierro, *Appl. Catal. A: Gen.* 2006, **297**, 60.
339. M.C. Alvarez-Galvan, R.M. Navarro, F. Rosa, Y. Briceno, F. Gordillo, J.L.G. Fierro, *Int. J. Hydrogen Energy* 2008, **33**, 652.
340. M.C. Alvarez-Galvan, R.M. Navarro, F. Rosa, Y. Briceno, M.A. Ridao, J.L.G. Fierro, *Fuel* 2008, **87**, 2502.
341. F. Rosa, E. Lopez, Y. Briceno, D. Sopena, R.M. Navarro, M.C. Alvarez-Galvan, J.L.G. Fierro, C. Bordons, *Catal. Today* 2006, **116**, 324.
342. P. Erri, P. Dinka, A. Varma, *Chem. Eng. Sci.* 2006, **61**, 5328.
343. R.M. Navarro, M.C. Alvarez-Galvan, J.A. Villoria, I.D. Gonzalez-Jimenez, F. Rosa, J.L.G. Fierro, *Appl. Catal. B: Env.* 2007, **73**, 247.
344. N. Mota, M.C. Alvarez-Galvan, J.A. Villoria, F. Rosa, J.L.G. Fierro, R.M. Navarro, *Top. Catal.* 2009, **52**, 1995.
345. J.A. Villoria, M.C. Alvarez-Galvan, R.M. Navarro, Y. Briceno, F. Gordillo, F. Rosa, J.L.G. Fierro, *Catal. Today* 2008, **138**, 135.
346. D.J. Liu, M. Krumpelt, *Int. J. Appl. Ceram. Tech.* 2005, **2**, 301.
347. D.J. Liu, M. Krumpelt, H.T. Chien, S.H. Sheen, *J. Mater. Eng. Perform.* 2006, **15**, 442.
348. J.R. Mawdsley, T.R. Krause, *Appl. Catal. A: Gen.* 2008, **334**, 311.

This page intentionally left blank

CHAPTER 9

SUPPORTED METALS FOR APPLICATION IN FUEL CELLS

Sergio Rojas, María Victoria Martínez-Huerta and M.A. Peña

Instituto de Catálisis y Petroleoquímica, CSIC, C/Marie Curie, Cantoblanco, 28049 Madrid, Spain

9.1 Introduction

In the preceding chapter, different catalytic technologies for hydrogen production have been described, indicating its role as an energy vector, and as the most appropriate fuel for the implementation of a sustainable energy economy. Although hydrogen can be used in conventional combustion devices, the most efficient way of application is through the use of fuel cells (FC). The FC technology dates from the mid-19th century, but its first practical use arrived with the first space flights, as an energy source in spacecrafts. There are several fields of application of the FC technology, but probably the highest current interest is in the transportation sector, where the combination of batteries, FCs, and a hydrogen tank could be the only way of manufacturing zero emission vehicles with a long range of autonomy.[1] If the hydrogen used in this vehicle is of a renewable origin, the life cycle assessment for this application can be considered fully sustainable.

An FC is an electrochemical device that allows the transformation of the chemical energy of a fuel directly into electrical energy.[2,3]

It is not a heat engine, limited by the thermal efficiency given by the Carnot cycle. As a consequence, the efficiency of FCs is usually higher than the standard internal combustion engines used in transportation, with values always higher than 60% for the transformation of the chemical energy in electricity. An FC works as other similar electrochemical systems, including: an anode, where the fuel is oxidized releasing electrons (these electrons are the source of the electrical power in an external circuit); a cathode, where an oxidant (usually oxygen, from the air in terrestrial applications) is reduced, closing the external circuit with the flowing electrons from the anode; and a electrolyte that closes internally the circuit connecting anode and cathode with ions exchange, but that is an electronic insulator to avoid electron losses from the external circuit. There are several types of FCs and the main difference between them is the kind of electrolyte that is used: Solid oxide fuel cells (SOFC), where the electrolyte is an oxide (usually Y_2O_3 doped with ZrO_2) that transports oxide ions (O^{2-}) at high temperature (>800°C); molten carbonate fuel cells (MCFC) use a mixture of carbonates (Li_2CO_3-K_2CO_3), that are liquid at the operation temperature (600–700°C), exchanging carbonate ions (CO_3^{2-}); phosphoric acid fuel cells (PAFC), working at *ca.* 200°C, have liquid phosphoric acid as electrolyte with protons (H^+) as charge carriers; alkaline fuel cells (AFC) are based in KOH with transportation of hydroxyls (OH^-) at *ca.* 100°C; finally, proton exchange membrane fuel cells (PEMFC), which also work at *ca.* 100°C, use a solid proton conducting membrane as electrolyte.

Since the working conditions (temperature and electrolyte environment) are very different depending on the type of FC, the used materials are very also varied. One of these materials is the electrocatalyst that is used in the electrodes, anode and cathode.[3,4] A catalyst is necessary in the surface of the electrode for an efficient rate of the electrochemical half-reactions of oxidation and reduction occurring in anode and cathode. From the different types of FCs, PEMFCs have been intensely studied during the last years, and they are the clearest candidates for transportation and portable applications. The catalyst used in the electrodes of this family of

FCs is a supported metal catalyst. Throughout this chapter, the different electrocatalysts that are used in PEMFCs will be described. We will see that PEMFC electrocatalysts are supported metals of high loading, usually higher than 30 wt%, but they should maintain a high metal dispersion, with a metal particles size typically below 4 nm and an active surface area (ASA) for the metal in the range of 70–120 m^2g^{-1}.[3,5,6] We will see that, depending on the electrode and the fuel used, the optimized composition of the electrocatalysts will change, but platinum-based catalysts are still necessary for obtaining a catalyst of high performance for possible commercial applications of the FCs.

For the choice of a specific catalyst, the first parameter to be considered is the fuel used in the FCs, and that is going to be oxidized at the anode. Pure hydrogen is the most suitable fuel for the PEMFCs, producing high current densities at high potentials in the presence of supported Pt anode catalysts. But if hydrogen is produced from reforming of hydrocarbons (see Chapter 8), CO and CO_2 can be present as impurities in the fuel, acting as poisons for the catalytic sites.[3,7] In this case, the catalysts should be modified in order to be "tolerant" with these impurities, mainly with CO, which has the more significant effect.[6] Other fuels that are being considered as alternatives to hydrogen are methanol and ethanol. The main advantage of both is that they are liquid fuels, and the storage problems compared with hydrogen are simplified, since their power density in terms of energy by volume of fuel is much higher. Methanol is a commodity chemical and its distribution as fuel can be easily adopted. Ethanol has the advantage of its renewable origin, when it is obtained from biomass. Both alcohols have the drawback of very slow kinetics of the corresponding oxidation anodic half-reaction, requiring electrocatalysts of a very high activity, with novel formulations.[6,8–10] Something very similar happens with the cathodic electrocatalysts, since the kinetics are much lower than the electrooxidation of hydrogen. The design and synthesis of an active cathode electrocatalyst for the oxygen reduction reaction (ORR) is another of the most important challenges in PEMFCs science and technology.[11–15] The amount of platinum contained in current

PEMFCs, indeed in those using hydrogen as fuel, is still higher than the required one for large-scale applications, mainly in the transportation sector.[16] Therefore, one of the most important short-term objectives for the catalytic technology is the reduction of the noble metals loadings of the electrodes,[17,18] and also its substitution for non-noble metal catalysts (NNMCs).[10,14,15,18]

There are non-catalytic components in the PEMFCs that can have an important influence in the design of the electrocatalysts. First of all is the proton exchange membrane, which is the temperature-controlling component in the current technology. The most common membrane used is a layer of solid polymeric electrolyte (ionomer), of several microns of thickness, which should be maintained wet to keep the proton conductivity.[19] To avoid the loss of water, the operating temperature must to be lower than 100°C for the most used membrane material, Nafion®. Research in this field is working towards membranes that can operate at up to 200°C. This means that catalysts used in these intermediate-temperature FCs will be of a different design, with lower requirements than those working at 100°C. The other component is the gas diffusion layer (GDL), which allow the reactants (fuel or oxygen) to reach the catalyst surface, and the products (water, and CO_2 if alcohols are used as fuels) to leave the FCs. This is a porous layer material, of several microns of thickness, which should thoroughly manage the gradient and diffusion of reactant and products in the surrounding of the catalytic active sites. The catalyst powder is usually dispersed on the internal surface of the GDL (the one that will be in contact with the proton exchange membrane), or on the surface of the membrane, with the GDL placed directly in contact with the catalyst. A membrane with two layers of catalytic powder, one at each side, is a MEA (membrane electrode assembly) of three layers. When the GDLs are added to the membrane, we have a MEA of five layers. Dispersion of the catalytic powder in the MEA and the behaviour of the GDL will have a large influence on the performance of the PEMFCs and usually several discrepancies are found in the literature for the same catalyst due to differences in the assembly of the different components of the FC.[16,20]

The singular requirements of the active sites of the PEMFCs electrocatalysts must be taken into account when the electrode is designed. At every catalytic site, electrons and protons are generated (anode) or are consumed (cathode). Therefore, every catalytic site should be in contact with the conductive media of both electrons and protons. The first condition is fulfilled by using a conductive material as catalytic support of the metal particles, such as carbon black.[21] Also the GDL are based in electronic porous conductors, as graphitic carbon papers or cloths. However, the proton conductivity is reached only by an appropriate design of the electrode layer, adding to the catalyst, during the conformation of the electrode layer, micelles of the ionomer that should be in contact with the catalytic centers.[22,23] Regarding the use of carbon materials as catalyst support, several modifications of the support are also possible, which allow the introduction of new properties in the catalyst.

9.2 Hydrogen Oxidation Reaction

Studies on hydrogen oxidation reaction (HOR) electrocatalysis have built up a foundation for all modern electrocatalysis. In general, electrocatalysis can be considered as a specific type of heterogeneous catalysis whereby reactants and products adsorb onto the catalyst surface during the reaction process. Since the catalyzed electrochemical reaction occurs at the catalyzed electrode/electrolyte interface, the intrinsic kinetic rate of an electrochemical reaction (measured by the exchange current density) strongly depends on the potential difference between the catalyst surface and the electrolyte, as well as on the type of catalyst and its surface morphology.[24] Not surprisingly, virtually every electrochemical reaction where chemical bonds are broken or formed is electrocatalytic, and the kinetics vary by many orders of magnitude for different electrode materials. This is true even for the simplest electrochemical reaction where chemical bonds are broken, as for the hydrogen oxidation reaction,

$$H_2 + 2\ e^- \rightarrow 2H^+ + 2\ e^-. \tag{9.1}$$

Current voltage correlations measured for the Butler–Volmer equation (Eq. 9.2), describe mathematically the current-voltage correlation for a reversible electrochemical reaction, for instance, the anodic oxidation of hydrogen (index a) and cathodic hydrogen evolution (index c).

$$j = j_0 \, (\exp \, [\alpha_a F\eta/RT] - \exp -[\, \alpha_c F\eta/\, RT]), \qquad (9.2)$$

where, j is the current density, η is the overpotential or the difference between actual electrode potential E and equilibrium potential E_0 ($\eta = E - E_0$), and the coefficients α_a and α_c in the exponent are the charge transfer. In the Butler–Volmer equation, the exchange current density, j_0, as the quantity describing charge exchange per unit surface at equilibrium potential (equal in magnitude to either cathodic and anodic currents), is an indicator for electrocatalysis. Table 9.1 collates the exchange current densities of the hydrogen evolution reaction at different electrode materials. According to the data in this table, the metals contained in the group of the platinum metals are good electrocatalysts for this reaction, whereas mercury, for which an exceedingly low exchange current density is reported, is not an electrocatalyst at all.

Table 9.1 Exchange current densities of the hydrogen evolution/anodic oxidation reaction at different electrode materials in aqueous 1M H_2SO_4 solution at ambient temperature.[25]

Metal	j_0 (A·cm^{-2})
Palladium, Pd	$1.0 \cdot 10^{-3}$
Platinum, Pt	$7.9 \cdot 10^{-4}$
Rhodium, Rh	$2.5 \cdot 10^{-4}$
Iridium, Ir	$2.0 \cdot 10^{-4}$
Nickel, Ni	$6.3 \cdot 10^{-6}$
Gold, Au	$3.9 \cdot 10^{-6}$
Tungsten, W	$1.2 \cdot 10^{-6}$
Lead, Pb	$1.0 \cdot 10^{-12}$
Mercury, Hg	$5.0 \cdot 10^{-13}$

The adsorption of hydrogen on metal electrodes such as platinum has been studied extensively in electrochemical systems over the last several decades.[26,27] The mechanism for the hydrogen oxidation reaction on a Pt electrode in an acid electrolyte proceeds through two pathways, Tafel–Volmer and Heyrosky–Volmer, both of which involve the adsorption of molecular hydrogen (H_{ad}), followed by a charge transfer step:

Tafel: $$Pt + H_2 \rightarrow 2Pt\text{-}H_{ad} \tag{9.3}$$

Heyrosky: $$Pt + H_2 \rightarrow Pt\text{-}H_{ad} + H^+ + e^- \tag{9.4}$$

Volmer: $$Pt\text{-}H_{ad} \rightarrow Pt + H^+ + e^-. \tag{9.5}$$

It has been established that H_{ad} is the reactive intermediate in the HOR, and therefore the kinetics of the HOR is mainly determined by the interaction between H_{ad} and the Pt surface atoms.[26] There are two different possible states of adsorbed hydrogen. One is the H_{upd} (the underpotentially deposited hydrogen), which is the "strongly" adsorbed stated formed on the surface at potentials more positive than the Nernst potential, and the other is the H_{opd} (the overpotentially deposited hydrogen), which is the "weakly" adsorbed state formed close to or negative with respect to the Nernst potential.[26]

An approach to explain the particular role of platinum as an electrocatalyst for anodic hydrogen oxidation and cathodic hydrogen evolution is correlating the catalytic activity of different metals for this reaction and the strength of the adsorption enthalpy of hydrogen on these metals in Fig. 9.1.[27–29] This figure reveals, in the so-called volcano curve, a maximum of obtained current densities and hence electrocatalytic activities for intermediate Me–H bond strengths. The compromise between having a sufficient heat of adsorption for breaking the H–H bond, but not too large as to prevent the desorption of intermediates, is fulfilled by the platinum metals,[30] and explains the fast kinetics of this reaction over Pt catalysts.

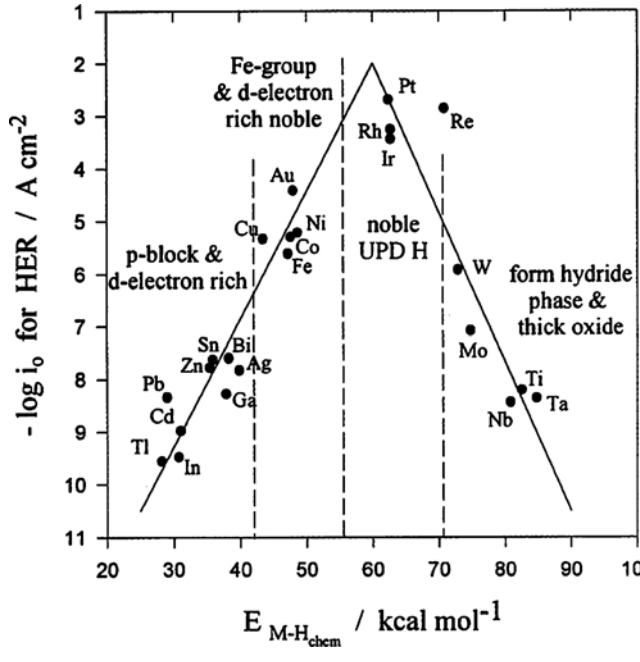

Figure 9.1 Volcano curve for the electrocatalysis of the HER at various metals in terms of dependence of log i_0 values on metal-to-H bond energy.[27]

The major effort in HOR electrocatalysis has been focused on understanding the rate dependency on the atomic-scale morphology of a platinum single-crystal surface. Recently, catalysis studies on well-defined Pt single-crystal electrodes clearly demonstrated that the HOR kinetics on Pt (hkl) vary with a crystal face that has "structure sensitivity".[26,31] This sensitivity is mainly caused by the structure-sensitive adsorption of hydrogen and electrolyte anions. Depending on the surface structure of the well-defined Pt, i.e. (110), (100), or (111), the influence of the H_{upd} state on the HOR is different, resulting in different mechanisms taking place.[32]

Although the HOR displays fast kinetics on pure Pt catalyst surfaces, one of the main disadvantages of the use of pure Pt is its high price and the possibility of depleting these mineral reserves if fuel cells were to be widely used. It is important to note that the current goal set by the USA Department of Energy (DOE) aims for specific power

(including area specific power) of 0.3–0.2 mg_{Pt}/cm^2 (2010 leading to 2015 targets). Since the cost targets are \$5 and \$3/kW (2010 and 2015 targets), an even more ambitious target may be needed depending on the increase in cost of Pt (currently priced at \$1500/t-oz, on average).[33] From an automotive perspective, a prior review by Gasteiger *et al.*[16] has pointed out that for automotive application, the current state of the art (with H_2/Air at 80°C), which is at approximately 0.7 W/cm^2 at 0.68V (for 58% energy conversion) corresponding to 0.85–1.1 g_{Pt}/kW requires a transition to 0.2 g_{Pt}/kW at ≥ 0.65V. This can be envisaged as a dual effort wherein (a) MEA power density is improved to 0.8–0.9 W/cm^2 MEA at ≥ 0.65V by increasing Pt utilization and lowering mass transport and ohmic contributions, and (b) increasing the inherent activities of the reaction zone by changing the nature of the conventional supported Pt electrocatalysts (Pt nanoparticles) *via* a means such as alloying and modification of surface morphology.

In the 1960s and 1970s exceptionally high loadings of 4–40 mg/cm^2 Pt and Pd black catalysts were utilized in making membrane electrode assemblies. This approach has two major hurdles: (a) the high loading of the noble metal, and (b) the loss of mass activity due to particle agglomeration resulting in the decrease of the effective surface area. The revolutionary step was to develop supported electrocatalysts, as previously employed in gas-phase heterogeneous catalysis.[34] In this context, the introduction of high surface area carbon blacks in 1988 for supporting precious metals decreased the catalysts loading by ten to hundred of orders of magnitude down to loadings of 0.4–0.5 mg/cm^2.[35]

Since catalyst performance for the HOR is strongly dependent on the total active surface area, supported catalysts have been developed to maximize the catalyst surface area. This issue is discussed in more detail in Section 9.8.

9.3 H_2/CO Electrooxidation

9.3.1 *Pt electrocatalysts*

In a PEMFC, when operating with pure hydrogen at practical current densities, the anode potential is typically less than + 0.1V (*vs.* RHE).

Under such operating conditions the cell potential is only slightly lower than the cathode potential and the MEA performance essentially reflects the cathode operation. However, when using reformate as a fuel, the CO in the reformate stream binds very strongly to the Pt electrocatalyst sites in the anode layer, at the typical MEA operating temperature of 80°C. The adsorbed CO prevents the dissociative electrosorption of hydrogen and dramatically lowers the cell potential produced by the MEA.[36] This is demonstrated in Fig. 9.2 by the effect of ppm levels of CO on a MEA with a Pt anode. The cell operating temperature was 80°C and CO concentrations of 25, 50, 100, and 250 ppm were used in the fuel gas.[37] It was found that for hydrogen and 25 ppm CO, the cell polarization curve looked similar to the curve without CO, only with a more negative slope. However, for CO concentration greater than 100 ppm, the polarization curve had two distinct slopes. The lower slope was explained by the adsorption and oxidation kinetics of hydrogen and CO at the anode. At increasing concentrations, CO could be oxidized to CO_2, thus leading to higher reaction rates for hydrogen adsorption and oxidation.

Despite its importance for low-temperature fuel cells, the exact mechanism of CO oxidation on Pt and the role of co-catalysts are still far from being understood.[38] It is generally accepted that the oxidation of CO proceeds according to a Langmuir–Hinshelwood mechanism, suggested by Gilman more than 40 years ago.[39] According to this model, water needs to be activated on a free site on the surface, leading to surface-bonded OH:

$$H_2O + * \leftrightarrow OH_{ads} + H^+ + e^- , \tag{9.6}$$

where the * denotes a free site on the platinum surface. The surface-bonded OH is the oxygen donor reacting with surface-bonded CO to form CO_2:

$$CO_{ads} + OH_{ads} \rightarrow CO_2 + H^+ + e^- + 2*. \tag{9.7}$$

In addition, CO was found to be a poisoning adsorbate during the oxidation of methanol and other small organic molecules.[40] In the

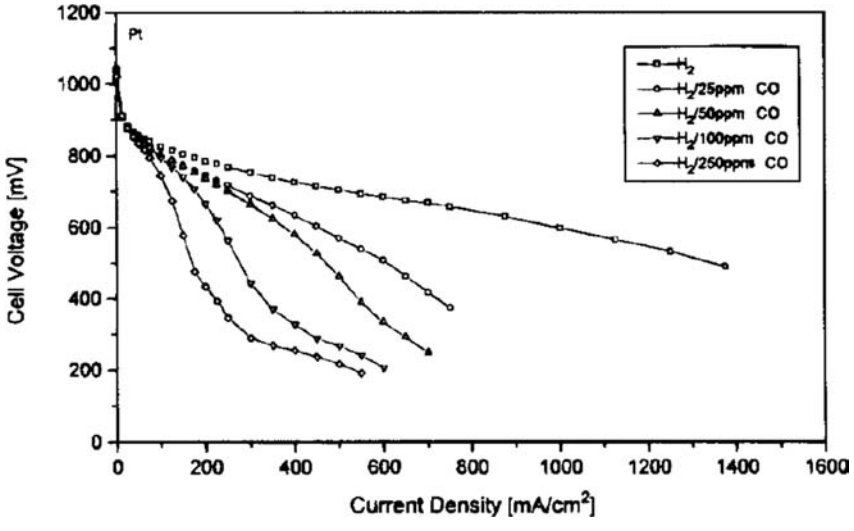

Figure 9.2 Illustration of the effect of CO on a PEMFC.[37]

case of methanol, CO formed along its dissociative adsorption on pure Pt covers a considerable fraction of the electrode surface in a matter of seconds. At potentials below 0.40V, the reaction cannot progress due to the inability of platinum to form OH for further oxidation, and the current falls to negligible values. Consequently, an important, although not unique, aspect of the catalysis of methanol oxidation is related to the catalysis of CO oxidation.

For many years it has been well known that CO electrooxidation on platinum is a structure-sensitive reaction.[41,42] Studies with single-crystal electrodes have shown that the kinetic parameters depend not only on the surface composition of the catalyst but also on the symmetry of the surface and that the presence of steps and defects alters significantly the reaction rate.[43] As a consequence, the surface structure of the nanoparticles should also affect the performance for the oxidation of CO. Understanding how the different variables affect CO oxidation on Pt nanoparticles dispersed on carbon requires the control of the platinum surface in a similar way as has been achieved for single-crystal electrodes. In this sense, the influence of the surface site distribution on CO oxidation using nanoparticles of well-defined

shapes has been reported.[44,45] For the carbon supported nanoparticle electrodes, the shape is generally more complex than that found for single-crystal electrodes, since it is affected by the surface structure and nanoparticle size and aggregation. López-Cudero *et al.*[46] have studied the CO oxidation on platinum nanoparticles deposited on carbon with different platinum loadings (from 10% to 50%), where the increasing loading leads to nanoparticle agglomeration. The results demonstrate that CO oxidation takes place at lower potentials when agglomeration takes place, since the adsorbed OH and CO species that participate in the reaction are on different nanoparticles, that is, it is an inter-particle process.

Nevertheless, the development of CO tolerant catalysts for PEMFCs is an important issue that needs to be addressed. The impurities in the hydrogen fuel remain a topic for research, although modern reformers typically produce a hydrogen stream with trace amounts of CO, for instance 1–50 ppm. However, even low CO concentrations (< 5 ppm) can poison the catalytic Pt surface of the anode, and reduce the cell performance.[37]

9.3.2 *CO tolerant catalysts*

It is generally considered that the use of CO tolerant electrocatalysts is the most promising way for solving the CO poisoning problem in PEMFCs. Since the mid-1960s, work to promote the CO tolerance has involved the modification of the catalytic platinum surface by the addition of a second metal to platinum.[47,48] It is well established that binary systems of CO tolerant electrocatalysts, with Pt as one of the components, can exhibit a substantial resistance to the presence of CO in the fuel stream. It has been found that the use of a second element with Pt, such as Ru, Sn, Co, Ta, Fe, Ni, Au, Mo, W, Ti, etc., in the form of an alloy or a co-deposit yields significant improvement in the CO tolerance behaviour, relative to pure Pt.[48–58]

Among these various Pt-based systems, the most commonly used is the PtRu/C whose study started as early as the 1960s as a very promising alloy for the methanol oxidation.[59] To date, Pt-Ru alloys, typically around the 1 : 1 composition, are the only ones to have

been introduced commercially and their preparation conditions and inter-metallic interactions have been extensively studied.[60,61] During the 1970s the group of Watanabe–Motoo[62–64] considered the possible nature of high Pt-Ru activity by formulating the mechanism of bifunctional catalysis. According to their theory, the ruthenium centers are responsible for generation of active oxygen species at potentials much lower than platinum.

$$Ru + H_2O \rightarrow RuOH + H^+ + e^- \quad E^0 \approx 0.2V_{NHE}. \tag{9.8}$$

Finally, following a Langmuir–Hinshelwood mechanism, adsorbed CO reacts with adsorbed OH to give CO_2, which is only possible if the final oxidation step occurs between CO adsorbed at Pt and OH adsorbed at Ru,[65] as shown in Fig. 9.3(a).

A second mechanism concerning an electronic effect resulting from the interaction of Ru with Pt was also proposed. This mechanism became widely accepted especially after the *in situ* FTIR work of the Iwasita–Vielstich team in the early 1990s and is associated with an energy shift of the Pt d electronic states caused by the second element, and resulting in a weakening of the Pt–CO bond, as seen more graphically in Fig. 9.3(b).[40,66]

However there are still many controversies about the nature of the CO tolerance mechanism. As most of the reactions taking place are structure-sensitive, the need for more nanoscale level studies is essential. Recently Watanabe *et al.*[67] reported that the bifunctional theory cannot be accepted for the Pt-non-precious metal alloys, such as PtFe,

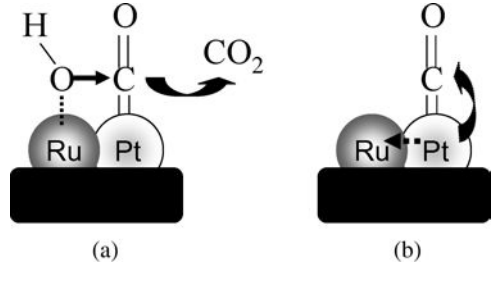

Figure 9.3 Bifunctional (a) and ligand (b) effects.

PtCo, and PtNi, and this was related to the formation of a Pt-skin layer on the alloy particles. However, for Pt alloys with precious metals such as Ru, Os, or Re, the bifunctional mechanism is operative because of the stability of these elements in the Pt surface. With the introduction and evolution of more powerful characterization techniques such as XAS, it has been possible to perform more detailed studies of the crystalline phases present in a catalyst. The work of McBreen and Mukerjee[68] has shown clearly that in Pt-Ru alloys, the Ru increased the Pt d-band vacancies and decreased the Pt–Pt bond distances. The wider conclusion of this work was that a fine-tuning of the electronic structure and the electrocatalysis is necessary in order to design an even more CO tolerant and active catalyst.

Other bimetallic alloys such as Pt-Mo[69–71] and Pt-Sn[72] have also shown good CO tolerance, even better than that showed by the Pt-Ru alloys, depending on the carbon monoxide concentration in the fuel stream. Nevertheless, they have not yet been introduced into commercial applications, probably because PEMFCs need to perform well under a variety of operating conditions for long periods of time with minimal degradation in performance. Non-noble elements such as Mo and Sn have the potential to corrode during operation, which may impact on long-term stability. Moreover, although these alloys are more tolerant to CO than pure Pt, the hydrogen oxidation overpotentials in the presence of CO are still very high relative to the hydrogen overpotentials in a CO-free gas feed.

Bimetallic PtMo alloy catalysts have thus attracted considerable attention as a result of their high catalytic activity in H_2 oxidation using a CO/H_2 feed.[51–53,57,69,71,73–88] Such enhanced performance was ascribed to (i) the lack of adsorption of CO on Mo, leaving more adsorption sites for oxygen containing species that are acting as CO oxidation reagents within the frame of a bifunctional mechanism, or (ii) changes in Pt-Pt atomic distance which modifies the Pt-CO adsorption energy.[89] Grgur *et al.*[51,74,90] reported the electrochemical oxidation of H_2, CO, and CO/H_2 on well-characterized PtMo bulk alloys or carbon supported PtMo catalysts in sulfuric acid solution. Their work suggested a similar bifunctional mechanism as with Ru for Mo in PtMo alloy, an increase in free Pt sites by the oxidative

removal of adsorbed CO. Mukerjee *et al.*[71,81,82] showed a two- to three-fold enhancement of the CO tolerance of PtMo in a PEM fuel cell compared to that of PtRu, which was ascribed to the onset of CO oxidation at very low potentials (≈ 100 mV). Papageorgopoulos *et al.*[57] related the increased tolerance to the ability of PtMo to promote the CO oxidation process at very low potentials. This was attributed to oxygen transfer from Mo oxyhydroxide species, with only the OH species of the oxyhydroxide states (predominantly $MoO(OH)_2$) being reactive with adsorbed CO.[74] In a more recent work, Liu *et al.*[52] has proposed a different mechanism to the bifunctional one. PtMo core-shell particles have been prepared that present higher CO tolerance and increased activity in the H_2/CO oxidation than commercial Pt/C and PtRu/C catalysts. It is considered likely that the electronic effect of the MoO_x core on Pt shell weakens the Pt–CO bond, which may dramatically reduce the oxidation overpotential.

A different mechanism altogether is proposed in the work of Santiago *et al.*[69,80] Different layers of Pt/C and Mo/C were combined and an excellent CO tolerance was observed. In that case there was no contact between the Mo and Pt particles (or atoms), implying that the CO tolerance cannot be associated with the electronic or bifunctional mechanisms. In their opinion, these high CO tolerances were caused by a lowering of the CO concentration in the gas channels inside the electrode, promoted by the modified Mo/C diffusion layer. There is no contact between Mo/C and any electrochemical interface, so this can only be achieved through a chemical reaction of CO catalyzed by the Mo sites. The reaction that the report suggests is the well-known water-gas shift reaction (WGS):

$$CO + H_2O \leftrightarrow CO_2 + H_2. \tag{9.9}$$

This reaction involves the conversion of CO to CO_2 without direct participation of protons and electrons, and compounds of molybdenum have shown potential for application as WGS catalysts.

The working principle of the PtSn electrocatalysts for the electrooxidation of CO is akin to that of PtRu; nucleation of $–OH_{ad}$

species occur at lower potentials on Sn than on Pt because Sn is more oxophilic than Pt. In contrast to PtRu, the PtSn electrocatalyst is a real bifunctional electrocatalyst; that is, CO adsorbs on Pt and Sn nucleates $-OH_{ad}$. It is unlikely that CO adsorbs on Sn.[4,91,92]

The $Pt_3Sn(111)$ surface has the highest activity for the electrooxidation of CO_{ad} and H_2/CO in acid medium reported thus far. The onset potential for the oxidation process is shifted by *ca.* 700 mV compared to pure Pt.[4] This result also applies to Pt_3Sn/C.[93,94]

9.4 Electrooxidation of Methanol

Direct Methanol Fuel Cells (DMFC) have the potential to have greater power density, longer runtime, instant recharging and lower weight than conventional batteries.[95–102] Currently, the lifetime of portable devices is still limited by how long they can operate as truly portable devices by the quantity of energy that can be stored within the batteries. The energy density of fuel cells is high if the power demand is small and the energy demand is large. DMFCs usually operate under ambient conditions and methanol as fuel has simpler and safer handling, since it is in liquid form at ambient condition. Also, methanol shows good electrochemical activity with a high energy density (6 kWh kg^{-1}).[99]

Much research effort involves attempts to enhance performance by improving characteristics of the components, including polymer electrolyte membranes, catalysts, membrane electrode assemblies (MEAs), stack assemblies, and packaging technology. DMFCs are flexible in power output from sub-watt to several hundred watts and thus are considered to be applicable to various portable electronics such as cellular phones, laptop computers, or television sets. DMFCs are roughly classified by their electric capacity and micro DMFCs are generally defined as those with less than 5W. The micro fuel cells could be potentially used as power sources for portable electronics. Recently, many companies including Motorola, Samsung, Toshiba, DuPont, Polyfuel, NEC, MTI (Mechanical Technologies Inc.), LG Chem, Casio, Smart Fuel Cell, etc. entered into this business.

A single cell in a DMFC has a maximum thermodynamic voltage of 1.18V at 25°C. The reactions that take place in a DMFC are given below:

Anode: $CH_3OH + H_2O \rightarrow CO_2 + 6H^+ + 6e^-$ $E^0 = 0.046$ V (9.10)

Cathode: $3/2O_2 + 6H^+ + 6e^- \rightarrow 3H_2O$ $E^0 = 1.229$ V (9.11)

Overall: $CH_3OH + 3/2O_2 \rightarrow CO_2 + 2H_2O$ $E^0 = 1.183$ V. (9.12)

As seen in the reaction, the oxidation of methanol involves six electrons and overall potential is almost the same as the oxidation of hydrogen. However, the energy density of the DMFCs is still far from that expected due to the methanol crossover and the high over voltage at the electrodes.[95] The crossover of methanol from the anode to the cathode has serious consequences in reducing its coulombic and voltage efficiencies. The main reason for the crossover is that the methanol fuel is soluble in water over the full range of composition from 0 to 100%. As a consequence, the diffusion rate of methanol from the anode to the cathode through the electrolyte is extremely high (corresponding to an equivalent current loss larger than 100 mA/cm^2 under open circuit conditions). On the other hand, the anode suffers from high activation overpotentials due to the slow kinetics of the methanol oxidation reaction. This detrimental effect reduces the cell voltage and severely affects the voltage efficiency of the system. DMFCs generally need higher metal loadings, sometimes more than ten times greater than the hydrogen-fed PEMFCs, due to the slow electrode reactions.

Understanding the nature of this overpotential is a key feature to the development of better fuel-cell catalysts, and also involves understanding the reactivity of intermediates in methanol oxidation. Spectroscopic studies have shown that the electrooxidation of CH_3OH (Eq. 9.10) on Pt is thought to follow a dual path mechanism at sufficiently high potentials[38,103] that involves both "indirect" and "direct" pathways (Fig. 9.4). The indirect path, which proceeds through the formation of CO, is shown in the center of Fig. 9.4

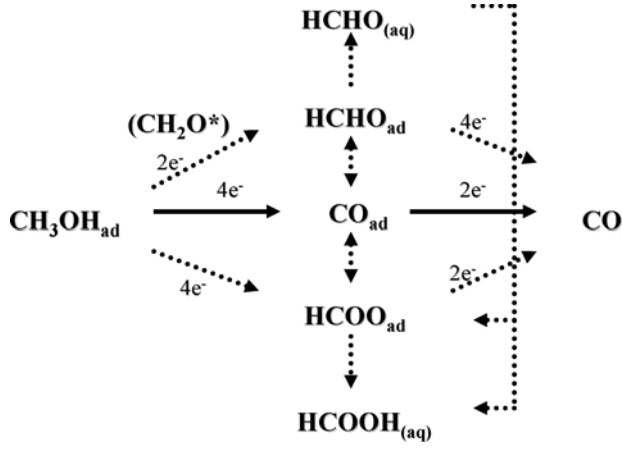

Figure 9.4 The initial steps in dual path mechanism for the electrocatalytic oxidation of methanol over Pt to CO_2, adapted from Neurock.[103])

(solid line). The direct paths, which lead to the formation of formaldehyde and formic acid, are shown at the top and bottom, respectively. The formaldehyde that forms can also react in solution to form formic acid or adsorbed formate. The interconversion of these steps is sketched by the dotted line. A more detailed set of possible elementary steps and how these may interconvert is given by Koper *et al.*[104,105]

Therefore, a catalyst for methanol oxidation should be able to (a) dissociate the C–H bond and (b) facilitate the reaction of the resulting residue with some O containing species, especially CO, to form CO_2.[40] On a pure Pt electrode, which is known to be a good catalyst for breaking the C–H bond, the two processes necessary for complete oxidation occur in different potential regions:

- Process (a) involving the adsorption of methanol molecules, requires several neighbouring places at the surface and, due to the fact that methanol is not able to displace adsorbed H atoms, adsorption can only begin at potentials where enough Pt sites become free from H, i.e. *ca.* 0.2V *vs.* RHE for a polycrystalline Pt electrode;

- The second process (b) is crucial and requires dissociation of water, which is the oxygen donor for the reaction. On a pure Pt electrode, sufficient interaction of water with the catalyst surface is only possible at potentials above 0.4–0.45V *vs.* RHE.

$$H_2O_{ad} + Pt \rightarrow Pt\text{-}OH + H^+ + e^-. \quad (9.13)$$

Thus, on pure Pt, methanol oxidation to CO_2 cannot begin below 0.45V. However, the adsorbate layer does not exhibit good reactivity below at least 0.7V, i.e. at potentials without technological interest. Several binary and ternary catalysts have been proposed for methanol oxidation, most of them based on modifications of Pt with some other metal including Ru, Mo, Rh, Os, Sn, Ni, Zr, Mo, W, Ti, and Ir.

At present, there is a general consensus that PtRu offers the most promising results, and has been the benchmark bimetallic catalyst since the mid-1960s.[59] The reason for the enhanced rate of methanol oxidation on PtRu is often invoked by the bifunctional mechanism[106] (see Section 9.3.1), where the first step of the reaction is adsorption of methanol:

$$CH_3OH_{(sol)} \rightarrow (CO)_{ad} + 4H^+ + 4e^-. \quad (9.14)$$

$(CO)_{ad}$ are CO species adsorbed either on Pt or Ru. Moreover, the effect of modification in Pt electronic environment, induced by Ru through increase in Pt d-band vacancies, has been emphasized[68] (see Section 9.3.1).

According to the bifunctional model, Anderson *et al.* calculated H_2O binding energies with respect to substituted atoms in a Pt alloy cluster.[107] Elements to the left of Pt in the periodic Table (i.e. Groups 3–9) bind H_2O more strongly than Pt, with the exception of Rh and Ir. Elements to the right, Groups 11–16, bind H_2O more weakly than Pt with no exceptions. The strongest binding energy (about 2.5 eV) was obtained for Ru, followed by Cr, Mo, and W. Following H_2O_{ad} the second step is the breaking of the OH bond and release of H. First principle theoretical calculations predicted

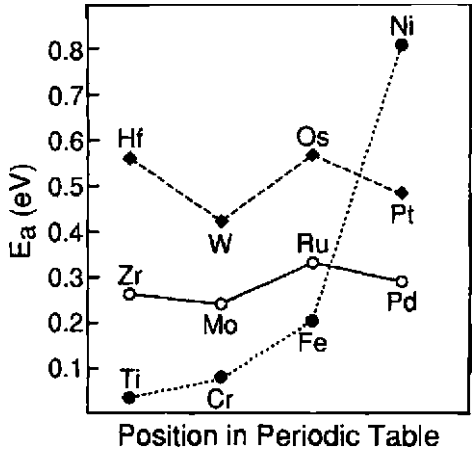

Figure 9.5 Activation energies (E_a) for OH bond scission when H_2O is bonded to a substitutional transition metal atom.[107]

that alloying with elements such as Ti, Cr, Fe, Mo, Pd, and Zr lead to lower activation energies for bond breaking in H_2O_{ad} compared to Ru (Fig. 9.5). In principle, they could be suitable as a Pt co-catalyst toward CH_3OH electrooxidation in a similar manner to Ru. These theoretical studies invite the question as to how binary catalyst formulations Pt-M (with M other than Ru, such as Mo, Sn, Ni, W, Os) compare experimentally with Pt and PtRu.

Mukerjee and Urian[78] compared the activity of PtMo/C (3 : 1 atomic ratio) with PtRu/C (1 : 1 atomic ratio) and Pt/C under conditions relevant for DMFCs. During polarization in 1M CH_2OH at 363 K, using Nafion 117 and 4 mg cm^{-2} catalyst load, the electrode potential at 100 mA cm^{-2} was about 170 mV more positive for PtMo compared to PtRu. Moreover, PtMo performed slightly worse than pure Pt alone. The effect of Mo as an alloying element with respect to CH_3OH oxidation was in sharp contrast with its beneficial role for enhancing the CO tolerance of Pt from a reformate feed. This indicates a major difference between CO and CH_3OH electrooxidation catalysis. Using XANES (X-ray absorption near-edge structure) the oxidation of Mo was observed at $E \geq 0V$ *vs.* RHE generating Mo(V), most likely a Mo oxo-hydroxide. The latter species was considered

responsible for CO oxidation from reformate feed; however, it was inactive in the case of methanol oxidation.[78] Consequently, the real experimental situation for PtMo is more complex than the bifunctional mechanism would suggest.

In the case of PtRu catalysts, a significant amount of work has been carried out and various theoretical and experimental techniques have been brought to bear in order to reveal the details for the PtRu catalytic/co-catalytic effect.[59] An interesting aspect of the Ru effect relates to the effect of the temperature and the optimum Pt : Ru ratio. Gasteiger *et al.* showed that dissociative methanol adsorption can occur on Ru sites as well, but it is a temperature-activated process.[108] Therefore, at low temperatures (e.g. 298 K) a higher Pt : Ru atomic ratio (above 1 : 1) is required to facilitate the dissociative adsorption and dehydrogenation of methanol preferentially on Pt, whilst at high temperatures (e.g. 333 K and above) a surface richer in Ru is beneficial (e.g. 1 : 1 at. ratio) since Ru becomes active for chemisorption and the rate determining step switches to the reaction between CO_{ad} and OH_{ad}.[108]

The oxidation state of the Ru component is still a topic of discussion. While some authors refer to the active ruthenium compound mainly as metallic Ru^0 in a bimetallic alloy,[109–111] early research revealed that hydrous ruthenium oxide as a part of bimetallic PtRu electrodes is the most active catalyst for methanol oxidation.[112–117] According to this latter point, Rolison *et al.*[112,113] emphasized the importance of hydrous ruthenium oxides because the $RuO_2{\bullet}xH_2O$ speciation of Ru in nanoscale PtRu blacks shows both high electron and proton conductivity, which results in a much more active catalyst for methanol oxidation. Cao *et al.*[115] showed that a new nanocomposite $Pt/RuO_2{\bullet}xH_2O$ supported on carbon nanotubes presented higher activity in the methanol electrooxidation as compared to that of PtRu commercial catalysts. The superior performance was attributed to the presence of $RuO_2{\bullet}xH_2O$ species. Recently, Gómez de la Fuente *et al.*[117] revealed that a combination of the electrocatalytic nature of $RuO_2{\bullet}xH_2O$ species and functionalized carbon black in PtRu/C catalysts greatly improves the performance in a single DMFC.

In order to improve the lifetime of the DMFCs and PEMFCs fuelled with H_2 from hydrocarbon reforming, without increasing cost or losing performance, exploring ternary anode catalysts is one of the most interesting and low-cost approaches.[118,119] However, ternary electrocatalysts must be resistant to changes in morphology and surface properties, and their stability may be a determining factor in the useful lifetime of these systems. The range of compositions that can be studied in such systems is enormous and realistically can only be mapped well through the use of high throughput materials science methods. Several CO tolerant Pt containing anodes exist, including PtRuSn, PtRuW, PtRuMo, PtRuOs, and PtRuPd.[24]

The crystal structure of pure Pt is face-centered cubic (fcc), while that of Ru is hexagonal close packed (hcp). For Ru atomic fractions up to about 0.7, Pt and Ru form a solid solution with Ru atoms replacing Pt atoms on the lattice points of the fcc structure. The lattice constant decreases from 0.3923 (pure Pt) to 0.383 nm (0.675 atomic fraction of Ru). In contrast to bulk Pt-Ru alloys, it has to be remarked that in carbon supported catalysts the amount of Ru alloyed with Pt is lower than the nominal Ru content in the material;[6] the amount of Ru alloyed with Pt depends on the preparation method of the supported catalyst. In Pt-Ru-M catalysts, the third metal is an oxophilic element as W, Mo, Os, Ni, Ir, etc. Some of these elements can be fully alloyed, while several form alloys to a limited extent or not at all with Pt.[120]

Ternary electrocatalysts based on PtRuMo nanoparticles have attracted major attention in recent years for PEMFCs fuelled with H_2/CO or low molecular weight alcohols.[53,57,121–132] However, the synergistic mechanisms of Pt, Ru, and Mo working together is still not clear and further studies are required. Recently a novel two step method for the preparation of ternary PtRuMo catalysts has been developed.[126,128] These catalysts display an important negative shift in the CO_{ads} oxidation potential in Differential Electrochemical Mass Spectroscopy (DEMS) experiments and surprising activity enhancement after the aging of the catalyst *via* methanol oxidation,

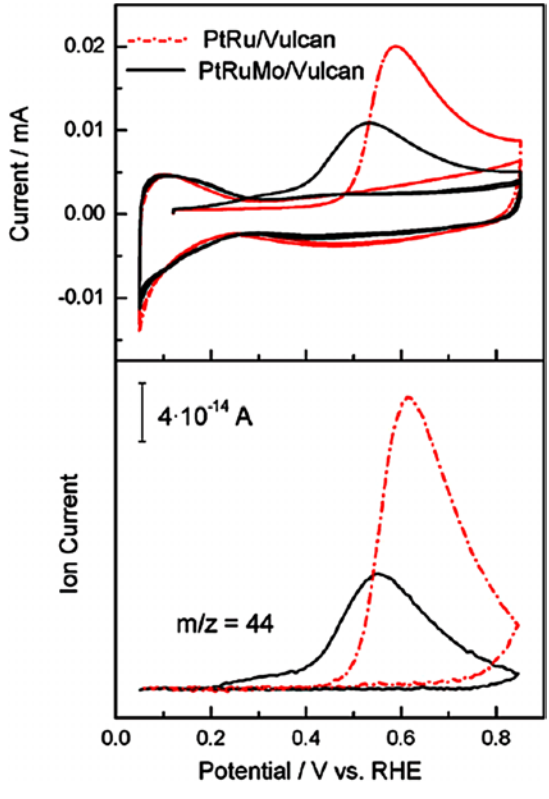

Figure 9.6 Voltammograms for the oxidation of CO in 0.5M H_2SO_4 at 25°C of PtRu/Vulcan XC-72R and PtRuMo/Vulcan XC-72R, and the corresponding MS signal for CO_2 production (m/z = 44).[128]

compared with literature reported binary catalysts and commercial catalysts. CO-stripping voltammetry results showed that the addition of Mo to a PtRu/C system led to a reduction in both onset potential and CO-stripping area (Fig. 9.6). These results suggest that catalysts with composition below 10 at. % Mo are worth examining further as candidates for the anode in improved CO tolerant fuel cells. A more detailed study of the electro-activation through the aging of the ternary catalysts, revealed the important role of the electrochemical reduction, through which the catalyst is been restructured to obtain a more active form.[127]

9.5 Electrooxidation of Ethanol

Ethanol is considered as the ideal fuel for the so-called direct alcohol fuel cells (DAFCs). This is because ethanol has a number of advantages over methanol; it can be produced in a sustainable manner, easily stored and transported, and is less toxic or corrosive than methanol. The theoretical mass energy of ethanol is 8.0 kWh kg^{-1} compared to 6.1 kWh kg^{-1} for methanol. The complete oxidation of ethanol releases 12 electrons per molecule; its standard electromotive force E^0_{Eq} = 1.145V, is similar to that of methanol.[133–136]

However, a number of issues, particularly those related to the performance of the electrocatalyst, should be improved in order to implement direct ethanol fuel-cell (DEFC) technology. Among them, the major challenge is developing electrocatalysts that can break the C–C bond at relative low potentials.

The mechanism of the electrooxidation of ethanol in acid media over a Pt surface has been studied.[135,137] It involves the electrochemical adsorption of ethanol by the alpha carbon (the one bearing the OH group) onto Pt sites releasing one electron and one proton[137] (Eqs 9.15 and 9.16). In successive dehydrogenation steps, acetaldehyde and acetic acid are produced. Acetaldehyde can readsorb on Pt as acetyl species and be dissociated into CH_x fragments and CO that can be completely oxidized to CO_2 at electrode potentials >0.5 eV. In the optimal scenario, when the C–C bond is dissociated and the fragments are oxidized into CO_2, the total number of electrons released per molecule of ethanol is 12. Despite the ability of Pt to activate the C–C bond, bare-Pt is not a suitable electrocatalyst for ethanol fuel cells since the process requires high overpotentials and, even at those high potentials, the reaction kinetics are slow. As a matter of fact, the actual efficiency of ethanol electrooxidation to CO_2 over on Pt catalysts, as determined by electrochemical infrared reflection-absorption spectroscopy (EC-IRAS) and differential electrochemical mass spectrometry (DEMS), is low; acetaldehyde and acetic acid, in different proportions being the main products.[133,138,139]

An efficient ethanol electrooxidation catalyst should combine at least two features: (i) high tolerance to CO and other intermediate species generated over the surface of the electrocatalyst during alcohol electrooxidation; and (ii) ability to break the C–C bond of the ethanol molecule under mild conditions. The most relevant features for the designing of CO tolerant electrocatalysts have been described above; namely, Pt modification with more oxophilic metals such as Ru,[140] Mo[126] or Sn[93] renders the best electrocatalysts. This is because such oxophilic atoms promote the formation of $-OH_{ad}$ species (involved in the CO_{ad} oxidation reaction) at potentials that are more negative than that on pure Pt (Eq. 9.17). Among those, Sn-modified Pt electrocatalysts are the most active formulations.[4,94,141,142] There is also widespread consensus that the Pt_3Sn phase is the most active one in the CO reaction and early stages of the ethanol electrooxidation process.[91,94,143]

$$Pt + CH_3\text{-}CH_2OH \rightarrow Pt\text{-}OCH_2\text{-}CH_3 + H^+ + e^- \qquad (9.15)$$

$$Pt + CH_3\text{-}CH_2OH \rightarrow Pt\text{-}CHOH\text{-}CH_3 + H^+ + e^- \qquad (9.16)$$

$$Pt\text{-}CO_{ads} + Sn\text{-}OH_{ads} \rightarrow Pt + Sn + CO_2 + H^+ + e^-. \qquad (9.17)$$

Although PtSn/C are the best binary electrocatalysts for the electrooxidation of ethanol, the main reaction products are acetic acid (AA) and acetaldehyde (AAL).[139]

Several approaches to the designing of efficient electrocatalysts for the electrooxidation of ethanol have been reported. Some of them focused on the structure of the catalytic particles. For instance, by generating high-index faceted Pt particles, the catalytic activity and selectivity to CO_2 of Pt/C can be improved.[144,145] The same is true for PtNi/C catalysts.[146] However, high-index planes are not stable in nanoparticles, hence the mass activity of those catalysts is low. Most studies, however, deal with bimetallic particles, typically Pt-M (M = W, Pd, Rh, Re, Mo)[118,119,134,135,138,147–153] with PtSn and PtRu being the most active. The predominant role of the Pt_3Sn phase has been recently reported.[94,154] Features such as the

actual catalyst morphology or the Pt to Sn stoichiometry have not previously been identified.

The addition of a third metal function (Ru, In, W) to PtSn/C catalysts has been reported to increase CO_2 selectivity and/or improve the performance of ethanol electrooxidation in a single cell.[133,155–160] In this context, the incorporation of Rh to the formulation of electrocatalyst for ethanol electrooxidation is receiving increasing attention.[159–164] In fact, in the field of heterogeneous catalysis for ethanol reforming it is well established that Rh plays a key role in the dissociation of the C–C bond.[165] On the other hand it has also been demonstrated that Rh(111) surfaces lack suitable electrocatalytic properties for the electrooxidation of CO_{ad} and ethanol.[166]

No catalysts with propensity for the complete oxidation of ethanol in acid medium have been reported.

9.6 Oxygen Reduction Reaction

The oxygen reduction reaction (ORR) is a very important reaction in energy conversion processes. In proton exchange membrane fuel cells (PEMFCs) the ORR is the half-cell reaction occurring at the cathode. From a kinetic point of view, the ORR is the slowest of the catalytic processes that take place within a fuel cell and hence it limits the overall performance of the PEMFCs. The exchange current density (j_0) is about 10^{-6} mA/cm^2 on a smooth Pt surface; about six orders of magnitude slower than the HOR. Therefore, driving the ORR at sufficient reaction rates, accounts for the largest part of the overpotential of a fuel cell. Hence, enormous efforts have been, and still are, focused towards understanding the reaction mechanism, structure related parameters, and to developing more active catalysts.[167–169]

The oxygen reduction reaction can proceed by two pathways in aqueous electrolytes.[170] The first one, the so-called "direct" pathway, involves releasing four electrons per oxygen molecule to yield H_2O. The "indirect" pathway involves releasing two electrons to yield hydrogen peroxide (H_2O_2) that in successive steps can produce water. Two further pathways, which are combinations of the above, can be envisaged. The "series" pathway implies sequential two or

four electron reduction steps to achieve total reduction of O_2 to H_2O accompanied by formation of H_2O_2. The "parallel" pathway is a combination of the "direct" and "series" pathways. The direct route is the preferred one in fuel cells because of its higher Faradaic efficiency and because it avoids the formation of H_2O_2. In the less active metals such as Au and Hg the reaction proceeds *via* two electron reduction. This process could be of potential interest for the production of H_2O_2. On Pt, the most active metal for ORR, the reaction proceeds *via* four electron transfer. This feature is consistent with the lack of observation for H_2O_2 in rotating-ring disk-electrode (RRDE) experiments.

In the acid medium, Pt is the most active metal for the ORR and it drives the reaction *via* the four electron process. In fact, Pt was the preferred catalyst for fuel-cell applications from as early as the 1960s. Due to high Pt price and scarcity, many strategies were proposed for decreasing its usage within the fuel cell.

The most obvious approach to improving Pt efficiency is attained by increasing the surface area by supporting it as nanosized Pt particles on graphite-type carriers. Using this approach the Pt-loading can be decreased by several orders of magnitude. However, even the most active Pt catalyst, based upon nanosized Pt particles of *ca.* 3 nm deposited on graphite type carbon, have a mass activity of *ca.* 160 mA/mg_{Pt}, well below the figure of merit of 450 mA/mg_{Pt} requested by the DOE[16] to achieve a target of \$45/kW for direct hydrogen fuel cells for transportation by 2010. Several strategies geared towards increasing further the Pt mass activity are under investigation.

The most promising ones are based upon (supported) Pt-based alloys. Numerous carbon supported bimetallic catalysts for the ORR have been studied, amongst them, PtCo,[171,172] PtAu,[173,174] PtV,[175] PtFe,[176] PtZn;[177] further PtM/C can be found in Refs. 12 and 178.

A number of studies dealing with non-noble metal catalysts (NNMCs) have appeared in recent years.[15,179–184] The main advantage of this type of catalyst is their low cost compared to Pt-based systems. In the next sections, relevant features to the ORR and the current status of catalyst development will be discussed.

9.6.1 *Reaction mechanism*

The oxygen reduction reaction is a multi-electron process involving numerous steps and intermediate species. As stated above, ORR may proceed *via* four or two electron transfer in aqueous acidic medium. The most relevant reactions pathways and their thermodynamic electrode potentials in acidic medium are shown below:

$$O_2 + 4H^+ + 4e^- \rightarrow H_2O \qquad E^0 = 1.229V \tag{9.18}$$

$$O_2 + 2H^+ + 2e^- \rightarrow H_2O_2 \qquad E^0 = 0.695V \tag{9.19}$$

$$H_2O_2 + 2H^+ + 2e^- \rightarrow H_2O \qquad E^0 = 1.776V. \tag{9.20}$$

The actual mechanism and the reaction kinetic depend, among other aspects, on the nature of the catalyst, the electrolyte, and the overpotential (η). The most accepted reaction scheme (see Fig. 9.7) for the ORR was given by Wroblowa *et al.*[185]

Despite numerous efforts, the ORR reaction mechanism remains elusive. Recently, theoretical calculations have been used to identify the rate limiting step and the nature of the key intermediate species in the ORR.[186–189]

The first step of the oxygen reduction on Pt, i.e. oxygen adsorption, can proceed through either dissociative or associative steps. In the dissociative route, O_2 dissociates on the Pt surface upon adsorption, a process akin to that observed under ultra-high vacuum (UHV)

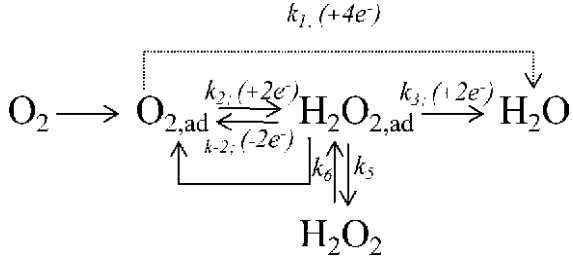

Figure 9.7 Reaction pathway for the ORR in acid solution, adapted from Wroblawa *et al.*[185]

conditions.[190] In the associative mechanism, O_2 binds to the Pt surface where it is reduced to a superoxide ion. More likely, this process is accompanied with the transfer of one proton.[167] The observation of superoxide, or other intermediate species, in acid medium remains elusive, probably because of its high tendency to become rapidly protonated in this medium.[167] Shao *et al.*[191] have reported the observation of a superoxide anion as intermediate in the ORR on Pt electrodes at pH 11. Observation of such species in acid medium has been achieved, however, in Bi-modified Au electrodes.[192] The associative route has been the most accepted one. However, it is not unusual in recent literature to find studies in which atomic adsorbed species are considered.[189,193] In fact, theoretical calculations show that the dissociation mechanism could be the most favorable one on Pt(111) surfaces.[194]

Recently, experimental results suggest that a series pathway *via* an H_2O_{2ad} intermediate is the most plausible pathway.[26,195] Some authors suggest that both mechanisms could operate at 0.80V.[187]

Appleby[196] proposed that the initial electron transfer to an adsorbed oxygen molecule is the rate determining step on group Ib and VIII metals. He also acknowledges that the process might well be accompanied by proton involvement. Other recent works share the idea that the rate limiting step is the addition of the first electron to O_{2ad}[26] forming OOH_{ad}.[197] Nørskov *et al.*[189] identified the strong adsorption of oxygen on Pt(111) at high potential as the origin of the overpotential. By lowering the potential, proton and electron transfer becomes more facile and the ORR may proceed. In this work, they also reported that both associative and dissociative paths can operate for the ORR; the predominance of each depending on the electrode potential. In this line, the reaction pathway and the rate determining step depend on the operation potential. At the equilibrium potential of 1.23V, OH removal is the rate limiting step; however, at 0.80V the strength of oxygen adsorption, with OH removal *via* hydrogenation or O–O bond scission are the rate limiting steps for surfaces with stronger and weaker oxygen binding, respectively.[187]

The kinetics of electrochemical O_2 reduction on Pt has been studied extensively.[193,198–200] There is a general consensus that it shows first order kinetics in O_2. By following the Butler–Volmer approach, the rate expression for the ORR can be expressed by the relationship between kinetic current, i, and potential, E:

$$i = nFkcO_2(1-\theta_{ad})\exp\left(\frac{-\beta FE}{RT}\right)\exp\left(\frac{-\Delta G°ad}{RT}\right) \qquad (9.21)$$

where i is the observed current, CO_2 is the concentration of O_2, θ_{ad} is the coverage of adsorbed species (anions from the electrolyte and OH_{ad}), n is the number of electrons, E is the applied potential, and β is the symmetry factor. From this expression it can be derived that the rate for the ORR is determined by either the number of free Pt sites for the adsorption of O_2, $(1 - \theta_{ad})$ term, and/or by the change of Gibbs energy of adsorption of reaction intermediates. This equation illustrates the strong effect of anion adsorption in the kinetic of the ORR. This is because anions adsorb at the same sites as O_2. This is the reason for the lower kinetics of the ORR in acid medium as compared to alkaline. For a detailed overview regarding the kinetic analysis for the ORR the reader is referred to Refs. 16, 193, 198–202. A typical device for the analysis of the kinetic parameters of the ORR is plotting log i *vs.* η (overpotential); the so-called Tafel plot.[203] In acidic solutions two Tafel slopes for the ORR are usually reported. At potential regions where the electrode is covered by an oxide layer, (1.1–0.8 V) the Tafel slope is −60 mVdecade^{-1} whereas at potentials from *ca.* 0.8 to 0.35 V the electrode is oxide free and the Tafel slope is −120 mVdecade^{-1}.[169] For a detailed analysis of the double Tafel slope advanced readers are referred to Ref. 198.

A very interesting, although not unusual feature in catalysis, is the finding that the activity of the different metals for the ORR with respect to specific properties (descriptors) such as the strength of oxygen adsorption on those metals[204] or the Pauli electronegativity[205] follows a volcano relationship.[206] Both geometric aspects such as particle size,[207–210] inter-particle distance, exposed surface or electrolyte adsorption (*vide supra*), and electronic aspects such as d-band

vacancies or the work function are known to influence the performance of electrocatalysts for the ORR.

Volcano type relationships between reaction rates and adsorption energies are well known in heterogeneous catalysis.[206,211,212] The reason for this type of performance can be rationalized by assuming that the adsorption properties of atoms and small molecules on transition metals depend on the electronic structure of the metal surface, which in turn depends on the catalyst's structure and composition. For the transition metals, the coupling between the adsorbate valence states and the metal d-states accounts for the activity variations.[211] The higher in energy the d-states are relative to the highest occupied state, the stronger the interaction with adsorbate states. For instance, density-functional theory studies report that modifying the surface electronic properties of Pt(111) by subsurface 3d transition metals results in weaker dissociative adsorption energy of hydrogen and oxygen.[213]

A very interesting effect emerges from the discussion above; the electronic structure of a metal surface, namely Pt, can be changed by alloying or by inserting foreign atoms in lower layers. This will affect strongly the adsorption energy of oxygen (or other adsorbates) therefore modifying the catalytic performance.

Finally, it should be remarked that a catalyst for the ORR should provide a balance between being sufficiently active to activate O_2 and releasing it as H_2O, and noble enough not to be oxidized itself by water oxidation which may occur at the typical potentials for cathode operation.

9.6.2 *Electrocatalysts for the ORR*

It is well established that the reaction rate of the ORR on Pt (hkl) surfaces is structure-sensitive.[214,215] This is because of the different adsorption strengths of the electrolytes; the stronger the adsorption, the more pronounced the structural effect. Remarkably, the same activation energy in both acid (*ca.* 42 kJ/mol) and alkaline solution (*ca.* 40 kJ/mol), at the reversible potential, and at 0.8 V, has been reported.[26] This feature indicates that the structure sensitivity arises from geometrical factors in the pre-exponential term of Eq. (9.21).

The kinetics of the ORR on Pt (hkl) surfaces vary with the crystal face in a different manner depending on the electrolyte. In H_2SO_4 this follows the order Pt(111) <Pt(100) <Pt(110). In $HClO_4$, the activity of those Pt planes for the ORR follows the order Pt(100) <Pt(110) ≈ Pt(111) and are significantly higher than in H_2SO_4. The strong inhibition of the ORR in Pt(111) is due to the strongest adsorption of the (bi)sulphate ions on this crystal surface.[216] This inhibition affects only the reaction rate, but it does not modify the product distribution in the kinetically controlled region, i.e. H_2O_2 is not produced. A deeper discussion on this issue is out of the scope of this chapter. A comprehensive report on the nature of pure metal single crystals for ORR can be found in Ref. 26. It is often difficult, however, to correlate the knowledge derived from the studies of the ORR on Pt(hkl) to the designing of real fuel-cell catalysts. This is because experimental conditions for ORR studies on supported catalysts are very different to those employed in single-crystal measurements. One of the few studies in which similar reaction conditions are reported is found in Peuckert.[217] Furthermore, even though well-characterized single crystals are reasonable models for highly faceted particles, the actual population of the low-index planes, kinks and steps of the nanoparticles, cannot be accurately determined. This feature is even more critical for supported catalysts that usually display a more or less broad distribution of particles of different sizes. On the other hand, it is accepted that the equilibrium shape of fcc structure (like that of Pt) adopts a cubo-octahedron habit to minimize its surface energy.[218] The basic cubo-octahedron consists of eight octahedral <111> and six <100> crystal faces bound by edge and corner atoms (displaying the lower coordination number). Figure 9.8 shows how the mass activity of Pt particles for the ORR varies with their size.[209] More importantly, a remarkable correlation of the ORR activity with the surface averaged distribution of the <100> crystal faces is found. This evidence is in line with the higher intrinsic activity of Pt(100) than Pt(111) for the ORR in H_2SO_4 (*vide supra*). The rapid decline for the ORR activity for particles below ≈ 4 nm is in good agreement with the decreasing of the fraction of (100) faces on the surface of such small particles.

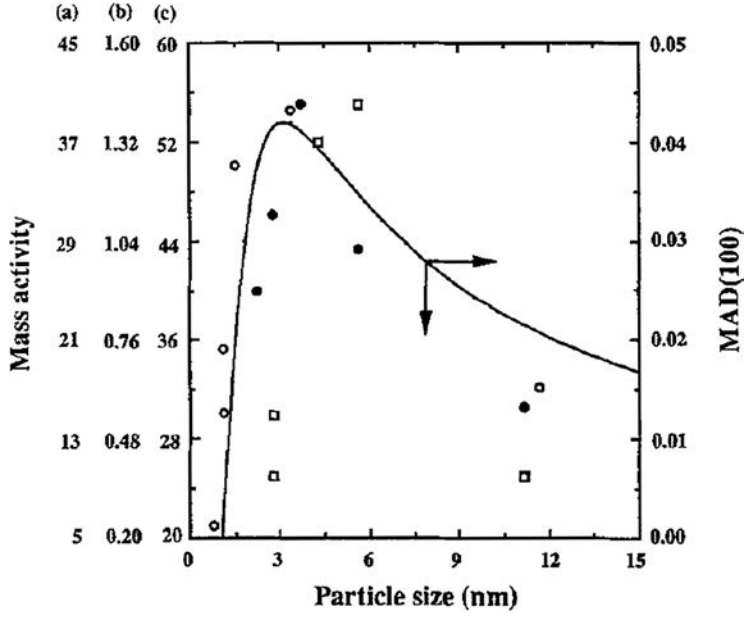

Figure 9.8 Variation of Pt mass activity and activity of the Pt(100) surface for the ORR as a function of particle size in different electrolytes; open circles 98% H_3PO_4 180°C; full circles 0.5 M H_2SO_4 25°C and open squares 97% H_3PO_4 at 177°C.[209]

While the studies above demonstrate that certain surfaces show superior activity for the ORR, it is difficult (to say the least) to synthesize Pt catalysts exposing only a desired individual surface. Therefore, other approaches are required in order to increase the activity for the ORR.

We have hinted above that by alloying, the surface structure and electronic density of a given surface can be modified. Accordingly, the interaction with adsorbates, and hence the catalytic performance, can be engineered. A great deal of effort has been devoted to the preparation, characterization, and study of alloys of the composition Pt_3X (X = Fe, Co, Ni, Cr, Mn). In a seminal work, Jalan and Taylor identified carbon supported PtCr alloy as the most active alloy for the ORR in phosphoric acid fuel cells.[219] They also proposed PtNi and PtCo as the next best alloys. This line of research was further explored by other groups;[220] Mukerjee *et al.*;[205,221,222]

Watanabe *et al.*[223–225] For instance, a ten-fold enhancement in the performance of PtNi for the ORR at 0.8 V is reported for a Ni content of *ca.* 30%$_{at}$.[225] The promotional effect was found also for PtFe and PtCo alloys,[223,224] and carbon supported bimetallic particles.[205,221] The results were rationalized in terms of the shortening of Pt-Pt distance due to the alloying,[221] preferential exposure of the <100> surface,[220] or to the modification of the Pt d-band vacancies and modification of the Pt-Pt bond distance due to alloying.[205] Figure 9.9 depicts the correlation of the current recorded at 900 mV on different carbon supported Pt-M alloys with the d-orbital vacancy of Pt and the bond distance.

It appears that by alloying, OH_{ad} formation is suppressed in the order Pt < PtNi < PtCo < PtFe < PtCr, matching the actual performance

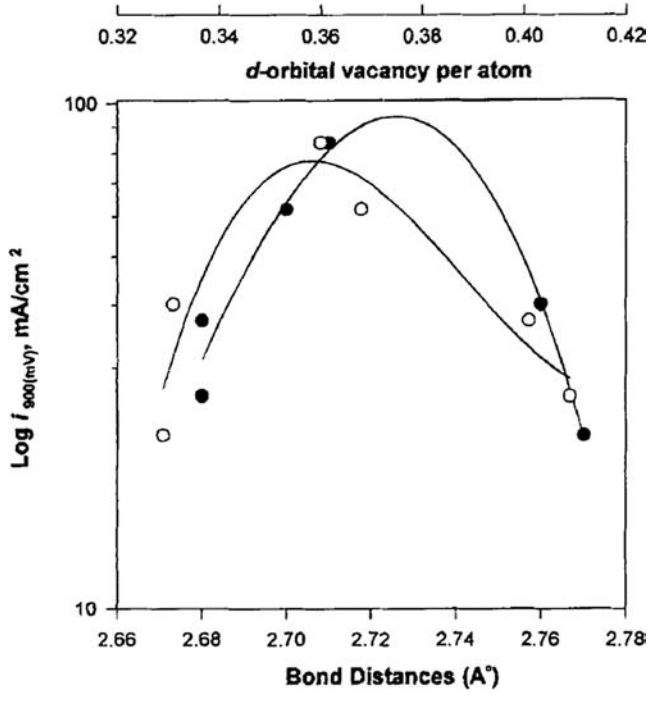

Figure 9.9 Correlation of the activity for the ORR on Pt and Pt bimetallic (circles) electrocatalysts with Pt–Pt bond distance (full circles) and d-orbital vacancy of Pt (open).[205]

of those carbon supported bimetallic electrodes on the ORR.[222] This is because, as discussed above, OH_{ad} competes with O_2 adsorption, so impeding the formation OH_{ad} which will result in more available sites of O_2 adsorption, i.e. the difference in the ORR kinetics lie in the pre-exponential term in Eq. (9.21) rather than in a different reaction pathway.

Interestingly, in the works of Watanabe *et al.*[207,224] it was implied that the actual composition of the bimetallic PtNi alloys was not uniform and instead solids with a Pt-skin on the alloy surface were formed. They went further by suggesting that the performance of the bimetallic electrode for the ORR is enhanced only if the Pt-skin is thin enough so that the electronic structure of the surface can be modified by that of the bulk alloy. This line of research was taken forward by the groups at the Lawrence Berkeley National Laboratory and the Argonne National Laboratory.[226–230] In brief, it was shown that the performance of Pt_3M bulk alloys (M = Ni, Co, V, Ti, Fe) depended strongly on the composition of the outermost layer, which can be engineered by means of treating the alloy in the appropriate reaction conditions; annealing at 1000 K or mildly sputtered with a 0.5 keV beam of Ar^+ ions, either operation being performed under UHV (ultra-high vacuum).[226] Thus, the exact composition of the topmost atomic layer of the alloys as determined by LEIS (low energy ion scattering) can be the same as that in the bulk alloy after sputtering (that is, $75\%_{at}$ of Pt and $25\%_{at}$ of the foreign metal) or pure Pt in the outmost layer due to surface segregation after annealing. In this latter case, Pt surface enrichment is balanced with Pt depletion from the second and third atomic layers of the alloy. These types of alloys were termed "Pt-skin".[227–230] Whereas the Pt-skin type alloy maintains its structure in the electrochemical environment, the sputtered surface is not stable and the 3d metal dissolved in the electrolyte leads to a Pt-enriched surface. However, in contrast to the Pt-skin alloy, the next atomic layers show the same composition as that of the bulk alloy. These solids are termed Pt-skeleton. The most interesting finding is that the performance for the ORR of the three alloys, displaying the same bulk composition but different structure within the one to three

outmost atomic layers was very different. Thus, the activity of the ORR increases in the order Pt < Pt-skeleton < Pt-skin.

UPS (ultraviolet photoelectron spectroscopy) shows that the d-band center of the Pt_3M surfaces is structure-sensitive, being downshifted due to alloying. Furthermore, the downshifting is more pronounced for the annealed surfaces, in good agreement with theoretical predictions for the modification of Pt(111) with subsurface 3d transition metals.[213] The plotting of the d-band center position *vs.* the specific activity for the ORR on Pt_3M surfaces recorded at 900 mV shows a volcano type relationship (Fig. 9.10).

Not only does the performance depend on the nature of the foreign metal but also on the preferential surface exposed. Thus, the $Pt_3Ni(111)$-skin surface exhibits the highest catalytic activity recorded for the ORR, i.e. a total 90-fold increase with respect to that of Pt/C.[229] This value corresponds to a TOF (turn-over frequency) of $\approx 2800\ s^{-1}$, a value well above the figures reported for Pt/C and PtM/C of $\approx 25\ s^{-1}$, and $\approx 60\ s^{-1}$, respectively.[231] Wu *et al.*[232] have reported a facile method for synthesizing Pt_3Ni nanoparticles with a dominant exposure of {111} facets.

Two reasons might account for the enhanced activity for the ORR on the Pt_3M surfaces; a higher activity for the dissociation of O_2 and/or a higher fraction of Pt sites available for O_2 adsorption. The former aspect was discarded by periodic density-functional theory calculations.[233] On the other hand, it was demonstrated that the modification of the electronic properties of the Pt_3M alloys, i.e. the d-band center, resulted in a shift towards less positive potentials in H_{upd} formation (underpotentially deposited hydrogen takes place between $0.05 < E < 0.4V$ in pure Pt) and towards more positive potentials in OH_{ad} formation (hydroxyl layer formation from water discharge takes place at above 0.6V on pure Pt) relative to pure Pt. Both features illustrate how the coverage by H_{upd} and OH_{ad} (θ_{Hupd} and θ_{oHad}) are reduced due to d-band downshifting due to alloying. As discussed above, the kinetics for the ORR are dominated by the coverage of adsorbed ions and spectator species, mainly OH_{ad}. Thus, decreasing the θ_{oHad} term by alloying (modifying the d-band center) would lead to an enhancement in the kinetics of the ORR by

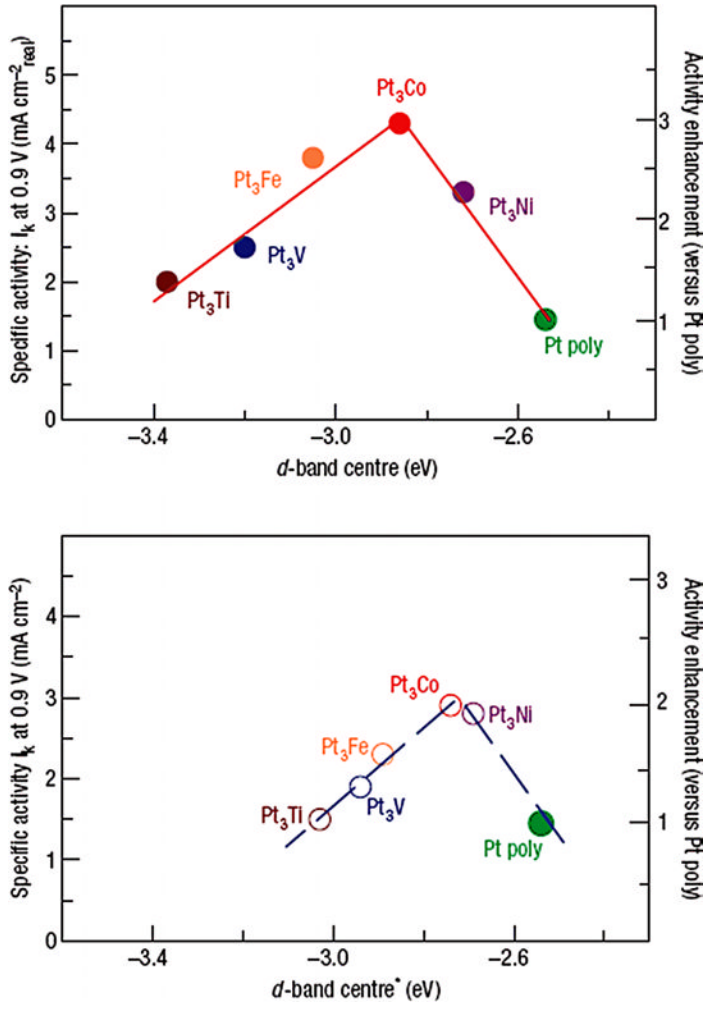

Figure 9.10 Correlation between specific activity for the ORR at 0.9 V and the d-band center for different Pt-skin and Pt-skeleton type catalysts. Note how Pt_3Co is atop both curves.[230]

increasing the number of free Pt sites for the adsorption of O_2. This applies to the alloys showing a moderate shifting of the d-band center i.e. Pt_3Ni and Pt_3Co. On the other hand, when the d-band center is too far from the Fermi level (as for Pt_3V and Pt_3Ti alloys) even if the surface of the electrodes is (almost) free from OH_{ad} and anions,

the adsorption of O_2 is too weak to permit a catalytic reaction, i.e. desorption of O_2 is very fast, and the reaction is limited by electron and proton transfer processes. In summary, the adsorption strength of oxygen atoms to the surface of the electrodes is an excellent descriptor for the ORR; thus, electrodes with slightly weaker energy for oxygen adsorption than Pt will display improved performance for the ORR.

Very recently Nørskov *et al.* have proposed that alloys of Pt with early transition metals such as Sc and Y can be more active and stable under fuel-cell environment than the alloys with late transition metals. Those alloys do also display a Pt-enriched topmost atomic layer whereas for the atomic layers below, the Pt_3M bulk stoichiometry is maintained. Thus, the activity of Pt_3Y for the ORR is superior to that of Pt_3Ni bulk alloy and very close to that reported for $Pt_3Ni(111)$.[234]

The results obtained with bulk alloys can be also translated to more practical carbon supported PtM catalysts. In general, a certain increase in the mass activity (A/g_{Pt}) for the ORR reaction was found in PtM (M = Cr, V, Mn, Ni, Co) as compared to Pt/C. Again, it is difficult to extract accurate conclusions to explain the role of the foreign metal on the activity of carbon supported bimetallic (or polymetallic) electrocatalysts for the ORR since features such as particle size and size distribution, or metal loading cannot always be eliminated by normalization procedures. Paulus *et al.*[200,235] studied the performance of PtCo/C and PtNi/C in comparison with Pt/C with the same metal loading (20 wt%) and particle size (4 ± 2 nm). They found a promotion of around 1.5 times per Pt atom for the $25\%_{at}$ alloys (Pt_3Ni/C and Pt_3Co/C) with respect to Pt/C and a more significant increase of two- to three-fold for PtCo/C. Surprisingly, the activity of PtNi/C was found to be less active than Pt/C.

An important conclusion derived from those studies is that it is possible to reduce the Pt-loading of the catalyst by placing it selectively as a monolayer in the outmost surface of the particles. This line of research has been also explored extensively by Adzic and coworkers.[191,236–239] They have shown that by depositing a monolayer of Pt on Au(111), Rh(111), Pd(111), Ru(0001), and Ir(111) surfaces, the

activity for the ORR follows a volcano-type curve with the d-band center determined by DFT calculations with Pt/Pd(111) falling on top of the curve. The next logical step is developing methods for preparing Pt "monolayer" electrocatalysts in which a layer of Pt (or Pd) is placed on a carbon supported non-noble metal, i.e. a so-called egg-shell or core-shell structure. These catalysts show up to a 20-fold increase in Pt mass activity compared to all Pt electrocatalysts. The major advantages of this approach are a higher utilization of Pt since most of them are located on the surface of the particles and a higher stability because of the decreased oxidation of the Pt monolayer.

One approach for preparing carbon supported, non-noble metal core, Pt shell type particles is depicted in Fig. 9.11. First, a bulk alloy of Co(Ni)Au(Pd) is formed on the carbon support by reduction of the metal salt precursors. Surface segregation of the noble metal is achieved by hydrogen treatment at temperatures between 600 and 850°C. After this, a Cu monolayer is deposited at underpotential (Cu UPD) and displaced by Pt atoms.[240]

Details on the scale-up synthesis of Pt monolayer electrocatalysts for the ORR can be found in reference.[239] The activity of the Pt monolayer can be further increased by depositing it onto a core of inter-metallic structures such as PtPb or PtFe.[241] The Pt/PtPb catalyst showed a current density of 2.7 $mA/cm^2_{geometric}$ at E = 900 mV. Furthermore, the Pt/PtPb catalyst is stable after 6,000 cycles between 0.6 and 1.13V and shows better stability than carbon supported Pt/PtPb.

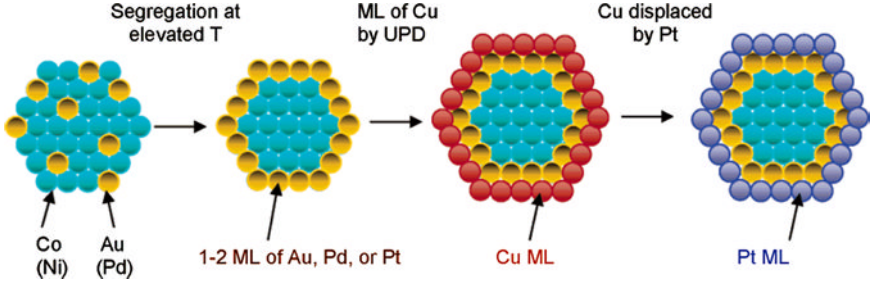

Figure 9.11 Model for the synthesis of Pt monolayer catalyst on non-noble metal-noble metal core-shell nanoparticles.[236]

The most active catalysts in terms of noble metal mass-based activity developed so far for the ORR are termed "de-alloyed" Pt electrocatalysts.[242–249] In line with the "Pt monolayer" electrocatalysts and "Pt-skin" electrocatalysts discussed above, the catalytic particles display a core-shell type structure in which the noble metal, Pt, is located preferentially in the outermost layers whereas the core of the structure is enriched in non-noble metals such as Cu. In contrast to the previous approaches, the Pt layer can be much thicker than a single monolayer. In this way, their performance is not only governed by the ligand and geometric effects as in the Pt monolayer and Pt-skin electrocatalyst, but also the ensemble effect can play a central role in their performance.[247] Both bimetallic PtCu/C and trimetallic PtCuCo/C with different atomic stoichiometries have been studied. The preparation consists of the impregnation of aqueous Cu and Co salt solutions onto carbon supported Pt nanoparticles and subsequent freeze-drying reductive annealing steps.[242] The obtained solids are subjected to an electrochemical dissolution (de-alloying) process by successive cycling in acid medium. A further advantage of this approach is that the *in situ* voltammetric de-alloying process can be done inside fuel-cell electrode layers.[244] The $Pt_{25}Cu_{75}$ de-alloyed particles show a Pt mass activity improvement by a factor of 4.1 with respect to the standard Pt in the MEAs. In fact, $Pt_{20}Cu_{20}Cu_{60}$ particles exhibited an ORR activity of up to 0.5 A/mg_{Pt}, a value well above the DOE target of 0.445 A/mg_{Pt}.[16]

Another important niche for improvement is the development of methanol tolerant cathode electrocatalysts for direct methanol fuel cells (DMFCs). Although methanol is fed at the anode side of a DMFC, it is not unlikely that some methanol might reach the cathode electrode. This effect, known as the methanol crossover effect, causes a severe loss of activity of the Pt electrode for the ORR due to the competition of methanol and oxygen for the active sites. Furthermore, mixed potentials, which result from the oxygen reduction reaction and the methanol oxidation occurring simultaneously, result in severe cell voltage losses, generate additional water, and increase the required oxygen ratio. It has been observed, that by

alloying Pt with Cr, Co, Ni, or Fe, catalysts with improved tolerance to methanol are obtained. It is not clear, however, how those catalysts develop a higher tolerance to methanol. Recently, Antolini *et al.*[250] have tried to rationalize such effects on the basis of methanol adsorption and/or CO oxidation properties of binary systems. They proposed that the most successful method of improving methanol tolerance is by decreasing the methanol adsorption ability of Pt by its alloying with metals such as Cr,[251,252] Co,[253] Ni,[254] Au,[174,255] or Fe.[256] Recently it has been reported that Ru addition to PtCo/C results in catalysts with improved tolerance to methanol under typical ORR reaction conditions i.e. potentials more positive than 0.7 V *vs.* NHE and O_2 saturated acid electrolyte.[257] This is because under these reaction conditions, upper oxide Ru species are stable and hinder methanol adsorption. Another interesting alternative is the Ru-based chalcogenides. In particular Ru_xSe_y-based electrocatalysts have received a great deal of attention because of their high tolerance to methanol, even if their performance as electrocatalysts for the ORR is inferior to Pt/C by ≈40%.[15,258]

9.7 Preparation of Carbon Supported Platinum

Structural characteristics of the nanoparticles such as chemical state, type of crystal phase, degree of alloying, or particle size depend widely on the preparation method. In recent years, methodological development for carbon supported nanoparticles preparation has been one of the major topics in electrocatalysts exploration. Among the notable variants in approaches, there are three important methods for preparing carbon supported Pt-based catalysts, including the impregnation method, colloidal method, and microemulsion method. All of these include a chemical step for dispersing the catalyst onto the carbon particles.[8,29,118,259] Whatever the approach, all methods aim to obtain well-dispersed nanosized metallic particles. Figure 9.12 shows four TEM images of different electrocatalysts, illustrating the effect of the support for avoiding Pt agglomeration and bimetallic and ternary particles deposited on carbon black.

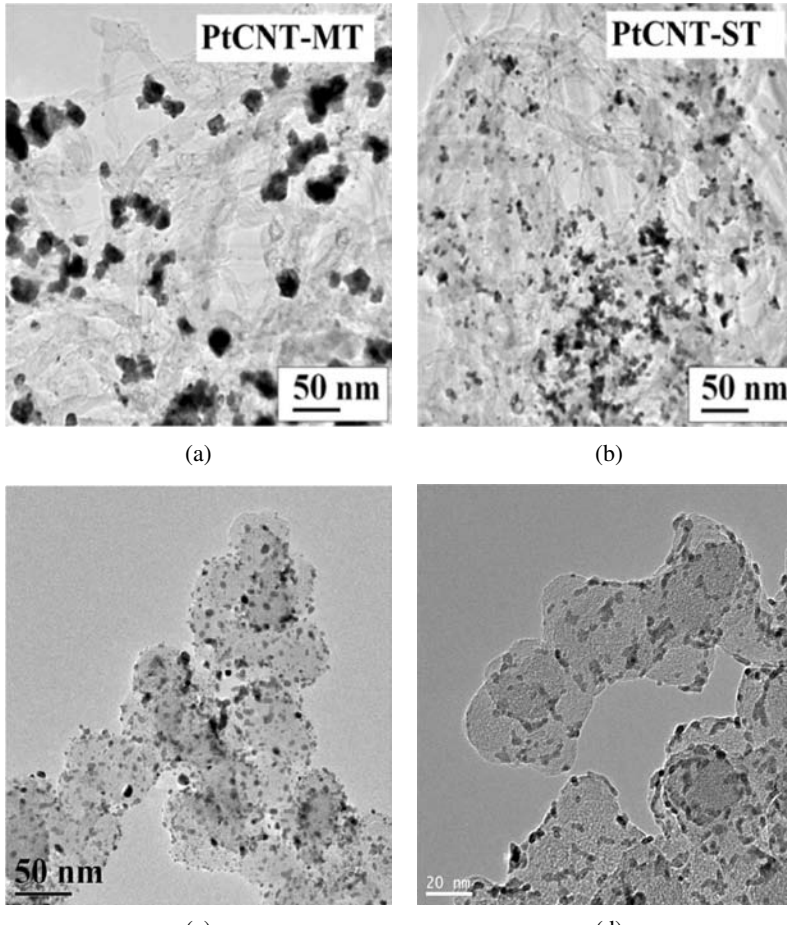

Figure 9.12 Pt particles deposited on (a) Mild treatment functionalized MWCNTs, (b) Strong treatment functionalized MWCNTs, (c) 40 wt% Pt_3Sn/C, and (d) Ternary Mo-PtRu/C, adapted from Rojas *et al.*[260,261]

9.7.1 *Synthesis methods*

9.7.1.1 *Impregnation method*

Among these methods, the impregnation-reduction approach is one of the oldest. Impregnating the carbon by aqueous or non-aqueous, organic solvents containing metal salts assisted by the addition of

dissolved wetting agents, followed by drying the impregnated material leads to a relatively homogeneous distribution of metal salts on the carbon material. As a catalyst support, carbon black plays a major role in terms of penetrating and wetting the precursors, and it can also limit nanoparticle growth. Many studies have indicated that synthetic conditions, such as the nature of the metal precursors used, the reduction method, and the heating temperature, are also crucial in the impregnation process.

9.7.1.2 *Colloidal method*

The current state of the art carbon supported electrocatalyst is made using variants of the colloidal approach. A common approach is to dissolve the metal salt solution in an appropriate solvent followed by reduction to form a colloid. A wide variety of recipes using reducing agents, organic stabilizers, or shell-removing approaches have also been developed in recent years. The patents most frequently referred to in this field are from United Technologies by Petrow and Allen.[34] Sols of the metal are obtained for instance by an initial formation of a metastable platinum–sulfito complex, which is inert at ambient temperature but decomposes and produces the small Pt-crystallites at temperatures in excess of 60°C. Thus a relatively well-defined crystal size between 2 to 6 nm can be obtained.

For the preparing of nanodispersed electrocatalysts which are composed of two, three or even more elements, the procedure of Bönnemann became very popular.[262,263] This preparation method produces a well-defined molecular mixture and where possible well-defined alloys of the elements in the electrocatalyst particles of nanometer size. It is essentially based on reductive precipitation of metals from their salt solutions in aprotic media by a borohydride, a very strong reductant. The objective is the forced co-deposition of metals irrespective of their redox potential or different degree of nobility.

The "alcohol reduction process" by Toshima and Yonezawa[264] is widely applicable for the preparation of colloidal precious metals of small and uniform metal nanoparticles. Refluxing of alcoholic

solutions of metal ions stabilized by organic polymers such as poly(vinylpyrrolidone) (PVP), poly(vinyl alcohol) (PVA), and poly (methylvinyl ether) gives homogeneous colloidal dispersions of the corresponding metal nanoparticles. Alcohols, such as ethanol, methanol, 2-propanol, glycol, or ethoxyethanol, function as a solvent as well as a reductant and are oxidized to aldehydes or ketones.

9.7.1.3 *Synthesis by microemulsion*

A microemulsion is a thermodynamically stable, optically clear dispersion of two immiscible liquids such as water and oil, stabilized by the presence of a surfactant and, in some cases, a co-surfactant.[140,171,265–267] The synthesis of nanoparticles by microemulsions has two main advantages. On the one hand, particle size can be controlled by adjusting the size of the micelle containing the metal precursors. Therefore, thermal treatments for particle size control can be avoided. On the other hand, since the micelles have the same composition, i.e. metal precursors are distributed homogeneously; the nucleation of metallic particles renders particles of the same composition. This latter feature is very important for the synthesis of bimetallic (or ternary) catalysts. The main drawback of the microemulsion, or any other approach using surfactants, is surfactant removal. Severe thermal treatments are required in order to achieve complete removal of the surfactant which may result in particle aggregation and/or surface enrichment, or complete phase segregation of the components of the bimetallic samples.[268]

Typically, a metal salt precursor is dissolved in water and dispersed in an oil phase, using a surfactant as stabilizing agent. Under particular conditions (constituent relative concentration and nature), a microemulsion is obtained. In the microemulsion phase, water droplets containing the metal precursor are surrounded by surfactant molecules. These surfactant stabilized water droplets can be pictured as nano-reactors, preventing the excess aggregation of the particles and yielding nanosized samples. As a general rule, the size of the water droplet determines the size of the metal particles, particularly when anionic surfactants are used. This preparation

method allows control of the metal particle size, that is, to achieve a given particle size with a narrow particle size distribution regardless of metal content.

9.7.2 *Synthesis of bimetallic and ternary catalysts*

9.7.2.1 *Preparation of carbon supported PtRu catalysts*

The impregnation method is the most widely used, and is a simple and straightforward chemical preparation technique for PtRu catalyst preparation.[269–278] During the impregnation step, Pt and Ru precursors are mixed with high surface area carbon black in aqueous solution to form a homogeneous mixture. The chemical reduction step can be carried out by liquid-phase reduction using Na_2SO_3, $NaBH_4$, $Na_4S_2O_5$, N_2H_4, or formic acid as a reductive agent, or gas-phase reduction using a flowing hydrogen stream as a reducing agent at elevated temperature. During the impregnation process, many factors can affect the composition, morphology, and dispersion of PtRu/C catalysts, resulting in the variation of catalytic activity. Generally, metal chloride salts (e.g. H_2PtCl_6 and $RuCl_3$) are commonly used as precursors in the impregnation-reduction process due to their ready availability. An alternative process has been suggested using metal sulphite salts (e.g. $Na_6Pt(SO_3)_4$, $Na_6Ru(SO_3)_4$ as precursors, which can be prepared from the chloride metal salts. Other Cl-free compounds such as $Pt(NH_3)_2(NO_2)_2$, $RuNO(NO_3)_x$, $Pt(NH_3)_4(OH)_2$, $Pt(C_8H_{12})(CH_3)_2$, and $Ru_3(CO)_{12}$ were also used as metal precursors in the impregnation method.

Some strategies for developing a polyol process capable of generating well-dispersed alloyed PtRu nanoparticles deposited on carbon supports have been also investigated.[264,279–281] Recently, Sau *et al.*[280] reported how, by careful selection of the polyol, reaction pH, temperature, and modality of combining the reactants, it was possible to control not only the size and dispersion of the bimetallic nanoparticles but also the relative spatial distribution of the two elements.

Watanabe *et al.*[62] reported a preparation procedure for a highly dispersed PtRu catalyst through co-deposition of colloidal Pt and Ru oxides on carbon in aqueous media, followed by a reduction with

bubbling hydrogen. A modified Watanabe's route using metal sulphite salts, with a final thermal treatment in a H_2 atmosphere, was successful in producing a catalyst with a better performance.[275,282] This metal oxide colloids route can prepare a PtRu catalyst with much higher specific surface area compared with that of a conventional impregnation method. However, the particle growth and agglomeration control in this route seem to be problematic.

By the Bönnemann method,[283] PtRu catalysts with well-defined, completely alloyed particles and a very narrow particle size distribution (< 3 nm) were obtained, and showed comparable activity with that of state of the art commercially available catalyst. To simplify the preparation steps and avoid using chloride containing stabilizers, Paulus *et al.*[284] developed a modified route by using organoaluminium molecules (e.g. $Al(CH_3)_3$) as both the reductive agent and stabilizer.

The microemulsion method has been also developed for preparing PtRu nanoparticles.[140,285,286] Aqueous phase should contain platinum and ruthenium salts, with reducing agent and surfactants for microemulsification being located in organic phase. Triton X-100 and isopropanol were used for the latter purpose.[286]

9.7.2.2 *Preparation of carbon supported PtSn*

The impregnation-reduction method has been frequently used for the synthesis of PtSn supported on inorganic carriers such as SiO_2, Al_2O_3, or SAPO, but this approach has rarely been employed for the synthesis of carbon supported electrocatalysts.[287–290] In general, the metal content in those samples is *ca.* 1–2 wt%, well below the demands of a state of the art fuel-cell electrocatalyst. A number of routes have been explored for the synthesis of carbon supported bimetallic PtSn samples. In general, they lead to materials composed of a wide range of phases, such as metallic and/or oxide Pt, Sn oxides, or PtSn solid solutions of different stoichiometry.

Lamy *et al.* stated that the Bönnemann method renders the most active electrocatalysts, allowing some control of the different metallic phases.[148,266] The microemulsion method[266] and especially the polyol method[291] have been proposed as the most suitable approaches for

synthesizing nanosized carbon supported bimetallic PtSn samples. The latter method affords Sn species in multivalence states[292,293] that, according to some reports, could be beneficial for the final activity of the catalysts.[294] Nevertheless, the exclusive formation by the polyol method of alloyed PtSn phases, along with a variable amount of SnO_2, is also reported.[295] These methods yield only partially alloyed particles due to the lack of thermal treatments imposed by the use of low boiling point solvents. A high-temperature colloidal approach has recently been proposed for the synthesis of Pt_3Sn nanoparticles.[296] Other approaches focus on the modification of the surface of carbon supported Pt particles with Sn-organic precursor. In general, these routes lead to the exclusive formation of Pt_3Sn.[94,297,298] Hydrothermal treatment[299] and the Pechini–Adams method[300] have recently been proposed for the synthesis of carbon supported PtSn bimetallics, which yield samples of a composition similar to those reported by other methods. An interesting approach to fix the Pt to the Sn atomic stoichiometry of the samples is the use of Pt-Sn complexes as metallic precursors.[301,302] Finally, and regardless of the synthesis method, obtaining the most desired Pt_3Sn phase requires thermal treatment in a reducing atmosphere.

Whichever the synthesis route and the electrocatalytic performance, a certain lack of consistency between different electrocatalysts has been pointed out,[301] suggesting the coexistence of a number of metal and/or oxidized phases in those systems. On the other hand, most reports fail to give the actual metallic loading of the final catalysts, or the Pt to Sn stoichiometry of the particles, or, more importantly for the sake of reproducibility of the methods, the target metal loading and Pt : Sn atomic ratio.

Recently, García-Rodríguez *et al.* have reported the synthesis of high metal-loaded Pt_3Sn/C by the impregnation-reduction method.[261] The method, when properly controlled, renders Pt_3Sn nanosized particles of controlled stoichiometry. Furthermore neither Pt nor Sn losses are observed. The key feature during the synthesis of the nanoparticles is to avoid Sn losses, as polymeric SnClx species, during the thermal treatments. This is possible by ensuring a controlled hydrolytic precipitation of the Sn precursor.

9.7.2.3 *Preparation of carbon supported ternary catalysts*

PtRu is the base binary catalyst for the synthesis of ternary catalysts serving as anode materials in low-temperature fuel cells. Various preparation methods of carbon supported ternary catalysts have been proposed: (1) synthesis of the ternary nanoparticles, followed by deposition onto the carbon surface (one step method); (2) deposition of all the precursors on the carbon support, followed by reduction (one step method); (3) deposition of the precursor of the third metal on preformed PtRu/C, followed by reduction (two step method). Many investigations have been made to improve the performance of the PtRu binary catalysts with the incorporation of a third metal, such as W, Mo, Sn, Os, etc.

The synthesis methods used for the preparation of carbon supported PtRuMo nanoparticles could be classified as adsorption of metal colloids onto the carbon surface, or impregnation of carbon support with metals precursor solution. Additionally, the incorporation of the metals has been carried out in a (1) one step method or with simultaneous incorporation of the three metals, and in (2) two step methods or sequential incorporation of Mo and PtRu nanoparticles:

(1) One step methods. PtRuMo/C catalysts obtained by the impregnation manner[57,303] revealed that the addition of a relatively small amount of Mo results in an electrocatalyst with a higher activity in CO or methanol electrooxidation than with the PtRu/C system. Moreover, Benker *et al.*[303] studied the effect of molybdenum precursor, and the physico-chemical characterization indicated that only traces of molybdenum were present in the samples when $Mo(CO)_6$ was used for the synthesis, while ammonium molybdate was an appropriate precursor for the synthesis of PtRuMo/C catalysts. On the other hand, a colloidal method developed by Bönnemann *et al.*[262] was used to prepare carbon supported PtRuMo nanoparticles[53,123] and established that this method provided a better tool for synthesizing PtRuMo (1 : 1 : 1) nanoparticles deposited on a carbon substrate, being more

effective in a cell operated in H_2/CO, than the impregnation method, and similar to a commercial PtRu/C catalyst. Oliveira Neto *et al.*[123] prepared ternary Pt-Ru-Mo/C (1 : 1 : 0.5 and 1 : 1 : 1) electrocatalysts by this colloidal process. Cyclic voltammetry showed that addition of Mo is very promising for methanol oxidation, and better than PtRu catalysts by the same method.

(2) Two step methods. Hou *et al.*[122] prepared a PtRu-H_xMoO_3/C with atomic ratio *ca.* 1 : 1 : 1 by a composite support method. First of all, they synthesized a composite carrier with H_xMoO_3 colloid using ammonium molybdate as precursor and, subsequently, Pt and Ru metals were added by impregnation using formaldehyde as the reducing agent. The dispersion of noble metals in PtRu-H_xMoO_3/C was not affected by the addition of transitional molybdenum oxide, which exists in amorphous form. Such a structure improved the performance in a single cell set-up using H_2/CO mixture. On the other hand, the incorporation of Mo to PtRu/Vulcan was carried out by Pasupathi *et al.*[130] subliming appropriate amounts of molybdenum (II) acetate under vacuum at fixed temperatures in a flask also containing the binary PtRu/Vulcan catalyst. They observed that CO-stripping peak was shifted to a lower potential when compared to PtRu, however methanol oxidation on PtRuMo (1 : 0.6 : 0.25)/Vulcan did not show any increase in their activity when compared with PtRu. Recently, our group has prepared PtRu-MoO_x nanoparticles following two step procedures[126,128] by combination of impregnation and colloidal methods. We have investigated the incorporation of firstly MoO_x over carbon support followed by the addition of PtRu nanoparticles by sulfito-complex route to obtain PtRuMo (1 : 0.9 : 0.2)/C catalysts,[126] and in the opposite way, the addition of MoO_x over PtRu/C systems to obtain PtRuMo (1 : 0.9 : 0.7)/C catalysts.[128] Both methods provide highly CO tolerant catalysts. From differential electrochemical mass spectrometry, a significantly negative shift of about 0.2 V in the onset potential for CO_2 was established for these systems with respect to a commercial PtRu/C (Johnson Matthey).

PtRuMo ternary metal nanoparticles with a narrow size distribution (2.4 ± 0.7 nm) were prepared by microemulsion,[304] but without carbon support. Their characterization on the carbon electrode gave higher activity and longer stability for methanol oxidation than that of PtRu and pure Pt nanoparticles/carbon electrode.

9.8 Catalyst Supports

Due to the unique characteristics of the electrocatalysts for PEMFCs, some of the requirements of the support are common with other metal supported catalysts, but also some specific details should be taken into account:

- High surface area: since a noble metal is used in a reaction at low temperature, a very high dispersion of the active metal is required, with a support that allows the stabilization of small metal particles. Nevertheless, there are also some structure-sensitive half-reactions (e.g. ORR) involved, that implies poorer kinetics at lower metal particles size, due to geometric effects. Additionally, the morphology of the metal particle also plays an important role in determining catalytic activity, as well as the formation of alloys between metals, and this is not always obtained by increasing the surface area. Practical applications will use a support of 150–250 m^2g^{-1}.
- Electronic conductivity: electrons generated or required for the half-reaction should move to/from the active center, and this is attained by providing appropriate contact of the active metal with a conductive support, which will be in close contact with the whole electrode. Therefore, the support should be of high electronic conductivity, and the interactions between the metal phase and the support should be optimized.
- Mesopore structure: it will make an important contribution to the high surface area of the support, but the main objective is that it should be appropriate for the diffusion of the reactants and products of both half-reactions of the FC, and also should be appropriate for accommodation of metal particles of the appropriate size (2–5 nm) and the micelles of ionomer for

proton conductivity. Practical applications require a mesoporous area greater than 75 m^2g^{-1}.

- Stability: as in other metal supported catalyst, the support should contribute towards maintaining the shape and size of the metal particles, avoiding sintering under the working conditions: acidic media, and very oxidative (cathode) and reductive (anode) atmospheres. However in PEMFCs there is another relevant factor: the corrosion of the support. This can be produced directly by oxygen oxidation in the cathode or by electrochemical routes, due to the generated voltages in the FC electrodes.
- Bifunctional catalyst: in some cases, the support can provide additional active centers that can account for activation of the intermediates produced, depending on the reaction mechanism operating at the electrode. In this sense, and due to the role of water, the hydrophobicity and/or hydrophilicity of the support can also be an important factor in the reaction mechanism.

Taking into account all these factors, it has been found that the most appropriate supports for PEMFCs catalysts are carbon blacks of *ca.* 250 m^2g^{-1} BET surface area, and the most widely used is Vulcan XC-72R commercialized by Cabot.[305–307] Due to the importance of the surface chemistry of these supports, and its influence in the supported active metal phase,[307,308] different chemical modifications of the support have been also investigated. The chemical nature of the carbon surface produces different electronic interactions between the noble metals and the carbon support, and affects the metal particle morphology,[308] and influences the catalytic activity.[21] Additionally, during the last few years, new alternative materials to carbon blacks have also been used, especially on the basis of their porous structure (nanotubes, mosoporous carbons) or their microstructure (nano- and microfibers, and microspheres).[309–312]

9.8.1 *Carbon blacks*

Carbon black is often employed as a support for noble metals in the electrodes of solid polymer fuel cells. This support is of special interest due to the high surface area that allows fine dispersion,

stabilization of small metallic particles, and drastically reduces the metal loadings.[306,313] These carbons are prepared by pyrolysis of hydrocarbons in inert or low O_2 containing atmospheres.[307,309] Although they can be produced with a wide range of surface areas, there are some limits for the application to PEMFCs electrocatalysts. For suitable dispersions of the noble metals, areas below 100 m^2g^{-1} are not usually used. Increasing the surface area has a little effect on the Pt dispersion,[314,315] but sufficiently high dispersion is obtained for carbon blacks with surface areas in the range of 150–250 m^2g^{-1}. Carbon blacks with higher surface area have lower electronic conductivity, and the performance of the electrode decreases quickly. Additionally, increasing the surface area in carbon blacks implies a higher volume of micropores, which are not appropriate for these electrocatalysts as we will see below.

A clear effect of porous structure in the catalytic activity was found by Uchida *et al.*[316] in Pt-Ru supported on carbon blacks of different surface areas. Pt dispersion increases with the surface area as expected, but the activity for methanol electrooxidation is higher for lower dispersions. This effect is due to the porous structure of the support, and the maximum activity was found when the mesoporous volume was higher, not for the maximum metal dispersion. Pt dispersed in pores of lower diameter (mainly in micropores) is not active, since the micelles of the ionomer cannot enter, and there is no proton conductivity at the active centers. Additionally, the diffusion of methanol should also be optimized, and it is not fast enough in the micropores of the support. In this sense, Rao *et al.*[317] successfully prepared electrocatalysts with high dispersions of Pt-Ru on carbon blacks of surface area lower than 100 m^2g^{-1}, and with very low micropore content. They found that for catalysts of higher area, the activity for the electrooxidation of methanol does not increase, and in some cases decreases, due to the participation of pores of low diameter in the development of the surface area. Again, the micelles of ionomer cannot enter in these micropores and the metal inside them is not active. The optimal value of the pore size can be different depending on the application of the electrode (cathode, anode, hydrogen, methanol, etc.), synthesis conditions, size of the micelles

of the ionomer, etc. As an illustration, Uchida *et al.*[316] found an optimal value of 3–8 nm, while Rao *et al.*[317] indicate that the pore size should be greater than 20 nm.

The performance of carbon blacks can be improved by different chemical and physical treatments. Usually, these treatments of the support are essential to remove (partially) surface contaminants, which will decrease the surface area of the deposited Pt.[318] But additional surface chemical modifications are produced. As examples, the wettability and adsorptive behaviour of a carbon, as well as its catalytic and its electrical properties, are influenced by the nature and extent of the oxygen complexes. It is known that the surface of the carbon black can be modified by oxidation treatments with HNO_3, H_2O_2, or O_3, and several types of surface functional groups (acid and redox), containing oxygen and nitrogen, can be produced as a consequence of these treatments.[305,308,319–321] Thus, carboxylic, phenolic, carbonyls, anhydrides, lactones, peroxides, and quinones have been suggested as acidic surface groups produced by oxidation treatments. Surface oxygen complexes of the support exhibit an outstanding role in this field due to their double function: (a) they are anchorage sites for the metal precursor during catalyst preparation, and (b) they can act as active centers in multifunctional catalysts due to their acid-base or redox properties. It is known that the presence of oxygen surface complexes influences the surface behaviour of carbons to a great extent.[322–324] When the support is a hydrophobous material, like carbon, surface complexes also contribute to improve its wettability and hence make the impregnation with polar solvents easier. In liquid feed fuel cells it can be desirable to make components in the anode (e.g. catalyst layer) more wettable by liquid fuel stream in order to improve access of the reactant to the electrocatalyst sites. Nevertheless, the whole impact of the chemical and physical properties of the carbon surface on the electrocatalytic performance is not yet sufficiently understood, especially for the more complex half-reactions such as the electrooxidation of methanol or ethanol.

The extension and nature of the surface groups produced by the different treatments on the carbon supports can be checked by TPD,

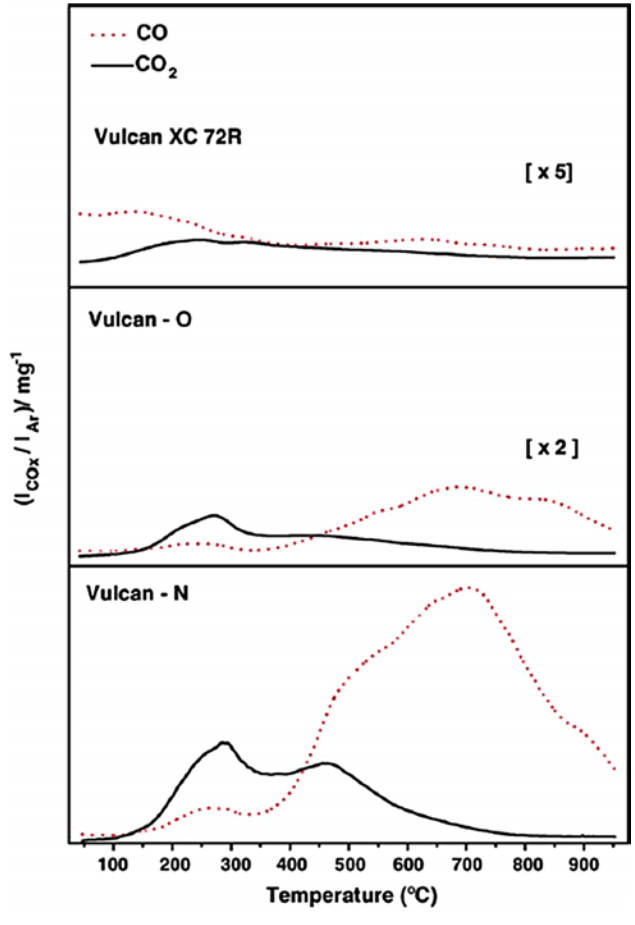

Figure 9.13 TPD under Ar of Vulcan XC-72R, Vulcan-O (H_2O_2-treated) and Vulcan-N (HNO_3-treated).[326]

FTIR, and XPS. Figure 9.13 depicts both the CO and CO_2 desorption profiles under Ar of Vulcan XC-72R and the same carbon black after treatment with H_2O_2 (Vulcan-O) and HNO_3 (Vulcan-N).[325,326] It may be observed that H_2O_2 and, particularly, HNO_3 treatments generated much enhanced oxidation that resulted in large CO_2 and CO signals between 100–600°C and 400–900°C, respectively, compared with the untreated carbon Vulcan XC-72R. Surface oxygen groups decomposed upon heating under inert atmosphere; the most acidic groups

(carboxylic groups and their derivatives, such as lactones and anhydrides) evolved CO_2, and the least acidic groups (quinones, hydroquinones, ethers, carbonyls, and phenols) evolved CO. The appearance of distinct species after HNO_3 treatment is evident from the FTIR spectra.[327,328] Figure 9.14 shows that the treatment of Vulcan with HNO_3 generates four bands of interest: (i) 1740 cm^{-1}, associated with CO stretching mode in lactones and carboxylic groups; (ii) 1590 cm^{-1}, associated with aromatic stretching mode, quinonic structures, and carboxylate groups; (iii) 1390 cm^{-1}, associated with –O–H bending vibrations in phenolic and carboxylic OH; and (iv) a broad band centered around 1230 cm^{-1} associated with C–O stretching vibrations, and which could indicate the existence of aromatic ethers, such as lactonic structures, phenols, and carboxylic groups.[329,330] The functionalization of the surface is also confirmed by XPS, where the analysis of the O1s core levels reveals that the amount of surface oxygen increases following this trend: Vulcan-N ≫ Vulcan-O > Vulcan.[327,328]

It should also be considered that during the synthesis of the metal electrocatalyst on a functionalized carbon, the surface groups can

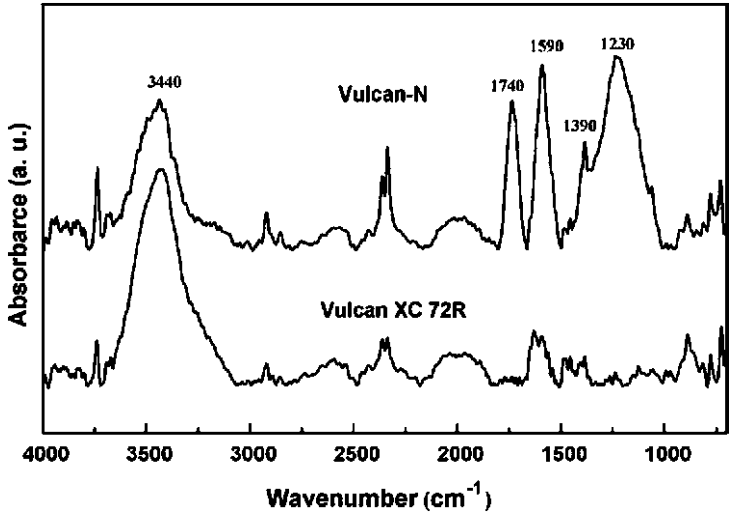

Figure 9.14 FTIR spectra of Vulcan XC-72R and Vulcan-N (HNO_3-treated).[117]

also change, with a final composition in the catalyst that will partially differ from the initial groups in the functionalized carbon. FTIR spectroscopy can detect these differences, which will depend on the synthesis (impregnation or colloidal methods), and could indicate a certain degree of interaction between metal and the oxygen containing surface groups of the support.[327]

Possible negative effects of the carbon pre-treatment, mainly when HNO_3 is used, can be the reduction in BET surface and of the electronic conductivity. Nevertheless, the decrease of surface area is not significant, and no other differences in textural properties evaluated by N_2 adsorption–desorption isotherms have been found.[328] Besides, in HNO_3-treated carbons, XP spectra showing a low intensity broad peak at *ca.* 291 eV due to π-π^* transition, are characteristic of pure graphitic samples and they can be taken as an indirect measure of the graphitic character of carbon black.[313] The shape of this peak is similar for all samples and only a minor area decrease could be detected for the Vulcan-N sample indicating that the graphite nature of the carbon is preserved.[326,328]

The varying role of oxygenated functionalities on the formation of the dispersed platinum is well recognized.[331–334] However, conflicting points of view regarding the effect of the metal dispersion, the oxidation state of the metal, and the nature of the metal support interaction on the catalytic behaviour are found in the literature. There is no clear relationship between the amount of oxide surface groups in the carbon and the amount of anchored metal. Some authors find an effect of oxygen containing groups acting as anchors for Pt particles, increasing the dispersion;[335] but some data indicate an opposite effect,[314,332,333,336,337] the absence of any effect at all, or a volcano dependence of Pt dispersion on the concentration of chemisorbed oxygen.[338]

In some cases, agglomeration of small metal nanoparticles on the catalysts using the functionalized support has been observed, but maintaining the average metal particle size.[325,326,328] In these cases, PtRu crystallites of 2–3 nm are found to be aggregated only in some of the areas of the support. Quantitative evaluation of PtRu content by XPS revealed that the concentration of the metals in the

external exposed surface was much lower on a functionalized catalyst (7 wt%) than on the non-functionalized (21 wt%) counterpart, indicating that the metal is placed in the porous structure after support functionalization. A similar effect has been found in re-activated carbons, where the development of meso- and/or macropores is obtained.[339] In this case, the catalytic performance for methanol electrooxidation is directly related to the inter-particle distance inside these pores for the same average metal size, that is, closer inter-Pt distanced catalysts have better catalytic activity.

Carbon surface groups have a differential effect on the dispersion and the metal phases formed, depending on the synthesis method used for the preparation of the catalysts.[326,327] Catalysts obtained by the colloidal method supported on functionalized carbon exhibit less or even no Pt^{4+} species. Arico *et al.*[340] observed an increase of oxidized Pt species in a PtRu/carbon catalyst with respect to the Pt/carbon sample, which would explain the development of metal support interactions due to the change of catalyst preparation conditions. Simultaneously, acid groups on the surface of carbon could affect the oxidation state of platinum, which is less oxidized on HNO_3, and especially on H_2O_2-treated support, than over the VulcanXC-72R, indicating a higher oxidation resistance using the acidic support than for the untreated one,[341] but always dependent on the preparation method. Additionally, the presence of $RuO_2 \cdot xH_2O$ phases has been evidenced in catalysts obtained by the sulfito-complex route ($Na_2S_2O_5$)[62] on HNO_3-treated Vulcan.[117] Nevertheless, surface oxygen containing groups of the support seem to be unable to stabilize the anhydrous precursors of platinum and ruthenium in catalysts obtained by Bönnemann's method (use of the reducing agent $NOct_4[BEt_3H]$),[342] which yield crystalline RuO_2.[117]

An alternative to the oxidative pre-treatment of the support is the oxidative treatment of the supported metal catalyst. This has been explored in ternary catalysts, such as the Pt-Ru-Mo system.[126] Oxidation with aqueous H_2O_2 during the preparation of catalysts mainly affects the atomic ratio of Pt/Mo and increases the extent of oxidation of surface with no influence on the sample nanostructure.

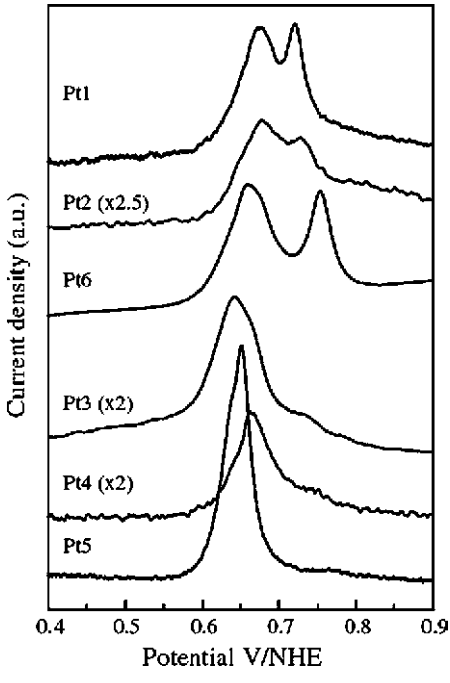

Figure 9.15 CO_{ad}-stripping voltammograms of Pt/C catalysts prepared over treated (Pt3, Pt4, Pt5) and untreated carbons (Pt1, Pt2, Pt6).[328]

As a consequence of the treatment of the support and the metal phases formed during the synthesis, the electrochemical behaviour of the catalysts is clearly altered. Figure 9.15 shows the CO-stripping voltammograms of Pt/C catalysts prepared over treated (H_2O_2 or HNO_3) and non-treated carbons.[328] Treated catalysts (Pt3, Pt4, Pt5) display a single, if broad, CO-stripping peak. Catalysts prepared on untreated Vulcan carbon (Pt1, Pt2, Pt6) displayed two distinct CO-stripping peaks. These two distinct CO oxidation processes are likely associated with the ability towards nucleation of oxygen species in the vicinities of the different CO_{ad} zones. On the other hand, a single CO-stripping peak is due to the homogenization of the sample surface after the treatment. The ability of Pt/C samples towards CO oxidation depended to a larger extent on the nature of the support than on the nature of the Pt particles (either shape or size), although both aspects should be considered.

Apart from the different effects considered on the surface structure of the catalysts, a beneficial effect of the oxidative treatments in the electrocatalytic behaviour is generally found, regardless of their influence on the dispersion of the metals. Platinum catalysts supported on electrochemically oxidized glassy carbon have been studied by Jovanovic *et al.*[323] Electrochemical treatment of a glassy carbon support does not affect significantly the real Pt surface area but leads to a better distribution of platinum on the substrate and shows a remarkable increase in methanol oxidation, resulting in greater than one order of magnitude improvement over Pt/glassy carbon electrode. The oxidation of the substrate by ozone treatment also affects the performance of PtRu/C.[324] Electrochemical measurements showed that the catalysts supported on the carbon after ozone treatment had higher activity for methanol electrooxidation than PtRu/C supported on the untreated carbon black. The PtRu/C electrocatalysts prepared by the colloidal method after pretreating the carbon black substrate with HNO_3 and, especially with H_2O_2, displayed higher activity per area unit metal than the commercial Johnson Matthey version.[326] Both the chemical treatment of Vulcan XC-72R substrate and the preparation method affect to a significant extent the activity of the samples. For ternary systems like Pt-Ru-Mo, the presence of MoOx and a more oxidized surface of a treated carbon support avoids the bonding of CO to PtRu,[126] producing a CO tolerant catalyst that is more active for methanol electrooxidation. *In situ* FTIR studies in the presence of dissolved CO show that lesser amounts of CO are adsorbed on PtRu-MoOx catalysts than on the binary catalyst, and this is particularly remarkable for the samples treated with H_2O_2.

Figure 9.16 shows the methanol electrooxidation evaluated by chronoamperometry on a PtRu/C catalyst[325] compared with a commercial version (Johnson Matthey).[326] The electrocatalyst prepared by pre-treating the carbon black substrate with hydrogen peroxide (CPRO) displayed substantially higher activity than the commercial version, although the metal dispersion was lower. The remarkable increase in activity of the CPRO electrocatalyst must be determined by the type and surface density of the O containing groups

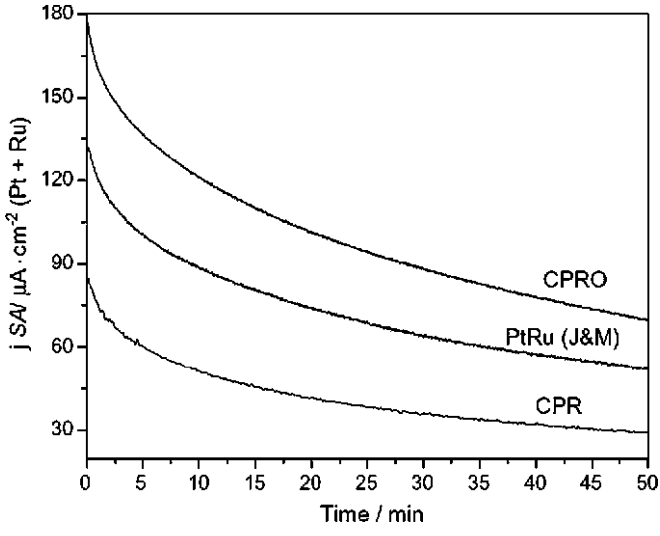

Figure 9.16 Chronoamperograms at 500 mV (RHE) for the oxidation of methanol at room temperature of PtRu/C catalysts.[325]

developed after the H_2O_2 treatment. The increase in methanol electrooxidation activity over the less dispersed sample could be due to the treatment improving the accessibility of the metal precursor within the mesoporous structure of the carbon. Pt-Ru particles are located within the mesoporous structure, accessible to CO and methanol reactants. The higher concentration of oxidized groups on the surface of CPRO catalysts could facilitate the accessibility of methanol and CO reactants to the electro-active surface and participate in the oxidation of the absorbed intermediate species formed in methanol dissociation.

Alternative treatments with organic materials such as polypyrrole, for the generation of specific nitrogen surface groups, lead to a higher dispersion of platinum on the surface and an increase in the electrooxidation of methanol.[343] Nitrogen containing carbons (pyridinic), prepared by pyrolysis of acetonitrile over Vulcan, have also been used in non-noble metal catalysts for ORR electrodes.[344] The most usual organic treatment is when a sulfonated polymer (ionomer) is added to the surface, in order to increase the proton

conductivity, with better mass transport for overall operation of the DMFCs.[345] Also thermal activation of the support is possible at high temperature (800–1100°C) when an inert or reducing atmosphere is used, or low temperature (400–500°C) when an oxidant (air, water) is included in the steam. These thermal pre-treatments of the support can increase the platinum electro-active area of the final catalysts.[318,332] However the thermal treatment also modifies the surface of the carbon support, since an increase in the activity for ORR was found for Pt/C catalysts without modification of the metal particle size after a thermal treatment in N_2.[346] Some of the thermal treatments could produce a drastic change in the porous structure of the support, resulting in a significant decrease in micro- and mesoporosity.[347]

9.8.2 *New carbon materials*

Carbon blacks with an appropriate pre-treatment for functionalization of the surface have been shown as the most suitable support for PEMFC catalysts in practical applications. Nevertheless, there are several barriers that the use of this kind of support cannot resolve:

- Corrosion problems: from the different issues related to the durability of the MEAs in the PEMFCs, corrosion of the carbon support is one of the most significant in terms of improving the stability of the electrodes. Carbon blacks are relatively stable with respect to other kind of carbons, but still their behaviour is not ideal for long-term use of FCs.
- Reduction of noble metal loading: a significant reduction has been achieved since the late 1990s, but an approximately five-fold reduction of the amount of platinum is required for large-scale application, due to both cost and Pt supply considerations.[16] This objective seems to be difficult to attain by using carbon blacks as support. This is particularly important for the cathode, since the limitation on the kinetics of the ORR requires higher loadings of Pt.

- Mesoporous structure: we have seen that the porous structure of the support can be optimized for obtaining active metallic centers with proton and electronic conduction, and appropriate mass transfer of reactants and products. However, the design of the mesoporous structure is limited using carbon blacks.

With the objective of dealing with these issues, the use of alternative carbon materials as supports for electrocatalysts has been investigated. Corrosion problems could be the most important limitation for commercialization of FCs, since there are several limits of durability that should be guaranteed for practical use. Carbon is electrochemically unstable at potentials above 0.207 V in acidic electrolyte:[348–353]

$$C + H_2O \rightarrow CO_2 + 4H^+ + 4e^-. \quad (9.22)$$

Carbon can be also consumed by the heterogeneous water-gas reaction:

$$C + H_2O \rightarrow H_2 + CO. \quad (9.23)$$

Both processes can also take place during incomplete oxidation, leading to the formation of oxygenated surface groups. Therefore, the durability of the carbon support is mainly a question of kinetics, and the presence of a metal on the surface of the support increases the corrosion rate, especially when it is well dispersed.[354] In the same sense, a high surface area of the support also increases the rate of corrosion.[316] Corrosion of carbon causes loss of the support, producing carbon oxides that eventually can be poisons for the catalytic centers. Moreover, the porous structure tends to collapse, the surface textural characteristics of the support (including interaction with the ionomer) are lost, and anchoring of the metal particles fails, leading to indirect leaching and/or sintering of the active phase.

Corrosion resistance increases clearly when the degree of graphitization of the carbon support increases.[306,348,349] Different carbon blacks have been tested for corrosion resistance[355] and also

thermal treatments have been used to increase it.[316] However, the use of alternative carbon supports has been studied as a better solution. These alternative support materials should have characteristics similar to carbon blacks, from the point of view of electrocatalysts support, but increasing the graphitic character, for a higher corrosion resistance. Corrosion problems are produced in the cathode (although in start-up/shutdown of the FC, or with low fuel feed, anode corrosion can take place,[351,352] therefore most of the research regarding alternative supports has been devoted to electrochemical ORR). Additionally, reducing Pt-loading of cathodes is one of the challenges for FC cost reduction, and both objectives, corrosion resistance and low Pt content in the catalysts are investigated when new carbon materials are studied as support.

Carbon nanotubes (CNT) and carbon nanofibers (CNF) are promising materials with potentially useful characteristics, and several revisions regarding their role as supports of FCs electrocatalysts can be found.[309–312,356] The main problem for their practical application is the preparation methods, which have very low yield and several steps of purification are always needed, mainly for removal of unwanted amorphous carbon. Additionally, the conditions of the catalysts' preparation methods should be more precise for control of the metal particle deposition and distribution on the surface of the CNT and CNF, and changing slightly the parameters of the synthesis, the catalytic results are different.[357] It is interesting to note that for both supports, surface modification is necessary, usually by means of pre-treatment with HNO_3, since there are insufficient surface centers for anchoring of the metal precursors.[358] When a well-dispersed catalyst is obtained, CNTs and CNFs display better corrosion resistance than carbon blacks such as Vulcan.[359–365] However, it has also been found that the electroactivity is also higher than in carbon black supported catalysts, using lower Pt-loadings, for ORR, and also for CO and methanol electrooxidation.[115,364,366–372] In some of these catalysts, the functionalization with nitrogen groups has an additional beneficial effect[344,365] in both durability and catalytic activity. Nevertheless, in ternary Pt-Ru-Mo systems, a detrimental effect of oxygen functionalization was found regarding the stabilization of

MoO_x species.[128] Increasing the catalytic activity with lower Pt-loading catalysts when CNTs and CNFs are used as support is still not well explained, but could be related to their good electronic conductive characteristics, improved mass transfer of reactants and/or products, or modification of the nature of the metal particles.[311,361] Regarding this last point, it is interesting to note the possible interaction of Pt precursors with π electrons of the grapheme sheets (C-π sites). The amount of these sites is modified by chemical pre-treatments of CNTs and CNFs, and depending on the number of C-π and O- or N-functionalized sites, the loading, dispersion and size of metal particles will be different.[260]

Mesoporous carbons are also used as an alternative when the optimization of the mesopores is wanted (2–50 nm). This type of carbon can be prepared using a mesoporous silica as template, such as SBA-15 or MCM-41, and a carbon source, like sucrose, which is impregnated in the porous structure. After carbonization and removal of template with HF or NaOH, the mesoporous carbon is obtained. Depending on the template, ordered or disordered mesoporous can be obtained. If Pt particles and ionomer micelles are placed in this porous structure, the internal diffusion transfer during the electrochemical reaction is controlled. Very similar objectives are obtained using carbon gels, where microspheres and microbeads are obtained to produce meso- and macroporosity. The application of these supports to FCs electrocatalysts has been recently reviewed.[309,310,373] In all the cases these carbons need, like CNTs and CNFs, some kind of surface activation before dispersion of the metal active phase, and, in general, ordered porous structures are preferred for higher values of the catalytic activity.

9.9 Conclusions and Future Trends

The basis of the science of the current PEMFCs does not differ from that of the first FCs used in the space flights during the 1960s. Nevertheless, the development of this technology, especially during the last 15 years, has permitted changes from very reliable but expensive components to components that are still durable and very

close to being economically viable, because of their competiveness. Regarding the catalytic technology of the PEMFCs, we have progressed from the platinum-blacks of the first FCs prototypes to very advanced supported catalysts with a high level of nano-structured design. This has permitted a significant reduction of the noble metal loading of the electrodes since the 1990s, maintaining or, indeed, increasing the performance of the FC. However, an additional, approximately five-fold, reduction of the amount of platinum should be obtained for both large-scale production and to make these devices competitive in the real world with vehicles based on internal combustion engines. In this sense, any catalytic research with the objective of reduction of noble metals content, but maintaining catalytic efficiency and durability, will have a direct impact on the FCs technology. Another important field of research is the use of bi- and trimetallic catalysts. The main objective is operation with hydrogen from reforming of hydrocarbons, containing CO, and the electrooxidation of methanol, using the Pt-Ru system. However, the current objective is also the design of Pt-M or Pr-Ru-M metallic particles with an appropriate nanostructure (e.g. type core-shell) that allows for both a reduction in the platinum loading and an increase in the electrocatalytic activity.

Consequently, over the next period, research in electrocatalysis for PEMFCs should be mainly oriented towards a reduction of the platinum content, not just due to its price but also to the restriction in its supply, which can produce unwanted market fluctuations since platinum producing countries are very limited. Partial or total substitution of platinum by alternative metals, maintaining the catalytic performance, would be the ideal solution. Nevertheless, the durability of the catalyst is one of the most important issues regarding the reliability of the FCs, and it should be taken into account for the production of metal particles and supports of enough endurance. Finally, it is interesting to note the possibility of PEMFCs working at a temperature higher than 100°C, up to 200°C, using alternative membranes that are still to be developed, or the use of alkaline FCs with solid membranes very similar to the PEMFCs. These FCs will have a higher electrical performance, and the catalytic system to be

used in these "high-temperature" PEMFCs or alkaline "PEMFCs" will have new requirements. Noble metal loading will probably be lower, but durability issues will be more demanding.

Acronyms

AA:	Acetic Acid
AAL:	Acetaldehyde
AFC:	Alkaline Fuel Cell
ASA:	Active Surface Area
CNT:	Carbon Nanotubes
CNF:	Carbon Nanofibers
CVD:	Chemical Vapour Deposition
DAFC:	Direct Alcohol Fuel Cell
DEFC:	Direct Ethanol Fuel Cell
DEMS:	Differential Electrochemical Mass Spectroscopy
DMFC:	Direct Methanol Fuel Cell
DOE:	Department of Energy
EC-IRAS:	Electrochemical Infrared Reflection-Absorption Spectroscopy
FC:	Fuel Cell
GDL:	Gas Diffusion Layer
HOR:	Hydrogen Oxidation Reaction
MCFC:	Molten Carbonates Fuel Cell
MEA:	Membrane Electrode Assembly
MS:	Mass Spectrometry
MWCNT:	Multiwall Carbon Nanotubes
NHE:	Normal Hydrogen Electrode
NNMC:	Non-Noble Metal Catalysts
ORR:	Oxygen Reduction Reaction
PAFC:	Phosphoric Acid Fuel Cell
PEMFC:	Proton Exchange Membrane Fuel Cell
RHE:	Reference Hydrogen Electrode
RRDE:	Rotating-Ring Disk-Electrode
SEM:	Scanning Electron Microscopy
SOFC:	Solid Oxide Fuel Cell
SWCNT:	Singlewall Carbon Nanotubes
TEM:	Transmission Electron Microscopy

TOF:	Turn-Over Frequency
t-oz:	troy ounce
TPD:	Thermal Programmed Desorption
UHV:	Ultra-High Vacuum
UPD:	Underpotential Depostion
UPS:	Ultraviolet Photoelectron Spectroscopy
XANES:	X-ray Absorption Near-Edge Structure
XAS:	X-ray Absorption Spectroscopy

References

1. J.M. Andújar, F. Segura, *Renew. Sust. Energ. Rev.* 2009, **13**, 2309.
2. W. Vielstich, A. Lamm, H.A. Gasteiger (Eds.) *Handbook of Fuel Cells. Fundamentals, Technology and Applications,* John Wiley & Sons, Chichester, 2003.
3. G. Hoogers, D. Thompsett, *CATTECH* 1999, **3**, 106.
4. N.M. Markovic, P.N. Ross, *CATTECH* 2000, **4**, 110.
5. K.Y. Chan, J. Ding, J. Ren, S. Cheng, K.Y. Tsang, *J. Mater. Chem.* 2004, **14**, 505.
6. E. Antolini, *Mat. Chem. Phys.* 2003, **78**, 563.
7. X. Cheng, Z. Shi, N. Glass, L. Zhang, J.J. Zhang, D.T. Song, Z.S. Liu, H.J. Wang, J. Shen, *J. Power Sources* 2007, **165**, 739.
8. H. Liu, C. Song, L. Zhang, J. Zhang, H. Wang, D.P. Wilkinson, *J. Power Sources* 2006, **155**, 95.
9. S. Wasmus, A. Küver, *J. Electroanal. Chem.* 1999, **461**, 14.
10. A. Serov, C. Kwak, *Appl. Catal. B: Env.* 2009, **90**, 313.
11. C.W.B. Bezerra, L. Zhang, H.S. Liu, K.C. Lee, A.L.B. Marques, E.P. Marques, H.J. Wang, J.J. Zhang, *J. Power Sources* 2007, **173**, 891.
12. Y.H. Bing, H.S. Liu, L. Zhang, D. Ghosh, J.J. Zhang, *Chem. Soc. Rev.* 2010, **39**, 2184.
13. J.W. Lee, B.N. Popov, *Solid State Electrochem.* 2007, **11**, 1355.
14. G.F. Wang, M.A. Van Hove, P.N. Ross, M.I. Baskes, *J. Phys. Chem. B* 2005, **109**, 11683.
15. Y. Feng, N. Alonso-Vante, *Phys. Status. Solidi. B* 2008, **245**, 1792.
16. H. A. Gasteigerg, S. S. Kocha, B. Sompalli, F.T. Wagner, *Appl. Catal. B: Env.* 2005, **56**, 9.

17. J.H. Wee, K.Y. Lee, S.H. Kim, *J. Power Sou*rces 2007, **165**, 667.
18. L. Zhang, J. Zhang, D.P. Wilkinson, H. Wang, *J. Power Sources* 2006, **156**, 171.
19. M. Doyle, G. Raendran, in *Handbook of Fuel Cells. Fundamentals, Technology and Applications 3*, Eds.: W. Vielstich, H.A. Gasteiger, A. Lamm, John Wiley & Sons, Chichester, 2003, 351.
20. V. Mehta, J.S. Cooper, *J. Power Sources* 2003, **114**, 32.
21. A.L. Dicks, *J. Power Sources* 2006, **156**, 128.
22. S. Litster, G. McLean, *J. Power Sources* 2004, **130,** 61.
23. T. Tada, in *Handbook of Fuel Cells. Fundamentals, Technology and Applications 3*, Eds.: W. Vielstich, H.A. Gasteiger, A. Lamm, John Wiley & Sons, Chichester, 2003, 481.
24. S. Ye, in *PEM fuel cell electrocatalysts and catalyst layers. Fundamentals and applications*, Ed.: J. Zhang, Springer, Vancouver, 2008, 759.
25. D.T. Sawyer, A. Sobkowiak, J.L. Roberts, *Electrochemistry for Chemists*, John Wiley, New York, 1995.
26. N.M. Markovic, P.N. Ross, *Surf. Sci. Reports* 2002, **45**, 11.
27. B.E. Conway, B.V. Tilak, *Electrochim. Acta* 2002, **47**, 3571.
28. S. Trasatti, *J. Electroanal. Chem.* 1972, **39**, 163.
29. H. Wendt, E.V. Spinace, A. Oliveira Neto, M. Linardi, *Quim. Nova* 2005, **28**, 1066.
30. W. Vielstich, T. Iwasita, in *Handbook of Heterogeneous Catalysts*, Eds.: G. Ertl, H. Knözinger, F. Schüth, J. Weitkamp, Wiley-VCH, Verlag, 1997, 2090.
31. N. Markovic, in *Handbook of Fuel Cells. Fundamentals, Technology and Applications 2*, Eds.: W. Vielstich, A. Lamm, H.A. Gasteiger, John Wiley & Sons, Chichester, 1973, 368.
32. N.M. Markovic, P.N. Ross, *Interfacial Electrochemistry: Theory, Experiments, Applications*, Ed.: A. Wieckowski, Marcel Dekker, New York, 1999, 821.
33. N. Ramaswamy, T.M. Arruda, W. Wen, N. Hakim, M. Saha, A. Gullá, S. Mukerjee, *Electrochim. Acta* 2009, **54**, 6756.
34. H.G. Petrow, R.J. Allen, US Patent No. 3,992,331, 1976.
35. S. Srinivasan, E.A. Ticianelli, C.R. Derouin, A. Redondo, *J. Power Sources* 1988, **22**, 359.
36. S. Gottesfeld, J. Pafford, *J. Electrochem. Soc.* 1988, **135**, 2651.

37. H.F. Oetjen, V.M. Schmidt, U. Stimming, F. Trila, J. *Electrochem. Soc.* 1996, **143**, 3838.
38. M.T.M. Koper, S.C.S. Lai, E. Herrero, in *Fuel cell catalysis. A surface science approach.*, Ed.: M.T.M. Koper, Wiley-Blackwell, New Jersey, 2009, 159.
39. S. Gilman, *J. Phys. Chem.* 1964, **68**, 70.
40. T. Iwasita, in *Handbook of Fuel Cells. Fundamentals, Technology and Applications 2*, Eds.: W. Vieltich, A. Lamm, H.A. Gasteiger, John Wiley & Sons, Chichester, 2003, 603.
41. S.C. Chang, L.W. Leung, M.J. Weaver, *J. Phys. Chem.* 1989, **93**, 5341.
42. C. Lamy, J.M. Léger, J. Clavilier, R. Parsons, *J. Electroanal. Chem.* 1983, **150**, 71.
43. N.P. Lebedeva, M.T.M. Koper, E. Herrero, J.M. Feliu, R.A. van Santen, *J. Electroanal. Chem.* 2000, **487**, 37.
44. J. Solla-Gullón, F.J. Vidal-Iglesias, E. Herrero, J.M. Feliu, A. Aldaz, *Electrochem. Commun.* 2006, **8**, 189.
45. S. Kinge, C. Urgeghe, A. Battisti, H. Bönnemann, *Appl. Organomet. Chem.* 2008, **22**, 49.
46. A. López-Cudero, J. Solla-Gullón, E. Herrero, A. Aldaz, J.M. Feliu, *J. Electroanal. Chem.* 2010, **644**, 117.
47. J.O.M. Bockris, H. Wroblowa, *J. Electroanal. Chem.* 1964, **7**, 428.
48. S.J. Lee, S. Mukerjee, E.A. Ticianelli, J. McBreen, *Electrochim. Acta* 1999, **44**, 3283.
49. H.A. Gasteiger, N. Markovic, P.N. Ross Jr, E.J. Cairns, *J. Electrochem. Soc.* 1964, **141**, 1795.
50. Y.Y. Tong, S.K. Hee, P.K. Babu, P. Waszczuk, A. Wieckowski, E. Oldfield, *J. Am. Chem. Soc.* 2002, **124**, 468.
51. B.N. Grgur, G. Zhuang, N.M. Markovic, J.P.N. Ross, *J. Phys. Chem. B* 1997, **101**, 3910.
52. Z. Liu, J.E. Hu, Q. Wang, K. Gaskell, A.I. Frenkel, G.S. Jackson, B. Eichhorn, *J. Am. Chem. Soc.* 2009, **131**, 6924.
53. M. Götz, H. Wendt, *Electrochim. Acta* 1998, **43**, 3637.
54. K. Wang, H.A. Gasteiger, N.M. Markovic, P.N. Ross, *Electrochim. Acta* 1996, **41**, 2587.
55. H. Abe, F. Matsumoto, L.R. Alden, S.C. Warren, H.D. Abruña, F.J. Di Salvo, *J. Am. Chem. Soc.* 2008, **130**, 5452.

56. M. Watanabe, H. Igarashi, T. Fujino, *Electrochemistry* 1999, **67**, 1194.
57. D.C. Papageorgopoulos, M. Keijzer, F.A. de Bruijn, *Electrochim. Acta* 2002, **48**, 197.
58. D.A. Stevens, J.M. Rouleau, R.E. Mar, A. Bonakdarpour, R.T. Atanasoski, A.K. Schmoeckel, M.K. Debe, J.R. Dahn, *J. Electrochem. Soc.* 2007, **154**, B566.
59. O.A. Petrii, *J. Solid State Electrochem.* 2008, **12**, 609.
60. R. Parsons, T. Van der Noot, *J. Electroanal. Chem.* 1988, **257**, 9.
61. J.S. Spendelow, P.K. Babu, A. Wieckowski, *Curr. Opin. Solid State Mater. Sci.* 2002, **9**, 37.
62. M. Watanabe, M. Uchida, S. Motoo, *J. Electroanal. Chem.* 1987, **229**, 395.
63. M. Watanabe, S. Motoo, *J. Electroanal. Chem.* 1975, **60**, 267.
64. M. Watanabe, S. Motoo, *J. Electroanal. Chem.* 1975, **60**, 259.
65. M.T.M. Koper, J.J. Lukkien, A.P.J. Jansen, R.A. van Santen, *J. Phys. Chem. B* 1999, **103**, 5522.
66. T. Iwasita, *Electrochim. Acta* 2002, **47**, 3663.
67. M. Watanabe, in *Handbook of Fuel Cells. Fundamentals, Technology and Applications 2*, Eds.: W. Vielstich, H.A. Gasteiger, A. Lamm, John Wiley & Sons, Chichester, 2003, 408.
68. J. McBreen, S. Mukerjee, *J. Electrochem. Soc.* 1995, **142**, 3399.
69. E.I. Santiago, M.S. Batista, E.M. Assaf, E.A. Ticianelli, *J. Electrochem. Soc.* 2004, **151**, A944.
70. F.A. de Bruijn, D.C. Papageorgopoulos, E.F. Sitters, G.J.M. Janssen, *J. Power Sources* 2002, **110**, 117.
71. S. Mukerjee, S.J. Lee, E.A. Ticianelli, J. McBreen, B.N. Grgur, N.M. Markovic, P.N. Ross, J.R. Giallombardo, E.S. de Castro, *Electrochem. Solid-State Lett.* 1999, **2**, 12.
72. H.A. Gasteiger, N.M. Markovic, P.N. Ross Jr, *J. Phys. Chem.* 1995, **99**, 8945.
73. B.N. Grgur, N.M. Markovic, P.N. Ross, *Electrochim. Acta* 1998, **43**, 3631.
74. B.N. Grgur, N.M Markovic, P.N. Ross, *J. Electrochem. Soc.* 1999, **146**, 1613.
75. P. Gouerec, M.C. Denis, D. Guay, J.P. Dodelet, R. Schulz, *J. Electrochem. Soc.* 2000, **147**, 3989.

76. S. Ball, A. Hodgkinson, G. Hoogers, S. Maniguet, D. Thompsett, B. Wong, *Electrochem. Solid-State Lett.* 2002, **5**, A31.
77. E.M. Crabb, M.K. Ravikumar, Y. Qian, A.E. Russell, S. Maniguet, J. Yao, D. Thompsett, M. Hurford, S.C. Ball, *Electrochem. Solid-State Lett.* 2002, **5**, A5.
78. S. Mukerjee, R.C. Urian, *Electrochim. Acta* 2002, **47**, 3219.
79. T. Ioroi, K. Yasuda, Z. Siroma, N. Fujiwara, Y. Miyazaki, *J. Electrochem. Soc.* 2003, **150**, A1225.
80. E.I. Santiago, G.A. Camara, E.A. Ticianelli, *Electrochim. Acta* 2003, **48**, 3527.
81. R.C. Urian, A.F. Gull, S. Mukerjee, *J. Electroanal. Chem.* 2003, **554–555**, 307.
82. S. Mukerjee, R.C. Urian, S.J. Lee, E.A. Ticianelli, J. McBreen, *J. Electrochem. Soc.* 2004, **151**, A1094.
83. J.M. Jaksic, L. Vracar, S.G. Neophytides, S. Zafeiratos, G. Papakonstantinou, N.V. Krstajic, M.M. Jaksic, *Surf. Sci.* 2005, **598**, 156.
84. N.P. Lebedeva, G.J.M. Janssen, *Electrochim. Acta* 2005, **51**, 29.
85. T. Ioroi, T. Akita, S.I. Yamazaki, Z. Siroma, N. Fujiwara, K. Yasuda, *Electrochim. Acta* 2006, **52**, 491.
86. G. Papakonstantinou, F. Paloukis, A. Siokou, S.G. Neophytides, *J. Electrochem. Soc.* 2007, **154**, B989.
87. P. Roquero, L.C. Ordoñez, O. Herrera, O. Ugalde, J. Ramírez, *Int. J. Chem. Reactor Eng.* 2007, **5**, 1.
88. T.R. Ralph, M.P. Hogarth**,** *Platinum Met. Rev.* 2002, **46**, 3.
89. Y. Ishikawa, M.S. Liao, C.R. Cabrera, *Surf. Sci.* 2002, **513**, 98.
90. B.N. Grgur, N.M. Markovic, P.N. Ross, *J. Phys. Chem. B* 1998, **102**, 2494.
91. V.R. Stamenkovic, M. Arenz, B.B. Blizanac, K.J.J. Mayrhofer, P.N. Ross, N.N. Markovic, *Surf. Sci.* 2005, **576**, 145.
92. T.E. Shubina, M.T.M. Koper, *Electrochim. Acta* 2002, **47**, 3621.
93. M. Arenz, V.R. Stamenkovic, B.B. Blizanac, K.J. Mayrhofer, N.M. Markovic, P.N. Ross, *J. Catal.* 2005, **232**, 402.
94. S. García-Rodríguez, F. Somodi, I. Borbáth, J.L. Margitfalvi, M.A. Peña, L.G. Fierro, S. Rojas, *Appl. Catal. B* 2009, **91**, 83.
95. A.S. Arico, R. Srinivasan, V. Antonucci, *Fuel Cells* 2001, **1**, 133.

96. A. Hamnett, in *Handbook of Fuel Cells. Fundamentals, Technology and Applications 1*, Eds.: W. Vielstich, H.A. Gasteiger, A. Lamm, John Wiley & Sons, Chichester, 2003, 305.
97. S.K. Kamarudin, W.R.W. Daud, S.L. Ho, U.A. Hasran, *J. Power Sources* 2007, **163**, 743.
98. U.B. Demirci, *J. Power Sources* 2007, **169**, 239.
99. U.B. Demirci, *J. Power Sources* 2007, **173**, 11.
100. P. Agnolucci, *Int. J. Hydrogen Energ.* 2007, **32**, 4306.
101. R. Rashidi, I. Dincer, G.F. Naterer, P. Berg, *J. Power Sources* 2009, **187**, 509.
102. S.K. Kamarudin, F. Achmad, W.R.W. Daud, *Int. J. Hydrogen Energ.* 2009, **34**, 6902.
103. M. Neurock, in *Handbook of Fuel Cells. Fundamentals, Technology and Applications 5*, Eds.: W. Vielstich, H. Yokokawa, H.A. Gasteiger, John Wiley & Sons, Chichester, 2009, 152.
104. S. Lai, N. Lebedeva, T. Housmans, M.T.M. Koper, *Top. Catal.* 2007, **46**, 320.
105. T.H.M. Housmans, A.H. Wonders, M.T.M. Koper, *J. Phys. Chem. B* 2006, **110**, 10021.
106. H.A. Gasteiger, N. Markovic, P.N. Ross Jr, E.J. Cairns, *J. Phys. Chem.* 1993, **97**, 12020.
107. A.B. Anderson, E. Grantscharova, S. Seong, *J. Electrochem. Soc.* 1996, **143**, 2075.
108. H.A. Gasteiger, N. Markovic, P.N. Ross Jr, E.J. Cairns, *Catal.Today* 1994, **38**, 445.
110. D. Chu, S. Gilman, *J. Electrochem. Soc.* 1996, **143**, 1685.
111. G. Wu, L. Li, B.Q. Xu, *Electrochim. Acta* 2004, **50**, 1.
112. J.W. Long, R.M. Stroud, K.E. Swider-Lyons, R. Rolison, *Phys. Chem. B* 2000, **104**, 9772.
113. D.R. Rolison, P.L. Hagans, K.E. Swider, J.W. Long, *Langmuir* 1999, **15**, 774.
114. Z.G. Chen, X.P. Qiu, L.B. Lu, S.C. Zhang, W.T. Zhu, L.Q. Chen, *Electrochem. Commun.* 2005, **7**, 593.
115. L. Cao, F. Scheiba, C. Roth, F. Schweiger, C. Cremers, U. Stimming, H. Fuess, L.Q. Chen, W.T. Zhu, X.P. Qiu, *Angew. Chem. Int. Ed.* 2006, **45**, 5315.

116. M.K. Jeon, J.Y. Won, S.I. Woo, *Electrochem. Solid-State Lett.* 2007, **10**, B23.
117. J.L. Gómez de la Fuente, M.V. Martínez–Huerta, S. Rojas, P. Hernández-Fernández, P. Terreros, J.L.G. Fierro, M.A. Peña, *Appl. Catal. B: Env.* 2009, **88**, 505.
118. E. Antolini, *Appl. Catal. B: Env.* 2007, **74**, 324.
119. E. Antolini, *Appl. Catal. B: Env.* 2007, **74**, 337.
120. E. Gyenge, in *PEM fuel cell electrocatalysts and catalyst layers. Fundamentals and applications.* Ed.: J. Zhang, Springer, New York, 2009, 165.
121. A. Lima, C. Coutanceau, J.M. Léger, C. Lamy, *J. Appl. Electrochem.* 2001, **31**, 379.
122. Z. Hou, B. Yi, H. Yu, Z. Lin, H. Zhang, *J. Power Sources* 2003, **123**, 116.
123. A. Oliveira Neto, E.G. Franco, E. Arico, M. Linardi, E.R. González, *J. Eur. Ceram. Soc.* 2003, **23**, 2987.
124. A. Bauer, E.L. Gyenge, C.W. Oloman, *J. Power Sources* 2007, **167**, 281.
125. Z.B. Wang, G.P. Yin, Y.G. Lin, *J. Power Sources* 2007, **170**, 242.
126. M.V. Martínez-Huerta, J.L. Rodríguez, N. Tsiouvaras, M.A. Peña, J.L.G. Fierro, E. Pastor, *Chem. Mater.* 2008, **20**, 4249.
127. M.V. Martínez-Huerta, N. Tsiouvaras, M.A. Peña, J.L.G. Fierro, J.L. Rodríguez, E. Pastor, *Electrochim. Acta* 2010, **66**, 7634.
128. N. Tsiouvaras, M.V. Martínez-Huerta, R. Moliner, M.J. Lazaro, J.L. Rodríguez, E. Pastor, M.A. Peña, J.L.G. Fierro, *J. Power Sources* 2009, **186**, 299.
129. N. Tsiouvaras, M.A. Peña, J.L.G. Fierro, E. Pastor, M.V. Martínez–Huerta, *Catal. Today* 2010, **158**, 12.
130. S. Pasupathi, V. Tricoli, *J. Solid State Electrochem.* 2008, **12**, 1093.
131. N. Tsiouvaras, M.V. Martínez–Huerta, O. Paschos, U. Stimming, J.L.G. Fierro, M.A. Peña, *Int. J. Hydrogen Energy* 2010, **35**, 11478.
132. Z.B. Wang, P.J. Zuo, G.P. Yin, *Fuel Cells* 2009, **2**, 106.
133. S. Rousseau, C. Coutanceau, C. Lamy, J.M. Léger, *J. Power Sources* 2006, **158**, 18.
134. C. Lamy, A. Lima, V. LeRhun, F. Delime, C. Coutanceau, J.M. Léger, *J. Power Sources* 2002, **105**, 283.
135. F. Vigier, S. Rousseau, C. Coutanceau, J.M. Léger, C. Lamy, *Top. Catal.* 2006, **40**, 111.
136. S. Song, Y. Wang, P. Shen, *Chin. J. Cat.* 2007, **28**, 752.

137. G.A. Camara, R.B. De Lima, T. Iwasita, *Electrochem. Commun.* 2004, **6**, 812.
138. H. Wang, Z. Jusys, R.J. Behm, *J. Power Sources* 2006, **154**, 351.
139. Q. Wang, G.Q. Sun, L.H. Jiang, Q. Xin, S.G. Sun, Y.X. Jiang, S.P. Chen, Z. Jusys, R.J. Behm, *Phys. Chem. Chem. Phys.* 2007, **9**, 2686.
140. S. Rojas, F.J. García-García, S. Järas, M.V. Martínez-Huerta, J.L.G. Fierro, M. Boutonnet, *Appl. Catal. A: Gen.* 2005, **285**, 24.
141. W. Zhou, Z. Zhou, S. Song, W. Li, G. Sun, P. Tsiakaras, Q. Xin, *Appl. Catal. B: Env.* 2003, **46**, 273.
142. V. Radmilovic, T.J. Richardson, S. J. Chen, P.N. Ross Jr, *J. Catal.* 2005, **232**, 199.
143. C. Dupont, Y. Jugnet, D. Loffreda, *J. Am. Chem. Soc.* 2006, **128**, 9129.
144. J. Shin, W.J. Tornquist, C. Korzeniewski, C.S. Hoaglund, *Surf. Sci.* 1996, **364**, 122.
145. Z.Y. Zhou, Z.Z. Huang, D.J. Chen, Q. Wang, N. Tian, S.G. Sun, *Angew. Chem. Int. Ed.* 2010, **49**, 411.
146. N. Tian, Z.Y. Zhou, S.G. Sun, Y. Ding, L.W. Zhong, *Science* 2007, **316**, 732.
147. E. Antolini, *J. Power Sources* 2007, **170**, 1.
148. C. Lamy, S. Rousseau, E.M. Belgsir, C. Coutanceau, J.M. Léger, *Electrochim. Acta* 2004, **49**, 3901.
149. F. Vigier, C. Coutanceau, A. Perrard, E.M. Belgsir, C. Lamy, *J. Appl. Electrochem.* 2004, **34,** 439.
150. F. Vigier, C. Coutanceau, F. Hahn, E.M. Belgsir, C. Lamy, *J. Electroanal. Chem.* 2004, **563**, 81.
151. F. Colmati, E. Antolini, E.R. González, *J. Electrochem. Soc.* 2007, **154**, B39.
152. F. Colmati, E. Antolini, E.R. González, *Appl. Catal. B: Env.* 2007, **73**, 106.
153. J. Datta, S. Singh, S. Das, N.R. Bandyopadhyay, *Bull. Mater. Sci.* 2009, **32**, 643.
154. V.R. Stamenkovic, M. Arenz, C.A. Lucas, M.E. Gallagher, P.N. Ross, N.M. Markovic, *J. Am. Chem. Soc.* 2003, **125**, 2736.
155. P.J. Barczuk, A. Lewera, K. Miecznikowski, A. Zurowski, P.J. Kulesza, *J. Power Source*s 2009, **195**, 2507.
156. W.J. Zhou, W.Z. Li, S.Q. Song, Z.H. Zhou, L.H. Jiang, G.Q. Sun, Q. Xin, K. Poulianitis, S. Kontou, P. Tsiakaras, *J. Power Sources* 2004, **131,** 217.

157. E.V. Spinace, M. Linardi, A.O. Neto, *Electrochem. Commun.* 2005, **7**, 365.
158. J. Mann, N. Yao, A.B. Bocarsly, *Langmuir* 2006, **22**, 10432.
159. A. Kowal, M. Li, M. Shao, K. Sasaki, M.B. Vukmirovic, J. Zhang, N.S. Marinkovic, P. Liu, A.I. Frenkel, R.R. Adzic, *Nat. Mater.* 2009, **8**, 325.
160. A. Kowal, S.L. Gojkovic, K.S. Lee, P. Olszewski, Y.E. Sung, *Electrochem. Commun.* 2009, **11**, 724.
161. J.P.I. de Souza, S.L. Queiroz, K. Bergamaski, E.R. González, F.C. Nart, *J. Phys. Chem. B* 2002, **106**, 9825.
162. F.H.B. Lima, E.R. González, *Appl. Catal. B: Env.* 2008, **79**, 341.
163. F.H.B. Lima, E.R. González, *Electrochim. Acta* 2008, **53**, 2963.
164. F.H.B. Lima, D. Profeti, W.H. Lizcano-Valbuena, E.A. Ticianelli, E.R. González, *J. Electroanal. Chem.* 2008, **617**, 121.
165. P.Y. Sheng, A. Yee, G.A. Bowmaker, H. Idriss, *J. Catal.* 2002, **208**, 393.
166. L.W.H. Leung, M.J. Weaver, *J. Phys. Chem.* 1989, **93**, 7218.
167. E. Yeager, *Electrochim. Acta* 1984, **29**, 1527.
168. S. Mukerjee, S. Srinivasan, in *Handbook of Fuel Cells, Fundamentals, Technology and Applications 2*, Eds.: W. Vielstich, H.A. Gasteiger, A. Lamm, John Wiley & Sons, Chichester, 2003, 502.
169. M. Gattrell, M. MacDougall, in *Handbook of Fuel Cells. Fundamentals, Technology and Applications 2*, Eds.: W. Vielstich, H.A. Gasteiger, A. Lamm, John Wiley & Sons, Chichester, 2003, 443.
170. R.R. Adzic, in *Electrocatalysis*, Eds.: J. Lipkowski, P.N. Ross, Wiley/VCH, New York, 1998, 197.
171. P. Hernández–Fernández, S. Rojas, P. Ocón, J.L. Gómez de la Fuente, P. Terreros, M.A. Peña, J.L.G. Fierro, *Appl. Catal. B: Env.* 2007, **77**, 19.
172. A. Sarkar, A.V. Murugan, A. Manthiram, *Langmuir* 2009, **26**, 2894.
173. R.R. Adzic, J. Zhang, K. Sasaki, E. Sutter, *Science* 2007, **315**, 220.
174. P. Hernández-Fernández, S. Rojas, P. Ocón, J.L. Gómez de la Fuente, J. San Fabián, J. Sanza, M.A. Peña, F.J. García-García, P. Terreros, J.L.G. Fierro, *J. Phys. Chem. C* 2007, **111**, 2913.
175. L.G.R.A. Santos, K.S. Freitas, E.A. Ticianelli, *Electrochim. Acta* 2009, **54**, 5246.
176. A.R. Malheiro, J. Pérez, H.M. Villullas, *J. Electrochem. Soc.* 2009, **156**, B51.

177. A. Sode, A. Musgrove, D. Bizzotto, *J. Phys. Chem. C* 2010, **114**, 546.
178. H. Yano, M. Kataoka, H. Yamashita, H. Uchida, M. Watanabe, *Langmuir* 2007, **23**, 6438.
179. M. Lefevre, E. Proietti, F. Jaouen, J.P. Dodelet, *Science* 2009, **324**, 71.
180. F. Jaouen, J.P. Dodelet, *Electrochim. Acta* 2007, **52**, 5975.
181. F. Charreteur, F. Jaouen, S. Ruggeri, J.P. Dodelet, *Electrochim. Acta* 2008, **53**, 2925.
182. F. Jaouen, J.P. Dodelet, *J. Phys. Chem. C* 2009, **113**, 15422.
183. F. Jaouen, J. Herranz, M. Lefèvre, J.-P. Dodelet, U.I. Kramm, I. Herrmann, P. Bogdanoff, J. Maruyama, T. Nagaoka, A. Garsuch, J.R. Dahn, T. Olson, S. Pylypenko, P. Atanassov, E.A. Ustinov, *ACS Appl. Mater. Interfaces* 2009, **1**, 1623.
184. R. Bashyam, P. Zelenay, *Nature* 2006, **443**, 63.
185. H.S. Wroblowa, P. Yen Chi, G. Razumney, *J. Electroanal. Chem.* 1976, **69**, 195.
186. Z. Shi, J. Zhang, Z.-S Liu, H. Wang, D.P. Wilkinson, *Electrochim. Acta* 2006, **51**, 1905.
187. A.U. Nilekar, M. Mavrikakis, *Surf. Sci.* 2008, **602**, L89.
188. S. Venkatachalam, T. Jacob, in *Handbook of Fuel Cells. Fundamentals, Technology and Applications 5*, Eds.: W. Vielstich, H. Yokokawa, H.A. Gasteiger, John Wiley & Sons, Chichester, 2009, 133.
189. J.K. Nørskov, J. Rossmeisl, A. Logadottir, L. Lindqvist, J.R. Kitchin, T. Bligaard, H. Jónsson, *J. Phys. Chem. B* 2004, **108**, 17886.
190. L. Vattuone, L. Savio, M. Rocca, *Surf. Sci. Reports* 2008, **63**, 101.
191. M.H. Shao, T. Huang, P. Liu, J. Zhang, K. Sasaki, M.B. Vukmirovic, R.R. Adzic, *Langmuir* 2006, **22**, 10409.
192. X. Li, A.A. Gewirth, *J. Am. Chem. Soc.* 2005, **127**, 5252.
193. V.P. Zhdanov, B. Kasemo, *Electrochem. Commun.* 2006, **8**, 1132.
194. E. Leiva, C. Sánchez, in *Handbook of Fuel Cells, Fundamentals, Technology and Applications 2*, Eds.: W. Vieltich, A. Lamm, H.A. Gasteiger, John Wiley & Sons, Chichester, 2004, 93.
195. S. Song, H. Zhang, X. Ma, Z. Shao, R.T. Baker, B. Yi, *Int. J. Hydrogen Energ.* 2008, **33**, 4955.
196. A.J. Appleby, *Catal. Rev.* 1970, **4**, 221.
197. A.B. Anderson, J. Roques, S. Mukerjee, V.S. Murthi, N.M. Markovic, V.R. Stamenkovic, *J. Phys. Chem. B* 2005, **109**, 1198.

198. J.X. Wang, F.A. Uribe, T.E. Springer, J.L. Zhang, R.R. Adzic, *Faraday Discussions*. 2008, **140**, 347.
199. J.X. Wang, J. Zhang, R.R. Adzic, *J. Phys. Chem. A* 2007, **111**, 12702.
200. U.A. Paulus, A. Wokaun, G.G. Scherer, T.J. Schmidt, V.R. Stamenkovic, N.M. Markovic, P.N. Ross, *Electrochim. Acta* 2002, **47**, 3787.
201. J. Pérez, E.R. González, E.A. Ticianelli, *Electrochim. Acta* 1998, **44**, 1329–1339.
202. K.C. Neyerlin, W. Gu, J. Jorne, H.A. Gasteiger, *J. Electrochem. Soc.* 2006, **153**, A1955.
203. A.J. Bard, L.R. Faulkner, *Electrochemical Methods: Fundamentals and Applications*, 2nd Edition, John Wiley & Sons, Hoboken, 2001.
204. F.H.B. Lima, J. Zhang, M.H. Shao, K. Sasaki, M.B. Vukmirovic, E.A. Ticianelli, R.R. Adzic, *J. Phys. Chem. C* 2007, **111**, 404.
205. S. Mukerjee, S. Srinivasan, M.P. Soriaga, J. McBreen, *J. Electrochem. Soc.* 1995, **142**, 1409.
206. J.K. Nørskov, T. Bligaard, B. Hvolbaek, F. Abild-Pedersen, I. Chorkendorff, C.H. Christensen, *Chem. Soc. Rev.* 2008, **37**, 2163.
207. M. Watanabe, H. Sei, P. Stonehart, *J. Electroanal. Chem.* 1989, **261**, 375.
208. N. Markovic, H. Gasteiger, P.N. Ross, *J. Electrochem. Soc.* 1997, **144**, 1591.
209. K. Kinoshita, *J. Electrochem. Soc.* 1990, **137**, 845.
210. S. Mukerjee, *J. Appl. Electrochem.* 1990, **20**, 537.
211. J.K. Nørskov, T. Bligaard, J. Rossmeisl, C.H. Christensen, *Nat. Chem.* 2009, **1**, 37.
212. B. Hammer, J.K. Nørskov, in *Advances in Catalysis 45*, Eds.: C.G. Bruce, K. Helmut, Academic Press, London, 2000, 71.
213. J.R. Kitchin, J.K. Nørskov, M.A. Barteau, J.G. Chen, *J. Chem. Phys.* 2004, **120**, 10240.
214. N.M. Markovic, T.J. Schmidt, V.R. Stamenkovic, P.N. Ross, *Fuel Cells* 2001, **1**, 105.
215. M.D. Maciá, J.M. Campiña, E. Herrero, Feliu, *J. Electroanal. Chem.* 2004, **564**, 141.
216. A. Kolics, A. Wieckowski, *J. Phys. Chem. B* 2001, **105**, 2588.
217. M. Peuckert, T. Yoneda, R.A.D. Betta, M. Boudart, *Prog. Surf. Sci.* 1986, **80**, 92.
219. V. Jalan, E.J. Taylor, *J. Electrochem. Soc.* 1983, **130**, 2299.

220. B.C. Beard, N. Philip, J. Ross, *J. Electrochem. Soc.* 1990, **137**, 3368.
221. S. Mukerjee, S. Srinivasan, *J. Electroanal. Chem.* 1993, **357**, 201.
222. M. Teliska, V.S. Murthi, S. Mukerjee, D.E. Ramaker, *J. Electrochem. Soc.* 2005, 1**52**, A2159.
223. T. Toda, H. Igarashi, M. Watanabe, *J. Electroanal. Chem.* 1999, **460**, 258.
224. T. Toda, H. Igarashi, H. Uchida, M. Watanabe, *J. Electrochem. Soc.* 1999, **146**, 3750.
225. T. Toda, H. Igarashi, M. Watanabe, *J. Electrochem. Soc.* 1998, **145**, 4185.
226. V.R. Stamenkovic, T.J. Schmidt, P.N. Ross, N.M. Markovic, *J. Phys. Chem. B* 2002, **106**, 11970.
227. V.R. Stamenkovic, B.S. Mun, K.J.J. Mayrhofer, P.N. Ross, N.M. Markovic, J. Rossmeisl, J. Greeley, J.K. Nørskov, *Angew. Chem. Int. Ed.* 2006, **45**, 2897.
228. V.R. Stamenkovic, B.S. Mun, K.J.J. Mayrhofer, P.N. Ross, N.M. Markovic, *J. Am. Chem. Soc.* 2006, **128**, 8813.
229. V.R. Stamenkovic, B. Fowler, B.S. Mun, G.F. Wang, P.N. Ross, C.A. Lucas, N.M. Markovic, *Science* 2007, **315**, 493.
230. V.R. Stamenkovic, B.S. Mun, M. Arenz, K.J.J. Mayrhofer, C.A. Lucas, G. Wang, P.N. Ross, N.M. Markovic, *Nat. Mater.* 2007, **6**, 241.
231. H.A. Gasteiger, N.M. Markovic, *Science* 2009, **324**, 48.
232. J. Wu, J. Zhang, Z. Peng, S. Yang, F.T. Wagner, H. Yang, *J. Am. Chem. Soc.* 2009, **132**, 4984.
233. Y. Xu, A.V. Ruban, M. Mavrikakis, *J. Am. Chem. Soc.* 2004, **126**, 4717.
234. J. Greeley, I.E.L. Stephens, A.S. Bondarenko, T.P. Johansson, H.A. Hansen, T.F. Jaramillo, J. Rossmeisl, I. Chorkendorff, J.K. Nørskov, *Nat. Chem.* 2009, **1**, 552.
235. U.A. Paulus, A. Wokaun, G.G. Scherer, T.J. Schmidt, V.R. Stamenkovic, V. Radmilovic, N.M. Markovic, P.N. Ross, *J. Phys. Chem. B* 2002, **106**, 4181.
236. J. Zhang, F.H.B. Lima, M.H. Shao, K. Sasaki, J.X. Wang, J. Hanson, R.R. Adzic, *J. Phys. Chem. B* 2005, **109**, 22701.
237. J. Zhang, M.B. Vukmirovic, Y. Xu, M. Mavrikakis, R.R. Adzic, *Angew. Chem. Int. Ed.* 2005, **44**, 2132.
238. R.R. Adzic, J. Zhang, K. Sasaki, M.B. Vukmirovic, M. Shao, J.X. Wang, A.U. Nilekar, M. Mavrikakis, J.A. Valerio, F. Uribe, *Top. Catal.* 2007, **46**, 249.

239. K. Sasaki, J.X. Wang, H. Naohara, N. Marinkovic, K. More, H. Inada, R.R. Adzic, *Electrochim. Acta* 2010, **55**, 2645.
240. A. Sarkar, A. Manthiram, *J. Phys. Chem. C* 2010, **114**, 4725.
241. T. Ghosh, M.B. Vukmirovic, F.J. DiSalvo, R.R. Adzic, *J. Am. Chem. Soc.* 2010, **132**, 906.
242. S. Koh, J. Leisch, M.F. Toney, P. Strasser, *J. Phys. Chem. C* 2007, **111**, 3744.
243. S. Koh, P. Strasser, *J. Am. Chem. Soc.* 2007, **129**, 12624.
244. R. Srivastava, P. Mani, N. Hahn, P. Strasser, *Angew. Chem. Int. Ed.* 2007, **46**, 8988.
245. R. Srivastava, P. Mani, P. Strasser, *J. Power Sources* 2009, **190**, 40.
246. C. Yu, S. Koh, J.E. Leisch, M.F. Toney, P. Strasser, *Faraday Discussions.* 2009, **140**, 283.
247. P. Strasser, in *Handbook of Fuel Cells. Fundamentals, Technology and Applications 5*, Eds.: W. Vielstich, H. Yokokawa, H.A. Gasteiger, John Wiley & Sons, Chichester, 2009, 30.
248. P. Strasser, *Rev. Chem. Eng.* 2009, **25**, 255.
249. P. Strasser, Q. Fan, M. Devenney, W.H. Weinberg, P. Liu, J.K. Nørskov, *J. Phys. Chem. B* 2003, **107**, 11013.
250. E. Antolini, T. Lopes, E.R. González, *J. Alloys Compd.* 2008, **461**, 253.
251. H. Yang, N. Alonso-Vante, J.-M Léger, C. Lamy, *J. Phys. Chem. B* 2004, **108**, 1938.
252. E. Antolini, J.R.C. Salgado, L.G.R.A. Santos, G. García, E.A. Ticianelli, E. Pastor, E.R. González, *J. Appl. Electrochem.* 2006, **36**, 355.
253. J.R.C. Salgado, E. Antolini, E.R. González, *Appl. Catal. B: Env.* 2005, **57**, 283.
254. H. Yang, C. Coutanceau, J.M. Léger, N. Alonso-Vante, C. Lamy, *J. Electroanal. Chem.* 2005, **576**, 305.
255. P. Hernández-Fernández, S. Rojas, P. Ocón, A. de Frutos, J.M. Figueroa, P. Terreros, M.A. Peña, J.L.G. Fierro, *J. Power Sources* 2008, **177**, 9.
256. K. Scott, W. Yuan, H. Cheng, *J. Appl. Electrochem.* 2007, **37**, 21.
257. M. Montiel, P. Hernández-Fernández, J.L.G. Fierro, S. Rojas, P. Ocón, *J. Power Sources* 2009, **191**, 280.
258. M. Montiel, S. García-Rodríguez, P. Hernández-Fernández, R. Díaz, S. Rojas, J.L.G. Fierro, E. Fatás, P. Ocón, *J. Power Sources* 2010, **195**, 2478.

259. S.H. Liu, R.F. Lu, S.J. Huang, A.Y. Lo, S.H. Chien, S.B. Liu, *Chem. Commun.* 2006, **32**, 3435.
260. P. Hernández-Fernández, M. Montiel, P. Ocón, J.L. Gómez de la Fuente, S. García-Rodríguez, S. Rojas, J.L.G. Fierro, *Appl. Catal. B: Env.* 2010, **99**, 343.
261. S. García–Rodríguez, M.A. Peña, J.L.G. Fierro, S. Rojas, *J. Power Sources* 2010, **195**, 5564.
262. H. Bönnemann, W. Brijoux, R. Brinkmann, E. Dinjus, T. Joussen, B. Korall, *Angew. Chem. Int. Ed.* 1991, **30**, 1312.
263. H. Bönnemann, G. Khelashvili, *Appl. Organomet. Chem.* 2010, **24**, 257.
264. N. Toshima, T. Yonezawa, *New. J. Chem.* 1998, **22**, 1179.
265. S. Eriksson, U. Nylén, S. Rojas, M. Boutonnet, *Appl. Catal. A: Gen.* 2004, **265**, 207.
266. C. Coutanceau, S. Brimaud, C. Lamy, J.M. Léger, L. Dubau, S. Rousseau, F. Vigier, *Electrochim. Acta* 2088, **53**, 6865.
267. M.P. Pileni, *Crys. Res. Tech.* 1998, **33**, 1155.
268. S. Brimaud, C. Coutanceau, E. Garnier, J.M. Léger, F. Gérard, S. Pronier, M. Leoni, *J. Electroanal. Chem.* 2007, **602**, 226.
269. E.S. Steigerwalt, G.A. Deluga, D.E. Cliffel, C.M. Lukehart, *J. Phys. Chem. B* 2001, **105**, 8097.
270. E.S. Steigerwalt, G.A. Deluga, C.M. Lukehart, *J. Phys. Chem. B* 2002, **106**, 760.
271. M. Neergat, D. Leveratto, U. Stimming, *Fuel Cells* 2002, **2**, 25.
272. M.S. Nasher, A.L. Frenkel, D. L. Adler, J.R. Shapley, R.G. Nuzzo, *J. Am. Chem. Soc.* 1997, **119**, 7760.
273. D.L. Boxall, G.A. Deluga, E.A. Kenik, W.D. King, C.M. Lukehart, *Chem. Mater.* 2001, **13**, 891.
274. N. Jha, A. Leela Mohana Reddy, M.M. Shaijumon, N. Rajalakshmi, S. Ramaprabhu, *Int. J. Hydrogen Energ.* 2008, **33**, 427.
275. V. Radmilovic, H.A. Gasteiger, P.N. Ross, *J. Catal.* 1995, **154**, 98.
276. B. Yang, Q.Y. Lu, Y. Wang, L. Zhuang, J.T. Lu, P.F. Liu, *Chem. Mater.* 2003, **15**, 3552.
277. Y. Takasu, T. Fujiwara, Y. Murakami, K. Sasaki, M. Oguri, T. Asaki, W. Sugimoto, *J. Electrochem. Soc.* 2000, **147**, 4421.
278. T.C. Deivaraj, J.Y. Lee, *J. Power Sources* 2005, **142**, 43.
279. C. Bock, B. MacDougall, Y. LePage, *J. Electrochem. Soc.* 2004, **151**, A1269.

280. T.K. Sau, M. López, D.V. Goia, *Chem. Mater.* 2009, **21**, 3649.
281. H. Nitani, T. Nakagawa, H. Daimon, Y. Kurobe, T. Ono, Y. Honda, A. Koizumi, S. Seino, T.A. Yamamoto, *Appl. Catal. A: Gen.* 2007, **326**, 194.
282. H.P. Liang, H.M. Zhang, J.S. Hu, Y.G. Guo, L.J. Wan, C.L. Bai, *Angew. Chem.* 2004, **116**, 1566.
283. H. Bönnemann, P. Britz, W. Vogel, *Langmuir* 1998, **14**, 6654.
284. U.A. Paulus, U.Endruschat, G.J. Feldmeyer, T.J. Schmidt, H. Bönnemann, R.J. Behm, *J. Catal.* 2000, **195**, 383.
285. Z. Liu, J.Y. Lee, M. Han, W. Chen, L.M. Gan, *J. Mater. Chem.* 2002, **12**, 2453.
286. X. Zhang, K.Y. Chan, *Chem. Mater.* 2003, **15**, 451.
287. A.E. Aksoylu, M.M.A. Freitas, J.L. Figueiredo, *Appl. Catal. A: Gen.* 2000, **192**, 29.
288. F. Coloma, A. Sepúlveda–Escribano, J.L.G. Fierro, F. Rodríguez-Reinoso, *Appl. Catal. A: Gen.* 1996, **136**, 231.
289. M.C. Román–Martínez, J.A. Macía-Agulló, I.M.J. Vilella, D. Cazorla-Amorós, H. Yamashita, *J. Phys. Chem. C* 2007, **111**, 4710.
290. J. Ribeiro, D.M. Dos Anjos, J. M. Léger, F. Hahn, P. Olivi, A.R. De Andrade, G. Tremiliosi-Filho, K.B. Kokoh, *J. Appl. Electrochem.* 2008, **38**, 653.
291. L.H. Jiang, Z. H. Zhou, W.Z. Li, W.J. Zhou, S.Q. Song, H.Q. Li, G.Q. Sun, Q. Xin, *Energy Fuels* 2004, **18**, 866.
292. Z. Liu, B. Guo, L. Hong, T.H. Lim, *Electrochem. Commun.* 2006, **8**, 83.
293. A.O. Neto, R.R. Dias, M.M. Tusi, M. Linardi, E.V. Spinacé, *J. Power Sources* 2007, **166**, 87.
294. L. Jiang, H. Zang, G. Sun, Q. Xin, *Chin. J. Catal.* 2006, **27**, 15.
295. L. Jiang, G. Sun, S. Sun, J. Liu, S. Tang, H. Li, B. Zhou, Q. Xin, *Electrochim. Acta* 2005, **50**, 5384.
296. Z. Liu, D. Reed, G. Kwon, M. Shamsuzzoha, D.E. Nikles, *J. Phys. Chem. C* 2007, **111**, 14223.
297. J. Llorca, P.R. de la Piscina, J.L.G. Fierro, J. Sales, N. Homs, *J. Catal.* 1995, **156**, 139.
298. E.M. Crabb, R. Marshall, D. Thompsett, *J. Electrochem. Soc.* 2000, **147**, 4440.
299. D.-H. Lim, D.-H. Choi, W.-D. Lee, H.-I. Lee, *Appl. Catal. B: Env.* 2009, **89**, 484.

300. F.L.S. Purgato, P. Olivi, J.M. Léger, A.R. de Andrade, G. Tremiliosi-Filho, E.R. González, C. Lamy, K.B. Kokoh, *J. Electroanal. Chem.* 2009, **628**, 81.
301. D.L. Boxall, E.A. Kenik, C.M. Lukehart, *Chem. Mater.* 2002, **14**, 1715.
302. R. Tarozaitė, L. Tamašauskaitė Tamašiūnaitė, V. Jasulaitienė, *J. Solid State Electrochem.* 2009, **13**, 721.
303. N. Benker, C. Roth, M. Mazurek, H. Fuess, *J. New Mater. Electrochem. Syst.* 2006, **9**, 121.
304. X. Zhang, F. Zhang, K.Y. Chan, *J. Mater. Sci.* 2004, **39**, 5845.
305. H.P. Boehm, *Carbon* 1994, **32**, 759.
306. E. Auer, A. Freund, J. Piestch, T. Tacke, *Appl. Catal. A: Gen.* 1998, **173**, 259.
307. F. Rodríguez-Reinoso, *Carbon* 1998, **36**, 159.
308. X. Yu, S. Ye, *J. Power Sources* 2007, **172**, 133.
309. E. Antolini, *Appl. Catal. B: Env.* 2009, **88**, 1.
310. Y.Y. Shao, J. Liu, Y. Wang, Y.H. Lin, *J. Mater. Chem.* 2009, **19**, 46.
311. J. Nakamura, in *Molecular catalysts for energy conversion*, Eds.: T. Okada, M. Kaneko, Springer, Heidelberg, 2009, 185.
312. K. Lee, J.J. Zhang, H. J. Wang, D.P. Wilkinson, *J. Appl. Electrochem.* 2006, **36**, 507.
313. D. Pantea, H. Darmstadt, S. Kaliaguine, C. Roy, *Appl. Surf. Sci.* 2003, **217**, 181.
314. M.A. Fraga, E. Jordao, M.J. Mendes, M.M.A. Freitas, J.L. Faria, J.L. Figueiredo, *J. Catal.* 2002, **209**, 355.
315. Y. Takasu, T. Kawaguchi, W. Sugimoto, Y. Murakami, *Electrochim. Acta* 2003, **48**, 3861.
316. M. Uchida, Y. Aoyama, M. Tanabe, N. Yanagihara, N. Eda, A. Ohta, *J. Electrochem. Soc.* 1995, **142**, 2572.
317. V. Rao, P.A. Simonov, E.R. Savinova, G.V. Plaksin, S.V. Cherepanova, G.N. Kryukova, U. Stimming, *J. Power Sources* 2005, **145**, 178.
318. A.L.N. Pinheiro, A. Oliveira-Neto, E.C. de Souza, J. Pérez, V.A. Paganin, E. A. Ticianelli, E.R. González, *J. New Mater. Electrochem. Syst.* 2003, **6**, 1.
319. J.S. Noh, J.A. Schwarz, *Carbon* 1990, **28**, 675.
320. S.R. de Miguel, J.C. Heinen, A.A. Castro, O.A. Scelza, *React. Kinet. Catal. Lett.* 1989, **40**, 331.
321. A. Guha, W.J. Lu, T.A. Zawodzinski, D.A. Schiraldi, *Carbon* 2007, **45**, 1506.

322. Y. Otake, R.G. Jenkins, *Carbon* 1993, **31**, 109.
323. V.M. Jovanovic, S. Terzic, A.V. Tripkovic, K.D. Popovic, J.D. Lovic, *Electrochem. Commun.* 2004, **6**, 1254.
324. Z.B. Wang, G.P. Yin, P.F. Shi, *Carbon* 2006, **44**, 133.
325. J.L. Gómez de la Fuente, M.V. Martínez-Huerta, S. Rojas, P. Terreros, J.L.G. Fierro, M.A. Peña, *Carbon* 2005, **43**, 3002.
326. J.L. Gómez de la Fuente, M.V. Martínez-Huerta, S. Rojas, P. Terreros, J.L.G. Fierro, M.A. Peña, *Catal. Today* 2006, **116**, 422.
327. J.L. Gómez de la Fuente, F.J. Pérez-Alonso, M.V. Martínez-Huerta, M.A. Peña, J.L.G. Fierro, S. Rojas, *Catal. Today* 2009, **143**, 69.
328. J.L. Gómez de la Fuente, S. Rojas, M.V. Martínez-Huerta, P. Terreros, M.A. Peña, J.L.G. Fierro, *Carbon* 2006, **44**, 1919.
329. C. Prado-Burguete, A. Linares-Solano, F. Rodríguez-Reinoso, C. Salina-Martínez de Lecea, *J. Catal.* 1989, **115**, 98.
330. J.L. Figueiredo, M.F.R. Pereira, M.M.A. Freitas, J.J.M. Órfão, *Carbon* 1999, **37**, 1379.
331. G.C. Torres, E.L. Jablonski, G.T. Baronetti, A.A. Castro, S.R. de Miguel, O.A. Scelza, M.D. Blanco, M.A. Peña, J.L.G. Fierro, *Appl. Catal. A: Gen.* 1997, **161**, 213.
332. P.L. Antonucci, V. Alderuci, N. Giordano, D.L. Cocke, H. Kim, *J. Appl. Electrochem.* 1994, **24**, 58.
333. M.C. Román-Martínez, D. Cazorla-Amorós, A. Linares-Solano, C. Salinas-Martínez de Lecea, H. Yamashita, M. Anpo, *Carbon* 1995, **33**, 3.
334. Y. Verde, G. Alonso, V. Ramos, H. Zhang, A.J. Jacobson, A. Keer, *Appl. Catal. A: Gen.* 2004, **277**, 201.
335. C.K. Poh, S.H. Lim, H. Pan, J.Y. Lin, J.Y. Lee, *J. Power Sources* 2008, **176**, 70.
336. K.L. Yeung, E.E. Wolf, *J. Catal.* 1992, **135**, 13.
337. F. Coloma, A. Sepúlveda-Escribano, J.L.G. Fierro, F. Rodríguez-Reinoso, *Langmuir* 1994, **10**, 750.
338. P.A. Simonov, V.A. Likholobov, in *Catalysis and Electrocatalysis at Nanoparticle Surfaces*, Eds.: A. Wieckowski, E.R. Savinova, C.G. Vayenas, Marcel Dekker Inc, New York, 2003, 409.
339. G.G. Park, T.H. Yang, Y.G. Yoon, W.Y. Lee, C.S. Kim, *Int. J. Hydrogen Energ.* 2003, **28**, 645.

340. A.S Arico, P. Creti, H. Kim, R. Mantegna, N. Giordano, V. Antonucci, *J. Electrochem. Soc.* 1996, **143**, 3950.
341. Y. Yazawa, H. Yoshida, T. Hattori, *Appl. Catal. A: Gen.* 2002, **237**, 139.
342. H. Bönnemann, W. Brijoux, R. Brinkmann, R. Fretzen, T. Joussen, R. Koppler, B. Korall, P. Neiteler, J. Richter, *J. Mol. Catal.* 1994, **86**, 129.
343. B. Choi, H. Yoon, I.S. Park, J. Jang, Y.E. Sung, *Carbon* 2007, **45**, 2496.
344. P.H. Matter, L. Zhang, U.S. Ozkan, *J. Catal.* 2006, **239**, 83.
345. H. Kim, W. Lee, D. Yoo, *Electrochim. Acta* 2007, **52**, 2620.
346. J.H. Tian, F.B. Wang, Z.Q. Shan, R.J. Wang, J.Y. Zhang, *J. Appl. Electrochem.* 2004, **34**, 461.
347. C. Prado-Burguete, A. Linares-Solano, F. Rodríguez-Reinoso, C. Salinas-Martínez de Lecea, *J. Catal.* 1991, **128**, 397.
348. F.T. Wagner, S.G. Yan, P.T. Yu, in *Handbook of Fuel Cells. Fundamentals, Technology and Applications 5*, Eds.: W. Vielstich, H. Yokokawa, H.A. Gasteiger, John Wiley & Sons, Chichester, 2009, 250.
349. Y.Y. Shao, G.P. Yin, Y.Z. Gao, *J. Power Sources* 2007, **171**, 558.
350. K.G. Gallagher, R.M. Darling, T.F. Fuller, in *Handbook of Fuel Cells. Fundamentals, Technology and Applications 6*, Eds.: W. Vielstich, H. Yokokawa, H.A. Gasteiger, John Wiley & Sons, Chichester, 2009, 819.
351. S.S. Zhang, X.Z. Yuan, J.N.C. Hin, H.J. Wang, K.A. Friedrich, M. Schulze, *J. Power Sources* 2009, **194**, 588.
352. S.S. Zhang, X.Z. Yuan, H.J. Wang, W. Merida, H. Zhu, J. Shen, S.H. Wu, J.J. Zhang**,** *Int. J. Hydrogen Energ.* 2009, **34**, 388.
353. W. Schmittinger, A. Vahidi, *J. Power Sources* 2008, **180**, 1.
354. D.A. Stevens, J.R. Dahn, *Carbon* 2005, **43**, 179.
355. J.J. Wang, G.P. Yin, Y.Y. Shao, S. Zhang, Z.B. Wang, Y.Z. Gao, *J. Power Sources* 2007, **171**, 331.
356. P. Serp, M. Corrias, P. Kalck, *Appl. Catal. A: Gen.* 2003, **253**, 337.
357. W.Z. Li, C.H. Liang, W.J. Zhou, J.S. Qiu, Z.H. Zhou, G.Q. Sun, Q. Xin, *J. Phys. Chem. B* 2003, **107**, 6292.
358. N. Rajalakshmi, H. Ryu, M.M. Shaijumon, S. Ramaprabhu, *J. Power Sources* 2005, **140**, 250.
359. X. Wang, W.Z. Li, Z.W. Chen, M. Waje, Y.S. Yan, *J. Power Sources* 2006, **158**, 154.
360. Y. Shao, G. Yin, J. Zhang, Y. Gao, *Electrochim. Acta* 2006, **51**, 5853.

361. Y.Y. Shao, G.P. Yin, Y.Z. Gao, P.F. Shi, *J. Electrochem. Soc.* 2006, **153**, A1093.
362. F. Yuan, H.K. Yu, H. Ryu, *Electrochim. Acta* 2004, **50**, 685.
363. F.L. Yuan, H.J. Ryu, *Nanotechnology* 2004, **15**, S596.
364. T. Yoshitake, Y. Shimakawa, S. Kuroshima, H. Kimura, T. Ichihashi, Y. Kubo, D. Kasuya, K. Takahashi, F. Kokai, M. Yudasaka, S. Iijima, *Physica B* 2002, **323**, 124.
365. T. Maiyalagan, B. Viswanathan, U. Varadaraju, *Electrochem. Commun.* 2005, **7**, 905.
366. C.A. Bessel, K. Laubernds, N.M. Rodríguez, R.T.K. Baker, *J. Phys. Chem. B* 2001, **105**, 1115.
367. A. Kongkanand, S. Kuwabata, G. Girishkumar, P. Kamat, *Langmuir* 2006, **22**, 2392.
368. G.L. Che, B.B. Lakshmi, E.R. Fisher, C.R. Martin, *Nature* 1998, **393**, 346.
369. B. Rajesh, V. Karthik, S. Karthikeyan, K.R. Thampi, J.M. Bonard, B. Viswanathan, *Fuel* 2002, **81**, 2177.
370. H. Tang, J.H. Chen, Z.P. Huang, D.Z. Wang, Z.F. Ren, L.H. Nie, Y.F. Kuang, S.Z. Yao, *Carbon* 2004, **42**, 191.
371. T. Matsumoto, T. Komatsu, H. Nakano, K. Arai, Y. Nagashima, E. Yoo, T. Yamazaki, M. Kijima, H. Shimizu, Y. Takasawa, J. Nakamura, *Catal. Today* 2004, **90**, 277.
372. T. Matsumoto, T. Komatsu, K. Arai, T. Yamazaki, M. Kijima, H. Shimizu, Y. Takasawa, J. Nakamura, *Chem. Commun.* 2004, **7,** 840.
373. H. Chang, S.H. Joo, C. Pak, *J. Mater. Chem.* 2007, **17**, 3078.

This page intentionally left blank

CHAPTER 10

SUPPORTED METALS IN VEHICLE EMISSION CONTROL

A. Martínez-Arias[1], José C. Conesa[1], M. Fernández-García[1] and J. A. Anderson[2]

[1]*Instituto de Catálisis y Petroleoquímica, CSIC, C/Marie Curie, Cantoblanco, 28049 Madrid, Spain*

[2]*Surface Chemistry and Catalysis Group, Department of Chemistry, University of Aberdeen, Kings College, Aberdeen, Scotland, UK*

10.1 Introduction

The transport sector is recognized as one of the main anthropogenic sources of atmospheric pollution. This is a consequence of the conditions employed during flame combustion of fossil fuels in the vehicle engines, which in addition to carbon dioxide and water formed as main products, generate a small portion of pollutants as a result of incomplete combustion processes, or due to high-temperature radical reactions involving N and O, or due to their presence in the fuel (typically S and N containing compounds).[1] The characteristics of the exhaust emission depend on the type of engine, as summarized in Table 10.1 for the main type of engines employing typical gasoline or diesel fuels found in the market.

Catalytic technologies are usually employed to deal with pollutants emitted by the exhaust systems of motor vehicles and which are subject to regulation (nitrogen oxides, hydrocarbons, CO and particulates). Specific catalysts have been developed in each case as a function of the regulatory requirements and particular characteristics

Table 10.1 General characteristics of the exhaust emission as a function of the type of engine. A range of values appears generally as a function of the driving conditions, the origin or blend of the fuel employed, the particular type of engine, etc.[1–5]

Exhaust component[a] or condition	Diesel engine	Gasoline stoichiometric engine	Gasoline direct injection lean-burn engine[b]
Nitrogen oxides[c]	200–1000 ppm	100–4000 ppm	800–2300 ppm
Total hydrocarbons[d]	10–330 ppm	400–5000 ppm	350–1500 ppm
CO	150–1200 ppm	0.1–6%	0.5–0.9%
O_2	5–15%	0.2–2%	0.6–7%
H_2O	1–7%	10–12%	10–12%
CO_2	3–13%	10–18%	10–15%
Sulfur oxides[e]	10–100 ppm	15–60 ppm	10–50 ppm
Particulates	50–400 mg m^{-3}		
Temperature	RT–973 K	RT–1373 K	RT–1173 K
A/F[f] (λ)[g]	45 – 18 (3 – 1.2)	≈14.7 (≈1)	40 – 30 (2.7 – 2); 14.6 (≈1)[h]

[a]Additionally around 70% of N_2;[1] H_2 also appears typically in a proportion of 1/3 with respect to CO.[2,6] [b]Differences between the lean and stoichiometric condition in this engine affect mainly the O_2 concentration but also the other components.[5,7] [c]NO + NO_2. [d]A large variety of hydrocarbons can be produced as a function of the type of fuel employed.[1] [e]Mainly SO_2, in a vol.% of around 1/20 of the wt% sulfur content in the fuel. [f]Air-to-fuel mass ratio employed in the fuel combustion. [g]λ = (actual A/F)/(stoichiometric A/F). [h]Oscillating between lean-burn (most of the time) and quasi-stoichiometric condition.

of the emission. Thus, three-way catalysts are highly efficient at controlling emissions produced by engines operated at stoichiometry (conversion levels above 90% are achieved during a regular driving cycle for the three main pollutants regulated in this case). In the case of diesel engines operating under lean-burn conditions, there appear to be important difficulties to catalyze the reduction of NO_x as a consequence of the relatively high concentration of oxygen (main oxidant competitor) present in the exhaust emission. The main efforts in this respect are directed towards controlling NO_x emissions (so-called de-NO_x catalysts) through their reaction with reductant gases present in the exhaust or introduced externally (mainly NH_3 derived from urea decomposition or hydrocarbons within selective catalytic reduction processes). Partial solutions in

this sense are also provided by commercially available oxidation catalysts and filters which are able to control emissions of reductant pollutants (hydrocarbons, CO, and particulates). On the other hand, NO_x storage-reduction catalysts (NSR) have been developed to treat mixed oscillating emissions produced by lean-burn gasoline direct injection engines. This chapter develops the main principles of these types of catalysts focusing on the fundamental aspects of the catalytic behavior of supported metals (or other closely interacting components that affect their properties) that constitute the main active part of the systems. Some recent reviews are available which have focused mainly on the practical aspects of these systems.[1,3,6,8]

10.2 Emissions Produced at Stoichiometric Conditions

10.2.1 *Classical TWC*

The elimination of nitrogen oxides (NO_x for short, which refers to NO and NO_2; the need to control N_2O has only been recognized more recently) in automobile exhaust gas, which were first regulated in the late 1970s, led to the development of the so-called three-way catalysts (TWCs), which had to suppress the three, then relevant, pollutants: CO, HC (hydrocarbons) and NO_x. Although NO is thermodynamically unstable with respect to decomposition to N_2 and O_2, kinetically this reaction is very difficult to achieve, and no catalyst has been found to date which allows its completion under the conditions found in a car exhaust system. Therefore NO_x levels are normally suppressed through reduction with one or both of CO and HC, while the latter two are eliminated by oxidation with O_2 and NO_x. Although all of the platinum group metals were found to have high activity in these processes (and of them Os, Ir, and Ru were discarded due to their tendency to form volatile oxides), it was soon realized that NO_x reduction was not readily achieved in the presence of excess O_2. Since incompletely combusted CO and HC also had to be eliminated, strict control of fuel injection at the engine in order to achieve an overall air-to-fuel ratio close to the stoichiometric value (i.e. one leading to only N_2, CO_2, and H_2O after full reaction)

was implemented through the use of oxygen partial pressure sensors at the exhaust manifold. Even so, oscillations in the A/F ratio as a consequence of the oxygen sensor providing engine feedback remained in the oxidant/reductant ratio of the exhaust, due to the transient and inertial characteristics of the systems used, and, in order to compensate, other components (oxygen buffers, typically ceria-related compounds) were added to catalyst formulation which allowed excess oxygen to be consumed when present and delivered to achieve full conversion of reductants when these latter are in excess. Figure 10.1 illustrates the importance of the air-fuel ratio control in terms of the overall conversion achieved for the main three main pollutants.

A classical TWC formulation was established, using a mixture of Pt and Rh in typically a 5 : 1 weight ratio as a precious metal catalyst, and cerium oxide as an oxygen buffer. All these ingredients were dispersed on a layer of porous alumina (the "washcoat"), possibly stabilized against sintering with appropriate additives, and deposited on a metallic or ceramic honeycomb-type rigid structure. A considerable volume of work was performed in the following 15–20 years to optimize and understand the operation of these typical catalysts, which has been covered extensively in the available literature; the principal features of these systems are summarized in a number of reviews.[1,8–13] Briefly, Rh was included in these catalysts as a key component for NO removal due to its specificity to promote NO dissociation,[14] followed by re-combination of N atoms to produce N_2; the remaining O atom was then eliminated by adsorption of CO and reaction to give CO_2, the overall reaction being:

$$CO + NO \rightarrow CO_2 + \frac{1}{2} N_2. \qquad (10.1)$$

The adsorbed N atoms can also combine with undissociated adsorbed NO, producing N_2O; if the latter desorbs and does not react further, the global reaction is:

$$CO + 2NO \rightarrow CO_2 + N_2O. \qquad (10.2)$$

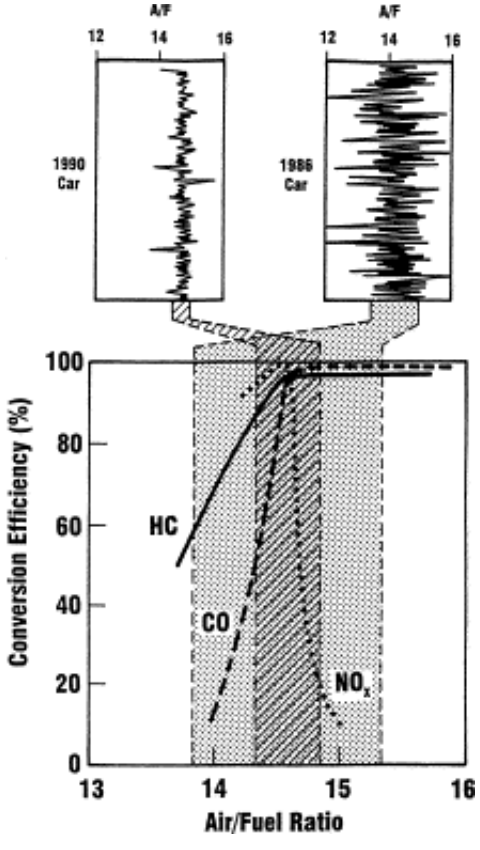

Figure 10.1 Three-way catalyst conversion efficiency for the three main pollutants as a function of the air-fuel ratio. Representative air-fuel ratios achieved for 1986 and 1990 vehicles are also plotted[8] (reproduced with permission from Elsevier Science).

N_2O may appear as a reaction product in important amounts, especially in the lower temperature range of activity in which the amount of associatively adsorbed NO is large and catalytic activity for N_2O decomposition is low. Traditionally N_2O has not been considered a serious pollutant; and as it was not included in the legal regulations, no efforts were made to avoid its formation and emission. However, there is now concern regarding N_2O emissions, among other things because they contribute to the greenhouse effect, and the work on

TWCs pays attention to their generation and minimization. Adsorbed N atoms may also combine with CO, generating NCO species which readily diffuse to the support and become stabilized there; the build-up of these adsorbed species, readily detected in IR spectra, is a fingerprint for the onset of NO conversion activity. Detailed aspects of the mechanisms of all these steps relevant for NO reduction with CO, as well as references to earlier studies, are given in a recent kinetic analysis of this process.[15]

On the other hand, the oxidation of CO and unburnt HC by oxygen is catalyzed satisfactorily mainly by the Pt component, according to reactions:

$$CO + \frac{1}{2}\ O_2 \rightarrow CO_2 \tag{10.3}$$

$$C_nH_{2m} + \left(n + \frac{m}{2}\right)\ O_2 \rightarrow n\ CO_2 + mH_2O. \tag{10.4}$$

It is important to note that, although the initial role of the ceria component in the catalyst was to provide the needed oxygen buffering capacity, the activity of the above reactions is influenced by metal-ceria interactions. In the first place, the oxygen buffering activity of ceria is significantly enhanced by platinum group metals; i.e. the presence of direct contact between the metal and the oxide accelerates the reduction of CeO_2 by CO[16] or H_2[17] (which is also present in the exhaust gas over the catalyst, either because of its production by the engine in small amounts or because the catalyst promotes its formation from CO or HC and water *via* the water-gas shift or reforming reactions, respectively). In the case of CO, this enhancement is normally presumed to occur through reaction at the metal-oxide interface between metal-adsorbed CO and oxygen atoms of the ceria surface, and indeed the production of CO_2 by reaction of CO with Pt/CeO_2 was found to increase with specific surface area of Pt;[16] in the case of H_2, spillover of adsorbed hydrogen atoms to the buffering oxide, generating Ce^{3+} and OH^- groups (the latter then desorbing as water) could be the key mechanism. Actually, the ease of reduction of the support with H_2 is such that it interferes with the standard methods of metal surface area

determination by hydrogen chemisorption (see Chapter 4); it has been proposed that this problem can be avoided if the measurement is made at low temperature (−80°C).[18] On the other hand, it must be noted that this spillover phenomenon, as well as other catalytic properties, is strongly decreased, or even absent, if the catalyst contains chlorine, which in ceria supported catalysts is often the case if a chloride salt is used to deposit the metal.[18] This is related to the ability of ceria to retain strongly Cl at its surface, especially after reduction treatments, so that an oxychloride, CeOCl phase (or a precursor thereof), stabilizing Ce^{3+} is formed; such a phase has been even detected by XRD.[19]

As a result of the mentioned interactions, both the activity for catalytic CO oxidation (even in the absence of oscillations in the gas phase composition) and the oxygen buffering efficiency are improved by the existence of such contacts. Therefore when catalyst aging produces sintering of both metal and ceria components on the alumina support, with the consequent decrease in the number of those contacts, catalyst performance is degraded, more than what would be expected on the basis of the decrease in the surface areas alone.

NO reduction activity has been observed to be enhanced by contacts between the metal and ceria.[15,20] This is interpreted through a somewhat similar mechanism, in which metal-adsorbed NO dissociates at the metal-oxide interface, probably by interacting with anion vacancy sites produced by previous reduction at the ceria surface, transferring the O atom to the oxide which is thus re-oxidized. It should be mentioned, however, that some NO reduction can occur also in the absence of metal on a reduced ceria surface,[21] leading to N_2O (and/or N_2) production and ceria re-oxidation through formation of an intermediate hyponitrite species.

Finally, it is worth remarking that, while many of the published studies have concentrated on processes involving CO with NO and O_2, hydrocarbons may need to be included as reactants if one wants to obtain a more realistic picture, mainly because the latter can produce significant amounts of adsorbed C_xH_y species on the metal which are able to interfere with the reactions of the other species.

Indeed it has been reported, that in some cases, NO reduction activity is lower in the presence of HC.[22]

10.2.2 *Modern TWC*

The increasingly stricter emissions limits implanted worldwide since the early 1990s forced new aspects and requirements in TWCs to be considered. Above all, it was clear that most of the emissions remaining with the then current technologies (and consisting mainly of unburnt HC) were produced in the first moments of engine operation, when the catalyst under the exhaust gas has not yet reached the temperature necessary for light-off. Attempts to minimize this problem have followed several strategies, which do not exclude mutually: (a) to increase the temperature rise at the catalyst, either by decreasing the thermal capacity and/or conductance of the exhaust tubing and honeycomb materials, by locating the catalyst much closer to the engine manifold outlet or by artificially heating the catalyst (electrically or by burning added fuel at an appropriate location); (b) to use catalysts with lower light-off temperatures, at least for the HC and CO oxidation reactions (which thus contributes to a more rapid temperature rise); (c) to insert an adsorbent of HCs before the catalyst which traps these when the exhaust gas is cooler and releases them at higher temperature when light-off conditions have been reached, and the catalyst can efficiently burn the hydrocarbons.

Locating the catalyst near the engine outlet was soon recognized to be a particularly convenient method. However, such a close coupling of engine and catalyst implied that the latter would reach, upon continued operation, much higher temperatures (possibly above 1000°C) than in the classic TWC technology; this problem imposed on the catalyst additional strong requirements of resistance to thermal sintering and deactivation. Furthermore, the new regulations demanded not only a lower level of emissions, but also their retention during a longer time interval (for example, the Tier 2 regulation in the USA imposes a catalyst lifetime of 120,000 miles), which also demands an improvement in resistance to deactivation.

Two main changes in catalyst formulation appeared to satisfy these needs.

10.2.2.1 *New oxygen buffering oxides*

One early change was the substitution of cerium oxide by mixed oxides based on the latter. Most interesting for this are solid solutions of cerium and zirconium dioxides (with typically Zr cation fractions between 0.3 and 0.5), which have two main advantages: firstly, they are more refractory than pure ceria (have higher melting point) and consequently lose surface area to lower extent under high temperatures; and secondly, and possibly more importantly, this mixed oxide provides oxygen buffering capacity under TWC conditions not only from its external surface as is the case of ceria, but also from its bulk (as oxygen vacancies inside the latter are formed much more readily), so that even if its surface area diminishes upon aging, its buffering efficiency decreases to a much lower extent. Although the study of such an oxidic catalyst component is not of direct concern in a chapter devoted to the role of supported metals, it is worthwhile considering ceria-zirconia here in that it strongly influences the catalytic behavior of the metallic component.

The structure and redox properties of ceria-zirconia solid solutions have been extensively studied following the discovery over a decade ago of their striking ability for O_2 uptake and release.[23,24] These materials have a fluorite-type structure (the same as pure ceria), with purely cubic crystal symmetry for high Ce cation fraction (above *ca.* 80%) and a tetragonal lattice (the so-called t' phase) when this fraction is below *ca.* 65%; the composition range in-between presents a cubic crystal cell shape together with an internal tetragonal symmetry of the atom positions (the so-called pseudocubic phase t").[25] It must be noted however that the frontiers between the existence of these phases depend on preparation methods and especially on the degree of dispersion: small crystallite sizes, for example, allow the presence of phase t" for Ce cation fractions around 50%, for which phase t' would be normally more stable. It has been found that upon reduction these mixed oxides can be

extensively reduced in the bulk even at temperatures around 750 K, in contrast with pure ceria for which only the external surface is reduced under these conditions and much higher temperatures are required to reduce the bulk oxide.[24] This is normally ascribed to the higher stability of anion vacancies in ceria-zirconia, due to the tendency of the smaller Zr cation to decrease its coordination number below 8 (the value in the regular fluorite structure); indeed in the simple limiting case of 50% cationic ratio and full reduction of Ce to Ce^{3+} (the stable Zr^{4+} state is not significantly reduced in catalytically relevant conditions) the thermodynamically favored state has the composition $Ce_2Zr_2O_7$ with both anion vacancies and cations ordered in the pyrochlore structure in which Zr and Ce coordinations are 6 and 8, respectively. Still, a number of questions remain unanswered concerning the properties of these solid solutions. First, it has been observed that cycles of high- and low-temperature redox treatments in this material can lead to the appearance and disappearance of an exceptional ability to lose oxygen from the bulk at temperatures as low as 675 K;[26,27] the reason for this behavior is not yet known, although subtle surface structural rearrangements seem to be involved.[28] Secondly, severe calcination treatments of these solid solutions (around 1273 K) lead to their decomposition into two separate solid solution phases one being richer and the other poorer in Ce,[29] which is disadvantageous for the oxygen buffering properties. Although computer modeling of these solid solutions gives some justification to this decomposition,[30] the observations that some preparations are more resistant than others, even in cases in which they present the same structural characteristics,[25] and that redox cycling at similar temperatures does not produce the same effects,[31] are not yet well understood. It has been proposed that small cation composition inhomogeneities, which might be detectable only with specialized techniques,[32] could be a key factor favoring this high-temperature decomposition.[25] Particle size effects can also be considered, given the fact that the effect is also retarded when the mixed oxide is highly dispersed on alumina.[33]

Even if these details of the ceria-zirconia oxides remain unsolved, the introduction of these mixed oxides into modern

TWCs due to their good buffering and refractory properties have activated a new wave of studies to verify if these mixed oxides influence the behavior of catalytic metals in the same way as the more widely studied CeO_2. The majority of these studies use unsupported ceria-zirconia, since preparing this latter material dispersed on alumina or a similar carrier with good structural control so avoiding mutual segregation of Zr and Ce, is not straightforward. In general, ceria-zirconia influence and promote the reactivity of the metal catalyst in a similar manner. Within this similarity in behavior, one of the observations made is that the intrinsic rate of reduction of $Pt/(Ce,Zr)O_2$ by CO is higher than that of Pt/CeO_2, even in its initial stages; furthermore, the maximum rate of oxide reduction occurs at much lower metal loadings.[16] On the other hand, TWC performance in catalysts (at least when not aged) may be poorer with $M/(Ce,Zr)O_2$ than with M/CeO_2 combinations; this was verified in some cases with Rh[34,35] and Pd.[36] In the latter case, EPR experiments suggest that a CeO_2 containing catalyst was better than a $(Ce,Zr)O_2$-based one in providing the type of reactive oxygen surface vacancies of interest. The same work indicated, on the other hand, that the tendency for the metal to be deposited preferentially on the surface of the buffering oxide (rather than on the alumina carrier) was more marked for $(Ce,Zr)O_2$ than for CeO_2.[36] In any case, the major difference between ceria and ceria-zirconia lies, as mentioned above, in the higher refractory character of the latter, giving it a greater resistance to sintering (and, additionally, improving the resistance to loss of area of the alumina carrier),[33] and in its ability to involve the anions from the bulk, not only those from the surface, in the oxygen buffering activity (which also reduces the importance of the oxide surface area decrease occurring upon aging).

Although ceria-zirconia is by far the main (mixed) oxide replacing ceria nowadays as the oxygen buffer, it is worth mentioning that some other modifications to this component have been proposed as being of benefit. In particular, addition of other redox-active lanthanides such as Tb and Pr to ceria (or ceria-zirconia) has been studied and found to improve the oxide buffering capacities and/or the stability against sintering.[31,37,38] Finally, it must be mentioned that

Pd, which as indicated below is being used now as the main TWC metal, has by itself, in the amounts typically included in the catalysts, a significant contribution to oxygen buffering through its reversible oxidation to PdO.[8]

10.2.2.2 *The shift towards the use of palladium*

The other significant change to TWC formulation has been the use of palladium, at least as a substitute for platinum, since Pd is recognized to be a good catalyst for oxidation of hydrocarbons and CO, and to have good resistance to thermal sintering. This trend had been desired during the early development of the first TWC formulations, if only because of the price of Pd (several times lower at that time than Pt and much lower than Rh), but could not be realized at this stage due to the greater sensitivity of Pd to poisoning by lead, sulfur, and other pollutants coming from the fuel and lubricant formulations employed at that time. As the limits allowed for these latter elements in the exhaust gas were decreased, the use of Pd again became feasible, and so a new generation of catalysts arose where Pd was used instead of Pt, and even replaced Rh as NO_x reduction catalyst. The resulting worldwide increase in demand for Pd was such that the market price of this latter increased and surpassed that of Pt during 2000 and 2001; later, catalyst improvements have allowed the use of lower amounts of Pd, and recently (end of year 2003 data) the Pd prices have again become lower than those of Pt: *ca.* 200 $/oz for Pd *vs. ca.* 800 $/oz for Pt, a proportion nearly equal to that prevailing in the early 1990s (and it is noteworthy that now Rh, having been significantly replaced by Pd in TWCs, has a price of *ca.* 500 $/oz, between those of Pt and Pd, while formerly it was the most expensive of the three). Many TWCs now include Pd as the major or as the only Pt group metal component (and in a number of cases it is contained in two different regions or layers of the catalyst, which have different support and/or promoters, in order to achieve good activity in all three TWC reactions). Correspondingly the number of studies on such systems has increased significantly. Now a significant tendency in TWC technology is

towards using a mainly Pd-based compact catalyst located close to the engine outlet (where there are more space constraints), which functions mainly in the oxidation of HC and as promoter of a rapid establishment of light-off conditions, in addition to another catalyst of larger volume, located under the vehicle at greater distance from the engine, which completes the TWC function.

Pd has a relatively good intrinsic activity for the CO + O_2 reaction. On an alumina support, it is intermediate between those of Pt and Rh[39] and, as in these other metals, its kinetics displays minus first order (−1) with respect to CO under typical TWC temperatures, as CO is strongly adsorbed and reaction is controlled by the availability of free metal surface for O_2 adsorption. For this reason, in temperature-programmed experiments the reaction only initiates when CO coverage begins to decrease, as confirmed by *in situ* DRIFTS studies for Pd on silica[40] or alumina.[41] The reaction is structure-insensitive,[40] and thus is faster for highly dispersed metal; in fact it has been proposed as a possible method for determining Pd dispersion on alumina.[42] The situation changes if a redox promoter such as ceria is present and in contact with the metal; CO oxidation activity then increases, and may become important at low temperatures where normally high CO coverage would completely inhibit the reaction, so that even full CO conversion may appear at close to room temperature.[41] It is generally accepted that this is due to a reaction, occurring at the metal support interface sites, between Pd-adsorbed CO and oxygen atoms of the oxide surface; indeed *in situ* DRIFTS data in such a case show that CO coverage of the metal remains complete at temperatures at which the reaction is fast,[41] and a similar observation applies when ceria-zirconia, rather than ceria, is used as promoter, as illustrated in Fig. 10.2.[43]

The IR spectra of CO adsorbed on different well-characterized chemical states and surfaces of Pd[44,45] have helped in interpreting results for this system. Use of this technique has confirmed, for example, that CO adsorption on pre-oxidized supported Pd forms Pd^0 sites even at room temperature[41] even in a stoichiometric CO + O_2 mixture, although the bulk of the metal probably remains oxidized until significantly higher temperatures. This approach of

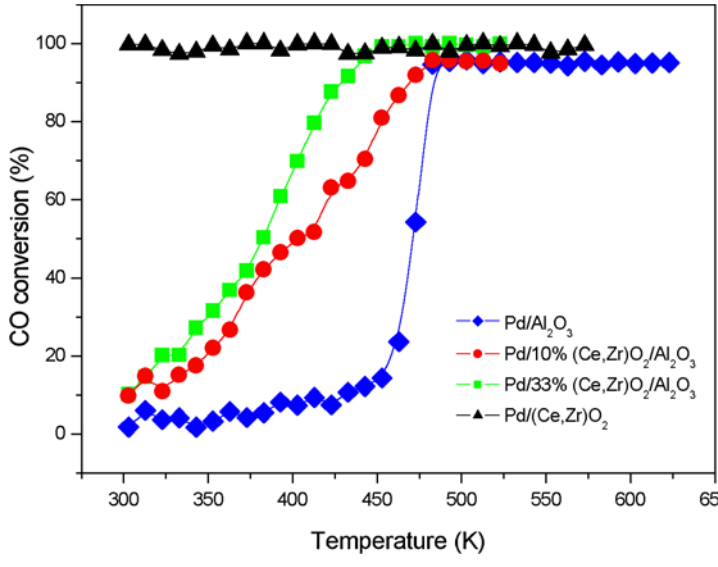

Figure 10.2 Catalytic activity for CO oxidation under stoichiometric conditions over 1 wt% Pd catalysts with different contents of $(Ce,Zr)O_2$ promoter.[43]

course provides information only on molecularly adsorbed forms of CO; dissociation of CO, on the other hand, can occur giving deposited C in a Boudouard-type reaction as proved by CO_2 evolution in TPD experiments at $T \geq 523$ K.[46–48]

The NO + CO reaction on Pd is, contrarily to CO oxidation, structure-sensitive, and proceeds at a greater specific rate on larger Pd particles.[49] In this reaction, the rate limiting step is generally considered to be the dissociation of NO,[50] although other authors have proposed that re-combination of rather stable adsorbed N atoms to give N_2 is the slower step.[51] If the reaction is carried out in a stoichiometric CO + NO + O_2 mixture (with $P(O_2) > P(NO)$ in most cases), it has been observed that CO oxidation proceeds at lower rates than in the absence of NO.[52] One likely reason for this is the oxidation of the Pd surface by NO, evidenced in the latter work by *in situ* DRIFTS, coupled with the fact that cationic Pd is less active than Pd^0 for CO oxidation. This oxidation of Pd by NO would occur through dissociation of NO, thus implying that, at least in this work,

that such dissociation (which may take place relatively easily on step sites but not on flat (111) type surfaces)[53] would not be the rate determining step; even if the resulting O atom may be readily scavenged by CO. The remaining N atom, the presence of which implies an oxidized state of neighboring Pd, would be less easily eliminated. It should be added here that the dissociation of NO seems to be enhanced by the presence of ceria or a similar promoter,[54] the process occurring presumably *via* interaction of Pd-adsorbed NO with neighboring anion vacancy sites of the promoter oxide surface.

The above results imply that the redox state of Pd may vary significantly during a reaction run. The chemical state can be monitored with different *in situ* techniques: FTIR for the surface; XAFS, Raman, or XRD for the bulk. In principle, at sufficiently high temperatures (*ca.* 1100 K under air) a promoted alumina supported PdO of relatively high particle size would decompose in the bulk giving Pd metal (which also re-oxidizes under air at 950 K).[55] Under a stoichiometric CO + NO + O_2 atmosphere, on the contrary, bulk reduction of highly dispersed PdO starts at *ca.* 400 K and is complete at *ca.* 600 K, while DRIFTS data on the same material and under similar conditions, show that surface reduced Pd^0 species begin to appear even at around room temperature.[56] It should be considered, in any case, that the underlying support affects the redox state of Pd. Indeed ceria facilitates re-oxidation of Pd by O_2,[57] and interaction under vacuum of deposited Pd^0 with an oxidized (Ce,Zr)O_2 mixed oxide leads to oxidation of the metal by the oxide.[58] This is probably related to the very similar values of the heat of adsorption of O_2 over Pd and reduced ceria-zirconia.[59] Recent analyses of these issues under redox oscillating conditions by combining energy-dispersive extended X-ray absorption fine-structure spectroscopy with infrared and mass spectrometry (to monitor reactants and products concentrations) at high time resolution, within single *in situ* experiments, have allowed dynamic observation and quantification of adsorbed intermediates formed during CO/NO or CO/NO + O_2 redox cycling as well as exploration of induced size and shape or chemical changes of the Pd nanoparticles. In doing so, the existence of novel, non-oxidative, redispersion mechanisms for

the palladium nanoparticles has been demonstrated, for which oxidation of the Pd nanoparticles only occurs after the nanoparticles have undergone significant size/morphological alteration (i.e. redispersion which occurs within seconds).[60,61] Such Pd size/shape changes taking place under cycling conditions may strongly influence N_2 formation through a direct effect on N–O dissociation and N–N- coupling steps.[62] On the other hand, potential Pd particle size-dependences on the catalytic properties observed under such redox cycling conditions display significant differences with respect to expected results based on non-cycling measurements, typically performed with a fixed (most times stoichiometric) gas atmosphere.[63] The most particularly interesting results in this sense concern, firstly, the absence of a marked size-sensitivity for all relevant N_2 formation steps. This takes into account both the NO dissociation step but particularly the N–N-coupling. Differences among samples exhibiting different Pd sizes in N_2 formation are mostly justified by the metal surface area available and by the fact that the presumed size-sensitivity of the two elemental steps does not influence N_2 formation. On the other hand, CO_2 formation seems dominated by the CO desorption step and, contrarily to prototypical assumptions originated from measurements at non-cycling conditions, may present an important size-dependence. The growth of the Pd particle size was thus found detrimental for production of CO_2. The structure–activity relationship for Pd particles in CO and NO elimination reactions would thus display a characteristic size-dependence upon dynamic conditions, far from that predicted by non-cycling measurements.[63]

Another potentially important aspect of the interaction between supported Pd and ceria or ceria-zirconia in the support, arises in relation to the effects of high temperature or other aging treatments. While deposition of Pd by impregnation (e.g. from the nitrate salt) on a ceria-(or ceria-zirconia-) alumina support may preferentially deposit Pd on the promoter oxide surface,[36,43] aging and the ensuing particle size growth of both metal and promoter components may end up segregating them from one another and decreasing their mutual contact, with a consequent decrease in

activity for the $CO + O_2$ reaction until reaching the same level found on an equally aged ceria-free support.[64] It is noteworthy that such a negative effect of aging on catalytic activity is much smaller if the reaction is carried out in the presence of hydrocarbon, which reflects the previously mentioned poisoning effect of the latter on some TWC reactions, and highlights the importance of the nature of the reactant mixture (in terms of the possible mutual catalytic interferences) on the overall catalytic performance.[2,65] On the other hand, on a pure ceria or ceria-zirconia support (as well as on promoted alumina) severe aging may produce encapsulation of the metal, as revealed by changes in its crystal cell dimension,[66] as well as directly by HREM.[67] For less severe reducing treatments, decoration of the Pd surface by diffusing cerium oxide entities, in a manner similar to the classical SMSI effect,[68] may occur as revealed by TEM[69] or IR data,[44] leading also to activity loss. Electronic interactions (with influence on catalytic properties) following less severe treatments, or on the other hand Ce-Pd solid solution formation for stronger reduction conditions, have also been reported.[69] It has been claimed that reversal of this coverage by mild re-oxidation and re-reduction may occur, although it is possible that the process is not completely reversible.[69] IR data suggest that in such cases, the liberation of free Pd^0 surface occurs preferentially on the (111) surface, while the more reactive (100) surface and edge sites would remain covered.[42] Modifications of the interactions between Pd and the Ce containing promoter resulting from changes in the latter have also been noted after aging treatments either under laboratory (thermal aging leading to Ce enrichment at the surface of Ce-Zr mixed oxide)[70] or real (chemical poisoning by phosphorus leading to stabilization of $CePO_4$ phases)[71] conditions.

10.2.2.3 *Promotion of Pd by base metals*

Pd-only TWCs display limitations with respect to their ability to reduce NO and, particularly, in their selectivity towards N_2 at low temperatures.[72,73] Modification of Pd by the introduction of a second, cheaper, metal would appear to offer a viable solution from an

economical and catalytic point of view.[74] It is well known that the resulting bimetallic catalyst may display special features not anticipated by simple interpolation of the reactivity of the constituents. Although the complexity of TWC systems, where the metal components can be present over the alumina and/or the promoter, makes the study of bimetallic systems rather difficult, the main physicochemical effects exerted by the second metal on the noble metal component allow a simple classification of bimetallic systems, somewhat independent of the specific kinetic and thermodynamic features of the metal-metal contact. First of all, catalysts are found where the introduction of the second metal (M) may generate a binary phase, either in the oxidized and/or reduced chemical states. This is typically the case for Cu[75–77] or Cr.[36,56,77,78] A classic explanation of the differential behavior with respect to the monometallic Pd system makes use of the interrelated structural (or ensemble) and electronic effects. This is typically applied to the zero-valent state but can also loosely embrace oxidized or partially reduced states where the noble metal displays catalytic activity.[56] As previously mentioned, NO reduction (by CO) is known to be a structure-sensitive reaction and thus both factors, structural and electronic are rather important when interpreting reactivity. Structural effects are related to the generation or removal of certain surface sites while electronic factors are more subtle and induce changes in surface valence states. Electronic effects can play a catalytic role even in the case of an alloy dominated by Pd at the surface since modification of Pd electronic valence states with base metals located in sub-surface regions strongly modifies the NO dissociation and/or N-coupling steps.[79] A second class of bimetallic systems may present modified catalytic behavior as a consequence of the new "Pd" interface to the reactants. This may occur if the interaction of the second metal with the promoter or support is stronger,[76] in turn modifying the initial state of the noble metal, but also by formation of different interactions between Pd and this new component. The latter, in particular, affects the catalytic behavior when a Pd(0)-M^{n+} interface is created with redox capabilities due

to the second metal, as may be the case of Cr,[56] Ni,[67,80,81] Mo,[82,83] and Mn.[84] This second class of system is able to create new surface active sites for reaction or to block Pd sites which are present in the unmodified Pd system, having an important catalytic effect mostly through altering the temperature onset of metallic Pd formation.

10.3 Lean-Burn Emissions

In a diesel engine, the fuel is injected into an air charge which is highly compressed until a temperature is reached (973–1173 K) whereby spontaneous combustion of the fuel occurs. Thus, it is a compression-ignited process in contrast to the spark-ignited process employed in Otto engines. This brings as a consequence a change in the characteristics of the exhaust emission, which in turn depend on the specific diesel engine employed in each case.[1,6,85] General differences in comparison with spark-ignited engines employed under stoichiometric combustion can be highlighted. In the first place, since fuel is combusted under lean conditions (Table 10.1), excess oxygen is present in the exhaust. In second place, relatively lower NO_x concentrations are found than in engines operating under stoichiometric conditions. In contrast, a far higher amount of particulate matter (PM) is produced. The nature of such particulate matter is complex since it contains a mixture of solid (essentially located at the particles core) and liquid (remaining essentially adsorbed at the surface) components. The solid fraction is mainly composed of dry carbon or soot; the liquid portion can contain mainly unburned fuel or lubricating oil (collectively denoted as SOF or soluble organic fraction) and sulfuric acid (resulting from oxidation of SO_2 and on the whole resulting from burning of sulfur compounds present in the fuel) plus water.[1,85] Other minor components of the particulate matter include metals, inorganic oxides and/or sulfates.[1] Another significant difference with respect to the emission produced in spark-ignited engines operating under stoichiometric conditions, concerns the temperature of the exhaust

emission which is significantly lower (423–523 K *vs.* 773–873 K can be considered as an average temperature in each case under normal driving conditions).[1,85,86] Fortunately, the hydrocarbons present in the diesel exhaust (forming part of the gas or SOF portions) are globally more readily oxidized than those emitted by stoichiometric spark-ignited engines because of their higher average carbon number.[1,6,87] Three-way catalysts are not in general efficient enough to control the lean-burn emissions, although support formulations similar to those employed for TWC can operate as effective oxidation catalysts in certain temperature ranges.[88] Different review papers are available in which details of catalytic and non-catalytic approaches to deal with these types of emissions are described.[1,6,85] Among the catalytic treatments of lean-burn emissions, oxidation catalysis in flow-through systems, treatment of particulate matter with catalytic filters, hydrocarbon selective catalytic reduction of NO_x, and selective reduction of NO_x by external introduction of NH_3 (through urea decomposition) can be highlighted as processes in which supported metal catalytic systems play a fundamental role, as described in the following sections.

10.3.1 *Oxidation catalysts*

Diesel oxidation catalysts (Fig. 10.3) target the oxidation of soot, hydrocarbons, and CO, although flow-through systems employed for this purpose are fairly inefficient at treating the solid portion of the emission (usually less than 5% of the soot becomes oxidized as a consequence of the low contact time since catalysts are designed

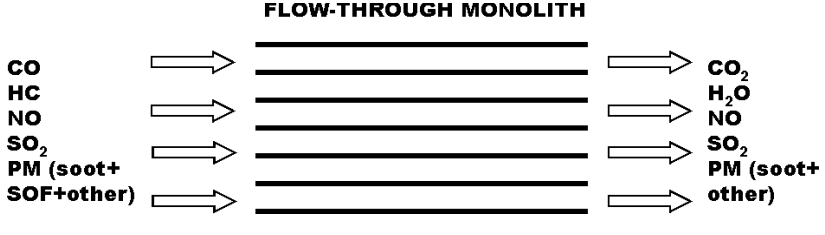

Figure 10.3 Operational concept of a diesel oxidation flow-through catalyst.

to avoid pressure drop by clogging).[1,85,87] Their oxidizing power must however be tuned in order to minimize SO_2 oxidation since formation of SO_3 and further interaction with water leads to the generation of sulfuric acid, which adds to the total particulate mass. Due to the relatively low operating temperature of these systems, supported noble metals (mainly Pt, but also Pd, and, to a lesser extent, Rh) with high oxidation activity are employed in their formulation. Among these, generally speaking the oxidation activity for CO, hydrocarbons, and SO_2 decreases in the order Pt > Pd > Rh.[1] This, along with its relatively lower availability, generally leads to the use of Rh in this type of catalyst being discarded. On the other hand, the composition of the support oxides forming the catalyst washcoat (which can include a number of different oxides such as alumina, titania, ceria, zirconia, vanadia, silica, etc.)[88–90] is usually selected to minimize the adsorption of the sulfur oxides and SOF.[1] This aims to prevent sulfate storage that could desorb as sulfuric acid at high temperatures, as well as avoiding condensation of the SOF in the pores of the catalyst that might retard its catalytic abatement. Among the washcoat metal oxides, vanadia provides interesting activity in terms of avoiding sulfate forming reactions while titania and silica appear relatively inert to sulfate adsorption, thereby being of interest for this application.[90,91] Nevertheless, the selected composition is in each case tailored as a function of the specific operating conditions. Thus, if average operating temperatures are below 523 K, very active oxidation catalysts (Pt-based) are employed because the rate of SO_2 oxidation is low for $T < 573$ K. However, a less active catalyst will be required to minimize SO_2 oxidation if higher temperatures predominate during catalyst operation. In this sense, alloys of Pt-Rh-Pd or of Pt with base metals and/or compositional modifications in the washcoat metal oxides are the main approaches employed to reach the best compromise.[6,85,87–89] Mechanistic aspects for CO and/or hydrocarbon oxidation reactions are similar to those already addressed for TWC operation (see above). Thus, a general trend of increasing CO oxidation activity and decreasing hydrocarbon oxidation activity is usually observed with increasing Pt dispersion over the support oxides.[89,92]

10.3.2 *Treatment of soot*

The gas-solid reaction involved in non-catalytic soot combustion is a relatively slow process.[85,93] Catalytic assistance (gas-solid-solid process) provides an increase in the rate of soot oxidation, although the process efficiency is mainly determined by the type of contact (tight or loose) established between the soot and the catalyst.[85,87,93,94] As mentioned above, flow-through systems are not effective for soot oxidation due to the relatively short contact time (and/or little contact points) between the soot and the catalyst. As a consequence, effective abatement of soot requires employment of filters that allow the trapping (even if loosely) of the solid portion of the exhaust until more or less complete combustion is achieved during the filter regeneration process.[85,95] An approach aimed at achieving tight catalyst-soot contact consists of the use of fuel additives (in the form of fuel soluble compounds of Mn, Fe, Cu, Ce, and Pt). In this approach, the introduced metal serves, after combustion in the engine, as a nucleus for soot deposition in such a way that a well-dispersed metal is entrapped in the soot particle in order to achieve a close soot-catalyst contact that facilitates soot oxidation in the filter.[85] The use of catalysts with relatively low melting points such as pyrovanadates, oxides of vanadium and molybdenum, and those based on different metal chlorides, molten salts, or K-doped systems also aims at increasing the contact points between soot and catalyst by taking advantage of the increased catalyst mobility.[85,95–101] A significant drawback of these high mobility catalysts is the possibility that they can be volatilized during soot oxidation resulting in loss of the catalyst and toxic emissions.[85,96,102]

Another well-recognized approach for soot abatement is the use of a supported Pt oxidation pre-catalyst (upstream of the filter) aimed at producing NO_2 (from NO oxidation), which decreases the non-catalyzed oxidation temperature of soot by approximately 200 K (from *ca.* 773 to 573 K) relative to air oxidation.[85,90,103] This is one of the basic concepts involved in the so-called NO_x-aided CRT (continuously regenerated trap), which is proposed as one of the most efficient technologies for soot abatement (Fig. 10.4).[85,104] Under

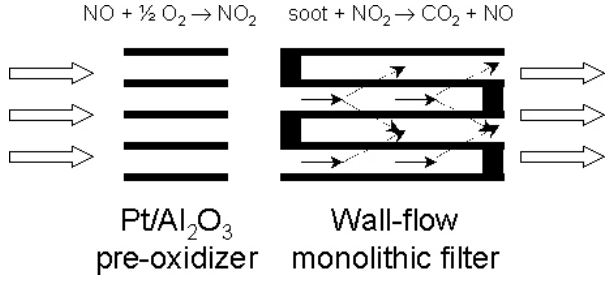

Figure 10.4 Basic scheme of the operational principle of the NO_x-aided CRT system for soot abatement.

practical operating conditions, the oxidation pre-catalyst overall converts 90% of the CO and hydrocarbons and 20–50% of the NO to NO_2.[105] Downstream, the particulate matter is trapped on a wall-flow monolith and subsequently oxidized by the NO_2.

Nevertheless, the use of a supported noble metal catalyst (usually Pt) for soot oxidation under loose contact conditions (proposed to be closer to the practical condition) results in a significant decrease in the soot oxidation temperature.[85,103,106,107] Thus, incorporation of the soot in a Pt/SiC foam catalyst allows the soot oxidation rate to be doubled (and also the maximum rate temperature to be decreased) with respect to a "non-catalyzed" situation in which the soot is incorporated into the Pt-free SiC foam (with Pt/SiC foam located upstream to promote NO oxidation). In turn, a considerable decrease in the maximum rate temperature is observed when employing NO + O_2 instead of O_2 as oxidant in the Pt/SiC-soot configuration.[107] On the basis mainly of these results, a catalytic role for NO is proposed in a recycle reaction as follows:

$$NO + \frac{1}{2}\ O_2 \overset{Pt}{\longleftrightarrow} NO_2 \tag{10.5}$$

$$NO_2 + C \rightarrow CO + NO \tag{10.6}$$

or

$$2NO_2 + C \rightarrow CO_2 + 2NO \tag{10.7}$$

in such a way that the NO produced during soot oxidation reactions (10.6) and (10.7) can be reutilized for NO oxidation in reaction (10.5).[107] In addition, a positive effect of including water in the oxidant reactant mixture is observed and attributed either to facilitation of NO_2 adsorption at the active site on the soot particles, or in decomposing surface oxygen complexes presumed to be intermediates in the oxidation of diesel soot. The latter is supported by the fact that water also increases the oxidation of soot using oxygen alone.[107] Support effects in various oxide supported Pt catalysts under loose soot-catalyst configurations have been pointed out in several studies.[103,106,108] Only subtle differences in soot oxidation profiles are generally observed between the systems and attributed to promoting effects of oxides with enhanced oxygen handling properties (CeO_2 or La_2O_3)[103] or to an activity promotion induced by SO_2 in systems employing TiO_2-SiO_2 as support.[108] The enhanced lattice oxygen mobility has also been highlighted as an important factor to explain the higher soot oxidation activity by NO_x/O_2 observed for Ce-Zr mixed oxides in comparison with pure ceria.[109] On the other hand, in addition to noble metals catalysts, supported copper has also shown potentially useful properties for the soot-NO_x/O_2 process, including its redox characteristics and the extent of copper-support interactions, with these features often being cited as the key features which explain the catalytic activity observed for a series of systems supported on various oxides.[110]

10.3.3 *Catalysts for selective reduction of NO_x with hydrocarbons*

Selective catalytic reduction (SCR) of NO_x employing hydrocarbons (HCs) as reductants constitutes a promising catalytic approach in dealing with lean-burn emissions. Basically, as shown in the following scheme, the target is promoting the NO_x reduction reaction by the hydrocarbon in a flowing atmosphere in which the predominant oxidant is oxygen and considering also the presence of potential catalytic poisons such as SO_2 as well as water.

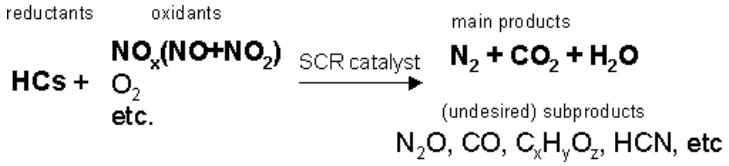

Scheme 10.1

In addition to the main products (nitrogen, carbon dioxide, and water), different subproducts can be formed as a result of partial oxidation or reduction processes. Such subproducts can be more harmful than the initial toxic reactants and as such, their formation is undesirable. Following the pioneering work by Iwamoto and coworkers which showed the activity of Cu/ZSM-5 for the process,[111,112] many systems have been tested for this reaction. Figure 10.5 gives a brief illustrative summary of different systems that have shown some success in the mentioned process.

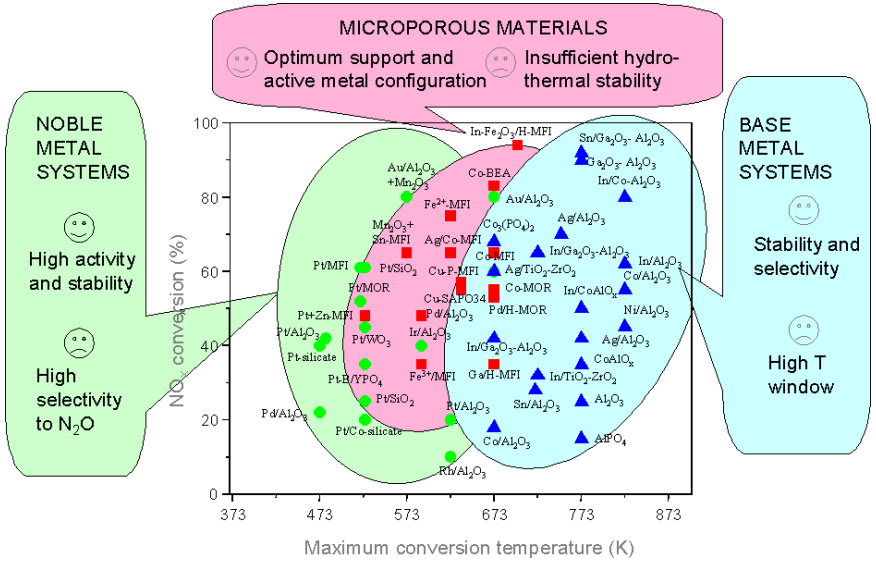

Figure 10.5 Catalytic activities of various systems for SCR of NO_x with hydrocarbons. A classification of the systems along with their general advantages and drawbacks is highlighted.

Following the approach by Iwamoto, a classification can be established on the basis of their catalytic behavior as platinum group metal and base metal systems while systems supported on microporous materials apparently provide optimum configuration of the catalytic components although their thermal stability is usually low, thus limiting their practical application.[111,113] Platinum group metal catalysts are the most active for the process although they have the drawback generally of forming substantial amounts of N_2O (a greenhouse gas — about 200 times more powerful than CO_2) and are ineffective at high temperature. Base metal systems are the least active (they only show activity at relatively high temperature) although they are usually fully selective to N_2 and can present improved thermal stability. In general terms, it will be shown that the extent of the selective reduction of NO_x depends on a series of factors such as the nature of the supported metal or of the hydrocarbon (or another co-reductant like H_2, CO, etc) employed as reductant, the type of support, as well as preparation parameters (metal precursor employed, type of pre-treatment, etc.).[112] In the following, the main catalytic properties of these systems are shown.

10.3.3.1 *Platinum group metal systems*

Various supported platinum group metal systems have been tested for the SCR process.[112] Among them, supported platinum systems appear to be the most active when jointly considering the NO_x reduction level achieved and the temperature range at which the catalyst is active, while palladium, rhodium, and iridium also show catalytic activity for the process and Rh and Ir apparently present higher selectivity to N_2.[112,114–118] Support effects are observed which generally depend on the type of hydrocarbon employed, the presence or absence of SO_2 in the reactant mixture or the type of impurities present in the support.[112] In this respect, a variety of materials like SiO_2, Al_2O_3, ZrO_2, sulfated alumina, zeolitic materials, and activated carbons have been employed as supports of the metals and tested for the process.[112–123]

General catalytic features

Figure 10.6 shows typical results observed for the NO SCR with n-octane over a supported Pt catalyst. As noted, the NO_x conversion fairly closely follows hydrocarbon oxidation at low temperature and presents a maximum at intermediate temperature after which combustion of the hydrocarbon with O_2 occurs. It can also be observed that appreciable amounts of N_2O are formed during NO reduction. Even a lower N_2 selectivity is apparently achieved when employing propene as reductant.[115] This relatively poor behavior in terms of N_2 selectivity appears independent of the support employed, in spite of the fact that overall NO_x conversions appear affected by this parameter.[112,115,123] In contrast, a certain enhancement in the N_2 selectivity has been reported to occur upon addition of promoters like Na, alkaline-earth or rare-earth oxides,[112,124] although a previous report including a number of promoters on Pt/Al_2O_3 (including alkaline

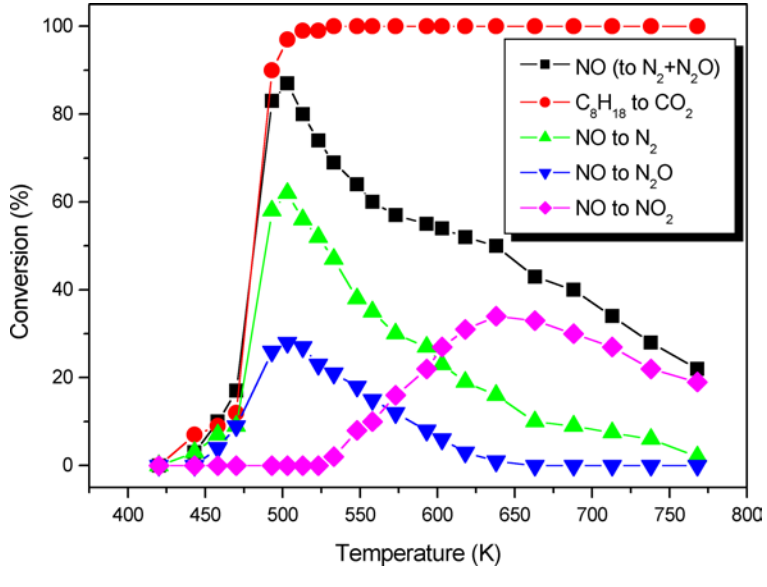

Figure 10.6 Catalytic activity observed for the NO SCR process with n-C_8H_{18} under lean conditions over a 0.3% Pt/Al_2O_3 catalyst,[122] (adapted with permission from Elsevier Science).

or alkaline-earth metals, transition metals, and rare earths) suggested no important effects in this respect.[125] The use of toluene as reducing agent appears to be another solution in this sense since no detectable amount of N_2O was observed during the selective NO_x reduction when using this reagent over Pt/Al_2O_3.[126]

Differences in NO_x conversion level are observed depending upon the type of hydrocarbon employed.[112] The selective reduction of NO_x appears more effective as the chain length or the degree of saturation of the hydrocarbon are increased, although deactivation phenomena (attributed to generation of carbonaceous deposits) may appear for relatively long chain hydrocarbons.[112,122,127] Support effects are apparent in this respect when comparing alkanes and alkenes (typically propane and propene).[112,128–130] Comparing Pt/SiO_2 and Pt/Al_2O_3 shows that the former is relatively ineffective when employing propane as reductant while it can be most active when using propene.[129,130] As will be noted below, important mechanistic consequences can be derived from this observation.[112] On the other hand, the influence of the presence of both H_2O and SO_2 in the reactant mixture also appears to depend strongly on the type of hydrocarbon employed. Thus, Pt/Al_2O_3 catalysts are appreciably less active in the presence of water when propane is used as reductant, a more moderate effect being observed when using propene.[129] Similarly, the presence of SO_2 significantly inhibits NO_x reduction when using propane as reductant.[131] This can be explained by the different deactivating effects taking place over the metal and support components of the catalyst along with consideration of the nature of the active site in each case.[131] Sulfur poisoning of the metal component (where the active sites are located when using propene as reductant) appears less relevant (even if a certain decrease in the overall activity is produced) as a consequence of its reversible character, while poisoning by sulfate species of the Al_2O_3 support (proposed as the active site when using propane as reductant) appears irreversible under normal reaction conditions, this result leading to decreases in catalytic activity.[131]

With respect to particle size effects, the catalytic activity apparently increases with decreasing Pt dispersion.[119,132] A similar result

has been observed for Ir containing systems, with the peculiarity that for Ir/Al_2O_3 the active state is only achieved following certain preconditioning of the sample (apparently the presence of CO + O_2 are required).[116] On the other hand, particle size effects on N_2 selectivity are less certain.[112]

Mechanistic aspects and nature of the active site

As treated in detail in the review work by Burch *et al.*,[112] three distinct mechanisms can be differentiated for the SCR of NO_x by hydrocarbons over Pt catalysts. The first one attributes a role of cyanide or isocyanate species in the formation of N_2 or N_2O. In this respect, although formation of such species under relatively mild (and dry) reaction conditions is well addressed in the literature (based on infrared experiments), it is not at all clear whether such species are real intermediates or mere spectators since there is no conclusive kinetic evidence correlating formation of N_2 and N_2O with the evolution of –CN or –NCO species. The absence of formation of isocyanate in the presence of water (due to its rapid hydrolysis) would oppose a significant involvement of this type of species in the reaction mechanism. A second mechanism proposes the involvement of organo-nitro and related species (resulting from hydrocarbon partial oxidation processes with O_2 or NO_x species, in a similar way as proposed for base metal systems, as indicated below) as relevant intermediates. However, although decomposition of these compounds in the pure state to N_2 or N_2O is a possible process, it is uncertain whether such specific chemical compounds play a role under realistic conditions and further experimental evidence is required to verify their role.[112] Nevertheless, this type of mechanism cannot be fully discarded from contributing to some extent under certain circumstances, particularly in cases where the catalyst remains in an oxidized state (because the reactant mixture is unable to activate the system into its more active metallic state) or when active sites are apparently located on the support (as proposed when using propane as reductant, as indicated above).

The highest NO_x reduction activity in this type of system appears to be achieved in cases where the reactant mixture is able to activate the surface of the metal to a metallic state (even under net-oxidizing conditions). In such a scenario, a mechanism similar to that operating for three-way catalysts is proposed. Thus, N_2 or N_2O are envisaged as being formed by direct dissociative adsorption of NO over the metallic surface followed by re-combination processes between the corresponding dissociated fragments and/or between these and adsorbed NO species.[112,133] Oxidation of the hydrocarbon is then expected to take place following interaction of chemisorbed hydrocarbon species with the adsorbed atomic oxygen species resulting from NO or O_2 dissociation.[112,133] Evidence in favor of this mechanism is mainly based on transient TAP reactor experiments, kinetic measurements, and steady state transient kinetic isotope experiments.[112] Support for this mechanism is also provided by kinetic differences found as a function of the type of hydrocarbon employed as reductant, which is assumed to be crucial in attaining an active metallic state for the noble metal.[112,130] Studies comparing propane and propene indicate that in the competitive adsorption between oxygen and the hydrocarbon, the unsaturated hydrocarbon (propene) competes strongly with oxygen in such a way that a metallic state is attainable and a substantial coverage with hydrocarbonaceous species can be attained. In contrast, the saturated hydrocarbon (propane) is not adsorbed in the presence of oxygen and the metal thus remains in an oxidized state unable to dissociatively adsorb NO. Full details of this mechanism can be found elsewhere.[112]

10.3.3.2 *Base metal systems*

The selective catalytic reduction (SCR) of NO_x using base or non-noble metal systems appears as a viable approximation to solve environmental problems related to the oxygen-rich exhaust streams of lean-burn engines. Cu-ZSM-5 was the first catalyst found which displayed good lean NO_x reduction activity,[134] and as a result of this discovery, the use of zeolite-based catalysts was extensively studied.

Although some of these systems, such as Co-MOR or Fe-ZSM-5,[135–137] as well as others, such as pillared-clay-based,[138] appear to have interesting properties, they appear to lack stability in the presence of water and sulfur containing streams after prolonged use. In contrast, it has been shown that bimetallic formulations such as In-Co supported on specific zeolites are highly active and stable in the presence of steam.[139,140]

A second approach makes use of oxides, such as Al_2O_3, TiO_2, ZrO_2 (and others), as supports, promoted with base metal cations. Among such cations, Co, Ni, Cu, Fe, Sn, Ga, Au, In, and Ag have all been tested, and their activity in the SCR of NO_x by hydrocarbons (HCs) has been reviewed.[112,141] These studies have mainly focused on alumina supported systems, which ensure hydrothermal stability up to high operating temperatures (1073 K), promoted with Ag[112,142,143] and In[144–146] as "active" components, as they appear as the most promising systems for operation under real conditions. Mixed supports like WO_3/ZrO_2 may also be of interest for achieving optimal catalytic performance.[147] In this section, we will review systems displaying acceptable hydrothermal stability and the corresponding implications for the establishment of an efficient system for the elimination of NO_x by HCs under lean conditions.

General features of the catalytic activity

Bimetallic In-Co systems in ferrierite and H-Beta appear the only zeolitic systems presenting high activity in presence of steam.[139,140,148] The limited information accessible in the literature, however, prevents a deep understanding of the situation. Studies mostly focus on methane/propene as hydrocarbons and show maximum activity for NO_x elimination in a broad temperature range going from 573 to 673 K. Steam does not affect activity in more than a few percent loss and in a totally reversible manner.

A more detailed scenario can be found for alumina supported systems. Figure 10.7 illustrates the typical catalytic behavior for the SCR of NO_x displayed by alumina supported systems, promoted with increasing loadings of a base metal. In this case, the catalytic activity

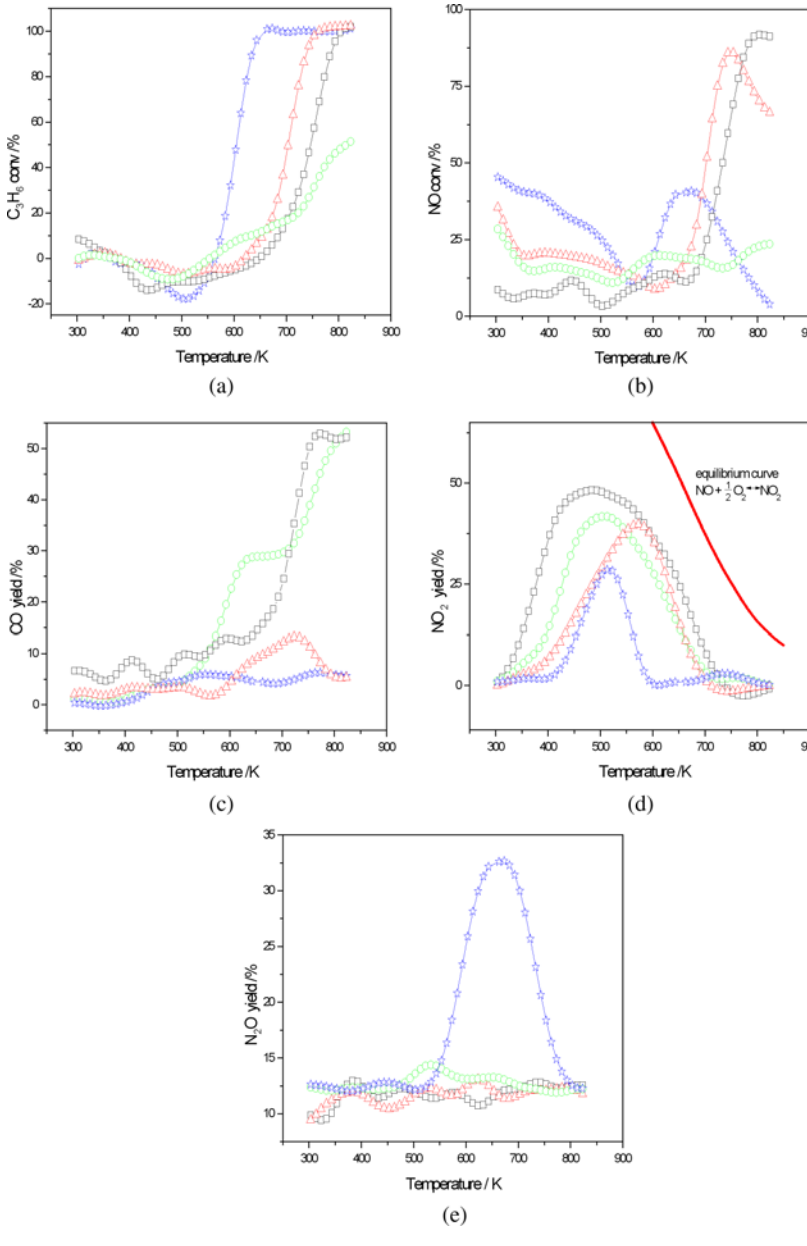

Figure 10.7 Conversion of propene (a) and of NO_x (b) to N_2 for Ag samples and the alumina support. Yields to CO (c), NO_2 (d), and N_2O (e) are shown. Circles, alumina; squares, 1.5% Ag/Al_2O_3; triangles, 4.5% Ag/Al_2O_3; stars, 6% Ag/Al_2O_3.[150]

during a light-off run is shown for the Ag promoted system using propene (C_3H_6) as reducing agent.[142] The NO and oxygen concentration used are those typically encountered in real exhaust gases and the hydrocarbon concentration is taken to be similar to that of NO_x (as commonly employed).

Hydrocarbons (HCs) from C_2 to C_{10} are commonly used to test activity. The efficiency of the HC in the SCR of NO_x in competition with the combustion reaction with oxygen increases with increasing molecular weight. This is probably due to the parallel increase in the heat of adsorption and decrease in the C–H bond strength.[149] Alkanes, alkenes, and oxygenated HCs have been studied in this reaction and the activity in the NO_x elimination frequently follows this order, with the lower light-off temperatures being displayed for the latter type of compounds. Independent of the nature of the HC and its molecular weight, its conversion follows the general pattern as described in Fig. 10.7(a). The Al_2O_3 support displays moderate activity in the presence of water while a progressive enhancement is observed with Ag loading up to *ca.* 6 wt%. Carbon containing products of the reaction are CO_2 and CO (Fig. 10.7(c)). Production of significant amounts of CO appears to be a characteristic of acidic supports,[142,143,150,151] and its elimination from the outlet has provided interesting clues concerning mechanistic aspects of the reaction.[143] In contrast, NO_x conversion (Fig. 10.7(b)) does not follow the HC oxidation pattern described. A clear maximum in activity is detected for samples having intermediate loadings (in this case, between 1.5 and 4.5 wt%) of the base metal. This appears to be a distinguishable characteristic of Ag- and In-based catalysts,[112,142–150] which can be extended to most of the systems used for the SCR reaction.[112] The support is able to eliminate NO_x even in presence of water but this is strongly promoted by the presence of the base metal above 673 K, with a sharp decrease for the 6 wt% Ag sample. This decrease always appears concomitantly with the increase in N_2O yield and loss of N_2 selectivity (Fig. 10.7(e)). The different activity and selectivity is directly related to the different nature of the active phase present under reaction conditions, as will be detailed in the following section. A final comment may be added to the performance of Ag

systems in the SCR-NO_x with biodiesel; in this case, particulates seem of critical importance and the systems display lower performance than when using diesel fuels.[152]

The presence of oxygen promotes the SCR-NO_x reaction, with a typical enhancement curve showing an increase up to *ca.* 2 vol.% and then leveling off.[112,141,144–149] When adding oxygenates to diesel exhaust streams it appears that the optimum enhancement of activity is observed for C_2 (ethanol, acetaldehyde) compounds. The promoting effect is typically attributed to a decrease in the concentration of carbonaceous deposits which otherwise block adsorption sites at the surface of the catalyst, together with a better interaction of C and N containing intermediates. A similar beneficial effect can be also attributed to the presence of water. Other beneficial effects of oxygen have been attributed to a promotion of NO_2 formation. This appears to work only for certain base metal catalysts (such as Au/Al_2O_3) in which an outstanding activity essentially attributed to this effect is obtained when physically mixed with Mn_2O_3 (Fig. 10.5),[153] while its role in the case of Ag or In systems appears more uncertain.[112] On the other hand, SO_2 is typically found in lean-burn exhaust streams and the presence of sulfate species brings about a reduction in the number of strong chemisorption sites for NO_x.[154,155] An inhibition of the SCR-NO_x by sulfur dioxide is observed in essentially all cases, but its extent depends significantly on the nature of the reductant and SO_2 concentration.[112] For Ag systems, the inhibition is minimized in cases where Cs is used as a co-promoting agent,[156] or when the Ag content (high loading) allows the presence of Ag(0), which seems to be redispersed by an effect of SO_2, under reaction conditions.[157] For In, the presence of Co induces similar effects which counteract the presence of SO_2.[146] It appears therefore that, as outlined below, multi-component formulations are needed to produce catalysts which can operate under real exhaust conditions. Additional stability in the presence of SO_2 can be reached by doping the alumina support with surface species such as TiO_2 or SiO_2.[158,159] This appears important in order to maintain activity at low temperatures.

A final point to mention is the fact that in the presence of H_2 in the inlet feed a significant decrease in light-off temperature is

produced (by *ca.* 100 K), but the physico-chemical basis for such behavior is still not clear.[160] Recent studies indicate that H_2 is particularly effective at low temperature (below *ca.* 650 K) and affects both NO_2 formation and subsequent surface storage of N compounds as well as diminishing the C-rich surface entities through an effective interaction with NO_2.[161,162] It also appears that H_2 promotion is more pronounced with short chain alkanes,[161] while it can also operate when using ethanol as reductant which can be related to promotion of its partial oxidation to acetaldehyde.[163]

Nature of the active phase

The composition and the preparation method of SCR catalysts have a dramatic influence on their activity and selectivity. This follows from the fact that, essentially in all cases, the presence of dispersed, oxidized species with strong interactions with the support appear to be essential in order to obtain reasonable activity in the SCR reaction and to limit the HC combustion reaction.[112,137,139,142–160] For zeolite supported samples, the metal-support interaction appears to play a crucial role and the presence of $(InO)^+$ species is commonly mentioned although their relevance under reaction conditions requires further exploration.[137,139,140,148] The presence of Co appears to modify the In and a redox interplay between cations, at least at the initial reaction state, is claimed.[139]

In the case of Ag, probably one of the promoter cations most widely studied, UV-vis, and XAFS techniques were able to indicate that isolated or highly dispersed Ag(I) cations yielded highly active and selective SCR catalysts. This was also a conclusion indirectly extracted by the fact that intermediate loadings of Ag were in fact adequate in order to optimize activity[112,142,164,165] and that addition of Cs also produces further stabilization of Ag(I) cations under reaction conditions.[156] However, the exact nature of the active phase was not revealed until recently when a XAFS (XANES and EXAFS) study was able to provide some further evidence. The XANES spectra of two active catalysts containing 1.5 and 4.5 wt%, and of Ag(I) containing reference samples are shown in Fig. 10.8(a).

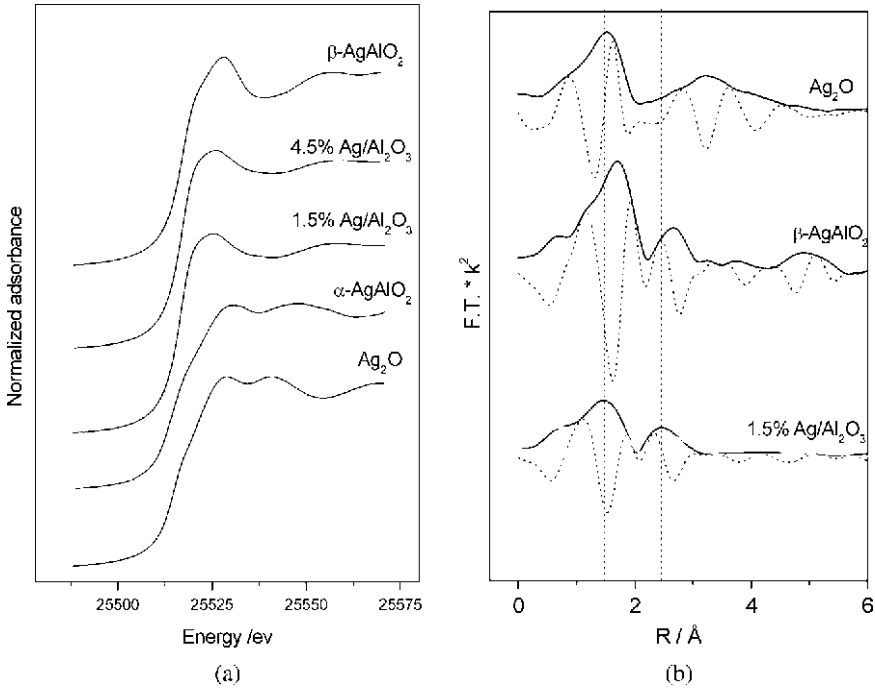

Figure 10.8 (a) XANES spectra of calcined Ag/Al_2O_3 catalysts and reference compounds. (b) FT of EXAFS spectra for an active Ag/Al_2O_3 catalyst and reference compounds (black line, calcined catalyst; gray line, post-reaction catalyst; full line, modulus; dashed line, imaginary part).[142]

The activity of these samples is displayed in Fig. 10.7, showing their qualities as SCR catalysts. Comparison of XANES spectra indicates that Ag(I) cations possess tetrahedral-like local coordination which closely resembles that of the ß-$AgAlO_2$ reference. The corresponding EXAFS spectra suggest significant local disorder around the Ag centers as well as a noticeable reduction in the average Ag-O first shell coordination distance with respect to those present in the more regular, tetrahedral-like local structure of the ß-$AgAlO_2$ material (Fig. 10.8(b)). Obviously, this local structure has notable differences with the linear structure characteristic of the Ag(I) oxide or alpha alumina (Fig. 10.8). It should be noted at this point that the linear (ß-Al_2O_3-type) $AgAl_{11}O_{17}$ aluminate has previously

been observed in calcined alumina supported silver catalysts but such samples do not display significant activity in the SCR reaction.[166] Although the promoter frequently exhibits a multiphase distribution in such samples, it may be the case that this phase usually contains excess Ag cations between the characteristic alumina layers of the beta alumina phase (allowing this phase to be described as $Ag_x(Ag_2O)_yAl_{11}O_{17}$), and its catalytic performance may be poor as a result of segregation of Ag_2O entities upon contact with the reducing agent under reaction temperatures. It may be concluded that the active Ag phases contain dispersed ions in a beta aluminate-like phase, which does not permit leaching of the promoter under reaction conditions; the stability of this phase is confirmed by EXAFS, which effectively demonstrates the low level of change suffered by the active samples (Fig. 10.8(b)). In contrast, samples showing poor SCR activity contain larger quantities of the base metal and typically suffer reduction of the active phase with the formation of reduced, zero-valent entities, which, frequently, are undetected by X-ray diffraction, indicating the formation of poorly crystalline or amorphous phases *via* a mechanism unknown at this moment.[112,142,150,164,165,167] The presence of the zero-valent chemical state can be readily monitored by the detection of N_2O resulting from NO dissociation during reaction.[142] In any case, although the formation of Ag(0) appears generally detrimental, as mentioned above, the presence of SO_2 in the reactant mixture seems to limit the negative consequences through a mechanism of redispersion of the zero-valent phase.[157]

The case of In on alumina is still relatively poorly investigated and apart from the fact that highly stable, dispersed, and oxidized species are required to obtain significant activity in the SCR reaction, further detailed information is not available.[144–146] The presence of Co as co-cation may allow a high dispersion to exist with stabilization of the previously mentioned In species.[144] Some studies have mentioned the importance of $(InO)^+$ species,[147] in a similar manner as found for zeolite supported systems. In contrast to In, the Co-only case has been thoroughly investigated as reviewed by Burch *et al.*[112]

Reaction mechanism

The overall reaction mechanism and the rate determining step of the SCR of NO over a given catalyst depend on the nature of the reductant and the experimental conditions employed. The mechanism is rather complicated and has not been fully elucidated for any given SCR catalyst. Nevertheless, a somewhat general (independent of the nature of the promoter phase) picture of the most significant steps which are likely to occur during the reaction can be drawn from the vast number of studies dedicated to this subject.

It is generally accepted that HC and NO molecules must be initially activated by formation of some oxidized, adsorbed intermediates, typically carboxylates, for the HC and NO_2, nitrite or nitrate compounds for NO.[112,142,150,168,169] Some of these activated, intermediate compounds are present on the alumina support alone, indicating that the support itself is able to promote the SRC of NO_x using HC as reducing agents. The non-noble metal is thought to play an important role in modifying the surface concentration and selectivity among these intermediates, enhancing the activity of the support. No clear general pattern for the activation mechanism for any of the reactant molecules, which is valid for all metals (or at least for Ag and In), can be extracted from studies published in the open literature. In the most widely studied case of the propene, acetate[165] or acrylate species[142,150] appear as likely intermediates, while for NO, studies performed to date would suggest that some specific nitrate groups are in fact the key intermediates.[112,142,150,165] Based on the kinetic isotope work of Cant and Cowan using methane as reductant,[170] abstraction of hydrogen from the HC was thought to be the rate determining step. However these authors were able to show that this was not the case with larger hydrocarbons,[170] probably due to the fact that the C–H bond strength decreases with increasing molecular weight. For oxygenated hydrocarbons, the principal C containing intermediates appear to be of enolic nature.[141] The rate determining step, at least in the case of propene, appears to be related to reaction of the activated, oxidized hydrocarbon intermediate on the alumina

support.[171] It would appear, therefore, that the main role of the base metal may be restricted to the initial steps of the reaction and is mainly related to activation of the reactant molecules, either on the silver surface and/or by modification of the acid/base (hydroxyls) properties of the alumina.[142,150,151] The coupling with N containing species occurs later and although very limited information is available on this aspect, the formation of isocyanate species is always mentioned. It can be noted, however, that strong indications for a role of gas phase reactions in determining N_2 selectivity are observed for both In[172] and Ag[143,173] samples. Experiments analyzing the influence of residence time after the catalysts, as well as the mixing of the SCR catalyst with several solids, indicate the importance of the gas phase reaction after the rate determining step and, in particular, in determining N_2 selectivity.

10.3.3.3 *Practical approaches*

Limitations in the activity of SCR catalysts under practical conditions due to a number of factors such as an inadequately wide temperature range showing sufficient activity, lack of hydrocarbon reductant in the exhaust gas (Table 10.1), influence of poisons, or varying flow rates of the exhaust gas, has led researchers to consider other non-catalytic or catalytic approaches to the problem.[4,86,174,175] Among the latter, auxiliary injection of reductant (either the diesel fuel itself, or selected hydrocarbons, or oxygenated organic reagents) has been considered as a practical solution to compensate for the lack of reductant or to increase the temperature window of catalyst operation,[4,175,176] while multilayer configurations including catalysts of different functionalities (basically combinations of platinum group and base metal catalysts) have been suggested.[4,177] Outstanding results in this respect have been obtained by combined injection of diesel fuel and oxidants (O_2 and H_2O) through use of partial oxidation catalysts. Generation of aldehydes in such a process has been shown to significantly increase the de-NO_x activity of $AgAlO_2/Al_2O_3$ catalysts.[175]

10.3.4 *Catalysts for NH_3- or urea-SCR*

The more stringent regulations proposed in Euro V (2009) or Euro VI (2014) proposals (or their equivalents in the USA or Japan), requiring further decreases in NO_x emissions, has led automotive manufacturers to consider other alternatives, given the considerable difficulties in achieving such objectives using hydrocarbon-SCR approaches, as exposed in the previous section. Among these, NSR technology, which will be discussed in Section 10.4, is considered most viable for light-duty vehicles. In turn, a catalytic strategy which could fulfill present or future regulations for both light- or heavy-duty vehicles (particularly trucks among the latter), has been commercially available since 2005, and is related to NH_3-SCR.[178,179] This is a well-established NO_x abatement technology in the case of stationary applications such as boilers, incinerators, or stationary diesel engines. Recent reviews proposing extension of its application to NO_x control in mobile sources are available.[178,180,181] The main reaction involved in the process is the so-called standard SCR in which both NO and O_2 act as oxidants of NH_3 (produced from decomposition of urea, which is considered as the most promising external NH_3 source due to safety and volume-restriction issues).[178,180,181]

$$4NH_3 + 4NO + O_2 \rightarrow 4N_2 + 6H_2O. \qquad (10.8)$$

Nevertheless, other reactions involving NO_2 as reactant, pure SCR process (without O_2 involvement), ammonium nitrate formation (with further decomposition), or partial unselective NO or NO_2 reduction yielding N_2O can also take place to some extent.[180,182,183] The use of NSR-produced NH_3 within combined NSR-SCR strategies has been also considered to enhance overall NO_x removal efficiency.[183–185]

Classical catalysts employed by industry for stationary processes have been shown to display acceptable performance in the more complex, as a consequence of the changing reaction atmosphere or temperature conditions as well as the generally higher spatial

velocity required, mobile applications.[178,180] They are based on anatase TiO_2-supported V_2O_5-WO_3 or V_2O_5-MoO_3.[178,180,181,186] Active sites are considered to be related to the V_2O_5 component while tungsten or molybdenum oxide apparently act mainly as stabilizers impeding TiO_2 phase transformation from anatase to rutile with consequential surface area loss. In turn, the use of TiO_2 as a support is associated with minimization of poisoning effects by SO_2.[186] As examined by theoretical calculations, taking into account experimental results, the reaction appears to start with the activation of ammonia on Brønsted acidic V-OH sites leading to formation of NH_4^+. This then reacts with NO to produce an NH_2NO complex which decomposes into N_2 and H_2O.[187] In this context, the stronger adsorption energy of NH_3 with respect to NO on this type of catalyst must be considered.[186] Nevertheless, a relevant mechanistic role for NO-derived surface species like nitrate or, most particularly, nitrite has been also pointed out.[183]

The classical vanadia system can apparently present some limitations for mobile applications, which have been related to the relatively low stability at high temperature of the titania support.[182] This has led to the use of new zeolite-based catalysts promoted by transition metals such as iron and copper.[178,182,188,189] Results comparing different iron containing catalysts supported on alumina, titania, and beta zeolite indicate the order of SCR performance to be Fe/zeolite >> Fe/TiO_2 > Fe/Al_2O_3 which was in the same order as the capacity to adsorb ammonia.[188] In addition to enhancing high-temperature NO_x abatement performance, zeolite-based catalysts are shown to improve low-temperature activity and to present a lower sensitivity to the use of non-ideal NO_2/NO_x ratios in the inlet mixture in comparison with vanadia-based catalysts.[178] Even though both Fe-zeolite and Cu-zeolite systems display high SCR activity, differences are found between them and have been related to their specific activity for the various reactions involved in the process.[182] In any case, as in the case of vanadia-based systems,[183] surface nitrates/nitrites which would further react with ammonia are considered as key intermediates in the reaction mechanism.[182,183]

On the other hand, considering the practical application, slip catalysts are generally required at the outlet of the SCR reactor in order to remove secondary emissions which typically include a certain concentration of ammonia, isocyanic acid (originating from incomplete urea decomposition), nitrous oxide, and nitrohydrocarbons.[178,181]

10.4 Mixed Oscillating Emissions

10.4.1 *NO_x storage and reduction catalysts*

Storage and reduction catalysts (NSR) offer the possibility of controlling NO_x emissions from automobile sources while permitting operation under predominantly lean-burn conditions.[190–193] The concept is based upon the storage of NO_x under lean conditions on an alkaline-earth oxide component, such as baria, which is then released during intermittent rich/stoichiometric periods where the stored NO_x is released and reduced by H_2, CO or HC over the noble metal component (Fig. 10.9).

The process has been thoroughly examined in two recent reviews which focus on mechanistic and fundamental issues associated with the system.[194,195] Given the focus of this book, our chapter will concern itself primarily with the roles performed by the metal component/s. Although the majority of studies involve Pt as the metal of choice,[190,193] studies involving Pd,[196–198] Rh,[192] and combinations of Pt and Rh,[199–202]

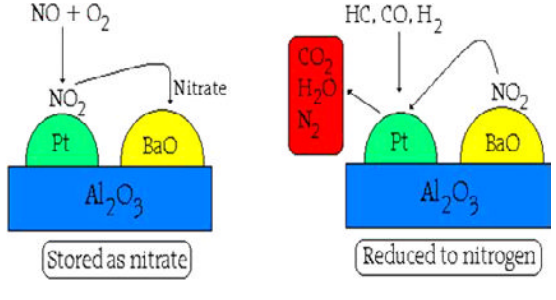

Figure 10.9 Operational concept of NSR catalyst.

Pt and Pd,[199] and Pt, Pd, and Rh,[203] have been performed. In principle the role of the noble metal[190,191] component is two-fold:

- Oxidation of NO to NO_2 which is catalyzed by the supported metal;
- Reduction of the released NO_x to N_2 by the reductants.

In the following section, the contribution of the noble metal component will be discussed with regard to its contribution (i) during the storage (lean conditions) process, then (ii) during the NO_x release and reduction process (stoichiometric/rich conditions) and, finally, (iii) involving the deactivation and reactivation due to sulfate poisoning.

(i) Although NO_x can be stored over BaO containing catalysts in the absence of the noble metal,[204–206] it is most readily stored when supplied in the form of NO_2,[204,206,207] but slow when NO_x is supplied in the form of NO,[208] confirming that the storage process is enhanced by the metal catalyzed oxidation of NO to NO_2. The extent of storage is therefore less in the absence of the noble metal.[207,209] Increasing the Pt loading from 0.02 to 0.2 wt% significantly enhances storage but only slight improvement is gained above this loading.[210] Such improvements as a function of metal loading/dispersion may not be apparent in cases where long storage periods are employed[211] but may be more prevalent when low temperatures are employed[212] and/or where "fast" sorption capacities are tested.[213] It is known that NO oxidation rate per site (TOF) is increased as dispersion is decreased in the case of Pt.[214] Fanson *et al.,*[215] in contrast to this widely accepted view, report that the oxidation of NO to NO_2 is not a critical step in the storage process and that NO is oxidized on the baria component by oxygen spilt over from Pt. Although NO may be directly adsorbed by baria in the form of nitrite species,[208,216] these may be slowly converted to nitrates, possibly by oxidation with NO_2[192,216] or by oxygen supplied by Pt.[208] In the case of oxidation of nitrites by NO_2, the reaction is thought to occur over the storage component[192,216] with no contribution from

the metal other than the initial oxidation of NO to provide the NO_2. Sensitivity to metal loading/dispersion[210,214] may be a consequence of exposure of Pt to NO/NO_2 which leads to oxidation of smaller particles to Pt^{2+} or Pt^{4+} which show reduced activity for NO oxidation.[217] Increasing Pt loading, in addition to avoiding oxidation of smaller more sensitive particles, may give increased storage due to the increased number of interactions with baria, thereby increasing the storage area.[199] However, loss of dispersion through sintering after heat treatment above 973 K under oxidizing conditions, leads to substantial losses of storage ability.[218] Pd shows higher NO_x storage ability than Pt[194,219] and Rh may perform better than Pt[220] although this may be limited[195] to specific supports.

In addition to its role in the oxidation process, there are some indications that the metal component may perform additional functions during storage other than merely oxidation of NO to NO_2. As the barium oxide exists primarily as carbonate in the prepared form as confirmed by XRD and FTIR studies,[221,222] there is a suggestion[223] that Pt enhances the decomposition of this barium carbonate and thus facilitates NO_x storage. However it is often difficult to make a direct comparison of Pt containing and Pt-free Ba/Al_2O_3 catalysts regarding bulk phases as XRD patterns of the as-prepared catalysts for the former tend to show lines due to bulk carbonate which are absent or less intense than in their Pt-free counterparts.[224] This is probably a consequence of the use of acidic H_2PtCl_6 as Pt precursor which appears to redisperse barium containing phases during the two-stage preparation procedure[225] although there is a suggestion that the blocking of sites for CO_2 adsorption by retained chloride ions may also play a role.[209] The appearance of weaker maxima at 1554 and 1324 cm^{-1} in FTIR spectra of Pt containing Ba/Al_2O_3 catalysts compared to Pt-free samples[209] may therefore be the consequence of different characteristics of the starting material rather than due to any advantages induced by a Pt catalyzed decomposition of carbonate species.

As the addition of Pt precursor may influence the subsequent dispersion of the baria component,[209,224,225] and nitrate formation is often observed to be limited to the surface regions of the storage

component rather than leading to bulk phases,[209,221,226] comparison of NO_x storage capacities in the presence and absence of the noble metal may provide misleading information concerning the role of Pt during the storage process. The NO_x storage capacity has been shown[209] to increase in the order, $Al_2O_3 < Ba/Al_2O_3 < Pt/Ba/Al_2O_3$ which provides support for the proposal[192,209,223] that the noble metal provides atomic oxygen which facilitates the uptake of NO_x by the baria. This may involve enhanced peroxide formation, which has been suggested[227] as a route to nitrate formation over supported baria in the absence of Pt. NO_x storage over baria in the absence of Pt as a supplier of atomic oxygen would therefore be limited to a few specific sites whose concentration is a function of dispersion and other preparation variables. This is consistent with the reduced NO_x uptakes observed in the absence of the metal.[207,209] Most models therefore involve oxidation of NO to NO_2 over the active metal, followed by spillover of NO_2 onto the storage component.[228] Further oxygen is required to convert NO_2 (N oxidation state IV) to NO_3^- (N oxidation state V). An alternative to the spillover of activated oxygen[192,223] to convert NO_2 to nitrate involves activated forms of NO_2.[223]

(ii) During a switch to rich mixture, the presence of Pt may lead to the catalytic decomposition of $Ba(NO_3)_2$.[226] Although the exact role of Pt in this process was not clear, this may be similar to the steps indicated by Balcon *et al.*[201] where NO_2 is released due to displacement by CO_2 which would be prevalent during the stoichiometric switch, and which provides a carbon-rich feed stream. Although stored NO_x is destabilized in the presence of propene leading to a lowering of its release temperature relative to experiments in air or nitrogen,[209,229] the release of NO_x occurs at temperatures significantly lower than the light-off temperature for the hydrocarbon, indicating that the stored NO_x decomposition is not driven by an increase in gaseous CO_2 concentration. Additionally, the extent of the destabilization was independent of the propene partial pressure.[229] Whereas Takahashi *et al.*[190] indicate that NO_x reduction efficiency is independent of the type of reductant but dependent

only on the stoichiometric ratio, there are indications that in terms of regenerating a nitrated trap catalyst, the order of efficiency is $H_2 > CO > HC$.[200,224,230] The differences in efficiency may arise from different reduction mechanisms for the different reductants, with hydrogen reducing NO_x *via* ammonia formation whereas use of CO may proceed *via* formation of surface cyanates and isocyanides.[231] The release and reduction mode mechanism is usually rather simplistically shown[190] as a reductant interacting with a metal site followed by reduction of stored NO_3^-. Using this model, it is unclear as to whether nitrate decomposition releases NO_2/NO followed by spillover to the metal and reaction, or whether activated reductant molecules are released by the metal where reaction proceeds with the stored NO_3^- over the baria. Olsson *et al.*[228] suggest that the specific pathway depends on the type of reductant employed, with propene for example undergoing reaction with NO_x on the metal. Propane, on the other hand, may undergo reaction with NO_2 on the support.[232] Under isothermal conditions, reduction using hydrogen is thought to involve a catalytic pathway involving Pt rather than *via* thermal decomposition.[233] Experiments using model catalysts show[224] that in the absence of reductant, less than 10% of NO_x is released as NO, whereas the presence of reductant leads to significant NO release which is independent of the presence of Pt. Results suggest that while formation of N_2 from stored NO_x requires the presence of reduced noble metal sites, formation of NO can take place over the support alone, probably by direct interaction between reductant and stored nitrate. The role of Pt in providing activated spillover reductant is important for the decomposition of certain forms of NO_x stored by the alumina.[224] Modeling studies also include[228] reaction steps which allow for spillover of hydrocarbon species from the metal component where they react directly with NO_x stored on the baria component. The fact that the light-off curves for C_3H_6 and hydrogen were displaced to higher temperatures in the presence of stored NO_x[209,224] illustrates that NO_x is reverse spilled over onto the platinum surface[228] during regeneration of the nitrated trap. Pd is believed to show better reduction ability compared to Pt.[195] If Pt is oxidized under lean conditions,[199,217] then this

may be rationalized, at least in part, due to the more facile conversion of Pd^{2+} to Pd compared to reduction of Pt.[198] Some NO_x is released during the initial lean to rich switch and this amount is temperature sensitive[211,234] but may also show sensitivity to Pt loading.[211]

(iii) The NO_x storage capacity of NSR catalysts is lowered as a function of time on-stream as a consequence of accumulation of sulfur as sulfate on the storage component.[235,236] The choice of noble metal or metal combination may be crucial in determining deactivation as there are indications that sulfate formation is promoted by Pt but inhibited by Rh.[237] Another report, however, indicated that the NO_x storage capacity was deactivated faster in the presence of SO_2 for an Rh containing catalyst than when Pt alone was employed.[199] Pt shows better sulfur tolerance than Pd.[195] The addition of transition metals such as Fe to the $Pt/Ba/Al_2O_3$ system may enhance durability[215,238] by inhibiting the growth of $BaSO_4$ particles which are formed.[238] In the absence of noble metals,[237] or in the absence of oxygen,[239] the extent of sulfate formation is reduced, probably indicating that the deactivation process involves oxidation of SO_2 to SO_3 over the metal component followed by SO_3 adsorption on the storage component. There are reports that $BaSO_4$ may be formed, however, even in the absence of Pt.[240] An alternative to the use of sulfur resistant storage materials using, for example, TiO_2 in place of BaO,[202] might involve a selection of metals or combination of metals which exhibit high selectivity for NO oxidation but low selectivity for SO_2 oxidation. In this context, Fridell and coworkers have investigated the addition of metal oxide additives including WO_3, MoO_3, V_2O_5, and Ga_2O_3 on the deactivation of $Pt/Ba/Al_2O_3$.[241] Although MoO_3 addition enhanced NO oxidation and showed the lowest SO_2 oxidation activity, the storage capacity of the modified catalyst declined faster than the unmodified $Pt/Ba/Al_2O_3$. The NO_x storage capacity may be readily regenerated under reducing conditions where the extent of deactivation is relatively low,[239,242] although, in more severe cases, even extended regeneration periods

fail to recover the initial storage capacity.[235,242] This transition in the ease by which sulfate may be removed may be associated with the transition from surface to bulk sulfates,[236] however, this is difficult to visualize given that bulk barium carbonate still retains NO_x storage ability and it is often found that NO_x storage is a surface rather than a bulk phenomenon.[221,226] It is also possible that sulfate particle size governs the ease by which this phase is decomposed.[238] The difficulty in complete regeneration following sulfate formation may be linked to the regeneration procedure employed, as this invariably involves exposure of the catalyst to a reducing atmosphere at high temperature which leads to the formation of sulfide species. Although some of this sulfide is associated with Ba,[235] there is also evidence that sulfide becomes associated with the metallic component,[203,236] which therefore hinders further regeneration *via* reduction. Pt and Pd both appear susceptible to sulfide formation,[203,236] while there is little evidence for sulfidation of Rh. A combination of Pt and Rh was found to provide good sulfur regeneration qualities.[199] For $Pt/Ba/Al_2O_3$ systems, the order of regeneration efficiency was found to be $H_2 > CO > C_3H_6$.[239] As the presence of water during the regeneration procedure may be beneficial, allowing for hydrolysis to remove surface sulfides,[203] the regenerating gas should contain hydrogen or hydrocarbon. Complete regeneration in hydrogen alone is not possible, even at elevated temperatures.[235] The addition of CO_2 to a hydrogen containing stream may also have benefits when attempting to regenerate sulfate poisoned catalysts, as the carbonate can displace S^{2-} under rich conditions.[235]

Acknowledgements

We thank Drs. A. Iglesias-Juez, A.B. Hungría, A. Kubacka, M.A. Newton, and Z. Liu, and Profs. J. Soria and G. Munuera for useful comments and discussions. Support from CICYT (Project MAT2000-1467), the EPSRC, and the Royal Society (London) is gratefully acknowledged.

References

1. E.S.J. Lox, B.H. Engler, in *Environmental Catalysis*, Eds.: G. Ertl, H. Knözinger, J. Weitkamp, Wiley-VCH, Weinheim, 1999, 1.
2. A. Martínez-Arias, M. Fernández-García, A.B. Hungría, A. Iglesias-Juez, K. Duncan, R. Smith, J.A. Anderson, J.C. Conesa, J. Soria, *J. Catal.* 2001, **204**, 238.
3. J. Kašpar, P. Fornasiero, N. Hickey, *Catal. Today* 2003, **77**, 419.
4. A. Obuchi, I. Kaneko, J. Oi, A. Ohi, A. Ogata, G.R. Bamwenda, S. Kushiyama, *Appl. Catal. B: Env.* 1998, **15**, 37.
5. W. Bögner, M. Krämer, B. Krutzsch, S. Pischinger, D. Voigtländer, G. Wenninger, F. Wirbeleit, M.S. Brogan, R.J. Brisley, D.E. Webster, *Appl. Catal. B: Env.* 1995, **7**, 153.
6. R.M. Heck, R.J. Farrauto, *Appl. Catal. A: Gen.* 2001, **221**, 443.
7. N. Takahashi, H. Shinjoh, T. Iijima, T. Suzuki, K. Yamazaki, K. Yokota, H. Suzuki, N. Miyoshi, S. Matsumoto, T. Tanizawa, T. Tanaka, S. Tateishi, K. Kasahara, *Catal. Today* 1996, **27**, 63.
8. M. Shelef, R.W. McCabe, *Catal. Today* 2000, **62**, 35.
9. K.C. Taylor, *Catal. Rev.* 1993, **35**, 457.
10. R. Heck, R. Farrauto, *Catalytic Air Pollution Control: Commercial Technology*, Van Nostrand Reinhold, New York, 1995.
11. A. Trovarelli, *Catal. Rev.* 1996, **38**, 439.
12. R.J. Farrauto, R.M. Heck, *Catal. Today* 1999, **51**, 351.
13. H.S. Gandhi, G.W. Graham, R.W. McCabe, *J. Catal.* 2003, **216**, 433.
14. S.H. Oh, G.B. Fisher, J.E. Carpenter, D.W. Goodman, *J. Catal.* 1986, **100**, 360.
15. J.H. Holles, M.A. Switzer, R.J. Davis, *J. Catal.* 2000, **190**, 247.
16. C.E. Hori, A. Brenner, K.Y. Simon Ng, K.M. Rahmoeller, D. Belton, *Catal. Today* 1999, **50**, 299.
17. C. de Leitenburg, A. Trovarelli, J. Kašpar, *J. Catal.* 1997, **166**, 98.
18. S. Bernal, F.J. Botana, J.J. Calvino, M.A. Cauqui, G.A. Cifredo, A. Jobacho, J.M. Pintado, J.M. Rodriguez-Izquierdo, *J. Phys. Chem.* 1993, **97**, 4118.
19. F. Le Normand, J. Barrault, R. Breault, L. Hilaire, A. Kiennemann, *J. Phys. Chem.* 1991, **95**, 257.
20. P. Bera, K.C. Patil, V. Jayaram, G.N. Subbanna, M.S. Hegde, *J. Catal.* 2000, **196**, 293.

21. A. Martínez-Arias, J. Soria, J.C. Conesa, X.L. Seoane, A. Arcoya, R. Cataluña, *J. Chem. Soc. Faraday Trans.* 1995, **91**, 1679.
22. H. Muraki, Y. Fujitani, H. Shinjoh, *Appl. Catal.* 1986, **22**, 325.
23. M. Ozawa, M. Kimura, A. Isogai, *J. Alloys Compd.* 1993, **193**, 73.
24. G. Ranga Rao, J. Kašpar, S. Meriani, R. di Monte, M. Graziani, *Catal. Lett.* 1994, **24**, 107.
25. J. Kašpar, P. Fornasiero, in *Catalysis by Ceria and Related Materials*, Ed.: A. Trovarelli, Imperial College Press, London, 2002, 217.
26. G. Balducci, P. Fornasiero, R. di Monte, J. Kašpar, S. Meriani, M. Graziani, *Catal. Lett.* 1995, **33**, 193.
27. R.T. Baker**,** S. Bernal, G. Blanco, A.M. Cordón, J.M. Pintado, J.M. Rodriguez-Izquierdo, F. Fally, V. Perrichon, *Chem. Commun.* 1999, **2**, 149.
28. P. Fornasiero, T. Montini, M. Graziani, J. Kašpar, A.B. Hungría, A. Martínez-Arias, J.C. Conesa, *Phys. Chem. Chem. Phys.* 2002, **4**, 149.
29. G. Colón, M. Pijolat, F. Valdivieso, H. Vidal, J. Kašpar, E. Finocchio, M. Daturi, C. Binet, J.C. Lavalley, R.T. Baker, S. Bernal, *J. Chem. Soc. Faraday Trans.* 1998, **94**, 3717.
30. J.C. Conesa, *J. Phys. Chem. B* 2002, **106**, 3402.
31. H.W. Jen, G.W. Graham, W. Chun, R.W. McCabe, J.-P. Cuif, S.E. Deutsch, O. Touret, *Catal. Today* 1999, **50**, 309.
32. A. Martínez-Arias, M. Fernández-García, A.B. Hungría, J.C. Conesa, G. Munuera, *J. Phys. Chem. B* 2003, **107**, 2667.
33. M. Fernández-García, A. Martínez-Arias, A.B. Hungría, A. Iglesias-Juez, J.C. Conesa, J. Soria, *Phys. Chem. Chem. Phys.* 2002, **4**, 2473.
34. P. Fornasiero, G. Ranga Rao, J. Kašpar, F. L'Erario, M. Graziani, *J. Catal.* 1998, **175**, 269.
35. H. Muraki, G. Zhang, *Catal. Today* 2000, **63**, 337.
36. A. Iglesias-Juez, A. Martínez-Arias, A.B. Hungría, J.A. Anderson, J.C. Conesa, J. Soria, M. Fernández-García, *Appl. Catal. A: Gen.* 2004, **259**, 207.
37. S. Bernal, G. Blanco, J.J. Delgado, J.M. Pintado, J.M. Rodríguez-Izquierdo, *J. Alloys Comp.* 2002, **344**, 347.
38. S. Roesch, P. Sermon, A. Wallum, P.N. Forrest, P. Kaur, *Top. Catal.* 2001, **16/17**, 1.
39. T. Bunluesin, E.S. Putna, R.J. Gorte, *Catal. Lett.* 1996, **41**, 1.
40. X. Xu, D.W. Goodman, *J. Phys. Chem.* 1993, **97**, 7711.

41. M. Fernández-García, A. Martínez-Arias, L.N. Salamanca, J. Coronado, J. Anderson, J.C. Conesa, J. Soria, *J. Catal.* 1999, **187**, 474.
42. D.R. Rainer, M. Koranne, S.M. Vesecky, D.W. Goodman, *J. Phys. Chem. B* 1997, **101**, 10769.
43. M. Fernández-García, A. Martínez-Arias, A. Iglesias-Juez, A.B. Hungría, J.A. Anderson, J.C. Conesa, J. Soria, *Appl. Catal. B: Env.* 2001, **31**, 39.
44. A. Badri, C. Binet, J.-C. Lavalley, *J. Chem. Soc. Faraday Trans.* 1996, **92**, 1603.
45. A. Bensalem, J.-C. Muller, D. Tessier, F. Bozon-Verduraz, *J. Chem. Soc. Faraday Trans.* 1996, **92**, 3233.
46. I.S. Stara, V. Matolin, *Surf. Sci.* 1994, **313**, 99.
47. V.H. Sandoval, C.E. Gigola, *Appl. Catal. A: Gen.* 1996, **148**, 81.
48. D. Ciuparu, A. Bensalem, L. Pfefferle, *Appl. Catal. B: Env.* 2000, **26**, 241.
49. X. Xu, P. Chen, D.W. Goodman, *J. Phys. Chem.* 1994, **98**, 9242.
50. A.S. Mamede, G. Leclercq, E. Payen, P. Granger, J. Grimblot, *J. Molec. Struct.* 2003, **651–653**, 353.
51. D.R. Rainer, S.M. Vesecky, W.S. Oh, D.W. Goodman, *J. Catal.* 1997, **167**, 234.
52. A. Martínez-Arias, A.B. Hungría, M. Fernández-García, A. Iglesias-Juez, J.A. Anderson, J.C. Conesa, *J. Catal.* 2004, **221**, 85.
53. I. Nakamura, T. Fujitani, H. Hamada, *Surf. Sci.* 2002, **514**, 409.
54. A. Martínez-Arias, M. Fernández-García, A. Iglesias-Juez, A.B. Hungría, J.A. Anderson, J.C. Conesa, J. Soria, *Appl. Catal. B: Env.* 2001, **31**, 51.
55. S.J. Cho, S.K. Kang, *J. Phys. Chem. B* 2000, **104**, 8124.
56. M. Fernández-García, A. Martínez-Arias, A. Iglesias-Juez, A.B. Hungría, J.A. Anderson, J.C. Conesa, J. Soria, *J. Catal.* 2003, **214**, 220.
57. J.Z. Shyu, K. Otto, W.L.H. Watkins, G.W. Graham, R.K. Belitz, H.S. Gandhi, *J. Catal.* 1988, **114**, 23.
58. M.Yu. Smirnov, G.W. Graham, *Catal. Lett.* 2001, **72**, 39.
59. I. Yang, O. Kresnawahjuesa, R.J. Gorte, *Catal. Lett.* 2001, **72**, 33.
60. M.A. Newton, C. Belver-Coldeira, A. Martínez-Arias, M. Fernández-García, *Nature Materials* 2007, **6**, 528.
61. M.A. Newton, C. Belver-Coldeira, A. Martínez-Arias, M. Fernández-García, *Angew. Chem. Int. Ed.* 2007, **46**, 8629.

62. A. Kubacka, A. Martínez-Arias, M. Fernández-García, M.A. Newton, *Catal. Today* 2009, **145**, 288.
63. A. Kubacka, A. Martínez-Arias, M. Fernández-García, M. Di Michiel, M.A. Newton, *J. Catal.* 2010, **270**, 275.
64. A. Martínez-Arias, M. Fernández-García, A. Iglesias-Juez, A.B. Hungría, J.A. Anderson, J.C. Conesa, J. Soria, *Appl. Catal. B: Env.* 2002, **38**, 151.
65. J.A. Botas, M.A. Gutiérrez-Ortiz, M.P. González-Marcos, J.A. González-Marcos, J.R. González-Velasco, *Appl. Catal. B: Env.* 2001, **32**, 243.
66. G.W. Graham, H.-W. Jen, W. Chun, R.W. McCabe, *J. Catal.* 1999, **182**, 228.
67. A.B. Hungría, J.J. Calvino, J.A. Anderson, A. Martínez-Arias, *Appl. Catal. B: Env.* 2006, **62**, 359.
68. G.L. Haller, D. Resasco, *Adv. Catal.* 1989, **36**, 173.
69. S. Bernal, J.J. Calvino, M.A. Cauqui, J.M. Gatica, C. Larese, J.A. Pérez Omil, J.M. Pintado, *Catal. Today* 1999, **50**, 175.
70. A. Iglesias-Juez, A. Martínez-Arias, M. Fernández-García, *J. Catal.* 2004, **221**, 148.
71. C. Larese, F. Cabello Galisteo, M. López Granados, R. Mariscal, J.L.G. Fierro, M. Furió, R. Fernández Ruiz, *Appl. Catal. B: Env.* 2003, **40**, 305.
72. R. Van Yperen, D. Linder, L. Mubmann, E.S. Lox, T. Kreuzer, *Stud. Surf. Sci. Catal.* 1998, **116**, 51.
73. R. Di Monte, P. Fornasiero, J. Kaspar, P. Rumori, G. Gubitosa, M. Graziani, *Appl. Catal. B: Env.* 2000, **24**, 157.
74. B. Coq, F. Figueras, *J. Mol. Catal. A: Chem.* **2001**, 173, 117.
75. M. Fernández-García, A. Martínez-Arias, A. Iglesias-Juez, A.B. Hungría, J.A. Anderson, J.C. Conesa, J. Soria, *J. Catal.* 2000, **194**, 385.
76. A.B. Hungría, A. Iglesias-Juez, A. Martínez-Arias, M. Fernández-García, J.A. Anderson, J.C. Conesa, J. Soria, *J. Catal.* 2002, **206**, 281.
77. A. Iglesias-Juez, A.B. Hungría, A. Martínez-Arias, J.A. Anderson, M. Fernández-García, *Catal. Today* 2009, **143**, 195.
78. A. Elhamdaoui, G. Begeret, J. Massadier, M. Primet, R. Renouprez, *J. Catal.* 1994, **148**, 47.
79. M. Fernández-García, J.C. Conesa, A. Clotet, J.M. Ricart, N. López, F. Illas, *J. Phys. Chem. B* 1998, **102**, 141.

80. A.B. Hungría, M. Fernández-García, J.A. Anderson, A. Martínez-Arias, *J. Catal.* 2005, **235**, 262.
81. A. Martínez-Arias, M. Fernández-García, A.B. Hungría, A. Iglesias-Juez, J.A. Anderson, *Catal. Today* 2007, **126**, 90.
82. T.E. Hoost, G.W. Graham, M. Shelef, O. Alexeev, B.C. Gates, *Catal. Lett.* 1996, **38**, 57.
83. M. Schmal, M.A.S. Baldanza, M.A. Vanice, *J. Catal.* 1999, **185**, 138.
84. J.F. Trillat, J. Massadier, B. Morawek, H. Praliaud, A.J. Renouprez, *Stud. Surf. Sci. Catal.* 1998, **116**, 103.
85. B.A.A.L. van Setten, M. Makkee, J.A. Moulijn, *Catal. Rev.* 2001, **43**, 489.
86. K.M. Adams, J.V. Cavataio, R.M. Hammerle, *Appl. Catal. B: Env.* 1996, **10**, 157.
87. B.J. Cooper, S.A. Roth, *Plat. Met. Rev.* 1991, **35**, 178.
88. R.J. Farrauto, K.E. Voss, *Appl. Catal. B: Env.* 1996, **10**, 29.
89. J.A.A. van den Tillaart, J. Leyrer, S. Eckhoff, E.S. Lox, *Appl. Catal. B: Env.* 1996, **10**, 53.
90. G. Corro, *React. Kinet. Catal. Lett.* 2002, **75**, 89.
91. M.R. Kim, D.H. Kim, S.I. Woo, *Appl. Catal. B: Env.* 2003, **45**, 269.
92. Y.-F. Yu Yao, *Ind. Eng. Chem. Prod. Res. Dev.* 1980, **19**, 293.
93. B.R. Stanmore, J.F. Brilhac, P. Gilot, *Carbon* 2001, **39**, 2247.
94. B.A.A.L. van Setten, J.M. Schouten, M. Makkee, J.A. Moulijn, *Appl. Catal. B: Env.* 2000, **28**, 253.
95. G. Saracco, N. Russo, M. Ambrogio, C. Badini, V. Specchia, *Catal. Today* 2000, **60**, 33.
96. G. Mul, F. Kapteijn, J.A. Moulijn, *Appl. Catal. B: Env.* 1997, **12**, 33.
97. S. Liu, A. Obuchi, J. Oi-Uchisawa, T. Nanba, S. Kushiyama, *Appl. Catal. B: Env.* 2001, **30**, 259.
98. C. Querini, M. Ulla, F. Requejo, J. Soria, U. Sedran, E. Miro, *Appl. Catal. B: Env.* 1998, **15**, 5.
99. G. Saracco, C. Badini, N. Russo, V. Specchia, *Appl. Catal. B: Env.* 1999, **21**, 233.
100. P. Ciambelli, V. Palma, P. Russo, S. Vaccaro, *J. Mol. Catal. A: Chem.* 2003, **204–205**, 673.
101. S. Liu, A. Obuchi, J. Uchisawa, T. Nanba, S. Kushiyama, *Appl. Catal. B: Env.* 2002, **37**, 309.

102. B.A.A.L. van Setten, C.G.M. Spitters, J. Bremmer, A.M.M. Mulders, M. Makkee, J.A. Moulijn, *Appl. Catal. B: Env.* 2003, **42**, 337.
103. B. Dernaika, D. Uner. *Appl. Catal. B: Env.* 2003, **40**, 219.
104. B.J. Cooper, J.E. Tos, *SAE Paper 890404*, 1989.
105. P. Hawker, N. Myers, G. Hüthwohl, H.Th. Vogel, B. Bates, L. Magnusson, P. Bronnenberg, *SAE Paper 970182*, 1997.
106. J. Oi-Uchisawa, A. Obuchi, R. Enomoto, J. Xu, T. Nanba, S. Liu, S. Kushiyama, *Appl. Catal. B: Env.* 2001, **32**, 257.
107. A. Setiabudi, M. Makkee, J.A. Moulijn, *Appl. Catal. B: Env.* 2003, **42**, 35.
108. J. Oi-Uchisawa, S. Wang, T. Nanba, A. Ohi, A. Obuchi, *Appl. Catal. B: Env.* 2003, **44**, 207.
109. I. Atribak, A. Bueno-López, A. García-García, *J. Catal.* 2008, **259**, 123.
110. F.E. López-Suárez, A. Bueno-López, M.J. Illán-Gómez, A. Adamski, B. Ura, J. Trawczynski, *Env. Sci. Technol.* 2008, **42**, 7670.
111. M. Iwamoto, *Stud. Surf. Sci. Catal.* 2000, **130**, 23 and references therein.
112. R. Burch, J.P. Breen, F.C. Meunier, *Appl. Catal. B: Env.* 2002, **39**, 283 and references therein.
113. Y. Traa, B. Burger, J. Weitkamp, *Microp. Mesop. Mater.* 1999, **30**, 3.
114. R. Burch, P.J. Millington, *Catal. Today* 1996, **29**, 37.
115. J. Pérez-Ramírez, J.M. García-Cortés, F. Kapteijn, G. Mul, J.A. Moulijn, C. Salinas-Martínez de Lecea, *Appl. Catal. B: Env.* 2001, **29**, 285.
116. M. Nawdali, E. Iojoiu, P. Gélin, H. Praliaud, M. Primet, *Appl. Catal. A: Gen.* 2001, **220**, 129.
117. C. Wögerbauer, M. Maciejewski, A. Baiker, U. Göbel, *J. Catal.* 2001, **201**, 113.
118. J. Pérez-Ramírez, J.M. García-Cortés, M.J. Illán-Gómez, F. Kapteijn, J.A. Moulijn, C. Salinas-Martínez de Lecea, *React. Kinet. Catal. Lett.* 2000, **69**, 385.
119. P. Denton, A. Giroir-Fendler, H. Praliaud, M. Primet, *J. Catal.* 2000, **189**, 410.
120. R. Burch, E. Halpin, J.A. Sullivan, *Appl. Catal. B: Env.* 1998, **17**, 115.
121. M. Inaba, Y. Kintaichi, H. Hamada, *Catal. Lett.* 1996, **36**, 223.
122. R. Burch, P. Fornasiero, B.W.L. Southward, *J. Catal.* 1999, **182**, 234.
123. J.M. García-Cortés, M.J. Illán-Gómez, A. Linares Solano, C. Salinas-Martínez de Lecea, *Appl. Catal. B: Env.* 2000, **25**, 39.

124. P. Vernoux, A.-Y. Leinekugel-Le-Cocq, F. Gaillard, *J. Catal.* 2003, **219**, 247.
125. R. Burch, T.C. Watling, *Appl. Catal. B: Env.* 1997, **11**, 207.
126. R. Burch, D. Otteri, *Appl. Catal. B: Env.* 1996, **9**, L19.
127. R. Burch, P. Fornasiero, B.W.L. Southward, *Chem. Commun.* 1998, **5**, 625.
128. M. Sasaki, H. Hamada, Y. Kintaichi, T. Ito, *Catal. Lett.* 1992, **15**, 297.
129. H. Hamada, *Catal. Today*, 1994, **22**, 21.
130. R. Burch, T.C. Watling, *Catal. Lett.* 1997, **43**, 19.
131. R. Burch, T.C. Watling, *Appl. Catal. B: Env.* 1998, **17**, 131.
132. F. Jayat, C. Lembacher, U. Schubert, J.A. Martens, *Appl. Catal. B: Env.* 1999, **21**, 221.
133. R. Burch, P.J. Millington, A.P. Walker, *Appl. Catal. B: Env.* 1994, **4**, 65.
134. M. Iwamoto, S. Yokoo, K. Saaki, S. Kagawa, *J. Chem. Soc. Faraday Trans. I* 1981, **77**, 1629.
135. I. Asensio, F. Dorado, J.L. Valverde, A. De Lucas, P. Sánchez, *Stud. Surf. Sci. Catal.* 2002, **142**, 731.
136. H.-Y. Chen, T. Voskoboinikov, W.H. Sachtler, *J. Catal.* 1998, **180**, 171.
137. T. Maunula, J. Ahola, H. Hamada, *Appl. Catal. B: Env.* 2006, **64**, 13.
138. G.A. Konin, A.N. Ilichev, V.A. Matyshak, T.I. Khomenko, V.N. Korchak, V.A. Sadykov, V.P. Doronin, R.V. Bunina, G.M. Alikina, T.G. Kuznetsova, E.A. Paukshtis, V.B. Fenelonov, V.I. Zaikovskii, A.S. Ivanova, S.A. Beloshapkin, A.Y. Rozovskii, V.F. Tretyakov, J.R.H. Ross, J.P. Breen, *Top. Catal.* 2001, **16/17**, 193.
139. A. Kubacka, J. Janas, B. Sulikowski, *Appl. Catal. B: Env.* 2006, **69**, 43.
140. Y. Shi, Q. Su, J. Chen, J. Wei, J. Yang, H. Pan, *Environ. Eng. Sc.* 2009, **26**, 1107.
141. H. He, X. Zhang, Q. Wu, C. Zhang, Y. Yu, *Catal. Surv. Asia* 2008, **12**, 38.
142. A. Iglesias-Juez, A.B. Hungría, A. Martínez-Arias, A. Fuerte, M. Fernández-García, J.A. Anderson, J.C. Conesa, J. Soria, *J. Catal.* 2003, **217**, 310.
143. K. Eranen, L-E. Lindfors, F. Klingstedt, D.Y. Murzin, *J. Catal.* 2003. **219**, 25.
144. G.E. Marnellos, E.A. Efthimiadis, I.A. Vasalos, *Appl. Catal. B: Env.* 2004, **48**, 1.

145. J. Li, J. Hao, L. Fu, T. Zhu, Z. Liu, X. Cui, *Reac. Knet. Catal. Lett.* 2003, **80**, 75.
146. Z. Liu, J. Hao, L. Fu, T. Shu, J. Li, X. Cui, *Appl. Catal. B: Env.* 2004, **48**, 37.
147. G. Jong, J. Li, D. Yang, J. Hao, *Appl. Catal. B: Env.* 2009, **91**, 123.
148. A. Kubacka, J. Janas, E. Wloch, B. Sulikowski, *Catal. Today* 2005, **6**, 1137.
149. K. Shimizu, A. Satsuma, T. Hattori, *Appl. Catal. B: Env.* 2000, **25**, 239.
150. A. Martínez-Arias, M. Fernández-García, A. Iglesias-Juez, A.B. Hungría, J.A. Anderson, J.C. Conesa, J. Soria, *Appl. Catal. B: Env.* 2000, **28**, 29.
151. T.N. Angelidis, N. Kruse, *Appl. Catal. B: Env.* 2001, **34**, 201.
152. X. Shi, Y. Yu, H. He, S. Shuai, H. Dong, R. Li, *J. Environ. Sci.* 2008, **20**, 177.
153. A. Ueda, M. Haruta, *Appl. Catal. B: Env.* 1998, **18**, 115.
154. R. Burch, E. Halpin, J.A. Sullivan, *Appl. Catal. B: Env.* 1998, **17**, 115.
155. F.C. Meunier, V. Zuzaniuk, J.P. Been, M. Olsson, J.R.H. Ross, *Catal. Today* 2000, **59**, 287.
156. I.H. Son, M.C. Kim, H.L. Koh, K.-L. Kim, *Catal. Lett.* 2001, **75**, 191.
157. X. She, M. Flytzani-Stephanopoulos, C. Wang, Y. Wang, C.H.F. Peden, *Appl. Catal. B: Env.* 2009, **88**, 98.
158. J. Li, Y. Zhu, R. Ke, J. Hao, *Appl. Catal. B: Env.* 2008, **80**, 202.
159. N. Jagtap, S.B. Umbakar, P. Miquel, P. Granger, M.K. Dongre, *Appl. Catal. B: Env.* 2009, **90**, 416.
160. R. Burch, J.P. Green, C.J. Hill, B. Krutzsch, B. Konrad, E. Jobson, L. Cider, K. Eranen, F. Klingsterd, L.-E. Lindfors, *Top. Catal.* 2004, **30–31**, 19.
161. V. Houel, P. Millington, R. Rajaram, A. Tsolakis, *Appl. Catal. B: Env.* 2007, **77**, 29.
162. J.P. Breen, R. Burch, C.J. Hill, *Catal. Today* 2009, **145**, 34.
163. R. da Silva, R. Cataluña, A. Martínez-Arias, *Catal. Today* 2009, **143**, 242.
164. K.A. Bethke, H.H. Kung, *J. Catal.* 1997, **172**, 93.
165. K. Shimizu, J. Shibata, H. Hyoshida, A. Satsuma, T. Hattori, *Appl. Catal. B: Env.* 2001, **30**, 151.
166. N. Bogdanchikova, F.C. Meunier, M. Avalos-Borja, J.P. Green, A. Petryakov, *Appl. Catal. B: Env.* 2002, **36**, 287.
167. A. Iglesias-Juez, M. Fernández-García, A. Martínez-Arias, Z. Schay, Zs. Koppány, A.B. Hungría, A. Fuerte, J.A. Anderson, J.C. Conesa, J. Soria, *Top. Catal.* 2004, **30-31**, 65.

168. K. Shimizu, H. Kawabata, A. Satsuma, T. Hattori, *J. Phys. Chem. B* 2000, **104**, 2885.
169. K. Hadjiivanov, *Catal. Rev.* 2000, **42**, 71.
170. N.W. Cant, A.D. Cowan, *Catal. Today* 1997, **35**, 89.
171. J.-H. Lee, A. Yezerets, M.C. Kung, H.H. Kung, *Chem. Comm.* 2001, **15**, 1404.
172. T. Maunula, Y. Kintaichi, M. Haneda, H. Hamada, *Catal. Lett.* 1999, **61**, 121.
173. A.Y. Stakheev, M. Thorhauge, P. Gabrielsson, N.N. Tolkachev, G.N. Baeva, G.O. Bragina, in *Preprints of the CAPoC6 Congress, Vol. 2.*, Eds.: N. Kruse, A. Frennet, J.-M. Bastin, T. Visart de Bocarmé, ULB, Brussels, 2003, 5.
174. A volume dedicated to the use of non-thermal plasmas in catalytic processes, including those of relevance to this section can be found in *Catal. Today* Vol. 89, Issues 1–2, 2004.
175. T. Nakatsuji, R. Yasukawa, K. Tabata, K. Ueda, M. Niwa, *Appl. Catal. B: Env.* 1998, **17**, 333.
176. C.U. Ingemar Odenbrand, J. Blanco, P. Avila, C. Knapp, *Appl. Catal. B: Env.* 1999, **23**, 37.
177. A. Obuchi, I. Kaneko, J. Uchisawa, A. Ohi, A. Ogata, G.R. Bamwenda, S. Kushiyama, *Appl. Catal. B: Env.* 1998, **19**, 127.
178. T. Johnson, *Plat. Met. Rev.* 2008, **52**, 23.
179. B. Amon, S. Fischer, L. Hoffmann, J. Zürbig, *Top. Catal.* 2001, **16/17**, 187.
180. M. Koebel, M. Elsener, M. Kleemann, *Catal. Today* 2000, **59**, 335.
181. P.L.T. Gabrielsson, *Top. Catal.* 2004, **28**, 177.
182. A. Grossale, I. Nova, E. Tronconi, D. Chatterjee, M. Weibel, *Top. Catal.* 2009, **52**, 1837.
183. P. Forzatti, L. Lietti, I. Nova, E. Tronconi, *Catal. Today* 2010, **151**, 202.
184. M. Weibel, N. Waldbüber, R. Wunsch, D. Chatterjee, B. Bandl-Konrad, B. Krutzsch, *Top. Catal.* 2009, **52**, 1702.
185. A. Lindholm, H. Sjövall, L. Olsson, *Appl. Catal. B: Env.* **98**, 112.
186. S. Roy, M.S. Hegde, G. Madras, *Appl. Ener.* 2009, **86**, 2283.
187. S. Soyer, A. Uzun, S. Senkan, I. Onal, *Catal. Today* 2006, **118**, 268.
188. Z. Liu, P. Millington, J.E. Ballie, R. Rajaram, J.A. Anderson, *Micropor. Mesopor. Mat.* 2007, **104**, 159.

189. M. Brandhorst, J. Zajac, D.J. Jones, J. Roziere, M. Womes, A. Jiménez-López, E. Rodríguez-Castellón, *Appl. Catal. B: Env.* 2005, **55**, 267.
190. N. Takahashi, H. Shinjoh, T. Iijima, T. Suzuki, K. Yamazaki, K. Yokota, H. Suzuki, N. Miyoshi, S. Matsumoto, T. Tanizawa, S. Tanaka, T. Tateishi, K. Kashara, *Catal. Today* 1996, **27**, 63.
191. S. Matsumoto, *Catal. Surveys, Jpn.* 1997, **1**, 111.
192. E. Fridell, M. Skogludh, B. Westerberg, S. Johansson, G. Smedler, *J. Catal.* 1999, **183,** 196.
193. J.M. Coronado, J.A. Anderson, *J. Molec. Catal.* 1999, **138,** 83.
194. W.S. Epling, L.E. Campbell, A. Yezerets, N.W. Currier, J.E. Parks, *Catal. Rev. Sci. Eng.* 2004, **46**, 163.
195. S. Roy, A. Baiker, *Chem. Rev.* 2009, **109**, 4054.
196. S. Salasc, M. Skogludh, E. Fridell, *Appl. Catal.* 2002, **36**, 145.
197. S. Roy, M.S. Hegde, *Catal. Commun.* 2008, **9**, 811.
198. P. Bera, K.C. Patil, V. Jayaram, G.N. Subbanna, M.S. Hedge, *J. Catal.* 2000, **196**, 293.
199. A. Amberntsson, E. Fridell, M. Skogludh, *Appl. Catal.* 2003, **46**, 429.
200. T. Lesage, C. Verrier, P. Bazin, J. Saussey, M. Daturi, *Phys. Chem. Chem. Phys.* 2003, **5**, 4435.
201. S. Balcon, C. Potvin, L. Salin, J.F. Tempère, G. Djéga-Mariadassou, *Catal. Letts.* 1999, **60**, 39.
202. H.Y. Huang, R.Q. Long, R.T. Yang, *Appl. Catal. B: Env.* 2001, **33**, 127.
203. L. Limousy, H. Mahzoul, J.F. Brilhac, F. Garin, G. Maire, P. Gilot, *Appl. Catal. B: Env.* 2003, **45**, 169.
204. N.W. Cant, M.J. Patterson, *Catal. Today* 2002, **73**, 271.
205. J. Despres, M. Koebel, O. Kröcher, M. Elsener, A. Wokaun, *Appl. Catal.* 2003, **43**, 389.
206. N.W. Cant, M.J. Patterson, *Catal. Letts.* 2003, **85**, 153.
207. F. Laurent, C.J. Pope, H. Mahzoul, L. Delfosse, P. Gilot, *Chem. Eng. Sci.* 2003, **58**, 1973.
208. F. Prinetto, G. Ghiooti, I. Nova, L. Castoldi, L. Lietti, E. Tronconi, P. Forzatti, *Phys. Chem. Chem. Phys.* 2003, **5**, 4428.
209. J.A. Anderson, B. Bachiller-Baeza, M. Fernández-García, *Phys. Chem. Chem. Phys.* 2003, **5**, 4418.
210. Y. Saito, K. Shimizu, T. Nobukawa, A. Satsuma, *Top. Catal.* 2010, **53**, 584.

211. Z. Liu, W.S. Epling, J.A. Anderson, *J. Phys Chem.* 2010, **115**, 952.
212. R.D. Clayton, M.P. Harold, V. Balakotaiah, C.Z. Wan, *Appl. Catal. B: Env.* 2009, **90** 662.
213. S.S. Chaugule, A. Yezerts, N.W. Currier, F.H. Ribeiro, W.N. Delgass, *Catal. Today* 2010, **151**, 291.
214. J.H. Lee, H.H. Kung, *Catal. Letts.* 1998, **51**, 4.
215. P.T. Fanson, M.R. Horton, W.N. Delgass, J. Lauterbach, *Appl. Catal. B: Env.* 2003, **46,** 393.
216. Ch. Sedlmair, K. Seshan, A. Jentys, J.A. Lercher, *J. Catal.* 2003, **214**, 308.
217. L. Olsson, E. Fridell, *J. Catal.* 2002, **210**, 340.
218. D.H. Kim, Y.-H. Chin, G.G. Muntean, A. Yezeretz, N.W. Currier, W.S. Epling, H.-Y. Chen, H. Hess, C.H.F. Peden, *Ind. Eng. Chem. Res.* 2006, **45,** 8815.
219. S. Salacs, M. Skoglundh, E. Fridell, *Appl. Catal. B: Env.* 2002, **36**, 145.
220. H.Y. Huang, R.Q. Long, R.T. Yang, *Energy Fuels* 2001, **15**, 205.
221. J.A. Anderson, M. Fernández-García, *I. Chem. Eng.* 2000, **78A**, 935.
222. F. Rodrigues, L. Juste, C. Potvin, J.F. Tempère, G. Blanchard, G. Djéga-Mariadassou, *Catal. Letts.* 2001, **72**, 59.
223. J.A. Anderson, D.J. Rosenberg, A.J. Paterson, *Stud. Surf. Sci and Catal.* 2001, **138**, 429.
224. Z. Liu, J.A. Anderson, *J. Catal.* 2004, **224**, 18.
225. A. Sepulveda-Escribano, M. Primet, H. Prauliaud, *Appl. Catal. A: Gen.* 1994, **108**, 221.
226. D. James, E. Fourré, M. Ishii, M. Bowker, *Appl. Catal. B: Env.* 2003, **45**, 147.
227. C. Hess, J.H. Lunsford, *J. Phys. Chem.* 2002, **106**, 6358.
228. L. Olsson, E. Fridell, M. Skogludh, B. Andersson, *Catal. Today*, 2002, **73**, 263.
229. J.A. Anderson, B. Bachiller-Baeza, M. Fernández-García, in *Catalysis in Application*, Eds.: S.D. Jackson, J.S.J. Hargreaves, D. Lennon, RSC, London, 2003, 296.
230. S. Matsumoto, Y. Ikeda, H. Suzuki, M. Ogai, N. Miyoshi, *Appl. Catal. B: Env.* 2000, **25**, 115.
231. I. Nova, L. Lietti, P. Forzatti, F. Prinetto, G. Ghiotti, *Catal. Today* 2010, **151**, 330.
232. R. Burch, T.L. Watling, *Stud. Surf. Sci. Catal.* 1998, **116**, 199.

233. I. Nova, L. Lietti, L. Castoldi, E. Tronconi, P. Forzatti, *J. Catal.* 2006, **239**, 244.
234. M. Al-Harbi, W.S. Epling, *Catal. Lett.* 2009, **130**, 121.
235. S. Pouston, R.R. Rajaram, *Catal. Today* 2003, **81**, 603.
236. Ch. Sedlmair, K. Seshan, A. Jentys, J.A. Lercher, *Catal. Today* 2002, **75**, 413.
237. H. Mahzoul, L. Limousy, J.F. Brilhac, P. Gilot, *J. Anal. Appl. Pyrol.* 2000, **56**, 179.
238. K. Yamazaki, T. Suzuki, N. Takahshi, K. Yokota, M. Sugiura, *Appl. Catal. B: Env.* 2001, **30**, 459.
239. Z. Liu, J.A. Anderson, *J. Catal.* 2004, **228**, 243.
240. D.H. Kim, J.H. Kwak, J. Szanyi, S.J. Cho, C.H.F. Peden, *J. Phys. Chem. C* 2008, **112**, 2981.
241. J. Dawody, M. Skoglundh, E. Fridell, *J. Mol. Catal. A: Chem.* 2004, **209**, 215.
242. C. Courson, A. Khalfi, H. Mahzoul, S. Hodjati, N. Moral, A. Kiennemann, P. Gilot, *Catal. Commun.* 2002, **3**, 471.

INDEX